

Nicolae Herisanu
Vasile Marinca *Editors*

Acoustics and Vibration of Mechanical Structures—AVMS 2019

Proceedings of the 15th AVMS,
Timisoara, Romania, May 30–31, 2019

Springer Proceedings in Physics

Volume 251

Indexed by Scopus

The series Springer Proceedings in Physics, founded in 1984, is devoted to timely reports of state-of-the-art developments in physics and related sciences. Typically based on material presented at conferences, workshops and similar scientific meetings, volumes published in this series will constitute a comprehensive up-to-date source of reference on a field or subfield of relevance in contemporary physics. Proposals must include the following:

- name, place and date of the scientific meeting
- a link to the committees (local organization, international advisors etc.)
- scientific description of the meeting
- list of invited/plenary speakers
- an estimate of the planned proceedings book parameters (number of pages/articles, requested number of bulk copies, submission deadline).

More information about this series at <http://www.springer.com/series/361>

Nicolae Herisanu · Vasile Marinca
Editors

Acoustics and Vibration of Mechanical Structures— AVMS 2019

Proceedings of the 15th AVMS, Timisoara,
Romania, May 30–31, 2019

 Springer

Editors

Nicolae Herisanu
Department of Mechanics
and Strength of Materials
University Politehnica Timisoara
Timisoara, Romania

Vasile Marinca
Department of Mechanics
and Strength of Materials
University Politehnica Timisoara
Timisoara, Romania

ISSN 0930-8989

ISSN 1867-4941 (electronic)

Springer Proceedings in Physics

ISBN 978-3-030-54135-4

ISBN 978-3-030-54136-1 (eBook)

<https://doi.org/10.1007/978-3-030-54136-1>

© Springer Nature Switzerland AG 2021

This work is subject to copyright. All rights are reserved by the Publisher, whether the whole or part of the material is concerned, specifically the rights of translation, reprinting, reuse of illustrations, recitation, broadcasting, reproduction on microfilms or in any other physical way, and transmission or information storage and retrieval, electronic adaptation, computer software, or by similar or dissimilar methodology now known or hereafter developed.

The use of general descriptive names, registered names, trademarks, service marks, etc. in this publication does not imply, even in the absence of a specific statement, that such names are exempt from the relevant protective laws and regulations and therefore free for general use.

The publisher, the authors and the editors are safe to assume that the advice and information in this book are believed to be true and accurate at the date of publication. Neither the publisher nor the authors or the editors give a warranty, expressed or implied, with respect to the material contained herein or for any errors or omissions that may have been made. The publisher remains neutral with regard to jurisdictional claims in published maps and institutional affiliations.

This Springer imprint is published by the registered company Springer Nature Switzerland AG
The registered company address is: Gewerbestrasse 11, 6330 Cham, Switzerland

Organizing Committee

Organized By

University Politehnica Timisoara, Acoustics and Vibration Laboratory
University of Nis, Noise and Vibration Laboratory
Romanian Academy, Center for Fundamental and Advanced Technical Research
Romanian Acoustical Society

Organizing Committee

Nicolae Herisanu, Chairman, University Politehnica Timisoara, Romania
Momir Prašević, Co-chairman, University of Nis, Serbia

Members

Viorel-Aurel Șerban, Rector—University Politehnica Timisoara, Romania
Vasile Marinca, University Politehnica Timisoara, Romania
Darko Mihajlov, University of Nis, Serbia
Ramona Nagy, University Politehnica Timisoara, Romania
Károly Menyhardt, University Politehnica Timisoara, Romania
Cosmina Vișaru, University Politehnica Timisoara, Romania
Marko Ličanin, University of Nis, Serbia

International Scientific Committee

Jan Awrejcewicz, Lodz University of Technology, Poland
Vasile Bacria, University Politehnica Timisoara, Romania
Malvina Baica, University of Wisconsin, USA
Liviu Bereteu, University Politehnica Timisoara, Romania
Polidor Bratu, ICECON Bucharest, Romania
Florin Breaban, University d'Artois, France
Veturia Chiroiu, Institute of Solid Mechanics, Bucharest, Romania
Liviija Cveticanin, University of Novi Sad, Serbia
Dragan Cvetković, University of Nis, Serbia
Gilbert-Rainer Gillich, "E.Murgu" University of Resita, Romania
Nicolae Herişanu, University Politehnica Timisoara, Romania
Metin O. Kaya, Istanbul Technical University, Turkey
Ivana Kovacic, University of Novi Sad, Serbia
J. A. Tenreiro Machado, Polytechnic Institute of Porto, Portugal
Vasile Marinca, Romanian Academy, Romania
Nuno Maia, University of Lisbon, Portugal
Emil Manóach, Bulgarian Academy of Sciences, Bulgaria
Dan B. Marghitu, Auburn University, USA
Darko Mihajlov, University of Nis, Serbia
Sotirios Natsiavas, Aristotle University of Thessaloniki, Greece
Kale Oyedeji, Morehouse College, Atlanta, GA, USA
Momir Prašćević, University of Nis, Serbia
M. Mehdi Rashidi, Tongji University, Shanghai, China
Mohsen Razzaghi, Mississippi State University, USA
Zlatan Šoškić, University of Kragujevac, Serbia
Sorin Vlase, "Transilvania" University Braşov, Romania
Jerzy Warminski, Lublin University of Technology, Poland

Preface

The Proceedings of the XV-th International Conference “Acoustics and Vibration of Mechanical Structures”—AVMS-2019 contains selected papers contributed to the Conference held during May 30–31, 2019 in Timișoara (Romania).

This book is organized on five chapters covering a broad range of topics related to acoustics and vibration problems, such as:

- Noise and vibration control;
- Noise and vibration generation and propagation;
- Effects of noise and vibration;
- Condition monitoring and vibration testing;
- Nonlinear acoustics and vibration;
- Analytical, numerical and experimental techniques for noise and vibration;
- Modeling, prediction and simulations of noise and vibration;
- Environmental and occupational noise and vibration;
- Noise and vibration attenuators;
- Biomechanics and bioacoustics.

There are presented some analytical, numerical and experimental techniques applicable to analyze linear and nonlinear noise and vibration problems.

Each paper went through a rigorous review process performed by the members of the International Scientific Committee and specialized external reviewers, and the accepted papers are reported in this volume.

We would like to express our sincere appreciation to keynote speakers and all contributors of the presented papers for sharing their knowledge and experiences with all the participants. We are also expressing our sincere thanks to the members of the International Scientific Committee for spending their valuable time to review the papers and also to the members of the Organizing Committee for ensuring the success of this Conference which would not have been possible without their efforts.

Finally, special thanks are given to Springer for producing this volume.

Timisoara, Romania

Nicolae Herisanu
Vasile Marinca

Contents

Analytical Approaches to Vibration Problems	
Modelling of Frictional Contacts in 3D Dynamics of a Rigid Body	3
Jan Awrejcewicz and Grzegorz Kudra	
Dynamics of the Impact with Benson Friction Model	13
Dan B. Marghitu and Dorian Cojocaru	
Vibrations of the Mass Variable Systems	25
Livija Cveticanin and Dragan Cveticanin	
An Approximate Analytical Solution of Transversal Oscillations with Quintic Nonlinearities	41
Nicolae Herisanu, Vasile Marinca, and Cristina Chilibaru-Opritescu	
Optimal Auxiliary Functions Method for Nonlinear Vibration of Doubly Clamped Nanobeam Incorporating the Casimir Force	51
Vasile Marinca and Nicolae Herisanu	
Study of the Vibrations of a System Consisting in Cantilever Beams	59
Maria-Luiza Beşliu-Gherghescu, Nicolae-Doru Stănescu, Nicolae Pandrea, and Dinel Popa	
Vibrations with Collisions of a Mechanical System with Elastic Elements	67
Ionuţ-Bogdan Dragna, Nicolae Pandrea, Nicolae-Doru Stănescu, and Dinel Popa	
Determination of the Dynamic Reactions for a Variable Compression Ratio Mechanism	75
Bogdan Mănescu, Nicolae-Doru Stănescu, Dinel Popa, and Nicolae Pandrea	

Improving the Accuracy of Estimates of the Frequencies Based on a Pseudo-sinc Function	85
Andrea Amalia Minda, Gilbert-Rainer Gillich, Ana-Maria Budai, Nicoleta Gillich, and Cristian Paul Chioncel	
Gears Dynamic Response to Vibrations	91
Valeriu Ionica, Ionut Geonea, Cosmin Miritoiu, and Alexandru Bolcu	
Dynamical Response of a Beam in a Centrifugal Field Using the Finite Element Method	101
Eliza Chircan, Maria Luminița Scutaru, and Ana Toderiță	
Environmental and Occupational Noise	
Development of Methodologies and Means for Noise Protection of Urban Areas—Project Results	117
Zlatan Šoškić, Milan Kolarević, Branko Radičević, Momir Praščević, and Vladan Grković	
Acoustic Treatment Solution of the Technical Room in Water Pumping Station—Case Study	131
Darko Mihajlov, Momir Praščević, Marko Ličanin, and Aleksandar Gajicki	
Solution of the Environmental Noise Problem Generated by HVAC Systems—Case Study	145
Marko Ličanin, Darko Mihajlov, Momir Praščević, Ana Đorđević, Miomir Raos, and Nenad Živković	
Coefficient of Sound Absorption of Polyamide PA12 Samples Manufactured by Selective Laser Sintering	155
Nebojša Bogojević, Branko Radičević, Aleksandar Vranić, and Snežana Ćirić Kostić	
Online Database of Industrial Noise Sources	165
Tanja Miodragović, Mladen Rasinac, Jelena Tomić, and Branko Radičević	
Studies on the Experimental Validation of the Theoretical Static Noise Field in the Neighbourhood of Agricultural Tractors	173
Petru Cardei, Cristian Sorica, Valentin Vladut, and Mihai Matache	
An Analysis of How Physical and Social Factors Influence the Efficiency of Crew Members of a Ship Running on the Danube	185
Laurentiu Picu, Eugen Rusu, and Mihaela Picu	
Mitigating Noise Pollution Level When Loading Useful Mineral Substances in CFR Wagons in Order to Increase Acoustic Comfort in Neighbouring Areas	205
Sorin Simion, Daniel Pupăzan, Angelica Călămar, Cristian Nicolescu, and Izabella Kovacs	

Research on Speech Changes Due to Environmental Noise 217
 Diana Cotoros, Ionel Șerban, Corneliu Drugă, and Anca Stanciu

Biomechanics and Bioacoustics

Angular Momentum About the Total Body Center of Mass Computed at Different Speeds 227
 Dan Ioan Stoia, Cosmina Vigaru, Andreea Nicoara, and Nicolae Herisanu

Analysis of Oscillatory Eye Movements as a Nystagmus, Manifested in the Visual System 235
 Mihaela Ioana Baritz and Alexandra Maria Lazar

Visual Aids Based on Ultrasonic Sensors to Increase Mobility of Patient with Blindness or Low Vision 243
 Mihaela Ioana Baritz and Mirela Gabriela Apostoaie

Numerical Investigation of an Idealized Overlapping Coronary Stents Configuration 251
 Alin Totorean, Iuliana-Claudia Totorean, Sandor Bernad, and Dan Gaita

Biomechanical Evaluation of Medical Rehabilitation for a Patient with Ankle Fracture 259
 Madalina Lupsa, Alin Totorean, Dan Ioan Stoia, and Alina Totorean

New Medical Rehabilitation System 267
 Cristian-Gabriel Alionte, Daniel-Constantin Comeagă, and Liviu-Marian Ungureanu

Designing and Creating a Smart Audiometer Using an Arduino Platform 277
 Corneliu Drugă, Ionel Șerban, Antonio Serbănescu, and Diana Cotoros

Influence of Whole Body Vibration Machines, for Sport Exercises, on the Human Balance and Stability 289
 Corneliu Drugă, Ionel Șerban, Diana Cotoros, and Angela Repanovici

Human Factor Balance Under the Influence of Variable Sound Frequency and Orientation 297
 Diana Cotoros, Ionel Șerban, Corneliu Drugă, and Anca Stanciu

The Effect of Vibration Exposure on Posterior Lower Limbs Skin Temperature During the Warm-up Process of Athletes 305
 Daniel Vlădaia, Adela Neamțu Popescu, Steliana Stanciu, Dorin Simoiu, and Liviu Bereteu

Modeling and Simulation of Mechanical Behavior of Spinal Ligaments with Applications in Traction Therapy	315
Adela Neamțu Popescu, Lucian Rusu, Ion Crăștiu, Alexandru Pavăl, and Liviu Bereteu	
Parameter Optimization for Biocompatible Polyamide Used in Selective Laser Sintering (SLS)	323
Dan Ioan Stoia, Liviu Marsavina, Alexandru Cosa, and Andreea Nicoara	
Vibration Problems in Industrial Processes	
Experimental Analysis of Noise and Chatter Detection in Milling Depending on the Cutting Parameters	333
Mladen Rasinac, Aleksandra Petrović, Branko Radičević, Vladan Grković, and Marina Ivanović	
Modal Analysis of a Gearbox Housing in Order to Avoid Resonance Frequencies	343
Attila Geroacs, Zoltan Korca, Vasile Cojocar, and Calin-Octavian Miclosina	
Dependence Between the Percussion Centre and the Uniformity of the Rotor Movement	351
Mircea Fenchea	
Comparative Analysis of the Voigt–Kelvin and Maxwell Models in the Compaction by Vibration Process	359
Cornelia-Florentina Dobrescu	
Parametric Analysis of Dynamic Insulation in the Action of the Seismic Movements of the Base-Insulated Buildings	367
Polidor Bratu, Cristina Oprețescu, Amalia Țârdea, Ovidiu Voicu, and Adrian Ciocodeiu	
Vibration of Fixing Device of the Reaction Chamber for Gamma-Ray Beam in the Project ELIADE	375
Sorin Vlase, Călin Itu, Paul Nicolae Borza, Gabriel Suliman, Cristian Petcu, and Maria Luminița Scutaru	
ANN Samples Generation Using 2D Dynamic FEM for Predicting Machining Vibrations	383
Andrei-Ionuț Berariu, Iulia-Maria Prodan, Cosmin-Ioan Niță, and Tudor Deaconescu	
Improved Model of a Vibrating Sieve	395
Maria Dragomir, Alina Ovanisof, and Roxana Alexandra Petre	
Vibration Analysis of High-Pressure Pneumatic Compressor	403
Ramona Nagy, Remus Stefan Maruta, and Karoly Menyhardt	

Structural Vibration

Vibroacoustic Diagnostics Based on the Experimental and Numerical Approach	415
Roman Zajac, Václav Otipka, Aleš Prokop, and Kamil Řehák	
Gear Shift Investigation Using Virtual Prototype	425
Aleš Prokop, Kamil Rehak, Roman Zajac, and Václav Otipka	
Numerical Dynamic Analysis of Gearbox Behaviour	433
Václav Otipka, Roman Zajac, Kamil Rehak, and Aleš Prokop	
Acoustic and Vibration Response Analysis of Heavy-Duty Gearbox ...	443
Kamil Rehak, Aleš Prokop, Roman Zajac, and Václav Otipka	
Application of Friction Pendulum Bearings in Multistory Buildings ...	453
Irena Gołębiowska and Maciej Dutkiewicz	
Spectral Element Analysis of Non-stationary Wind Acting on Overhead Transmission Line	463
Maciej Dutkiewicz and Marcela R. Machado	
Composed Isolation System Concept for Vibration Effects Mitigation on Bridge Structures	473
Fanel Scheaua	
Research of Acoustic Metamaterials at the University of Szeged, Faculty of Engineering	485
Péter Szuchy	
Crack Assessment Based on the Use of Severity-Adjusted Modal Curvatures of the Healthy Beam	499
Gilbert-Rainer Gillich, Cristian Tufisi, Magd Abdel Wahab, and Codruta Oana Hamat	
Influence of Eccentricity of Drive Mechanisms and Sieve Vibrations on the Quality of Seed Separation	505
Constantin Popa, Adrian Costache, Alina Ovanisof, and Roxana Alexandra Petre	
About the Forces and Moments that Influence the Behavior of a Friction Pendulum	515
Vasile Iancu and Lenuta Cindea	
The Influence of the Mesh Element Size on Critical Bending Speeds of a Rotor in the Finite Element Analysis	523
Ion Crăștiu, Dorin Simoiu, Calin Gozman-Pop, Paul Druța, and Liviu Bereteu	

Contributors

Magd Abdel Wahab Ghent University, Zwijnaarde, Belgium

Cristian-Gabriel Alionte Mechatronics and Precision Mechanics Department, University Politehnica of Bucharest, Bucharest, Romania

Mirela Gabriela Apostoaie Product Design, Mechatronics and Environment Department, Transilvania University Brasov, Brasov, Romania

Jan Awrejcewicz Lodz University of Technology, Lodz, Poland

Mihaela Ioana Baritz Product Design, Mechatronics and Environment Department, Transilvania University from Brasov, Brasov, Romania

Andrei-Ionuț Berariu Transilvania University of Brasov, Brașov, Romania

Liviu Bereteu Mechanics and Materials Strength Department, Politehnica University of Timișoara, Timișoara, Romania

Sandor Bernad Romanian Academy—Timisoara Branch, Timisoara, Romania

Maria-Luiza Beșliu-Gherghescu University of Pitesti, Pitesti, Romania

Nebojša Bogojević Faculty of Mechanical and Civil Engineering in Kraljevo, University of Kragujevac, Kraljevo, Serbia

Alexandru Bolcu Faculty of Mechanics, University of Craiova, Craiova, Romania

Paul Nicolae Borza Transilvania University of Brasov, Brașov, Romania

Polidor Bratu ICECON SA, Bucharest, Romania;
Faculty of Engineering and Agronomy, “Dunărea de Jos” University of Galați, Brăila, Romania

Ana-Maria Budai Universitatea “Eftimie Murgu” Resita, Resita, Romania

Angelica Călămar INCD INSEMEX Petroșani, Petroșani, Romania

Petru Cardei INMA, Bucharest, Romania

Cristina Chilibaru-Opritescu Politehnica University Timisoara, Timisoara, Romania

Cristian Paul Chioncel Universitatea “Eftimie Murgu” Resita, Resita, Romania

Eliza Chircan Transilvania University, Braşov, Romania

Lenuta Cindea Eftimie Murgu University, Resita, Romania

Adrian Ciocodeiu Institute of Solid Mechanics, Romanian Academy, Bucharest, România

Dorian Cojocaru Department of Mechatronics and Robotics, University of Craiova, Craiova, Romania

Vasile Cojocaru Department of Engineering Sciences, “Eftimie Murgu” University of Resita, Traian Vuia Square, Resita, Romania

Daniel-Constantin Comeagă Mechatronics and Precision Mechanics Department, University Politehnica of Bucharest, Bucharest, Romania

Alexandru Cosa Politehnica University Timisoara, Timisoara, Romania

Adrian Costache University Politehnica of Bucharest, Bucharest, Romania

Diana Cotoros University Transilvania of Brasov, Brasov, Romania

Ion Crâştiiu Mechanics and Materials Strength Department, Politehnica University of Timişoara, Timişoara, Romania

Livija Cveticanin University of Novi Sad, Novi Sad, Serbia;
Obuda University, Budapest, Hungary

Dragan Cveticanin Remming, Novi Sad, Serbia

Tudor Deaconescu Transilvania University of Brasov, Braşov, Romania

Cornelia-Florentina Dobrescu INCĐ URBAN-INCERC, Bucharest, Romania

Ana Đorđević Faculty of Electronic Engineering, Niš, Serbia

Ionuţ-Bogdan Dragna University of Pitesti, Pitesti, Romania

Maria Dragomir University Politehnica of Bucharest, Bucharest, Romania

Corneliu Drugă Transylvania University, Braşov, Romania

Paul Druţa Mechanics and Materials Strength Department, Politehnica University of Timişoara, Timişoara, Romania

Maciej Dutkiewicz Faculty of Civil, Architecture and Environmental Engineering and Architecture, University of Science and Technology in Bydgoszcz, Bydgoszcz, Poland

Mircea Fenchea “Politehnica” University of Timișoara, Timișoara, Romania

Dan Gaita University of Medicine and Pharmacy Victor Babes Timisoara, Timisoara, Romania;

Cardiology Department, Institute for Cardiovascular Diseases, Timisoara, Romania

Aleksandar Gajicki Institute of Transportation CIP, Belgrade, Serbia

Ionut Geonea Faculty of Mechanics, University of Craiova, Craiova, Romania

Attila Gerocs Department of Engineering Sciences, “Eftimie Murgu” University of Resita, Traian Vuia Square, Resita, Romania

Gilbert-Rainer Gillich Universitatea “Eftimie Murgu” Resita, Resita, Romania

Nicoleta Gillich Universitatea “Eftimie Murgu” Resita, Resita, Romania

Irena Gołębiowska Faculty of Civil, Architecture and Environmental Engineering and Architecture, University of Science and Technology in Bydgoszcz, Bydgoszcz, Poland

Calin Gozman-Pop Mechanics and Materials Strength Department, Politehnica University of Timișoara, Timișoara, Romania

Vladan Grković Faculty of Mechanical and Civil Engineering in Kraljevo, University of Kragujevac, Kragujevac, Serbia

Codruta Oana Hamat “Eftimie Murgu” University of Resita, Resita, Romania

Nicolae Herisanu Department of Mechanics and Strength of Materials, Politehnica University Timisoara, Timisoara, Romania;

Centre for Advanced Technical Research-CCTFA, Romanian Academy, Branch of Timisoara, Timisoara, Romania

Vasile Iancu Eftimie Murgu University, Resita, Romania

Valeriu Ionica Faculty of Mechanics, University of Craiova, Craiova, Romania

Călin Itu Transilvania University of Brasov, Brașov, Romania

Marina Ivanović Faculty of Mechanical and Civil Engineering, University of Kragujevac, Kraljevo, Serbia

Milan Kolarević Faculty of Mechanical and Civil Engineering in Kraljevo, University of Kragujevac, Kragujevac, Serbia

Zoltan Korka Department of Engineering Sciences, “Eftimie Murgu” University of Resita, Traian Vuia Square, Resita, Romania

Snežana Ćirić Kostić Faculty of Mechanical and Civil Engineering in Kraljevo, University of Kragujevac, Kraljevo, Serbia

Izabella Kovacs INCD INSEMEX Petroșani, Petroșani, Romania

- Grzegorz Kudra** Lodz University of Technology, Lodz, Poland
- Alexandra Maria Lazar** Product Design, Mechatronics and Environment Department, Transilvania University from Brasov, Brasov, Romania
- Marko Ličanin** Faculty of Occupational Safety, Niš, Serbia
- Madalina Lupsa** Politehnica University of Timisoara Romania, Timisoara, Romania
- Marcela R. Machado** Department of Mechanical Engineering, University of Brasilia, Brasilia, Brazil
- Dan B. Marghitu** Department of Mechanical Engineering, Auburn University, Auburn, AL, USA
- Vasile Marinca** Centre for Advanced Technical Research-CCTFA, Romanian Academy, Branch of Timisoara, Timisoara, Romania
- Liviu Marsavina** Politehnica University Timisoara, Timisoara, Romania
- Remus Stefan Maruta** Politehnica University Timisoara, Timisoara, Romania
- Mihai Matache** INMA, Bucharest, Romania
- Karoly Menyhardt** Politehnica University Timisoara, Timisoara, Romania
- Calin-Octavian Miclosina** Department of Engineering Sciences, “Eftimie Murgu” University of Resita, Traian Vuia Square, Resita, Romania
- Darko Mihajlov** Faculty of Occupational Safety, Niš, Serbia
- Andrea Amalia Minda** Universitatea “Eftimie Murgu” Resita, Resita, Romania
- Tanja Miodragović** Faculty of Mechanical and Civil Engineering, Kraljevo, Serbia
- Cosmin Miritoiu** Faculty of Mechanics, University of Craiova, Craiova, Romania
- Bogdan Mănescu** University of Pitesti, Pitesti, Romania
- Ramona Nagy** Politehnica University Timisoara, Timisoara, Romania
- Adela Neamțu Popescu** Mechanics and Materials Strength Department, Politehnica University of Timișoara, Timișoara, Romania
- Andreea Nicoara** Department of Mechanics and Strength of Materials, Politehnica University Timisoara, Timisoara, Romania
- Cristian Nicolescu** INCD INSEMEX Petroșani, Petroșani, Romania
- Cosmin-Ioan Niță** Transilvania University of Brasov, Brașov, Romania
- Cristina Oprețescu** ICECON SA, Bucharest, Romania

Václav Otipka Faculty of Mechanical Engineering, Brno University of Technology, Brno, Czech Republic

Alina Ovanisof University Politehnica of Bucharest, Bucharest, Romania

Nicolae Pandrea University of Pitesti, Pitesti, Romania

Alexandru Pavăl Mechanics and Materials Strength Department, Politehnica University of Timișoara, Timișoara, Romania

Cristian Petcu Institute of Atomic Physics, Bucharest, Romania

Roxana Alexandra Petre University Politehnica of Bucharest, Bucharest, Romania

Aleksandra Petrović Faculty of Mechanical and Civil Engineering, University of Kragujevac, Kraljevo, Serbia

Laurentiu Picu Dunarea de Jos, Galati University, Galati, Romania

Mihaela Picu Dunarea de Jos, Galati University, Galati, Romania

Constantin Popa University Politehnica of Bucharest, Bucharest, Romania

Dinel Popa University of Pitesti, Pitesti, Romania

Momir Prašćević Faculty of Occupational Safety, University of Niš, Niš, Serbia

Iulia-Maria Prodan Transilvania University of Brasov, Brașov, Romania

Aleš Prokop Faculty of Mechanical Engineering, Brno University of Technology, Brno, Czech Republic

Daniel Pupăzan INCD INSEMEX Petroșani, Petroșani, Romania

Branko Radičević Faculty of Mechanical and Civil Engineering in Kraljevo, University of Kragujevac, Kragujevac, Serbia

Miomir Raos Faculty of Occupational Safety, Niš, Serbia

Mladen Rasinac Faculty of Mechanical and Civil Engineering, University of Kragujevac, Kraljevo, Serbia

Kamil Řehák Faculty of Mechanical Engineering, Brno University of Technology, Brno, Czech Republic

Angela Repanovici Transylvania University, Brașov, Romania

Eugen Rusu Dunarea de Jos, Galati University, Galati, Romania

Lucian Rusu Mechanics and Materials Strength Department, Politehnica University of Timișoara, Timișoara, Romania

Fanel Scheaua “Dunarea de Jos” University of Galati, Engineering and Agronomy Faculty of Braila, MECMET Research Center, Galati, Romania

- Maria Luminița Scutaru** Transilvania University, Brașov, Romania
- Ionel Șerban** Transylvania University, Brașov, Romania
- Antonio Serbănescu** Transylvania University, Brașov, Romania
- Sorin Simion** INCD INSEMEX Petroșani, Petroșani, Romania
- Dorin Simoiu** Mechanics and Materials Strength Department, Politehnica University of Timișoara, Timișoara, Romania
- Cristian Sorica** INMA, Bucharest, Romania
- Zlatan Šoškić** Faculty of Mechanical and Civil Engineering in Kraljevo, University of Kragujevac, Kragujevac, Serbia
- Anca Stanciu** University Transilvania of Brasov, Brasov, Romania
- Steliana Stanciu** Mechanics and Materials Strength Department, Politehnica University of Timișoara, Timișoara, Romania
- Dan Ioan Stoia** Department of Mechanics and Strength of Materials, Politehnica University Timisoara, Timisoara, Romania
- Nicolae-Doru Stănescu** University of Pitesti, Pitesti, Romania
- Gabriel Suliman** Institute of Atomic Physics, Bucharest, Romania
- Péter Szuchy** Faculty of Engineering, University of Szeged, Szeged, Hungary
- Amalia Țârdea** ICECON SA, Bucharest, Romania
- Ana Toderiță** Transilvania University, Brașov, Romania
- Jelena Tomić** Faculty of Mechanical and Civil Engineering, Kraljevo, Serbia
- Alin Totorean** Politehnica University of Timisoara Romania, Timisoara, Romania
- Alina Totorean** University of Medicine and Pharmacy “Victor Babes”, Timisoara, Romania
- Iuliana-Claudia Totorean** University of Medicine and Pharmacy Victor Babes Timisoara, Timisoara, Romania;
Cardiology Department, Institute for Cardiovascular Diseases, Timisoara, Romania
- Cristian Tufisi** “Eftimie Murgu” University of Resita, Resita, Romania
- Liviu-Marian Ungureanu** Theory of Mechanisms and Robots Department, University Politehnica of Bucharest, Bucharest, Romania
- Cosmina Vigaru** Department of Mechanics and Strength of Materials, Politehnica University Timisoara, Timisoara, Romania
- Valentin Vladut** INMA, Bucharest, Romania

Sorin Vlase Transilvania University of Brasov, Braşov, Romania

Daniel Vlădaia Mechanics and Materials Strength Department, Politehnica University of Timișoara, Timișoara, Romania

Ovidiu Voicu Institute of Solid Mechanics, Romanian Academy, Bucharest, România

Aleksandar Vranić Faculty of Mechanical and Civil Engineering in Kraljevo, University of Kragujevac, Kraljevo, Serbia

Roman Zajac Faculty of Mechanical Engineering, Brno University of Technology, Brno, Czech Republic

Nenad Živković Faculty of Occupational Safety, Niš, Serbia

Analytical Approaches to Vibration Problems

Modelling of Frictional Contacts in 3D Dynamics of a Rigid Body



Jan Awrejcewicz  and Grzegorz Kudra 

Abstract There is considered a system of a spatial double pendulum with rigid movable obstacle, consisting of two links connected to each other and suspended on a shaft performing rotational motion about its horizontal axis according to a given function of time (kinematic driving). The links are connected by the use of two universal joints. The second link ends with a ball which can come into contact (impacts and permanent contact) with a planar and rotating obstacle situated below the pendulum. There is presented mathematical model of dynamics based on the Lagrange formulation. In this work, we use and expand our earlier developed models of contact forces (resulting friction force and rolling resistance). The friction models are based on the integral model developed assuming developed sliding on a planar contact area, where at each point, the classical Coulomb's friction law is valid. The integral models are then replaced by special approximations being more suitable for fast numerical simulations. In the present work, we model impacts with non-point frictional contacts assuming Hertzian compliance of the obstacle. The constructed models of 3D dynamics of a rigid body and the planned experimental investigations allow us to perform the tests of importance of the particular individual elements of the models and may lead to general conclusions about modelling and effective computer simulations of mechanical systems with 3D frictional contacts. We report bifurcation dynamics using bifurcation diagrams, Poincaré sections as well as the largest Lyapunov exponent.

1 Introduction

Pendulum-based mechanical systems serve as a paradigmatic model for analysis of many problems in nonlinear dynamics, mechanical engineering, biomechanics, control theory and mechatronics. Among different mechanical systems, one can encounter models based on spherical pendulum [1]. For example, in the work [2], the

J. Awrejcewicz (✉) · G. Kudra
Lodz University of Technology, Stefanowskiego 1/15, 90-924 Lodz, Poland
e-mail: jan.awrejcewicz@p.lodz.pl

© Springer Nature Switzerland AG 2021
N. Herisanu and V. Marinca (eds.), *Acoustics and Vibration of Mechanical Structures—AVMS 2019*, Springer Proceedings in Physics 251,
https://doi.org/10.1007/978-3-030-54136-1_1

authors analysed the problem of control of the spherical pendulum. In the paper [3], there is presented analysis of 3D frictionless double pendulum rotating with constant angular velocity about its vertical axis. Another example of a multi-pendulum system in 3D space is investigated in the work [4]. Since in robotics, many tasks require making and braking contact with different subjects, some group of works concerns the problems of pendulum dynamics with impact and friction phenomena [5, 6].

Real natural and engineering objects with frictional 3D contacts very often cannot be modelled using classical one-dimensional friction model. As examples, one can indicate rolling bearings, billiard ball, Celtic stone or other contact phenomena encountered for example in robotics. Exact numerical modelling and simulation require in general space discretization methods and lead to high computational costs. Looking for simplified but realistic models, Contensou proposed an integral model of resultant friction force assuming fully developed sliding and Coulomb friction law at each element of the contact area [7]. The integral model can be then approximated by the use of special algebraic functions in order to make the simulation faster [8]. Some authors developed approximations of the friction force and moment assuming special contact pressure distributions allowing to model rolling resistance [9, 10]. The approximated models were tested during modelling of the selected mechanical systems: wobblestone, billiard ball and full solid ellipsoid of the revolution [11–13].

In multibody system dynamics, the impact phenomena can be modelled as the so-called hard or soft impacts [14, 15]. However, the impacts are usually modelled as phenomena occurring at a certain point. Even if friction torque is taken into account, the coupling between friction force and moment is neglected.

In this work, we join the friction models developed and presented in the works [10–13] with impact model based on Hertzian stiffness and special model of nonlinear damping. The present work is continuation and extension of the conference papers [16, 17].

2 Mathematical Model

In Fig. 1a, there is presented a physical concept of the investigated double spatial pendulum, where one can observe the fixed frame F , three connected solids (the body 0, the pendulums 1 and 2) and the obstacle 3 in the form of the disc performing rotational motion. The solid 0 performs rotational motion with respect to the fixed frame. The solid 0, pendulum 1 and 2 are connected by the use of two Cardan–Hook joints. There are introduced the following coordinate systems: the fixed (global) reference frame O_1xyz , pendulum 1 fixed reference frame $O_1x_1y_1z_1$ and pendulum 2 fixed coordinate system $O_2x_2y_2z_2$. It is assumed that the origins O_1 and O_2 of the introduced coordinate systems lie in the centres of the corresponding Cardan–Hook joints (intersections of their axes) and that the body 0 rotates about the axis z .

It is assumed that the initial position of the system corresponds to the reference frames $O_1x_1y_1z_1$ and O_1xyz overlapping each other and the axes of the coordinate system $O_2x_2y_2z_2$ being parallel to the corresponding axes of the reference frame

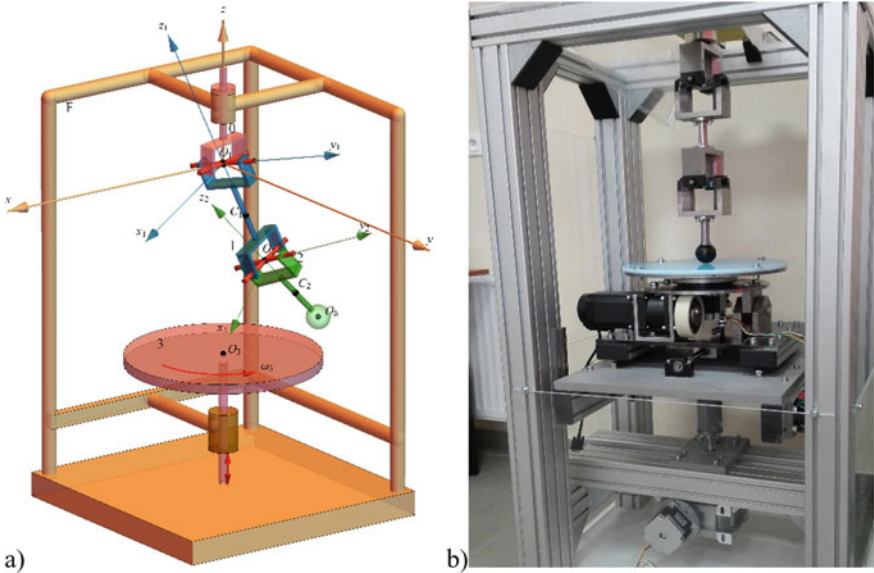


Fig. 1 Double pendulum with obstacle—model and experimental rig

$O_1x_1y_1z_1$. Then, the position of the system is described by the use of the following sequence of rotations: by angle ψ_1 about axis z_1 (rotation of the body 0), by angle θ_1 about axis x_1 , by angle φ_1 about axis y_1 , by angle θ_2 about axis x_2 and by angle φ_2 about axis y_2 . We assume also that the centre O_2 of the second Cardan–Hook joint lies on the axis O_1z_1 .

The second pendulum ends with a spherical solid of radius R_b and centred at the point O_3 which lies on the axis O_2z_2 . It is also assumed that the mass centres C_1 and C_2 of the both links lie on the axes O_1z_1 or O_2z_2 , respectively. Moreover, the axes of the reference frames $O_1x_1y_1z_1$ and $O_2x_2y_2z_2$ are the principal axes of inertia of the corresponding pendulums. The geometric and mass properties of the pendulums are defined by the following parameters: $L_1 = O_1O_2$, $L_2 = O_2O_3$, R_b , $e_1 = O_1C_1$, $e_2 = O_2C_2$, m_1 and m_2 (masses of the corresponding links), I_{xi} , I_{yi} and I_{zi} ($i = 1, 2$; the corresponding principal central moments of inertia of the link number i with respect to the axis parallel to the corresponding axis O_ix_i , O_ix_i or O_iz_i). It is assumed that the Cardan–Hook joints are massless. Moreover, the rotational motion of the body 0 is known in advanced as a kinematic driving of the system.

The spherical solid at the end of the second link can come into a contact with the obstacle 3, which has the form of a disc rotating around the axis z with angular velocity ω_3 . Vertical position of the obstacle is defined by the parameter z_{O_3} —describing the z coordinate of the disc’s centre O_3 . All the bodies are assumed to be rigid during modelling of their global dynamics. Introduced further local compliance of the bodies

in the vicinity of the contact is assumed to not influence global geometry of the system in a significant way.

Angular velocity $\omega = d\psi_1/dt$ of the body 0 is assumed to be the following function of time

$$\omega(t) = \omega_0 + q \cos \Omega t, \quad (1)$$

where ω_0 , q and Ω are parameters representing its constant component, amplitude and frequency.

The governing equations of motion are expressed using the Lagrange's formalism:

$$\frac{d}{dt} \left(\frac{\partial T}{\partial \dot{q}_i} \right) - \frac{\partial T}{\partial q_i} + \frac{\partial V}{\partial q_i} = \tau_i, \quad i = 1, 2, 3, 4 \quad (2)$$

where q_i is the i th generalized coordinate and element of the following vector

$$\mathbf{q} = \begin{bmatrix} q_1 & q_2 & q_3 & q_4 \end{bmatrix}^T = \begin{bmatrix} \theta_1 & \varphi_1 & \theta_2 & \varphi_2 \end{bmatrix}^T \quad (3)$$

and T —is kinetic energy, V —potential energy of gravity forces, τ_i —is the i th generalized force and the element of the following vector

$$\boldsymbol{\tau} = \begin{bmatrix} \tau_1 & \tau_2 & \tau_3 & \tau_4 \end{bmatrix}^T = \begin{bmatrix} \tau_{\theta_1} & \tau_{\varphi_1} & \tau_{\theta_2} & \tau_{\varphi_2} \end{bmatrix}^T. \quad (4)$$

The kinetic energy T of the system reads

$$\begin{aligned} T = & \frac{1}{2} m_1 (v_{C_1 x_1}^2 + v_{C_1 y_1}^2 + v_{C_1 z_1}^2) + \frac{1}{2} m_2 (v_{C_2 x_2}^2 + v_{C_2 y_2}^2 + v_{C_2 z_2}^2) \\ & + \frac{1}{2} (I_{x_1} \omega_{1x_1}^2 + I_{y_1} \omega_{1y_1}^2 + I_{z_1} \omega_{1z_1}^2) + \frac{1}{2} (I_{x_2} \omega_{2x_2}^2 + I_{y_2} \omega_{2y_2}^2 + I_{z_2} \omega_{2z_2}^2), \end{aligned} \quad (5)$$

and one can be presented using the following matrix notation

$$T(\mathbf{q}, \dot{\mathbf{q}}, \omega) = \frac{1}{2} \dot{\mathbf{q}}^T \mathbf{M}(\mathbf{q}) \dot{\mathbf{q}} + \dot{\mathbf{q}}^T \mathbf{b}_1(\mathbf{q}) \omega + \frac{1}{2} b_0(\mathbf{q}) \omega^2. \quad (6)$$

where \mathbf{v}_{C_1} and \mathbf{v}_{C_2} denote velocities of mass centres C_1 and C_2 of the first and the second link, $\boldsymbol{\omega}_1$ and $\boldsymbol{\omega}_2$ —stand for angular velocities of the bodies, while mass matrix $\mathbf{M}(\mathbf{q})$, $\mathbf{b}_1(\mathbf{q})$ and $b_0(\mathbf{q})$ are certain functions.

Potential energy $V(\mathbf{q})$ of gravitational forces reads as follows

$$V = m_1 g z_{C_1} + m_2 g z_{C_2}, \quad (7)$$

where z_{C_1} and z_{C_2} denote the coordinates along the axis z of the mass centres C_1 and C_2 .

The differential equations of motion can be finally presented in the following way

$$\mathbf{M}(\mathbf{q})\ddot{\mathbf{q}} + \mathbf{b}_1(\mathbf{q})\dot{\omega} + \mathbf{C}(\mathbf{q}, \dot{\mathbf{q}})\dot{\mathbf{q}} + \mathbf{c}_1(\mathbf{q}, \dot{\mathbf{q}})\omega + \mathbf{c}_2(\mathbf{q})\omega^2 + \mathbf{w}(\mathbf{q}) = \boldsymbol{\tau}, \quad (8)$$

where

$$\mathbf{C}(\mathbf{q}, \dot{\mathbf{q}}) = \frac{d\mathbf{M}(\mathbf{q})}{dt} - \frac{1}{2} \frac{\partial \dot{\mathbf{q}}^T \mathbf{M}(\mathbf{q})}{\partial \mathbf{q}},$$

$$\mathbf{c}_1(\mathbf{q}, \dot{\mathbf{q}}) = \frac{d\mathbf{b}_1(\mathbf{q})}{dt} - \frac{\partial \mathbf{b}_1^T(\mathbf{q})}{\partial \mathbf{q}} \dot{\mathbf{q}},$$

$$\mathbf{c}_2(\mathbf{q}) = -\frac{1}{2} \frac{\partial b_0(\mathbf{q})}{\partial \mathbf{q}},$$

$$\mathbf{w}(\mathbf{q}) = \frac{\partial V(\mathbf{q})}{\partial \mathbf{q}}.$$

The generalized forces are organized in the following way:

$$\boldsymbol{\tau} = \boldsymbol{\tau}_c + \boldsymbol{\tau}_b, \quad (9)$$

where $\boldsymbol{\tau}_c$ represents generalized contact forces and $\boldsymbol{\tau}_b = [\tau_{\theta_{1b}} \tau_{\varphi_{1b}} \tau_{\theta_{2b}} \tau_{\varphi_{2b}}]^T$ is a vector of damping torques in the corresponding joints.

Let us denote by A_2 and A_3 two points belonging to the bodies 2 and 3, respectively, where they can potentially come into a contact with each other. The elements of vector of generalized contact forces are computed in the following way

$$\tau_{ci} = \mathbf{F}_c \cdot \frac{\partial \mathbf{v}_{A_2}}{\partial \dot{q}_i}, \quad i = 1, 2, 3, 4 \quad (10)$$

where \mathbf{F}_c is resultant contact force acting on the ball of the second link at the point A_2 and \mathbf{v}_{A_2} is velocity of the point A_2 .

The set of admissible positions of the pendulum is limited by the obstacle, which undeformed surface is described by the equation $z = z_{O_3}$, where z is z -coordinate of a point lying on the surface and z_{O_3} is a constant parameter. It results in the following formula for distance h between the undeformed ball and the disc's surface

$$h = z_{O_b} - z_{O_3} - R_b, \quad (11)$$

where z_{O_b} denotes the corresponding global z -coordinate of the ball centre O_b .

The derivative of distance h with respect to time is expressed in the following way

$$\dot{h} = \mathbf{v}_{A_2} \cdot \mathbf{n}, \quad (12)$$

where \mathbf{n} is a unit vector normal to the obstacle.

One can write the following relation allowing to calculate velocity of the point A_3

$$\mathbf{v}_{A_3} = \boldsymbol{\omega}_3 \times \mathbf{r}_{A_3}, \quad (13)$$

where $\boldsymbol{\omega}_3$ is angular velocity of the obstacle rotating about the axis z and \mathbf{r}_{A_3} stands for the vector of the beginning at the point O_1 (lying on the rotation axis of the obstacle) and the end at the point A_3 .

Translational and angular sliding relative velocities at the centre of the contact area read

$$\begin{aligned} \mathbf{v}_s &= \mathbf{v}_{A_2} - \dot{h}\mathbf{n} - \mathbf{v}_{A_3}, \\ \boldsymbol{\omega}_s &= (\boldsymbol{\omega}_2 \cdot \mathbf{n})\mathbf{n} - \boldsymbol{\omega}_3. \end{aligned} \quad (14)$$

The damping torques in the joints $\boldsymbol{\tau}_b = \left[\tau_{\theta_1 b} \tau_{\varphi_1 b} \tau_{\theta_2 b} \tau_{\varphi_2 b} \right]^T$ are modelled in the following way

$$\tau_{\xi_i b} = -M_b \frac{\dot{\xi}_i}{\sqrt{\dot{\xi}_i^2 + \varepsilon_b^2}}, \quad \xi = \theta, \varphi; i = 1, 2, \quad (15)$$

where M_b and ε_b are constant parameters common for all the joints.

The contact force acting on the pendulum at the point A_2 consists of two components

$$\mathbf{F}_c = \mathbf{N} + \mathbf{T}, \quad (16)$$

where $\mathbf{N} = N\mathbf{n}$ is normal component of reaction, \mathbf{T} —resultant friction force reduced to the centre of the contact and \mathbf{n} —is unit vector normal to the disc's 3 surface.

The normal component is expressed in the following way

$$N = k|h|^{3/2}(1 - b\dot{h})\mathbf{1}(-h)\mathbf{1}(1 - b\dot{h}), \quad (17)$$

where k denotes the coefficient of the nonlinear stiffness of the Hertzian contact, b is coefficient of damping and $\mathbf{1}$ is the unit step function. In the case of the contact between a ball of radius R_b and an elastic semi-space, the coefficient of stiffness can be computed in the following way

$$k = \frac{4\sqrt{R_b}}{3\left(\frac{1-\nu_1^2}{E_1} + \frac{1-\nu_2^2}{E_2}\right)}, \quad (18)$$

where ν_1 and ν_2 are Poisson's coefficients of materials of the contacting bodies, while E_1 and E_2 are their Young's modulus.

The approximation of the resulting friction force for circular contact area, based on extensions of Padé approximants, assuming fully developed sliding and Coulomb friction model at each point of the contact, has the form [10–13]

$$\mathbf{T} = -\mu N \frac{\mathbf{v}_s}{\sqrt{\mathbf{v}_s^2 + b_T^2 a_r^2 \boldsymbol{\omega}_s^2 + \varepsilon^2}}, \quad (19)$$

where μ is coefficient of Coulomb friction, b_T —the parameter depending on the contact stress distribution, ε —the parameter introduced in order to regularize functions (19), a_r —radius of the corresponding Hertzian contact, while \mathbf{v}_s and $\boldsymbol{\omega}_s$ are relative linear and angular sliding velocities at the centre of the contact. The friction torque is neglected.

The size of the contact is calculated according to the following formula

$$a_r = \left(\frac{3}{4} N \left(\frac{1 - \nu_1^2}{E_1} + \frac{1 - \nu_2^2}{E_2} \right) R_b \right)^{1/3}. \quad (20)$$

3 Numerical Simulations

During the presented in this section numerical simulations the following set of geometrical and mass parameters (corresponding to the experimental stand under construction) remain constant: $m_1 = 4.59$ kg, $m_2 = 2.41$ kg, $I_{x_1} = I_{y_1} = 0.0315$ kg m², $I_{z_1} = 0.0078$ kg m², $I_{x_2} = 0.0084$ kg m², $I_{y_2} = 0.0055$ kg m², $I_{z_2} = 0.0038$ kg m², $L_1 = 0.228$ m, $L_2 = 0.175$ m, $e_1 = 0.122$ m, $e_2 = 0.0586$ m and $R_b = 0.025$ m. Moreover, we assume $g = 9.81$ m/s². The axes of the Cardan joints are assumed to be massless, since their masses are partially taken into account in the mass parameters of the links, i.e. the corresponding masses of the axes are assumed to move together with the link in which they are mounted. The test simulations performed for two different versions of the pendulum (for the full model with mass joints and for reduced model with massless swivels) exhibited no significant differences.

Moreover, we assume the following parameters of the resistance in the joints and properties of the contact: $M_b = 0.04$ N m, $\varepsilon_b = 0.4$ 1/s, $E_1 = E_2 = 0.01$ GPa, $\nu_1 = \nu_2 = 0.3$, $b = 0.5$ m⁻¹s, $\mu = 0.5$, $\varepsilon = 10^{-3}$ 1/s (regularization parameter) and $b_T = 0.681$. The last value was obtained based on optimizing the adjustment to the integral model of friction for circular contact area and Hertzian contact stress distribution. The parameters of the kinematic driving applied in the subsequent simulations are as follows: $\omega_0 = 0$ rad/s, $q = 3$ rad/s and $\Omega = 3$ rad/s. The obstacle rotates with constant angular velocity $\omega_0 = 5$ rad/s.

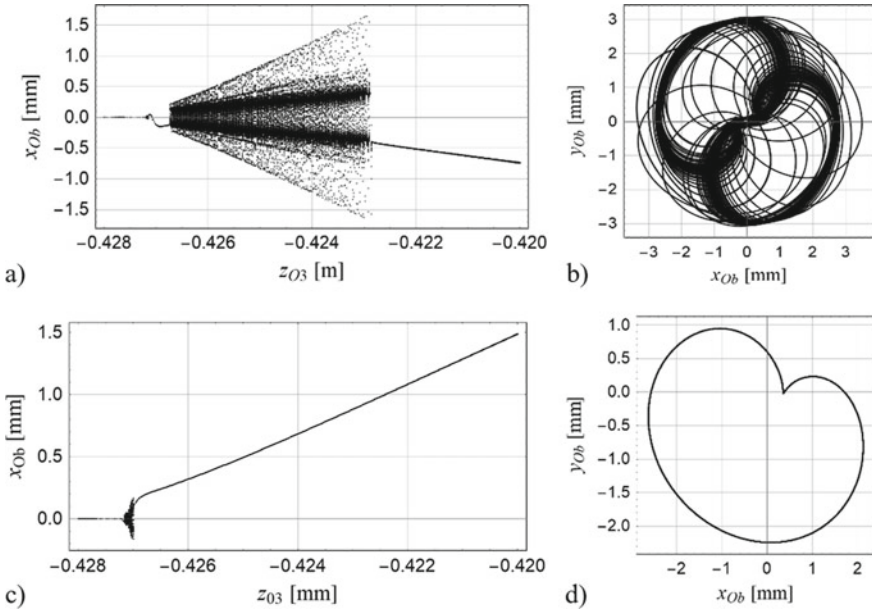


Fig. 2 Bifurcation diagrams with position of the obstacle z_{O3} as a control parameter for $b_T = 0.681$ (a) and $b_T = 0$ (c), along with the corresponding orbits for $z_{O3} = -0.424$ m (b—for $b_T = 0.681$, d— $b_T = 0$)

Figure 2 exhibits two bifurcation diagrams with (increasing) position of the obstacle z_{O3} as a control parameter for $b_T = 0.681$ (a) and $b_T = 0$ (c). The first case corresponds to model of friction force depending on local translational and angular sliding relative velocities (with optimized fitting to the integral model). The second case corresponds to classical friction model assuming a point contact. As one can observe, the introduced elements of modelling of the contact are crucial for bifurcation dynamics of the system. In the panels (b) and (d), there are presented the corresponding orbits for $z_{O3} = -0.424$ m: irregular orbit for $b_T = 0.681$ (b) and periodic attractor for $b_T = 0$ (d). Figure 3 exhibits the corresponding Poincaré section (a) and the process of computation of the largest Lyapunov exponents (b) of the attractor presented in Fig. 2b. One can conclude that the attractor is quasiperiodic. Note that since the system is non-autonomous with periodic forcing, there exists the second Lyapunov exponent equal to zero.

4 Concluding Remarks

In the works [16, 17] and the present paper, to our knowledge for the first time in the literature, there is presented an application of special class of reduced models of tangent contact forces based on approximations of the integral Contensou model

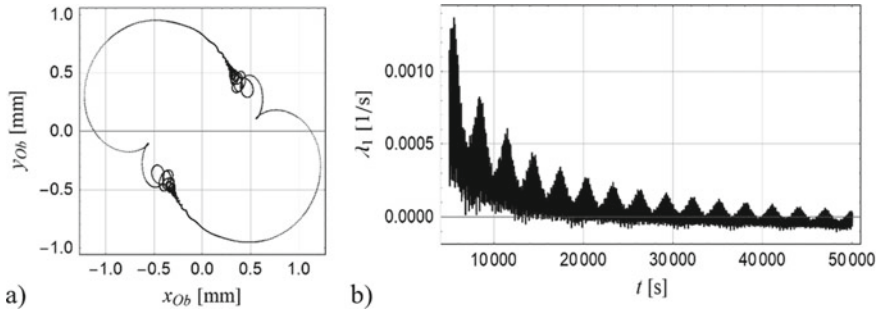


Fig. 3 Poincaré section of the orbit presented in Fig. 2b (a) and its largest Lyapunov exponent (b)

of friction, in modelling of impact dynamics of a rigid body in 3D space. Some components of the contact model, like rolling friction and spin friction, have been neglected. The authors of this work expect that influence of these elements on the system dynamics is negligible; however, it can be checked during further numerical and experimental investigations.

The investigated system can exhibit rich nonlinear dynamics and potentially new or rare bifurcation scenarios. The presented example of bifurcation dynamics shows the differences in simulation results, when applying the contact model for finite size of the contact and the model of friction force assuming a point contact, i.e. no relation between resultant friction force and rotational relative sliding motion of contacting surfaces. It proves the necessity of the use of the proposed models, when one can obtain fast and reliable numerical simulation of a rigid body dynamic with 3D frictional contacts.

The paper presents results which can be treated as a preparation stage before further joint numerical and experimental investigations. We are going to confirm experimentally the bifurcation scenarios exhibited by the model and usefulness of the developed models.

References

1. J. Shen, A.K. Sanyal, Dynamics and control of a 3D pendulum, in *Proceedings of 43rd IEEE Conference on Decision and Control*, Georgia, USA (2004), pp. 232–328
2. R.D. Peters, Chaotic motion from support constraints of a nondriven rigid spherical pendulum. *Int. J. Robust Nonlinear Control* **17**(16), 5352–5359 (1988)
3. S. Maiti, J. Roy, A.K. Mallik, J.K. Bhattacharjee, Nonlinear dynamics of a rotating double pendulum. *Phys. Lett. A* **380**(3), 408–412 (2016)
4. M. Ludwicki, J. Awrejcewicz, G. Kudra, Spatial double pendulum with axial excitation: computer simulation and experimental setup. *Int. J. Dyn. Control* **3**(1), 1–8 (2015)
5. S. Wu, F. Mou, Q. Liu, J. Cheng, Contact dynamics and control of a space robot capturing a tumbling object. *Acta Astronaut.* **151**, 532–542 (2018)
6. T. Wang, C. Chevallereau, D. Tlalolini, Stable walking control of a 3D biped robot with foot rotation. *Robotica* **32**(4), 551–571 (2014)

7. P. Contensou, Couplage entre frottement de glissement et de pivotement dans la théorie de la toupie, in *Kreiselp Probleme Gyrodynamik, IUTAM Symposium Celerina*, ed. by H. Ziegler (Springer, Berlin, 1962), pp. 201–216
8. V.P. Zhuravlev, The model of dry friction in the problem of the rolling of rigid bodies. *J. App. Math. Mech.* **62**(5), 705–710 (1998)
9. A.A. Kireenkov, Combined model of sliding and rolling friction in dynamics of bodies on a rough plane. *Mech. Solids* **43**(3), 412–425 (2008)
10. G. Kudra, J. Awrejcewicz, Approximate modelling of resulting dry friction forces and rolling resistance for elliptic contact shape. *Mech. A/Solids* **42**, 358–375 (2013)
11. G. Kudra, J. Awrejcewicz, Application and experimental validation of new computational models of friction forces and rolling resistance. *Acta Mech.* **226**(9), 2831–2848 (2015)
12. G. Kudra, M. Szewc, I. Wojtunik, J. Awrejcewicz, Shaping the trajectory of the billiard ball with approximations of the resultant contact forces. *Mechatronics* **37**, 54–62 (2016)
13. G. Kudra, M. Szewc, I. Wojtunik, J. Awrejcewicz, On some approximations of the resultant contact forces and their applications in rigid body dynamics. *Mech. Syst. Signal Process.* **79**, 182–191 (2016)
14. M. Machado, P. Moreira, P. Flores, H.M. Lankarani, Compliant contact force models in multi-body dynamics: Evolution of the Hertz contact theory. *Mech. Mach. Theory* **53**, 99–121 (2012)
15. G. Gilardi, I. Sharf, Literature survey of contact dynamics modelling. *Mech. Mach. Theor.* **37**(10), 1213–1239 (2012)
16. G. Kudra, J. Awrejcewicz, Modelling and simulation of bifurcation dynamics of spatial double pendulum with rigid limiters of motion, in *Proceedings of the International Conference on Structural Engineering Dynamics (ICEDyn)*, Ericeira, Portugal (2017), 10 pages
17. G. Kudra, M. Szewc, M. Ludwicki, K. Witkowski, J. Awrejcewicz, Modelling of rigid body dynamics with spatial frictional contacts, in *Vibration, Control and Stability of Dynamical Systems*, ed. by J. Awrejcewicz, M. Kaźmierczak, J. Mrozowski, P. Olejnik (DAB&M of TUL Press, Lodz 2017), pp. 231–240

Dynamics of the Impact with Benson Friction Model



Dan B. Marghitu and Dorian Cojocaru

Abstract An analytical model for the impact of a rigid link in planar pure rotation with a solid surface is developed. The free end of the link undergoes elastic and elastoplastic deformations during the compression phase of the impact. The restitution is considered elastic with a permanent deformation. During the impact, a friction force based on Benson model is employed. The differential impact equations are solved for different initial impact incident angle and distinct values of the coefficient of kinetic friction.

1 Introduction

An impact occurs in a very short interval of time in which the system has instantaneously change of velocities. Bhatt and Koechling analyzed the trace of the sliding velocity at the contact point for a three-dimensional impact [1]. Flow patterns that show the evolution of impact were defined. Also, three-dimensional parameters that govern the defining equations for the sliding behavior of the contact point were identified. The qualitative behavior during impact was determined based on the region which contains the parameters for a given impact configuration.

Yen and Wu proposed and verified experimentally a method to identify both the impact location and the transverse impact force history from strain responses on a rectangular plate [2]. A numerical verification of the method was performed by randomly generating the impact locations and the force histories and then performing forward calculations to obtain the corresponding strain responses. These responses were then used as the input data for the identification purposes.

D. B. Marghitu (✉)

Department of Mechanical Engineering, Auburn University, Auburn, AL 36349, USA
e-mail: marghitu@auburn.edu

D. Cojocaru

Department of Mechatronics and Robotics, University of Craiova, Craiova, Romania

© Springer Nature Switzerland AG 2021

N. Herisanu and V. Marinca (eds.), *Acoustics and Vibration of Mechanical Structures—AVMS 2019*, Springer Proceedings in Physics 251,
https://doi.org/10.1007/978-3-030-54136-1_2

An elasto-plastic contact law was proposed by Yigit for modeling the impact of a single flexible link [3, 4]. The contact law allows continuous transition between contact and non-contact phases and is capable of predicting impact force histories.

Marghitu and Hurmuzlu introduced a finite number of vibration modes to take into account the vibrational effect for the impact of a single straight bar [5]. Effects such as multicollisions, slip reversal, local vortex vector, and different configurations were accommodated automatically.

The chain reaction from impact on coaxial multibody systems was studied by Stronge [6]. Stronge studied three spheres connected by springs to analyze the external impact. The generated reaction force depends on the contact compliance and the mass of the adjacent spheres.

The planar collision of rigid bodies with the friction between the bodies was studied by Brach [7–9]. The general equations of impulse and momentum were used. The effect of the moment impulse on the angular velocities was taken into account through the use of a moment coefficient of restitution.

Kane and Levinson [10, 11] considered the generalized impulse and momentum equations for impact with friction. The impact equations include the generalized speeds before and after the impact. The system of equations was solved with two assumptions involving the velocity of separation and the normal and tangential impulse.

The planar body collisions with friction were studied by Wang and Mason [12]. Routh's graphical method was employed to analyze the frictional impact. Poisson's and Newton's methods were used for the impact analytical expressions. They show that Poisson's hypothesis does not violate energy conservation principles, while Newton's coefficient of restitution is not always correct.

Johansson and Klarbring developed an algorithm for rigid body impact with friction [13]. The impenetrability condition and Coulomb's law of friction are formulated as equations and solved together with the equations of motion using Newton's method. The impact process is described by the coefficient of friction, the coefficient of restitution, and a new introduced coefficient of tangential restitution. The new coefficient is determined experimentally.

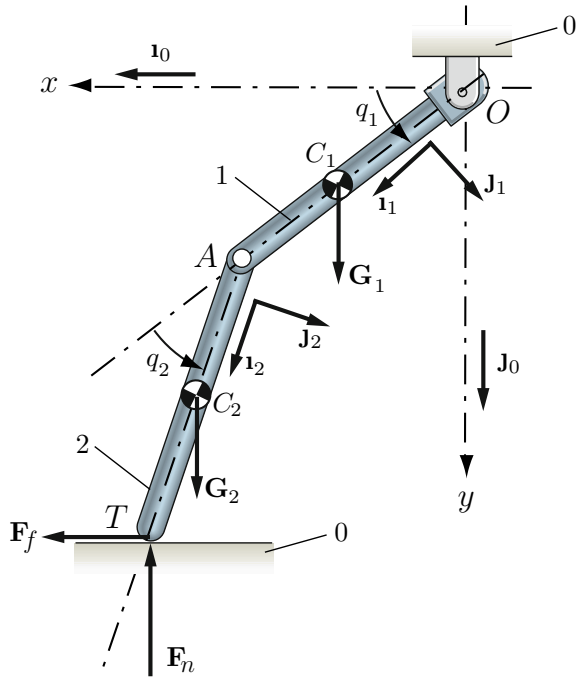
As it can be noticed from the previous literature, most of the cases involved impacts with Coulomb friction. In this study, during the impact a friction force based on Benson model is employed.

2 Mathematical Model

2.1 Kinematics

Figure 1 is a schematic representation of a kinematic chain with two links 1 and 2. The mass center of the link i is at C_i , $i = 1, 2$. The dimensions are $OC_1 = C_1A = L_1$ and $AC_2 = C_2T = L_2$. The "fixed" Newtonian reference frame (0), RF0, has the

Fig. 1 Impact of a chain with a surface



unit vectors $[\mathbf{i}_0, \mathbf{j}_0, \mathbf{k}_0]$. The reference frame (1), RF1, of unit vectors $[\mathbf{i}_1, \mathbf{j}_1, \mathbf{k}_1]$ is link 1 body attached. The vertical unit vectors \mathbf{j}_0 and \mathbf{j}_1 are fixed in both (0) and (1). The first generalized coordinate q_1 is the relative angle between the axes of (0) and (1). Link 1 is connected to link 2, and link 2 rotates relative to 1 about an axis fixed in both 1 and 2. The reference frame (2), of unit vectors $[\mathbf{i}_2, \mathbf{j}_2, \mathbf{k}_2]$ is body attached to link 2. The unit vectors \mathbf{k}_1 and \mathbf{k}_2 are fixed in both 1 and 2. The second generalized coordinate q_2 is the relative angle between the axes of (1) and (2).

The unit vectors $\mathbf{i}_1, \mathbf{j}_1,$ and \mathbf{k}_1 can be expressed in terms of $\mathbf{i}_0, \mathbf{j}_0,$ and \mathbf{k}_0 using the relation

$$\begin{bmatrix} \mathbf{i}_1 \\ \mathbf{j}_1 \\ \mathbf{k}_1 \end{bmatrix} = \begin{bmatrix} c_1 & s_1 & 0 \\ -s_1 & c_1 & 0 \\ 0 & 0 & 1 \end{bmatrix} \begin{bmatrix} \mathbf{i}_0 \\ \mathbf{j}_0 \\ \mathbf{k}_0 \end{bmatrix}, \tag{1}$$

where $s_1 = \sin q_1$ and $c_1 = \cos q_1$. The transformation matrix to express (1) in terms of (0) is

$$R_{10} = \begin{bmatrix} c_1 & s_1 & 0 \\ -s_1 & c_1 & 0 \\ 0 & 0 & 1 \end{bmatrix}. \tag{2}$$

The unit vectors \mathbf{i}_2 , \mathbf{j}_2 , and \mathbf{k}_2 can be expressed as

$$\begin{bmatrix} \mathbf{i}_2 \\ \mathbf{j}_2 \\ \mathbf{k}_2 \end{bmatrix} = \begin{bmatrix} c_2 & s_2 & 0 \\ -s_2 & c_2 & 0 \\ 0 & 0 & 1 \end{bmatrix} \begin{bmatrix} \mathbf{i}_1 \\ \mathbf{j}_1 \\ \mathbf{k}_1 \end{bmatrix}, \quad (3)$$

where $s_2 = \sin q_2$ and $c_2 = \cos q_2$. The transformation matrix to express (2) in terms of (1) is

$$R_{21} = \begin{bmatrix} c_2 & s_2 & 0 \\ -s_2 & c_2 & 0 \\ 0 & 0 & 1 \end{bmatrix}. \quad (4)$$

The generalized speeds u_1 , u_2 describe the motion of a system. The generalized speeds can be introduced as $u_i = \dot{q}_i$ or in our case another choice is

$$u_1 = \dot{q}_1 \quad \text{and} \quad u_2 = \dot{q}_1 + \dot{q}_2. \quad (5)$$

The angular velocity of link 1 with respect to reference frame (0) is

$$\boldsymbol{\omega}_{10} = \dot{q}_1 \mathbf{k}_1 = u_1 \mathbf{k}_1. \quad (6)$$

The angular velocity of link 2 with respect to reference frame (1) is

$$\boldsymbol{\omega}_{21} = \dot{q}_2 \mathbf{k}_1 = (u_2 - u_1) \mathbf{k}_1. \quad (7)$$

The angular velocity of the link 2 with respect to the fixed reference frame (0) is

$$\boldsymbol{\omega}_{20} = \boldsymbol{\omega}_{10} + \boldsymbol{\omega}_{21} = u_2 \mathbf{k}_1. \quad (8)$$

The angular acceleration of the link 1 in the reference frame (0) is

$$\boldsymbol{\alpha}_{10} = \ddot{q}_1 \mathbf{k}_1 = \dot{u}_1 \mathbf{k}_1. \quad (9)$$

The angular acceleration of the link 2 with respect to the reference frame (0) is

$$\boldsymbol{\alpha}_{20} = \frac{d}{dt} \boldsymbol{\omega}_{20} = \frac{{}^{(2)}d}{dt} \boldsymbol{\omega}_{20} + \boldsymbol{\omega}_{20} \times \boldsymbol{\omega}_{20} = \frac{{}^{(2)}d}{dt} \boldsymbol{\omega}_{20} = \dot{u}_2 \mathbf{k}_1, \quad (10)$$

where $\frac{{}^{(2)}d}{dt}$ is the partial derivative with respect to time in reference frame (2).

The velocities and the accelerations of the chain will be expressed in terms of q_i , u_i , and \dot{u}_i . The position vector of C_1 , the mass center of link 1, is

$$\mathbf{r}_{C_1} = L_1 \mathbf{i}_1, \quad (11)$$

and the velocity of C_1 in reference frame (0) is

$$\mathbf{v}_{C_1} = \frac{d}{dt} \mathbf{r}_{C_1} = \frac{{}^{(1)}d}{dt} \mathbf{r}_{C_1} + \boldsymbol{\omega}_{10} \times \mathbf{r}_{C_1}. \quad (12)$$

The position vector of C_2 , the mass center of link 2, is

$$\mathbf{r}_{C_2} = 2 L_1 \mathbf{i}_1 + L_2 \mathbf{i}_2. \quad (13)$$

The velocity of C_2 in reference frame (0) is

$$\mathbf{v}_{C_2} = \frac{d}{dt} \mathbf{r}_{C_2} = \frac{{}^{(2)}d}{dt} \mathbf{r}_{C_2} + \boldsymbol{\omega}_{20} \times \mathbf{r}_{C_2}. \quad (14)$$

The acceleration of C_1 is

$$\mathbf{a}_{C_1} = \frac{d}{dt} \mathbf{v}_{C_1} = \frac{{}^{(1)}d}{dt} \mathbf{v}_{C_1} + \boldsymbol{\omega}_{10} \times \mathbf{v}_{C_1}. \quad (15)$$

The acceleration of C_2 is

$$\mathbf{a}_{C_2} = \frac{d}{dt} \mathbf{v}_{C_2} = \frac{{}^{(2)}d}{dt} \mathbf{v}_{C_2} + \boldsymbol{\omega}_{20} \times \mathbf{v}_{C_2}. \quad (16)$$

2.2 Generalized Active Forces

The external weight forces exerted on the links 1 and 2 are \mathbf{G}_1 and \mathbf{G}_2 , respectively, and are expressed as

$$\mathbf{G}_1 = m_1 g \mathbf{J}_0 \quad \text{and} \quad \mathbf{G}_2 = m_2 g \mathbf{J}_0. \quad (17)$$

The contact point between link 2 and a solid surface is T . At the collision moment, an impact force, \mathbf{F}_n , is normal to the surface with the point of application at T . A friction force \mathbf{F}_f is acting at T and is tangent to the surface. The friction force is calculated using a Benson friction model [14]. The generalized active forces, Q_r , are

$$Q_r = \frac{\partial \mathbf{v}_{C_1}}{\partial u_r} \cdot \mathbf{G}_1 + \frac{\partial \mathbf{v}_{C_2}}{\partial u_r} \cdot \mathbf{G}_2 + \frac{\partial \mathbf{v}_T}{\partial u_r} \cdot (\mathbf{F}_n + \mathbf{F}_f), \quad r = 1, 2, \quad (18)$$

where

$$\mathbf{v}_T = \mathbf{v}_{C_2} + \boldsymbol{\omega}_{20} \times \mathbf{r}_{C_2 T},$$

is the velocity of the contact point T .

2.3 Generalized Inertia Forces

The inertia force of link $j = 1, 2$ is

$$\mathbf{F}_{in j} = -m_j \mathbf{a}_{C_j}, \quad (19)$$

where m_j is the mass of link j .

The inertia moment of link 1 in reference frame (0) is

$$\mathbf{M}_{in 1} = -\boldsymbol{\alpha}_{10} \cdot \bar{I}_{C1} - \boldsymbol{\omega}_{10} \times (\bar{I}_{C1} \cdot \boldsymbol{\omega}_{10}), \quad (20)$$

where $\bar{I}_{C1} = (I_{C1x} \mathbf{i}_1)\mathbf{i}_1 + (I_{C1y} \mathbf{j}_1)\mathbf{j}_1 + (I_{C1z} \mathbf{k}_1)\mathbf{k}_1$ is the central inertia dyadic of link 1. The central principal axes of link 1 are parallel to $\mathbf{i}_1, \mathbf{j}_1, \mathbf{k}_1$. The central principal moments of inertia associated with the principal axes are $I_{C1x}, I_{C1y}, I_{C1z}$, respectively. The inertia matrix associated with the central inertia dyadic of link 1 is

$$\bar{I}_{C1} \rightarrow \begin{bmatrix} I_{C1x} & 0 & 0 \\ 0 & I_{C1y} & 0 \\ 0 & 0 & I_{C1z} \end{bmatrix}. \quad (21)$$

The inertia moment of link 2 in reference frame (0) is

$$\mathbf{M}_{in 2} = -\boldsymbol{\alpha}_{20} \cdot \bar{I}_{C2} - \boldsymbol{\omega}_{20} \times (\bar{I}_{C2} \cdot \boldsymbol{\omega}_{20}), \quad (22)$$

where $\bar{I}_{C2} = (I_{C2x} \mathbf{i}_2)\mathbf{i}_2 + (I_{C2y} \mathbf{j}_2)\mathbf{j}_2 + (I_{C2z} \mathbf{k}_2)\mathbf{k}_2$ is the central inertia dyadic of link 2. The generalized inertia forces are

$$K_{in r} = \frac{\partial \mathbf{v}_{C_1}}{\partial u_r} \cdot \mathbf{F}_{in 1} + \frac{\partial \boldsymbol{\omega}_{10}}{\partial u_r} \cdot \mathbf{M}_{in 1} + \frac{\partial \mathbf{v}_{C_2}}{\partial u_r} \cdot \mathbf{F}_{in 2} + \frac{\partial \boldsymbol{\omega}_{20}}{\partial u_r} \cdot \mathbf{M}_{in 2}. \quad (23)$$

The kinematical equations of motion are

$$\dot{q}_1 = u_1 \quad \text{and} \quad \dot{q}_2 = u_2 - u_1. \quad (24)$$

The impact differential dynamical equations for the kinematic chain are

$$K_{in r} + Q_r = 0, \quad r = 1, 2. \quad (25)$$

The system of ordinary differential equations of motion (24) and (25) can be solved with numerical techniques, and the generalized coordinates q_r and the generalized speeds u_r are determined.

3 Application and Results

For the numerical application, a rigid link in pure rotation is considered. The link has the following characteristics: the length is $L = 0.30$ m, the diameter is $d = 0.05$ m, the radius is $R = d/2$, the density is $\rho = 7800$ kg/m³, the mass is $m = \pi R^2 L \rho$, and the mass moment of inertia about C is $I_C = m(L^2 + 3R^2)/12$ kg m².

The normal impact force is given by Jackson–Green [15, 16]. The Hertz theory is used for the first elastic phase of the impact and the last restitution phase. The first elastic phase is characterized by the force

$$F_n = \frac{4}{3} E R^{0.5} \delta^{1.5}, \quad (26)$$

where E and R are the reduced modulus of elasticity and radius [16]. The elastic deformation during impact is δ . A modified Jackson and Green model is used for the next elasto-plastic phase [17]

$$F_n = P_c \left\{ e^{-0.17 \left(\frac{\delta}{\delta_y} \right)^{\frac{5}{12}}} \left[\frac{\delta}{\delta_y} \right]^{1.5} + \frac{4H}{C_j S_y} \left[1 - e^{\left(\frac{-1}{78} \right) \left(\frac{\delta}{\delta_y} \right)^{\frac{5}{9}}} \left[\frac{\delta}{\delta_y} \right]^{1.1} \right] \right\}, \quad (27)$$

where [15, 16]

$$a = \sqrt{R \delta_y \left(\frac{\delta}{1.9 \delta_y} \right)^B}, \quad B = 0.14 e^{23 S_y / E}, \quad \frac{H}{S_y} = 2.84 - 0.92 \left[1 - \cos \left(\pi \frac{a}{R} \right) \right],$$

$$\delta_y = R \left(\frac{\pi C_j S_y}{2 E} \right)^2, \quad \text{and} \quad C_j = 1.295 e^{0.736 \nu}.$$

The yield strength of the weaker material is S_y , and the elastic displacement at which the yields begins is δ_y . The average normal pressure is H and the maximum deformation at the end of the compression phase is δ_m . The Poisson ratio is ν .

The elastic restitution is defined by

$$F_n = \frac{4}{3} E R^{0.5} (\delta - \delta_r)^{1.5}, \quad (28)$$

where the permanent deformation is [17]

$$\delta_r = \delta_m \left\{ 0.8 \left[1 - \left(\frac{\delta_m + 5.5}{6.5} \right)^{-2} \right] \right\}. \quad (29)$$

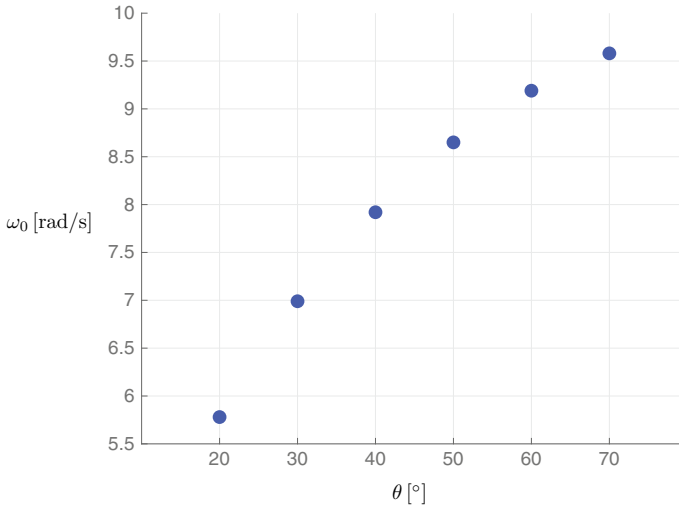


Fig. 2 Initial impact angular velocity ω_0

The friction force is given by a Benson friction model [14]

$$\mathbf{F}_f = -[\mu_k + (\mu_s - \mu_k) e^{-k_\mu |\mathbf{v}_T \cdot \mathbf{1}_0|}] |\mathbf{F}_n| \frac{(\mathbf{v}_T \cdot \mathbf{1}) \mathbf{1}_0}{|\mathbf{v}_T \cdot \mathbf{1}_0|}, \quad (30)$$

where μ_k is the kinematic coefficient of friction, μ_s is the static coefficient of friction, and k_μ is a constant.

Figure 2 shows the initial impact angular velocity of the link ω_0 [rad/s] as a function of the initial impact angle θ [°]. The initial impact angular velocity is the angular velocity at the beginning of the compression phase. For the next simulations, the following coefficients of friction are used $\mu_k = 0.15$ and $\mu_s = 0.20$. Figure 3 depicts the coefficient of restitution defined as $e = \omega_f / \omega_0$ as a function of the initial impact angle θ where ω_f is the final angular velocity at the end of the restitution phase. The coefficient of restitution is decreasing with the initial impact angle. Figure 4 shows the ration of the tangential velocities before and after impact v_{Txf} / v_{Tx0} as a function of the initial impact angle θ . This ratio is increasing with the initial impact angle. The permanent deformation during impact, δ_r , as a function of impact angle is shown in Fig. 5. For $\theta = 70^\circ$, the permanent deformation is decreasing with respect to δ_r at $\theta = 60^\circ$. For $\theta = 20^\circ - 60^\circ$, the permanent deformation is increasing with respect to the incident impact angle.

The next simulations are performed with an incident impact angle $\theta = 45^\circ$ and an initial impact angular velocity of the link $\omega_0 = 8.31$ rad/s. Figure 6 represents the coefficient of restitution, e , as a function of the kinetic coefficient of friction μ_k . The coefficient of restitution is increasing with the kinetic coefficient of friction. The ration of the tangential velocities before and after impact v_{Txf} / v_{Tx0} as a function of

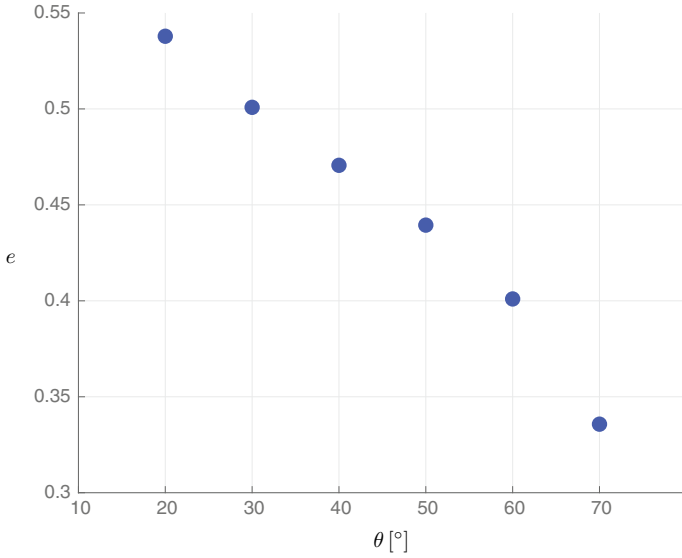


Fig. 3 Coefficient of restitution $e = \omega_f/\omega_0$

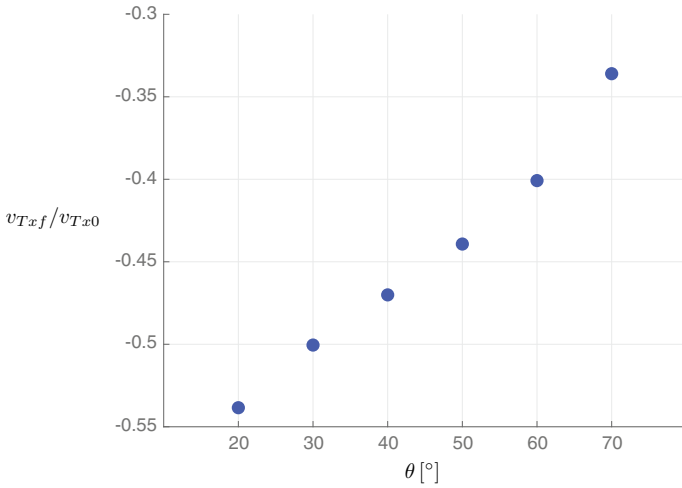


Fig. 4 Tangential velocity ratio v_{Txf}/v_{Tx0}

the kinetic coefficient of friction is shown in Fig. 7. The tangential velocity ratio is increasing with the kinetic coefficient of friction. Figure 8 shows the increase of the permanent deformation during impact, δ_r , as a function of the kinetic coefficient of friction μ_k .

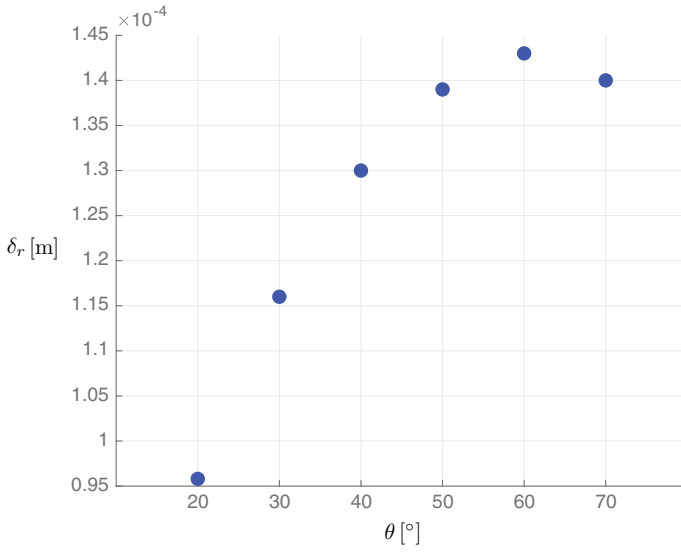


Fig. 5 Permanent deformation δ_r

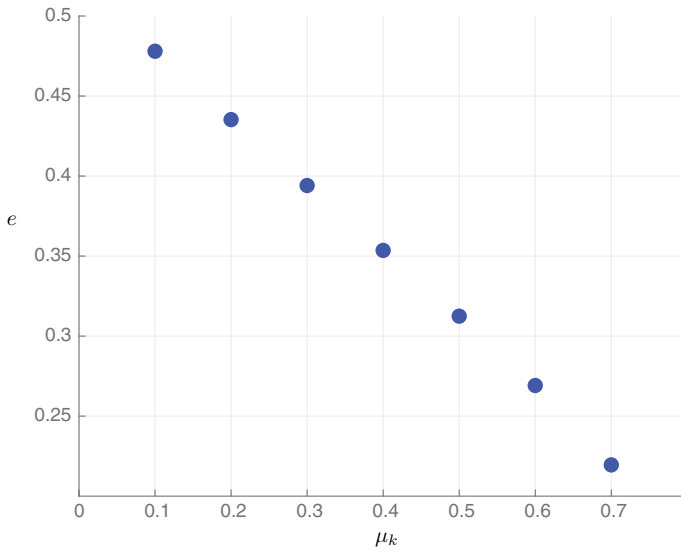


Fig. 6 Coefficient of restitution, e , as a function of kinetic coefficient of friction μ_k

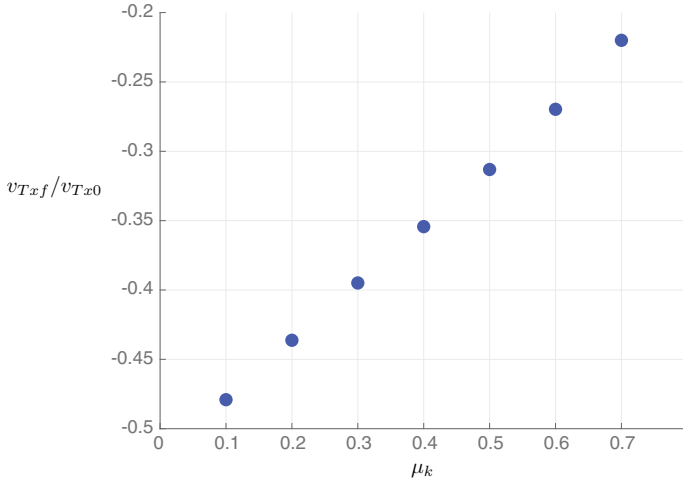


Fig. 7 Tangential velocity ratio v_{Txf}/v_{Tx0} versus kinetic coefficient of friction μ_k

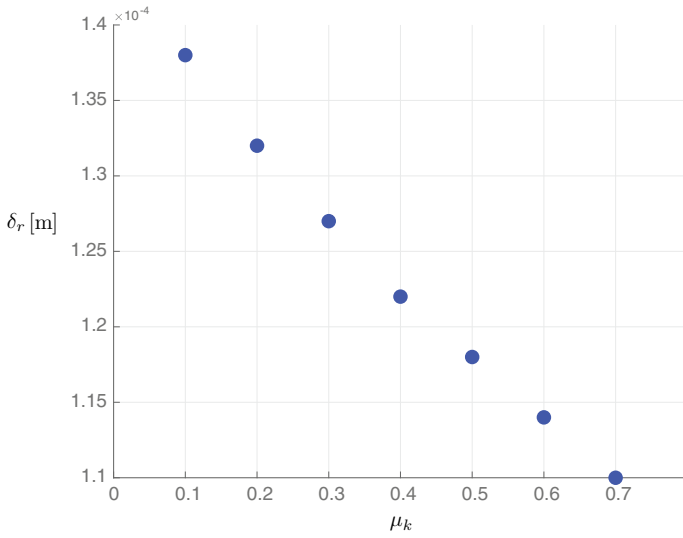


Fig. 8 Permanent deformation δ_r function of the kinetic coefficient of friction μ_k

4 Conclusions

The impact with friction of a link in pure rotation is studied. For the tangential force during the impact, a Benson friction model is selected. The coefficient of restitution is decreasing within incident impact angle and is decreasing with the kinetic coefficient of friction. Experimental results are needed to validate the impact model.

References

1. V. Bhatt, J. Koechling, Partitioning the parameter space according to different behaviors during three-dimensional impacts. *J. Appl. Mech.* **62**, 740–746 (1995)
2. C.-S. Yen, E. Wu, On the inverse problem of rectangular plates subjected to elastic impact, part II: experimental verification and further applications. *J. Appl. Mech.* **62**, 699–705 (1995)
3. A. Yigit, Flexural motion of a radially rotating beam attached to a rigid body. *J. Sound Vibr.* **121**, 201–210 (1988)
4. A. Yigit, On the use of an elastic-plastic contact law for the impact of a single flexible link. *J. Dyn. Syst. Meas. Control* **117**, 527–533 (1995)
5. D.B. Marghitu, Y. Hurmuzlu, Three-dimensional rigid-body collisions with multiple contact points. *J. Appl. Mech.* **62**, 725–732 (1995)
6. W.J. Stronge, Chain reaction from impact on coaxial multibody systems. *J. Appl. Mech.* **67**, 632–635 (2000)
7. R.M. Brach, Moments between impacting rigid bodies. *J. Mech. Des.* **103**, 812–817 (1981)
8. R.M. Brach, Friction, restitution, and energy loss in planar collisions. *J. Appl. Mech.* **51**, 164–170 (1984)
9. R.M. Brach, Rigid body collisions. *J. Appl. Mech.* **56**, 133–138 (1989)
10. T.R. Kane, P.W. Likins, D.A. Levinson, *Spacecraft Dynamics* (McGraw-Hill, New York, 1983)
11. T.R. Kane, D.A. Levinson, *Dynamics: Theory and Applications* (McGraw-Hill, New York, 1985)
12. Y. Wang, M.T. Mason, Two-dimensional rigid-body collisions with friction. *J. Appl. Mech.* **59**, 635–642 (1992)
13. L. Johansson, A. Klarbring, Study of frictional impact using a nonsmooth equations solver. *J. Appl. Mech.* **67**, 267–273 (2000)
14. E. Pennestri et al., Review and comparison of dry friction force models. *Nonlinear Dyn.* **83**, 1785–1801 (2016)
15. R.L. Jackson, I. Green, A finite element study of elasto-plastic hemispherical contact against a rigid flat. *ASME J. Tribol.* **127**(2), 343–354 (2005)
16. R.L. Jackson, I. Green, D.B. Marghitu, Predicting the coefficient of restitution of impacting elastic-perfectly plastic spheres. *J. Nonlinear Dyn.* **60**(3), 217–229 (2010)
17. H. Gheadnia, O. Cermik, D.B. Marghitu, Experimental and theoretical analysis of the elasto-plastic oblique impact of a rod with a flat. *Int. J. Impact Eng.* **86**, 307–317 (2015)

Vibrations of the Mass Variable Systems



Livija Cveticanin and Dragan Cveticanin

Abstract There are a significant number of systems with time-variable mass. The mass variation may be continual or discontinual. During discontinual mass change, a body with certain mass is added to or separated from an initial body. During this process, the position of acting parts is assumed to be unmovable, while their velocities have the jump-like variation. The effect of discontinual mass variation is evident during fracture of the body. The result of dynamic analysis of mass variation gives the prediction of kinematic properties of the separating and remaining bodies. It is concluded that the discontinual separation is the opposite process to the impact of bodies. Theoretical results are supported with an example of a windmill with bended or broken blades. If the separation or addition of mass is continual and slow, during mass variation a reactive force and a reactive torque occur, which are the product of mass time derivative and of the velocity change and the product of the time derivative of the moment of inertia moment and angular velocity, respectively. This force and torque excite vibration in the system. It is of interest to investigate the influence of the reactive force and torque on the oscillatory behavior of the system. Mathematical model of the system is formed, and methods for solving equations with slow time-variable parameters are developed. The obtained results are convenient for dynamic analysis. In this paper, the vibrations of the rotor, as a two-degree-of-freedom system, are considered. The effect of reactive force on the motion of the sieve for particle separation is also discussed.

L. Cveticanin (✉)

University of Novi Sad, Trg D. Obracovica 6, Novi Sad, Serbia

e-mail: cveticanin@uns.ac.rs

Obuda University, Nepszinhaz uU. 7, Budapest, Hungary

D. Cveticanin

Remming, B. Nusica 15, Novi Sad, Serbia

e-mail: dragan.cveticanin@remming.co.rs

© Springer Nature Switzerland AG 2021

N. Herisanu and V. Marinca (eds.), *Acoustics and Vibration of Mechanical Structures—AVMS 2019*, Springer Proceedings in Physics 251,

https://doi.org/10.1007/978-3-030-54136-1_3

1 Introduction

The problem of mass variable body is known for a long time (see [1]). In the seventeenth century, Galileo discovered the anomaly in the Moon motion which he believed is the function of the system mass variation. Lately, Laplace theoretically proved the phenomena of the secular acceleration of the Moon according to the influence of mass variation [2]. Dufour [3] explained that the mass of the Earth varies due to the falling shooting stars and also due to combustion or spending in the atmosphere. He found that the dust of shooting stars which falls on the surface of France in one year can cover a volume of 0.1 m^3 . Oppalzer [4] was the first to analyze the reason for secular acceleration of the Moon as the result of Earth and Moon mass increase. Namely, during a hundred year a 2.8 mm dust layer is formed on the Earth.

Since that time, a significant number of publications appear considering the mass variable systems. Mass variation may be continual or discontinual.

For the discontinual mass variation two processes are typical: mass addition and mass separation. The first process is usually considered as the plastic impact of two bodies. However, there are only few investigations in the discontinual mass separation [5–12].

For continual mass variation, Meshchersky [13] extended Newton's equation with the so-called reactive force. Solving this equation, results were obtained which were of crucial interest in developing of the rocket theory (see [14–18]). Nowadays, Meshchersky's equation is widely applied in systems with time-variable mass [12, 19] and specially in time-variable oscillators [20–25]. However, the equation is not convenient for explaining the dynamics of the body with simultaneous mass and geometry (i.e., moment of inertia) variation.

The aim of this paper is to extend the dynamics of the mass variable system to the dynamics of the mass variable body. The variation of the moment of inertia of the body is taken into consideration. Equations of general motion of the body with variable mass are formed.

As the special motion, the vibration of the body with variable mass is considered. The influence of mass variation on the dynamic properties is analyzed. As an example, vibrations of a sieve during mass separation are considered. The problem is mathematically described. The equation is solved analytically and numerically. The solutions are compared.

2 Discontinual Mass Separation

The term 'discontinual mass separation' means dividing of an initial rigid body into two rigid ones: a separating body and a remaining body (Fig. 1). The separation is assumed to be in a very short time during which the position of bodies is invariable [26]. However, linear and angular velocities of the initial, separating and remaining bodies differ. To calculate these values, the dynamics of bodies is divided into three

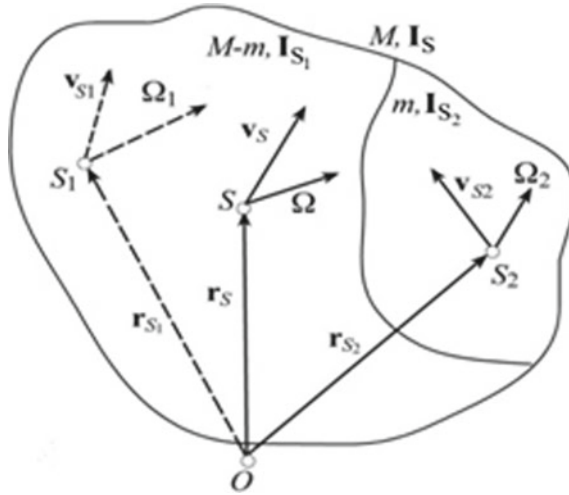


Fig. 1 Model of body separation

intervals: dynamics of the initial body, dynamics of discontinual mass separation and dynamics of the separating body and of the remaining body.

To describe the dynamics of the system, the principle of linear momentum and the principle of angular momentum are applied.

2.1 Principle of Linear Momentum

For the initial body with mass M and velocity of mass center v_S , the linear momentum is

$$K = M v_S \tag{1}$$

If the separated mass is m and the velocity of mass center is v_{S_2} , the linear momentum is

$$K_2 = m v_{S_2} \tag{2}$$

The linear momentum of the remaining mass is

$$K_1 = (M - m) v_{S_1} \tag{3}$$

where v_{S_1} is the unknown velocity of the mass center S_1 .

Assuming that all bodies during mass separation belong to a unique system (Fig. 1), we obtain the linear momentums \mathbf{K}_b before and \mathbf{K}_a after body separation. Linear momentum before mass variation is equal to linear momentum of the initial body

$$\mathbf{K}_b = \mathbf{K} = M\mathbf{v}_S \quad (4)$$

while the linear momentum after separation is a sum of the linear momentum which corresponds to the separating mass (2) and linear momentum of the remaining mass (3)

$$\mathbf{K}_a = \mathbf{K}_1 + \mathbf{K}_2 = m\mathbf{v}_{S2} + (M - m)\mathbf{v}_{S1} \quad (5)$$

Difference between the linear momentums \mathbf{K}_a and \mathbf{K}_b during mass separation is

$$\Delta\mathbf{K} = \mathbf{K}_a - \mathbf{K}_b = M(\mathbf{v}_{S1} - \mathbf{v}_S) - m(\mathbf{v}_{S1} - \mathbf{v}_{S2}) \quad (6)$$

Using the principle of linear momentum

$$\Delta\mathbf{K} = \mathbf{F}_r \Delta t \quad (7)$$

where \mathbf{F}_r is the resultant external force acting during the time Δt , it yields

$$\Delta\mathbf{K} \equiv M(\mathbf{v}_{S1} - \mathbf{v}_S) - m(\mathbf{v}_{S1} - \mathbf{v}_{S2}) = \mathbf{F}_r \Delta t. \quad (8)$$

2.2 Principle of Angular Momentum

The angular momentum of the initial body with respect to the fixed point O is (see Fig. 1)

$$\mathbf{L}_{Ob} = \mathbf{r}_S \times M\mathbf{v}_S + \mathbf{L}_S \quad (9)$$

where \mathbf{r}_S , \mathbf{v}_S , \mathbf{L}_S are the position vector, velocity and angular momentum of the mass center S , respectively. If the angular momentum of the separating body is

$$\mathbf{L}_{O2} = \mathbf{r}_{S2} \times m\mathbf{v}_{S2} + \mathbf{L}_{S2} \quad (10)$$

where \mathbf{r}_{S2} , \mathbf{v}_{S2} , \mathbf{L}_{S2} are the position vector, velocity and angular momentum of the mass center S_2 , respectively, and of the remaining body relating to the fixed point O is

$$\mathbf{L}_{O1} = \mathbf{r}_{S1} \times (M - m)\mathbf{v}_{S1} + \mathbf{L}_{S1} \quad (11)$$

where \mathbf{r}_{S1} , \mathbf{v}_{S1} , \mathbf{L}_{S1} are the position vector, velocity and angular momentum of the mass center S , respectively, the total angular momentum after body separation is

$$\mathbf{L}_{Oa} = \mathbf{L}_{O1} + \mathbf{L}_{O2} = \mathbf{r}_{S1} \times (M - m)\mathbf{v}_{S1} + \mathbf{L}_{S1} + \mathbf{r}_{S2} \times m\mathbf{v}_{S2} + \mathbf{L}_{S2} \quad (12)$$

The difference between the angular momentum before and after separation is

$$\Delta\mathbf{L}_O = \mathbf{L}_{S1} + \mathbf{L}_{S2} - \mathbf{L}_S + \mathbf{r}_{S1} \times (M - m)\mathbf{v}_{S1} + \mathbf{r}_{S2} \times m\mathbf{v}_{S2} - \mathbf{r}_S \times M\mathbf{v}_S \quad (13)$$

Introducing the position vectors \mathbf{r}_{S1} and \mathbf{r}_{S2} (Fig. 1)

$$\mathbf{r}_{S1} = \mathbf{r}_S + \boldsymbol{\rho}_{S1}, \mathbf{r}_{S2} = \mathbf{r}_S + \boldsymbol{\rho}_{S2} \quad (14)$$

the relation (10) transforms into

$$\Delta\mathbf{L}_O = \mathbf{L}_{S1} + \mathbf{L}_{S2} - \mathbf{L}_S + \boldsymbol{\rho}_{S1} \times (M - m)\mathbf{v}_{S1} + \boldsymbol{\rho}_{S2} \times m\mathbf{v}_{S2} - \mathbf{r}_S \times M\mathbf{v}_S \quad (15)$$

i.e., for (6) it is

$$\Delta\mathbf{L}_O = \mathbf{L}_{S1} + \mathbf{L}_{S2} - \mathbf{L}_S + \boldsymbol{\rho}_{S1} \times (M - m)\mathbf{v}_{S1} + \boldsymbol{\rho}_{S2} \times m\mathbf{v}_{S2} + \mathbf{r}_S \times \Delta\mathbf{K} \quad (16)$$

The relation (13) gives the dependence of the angular momentum on the linear momentum.

Otherwise, using (11) and the position of the mass center S

$$\mathbf{r}_S = \frac{M + m}{M}\mathbf{r}_{S1} + \frac{m}{M}\mathbf{r}_{S2} \quad (17)$$

we obtain

$$(M - m)\boldsymbol{\rho}_{S1} = -m\boldsymbol{\rho}_{S2} \quad (18)$$

Substituting (15) into (13), it is

$$\Delta\mathbf{L}_O = \mathbf{r}_S \times \Delta\mathbf{K} + \mathbf{L}_{S1} - \mathbf{L}_S + \mathbf{L}_{S2} - \boldsymbol{\rho}_{S2} \times m(\mathbf{v}_{S1} - \mathbf{v}_{S2}) \quad (19)$$

According to the principle of the angular momentum, variation of the angular momentum (16) in the time interval Δt is equal to the impulse \mathbf{J}^M , which is the sum of the impulse of the moment \mathbf{M}_O^{Fr} of the resultant force for the point O and of the impulse of the resultant torque \mathcal{M} , caused by active and reaction torques, i.e.,

$$\Delta\mathbf{L}_O = (\mathbf{M}_O^{Fr} + \mathcal{M})\Delta t = \mathbf{J}^M \quad (20)$$

Substituting (7) and (2.16) for mass separation, the relation (3.3) gives

$$\Delta \mathbf{L}_O \equiv \mathbf{r}_S \times \mathbf{F}_r \Delta t + \mathbf{L}_{S1} - \mathbf{L}_S + \mathbf{L}_{S2} - \boldsymbol{\rho}_{S2} \times m(\mathbf{v}_{S1} - \mathbf{v}_{S2}) = \mathbf{J}^M \quad (21)$$

Using the relation for the force moments according to fixed point O and the center of the initial mass S

$$\mathbf{M}_O^{Fr} = \mathbf{r}_S \times \mathbf{F}_r + \mathbf{M}_S^{Fr} \quad (22)$$

the final expression follows as

$$\Delta \mathbf{L}_O \equiv \mathbf{L}_{S1} - \mathbf{L}_S + \mathbf{L}_{S2} - \boldsymbol{\rho}_{S2} \times m(\mathbf{v}_{S1} - \mathbf{v}_{S2}) = (\mathbf{M}_S^{Fr} + \mathcal{M}) \Delta t \quad (23)$$

Relations (7) and (23) describe the dynamics of separation of a rigid body into two ones.

2.3 Dynamics of Separation of a Rigid Body into Two Without Impact

Assuming that the separation is without impact, the variation of the linear and angular momentum is zero, and the relations (6) and (23) transform into

$$(M - m)\mathbf{v}_{S1} = M\mathbf{v}_S - m\mathbf{v}_{S2} \quad (24)$$

$$\mathbf{L}_{S1} + \mathbf{L}_{S2} - \mathbf{L}_S - \boldsymbol{\rho}_{S2} \times m(\mathbf{v}_{S1} - \mathbf{v}_{S2}) = 0 \quad (25)$$

For the special case when the motion of bodies is translator, the relation (20) is satisfied. Then, due to (24), the linear velocity of the remaining body after separation is obtained. Otherwise, if the initial and remaining bodies have pure rotating motion around a fixed axle, the relation (24) is satisfied. Due to (20), the variation of the angle velocity is computed.

3 Continual Mass Separation

For infinitesimal small separating mass and infinitesimal small moment of inertia of the separating body, i.e.,

$$m = -\Delta M, \mathbf{I}_{S2} = -\Delta \mathbf{I} \quad (26)$$

velocity and angular momentum variations of the initial body are also infinitesimal

$$\Delta \mathbf{v} = \mathbf{v}_{S1} - \mathbf{v}_S, \Delta \mathbf{L}_S = \mathbf{L}_{S1} - \mathbf{L}_S \quad (27)$$

Using the notation

$$\mathbf{v}_{S1} = \mathbf{v}, \mathbf{v}_{S2} = \mathbf{u} \quad (28)$$

and the angular momentum of the separating body

$$\mathbf{L}_{S2} = \boldsymbol{\Omega}_2 \mathbf{I}_{S2} = \boldsymbol{\Omega}_2 \Delta \mathbf{I} \quad (29)$$

where $\boldsymbol{\Omega}_2$ is the angular velocity of the separating body and $\Delta \mathbf{I}$ is the tensor of moments of inertia, principles of linear and angular momentums (7) and (23) are

$$M \frac{\Delta \mathbf{v}}{\Delta t} - \frac{\Delta M}{\Delta t} (\mathbf{v} - \mathbf{u}) = \mathbf{F}_r \quad (30)$$

$$\frac{\Delta \mathbf{L}}{\Delta t} + \frac{\Delta \mathbf{I}}{\Delta t} \boldsymbol{\Omega}_2 - \boldsymbol{\rho}_{S2} \times \frac{\Delta M}{\Delta t} (\mathbf{v} - \mathbf{u}) = \mathbf{M}_S^{Fr} + \mathcal{M} \quad (31)$$

If the time tends to zero, relations transform into

$$M \frac{d\mathbf{v}}{dt} = \mathbf{F}_r + \frac{dM}{dt} (\mathbf{u} - \mathbf{v}) \quad (32)$$

$$\frac{d\mathbf{L}_S}{dt} = \mathbf{M}_S^{Fr} + \mathcal{M} + \boldsymbol{\rho}_{S2} \times \frac{dM}{dt} (\mathbf{u} - \mathbf{v}) + \frac{d\mathbf{I}}{dt} \boldsymbol{\Omega}_2 \quad (33)$$

For $\mathbf{L}_S = \mathbf{I} \boldsymbol{\Omega}$, where $\mathbf{I} = \mathbf{I}_S$ is the moment of inertia and $\boldsymbol{\Omega}$ is the angular velocity of rotation, the first time derivative is

$$\frac{d\mathbf{L}_S}{dt} = \mathbf{I} \frac{d\boldsymbol{\Omega}}{dt} + \boldsymbol{\Omega} \times \mathbf{I} \boldsymbol{\Omega} + \frac{d\mathbf{I}}{dt} \boldsymbol{\Omega} \quad (34)$$

Substituting (27) into (26), we obtain

$$M \frac{d\mathbf{v}}{dt} = \mathbf{F}_r + \phi \quad (35)$$

$$\mathbf{I} \frac{d\boldsymbol{\Omega}}{dt} + \boldsymbol{\Omega} \times \mathbf{I} \boldsymbol{\Omega} = \mathbf{M}_S^{Fr} + \mathcal{M} + \mathbf{M}_S^\phi + \mathfrak{R}_S \quad (36)$$

where

$$\phi = \frac{dM}{dt} (\mathbf{u} - \mathbf{v}) \quad (37)$$

is the well-known reactive force introduced by Meshchersky [13],

$$\mathbf{M}_S^\phi = \boldsymbol{\rho}_{S2} \times \frac{dM}{dt} (\mathbf{u} - \mathbf{v}) \quad (38)$$

is the moment of the reactive force according to the mass center S and

$$\mathfrak{M}_S = \frac{dI}{dt}(\Omega_2 - \Omega) \quad (39)$$

is the reactive torque. The reactive force and the reactive torque are the results of continual mass and moment of inertia variation in time. Reactive force is the product of mass variation and of relative velocity of mass variable body. Reactive torque is obtained by multiplying of time variation of the moment of inertia with relative angular velocity of mass variable body. Reactive force and reactive torque do not exist in dynamics of body with constant mass. Equation (28) defines the translational motion, while (29) the rotation around mass center S .

For practical reasons, it is convenient to rewrite vector differential (28) and (29) into scalar ones. Introducing the fixed coordinate system $Oxyz$, components v_x, v_y, v_z of the velocity \mathbf{v} , components u_x, u_y, u_z of the velocity \mathbf{u} and components F_x, F_y, F_z of the resultant \mathbf{F}_r , we rewrite (28) into

$$M \frac{dv_x}{dt} = F_x + \phi_x, M \frac{dv_y}{dt} = F_y + \phi_y, M \frac{dv_z}{dt} = F_z + \phi_z, \quad (40)$$

where the projections of the reactive force are

$$\phi_x = \frac{dM}{dt}(u_x - v_x), \phi_y = \frac{dM}{dt}(u_y - v_y), \phi_z = \frac{dM}{dt}(u_z - v_z) \quad (41)$$

For the reference system $S_{\xi\eta\zeta}$, fixed to the body with the origin S in center of body mass, inertial tensor I has nine components, but only six of them are independent: I_ξ, I_η, I_ζ are the moments of inertia, and $I_{\xi\eta}, I_{\eta\zeta}, I_{\zeta\xi}$ are centrifugal moments of inertia. If axes are principal and centrifugal moments of inertia that are zero, inertial tensor I has only three principal moments of inertia I_ξ, I_η, I_ζ . Angular velocity Ω has three components Ω_ξ, Ω_η and Ω_ζ , in this frame. If $\Omega_{2\xi}, \Omega_{2\eta}, \Omega_{2\zeta}$ are components of the angular velocity Ω_2 , M_ξ^Φ, M_η^Φ and M_ζ^Φ are body-axis components of M_S^Φ , M_ξ, M_η and M_ζ are body-axis components of M_S^{Fr} and $\mathcal{M}_\xi, \mathcal{M}_\eta$ and \mathcal{M}_ζ are projections of the torque vector \mathcal{M} , relation (29) gives equations

$$\begin{aligned} I_\xi \frac{d\Omega_\xi}{dt} + (I_\zeta - I_\eta)\Omega_\eta\Omega_\zeta &= M_\xi + \mathcal{M}_\xi + M_\xi^\Phi + \mathfrak{M}_\xi \\ I_\eta \frac{d\Omega_\eta}{dt} + (I_\xi - I_\zeta)\Omega_\xi\Omega_\zeta &= M_\eta + \mathcal{M}_\eta + M_\eta^\Phi + \mathfrak{M}_\eta \\ I_\zeta \frac{d\Omega_\zeta}{dt} + (I_\eta - I_\xi)\Omega_\xi\Omega_\eta &= M_\zeta + \mathcal{M}_\zeta + M_\zeta^\Phi + \mathfrak{M}_\zeta \end{aligned} \quad (42)$$

where the components of the reactive torque \mathfrak{M}_S are

$$\mathfrak{N}_\xi = \frac{dI_\xi}{dt}(\Omega_{2\xi} - \Omega_\xi), \mathfrak{N}_\eta = \frac{dI_\eta}{dt}(\Omega_{2\eta} - \Omega_\eta), \mathfrak{N}_\zeta = \frac{dI_\zeta}{dt}(\Omega_{2\zeta} - \Omega_\zeta) \quad (43)$$

Equations (40) and (42) are six scalar differential equations of motion of the body with variable mass.

4 Vibration of the Oscillator with Continual Mass Variation

Let us consider a one-degree-of-freedom oscillator modeled as a mass–spring system (Fig. 2). In general, the mathematical model of this oscillator is (42)₁

$$M \frac{dv_x}{dt} = F_x + \frac{dM}{dt}(u_x - v_x). \quad (44)$$

If it is assumed that the mass separation is with absolute velocity $u_x = 0$ and the elastic force in the spring is a nonlinear deflection function

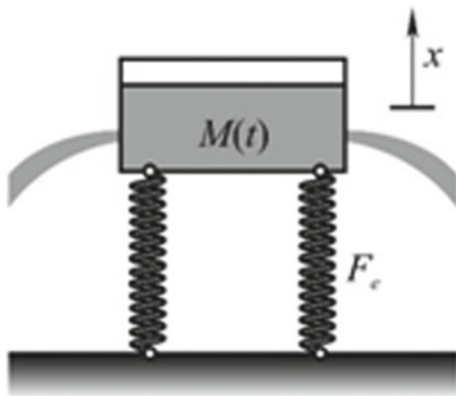
$$F_x = -kx|x|^{\alpha-1} \quad (45)$$

where k is a constant parameter and $\alpha \in \mathbb{R}$ (integer or non-integer not smaller than one) is the order of nonlinearity, the equation of motion is for $v_x = \dot{x}$

$$M\ddot{x} + kx|x|^{\alpha-1} = -\frac{dM}{dt}\dot{x} \quad (46)$$

Assuming that the mass variation is a slow time function, i.e., $M = M(\tau)$, where $\tau = \varepsilon t$ is the ‘slow time’ and $\varepsilon \ll 1$ is a small parameter, the (46) is rewritten as

Fig. 2 Model of the oscillator with variable mass



$$\ddot{x} + \omega^2(\tau)x|x|^{\alpha-1} = -\frac{\varepsilon}{M(\tau)} \frac{dM}{d\tau} \dot{x} \quad (47)$$

where

$$\omega^2(\tau) = \frac{k}{M(\tau)} \quad (48)$$

It is impossible to obtain the exact analytic solution of the (47).

In this paper, an asymptotic solving procedure is developed. It is based on the exact solution of the equation with constant parameters. Namely, if the small perturbation parameter ε is zero and the corresponding slow time is $\tau = 0$, the (47) transforms into

$$\ddot{x} + \omega^2(0)x|x|^{\alpha-1} = 0 \quad (49)$$

where $\omega^2(0) = \frac{k}{M(0)}$. However, the (49) has the exact solution [27] in the form of the Ateb (inverse beta) function [28]

$$x = Aca(\alpha, 1, \psi), \dot{x} = -\frac{2A\Omega}{\alpha+1}sa(1, \alpha, \psi), \ddot{x} = -\frac{2A\Omega^2}{\alpha+1}ca^{\alpha+1}(\alpha, 1, \psi) \quad (50)$$

where ψ is the phase angle of the function

$$\psi = \Omega t + \theta \quad (51)$$

Ω is the frequency of the function

$$\Omega^2 = \frac{\alpha+1}{2}\omega^2(0)A^{\alpha-1} \quad (52)$$

A and θ are constants of integration.

We assume the solution of (47) in the form (50), but with time-variable parameters $A(t)$ and $\psi(t)$, i.e., $\theta(t)$

$$x = A(t)ca(\alpha, 1, \psi(t)), \dot{x} = -\frac{2A(t)\Omega(t)}{\alpha+1}sa(1, \alpha, \psi(t)), \quad (53)$$

where

$$\Omega^2(t) = \frac{\alpha+1}{2}\omega^2(t)A^{\alpha-1}(t) \quad (54)$$

Differentiating (53)₁ and equating with (53)₂, the constraint follows

$$\dot{A}(t)ca(\alpha, 1, \psi(t)) - \frac{2A(t)\dot{\theta}(t)}{\alpha+1}sa(1, \alpha, \psi(t)) = 0 \quad (55)$$

Differentiating (53)₂, it is

$$\ddot{x} = -\frac{2(\dot{A}(t)\Omega(\tau) + A(t)\dot{\Omega}(\tau))}{\alpha + 1}sa(1, \alpha, \psi(t)) - \frac{2A(t)\Omega^2(\tau)}{\alpha + 1}ca^{\alpha+1}(\alpha, 1, \psi(t)) - \frac{2A(t)\Omega(\tau)\dot{\theta}(t)}{\alpha + 1}ca^{\alpha+1}(\alpha, 1, \psi(t)) \quad (56)$$

Substituting (53) and (53) into (47) and after some modification, it is

$$\begin{aligned} & -\frac{2(\dot{A}(t)\Omega(\tau) + A(t)\dot{\Omega}(\tau))}{\alpha + 1}sa(1, \alpha, \psi(t)) - \frac{2A(t)\Omega(\tau)\dot{\theta}(t)}{\alpha + 1}ca^{\alpha+1}(\alpha, 1, \psi(t)) \\ & = \frac{\varepsilon}{M(\tau)} \frac{2A(t)\Omega(\tau)}{\alpha + 1} \frac{dM}{d\tau} sa(1, \alpha, \psi(t)) \end{aligned} \quad (57)$$

(55) and (57) are two first-order equations which correspond to (47).

After uncoupling equations for \dot{A} and $\dot{\theta}$ and using the relations (48) and (54), it follows

$$\dot{A}(sa^2(1, \alpha, \psi) + ca^{\alpha+1}(\alpha, 1, \psi)) = -\frac{\varepsilon}{M} \frac{A}{\alpha + 1} \frac{dM}{d\tau} sa^2(1, \alpha, \psi) \quad (58)$$

$$A\dot{\theta}(sa^2(1, \alpha, \psi) + ca^{\alpha+1}(\alpha, 1, \psi)) = -\frac{\varepsilon A}{M} \frac{dM}{d\tau} sa(1, \alpha, \psi)ca(\alpha, 1, \psi) \quad (59)$$

Finally, for the identity [18]

$$sa^2(1, \alpha, \psi) + ca^{\alpha+1}(\alpha, 1, \psi) = 1 \quad (60)$$

it is

$$\dot{A} = -\frac{\varepsilon}{M} \frac{A}{\alpha + 1} \frac{dM}{d\tau} sa^2(1, \alpha, \psi), \quad A\dot{\theta} = -\frac{\varepsilon A}{M} \frac{dM}{d\tau} sa(1, \alpha, \psi)ca(\alpha, 1, \psi) \quad (61)$$

Equations (61) are the rewritten version of (47) into new variables: A and θ .

Bearing in mind that the Ateb functions are time periodic, the averaging of the equations over the period $T = \frac{2\pi\alpha}{\Omega}$ where $2\pi\alpha = 2B\left(\frac{1}{\alpha+1}, \frac{1}{2}\right)$ and B is the complete beta function is done. For

$$\begin{aligned} \frac{1}{T} \int_0^T sa^2(1, \alpha, \psi) d\psi &= \frac{\alpha + 1}{\alpha + 3}, \\ \frac{1}{T} \int_0^T sa(1, \alpha, \psi)ca(\alpha, 1, \psi) d\psi &= 0, \end{aligned} \quad (62)$$

averaged equations follow

$$\frac{\dot{A}}{A} = -\frac{1}{\alpha + 3} \frac{dM}{M}, \quad \dot{\theta} = 0 \tag{63}$$

Integrating the relations, it is obtained

$$A = A(0) \left(\frac{M(0)}{M} \right)^{\frac{1}{\alpha+3}}, \tag{64}$$

$$\psi = \theta(0) + A(0)^{\frac{\alpha-1}{2}} \int_0^t \left(\frac{M(0)}{M} \right)^{\frac{\alpha-1}{2(\alpha+3)}} \sqrt{\frac{\alpha+1}{2} \frac{k}{M(\tau)}} dt \tag{65}$$

Analyzing (64), it can be concluded: (a) If the order of the system is not varied and mass is increasing, amplitude of vibration decreases. Amplitude of vibration increases due to mass decrease.

(b) Order of nonlinearity has influence on the velocity of amplitude variation. If mass increases, velocity of amplitude decrease is higher for smaller orders of nonlinearity (Fig. 3a). Amplitude decreases the fastest in the linear oscillator, is approximately constant and corresponds to the initial one if the order of nonlinearity is extremely high. If mass is decreasing (Fig. 3b), the velocity of amplitude increase

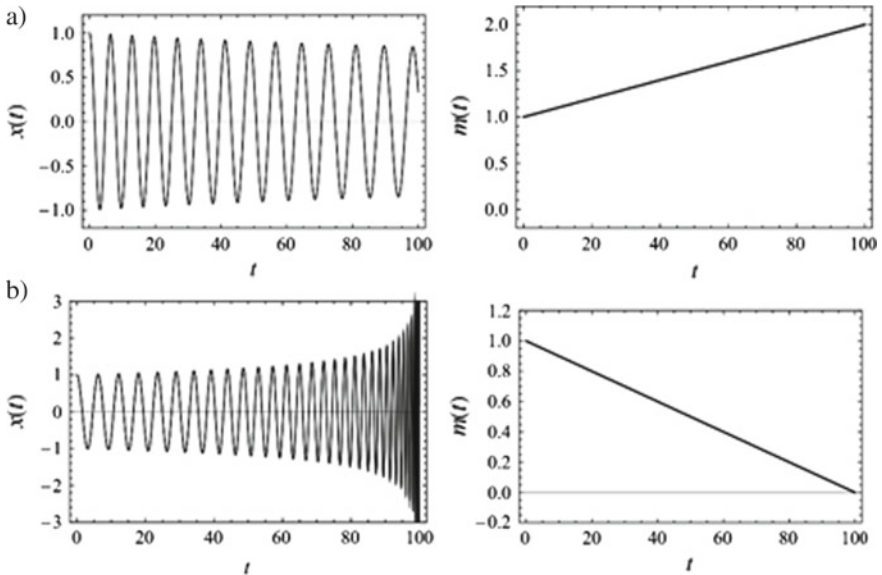


Fig. 3 Amplitude–time curves for various values of: **a** mass increases and **b** mass decreases

is higher for smaller orders of nonlinearity: Increase is the fastest for linear oscillator, while amplitude remains approximately constant for extremely high order of nonlinearity.

4.1 Reactive Force Is Omitted

In the most of published papers in vibrations of mass variable oscillators, the reactive force is omitted. For that case, the right side of the (47) is zero and the equations of vibration are

$$\dot{A} = \frac{\varepsilon}{M} \frac{A}{\alpha + 1} \frac{dM}{d\tau} sa^2(1, \alpha, \psi), \quad A\dot{\theta} = \frac{\varepsilon A}{M} \frac{dM}{d\tau} sa(\alpha, 1, \psi) ca(\alpha, 1, \psi) \quad (66)$$

The corresponding averaged equations are

$$\frac{\dot{A}}{A} = \frac{1}{\alpha + 3} \frac{dM}{M}, \quad \dot{\theta} = 0 \quad (67)$$

After integration, the amplitude and angle variation follow

$$A = A(0) \left(\frac{M}{M(0)} \right)^{\frac{1}{\alpha+3}}, \quad (68)$$

$$\psi = \theta(0) + A(0)^{\frac{\alpha-1}{2}} \int_0^t \left(\frac{M}{M(0)} \right)^{\frac{\alpha-1}{2(\alpha+3)}} \sqrt{\frac{\alpha+1}{2} \frac{k}{M(\tau)}} dt \quad (69)$$

Comparing the obtained solutions (64) and (68), it is obvious that the tendency of amplitude change is opposite for the two cases. Namely, if the mass is decreasing and the reactive force is assumed the amplitude of vibration increases. However, for the same mass decrease, if the reactive force is neglected the amplitude of vibration also decreases. This result is already obtained for the mass variable linear [29] and Duffing [30] oscillators. The result in the paper shows that it is generally the case for any oscillator with variable mass independently on the type of nonlinearity in elastic term.

5 Conclusion

The dynamics of the body with continual and discontinual mass variation is considered. In the rigid body which is separated into two parts, the linear and angular momentums are varying causing the change of the velocity of the mass center and of the angular velocity of the body. The linear and angular velocity variation is

jump-like, while the position of the parts is assumed to be invariant during separation. Based on the principles of the linear and angular momentum, the equations of motion for a body with continual mass variation are obtained. In the equations, the reactive force, reactive torque and moment of the reactive force occur. Reactive force and reactive torque are dynamic loadings which are evident only for those bodies whose mass is varying in time. The body which has the oscillatory motion and variable mass is considered. The one-degree-of-freedom oscillator is considered. Mathematical model of the system is formed using the equations developed in the paper. The equation is approximately solved using the Ateb functions. Two cases are analyzed: The reactive force is taken into consideration, and then, the reactive force is omitted. The results are quite opposite. It is concluded that in spite of the fact that the mass variation is small and slow the reactive force has to be taken into consideration. Otherwise, the obtained results are not correct.

Acknowledgements Investigation is supported by Faculty of Technical Sciences in Novi Sad (Proj. No. 05/2019).

References

1. I.V. Meshcherskij, *Rabotji po mehanike tel peremenoj massji* (Gos. Izd. tehniko-teoret.lit, Moscow, 1952)
2. A. Cayley, On a class of dynamical problems. Proc. R. Soc. London **III**, 506–511 (1857)
3. L. Ch. Dufour. Sur l'accélération séculaire du mouvement de la lune, *Comptes rendus des Seances de l'Ac. des Sc.* **LXII**, 840–842 (1866)
4. A. Oppalzer, Ueber die Ursache, welche den Unterschied zwischen der theoretischen berechneten Secularacceleration in der Laenge des Mondes und der thatsaechlichen bedingen kann. *Astron. Nachr.* **108**(2573), 67–72 (1884)
5. H. Gylden, Die Bahnbewegungen in einem Systeme von zwei Koerpern in dem Falle das Massen Veraenderungen unterworfen sind. *Astron. Nachr.* **109**(2593), 1–6 (1884)
6. I.V. Meshcherski. Odin chasnij sluchaj zadachi Gouldena. *Astronomische Nachrichten* **132**(3153), 9 (1893)
7. J. Fejoz. Quasiperiodic motions in the planar three-body problem. *J. Diff. Equat.* **183**, 303–341 (2002)
8. J. Fiol, R.E. Olson. Three- and four-body dynamics in fast heavy ion atom ionization. *J. Phys. B At. Mol. Opt. Phys.* **37**, 3947–3960 (2004)
9. L. Cveticanin, Particle separation form a four particle system. *Eur. J. Mech. A/Solids* **26**, 270–285 (2007)
10. J.E. Howard, Particle dynamics with variable mass and charge. *Phys. Lett. Sect. A Gener. At. Solid State Phys.* **366**(1–2), 91–96 (2007)
11. L. Cveticanin, D. Djukic, Dynamic properties of a body with discontinual mass variation. *Nonlinear Dyn* **52**(3), 249–261 (2008)
12. L. Cveticanin, *Dynamics of Bodies with Time Variable Mass* (Springer, Berlin, 2015)
13. I.V. Meshchersky, *Dinamika tochki peremenoj massji* (Peterburgski Universitet, Petersburg, Magistarskaja disertacija, 1897)
14. L. Meirovitch, General motion of a variable-mass flexible rocket with internal flow. *J. Spacecraft Rockets* **7**(2), 186–195 (1970)
15. J.W. Cornелиsse, H.F.R. Schoyer, K.F. Wakker, *Rocket Propulsion and Space Fleight Dynamics* (Pitman, London, 1979)

16. L. Cveticanin, Self-excited vibrations of the variable mass rotor/fluid system. *J. Sound Vib.* **212**(4), 685–702 (1998)
17. F.O. Eke, T.C. Mao, On the dynamics of variable mass systems. *Int. J. Mech. Eng. Educ.* **30**(2), 123–137 (2002)
18. T. Tran, F.O. Eke, Effects of internal mass flow on the attitude dynamics of variable mass systems. *Adv. Astronaut. Sci.* **119**(Issue SUPPL.), 1297–1316 (2005)
19. L. Cveticanin, Dynamics of the mass variable body, in *Dynamics of Mechanical Systems with Variable Mass*, eds. by H. Irschik, A. Belyaev, *Series CISM International Centre for Mechanical Sciences 557* (Springer, Berlin, 2014)
20. L. Cveticanin, M. Zukovic, D. Cveticanin, Oscillator with variable mass excited with non-ideal source. *Nonlinear Dynamics*, **92**(2), 673–682 (2018)
21. M.S. Abdalla, Canonical treatment of harmonic oscillator with variable mass. *Phys. Rev. A* **33**(5), 2870–2876 (1986)
22. M.S. Abdalla, Time-dependent harmonic oscillator with variable mass under the action of a driving force. *Phys. Rev. A* **34**(6), 4598–4605 (1986)
23. G. Crespo, A.N. Proto, A. Plastino, D. Otero, Information-theory approach to the variable-mass harmonic oscillator. *Phys. Rev. A* **42**(6), 3608–3617 (1990)
24. J. Flores, G. Solovey, S. Gill, Variable mass oscillator. *Am. J. Phys.* **71**(7), 721–725 (2003)
25. Ya.F. Kayuk, V.I. Denisenko, Motion of a mechanical system with variable mass - inertial characteristics. *Int. Appl. Mech.* **40**(7), 814–820 (2004)
26. H. Irschik, H.J. Holl, Mechanics of variable-mass-systems - Part I: balance of mass and linear momentum. *Appl. Mech. Rev.* **57**(2), 145–161 (2004)
27. L. Cveticanin, *Strong Nonlinear Oscillators: Analytical Solutions* (Springer, Berlin, 2018)
28. R. Rosenberg, The ateb(h)-functions and their properties. *Q. Appl. Math.* **21**(1), 37–47 (1963)
29. A.P. Bessonov, *Osnovji dinamiki mehanizmov s peremenoj masoj zvenjev* (Nauka, Moscow, 1967)
30. L. Cveticanin, The influence of the reactive force on a nonlinear oscillator with variable parameter. *J. Vib. Acoust. Trans. ASME* **114**(4), 578–580 (1992)

An Approximate Analytical Solution of Transversal Oscillations with Quintic Nonlinearities



Nicolae Herisanu, Vasile Marinca, and Cristina Chilibaru-Opritescu

Abstract Free damped vibrations of a hinged–hinged Euler–Bernoulli beam subject to a constant axial force at its free end is investigated. The quintic nonlinear equation of motion is derived from Hamilton’s principle and then solved using the optimal auxiliary function method (OAFM). Our proposed procedure is highly efficient and controls the convergence of the solutions, ensuring an excellent accuracy after the first iteration. Numerical values are also obtained in order to validate the analytical results.

1 Introduction

The nonlinear oscillations of the beams received considerable attention over many years. Structures like airplane wings, bridges, buildings, helicopter rotor blades, robot arms, or drill strings can be modeled as a beam-like member. It is very important to give an accurate analysis of the nonlinear vibration of these structures. Nonlinear dynamic problems have fascinated engineers, mathematicians, and physicists for a long time. Geometrically, nonlinear vibration of beams with different boundary conditions has long history. Many analytical and numerical studies were reported in the open literature.

Pakdemirli [1] showed that first discretizing the partial differential equation and then applying perturbation methods lead to incorrect results. An accurate solution is obtained by perturbation methods directly to the partial differential equations. Approximate method for analyzing the vibrations of an Euler–Bernoulli beam resting on a nonlinear elastic foundation is discussed by Nayfeh and Lacarbonara [2] in the cases of primary and subharmonic resonance. They proved that the approximate

N. Herisanu (✉) · C. Chilibaru-Opritescu
Politehnica University Timisoara, 300222 Timisoara, Romania
e-mail: nicolae.herisanu@upt.ro

N. Herisanu · V. Marinca
Centre for Advanced Technical Research-CCTFA, Romanian Academy, Branch of Timisoara,
300222 Timisoara, Romania

solutions based on discretization via the Galerkin method are contrasted with direct application of the multiple scales method.

The nonlinear characteristics of the parametric resonance of simply supported elastic beams are investigated by Son et al. [3] considering the instability in the lowest mode, whereas Ghayesh and Balar [4] considered the motion of the parametric vibrations of an axially moving Timoshenko beam taking into consideration two nonlinear models. Abe [5] proposed an accuracy improvement to the multiple scales method for nonlinear vibration analyses of continuous systems with quadratic and cubic nonlinearities. Based on differential quadrature method, Peng et al. [6] proposed a new semianalytic method for the geometrically nonlinear vibration of Euler–Bernoulli beams with different boundary conditions. The supercritical equilibrium solutions of an axially moving beam supported by sleeves with torsion springs are analyzed by Ding et al. [7]. The supercritical transport speed ranger, equilibria, and critical speeds of axially moving beams with hybrid boundary conditions are calculated from a nonlinear integro–partial–differential equation. Huang et al. [8] studied the fundamental and subharmonic resonances of an axially moving beam subject to periodic lateral force excitation. The incremental harmonic balance method was used to evaluate the nonlinear dynamic behavior.

Local bifurcations of a nonlinear beam under parametric excitation are studied by Zhang et al. [9], and Sedighi et al. [10] presented an analytical solution for vibrations of quintic nonlinear beam. Bayat and Pokar [11] implemented the variational approach for the Duffing equation with constant coefficients and for a restrained uniform beam carrying an intermediate lumped mass. Al-Qaisia and Hamdan [12] investigated the effect of an initial geometric imperfection on the in-plane nonlinear natural frequencies of an elastic Euler–Bernoulli beam resting on a Winkler elastic foundation. Bayat et al. [13] studied the nonlinear free vibration of a cylindrical shell by introducing the extended version of the Hamiltonian approach. Poorjamshidian et al. [14] presented the nonlinear vibration of a simple-supported flexible beam with constant velocity carrying a moving mass. The response time of the beam is obtained by means of a combination of the homotopy method and traditional perturbation. Wang et al. [15] considered the buckling of Euler–Bernoulli columns coupled with Eringen’s nonlocal theory under a tip load and uniformly distributed axial load. Analytical solutions for this type of clamped-free beam were derived.

The main objective of the present work is to propose an accurate procedure to obtain an analytical solution for vibrations of a beam with quintic nonlinearity. The optimal auxiliary function method (OAFM) is applied to find analytical approximate solutions of the governing nonlinear differential equations. An example is given which shows that our technique is simple, easy to use, and very accurate. This method is independent of the presence of small or large parameters and is based on the construction and determination of the linear operator and of the auxiliary functions, combined with a convenient way to optimally control the convergence of the solution. An accurate and explicitly analytical solution is obtained using only the first iteration.

2 The Governing Equation

In what follows, we consider a flexible Euler–Bernoulli beam of length l subjected by a constant axial force $P = P_0$ (Fig. 1).

The Cartesian coordinate system is adopted in the symmetric plane of the beam, and w is displacement of a point in the middle plane of the beam in y -direction. In Fig. 2 is considered an infinitesimal length of the Euler–Bernoulli beam with the ends F and G.

Applying the Hamilton’s principle, we obtain [9, 10]:

$$\delta \int_{t_1}^{t_2} L dt + \int_{t_1}^{t_2} \delta W dt = 0 \tag{1}$$

with L the Lagrange function and W the virtual work. The kinetic energy of the beam is $T = \frac{m}{2} \int_0^l (u_t^2 + v_t^2) dx$, m being the mass per unit length of the beam, and (u, v) are longitudinal and transversal displacement, respectively, of end F from Fig. 2. The strain potential energy of the beam is $U = \frac{1}{2E} \int_v \sigma^2 dv$, where we consider the linear relation between the stress and strain $\sigma = E\varepsilon$. The total strain of the point F is $\varepsilon = \varepsilon_0 + \varepsilon_1$ where the strain caused by the axial displacement of the beam is $\varepsilon_0 = \frac{ds-dx}{dx} = \sqrt{(1 + u_x)^2 + v_x^2} - 1$, and the strain of the point F located at the distance z from the middle plane, caused by the rotation of the cross-sectional plane $\theta(x, t)$ is $\varepsilon_1 = z \frac{d\theta}{ds} = z [W_{xx}(1 + W_x^2)^{-3/2}]$. By means of Taylor series, the strains ε_0 and ε_1 can be written in the form [9, 10]

Fig. 1 Flexible Euler–Bernoulli beam

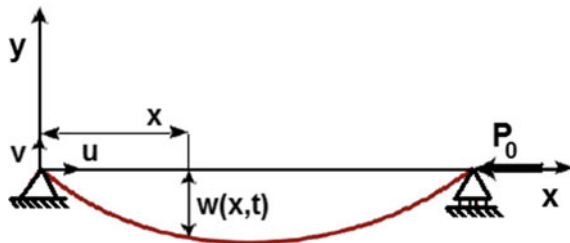
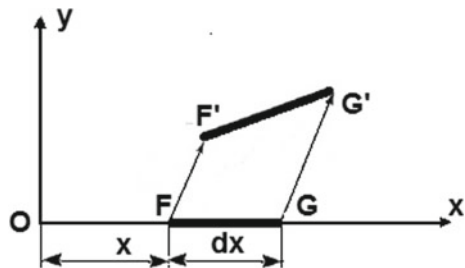


Fig. 2 A segment of an infinitesimal length



$$\varepsilon_0 = u_x + \frac{1}{2}W_x^2 - \frac{1}{8}W_x^4 - \frac{1}{2}u_x W_x^2 \quad (2)$$

$$\varepsilon_1 = z \left(W_{xx} - \frac{3}{2}W_x^2 W_{xx} \right) \quad (3)$$

where $u_x = \partial u / \partial x$. It follows that the strain potential energy of the beam is

$$U = \frac{EA}{2} \int_0^l \left[u_x + \frac{1}{2}W_x^2 - \frac{1}{8}W_x^4 - \frac{1}{2}u_x W_x^2 \right]^2 dx + \frac{EI}{2} \int_0^l \left[W_x^2 - \frac{3}{2}W_x^2 W_{xx} \right]^2 dx \quad (4)$$

where A is the area of the beam of length dx and $I = \int_0^l z^2 dA$.

The virtual work is given by the applied force P_0 and by the damping, such that

$$\int_{t_1}^{t_2} \delta W dt = - \int_{t_1}^{t_2} P_0 \delta u(l, t) dt - \int_{t_1}^{t_2} \int_0^l c W_t \delta W dx dt \quad (5)$$

where c is the damping coefficient.

If it is considered that no interaction occurs between transverse and longitudinal vibrations and therefore the longitudinal inertia can be neglected, then the governing equation of hinged–hinged beam subjected to axial constant force is

$$\begin{aligned} m W_{tt} + c W_t + EI \left(\frac{27}{2} W_x^2 W_{xx}^3 - 3 W_{xx}^3 - 3 W_x^2 W_{xxxx} + \frac{9}{4} W_x^4 W_{xxxx} + W_{xxxx} \right) \\ + P_0 \left(W_{xx} + \frac{3}{2} W_x^2 W_{xx} \right) = 0 \end{aligned} \quad (6)$$

Supposing the transverse deflection w in the form

$$w(x, t) = X(x)T(t) \quad (7)$$

where T is the amplitude of the fundamental transverse mode and X is the first eigenmode of the hinged–hinged Euler–Bernoulli beam, of the form $X(x) = \sin \pi x / l$, and applying the Galerkin method, from (6) we obtain

$$m \ddot{T} + c \dot{T} + \left(\frac{EI \pi^4}{l^4} - \frac{P_0 \pi^2}{l^2} \right) T - \left(\frac{P_0 \pi^4}{2l^4} + \frac{7EI \pi^6}{8l^6} \right) T^3 - \frac{27EI \pi^8}{20l^8} T^5 = 0 \quad (8)$$

Making the transformations

$$\begin{aligned}\bar{i} &= \left(\frac{EI}{ml^4}\right)^{1/2}, \bar{T} = \frac{lT}{r^2}, \mu = \frac{cl^2}{(mEI)^{1/2}}, \omega_n^2 = \pi^4 - \frac{P_0 l^2 \pi^2}{2EI l^4}, \\ \beta &= \left(\frac{P_0}{2EI} + \frac{7\pi^2}{8l^2}\right) \frac{r^4 \pi^4}{2EI l^4}, \delta = \frac{27}{20} \left(\frac{r\pi}{l}\right)^8\end{aligned}\quad (9)$$

where r is the radius of gyration of the beam cross section, then introducing the damping coefficient as

$$\mu(\bar{Y}) = \mu - \alpha \bar{Y}^2 + \gamma \bar{Y}^4 \quad (10)$$

And finally omitting the bar, we obtain the following nondimensional governing equation with constant excitation and quintic nonlinear term:

$$\ddot{T} + (\mu - \alpha T^2 + \gamma T^4)\dot{T} + \omega_n^2 T - \beta T^3 - \delta T^5 = 0 \quad (11)$$

Equation (11) describes the transversal vibrations of a hinged–hinged flexible beam subjected to a constant axial force. For the nonlinear differential equation with variable coefficients, we will use the OAFM [16–20].

3 OAFM for Nonlinear Differential Equation (11)

The initial conditions for (11) are

$$T(0) = a, \dot{T}(0) = 0 \quad (12)$$

where the amplitude a is unknown at this moment. The frequency of the system (11) is Ω , such that making the transformations

$$\tau = \Omega t, T(\tau) = ay(\tau) \quad (13)$$

The original Equation (11) can be rewritten in the form

$$y'' + \frac{1}{\Omega}(\mu - \alpha a^2 y^2 + \gamma a^4 y^4)y' + \frac{\omega_n^2}{\Omega^2}y - \frac{\beta}{\Omega^2}a^2 y^3 - \frac{\delta}{\Omega^2}a^4 y^5 = 0 \quad (14)$$

and the initial conditions (12) become

$$y(0) = 1, y'(0) = 0 \quad (15)$$

where primes denote differentiation with respect to τ .

The linear and nonlinear operators for (11) are, respectively

$$L(y) = y'' + y \quad (16)$$

$$N(y) = \left(\frac{\omega_n^2}{\Omega^2} - 1 \right) y + \frac{1}{\Omega} (\mu - \alpha a^2 y^2 + \gamma a^4 y^4) y' - \frac{\beta}{\Omega^2} a^4 y^5 \quad (17)$$

Assuming that the approximate analytical solution for (14) and (15) is

$$\bar{y}(\tau) = y_0(\tau) + y_1(C_i, \tau), \quad i = 1, 3, \dots, n \quad (18)$$

where C_i are the convergence-control parameters whose optimal values will be determined later. Then, the initial approximation $y_0(\tau)$ is obtained from equation

$$L(y_0(\tau)) = 0, \quad y_0(0) = 1, \quad y_0'(0) = 0 \quad (19)$$

The solution of (19) is

$$y_0(\tau) = \cos \tau \quad (20)$$

Substituting (20) into (17), we obtain

$$N(y_0(\tau)) = A_1 \cos \tau + A_2 \sin \tau + A_3 \cos 3\tau + A_4 \sin 3\tau + A_5 \cos 5\tau + A_6 \sin 5\tau \quad (21)$$

where

$$\begin{aligned} A_1 &= \frac{\omega_n^2}{\Omega^2} - 1 - \frac{10\delta a^4}{\Omega^2}, \quad A_2 = -\frac{1}{\Omega} \left(\mu - \frac{3}{4}\alpha a^2 + \frac{3}{8}\gamma a^4 \right), \quad A_3 = -\frac{5\delta a^4}{16\Omega^3} \\ A_4 &= \frac{\alpha a^2}{4\Omega} - \frac{5\delta a^4}{16\Omega}, \quad A_5 = -\frac{\delta a^4}{16\Omega^3}, \quad A_6 = -\frac{\gamma a^4}{16\Omega} \end{aligned} \quad (22)$$

The function given by (20) and (21) is “source” for the auxiliary functions, such that the first approximation $y_1(C_i, \tau)$ is obtained from the following equation:

$$\begin{aligned} y_1'' + y_1 &= (C_1 + 2C_2 \cos 2\tau + 2C_2 \sin 2\tau + 2C_3 \cos 4\tau + 2C_5 \sin 4\tau)(A_1 \cos \tau \\ &\quad + A_3 \cos 3\tau + A_6 \sin 5\tau), \\ y_1(0) &= y_1'(0) = 0 \end{aligned} \quad (23)$$

From (23), y_1 is immediately obtained, such that the approximate solution (18) becomes

$$\begin{aligned} \bar{y}(\tau, C_i) &= a \cos \tau + \frac{a}{8} (A_3 C_1 + A_1 C_2 + A_6 C_3 + A_1 C_4) (\cos \tau - \cos 3\tau) \\ &\quad + \frac{a}{8} (A_6 C_2 + A_1 C_3 + A_1 C_5) (3 \sin \tau - \sin 3\tau) + \frac{a}{24} (A_3 C_2 + A_1 C_4) \end{aligned}$$

$$\begin{aligned}
 &\times (\cos \tau - \cos 5\tau) + \frac{a}{24}(A_6C_1 + A_3C_3 + A_1C_5)(5 \sin \tau - \sin 5\tau) \\
 &+ \frac{a}{48}(A_3C_4 - A_6C_3)(\cos \tau - \cos 7\tau) + \frac{a}{48}(A_6C_2 + A_3C_5)(7 \sin \tau \\
 &- \sin 7\tau) - \frac{a}{80}A_6C_5(\cos \tau - \cos 9\tau) + \frac{a}{80}A_6C_4(9 \sin \tau - \sin 9\tau)
 \end{aligned}
 \tag{24}$$

where the values of the convergence-control parameters $C_i, i = 1, 2, \dots, 5$ are optimally determined.

4 Numerical Example

We illustrate the accuracy of our procedure, considering the case corresponding to the following values of the physical parameters involved in (11): $\gamma = 2.5; \alpha = 2.5; \delta = 0.8; \beta = 3.5; \mu = -0.05; \omega_n = 9.83$.

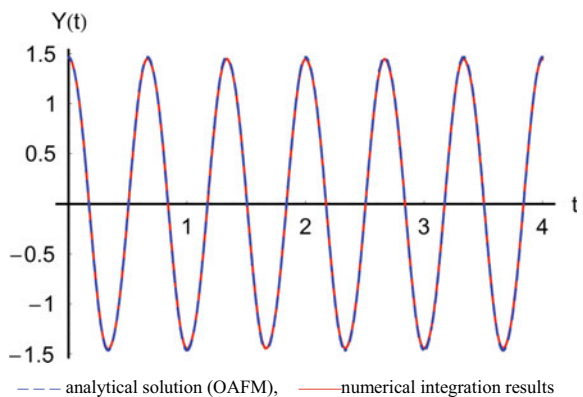
By means of the procedure described in [16], we obtain

$$\begin{aligned}
 C_1 &= 0.145927735933; C_2 = -0.128431942959; C_3 = -0.0043147480105; \\
 C_4 &= 0.070184012124; C_5 = -0.229972288472; \\
 a &= 1.464442738889; \Omega = 9.420966459723
 \end{aligned}
 \tag{25}$$

As depicted in Fig. 3, the analytical results and numerical integration results obtained using a fourth-order Runge–Kutta method are almost identical.

Note that our technique can be expanded to predict the beam response under different boundary conditions and also to other nonlinear problems.

Fig. 3 Comparison between the approximate solution (24) and numerical solution for $\gamma = 2.5; \alpha = 2.5; \delta = 0.8; \beta = 3.5; \mu = -0.05; \omega_n = 9.83$



5 Conclusions

In this work, we present a reliable procedure, namely the OAFM to analytically solve a nonlinear differential equation of transversal vibration of hinged–hinged flexible beam. Using Galerkin’s method and suitable transformations, the governing equation is transformed into a nonlinear differential equation. Our technique is valid even if the nonlinear differential equation does not contain any small or large parameters. Our construction is completely different in comparison with any other procedures known in the literature. We refer to the linear operator and to the auxiliary functions which contain several convergence-control parameters C_i , which ensure a fast convergence of the solution after the first iterations. This procedure is effective, explicit, and very accurate and can be applied to other nonlinear dynamical systems.

References

1. M. Pakdemirli, A comparison of two perturbation methods for vibrations of systems with quadratic and cubic nonlinearities. *Mech. Res. Commun.* **21**(2), 203–208 (1994)
2. A. Nayfeh, W. Lacarbonara, On the discretization of distributed-parameter systems with quadratic and cubic nonlinearities. *Nonlinear Dyn.* **13**, 203–220 (1997)
3. I.S. Son, Y. Uchiyama, W. Lacarbonara, H. Yabuno, Simply supported elastic beams under parametric excitation. *Nonlinear Dyn.* **53**, 129–138 (2008)
4. M.H. Ghayesh, S. Balar, Non-linear parametric and stability analysis of two dynamic models of axially moving Timoshenko beams. *Appl. Math. Model.* **34**, 2850–2859 (2010)
5. A. Abe, Accuracy improvement of the method of multiple scales for nonlinear vibration analyses of continuous systems with quadratic and cubic nonlinearities. *Math. Probl. Eng.* Art ID 890813 (2010)
6. J.S. Peng, Y. Lui, J. Yang, A semianalytical method for nonlinear vibration of Euler-Bernoulli beams with general boundary conditions. *Math. Probl. Eng.* Art ID 591786 (2010)
7. H. Ding, G.C. Zhang, L.Q. Chen, Supercritical equilibrium solutions of axially moving beams with hybrid boundary conditions. *Mech. Res. Commun.* **38**, 52–56 (2011)
8. J.L. Huang, R.K.L. Su, W.H. Li, S.H. Chen, Stability and bifurcation of an axially moving beam tuned to three-to-one internal resonances. *J. Sound Vib.* **330**, 471–485 (2011)
9. W. Zhang, X.W. Feng, W.Z. Jean, Local bifurcations and codimension-3 degenerate bifurcations of quintic nonlinear beam under parametric excitation. *Chaos, Solitons Fractals* **24**, 977–998 (2005)
10. H.M. Sedighi, K.H. Shirazi, J. Zare, An analytical solution of transversal oscillation of quintic non-linear beam with homotopy analysis method. *Int. J. Non-Linear Mech.* **47**, 777–784 (2012)
11. M. Bayat, I. Pokar, On the approximate analytical solution to non-linear oscillation systems. *Shock Vib.* **20**, 43–52 (2013)
12. A.A. Al-Qaisia, M.H. Hamdan, On nonlinear frequency veering and mode localizations of a beam with geometric imperfection resting on elastic foundation. *J. Sound Vib.* **332**, 4641–4655 (2013)
13. M. Bayat, I. Pokar, L. Cveticanin, Nonlinear vibration of stringer shell by means of extended Hamiltonian approach. *Arch. Appl. Mech.* **84**, 43–50 (2014)
14. M. Poorjamshidian, J. Sheiki, S.M. Moghadas, M. Nakhaie, Nonlinear vibrations analysis of the beam carrying a moving mass using modified homotopy. *J. Solid Mech.* **6**, 389–396 (2014)
15. C.M. Wang, H. Zhang, N. Challamel, Y. Xiong, Buckling of nonlocal columns with allowance for selfweight. *J. Eng. Mech.* **142**, 04016037 (2016)

16. N. Herisanu, V. Marinca, G. Madescu, F. Dragan, Dynamic response of a permanent magnet synchronous generator to a wind gust. *Energies* **12**(5), 915 (2019)
17. V. Marinca, N. Herisanu, The nonlinear thermomechanical vibration of a functionally graded beam on Winkler-Pasternak foundation, in *MATEC web of conferences*, vol. 148, p. 13004 (2018)
18. V. Marinca, N. Herisanu, Vibration of nonlinear nonlocal elastic column with initial imperfection. *Springer Proc. Phys.* **198**, 49–56 (2018)
19. N. Herisanu, V. Marinca, Free oscillations of Euler-Bernoulli beams on nonlinear Winkler-Pasternak foundation. *Springer Proc. Phys.* **198**, 41–48 (2018)
20. B. Marinca, V. Marinca, Approximate analytical solution for thin film flow of a fourth grade fluid down a vertical cylinder. *Proc. Rom. Acad. Ser.* **A19**, 69–76 (2018)

Optimal Auxiliary Functions Method for Nonlinear Vibration of Doubly Clamped Nanobeam Incorporating the Casimir Force



Vasile Marinca and Nicolae Herisanu

Abstract The optimal auxiliary functions method is implemented in this paper to derive an analytical approximate solution for the problem of nonlinear vibrations of doubly clamped nanobeam incorporating the Casimir force. A closed form solution is obtained. This model accounts for the inherent nonlinearity of the Casimir force and the geometric nonlinearity of mid-plane stretching. Our technique is optimized to accelerate the convergence of approximate solutions via the presence of the optimal convergence-control parameters. The procedure does not depend upon small or large parameters ensuring a very fast convergence, after the first iteration. Numerical developments are presented in order to validate the analytical approximate results.

1 Introduction

It is known that analytical approximate solutions of nonlinear differential equations which describe various phenomena in science and technology are often difficult to obtain. Micromechanical systems (MEMS), micro-sensors and actuators are an extension of microelectronics and integrated circuits technology. Because of their small size, low fabrication cost, performance and suitability for integration into complex functional engineering systems, they are important components of many commercial systems including metal alloy, accelerometers for airbag deployment in automobiles, single crystal silicon switches, filters, resonators, sensors, ink jet printer heads, atomic force microscopes, and so on. Nonlinearity usually arises from sources such as electrostatic actuation itself, squeeze-film damping, geometric nonlinearities and intermolecular forces, i.e., Casimir or van der Waals.

N. Herisanu (✉)

Politehnica University Timisoara, 300222 Timisoara, Romania

e-mail: nicolae.herisanu@upt.ro

V. Marinca · N. Herisanu

Centre for Advanced Technical Research-CCTFA, Romanian Academy, Branch of Timisoara, 300222 Timisoara, Romania

© Springer Nature Switzerland AG 2021

N. Herisanu and V. Marinca (eds.), *Acoustics and Vibration of Mechanical*

Structures—AVMS 2019, Springer Proceedings in Physics 251,

https://doi.org/10.1007/978-3-030-54136-1_5

Numerous analytical, numerical or experimental investigations have been conducted on the electrostatic and electrodynamic behaviors of the microbeams. Lin and Zhao [1] studied the bifurcation behavior of nanoscale electrostatic actuators taking into consideration the presence of the Casimir force. Stability analysis showed that one equilibrium point is Hopf point, and other is unstable saddle point when there are two equilibrium points. Hu [2] derived the total system energy expressions based on Euler–Bernoulli beam and by neglecting the fringing field capacitances. The closed form solution based on the full-order model is obtained by means of the minimum energy and the assumed mode methods. Using the reduced-order models, he showed that the fourth- and third-order models are not as accurate as the full-order one. Rhoads et al. [3] regarded a microbeam device which couples the inherent benefits of a resonator with purely parametric excitation with the simple geometry of a microbeam. An approximate analytical solution to the pull-in voltage of a microbridge considering the elastic boundary effect, fringing field capacitance, residual stresses and the distributed flexibility of the bridge is proposed by Hu et al. [4]. The accuracy of the obtained results is verified by comparison with FEM packages, other solutions and with experimental measured data. The static pull-in instability of electrostatically actuated microbridges and microcantilevers is investigated by Mojahedi et al. [5] using the homotopy perturbation method. Soroush et al. [6] introduced Adomian decomposition method in the study of the pull-in behavior and the interval stress resultants of the nano-actuator using a distributed parameter model. Also, the effects of the van der Waals and Casimir forces are taken into account.

Yin et al. [7] established a new non-classical Bernoulli–Euler beam invoking size effect for electrostatically actuated microbeams by using the modified couple stress theory. Nonlinear terms associated with the mid-plane stretching and the electrostatic force are considered. Askari and Tahani [8] used the homotopy analysis method and Galerkin decomposition procedure to determine analytical approximate solutions for oscillatory behavior of a nanobeam under the effect of the Casimir force. Numerical integration is utilized to find critical value of the Casimir parameter to describe the pull-in instability. Kong [9] gets the pull-in instability model for Bernoulli–Euler microbeams based on a modified couple stress theory and presented the approximate analytical solutions to the pull-in voltage and pull-in displacement on the electrostatically actuated microbeam.

Caruntu et al. [10] proposed the reduced-order model method (ROM) to investigate the nonlinear parametric dynamics of electrostatically actuated MEMS cantilever resonators. Fringe effect and damping forces are included, and the method of multiple scales and ROM are compared in this study. Younis [11] presented an exact analytical solution of the electrostatically actuated initially deformed cantilever beam problem. Simple analytical expressions are derived for two configurations: the curled and tilted configurations for beams of tip deflection of few microns and for largely deformed beams. The pseudo-spectral method is adopted by Maida and Bianchi [12] to numerically solve the problem of pull-in instability in a cantilever microbeam. They showed that poor approximation leads to very unphysical oscillatory attraction/repulsion forces along the cantilever.

A novel procedure based on the Sturm’s theorem for real-valued polynomials is developed by Omarov et al. [13] to predict and identify periodic and non-periodic solutions for a graphene-based MEMS lumped parameter model with general initial conditions. The procedure is supplemented numerically by using Python codes. Skrzypacz et al. [14] presented bifurcation analysis of dynamic pull-in for a lumped model. The restoring force of the spring is derived based on the nonlinear constitutive stress–strain law, and the driving force of the mass attached to the spring is based on the electrostatic Coulomb force, respectively.

In the present work, we have obtained an approximate analytical solution for the nonlinear vibrations of doubly clamped nanobeam taking into account the Casimir force. For this purpose, we apply the optimal auxiliary functions method in a proper manner. Our technique does not contain restrictive hypotheses and is very rapidly convergent, after the first iteration. The approximate solutions are nearly identical with numerical integration results obtained by means of a fourth-order Runge–Kutta method.

2 Nonlinear Equation for Nanobeam

We consider a clamped–clamped narrow nanobeam of length l , width b , thickness h and density ρ under the action of the Casimir force, as shown in Fig. 1.

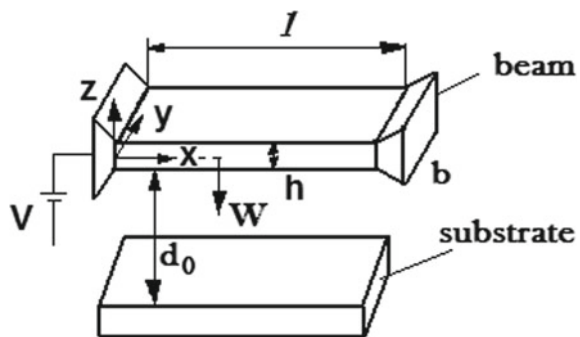
The distance between the beam and the stationary electrode is d_0 . In Fig. 1, x is the coordinate along the thickness, and W is deflection in the z -direction.

The Casimir force per unit length of the beam is [15]

$$F_c = \frac{\pi^2 \hbar c W}{240(d_0 - W)^4} \tag{1}$$

where $\hbar = 1.099 \times 10^{-34}$ Js is Planck’s constant divided by 2π and $c = 2.990 \times 10^8$ m/s is the speed of light in vacuum. If ν is Poisson’s ratio, I is the moment of inertia of cross section about y -axis, E is the effective Young’s modulus and incorporating

Fig. 1 Schematic of nanobeam with clamped–clamped boundary conditions



the von Karaman nonlinearity for mid-plane stretching, the equation of motion that governs the transverse deflection $W(x, t)$ of nanobeam, subjected to the Casimir force is as follow [8, 16]:

$$\rho b h \frac{\partial W(x, t)}{\partial t^2} + EI \frac{\partial^4 W(x, t)}{\partial t^4} - \left[N + \frac{E b h}{2l} \int_0^l \left(\frac{\partial W(x, t)}{\partial x} \right)^2 dx \right] \frac{\partial^2 W(x, t)}{\partial x^2} - F_c = 0 \quad (2)$$

where N is the axial loading. The kinematic boundary conditions for the nanobeam deflection of the double-clamped case are

$$W(0, t) = 0, \frac{\partial W(0, t)}{\partial x} = 0, W(l, t) = 0, \frac{\partial W(l, t)}{\partial x} = 0 \quad (3)$$

and the initial conditions are

$$W(x, 0) = 0, \frac{\partial W(x, 0)}{\partial t} = 0 \quad (4)$$

The following dimensionless variables are utilized

$$\hat{x} = \frac{x}{l}, \hat{t} = t \sqrt{\frac{EI}{\rho b k l^4}}, \hat{W} = \frac{W}{d_0}, \hat{N} = \frac{12l^2}{E b k^3} N, \alpha = 6 \left(\frac{d_0}{k} \right)^2, \lambda_4 = \frac{12l^4 \pi^2 \hbar c}{240 E k^3 d_0^5} \quad (5)$$

Using (2), the dimensionless equation of motion, dropping the hats, can be expressed as

$$\ddot{W} + W^{(IV)} - \left[\alpha \int_0^1 W'^2 dx + N \right] W'' - \frac{\lambda_4}{(1 - W)^4} = 0 \quad (6)$$

The boundary conditions (3) become

$$W(0, t) = 0, W'(0, t) = 0, W(1, t) = 0, W'(1, t) = 0 \quad (7)$$

where dot and prime denote derivative with respect to t and x , respectively.

By multiplying both sides of (6) by $(1 - W)^4$, we obtain

$$(1 - W)^4 + (1 - W)^4 W^{(IV)} - (1 - W)^4 \left[\alpha \int_0^1 W'^2 dx + N \right] W'' - \lambda_4 = 0 \quad (8)$$

3 Galerkin Formulation

Separating the dependence of the deflection on $W(x, t)$ into temporal and spatial by means of functions $u(t)$ and $X(x)$, respectively, we apply Galerkin procedure for (8):

$$W(x, t) = u(t) \frac{X(x)}{X(0.5)} \quad (9)$$

Within (9), $X(x)$ is a trial function satisfying the kinematic boundary conditions, and $u(t)$ is the midpoint deflection of the microbeam, and therefore, the eigenfunction for the clamped–clamped microbeam is known as

$$X(x) = \cosh \beta x - \cos \beta x - \frac{\cosh \beta - \cos \beta}{\sinh \beta - \sin \beta} (\sinh \beta x - \sin \beta x) \quad (10)$$

where $\beta = 4.730040745$. Substituting (9) into (8), and then multiplying (8) by $X(x)/X(0.5)$, and integrating on the domain $[0,1]$, we obtain the nonlinear equation [8]

$$(a_0 + a_1u + a_2u^2 + a_3u^3 + a_4u^4)\ddot{u} + b_0 + b_1u + b_2u^2 + b_3u^3 + b_4u^4 + b_5u^5 + b_6u^6 + b_7u^7 = 0 \quad (11)$$

with the initial conditions

$$u(0) = 0, \quad u'(0) = 0 \quad (12)$$

The expression of the coefficients a_i and b_i is known [8].

In what follows we apply OAFM [17–20] to obtain an analytic solution to (11) and (12). If Ω is the frequency of the system given nu (1), then making the transformation $\tau = \Omega t$, (11) can be rewritten as

$$\Omega^2(a_0 + a_1u + a_2u^2 + a_3u^3 + a_4u^4)u'' + b_0 + b_1u + b_2u^2 + b_3u^3 + b_4u^4 + b_5u^5 + b_6u^6 + b_7u^7 = 0 \quad (13)$$

where $u' = \partial u / \partial \tau$. The linear operator, the function $g(\tau)$ and the nonlinear operator are, respectively

$$\begin{aligned} L[u(\tau)] &= \Omega^2(u'' + u), \quad g(\tau) = b_0, \quad N[u(\tau)] \\ &= \Omega^2(a_0 - 1 + a_1u + a_2u^2 + a_3u^3 + a_4u^4) \\ &\quad + (b_1 - \Omega^2)u + b_2u^2 + b_3u^3 + b_4u^4 + b_5u^5 + b_6u^6 + b_7u^7 \end{aligned} \quad (14)$$

The approximate solutions of (13) can be expressed as

$$\tilde{u}(\tau) = u_0(\tau) + u_1(\tau) \quad (15)$$

such that the initial approximation $\theta_0(\tau)$ can be obtained from the linear equation.

$$\Omega_0^2(u_0'' + u_0) + b_0 = 0, \quad u_0(0) = u_0'(0) = 0 \quad (16)$$

Equation (16) has the solution

$$u_0(\tau) = -\frac{b_0}{\Omega^2}(1 - \cos \tau) \quad (17)$$

The nonlinear operator corresponding to (17) is

$$\begin{aligned} N[u_0(\tau)] = & A_0 + A_1 \cos \tau + A_2 \cos 2\tau + A_3 \cos 3\tau \\ & + A_4 \cos 4\tau + A_5 \cos 5\tau + A_6 \cos 6\tau + A_7 \cos 7\tau \end{aligned} \quad (18)$$

where $A_i, i = 0, 1, 2, \dots, 7$ are the coefficients of $\cos i\tau$ obtained from the substitution of (17) into (14).

The first approximation $u_1(\tau)$ can be obtained from equation

$$\begin{aligned} \Omega^2(u_1'' + u_1) = & (C_1 + 2C_2 \cos \tau + 2C_3 \cos 2\tau + 2C_4 \cos 3\tau)(A_1 \cos \tau + A_2 \cos 2\tau) \\ u_1(0) = u_1'(0) = & 0 \end{aligned} \quad (19)$$

Avoiding the secular term in (19), we obtain the condition

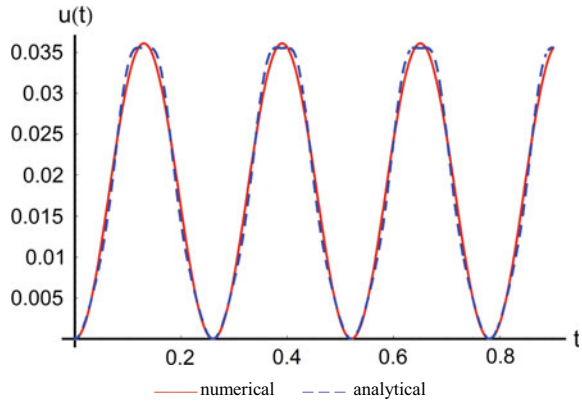
$$A_1(C_1 + C_3) + A_2(C_2 + C_4) = 0 \quad (20)$$

The solution of (19) is given by

$$\begin{aligned} u_1(\tau) = & (A_1 C_1^* + A_2 C_3^*)(1 - \cos \tau) + \frac{1}{3}(A_2 C_1^* + A_1 C_2^* + A_1 C_4^*)(\cos \tau - \cos 2\tau) \\ & + \frac{1}{8}(A_2 C_2^* + A_1 C_3^*)(\cos \tau - \cos 3\tau) + \frac{1}{15}(A_2 C_3^* + A_1 C_4^*) \\ & + \frac{A_2 C_4^*}{24}(\cos \tau - \cos 5\tau) \end{aligned} \quad (21)$$

where $C_i^* = C_i/\Omega^2$. From (17), (21) and (15), the approximate solution is known.

Fig. 2 Comparison between the approximate solution (15) and numerical integration results



4 Numerical Example

Considering $\alpha = 6$, $N = 20$, $\lambda_4 = 10$, by minimizing the residual of the initial (13) for \tilde{u} given by (15), the optimal values of the convergence-control parameters are obtained as $C_1 = 0.000180703067$, $C_2 = -0.000033253377$, $C_3 = -0.000162423645$, $C_4 = 0.000108804336$, and the approximate frequency $\Omega = 24.149754208745$. In this case, the approximate solution of (11) and (12) is well determined. In Fig. 2, the obtained analytical solution is compared with numerical integration results obtained by means of a fourth-order Runge–Kutta method.

5 Conclusions

In this work, an analytical solution is obtained for the nonlinear vibration of doubly clamped nanobeam subject to Casimir force. By means of OAFM, the dynamic response is explicitly obtained. The main advantage of our procedure in comparison with other methods consists in the involvement of the so-called auxiliary functions depending on several convergence-control parameters C_i . These parameters are optimally determined by means of rigorous techniques, leading to a rapid convergence, after the first iteration. This method does not contain restrictive hypotheses, is simple, accurate and very efficient in practice even for strongly nonlinear systems.


References

1. W.H. Lin, Y.P. Zhao, Nonlinear behavior for nanoscale electrostatic actuators with Casimir force. *Chaos, Solitons Fractals* **23**, 1777–1785 (2005)
2. Y.C. Hu, Closed form solutions for the pull-in voltage of micro curved beams subjected to electrostatic loads. *J. Micromech. Microeng.* **16**, 648–655 (2006)

3. J.F. Rhoads, S.W. Shaw, K.L. Turner, The nonlinear response of resonant microbeam systems with purely parametric electrostatic actuation. *J. Micromech. Microeng.* **16**, 890–899 (2006)
4. Y.C. Hu, P.Z. Chang, W.C. Chuang, An approximate analytical solution to the pull-in voltage of a micro bridge with an elastic boundary. *J. Micromech. Microeng.* **17**, 1870–1876 (2007)
5. M. Mojahedi, M.M. Zand, M.T. Ahmadian, Static pull-in analysis of electrostatically actuated microbeams with homotopy perturbation method. *Appl. Math. Model.* **34**, 1032–1041 (2010)
6. R. Soroush, A. Koochi, A.S. Kazemi, A. Noghrehabadi, H. Haddadpour, Investigating the effect of Casimir and van der Waals attraction on the electrostatic pull-in instability of nano-actuators. *Physica Scripta* **82**, Art ID 045801 (2010)
7. L. Yin, Q. Qian, L. Wang, Size effect on the static behavior of electrostatically actuated microbeams. *Acta Mech. Sin.* **27**(3), 445–451 (2011)
8. A.R. Askari, M. Tahani, An analytical approximation to nonlinear vibration of a clamped nanobeam in presence of the Casimir force. *Int. J. Aerosp. Lightweight Struct* **2**(3), 317–334 (2012)
9. S. Kong, Size effect on pull-in behavior of electrostatically actuated microbeams based on a modified couple stress theory. *Appl. Math. Model.* **37**, 7481–7488 (2013)
10. D. Caruntu, I. Martinez, K.N. Taylor, Voltage amplitude response of alternating current near half natural frequency electrostatically actuated MEMS resonators. *Mech. Res. Commun.* **52**, 25–31 (2003)
11. M.I. Younis, Analytical expressions for the electrostatically actuated curled beam problem. *Microsyst. Technol.* **21**(8), 1709–1717 (2015)
12. P.D. Maida, G. Bianchi, Numerical investigation of pull-in instability in a micro-switch MEMS device through the pseudo-spectral method. *Model. Simul. Eng.* ID 8543616 (2016)
13. D. Omarov, D. Nurakhmetov, D. Wei, P. Skrzypacz, On the application of Sturm’s theorem to analyses of dynamic pull-in for a grapheme-based MEMS model. *Appl. Comput. Mech.* **12**(1), 59–72 (2018)
14. P. Skrzypacz, S. Kadyrov, D. Nurakhmetov, D. Wei, Analysis of dynamic pull-in voltage of a grapheme MEMS model. *Nonlinear Anal. Real World Appl.* **45**, 581–589 (2019)
15. S.K. Lommoreaux, Resource letter of Casimir force. *Am. J. Phys.* **67**(10), 850–861 (1999)
16. R.C. Batra, M. Porfiri, D. Spinello, Vibrations and pull-in instabilities of micromechanical von Kármán elliptic plates incorporating the Casimir force. *J. Sound Vib.* **315**, 939–960 (2008)
17. N. Herisanu, V. Marinca, G. Madescu, F. Dragan, Dynamic response of a permanent magnet synchronous generator to a wind gust. *Energies* **12**(5), 915 (2019)
18. V. Marinca, N. Herisanu, Vibration of nonlinear nonlocal elastic column with initial imperfection. *Springer Proc. Phys.* **198**, 49–56 (2018)
19. N. Herisanu, V. Marinca, Free oscillations of Euler-Bernoulli beams on nonlinear Winkler-Pasternak foundation. *Springer Proc. Phys.* **198**, 41–48 (2018)
20. N. Herisanu, V. Marinca, Application of the optimal auxiliary functions method to a permanent magnet synchronous generator. *Int. J. Nonlinear Sci. Numer. Simul.* **20**, 399–406 (2019)

Study of the Vibrations of a System Consisting in Cantilever Beams



Maria-Luiza Beșliu-Gherghescu, Nicolae-Doru Stănescu , Nicolae Pandrea, and Dinel Popa

Abstract We consider a system consisting in two cantilever beams jointed one to another at the free ends. On the normal direction of the beams acts a force that produces the deformation of the beams. We assume that these deformations have great values, and we determine the equations which give the shape of the deformed beams and the axial force that acts upon the system. By variation of the normal force, one may obtain different shapes of beams and axial force. We present a numerical example for which we have drawn the diagrams of variation of the characteristic parameters.

1 Introduction

The biography discusses only the case of a single cantilever beam acted by different concentrated or distributed forces and moments. Various methods were proposed for the determination of the shape of the beam and its elongation at different points [1–8]. Consideration about the elastic elements is presented in [9], while a method for the elimination of the Lagrange multipliers is described in [10]. These methods were presented in detail in [11], and all of them are valid in some hypotheses, especially the length of the deformed beam is equal to the length of the non-deformed beam.

For small deformations of the cantilever beam, the general theory known from the strength of materials can be applied. Large deformations appear for high values of the forces and moments or in the cases of small values of the inertial parameters or Young's modulus. The last situation characterizes the beams obtained by additive manufacturing (AM), especially by fused deposition material (FDM).

General situation for a system consisting in many cantilever beams was not studied in the literature because of the complicate mathematics that intervenes in the modelling, the hypothesis of constant lengths of the beams does not hold true. In this paper, we consider a system of two cantilever beams linked one to another by

M.-L. Beșliu-Gherghescu · N.-D. Stănescu (✉) · N. Pandrea · D. Popa
University of Pitesti, Pitesti 110040, Romania
e-mail: s_doru@yahoo.com

© Springer Nature Switzerland AG 2021

N. Herisanu and V. Marinca (eds.), *Acoustics and Vibration of Mechanical Structures—AVMS 2019*, Springer Proceedings in Physics 251,
https://doi.org/10.1007/978-3-030-54136-1_6

a cylindrical joint and acted by a harmonic-type force at this point. The equations which offer the shapes of the deformed beams, the elongations of the beams and the horizontal force that appears in the beams are presented. A numerical example of such system is discussed, and some conclusions end the paper.

2 Mechanical System

The mechanical system is captured in Fig. 1. It consists in the cantilever beams O_1A and O_2A , jointed at the point A by a cylindrical joint. For each beam, one knows the geometrical and mechanical parameters. At the common point A , one acts with a vertical force P . The initial lengths of the two bars are L_{10} and L_{20} , respectively. The elasticity moduli are E_1 and E_2 , respectively, while the moments of inertia are I_1 and I_2 , respectively. We assume that both elasticity moduli and moments of inertia are function of the position (parameters x_1 and x_2 , respectively). The transversal force P is divided into two components P_1 acting upon the first cantilever beam O_1A and the

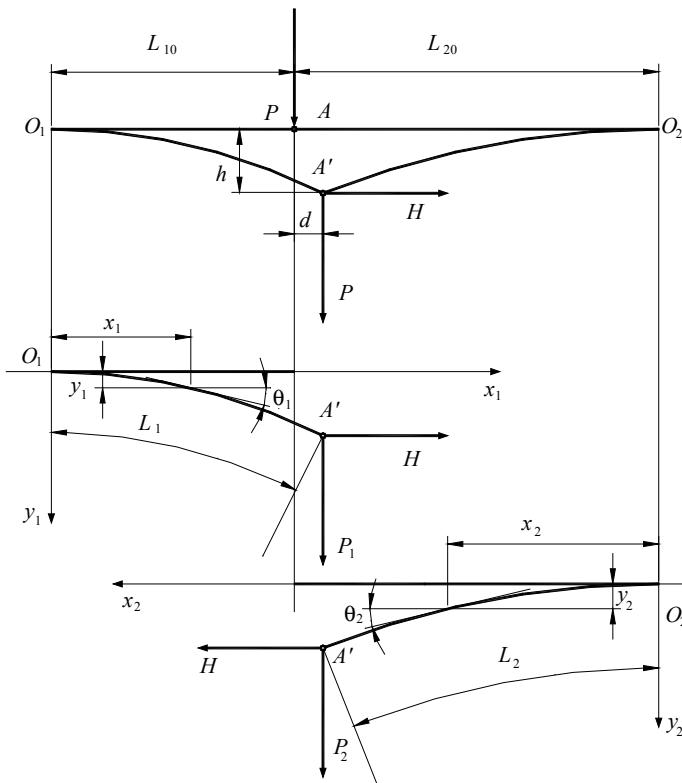


Fig. 1 Mechanical system

component $P_2 = P - P_1$ acting upon the second cantilever beam O_2A . Due to the action of the transversal force P , the two cantilever beams deform, their new lengths being L_1 and L_2 . The new position of point A is A' , which implies a horizontal displacement equal to d , and a vertical displacement equal to h . In the two cantilever beams appears a horizontal force denoted by H . In addition, the classical hypothesis of the strength of materials holds true.

It is proved [11] that the following equations may be obtained

$$L_1 = \int_0^{L_{10}+d} \sqrt{1 + (y_1')^2} dx_1, \quad (1)$$

$$L_2 = \int_0^{L_{20}-d} \sqrt{1 + (y_2')^2} dx_2, \quad (2)$$

$$\begin{aligned} L_1 &= L_{10} + \frac{1}{E_1(x_1)A_1(x_1)} \int_0^{L_{10}} (H \cos \theta_1 + P_1 \sin \theta_1) dx_1 \\ &= L_{10} + \frac{1}{E_1(x_1)A_1(x_1)} \int_0^{L_{10}} \frac{H + P_1 y_1'}{\sqrt{1 + (y_1')^2}} dx_1, \end{aligned} \quad (3)$$

$$\begin{aligned} L_2 &= L_{20} + \frac{1}{E_2(x_2)A_2(x_2)} \int_0^{L_{20}} (H \cos \theta_2 + P_2 \sin \theta_2) dx_2 \\ &= L_{20} + \frac{1}{E_2(x_2)A_2(x_2)} \int_0^{L_{20}} \frac{H + P_2 y_2'}{\sqrt{1 + (y_2')^2}} dx_2, \end{aligned} \quad (4)$$

$$P_1 + P_2 = P, \quad (5)$$

$$\frac{y_1''}{[1 + (y_1')^2]^{3/2}} = \frac{P_1(L_{10} - x_1) - H(h - y_1)}{E_1(x_1)I_1(y_1)}, \quad (6)$$

$$\frac{y_2''}{[1 + (y_2')^2]^{3/2}} = \frac{P_2(L_{20} - x_2) - H(h - y_2)}{E_2(x_2)I_2(x_2)}, \quad (7)$$

$$h = y_1(L_{10} + d) = y_2(L_{20} - d), \quad (8)$$

where $y_1' = \frac{dy_1}{dx_1}$, $y_2' = \frac{dy_2}{dx_2}$, $y_1'' = \frac{d^2y_1}{dx_1^2}$, $y_2'' = \frac{d^2y_2}{dx_2^2}$.

Some comments have to be added at the previous equations. Expressions (1) and (2) give the lengths of the deformed beams in the situation when one knows

the shape of them ($y_1 = y_1(x)$ and $y_2 = y_2(x)$). Equations (3) and (4) offer the lengths of the deformed beams from the theory of elasticity for a beam which is longitudinal elongated. Equation (5) is an expression for the decomposition of the total transversal force P . Expressions (6) and (7) give us the shapes of the beams, while the last equation (8) shows that the vertical deformations for the two cantilever beams are equal for them. In addition, (1)–(8) form a system of nonlinear integral differential equations with eight unknowns ($L_1, L_2, d, H, y_1, y_2, P_1$, and P_2).

The solution for the system of (1)–(8) is a very difficult task. One may assume that y_1 and y_2 may be developed into series,

$$y_1(x) = a_0 + a_1x + a_2x^2 + a_3x^3 + \dots, \quad (9)$$

$$y_1' = a_1 + 2a_2x + 3a_3x^2 + \dots, \quad (10)$$

and similar expressions for y_2 . The frontier conditions imply that $y_1(0) = 0$ and $y_1'(0) = 0$, wherefrom $a_0 = 0$ and $a_1 = 0$ (similarly for $y_2(x)$), that is,

$$y_1(x) = a_2x^2 + a_3x^3 + a_4x^4 + \dots, \quad y_2(x) = b_2x^2 + b_3x^3 + b_4x^4 + \dots \quad (11)$$

In this way, one may develop a trial-error procedure for solving the system (1)–(8).

Sometimes, the system may be added to a simpler form. One such situation is that in which the two cantilever beams are identical and the elasticity moduli and the moments of inertia have constant values along the beams ($E_1 = E_2 = E = ct$, $I_1 = I_2 = I = ct$). In this case, one obtains the following simplified form for the system of equations

$$L_1 = L_{10} + \frac{1}{EA} \int_0^{L_{10}} \frac{H + \frac{P}{2}y'}{\sqrt{1 + (y')^2}} dx, \quad (12)$$

$$L_1 = \int_0^{L_{10}} \sqrt{1 + (y')^2} dx, \quad (13)$$

$$\frac{y''}{[1 + (y')^2]^{3/2}} = \frac{\frac{P}{2}(L_{10} - x) - H(h - y)}{EI}, \quad (14)$$

$$h = y(L_{10}). \quad (15)$$

The simplest way to solve the system of (12)–(15) is to assume a known shape of the deformed cantilever beams. The case in which the shape is a parabola was discussed in [11].

3 Particular Solution of the System

In this study, we will consider that the shape is given by a function $y = a_n x^n$, where $n \geq 3$. It results in $y' = n a_n x^{n-1}$, $y'' = n(n-1)x^{n-2}$, $1 + (y')^2 = 1 + n^2 a_n^2 x^{2n-2}$, $h = a_n L_{10}^n$. Taking into account that

$$\int_0^{L_{10}} \frac{P}{2} (L_{10} - x) dx = \frac{P}{4} L_{10}^2, \int_0^{L_{10}} H(h - y) dx = H \frac{n a_n}{n+1} L_{10}^{n+1} \quad (16)$$

from (14) and (15), it results

$$H = \frac{n+1}{\sqrt{1 + n^2 a_n^2 L_{10}^{2n-2}}} \frac{EI}{L_{10}^2} + \frac{(n+1)P}{4n a_n L_{10}^{n-1}} \quad (17)$$

and expressions (12) and (13) lead to

$$L_{10} + \frac{1}{EA} \int_0^{L_{10}} \frac{H + \frac{P}{2} n a_n x^{n-1}}{\sqrt{1 + n^2 a_n^2 x^{2n-2}}} dx - \int_0^{L_{10}} \sqrt{1 + n^2 a_n^2 x^{2n-2}} dx = 0. \quad (18)$$

Using the relation (17), (18) is a nonlinear one with the unknown a_n . This equation can be solved with the aid of numerical methods. In addition, the angle θ at the point A, denoted by θ_f , has the expression

$$\sin \theta_f = \frac{1}{EI} \left(H \frac{n a_n}{n+1} L_{10}^{n+1} - \frac{P}{4} L_{10}^2 \right). \quad (19)$$

4 Numerical Example

As example, we consider the following situation: two identical cantilever beams for which the sections are squares of side $a = 0.003$ m, the lengths are $L_{10} = L_{20} = 0.3$ m. The excitation force is

$$P = P_0 + P_1 \sin(\omega t) + P_2 \sin(2\omega t) + P_3 \sin(3\omega t), \quad (20)$$

where $P_0 = 50$ N, $P_1 = 25$ N, $P_2 = 10$ N, $P_3 = 5$ N, $\omega = 20$ s⁻¹. The period of simulation is $t \in [0 \dots 5]$ s, while the step of simulation is selected $\Delta t = 10^{-3}$ s. The integrals in (18) are calculated using the Simpson rule, the step of integration being $\Delta x = L_{10}/100$. The elasticity moduli are $E_1 = E_2 = E = 2 \times 10^9$ Pa. It results

Table 1 Values of parameters for different values of the exponent n

n	a_n	H [N]	h [m]	θ_f [°]
2	0.3881913	161.4413419	0.0349372	13.11066004
3	1.1266249	164.9456759	0.0304189	16.91928297
4	3.3977716	171.0226902	0.0275220	20.15105633
5	10.4834847	177.4731071	0.0254749	23.00479786
6	32.8259942	183.7708766	0.0239301	25.57591923
7	103.8427031	189.7718622	0.0227104	27.91953344
8	330.9715613	195.4460183	0.0217150	30.07375196
9	1060.9348536	200.8014071	0.0208824	32.06596502
10	3416.1783028	205.8586803	0.0201722	33.91713753
20	465,758,204.67	244.5944225	0.0162400	47.27300159

in the area of the cross section for each beam $A = 9 \times 10^{-6} \text{ m}^2$, and the common moment of inertia $I = 6.75 \times 10^{-12} \text{ m}^4$.

In Table 1, we determined the mean parameters a_n , H , h and θ_f in function of the exponent n . One may easily observe that increasing the exponent, the coefficient a_n , the axial force H and the rotation angle at the end of each cantilever beam θ_f increase too, while the displacement of the free ends of each cantilever beam h decreases. These are expected results due to the shape of the deformed beams, $y = a_n x^n$. Moreover, the results for $n = 2$ are in excellent agreement with those reported in [11], where the integrals are directly calculated. In Fig. 2, we have drawn the variations of main parameters for different values of the exponent n . It is easy to observe that these variations are similar to the variation of the force P . When the exponent n increases, the variations of the main parameters increase too.

5 Conclusions

The paper presents a nonlinear model of calculation for the case of two cantilever beams jointed by a cylindrical joint. The shapes of the deformed beams are considered to be given by monomial forms for the simplicity of calculation. More general forms may use Airy type functions (in [7] is presented an example for a shell). It is proved that the results obtained by classical theory of the strength of materials are only approximate ones, so this method has to be extended to other practical cases.

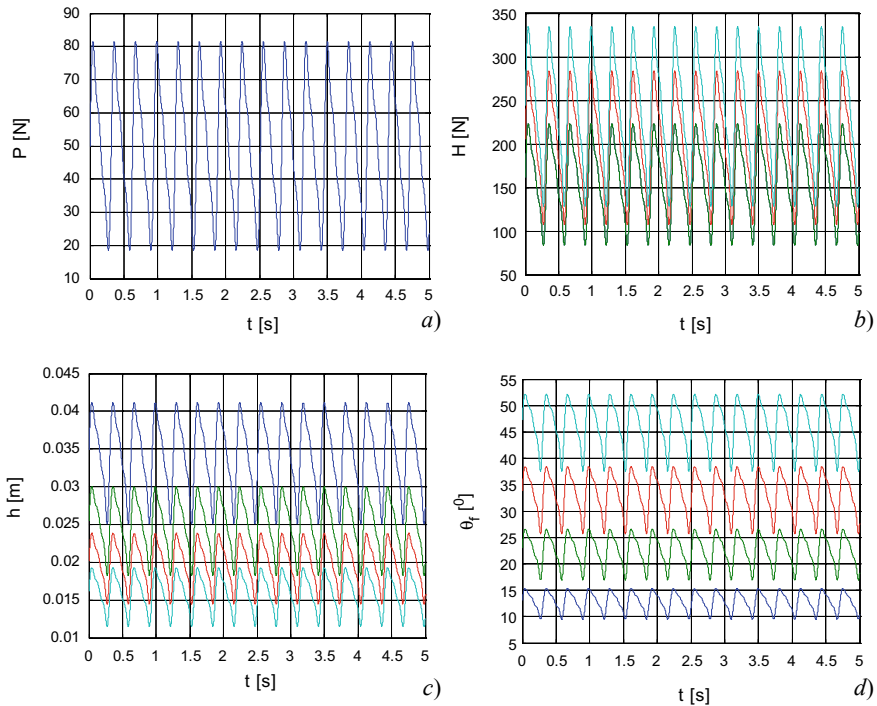


Fig. 2 Time history for: **a** $P = P(t)$; **b** $H = H(t)$ with $n = 2$ (blue), $n = 5$ (green), $n = 10$ (red) and $n = 20$ (light green); **c** $h = h(t)$ with $n = 2$ (blue), $n = 5$ (green), $n = 10$ (red) and $n = 20$ (light green); **d** $\theta_f = \theta_f(t)$ with $n = 2$ (blue), $n = 5$ (green), $n = 10$ (red) and $n = 20$ (light green)

References

1. D.G. Fertis, *Nonlinear Mechanics* (CRC Press, Boca Raton, 1999)
2. X. Huang, T.X. Yu, G. Lu, H. Lippmann, Large deflection of elastoplastic beams with prescribed moving and rotating ends. *Proc. Inst. Mech. Eng. Part C J. Mech. Eng. Sci.* **217**, 1001–1013 (2003)
3. P. Jiao, A.H. Alavi, W. Borchani, N. Lajnef, Small and large deformation models of post-buckled beams under lateral constraints. *Math. Mech. Solids* **24**(2), 386–405 (2019)
4. Y.A. Kang, X.F. Li, Large deflections of a non-linear cantilever functionally graded beam. *J. Reinf. Plast. Compos.* **29**(12), 1761–1774 (2010)
5. A.A. Nada, B.A. Hussein, S.M. Megahed, A.A. Shabana, Use of the floating frame of reference formulation in large deformation analysis: experimental and numerical validation. *Proc. IMechE Part K J. Multi-body Dyn.* **224**, 45–58 (2009)
6. O. Kopmaz, Ö. Gündoğdu, On the curvature of an Euler-Bernoulli beam. *Int. J. Mech. Eng. Educ.* **31**(2), 132–142 (2003)
7. P. Teodorescu, N.D. Stănescu, N. Pandrea, *Numerical Analysis with Applications in Mechanics and Engineering* (Wiley, Hoboken, 2013)
8. H. Yu, C. Zhao, B. Zheng, H. Wang, A new higher-order locking-free beam element based on the absolute nodal coordinate formulation. *Proc. IMechE Part C J. Mech. Eng. Sci.* **232**(19), 3410–3423 (2018)

9. S. Vlase, M. Marin, A. Öchsner, M.L. Scutaru, Motion equation for a flexible one-dimensional element used in the dynamical analysis of a multibody system. *Continuum Mech. Thermodyn.* **31**(3), 715–724 (2019)
10. S. Vlase, A method of eliminating Lagrangian multipliers from the equation of motion of interconnected mechanical systems. *J. Appl. Mech. Trans. ASME* **54**(1), 235–237 (1987)
11. N.D. Stănescu, M.L. Beşliu-Gherghescu, A. Rizea, D. Anghel, *Determination of the Shape of a Beam Obtained by Fused Deposition Material with General Loads* (IManEE, 2019) (in press)

Vibrations with Collisions of a Mechanical System with Elastic Elements



Ionuț-Bogdan Dragna, Nicolae Pandrea, Nicolae-Doru Stănescu ,
and Dinel Popa

Abstract In this paper, we present a mechanical system consisting in an arbitrary number of masses linked one to another by springs. The magnitudes of the vibrations are limited by some retainers located on the directions of vibrations. One knows the coefficients of restitution and the geometric and mechanical parameters of the system. The first index 0 mass is excited by a harmonic type force. We determine the equations of motion corresponding to each mass and the laws of motion, which, due to the collisions, are nonlinear ones. We also describe a numerical example for which we have drawn the diagrams of variation of the characteristic parameters.

1 Introduction

The modern approach of collisions is based on the theory of screws and uses the concept of inertance introduced in [22, 23]. The references [1–12, 14–17, 19–21, 24–36] discuss different aspects of collisions between two rigid bodies or between a rigid body and an obstacle considering or not the existence of friction at the contact point. The collisions are studied based on the hypotheses stated in [6, 22, 23], that is

- the impact forces are so high that one may neglect the other forces in system;
- collision consists in two phases: compression and expansion;
- positions remain constant during the shock;
- tangential stiffness is infinite.

For collisions without friction, one may prove [6, 22, 23] that the Newton, Poisson and energetic coefficients of restitution are equal and have values in interval $[0, 1]$. For collisions with friction, this equality between the coefficients of restitution is no longer valid, and there are examples [23] in which the coefficients of restitution may exceed 1. In addition, complex phenomena like jamb [3] may occur. It is also proved the existence of principal sliding directions [23].

I.-B. Dragna · N. Pandrea · N.-D. Stănescu (✉) · D. Popa
University of Pitesti, Pitesti 110040, Romania
e-mail: s_doru@yahoo.com

There exist numerous examples of vibrational systems with collisions. We deal only with the fundamental characteristics of mechanical vibrations [13, 18] and consider only the case of harmonic excitations. Elimination of the Lagrange multipliers is presented in [30].

2 The Mechanical System

The mechanical system is presented in Fig. 1. It consists in the rigid bodies denoted by $0, 1, 2, \dots, n$ that move without friction on horizontal bars. The rigid body 0 has an oscillatory motion in the form

$$x_0 = X_0 + A_0 \sin(\omega t), \quad (1)$$

where X_0 is its initial position.

The rigid bodies are linked one to another by springs of stiffness k_1, k_2, \dots, k_n and non-deformed lengths equal to the corresponding distances between horizontal bars, that is

$$l_p^0 = y_p. \quad (2)$$

On the n bars, there are situated some fixed stoppers situated (for a generic rigid body denoted by $p, 1 \leq p \leq n$) at the distances b_{ps} and b_{pd} , respectively, from the ends of the bars.

One considers as known the masses $m_p, 1 \leq p \leq n$, of the rigid bodies, and the coefficients of restitution r_p between the rigid body p and the stoppers situated on its own bar. We will denote by x_p the position of the rigid body p .

For an arbitrary spring p , its length at a moment of time is

$$l_p = \sqrt{y_p^2 + (x_{p+1} - x_p)^2}, \quad (3)$$

wherefrom one gets its elongation

$$\Delta l_p = l_p - l_p^0 = \sqrt{y_p^2 + (x_{p+1} - x_p)^2} - y_p. \quad (4)$$

The elastic force in the spring p has the expression

$$\mathbf{F}_p = k_p \Delta l_p = k_p \left[\sqrt{y_p^2 + (x_{p+1} - x_p)^2} - y_p \right]. \quad (5)$$

By isolating one generic rigid body $p < n$, the elastic forces \mathbf{F}_p and \mathbf{F}_{p+1} read

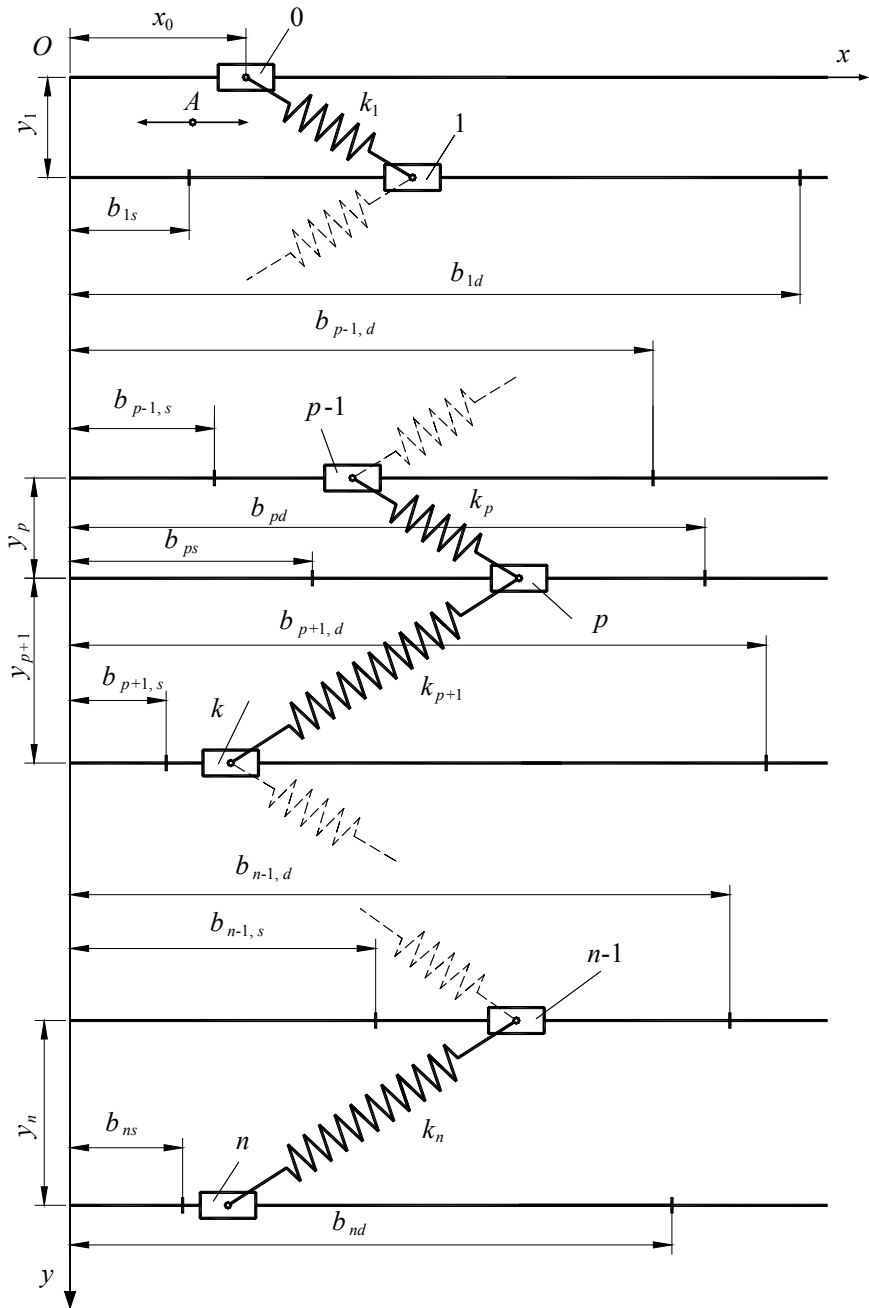


Fig. 1 Mechanical system

$$\mathbf{F}_p = k_p \Delta l_p \frac{(x_{p-1} - x_p)\mathbf{i} - y_p \mathbf{j}}{\sqrt{y_p^2 + (x_{p-1} - x_p)^2}}, \quad (6)$$

$$\mathbf{F}_{p+1} = k_{p+1} \Delta l_{p+1} \frac{(x_{p+1} - x_p)\mathbf{i} + y_{p+1} \mathbf{j}}{\sqrt{y_{p+1}^2 + (x_{p+1} - x_p)^2}}. \quad (7)$$

For a generic rigid body $p < n$, the force in horizontal direction is given by

$$F_{px} = (\mathbf{F}_p + \mathbf{F}_{p+1}) \cdot \mathbf{i} = k_p \frac{\sqrt{y_p^2 + (x_{p-1} - x_p)^2} - y_p}{\sqrt{y_p^2 + (x_{p-1} - x_p)^2}} (x_{p-1} - x_p) \\ + k_{p+1} \frac{\sqrt{y_{p+1}^2 + (x_{p+1} - x_p)^2} - y_{p+1}}{\sqrt{y_{p+1}^2 + (x_{p+1} - x_p)^2}} (y_{p+1} - y_p), \quad (8)$$

while for the last rigid body n , one gets

$$F_{nx} = \mathbf{F}_n \cdot \mathbf{i} = k_n \frac{\sqrt{y_n^2 + (x_{n-1} - x_n)^2} - y_n}{\sqrt{y_n^2 + (x_{n-1} - x_n)^2}} (x_{n-1} - x_n). \quad (9)$$

It results in the system of differential equations

$$\{\ddot{\mathbf{x}}\} = [\mathbf{M}]^{-1} \{\mathbf{F}\}, \quad (10)$$

where

$$\{\mathbf{x}\} = [x_1 \ x_2 \ \dots \ x_n]^T, \quad \{\mathbf{F}\} = [F_{1x} \ F_{2x} \ \dots \ F_{nx}]^T, \quad (11)$$

$$[\mathbf{M}] = \begin{bmatrix} m_1 & 0 & \dots & 0 \\ 0 & m_2 & \dots & 0 \\ \dots & \dots & \dots & \dots \\ 0 & 0 & \dots & m_n \end{bmatrix}, \quad [\mathbf{M}]^{-1} = \begin{bmatrix} m_1^{-1} & 0 & \dots & 0 \\ 0 & m_2^{-1} & \dots & 0 \\ \dots & \dots & \dots & \dots \\ 0 & 0 & \dots & m_n^{-1} \end{bmatrix}; \quad (12)$$

the system may be integrated if one knows the initial conditions at $t = 0$.

If at a given moment, the generic rigid body p suffers a collision with one stopper situated on its bar, then, between its velocity between the collision $\dot{x}_p(t_-)$ and its velocity after the collision $\dot{x}_p(t_+)$, the following relation holds true

$$\dot{x}_p(t_+) = -r_p \dot{x}_p(t_-). \quad (13)$$

If the generic rigid body p collides the left stopper, then the previous expression becomes

$$\dot{x}_p(t_+) = -r_p \dot{x}_p(t_-), \text{ with } \dot{x}_p(t_-) < 0, \tag{14}$$

while the collision takes place with the right stopper, one may write

$$\dot{x}_p(t_+) = -r_p \dot{x}_p(t_-), \text{ with } \dot{x}_p(t_-) > 0 \tag{15}$$

3 Numerical Example

As a numerical example, we consider $n = 3$, $m_1 = 1 \text{ kg}$, $m_2 = 2 \text{ kg}$, $m_3 = 3 \text{ kg}$, $y_1 = 0.1 \text{ m}$, $y_2 = 0.25 \text{ m}$, $y_3 = 0.3 \text{ m}$, $k_1 = 20 \text{ N/m}$, $k_2 = 10 \text{ N/m}$, $k_3 = 15 \text{ N/m}$, $X_0 = 0.3 \text{ m}$, $A_0 = 0.5 \text{ m}$, $\omega = 10 \text{ s}^{-1}$, $b_{1s} = 0.2 \text{ m}$, $b_{1d} = 0.35 \text{ m}$, $b_{2s} = 0.18 \text{ m}$, $b_{2d} = 0.4 \text{ m}$, $b_{3s} = 0.15 \text{ m}$, $b_{3d} = 0.5 \text{ m}$, $x_{10} = x_{20} = x_{30} = 0.3 \text{ m}$, $\dot{x}_{10} = \dot{x}_{20} = \dot{x}_{30} = 0 \text{ m/s}$, $r_1 = 0.6$, $r_2 = 0.7$, $r_3 = 0.9$, number of iterations $N = 50,000$, step of iterations $dt = 0.001 \text{ s}$.

Different other values are also selected for the parameters of the system: new values for the positions of the stoppers, different values for the stiffness, the coefficients of restitution (including the values 0 (plastic collision) and 1 (elastic collision)), positions of the horizontal bars, excitation. In all cases, the diagrams of variations have the same shape as in Fig. 2.

Analyzing the previous diagrams (Fig. 2, and those not represented in this papers), one may state

- the first rigid body has the most similar diagrams of variation for position and velocity as the excitation;

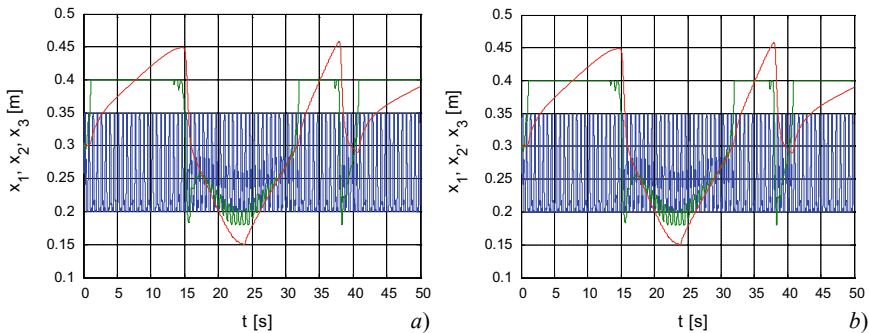


Fig. 2 Time history: **a** $x_1 = x_1(t)$ (blue), $x_2 = x_2(t)$ (green), $x_3 = x_3(t)$ (red); **b** $\dot{x}_1 = \dot{x}_1(t)$ (blue), $\dot{x}_2 = \dot{x}_2(t)$ (green), $\dot{x}_3 = \dot{x}_3(t)$ (red)

- the greatest number of collision appears for the first rigid body;
- increasing the index of the rigid body, the diagrams of variation for the position and velocity maintain a vague harmonic shape, the number of collisions decreases, and the time for which the rigid body is in continuous contact with one stopper increases;
- it is possible that at one or more rigid bodies, no collision occurs (the rigid body 3 in our case), that is, those rigid bodies have an oscillatory motion in an interval between the two corresponding stoppers;
- the number of collisions and the time of continuous contacts depend on the values of the coefficients of restitution. Increasing the values for coefficient of restitutions, the number of collisions increases, while the time of continuous contact decreases;
- smaller values for the distances between the stoppers lead to higher numbers of collisions.

4 Conclusions

In our paper, we consider a mechanical system for which we study its dynamics based on the possible collisions that may appear between one or many of its components and some stoppers situated along their directions of motion.

The study highlighted the complexity of the dynamics of such system and the absence of periodicity of the motion. In fact, it is possible that one rigid may stay in permanent contact with one of its stoppers, or another rigid may not collide at any of its own stoppers. The dynamics may become more complex if one considers nonlinear springs or another excitation (a non-harmonic one). These will be the goals of our future works.

References

1. J.A. Battle, Termination condition for three-dimensional inelastic collisions in multibody systems. *Int. J. Impact Eng.* **25**(7), 615–629 (2001)
2. J.A. Battle, The sliding velocity flow of rough collisions in multibody systems. *ASME J. Appl. Mech.* **63**(3), 804–809 (1996)
3. J.A. Battle, S. Cardona, The jamb (self locking) process in three-dimensional collisions. *ASME J. Appl. Mech.* **65**(2), 417–423 (1998)
4. R.M. Brach, Friction restitution and energy loss in planar collision. *ASME J. Appl. Mech.* **51**(1), 164–170 (1984)
5. R.M. Brach, Rigid body collision. *ASME J. Appl. Mech.* **56**(1), 133–138 (1989)
6. B. Brogliato, Kinetic quasi-velocities in unilaterally constrained Lagrangian mechanics with impacts and friction. *Multibody Syst. Dyn.* **32**, 175–216 (2014)
7. B. Brogliato, *Nonsmooth Mechanics*, 3rd edn. (Springer, Berlin, 2016)
8. F. Dimentberg, *The Theory of Screws and its Applications* (Nauka, Moscow, 1978)
9. H.A. Elkaranshaw, Rough collision in three-dimensional rigid multi-body systems. *Proc. Inst. Mech. Eng. Part K J. Multi-body Dyn.* **221**(4), 541–550 (2007)

10. P. Flores, J. Ambrósio, J.C.P. Claro, H.M. Lankarani, Influence of the contact-impact force model on the dynamic response of multi-body systems. *Proc. Inst. Mech. Eng. Part K J. Multi-body Dyn.* **220**(1), 21–34 (2006)
11. Glocker, C.: Energetic consistency conditions for standard impacts. Part I: Newton-type inequality impact laws. *Multibody System Dynamics* **29**, 77–117 (2013)
12. C. Glocker, Energetic consistency conditions for standard impacts. Part II: Poisson-type inequality impact laws. *Multibody Syst. Dyn.* **32**, 445–509 (2014)
13. D.J. Inman, *Engineering Vibration*, 4th edn. (Pearson Education, New Jersey, 2013)
14. M.G. Kapoulitsas, On the collision of rigid bodies. *J. Appl. Math. Phys. (ZAMP)* **46**, 709–723 (1995)
15. J.B. Keller, Impact with friction. *ASME J. Appl. Mech.* **53**(1), 1–4 (1986)
16. H.M. Lankarani, M.F.O.S. Pereira, Treatment of impact with friction in planar multibody mechanical systems. *Multibody Syst. Dyn.* **6**(3), 203–227 (2001)
17. B.D. Marghitu, Y. Hurmuzlu, Three-dimensional rigid body collisions with multiple contact points. *ASME J. Appl. Mech.* **62**(3), 725–732 (1995)
18. L. Meirovitch, *Fundamentals of Vibrations*, 2nd edn. (Waveland Press, Long Grove, 2010)
19. N. Pandrea, On the collisions of solids. *Stud. Res. Appl. Mech.* **40**(2), 117–131 (1990)
20. N. Pandrea, *Elements of the Mechanics of Solid Rigid in Plückerian Coordinates* (The Publishing House of the Romanian Academy, Bucharest, 2000)
21. N. Pandrea, About collisions of two solids with constraints. *Revue Romaine des Sciences Techniques, série de Mécanique Appliquée* **49**(1), 1–6 (2004)
22. N. Pandrea, N.D. Stănescu, A new approach in the study of frictionless collisions using inertances. *Proc. Int. Inst. Mech. Eng. Part C J. Mech. Eng. Sci.* **229**(12), 2144–2157 (2015)
23. N. Pandrea, N.D. Stănescu, A new approach in the study of frictionless collisions using inertances. *Proc. Int. Inst. Mech. Eng. Part C J. Mech. Eng. Sci.* **233**(3), 817–834 (2015)
24. E. Pennestri, P.P. Valentini, L. Vita, Dynamic analysis of intermittent-motion mechanisms through the combined use of Gauss principle and logical functions, in *IUTAM Symposium on Multiscale Problems in Multibody System Contacts Stuttgart February 2006, IUTAM Book series*, ed. by P. Eberhard (Springer, Heidelberg, 2006), pp. 195–204
25. F. Pfeiffer, On impact with friction. *Appl. Math. Comput.* **217**(3), 1184–1192 (2010)
26. N.D. Stănescu, L. Munteanu, V. Chiroiu, N. Pandrea, *Dynamical Systems. Theory and Applications* (The Publishing House of the Romanian Academy, Bucharest, 2007)
27. J.W. Stronge, Rigid body collision with friction. *Proc. R. Soc. A Math. Phys. Eng. Sci.* **431**(1881), 169–181 (1990)
28. J.W. Stronge, *Impact Mechanics* (Cambridge University Press, Cambridge, 2000)
29. A. Tavakoli, M. Gharib, Y. Hurmuzlu, Collision of two mass baton with massive external surfaces. *ASME J. Appl. Mech.* **79**(5), 051019 1–8 (2012)
30. S. Vlase, A method of eliminating Lagrangian multipliers from the equation of motion of interconnected mechanical systems. *J. Appl. Mech. Trans. ASME* **54**(1), 235–237 (1987)
31. R. Voinea, N. Pandrea, Contribution to a general mathematical theory of kinematic linkages, in *Proceedings of IFTOMM International Symposium on Linkages and Computer Design Method B* (Bucharest, 1973), pp. 522–534
32. Y. Wang, T.M. Mason, Two-dimensional rigid-body collisions with friction. *ASME J. Appl. Mech.* **59**(3), 635–642 (1992)
33. W.L. Yao, C. Bin, C.S. Liu, Energetic coefficient of restitution for planar impact in multi-rigid-body systems with friction. *Int. J. Impact Eng.* **31**(3), 255–265 (2005)
34. L. Woo, F. Freudenstein, Application of line geometry to theoretical kinematics and the kinematic analysis of mechanical systems. *J. Mech.* **5**(3), 417–460 (1970)
35. H.N. Yu, J.S. Zhao, F.L. Chu, An enhanced multi-point dynamics methodology for collision and contact problems. *Proc. Inst. Mech. Eng. Part C J. Mech. Eng. Sci.* **227**(6), 1203–1223 (2013)
36. M. Yuan, F. Freudenstein, Kinematic analysis of spatial mechanisms by means of screw coordinates. *ASME J. Eng. Ind.* **93**(1), 61–73 (1973)

Determination of the Dynamic Reactions for a Variable Compression Ratio Mechanism



Bogdan Mănescu, Nicolae-Doru Stănescu , Dinel Popa, and Nicolae Pandrea

Abstract We refer to a realistic variable compression ratio mechanism for which we determine the kinematic and dynamic parameters of the motion. As input parameter, we consider the position of one end of the lever which modifies the compression ratio. For this mechanism, we draw the variation of the characteristic parameters in function of the rotation angle of the crankshaft.

1 Introduction

The studies of such mechanism [1–8, 13–17] discuss the effects of variable compression mechanisms on the performances of the engines [3, 5, 14–18], different kinematic [4, 6, 8], or dynamic aspects [1, 7] highlighting the advantages of using of them. The possible variants of the realization of these mechanisms [2] are more than one thousands. The mechanism studied in this paper was firstly rejected by Freudenstein and Maki [2] because of its complexity, but nowadays it is successfully used by Nissan and PSA.

Some aspects concerning the kinematic and dynamic behavior of this mechanism are presented in [9–13].

2 Kinematic Analysis

The mechanism is captured in Fig. 1. It consists of the crank OA, schematized as a homogenous bar, the triangular homogenous shell ABC, the tiller BD also considered as a homogenous bar, the piston positioned at the point D, and the control lever CE, schematized as a homogenous bar. By vertical displacement of point E, one may

B. Mănescu · N.-D. Stănescu (✉) · D. Popa · N. Pandrea
University of Pitesti, 110040 Pitesti, Romania
e-mail: s_doru@yahoo.com

$$\dot{x}_{C_1} = -\frac{OA}{2}\omega \sin \varphi_1, \dot{y}_{C_1} = \frac{OA}{2}\omega \cos \varphi_1, v_{C_1} = \frac{OA}{2}\omega, \quad (9)$$

$$\omega_2 = \frac{\begin{vmatrix} -OA\omega \sin \varphi_1 & \sin \varphi_4 \\ \dot{y}_E - OA\omega \cos \varphi_1 & \cos \varphi_4 \end{vmatrix}}{AC \begin{vmatrix} \sin \varphi_2 & \sin \varphi_4 \\ \cos \varphi_2 & \cos \varphi_4 \end{vmatrix}}, \omega_4 = \frac{\begin{vmatrix} \sin \varphi_2 & -OA\omega \sin \varphi_1 \\ \cos \varphi_2 & \dot{y}_E - OA\omega \cos \varphi_1 \end{vmatrix}}{CE \begin{vmatrix} \sin \varphi_2 & \sin \varphi_4 \\ \cos \varphi_2 & \cos \varphi_4 \end{vmatrix}}, \quad (10)$$

$$\begin{cases} \dot{x}_B = -OA\omega \sin \varphi_1 - AC\omega_2 \sin \varphi_2 + CB\omega_2 \sin(\lambda - \varphi_2), \\ \dot{y}_B = OA\omega \cos \varphi_1 + AC\omega_2 \cos \varphi_2 - CB\omega_2 \cos(\lambda - \varphi_2), \end{cases} \quad (11)$$

$$\dot{x}_{C_3} = \frac{\dot{x}_B + \dot{x}_D}{2}, \dot{y}_{C_3} = \frac{\dot{y}_B + \dot{y}_D}{2}, \quad (12)$$

$$\dot{x}_D = 0, \dot{y}_D = \dot{y}_B \pm \frac{-2(e - x_B)\dot{x}_B}{2\sqrt{BD^2 - (e - x_B)^2}}, \quad (13)$$

$$\dot{x}_C = -OA\omega \sin \varphi_1 - AC\omega_2 \sin \varphi_2, \dot{y}_C = OA\omega \cos \varphi_1 + AC\omega_2 \cos \varphi_2, \quad (14)$$

$$\dot{x}_{C_2} = \frac{\dot{x}_A + \dot{x}_B + \dot{x}_C}{3}, \dot{y}_{C_2} = \frac{\dot{y}_A + \dot{y}_B + \dot{y}_C}{3}, \quad (15)$$

$$\dot{x}_{C_4} = \frac{\dot{x}_E + \dot{x}_C}{2}, \dot{y}_{C_4} = \frac{\dot{y}_E + \dot{y}_C}{2}, \quad (16)$$

$$\omega_3 = \frac{(\dot{y}_D - \dot{y}_B)(x_D - x_B) - (y_D - y_B)(\dot{x}_D - \dot{x}_B)}{(x_D - x_B)^2 + (y_D - y_B)^2}. \quad (17)$$

Similar relations are obtained for the accelerations:

$$\ddot{x}_A = -OA\omega^2 \cos \varphi_1, \ddot{y}_A = -OA\omega^2 \sin \varphi_1, a_{C_1} = \frac{OA}{2}\omega^2, \quad (18)$$

$$\ddot{x}_{C_1} = -\frac{OA}{2}\omega^2 \cos \varphi_1, \ddot{y}_{C_1} = -\frac{OA}{2}\omega^2 \sin \varphi_1, a_{C_1} = \frac{OA}{2}\omega^2, \quad (19)$$

$$\varepsilon_2 = \frac{\begin{vmatrix} -OA\omega^2 \cos \varphi_1 - AC\omega_2^2 \cos \varphi_2 - CE\omega_4^2 \cos \varphi_4 & \sin \varphi_4 \\ \ddot{y}_E + OA\omega^2 \sin \varphi_1 + AC\omega_2^2 \sin \varphi_2 + CE\omega_4^2 \sin \varphi_4 & \cos \varphi_4 \end{vmatrix}}{AC \begin{vmatrix} \sin \varphi_2 & \sin \varphi_4 \\ \cos \varphi_2 & \cos \varphi_4 \end{vmatrix}}, \quad (20)$$

$$\varepsilon_4 = \frac{\begin{vmatrix} \sin \varphi_2 & -OA\omega^2 \cos \varphi_1 - AC\omega_2^2 \cos \varphi_2 - CE\omega_4^2 \cos \varphi_4 \\ \cos \varphi_2 & \ddot{y}_E + OA\omega^2 \sin \varphi_1 + AC\omega_2^2 \sin \varphi_2 + CE\omega_4^2 \sin \varphi_4 \end{vmatrix}}{CE \begin{vmatrix} \sin \varphi_2 & \sin \varphi_4 \\ \cos \varphi_2 & \cos \varphi_4 \end{vmatrix}}, \quad (21)$$

$$\begin{cases} \ddot{x}_B = -OA\omega^2 \cos \varphi_1 - AC\varepsilon_2 \sin \varphi_2 - AC\omega_2^2 \cos \varphi_2 \\ \quad - CB\omega_2^2 \cos(\lambda - \varphi_2) + CB\varepsilon_2 \sin(\lambda - \varphi_2), \\ \ddot{y}_B = -OA\omega^2 \sin \varphi_1 + AC\varepsilon_2 \cos \varphi_2 - AC\omega_2^2 \sin \varphi_2 \\ \quad - CB\varepsilon_2 \sin(\lambda - \varphi_2) + CB\omega_2^2 \cos(\lambda - \varphi_2), \end{cases} \quad (22)$$

$$\ddot{x}_C = -OA\omega^2 \cos \varphi_1 - AC\omega_2^2 \cos \varphi_2 - AC\varepsilon_2 \sin \varphi_2, \quad (23)$$

$$\ddot{y}_C = -OA\omega^2 \sin \varphi_1 - AC\omega_2^2 \sin \varphi_2 + AC\varepsilon_2 \cos \varphi_2, \quad (24)$$

$$\ddot{x}_D = 0, \ddot{y}_D = \ddot{y}_B \pm \frac{(\dot{x}_B^2 + x_B \ddot{x}_B) \sqrt{BD^2 - (e - x_B)^2} - \frac{(e - x_B)^2 \dot{x}_B^2}{\sqrt{BD^2 - (e - x_B)^2}}}{BD^2 - (e - x_B)^2}, \quad (25)$$

$$\ddot{x}_{C_3} = \frac{\ddot{x}_B + \ddot{x}_D}{2}, \ddot{y}_{C_3} = \frac{\ddot{y}_B + \ddot{y}_D}{2}, \quad (26)$$

$$\ddot{x}_{C_2} = \frac{\ddot{x}_A + \ddot{x}_B + \ddot{x}_C}{3}, \ddot{y}_{C_2} = \frac{\ddot{y}_A + \ddot{y}_B + \ddot{y}_C}{3}, \quad (27)$$

$$\ddot{x}_{C_4} = \frac{\ddot{x}_E + \ddot{x}_C}{2}, \ddot{y}_{C_4} = \frac{\ddot{y}_E + \ddot{y}_C}{2}, \quad (28)$$

$$\begin{aligned} \omega_3 = & \frac{[(\ddot{y}_D - \ddot{y}_B)(x_D - x_B) - (y_D - y_B)(\ddot{x}_D - \ddot{x}_B)][(x_D - x_B)^2 + (y_D - y_B)^2]}{[(x_D - x_B)^2 + (y_D - y_B)^2]^2} \\ & - \frac{2[(\dot{y}_D - \dot{y}_B)(x_D - x_B) - (y_D - y_B)(\dot{x}_D - \dot{x}_B)]}{[(x_D - x_B)^2 + (y_D - y_B)^2]^2} \\ & \times [(x_D - x_B)(\dot{x}_D - \dot{x}_B) + (y_D - y_B)(\dot{y}_D - \dot{y}_B)]. \end{aligned} \quad (29)$$

3 Dynamic Analysis

We will denote by m_i and J_i the masses and moments of inertia, respectively, for the rigid bodies i , by R_{P_x} and R_{P_y} the components of the generic reactions at the generic point P , and by M_{e1} the equilibration moment. By isolation of the rigid bodies (Fig. 2), we obtain the equations of motion:

- for the rigid body 5:

$$m_5 \ddot{x} = 0 = N + R_{D_x}, m_5 \ddot{y}_D = R_{D_y} - m_5 g; \quad (30)$$

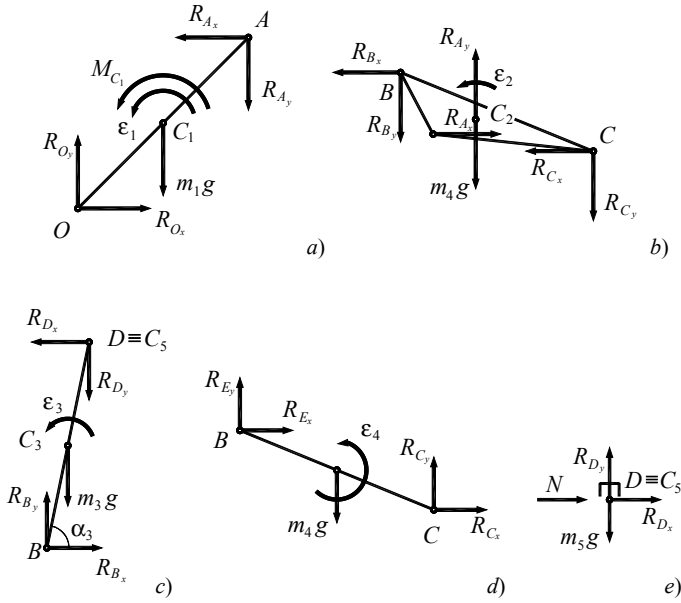


Fig. 2 Isolation of the rigid bodies: **a** rigid body 1; **b** rigid body 2; **c** rigid body 3; **d** rigid body 4; **e** rigid body 5

- for the rigid body 3:

$$m_3\ddot{x}_{C_3} = -R_{D_x} + R_{B_x}, m_3\ddot{y}_{C_3} = R_{B_y} - R_{D_y} - m_3g, \tag{31}$$

$$J_3\epsilon_3 = -(x_D - x_{C_3})R_{D_y} + (y_D - y_{C_3})R_{D_x} + (x_B - x_{C_3})R_{B_y} - (y_B - y_{C_3})R_{B_x}; \tag{32}$$

- for the rigid body 4:

$$m_4\ddot{x}_{C_4} = R_{E_x} + R_{C_x}, m_4\ddot{y}_{C_4} = R_{E_y} + R_{C_y} - m_4g, \tag{33}$$

$$J_4\epsilon_4 = (x_E - x_{C_4})R_{E_y} - (y_E - y_{C_4})R_{E_x} + (x_C - x_{C_4})R_{C_y} - (y_C - y_{C_4})R_{C_x}; \tag{34}$$

- for the rigid body 2:

$$m\ddot{x}_{C_2} = -R_{B_x} + R_{A_x} - R_{C_x}, m\ddot{y}_{C_2} = -R_{B_y} - R_{C_y} + R_{A_y} - m_2g, \quad (35)$$

$$J_2\varepsilon_2 = -(x_B - x_{C_2})R_{B_y} + (y_B - y_{C_2})R_{B_x} + (x_A - x_{C_2})R_{A_y} - (y_A - y_{C_2})R_{A_x} \\ - (x_C - x_{C_2})R_{C_y} + (y_C - y_{C_2})R_{C_x}; \quad (36)$$

- for the rigid body 1:

$$m\ddot{x}_{C_1} = -R_{A_x} + R_{O_x}, m\ddot{y}_{C_1} = -R_{A_y} + R_{O_y} - m_1g, \quad (37)$$

$$J_O\varepsilon_1 = -(x_A - x_O)R_{A_y} + (y_A - y_O)R_{A_x} + (x_{C_1} - x_O)m_1g - M_{e1}. \quad (38)$$

Assuming that the law of rotational motion of the crank OA is known, $\varphi_1(t) = \omega t$, (30)–(38) form a system of 14 linear equations with 14 unknowns (the reactions R_{O_x} , R_{O_y} , R_{A_x} , R_{A_y} , R_{B_x} , R_{B_y} , R_{C_x} , R_{C_y} , R_{D_x} , R_{D_y} , R_{E_x} , R_{E_y} , N , and the equilibration moment M_{e1}).

4 Numerical Example

For the numerical application, we consider the following values: $AB = 0.043$ m, $BC = 0.128$ m, $CA = 0.099$ m, $CE = 0.103$ m, $OA = 0.030$ m, $BD = 0.130$ m, $d = 0.086$ m, $e = 0$ m, $Y_E \in [0.100, 0.120]$ m, $\omega_1 = 100\pi$ rad/s, $\varphi_1 \in [0, 2\pi]$ rad, the diameter of the piston $d_p = 0.075$ m, position of the cylinder head $y_{ch} = 0.2088$ m, the thickness of the elements $thick = 0.008$ m, and the density of the material $\rho = 7800$ kg/m³. The iteration steps are: $dY_E = 0.00025$ m, and $d\varphi_1 = \frac{\pi}{180}$ rad. Some characteristic diagrams are captured in Fig. 3.

Analyzing the diagrams, we may state that:

- not all the reactions follow the same rule (increasing or decreasing) when the parameter Y_E increases. One may say nothing about the shape of these laws of variation;
- when Y_E increases, the axial force N (and consequently, the wear decreases), and the equilibration moment M_{e1} (and consequently, the necessary inertial moment of the flywheel) decrease;
- the compression ratio decreases when the parameter Y_E increases, the variation being almost a linear one;

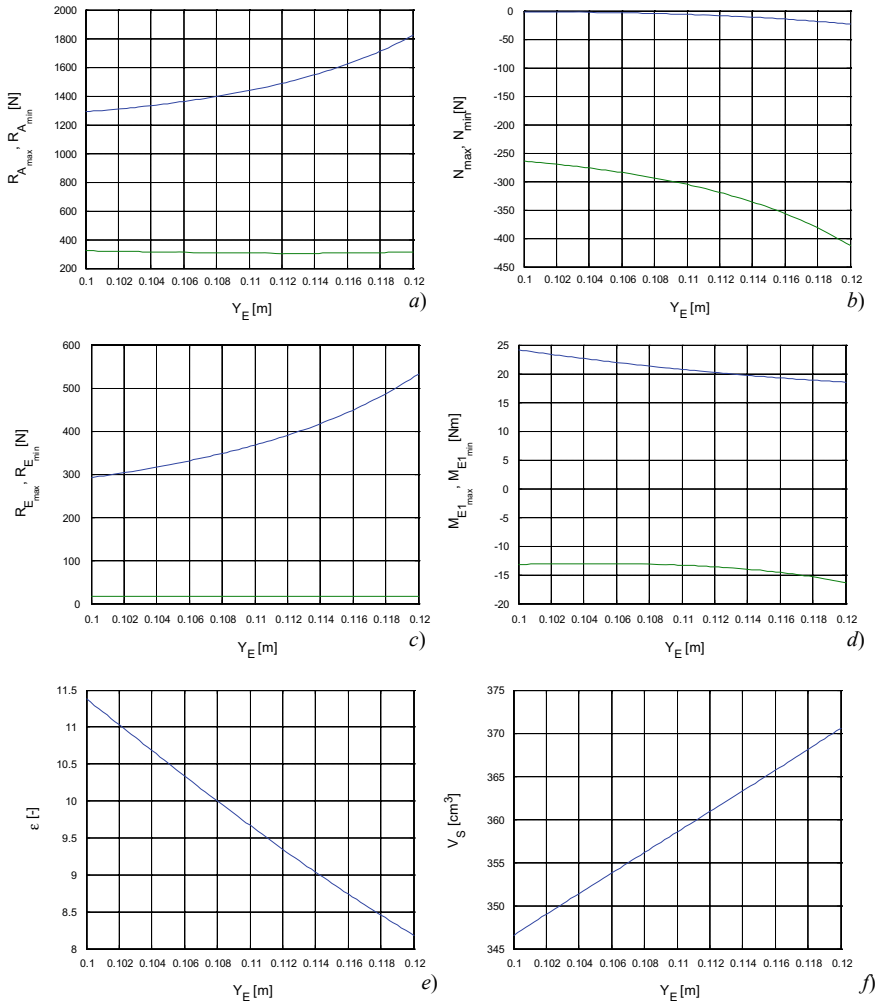


Fig. 3 Variations: **a** $R_{A_{max}} = R_{A_{max}}(Y_E)$ (blue), $R_{A_{min}} = R_{A_{min}}(Y_E)$ (green); **b** $N_{max} = N_{max}(Y_E)$ (blue), $N_{min} = N_{min}(Y_E)$ (green); **c** $R_{E_{max}} = R_{E_{max}}(Y_E)$ (blue), $R_{E_{min}} = R_{E_{min}}(Y_E)$ (green); **d** $M_{e_{imax}} = M_{e_{imax}}(Y_E)$ (blue), $M_{e_{imin}} = M_{e_{imin}}(Y_E)$; **e** compression ratio $\epsilon = \epsilon(Y_E)$; **f** unitary displacement volume $V_S = V_S(Y_E)$

- the same conclusion holds true for the unitary displacement volume, but in this case, it increases when parameter Y_E increases.

5 Conclusions

The reaction forces in the mechanism we determined for different values of the control parameter (position Y_E of the point E). The calculation is based on the kinematic analysis developed in our previous works and on the isolation of the rigid bodies. In addition, we also calculated the compression ratio and the unitary displacement volume, which has realistic values in all interval of variation for the parameter Y_E .

Our next works will be focused on the study of reactions in function of other geometrical and mechanical parameters.

References

1. S. Erkaya, Ş. Su, I. Uzmay, Dynamic analysis of a slider–crank mechanism with eccentric connector and planetary gears. *Mech. Mach. Theory* **42**, 393–408 (2007)
2. F. Freudenstein, E.R. Maki, Development of an optimum variable-stroke internal-combustion engine mechanism from the viewpoint of kinematic structure. *J. Mech. Transm. Autom. Des.* **105**, 259–266 (1983)
3. B. Govinda Rao, Y. Datta Bharadwaz, C. Virajitha, V. Dharma Rao, Effect of injection parameters on the performance and emission characteristics of a variable compression ratio diesel engine with plastic oil blends—an experimental study. *Energy Environ.* **29**(4), 492–510 (2018)
4. T. Hoeltgebaum, R. Simoni, D. Martins, Reconfigurability of engines: a kinematic approach to variable compression ratio engines. *Mech. Mach. Theory* **96**, 308–322 (2016)
5. T. Hu, S. Liu, I. Zhou, W. Li, Effects of compression ratio on performance, combustion, and emission characteristics of an HCCI engine. *Proc. Inst. Mech. Eng. Part D J. Automobile Eng.* **220**, 637–645 (2006)
6. G.G. Lowen, F.R. Tepper, R.S. Berkof, Balancing of linkages—an update. *Mech. Mach. Theory* **9**, 299–323 (1974)
7. G.G. Lowen, F.R. Tepper, R.S. Berkof, The quantitative influence of complete force balancing on the forces and moments of certain families of four-bar linkages. *Mech. Mach. Theory* **18**(3), 213–220 (1983)
8. Y. Lu, A.P. Roskilly, X. Yu, L. Jiang, L. Chen, Technical feasibility study of scroll-type rotary gasoline engine: a compact and efficient small-scale Humphrey cycle engine. *Appl. Energy* **221**, 67–74 (2018)
9. B. Mănescu, I. Dragomir, N.D. Stănescu, The transitory vibrations for a variable compression ratio mechanism, in *AVMS 2017, Acoustics and Vibration of Mechanical Structures - AVMS-2017, Proceedings of the 14th AVMS Conference*, Timisoara, Romania, 25–26 May 2017, ed. by N. Herişanu, V. Marinca (Springer International Publishing AG, Cham, 2017), pp. 375–380
10. B. Mănescu, I. Dragomir, N.D. Stănescu, N. Pandrea, Study of the influence of geometric parameters on the displacement of piston and compression ratio for a variable compression ratio mechanism. *Acta Technica Napocensis Ser. Appl. Math. Mech. Eng.* **60**(IV), 649–658 (2017)
11. B. Mănescu, I. Dragomir, N.D. Stănescu, N. Pandrea, A. Clenci, D. Popa, Aspects in the synthesis of a variable compression ratio mechanism, in *CAR2017 International Congress of Automotive and Transport Engineering—Mobility Engineering and Environment*. IOP Conference Series: Materials Science and Engineering, vol. 252 (2017), p. 012075
12. B. Mănescu, N.D. Stănescu, Dynamic analysis of a mechanism of an engine with variable compression ratio, in *IManEE 2019* (in press)
13. B. Mănescu, N.D. Stănescu, Kinematic analysis of a variable compression ratio mechanism, in *AMMA2018: International Congress of Automotive and Transport Engineering, Proceedings*

- of the 4th International Congress of Automotive and Transport Engineering (AMMA 2018)*, ed. by N. Burnete, B.O. Varga (Springer International Publishing AG, Cham, 2019), pp. 576–583
14. A. Paykani, A.H. Kakaee, P. Rahnama, R.D. Reitz, Progress and recent trends in reactivity-controlled compression ignition engines. *Int. J. Eng. Res.* **17**(5), 481–524 (2015)
 15. Y. Pogulyaev, O. Nikishin, A. Zheltov, The Kinematics of the swashplate engine with two rotating pairs. *Procedia Eng.* **206**, 1722–1727 (2017)
 16. S. Ramalingam, P. Chinnai, S. Rajendran, Influence of compression ratio on the performance and emission characteristics of annona methyl ester operated DI diesel engine. *Adv. Mech. Eng. ID 832470 1* (2014)
 17. T.J. Rychter, C.R. Stone, S.J. Charlton, A theoretical study of a variable compression ratio turbocharged diesel engine. *Proc. Inst. Mech. Eng. Part A J. Power Energy* **206**, 227–238 (1992)
 18. A. Shaik, N. Shenbaga Vinayaga Moorthi, R. Rudramoorthy, Variable compression ratio engine: a future power plant for automobiles—an overview. *Proc. Inst. Mech. Eng. Part D J. Automobile Eng.* **220**, 1159–1168 (2007)

Improving the Accuracy of Estimates of the Frequencies Based on a Pseudo-sinc Function



Andrea Amalia Minda , Gilbert-Rainer Gillich , Ana-Maria Budai , Nicoleta Gillich , and Cristian Paul Chioncel 

Abstract The methods currently used for frequency estimation do not provide accurate results as the obtained values depend on the acquisition time. To increase the estimates' accuracy, the authors propose a *pseudo-sinc* function that is dependent on the acquisition time but better reflect the physical phenomenon. The paper provides a new interpolation method developed to take into account more maximizer, obtained by iteratively cropping the source signal. The maximizer obtained in this way corresponds to an asymmetric pseudo-sinc function, which does not coincide with the assumptions generated by the commonly used interpolation methods. The method of interpolation using the pseudo-sinc function, developed by the authors, has as a direct practical application, the detection of changes in the mechanical characteristics of the engineering structures.

1 Introduction

The idea of low sensitivity in frequency evaluation stems from the fact that estimating the natural frequency by standard methods is influenced by acquisition time [1]. Advanced methods of processing the acquired signals involve the use of an interpolation algorithm. At present, the interpolation involves analyzing the maximizer and one or two neighbor spectral lines [2–7]. Frequency estimation from one spectrum increases the precision of the results but does not solve the problem of direct dependence on acquisition time. Another approach is cropping the signal and taking three maximizer from three spectra obtained from the same signal after cropping [8].

To accurately evaluate the frequencies of a signal, this study proposes a technique that involves the analysis of an overlapped spectrum composed of maximizer from different spectra obtained from a signal analyzed for different time lengths. In this way, the frequencies obtained become insensitive to the length of the signal and the errors are very small compared to those recorded by the standard methods. Through

A. A. Minda (✉) · G.-R. Gillich · A.-M. Budai · N. Gillich · C. P. Chioncel
Universitatea “Eftimie Murgu” Resita, 320085 Resita, Romania
e-mail: a.minda@uem.ro

© Springer Nature Switzerland AG 2021

N. Herisanu and V. Marinca (eds.), *Acoustics and Vibration of Mechanical Structures—AVMS 2019*, Springer Proceedings in Physics 251,
https://doi.org/10.1007/978-3-030-54136-1_9

the made analysis, we can also see that the maximizer are distributed by a non-symmetrical *pseudo-sinc* function with real frequency, justifying, at the same time, the opportunity to use such functions in spectral analyzes.

2 Leakage Phenomena and the Frequency Estimation of a Signal

It is considered a continuous harmonic signal with known angular frequency ω and amplitude A . The discrete form of the continuous signal according to [9] is $\{x\} = \{x[0], x[1], \dots, x[j], \dots, x[N - 1]\}$. Each element of this sequence has a real coefficient a_j , an imaginary coefficient b_j , and a modulus X_j resulted from the first two, which differ for different signal time lengths t_s . After ignoring some terms which are small if $\omega = 2\pi f$ is large enough, the modulus becomes:

$$X_j = \frac{\sin[\pi(f - j\Delta f)t_s]}{\pi(f - j\Delta f)t_s} = \text{sinc}[\pi(f - j\Delta f)t_s] \quad (1)$$

where Δf is the frequency resolution, f is the frequency of the generated signal, and j is the spectral line number. If the term $j\Delta f$ has values close to f the difference $f - j\Delta f \rightarrow 0$ and hence the *sinc* function is approaching the value 1 and the maximizer X_j approaches the real signal amplitude. If the value of $j\Delta f$ departs from f , the maximizer found with the *sinc* function gets a smaller value and a false frequency and amplitude is found. The phenomenon is known as leakage.

3 The Developed Pseudo-sinc Function

Modifying the length of the analyzed signal t_s , the maximizer for different signal lengths will not be symmetric and spectral lines will no longer be equidistant. This is highlighted in Fig. 1a, by plotting the *sinc* function with red line and the *pseudo-sinc* function with blue line. Therefore, we propose using a non-symmetrical *pseudo-sinc* function instead of the symmetric *sinc* function.

In the studies presented herein, we considered signals generated with $N_S = 15,000$ samples. For a certain value of f_{cor} , we choose a number of cycles n and calculate: the period T ; the original signal length $t_s = T \cdot n$; and the frequency resolution $\Delta f = 1/t_s$. To represent the *pseudo-sinc* function, for example, for $f_{\text{cor}} = 8$ Hz and for $n = 2$ cycles, we calculate the period $T = 0.125$ s and the number of samples of the original signal with length $t_s = 0.25$ s, which is $N_S = 3750$. Afterward, in order to plot the main lobe, we iteratively crop and add, respectively, 50 samples to the original signal. We compare the *pseudo-sinc* function with maximizer obtained from spectra achieved for signals with different time lengths.

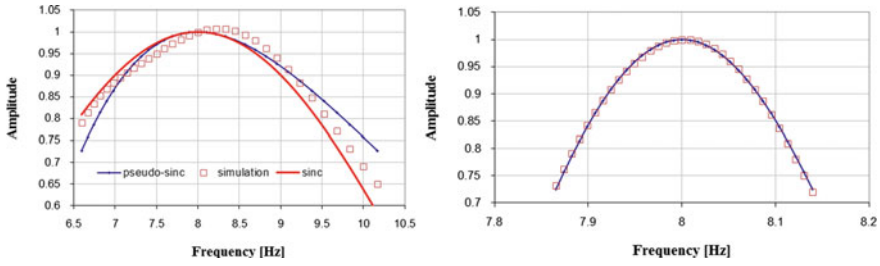
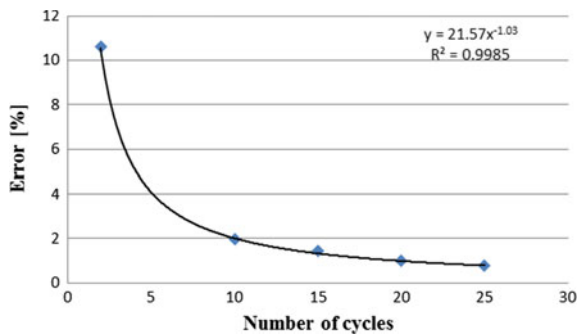


Fig. 1 Comparison between the pseudo-sinc function (continuous blue line), sinc function (red line), and maximizer achieved by simulation (square-shaped points) for $f = 8$ Hz and: **a** $n = 2$ cycles; **b** $n = 25$ cycles

The first approach concerns the study of the *pseudo-sinc* function, which is done by comparing this function with maximizer achieved by simulation from spectra generated with different signal lengths (Fig. 1). In Fig. 1a, we show the values for the main lobe of a signal with the frequency $f = 8$ Hz calculated for an original signal containing two cycles. One can notice a relatively large discrepancy between the maximizer obtained by simulation and the calculated *pseudo-sinc* function. The discrepancy observed in Fig. 1b fades and cannot be noticed when the analysis corresponds to $n = 25$ cycles, i.e., the analysis time is long enough. However, a big t_S cannot be achieved from free vibration signals used to detect damages as the vibration signal amplitude decreases quite quickly especially for high vibration modes. For such situations, the frequency is estimated by interpolation. Because we have shown the *sinc* function is inappropriate for this approach, and we propose a *pseudo-sinc* function that permits an accurate analysis in real operating conditions.

Analyzing for a given frequency the error that occurs between the values obtained by simulation for different number of cycles and the *pseudo-sinc* function, it is found that this error decreases by increasing the number of cycles. In Fig. 2, we show the error curve for a signal with $f = 8$ Hz and different number of cycles. We find that a small number of cycles do not provide adequate results, instead, if we choose a number of cycles bigger then $n = 20$, the error decreases significantly.

Fig. 2 Error curve for a signal with $f = 8$ Hz and different number of cycles



This analysis shows that the maximizer achieved from simulation accurately follow the *pseudo-sinc* function, so it can be used as a support for interpolation. This finding is especially useful for damage detection processes, where accurate frequency estimation is requested [10].

The second aspect of this paper is to determine the coefficients of an interpolation curve for a given frequency that allows us to determine the coefficients for any frequency. For a detailed analysis, we considered signals having frequencies of 8 Hz for three analysis time lengths, corresponding to 10, 20, and 30 cycles. At the initial time, all analyzed signals contain $N_S = 15,000$ samples.

Representing the amplitudes obtained for the analyzed cases and interpolating the points obtained for a given frequency signal for a certain number of cycles, we find that this is best done with a 5th degree polynomial [11], of the form:

$$y = C_5x^5 + C_4x^4 + C_3x^3 + C_2x^2 + C_1x + C_0 \tag{2}$$

For the signal with $f = 8$ Hz, we interpolate the amplitudes obtained at the main lobe for different number of cycles and obtain the curves in Fig. 3. Here, also the polynomial equation for each interpolation curve is displayed.

By normalizing the coefficients of the interpolation curves by dividing each coefficient C_k ($k = 0, \dots, 5$) to C_5 , which is the coefficient of x^5 , and taking only their value without taking into account their sign, we obtain the coefficients c_k given in Table 1.

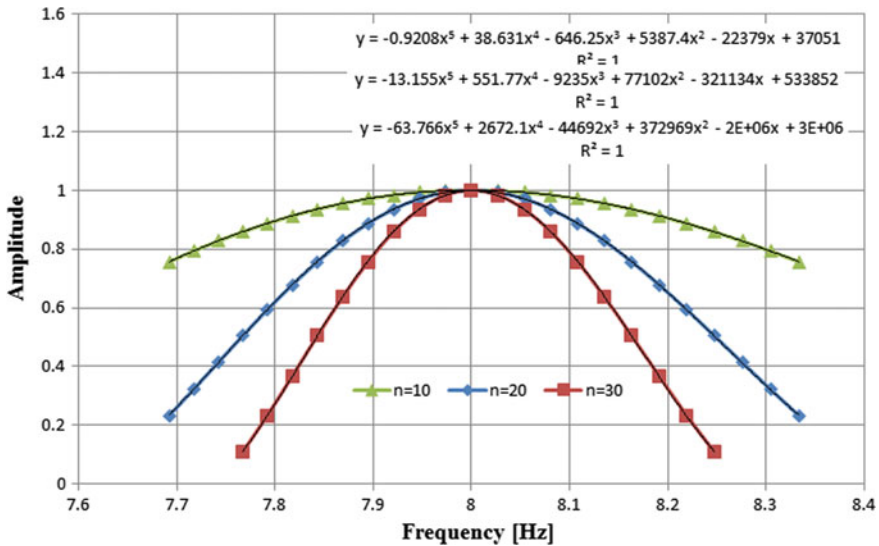


Fig. 3 Curves obtained by interpolation for the frequency $f = 8$ Hz and different number of cycles ($n = 10, 20,$ and 30)

Table 1 Values of the normalized coefficients c_k obtained from the interpolation function

n	c_5	c_4	c_3	c_2	c_1	c_0
30	1	-41.9047768	700.875074	-5849.02613	31,364.6771	-47,047.0157
20	1	-41.9437476	702.014443	-5861.04143	24,411.5545	-40,581.6801
10	1	-41.9537359	701.835361	-5850.78193	24,303.8662	-40,237.8367

Table 2 Normalized coefficients for the signals with the frequencies 8, 30, and 12 Hz

f (Hz)	c_5	c_4	c_3	c_2	c_1	c_0
8	1	41.94375	702.0144	5861.041	24,411.55	40,581.68
30 (estimation)	1	157.2891	9872.078	309,078.4	4,827,480	30,094,447
30 (interpolation)	1	157.6384	9893.785	309,762.7	4,838,192	30,161,130
Error (%)	0	0.221624	0.219402	0.220929	0.221401	0.221091
12 (estimation)	1	62.91562	1579.532	19,781.01	123,583.49	308,167.1
12 (interpolation)	1	62.91635	1579.576	19,781.79	123,586.6	308,175.3
Error (%)	0	0.001164	0.002772	0.003933	0.002481	0.00263

We have observed that, for a given number of cycles, knowing the normalized interpolation coefficients for a given frequency f_1 , we can calculate the normalized coefficients for any other frequency f_2 , by simply using the mathematical relationship:

$$c_k(f_2) = c_k(f_1) \left(\frac{f_2}{f_1}\right)^{5-k}, \quad k = 1, \dots, 5 \tag{3}$$

Based on relation (3), we calculated the normalized coefficients for signals having the frequencies $f = 30$ Hz and $f = 12$ Hz, starting from the normalized coefficients of the signal with the frequency $f_1 = 8$ Hz deduced for $n = 20$ cycles. These normalized coefficients are compared with those obtained by directly interpolating the points which we get from the maximizer for the two targeted frequencies. The values from direct interpolation and estimation, along with the achieved errors are presented in Table 2.

The small errors obtained if comparing the results achieved by estimation with the relation (3) and by directly interpolating the maximizer validate this relation.

4 Conclusions

In this paper, we analyze the variation of the maximizer obtained from the DFT of a signal if the analyzed signal length does not contain an entire number of cycles. It is shown that the maximizer are distributed after a *pseudo-sinc* function, because by

varying the signal length, the spectral lines are not anymore distributed equidistantly, so the *sinc* function cannot be used as interpolation support.

It was also found that, for any frequency, the errors are small enough to permit an accurate frequency estimation if the signal has a sufficiently length, i.e., a large number of cycles. Based on our expertise, we recommended to consider at least 25 cycles of the targeted frequency, in which case the error becomes less than 1%.

We have also found that the *pseudo-sinc* function follows a polynomial function of 5th degree and have shown that the coefficients for any frequency can be derived if the coefficients for another frequency are known.

The practical use of the proposed *pseudo-sinc* function consists in the support to estimate the true amplitude and frequency from measured signals, with direct application in vibration-based damage assessment.

References

1. D. Belega, D. Dallet, D. Petri, Accuracy of sine wave frequency estimation by multipoint interpolated DFT approach. *IEEE Trans. Instrum. Meas.* **59**(11), 2808–2815 (2010)
2. T. Grandke, Interpolation algorithms for discrete Fourier transforms of weighted signals. *IEEE Trans. Instrum. Meas.* **32**, 350–355 (1983)
3. B.G. Quinn, Estimating frequency by interpolation using Fourier coefficients. *IEEE Trans. Sig. Process.* **42**, 1264–1268 (1994)
4. V.K. Jain, W.L. Collins, D.C. Davis, High-accuracy analog measurements via interpolated FFT. *IEEE Trans. Instrum. Meas.* **28**, 113–122 (1979)
5. K. Ding, C. Zheng, Z. Yang, Frequency estimation accuracy analysis and improvement of energy barycenter correction method for discrete spectrum. *J. Mech. Eng.* **46**(5), 43–48 (2010)
6. P. Voglewede, Parabola approximation for peak determination. *Glob. DSP Mag.* **3**(5), 13–17 (2004)
7. E. Jacobsen, P. Kootsookos, Fast, accurate frequency estimators. *IEEE Sig. Process. Mag.* **24**(3), 123–125 (2007)
8. J.L. Ntakpe, G.R. Gillich, I.C. Mituletu, Z.I. Praisach, N. Gillich, An accurate frequency estimation algorithm with application in modal analysis. *Rom. J. Acoust. Vib.* **13**(2), 98–103 (2016)
9. K. Duda, Interpolation algorithms of DFT for parameters estimation of sinusoidal and damped sinusoidal signals, in *Fourier Transform-Signal Processing* (2012), pp. 1–32
10. G.R. Gillich, P.F. Minda, Z.I. Praisach, A.A. Minda, Natural frequencies of damaged beams—a new approach. *Rom. J. Acoust. Vib.* **9**(2), 101–108 (2012)
11. G.R. Gillich, A.A. Minda, Z.I. Korcka, Precise estimation of the resonant frequencies of mechanical structures involving a pseudo-sinc based technique. *J. Eng. Sci. Innov.* **2**(4), 37–48 (2017)

Gears Dynamic Response to Vibrations



Valeriu Ionica, Ionut Geonea, Cosmin Miritoiu, and Alexandru Bolcu

Abstract Gears work under heavy working conditions, subject to progressive damage that causes tooth wear or even tearing. In this paper, we analyze the dynamic behavior of the gear in time, based on a mechanical model with two degrees of freedom. We obtained the dynamic response by applying the Laplace transform with respect to mathematical model time, obtaining an algebraic system in the Laplace transformations of angular displacements. Their inversion led to the determination of the movements as time functions, their graphic representations highlighting the way they evolve. ADAMS modeling and simulation tools are used for the gear's dynamic response study.

1 Introduction

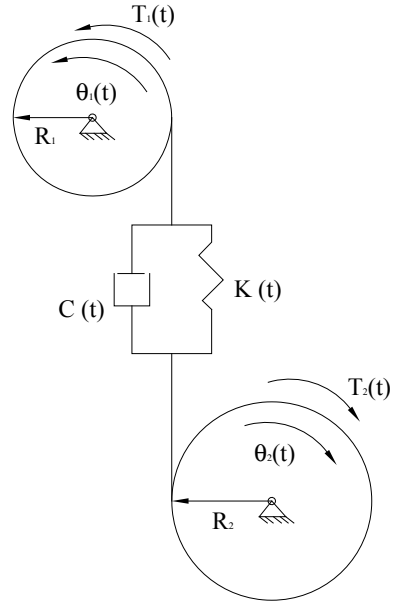
Maintenance is an important aspect for ensuring a satisfactory level of machine reliability over their lifetime [1, 2]. New maintenance strategies, such as conditional maintenance, have been extensively extended. This approach requires vibration analysis to be the most common technique for rotor maintenance [2–4].

Determining vibration displacements from the design phase will result in better gearing. These displacements we obtained with the Laplace unilateral transform in relation to time, the system of differential equations being linear, with constant coefficients. This modern method greatly facilitates integration because the transformed Laplace algebrizes the problem [5–8]. We obtained the dynamic response in the form of time functions [9]. Mathematical modeling is complemented by virtual simulation with multibody ADAMS software [10].

V. Ionica · I. Geonea (✉) · C. Miritoiu · A. Bolcu
Faculty of Mechanics, University of Craiova, Craiova, Romania
e-mail: igeonea@yahoo.com

© Springer Nature Switzerland AG 2021
N. Herisanu and V. Marinca (eds.), *Acoustics and Vibration of Mechanical Structures—AVMS 2019*, Springer Proceedings in Physics 251,
https://doi.org/10.1007/978-3-030-54136-1_10

Fig. 1 Mechanical model with two degree of freedom



2 Mechanical Model

Figure 1 shows the mechanical model with two degrees of freedom, which was obtained in the paper [9]. As a numerical application, we propose the values below.

$$I_1 = 257 \text{ Kg mm}^2; \quad I_2 = 4773 \text{ Kg mm}^2; \quad R_1 = 0.11 \text{ m}; \quad (1)$$

$$R_2 = 0.22 \text{ m}; \quad c = 10 \frac{\text{N s}}{\text{rad}}; \quad k = 0.9952 \frac{\text{N}}{\text{m}} \approx 1 \frac{\text{N}}{\text{m}}; \quad (2)$$

$$T_1 = 20 \text{ Nm}; \quad T_2 = 10 \text{ Nm} \quad (3)$$

3 Mathematical Model

The mathematical model obtained in Lagrange's formalism is the system of two differential equations with constant coefficients below:

$$\begin{cases} I_1 \frac{d^2\theta_1}{dt^2} + R_1 F_a(t) + R_1 F_e(t) = T_1 \\ I_2 \frac{d^2\theta_2}{dt^2} + R_2 F_a(t) + R_2 F_e(t) = -T_2 \end{cases} \quad (4)$$

θ_1, θ_2 are the angular displacements of the wheel and the sprocket around their axis of rotation, in degree; R_1 —input gear radius; R_2 —output gear radius; I_1 —moment of inertia of the wheel 1; I_2 —moment of inertia of the wheel 2; $T_i, i = \overline{1, 2}$ —torque; $F_a(t)$ —the damping force; $F_e(t)$ —elastic force.

$$F_a(t) = c(t) \left(R_1 \frac{d\theta_1}{dt} - R_2 \frac{d\theta_2}{dt} \right) \quad (5)$$

where $c(t)$ represent the damping coefficient.

$$F_e(t) = k(t)(R_1\theta_1 - R_2\theta_2) \quad (6)$$

where $k(t)$ represent the gearing stiffness.

Then, we will consider $c(t) = c = \text{constant}$ and $k(t) = k = \text{constant}$ so that, replacing the relations (2) and (3) in the system (1), we obtain the linear system with constant coefficients:

$$\begin{cases} I_1 \frac{d^2\theta_1}{dt^2} + R_1^2 c \frac{d\theta_1}{dt} - R_1 R_2 c \frac{d\theta_2}{dt} + R_1^2 k \theta_1 - R_1 R_2 k \theta_2 = T_1 \\ I_2 \frac{d^2\theta_2}{dt^2} - R_2^2 c \frac{d\theta_2}{dt} + R_1 R_2 c \frac{d\theta_1}{dt} - R_2^2 k \theta_2 + R_1 R_2 k \theta_1 = -T_2 \end{cases} \quad (7)$$

4 Dynamic Response

We obtained the dynamic response by applying the Laplace unilateral transform with relation with time, to mathematical model (7), obtaining an algebraic system in Laplace images of angular displacements as below:

$$\begin{cases} (I_1 s^2 + R_1^2 c s + R_1^2 k) \tilde{\theta}_1(s) - R_1 R_2 (c s + k) \tilde{\theta}_2(s) = \frac{T_1}{s} \\ R_1 R_2 (c s + k) \tilde{\theta}_1(s) + (I_2 s^2 - R_2^2 c s - R_2^2 k) \tilde{\theta}_2(s) = -\frac{T_2}{s} \end{cases} \quad (8)$$

By basically solving the system (4), we obtain the Laplace $\tilde{\theta}_i(s), i = \overline{1, 2}$ images of the angular displacements as follows:

$$\tilde{\theta}_i(s) = \frac{P_i(s)}{P(s)}, i = \overline{1, 2} \quad (9)$$

where

$$P(s) = s^2 [I_1 I_2 s^3 + c(R_1 I_2 - I_1 R_2^2) s^2 + (R_1^2 I_2 - I_1 R_2^2) s + R_1^2 R_2^2 c (k - 1)]; \quad (10)$$

$$P_1(s) = T_1 I_1 s^2 - R_2 c (T_1 R_2 + T_2 R_1) s - R_2 k (T_1 R_2 + T_2 R_1); \quad (11)$$

$$P_2(s) = T_2 I_1 s^2 + R_1 c(T_1 R_2 + T_2 R_1) s + R_1 k(T_1 R_2 + T_2 R_1); \quad (12)$$

$$k \approx 1 \left[\frac{N}{m} \right] \quad (13)$$

Applying the Laplace transform function to the functions (9), we obtain the desired time functions in the form below:

$$\theta_i(t) = \frac{1}{2f^3} \left[A_i(t) - \frac{B_i(t)}{C} \right], i = \overline{1, 2} \quad (14)$$

where

$$A_i(t) = (2c_i e^2 - 2c_i d f - 2b_i e f + 2a_i f^2 - 2c_i e f + 2b_i f^2 t + c_i f^2 t), i = \overline{1, 2} \quad (15)$$

$$B_i(t) = 2 \left[\cosh\left(\frac{et}{2d}\right) - \sinh\left(\frac{et}{2d}\right) \right] \cdot \{C [f(-b_i e + d^2) + c_i(e^2 - d f)] \cdot \cosh\left(\frac{C}{2d}t\right) + [f(-b_i e^2 + 2b_i d f + a_i e f) + c_i(e^3 - 3d f)] \cdot \sinh\left(\frac{C}{2d}t\right)\}; \quad (16)$$

$$C = \sqrt{e^2 - 4d f}; \quad (17)$$

$$d = I_1 I_2; e = c(R_1 I_2 - I_1 R_2^2); f = R_1^2 I_2 - I_1 R_2; \\ c_1 = -R_2(T_1 R_2 + T_2 R_1); c_2 = R_1(T_1 R_2 + T_2 R_1);$$

$$a_1 = T_1 I_1; a_2 = T_2 I_1; b_1 = -R_2 c(T_1 R_2 + T_2 R_1); b_2 = R_1 c(T_1 R_2 + T_2 R_1) \quad (18)$$

The application we proposed at the beginning of the paper led us to the graphical representations in Fig. 2.

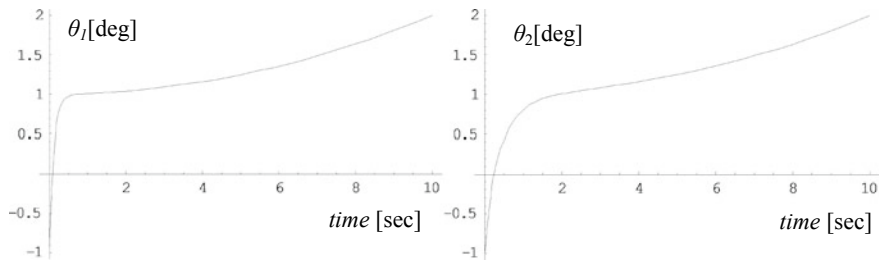


Fig. 2 Graphical representation of angular displacements $\theta_1 = \theta_1(t)$ and $\theta_2 = \theta_2(t)$

5 Dynamic Simulation in ADAMS of Gearing

To model the dynamic behavior of gear, ADAMS software is used. This allows the dynamic model of a gear by defining contact between tooth flanks. Contact forces are described by a mechanical contact model that is defined by parameters such as stiffness, contact force exponent, friction and damping coefficients, and penetration depth. MSC.ADAMS has the ability to perform rigid-elastic model calculations that are suitable for different contact models (gears). The rigid-elastic model is a compromise between rigid or elastic body modeling, in which the bodies in contact are considered rigid, but the contact surfaces are considered as deformable. The most appropriate method for defining contact parameters available in ADAMS is that of the impact method. The contact force calculated by this method is composed of two components: the elastic force produced by the deforming components and the damping force caused by the relative deformation velocity. The coefficient of friction between the flanks of the gears reaches values of 0.05, ..., 0.1.

The mathematical expression of the contact force in ADAMS is given by relation (19), with the notations exemplified in Fig. 3.

$$F = \begin{cases} K(x_0 - x)^e + CS\dot{x} & x < x_0 \\ 0 & x \geq x_0 \end{cases} \tag{19}$$

The parameters required to define the contact between the faces of the gear wheels are presented in Fig. 4. According to the Hertzian contact theory [11], the stiffness of two bodies in contact may be described by a pair of cylinders with the equivalent radius of the pair of gears in engagement. So, stiffness can be expressed as (20):

$$K = \frac{4}{3} R^{\frac{1}{2}} E^* = \frac{4}{3} \left[\frac{id_1 \cos \alpha_l \tan \alpha'_l}{2(1+i) \cos \beta} \right]^{\frac{1}{2}} E^*$$

$$\frac{1}{E^*} = \frac{1 - \nu_1^2}{E_1} + \frac{1 - \nu_2^2}{E_2}$$

$$\beta_b = a \tan(\tan \beta \cos \alpha_l) \tag{20}$$

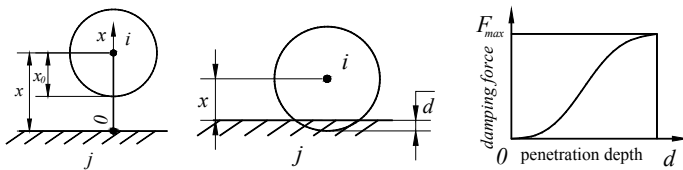


Fig. 3 Contact force model in ADAMS

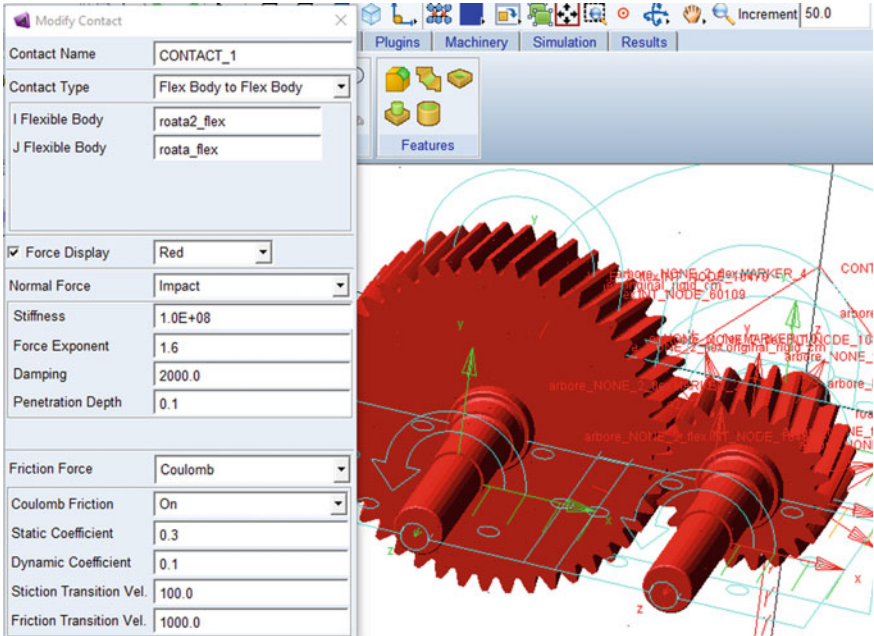


Fig. 4 Contact parameters for the gearbox in ADAMS

where d_1 —pinion pitch diameter; i —gear ratio; E_1, E_2 —Young’s module for the materials of the two wheels in contact; E^* —Young’s equivalent modulus; α'_t, α_t —pressure angle of the gear; ν_1, ν_2 —Poisson’s coefficients; β, β_b —helix angle of the teeth.

The contact parameters introduced into the ADAMS model are shown in Fig. 4.

ADAMS dynamic simulation determines the vibration modes of the bodies and deformations. Figure 5 shows the translation deformation of the center of the input gear.

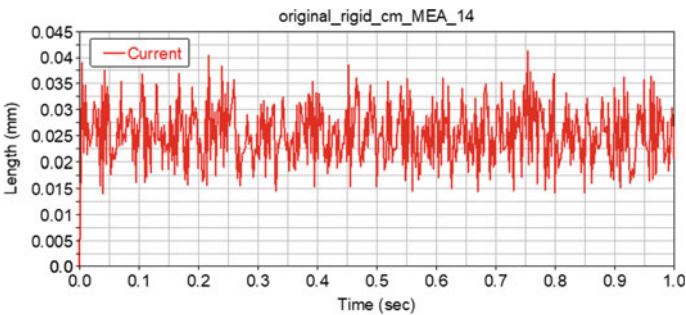


Fig. 5 Translational deformation of the pinion center of mass

Figures 6 and 7 show the angular deformation of the input and output gears.

In Figs. 8 and 9, the deformation speeds, both the translation and rotation of the marker attached to the center of the pinion are presented. The deformed shape of the input gear, corresponding to the vibration mode 7, is represented in Fig. 10. Also, the deformed shapes for the output gear (Fig. 11) and input shaft (Fig. 12) are represented.

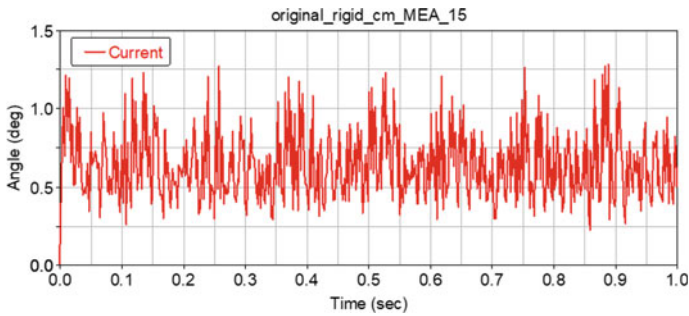


Fig. 6 Angular deformation of the input gear center of mass marker

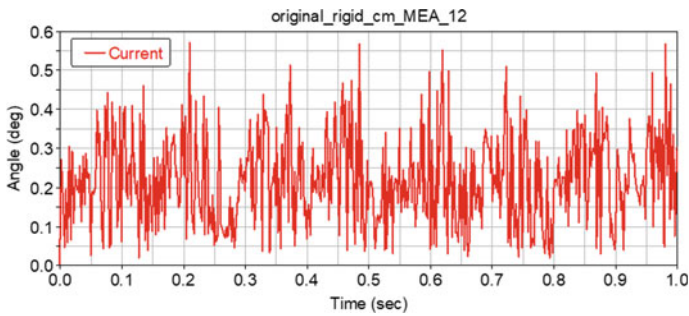


Fig. 7 Angular deformation of the output gear center of mass marker

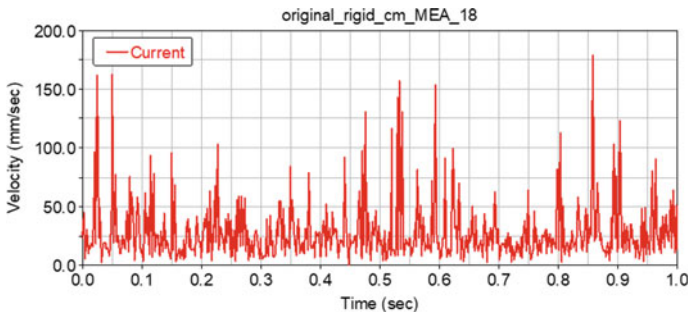


Fig. 8 Translational deformation velocity of the pinion center of mass marker

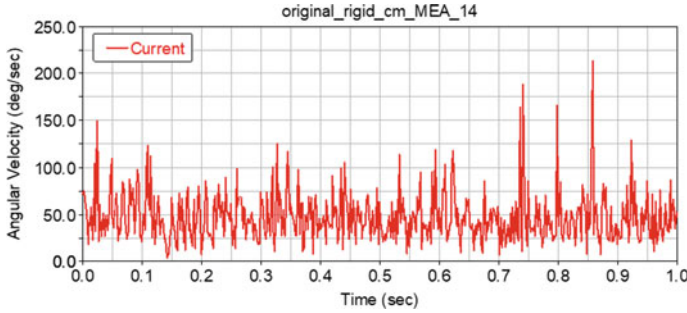


Fig. 9 Angular deformation velocity of the pinion center of mass marker

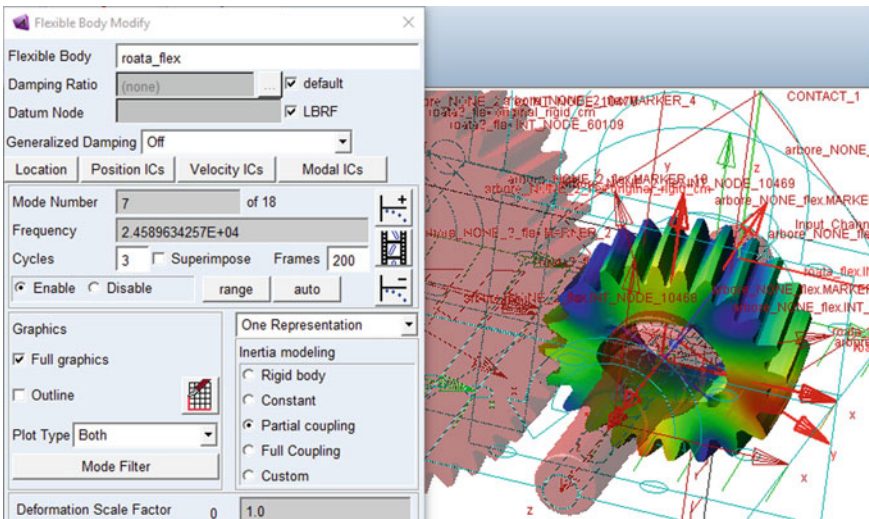


Fig. 10 Deformed shape of the input gear, for vibration mode 7

6 Conclusion

For preventive conditional maintenance, the vibration analysis that acts on gear teeth is very useful in the industrial design of gear mechanisms. In the paper, we developed an analytical model simulating the behavior of a vibratory gear. The analytical model is complemented by modeling and numerical simulation in ADAMS.

The angular displacements of the toothed gear and pinion were determined by the unilateral transformation with respect to Laplace's time, a modern method that leads to the so-called algebrasis of the problem, which ultimately solves an algebraic system, being easily adaptable to the calculation computation. The values obtained for angular displacements of the marker attached to the center of mass of the gears, by solving the mathematical model and by simulation in ADAMS, are comparable.

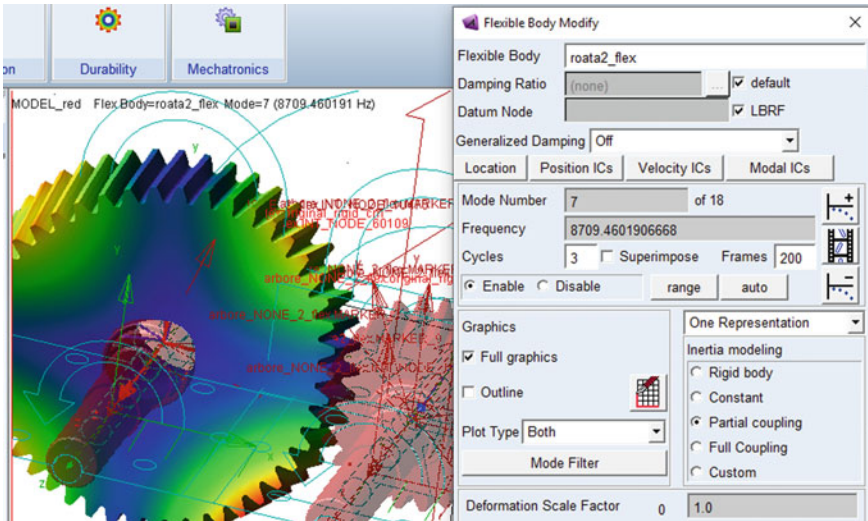


Fig. 11 Deformed shape of the output gear, for vibration mode 7

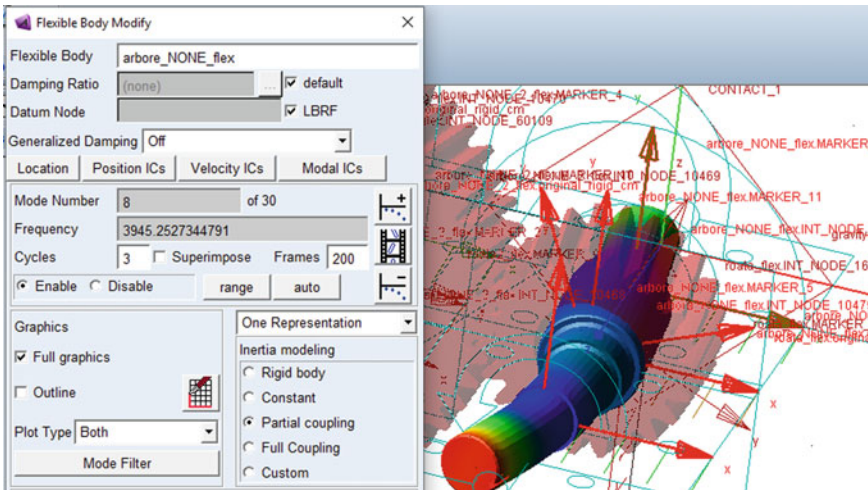


Fig. 12 Deformed shape of the input shaft, for vibration mode 8

References

1. V. Abousleiman, P. Velex, A hybrid 3d finite element/lumped parameter model for quasi-static and dynamic analyses of planetary/epicyclic gear sets. Mech. Mach. Theory **41**(6), 725–748 (2006)

2. D.Gh. Băgnaru, M.M. Stănescu, P. Cuță, Vibrations of the tool and tool holder unit for a shaper device, in *8th International Conference, Research and Development in Mechanical Industry, RaDMI 2008*, Užice, Serbia (2008), pp. 202–205
3. D.Gh. Băgnaru, On the vibration analysis of viscoelastic bars, the constituent elements of plane mechanisms, in *SYROM 97*, București (1997), pp. 25–30
4. D.Gh. Băgnaru, A. Hadăr, D. Bolcu, M.M. Stănescu, P. Cuță, The vibrations influence on the field of accelerations of the linear-elastic connecting rod of a mechanism connecting rod lug, in *Annals of DAAAM for 2009 & Proceedings*, vol. 20, issue 1 (2009), pp. 833–835
5. D.Gh. Băgnaru, M.M. Stănescu, D. Bolcu, P. Cuță, Approximate method in order to determine the displacement fields for the kinematic elements standing in vibration, in *Second International Congress Automotive, Safety and Environment, SMAT*, Craiova (2008), pp. 9–12
6. G.W. Blankenship, R. Singh, A comparative study of selected gear mesh interface dynamic models, in *International Power Transmission and Gearing Conference*, vol. 1 (ASME, 1992), pp. 137–146
7. C. Bard, *Modeling the dynamic behavior of gear transmissions* (L'institut National des Sciences Appliquées de Lyon, 1995)
8. R.R. Craig, M.C.C. Bampton, Coupling of substructures for dynamics analysis. *AIAA J.* **6**(7), 1313–1319 (1968)
9. H. Benmohamed, Y. Khadri, Y. Karmi, Numerical modeling of the vibratory behavior of gears with and without faults. *Rev. Sci. Technol. Synthèse* **36**, 153–169 (2018). (Département d'Electromécanique, LMI, Université Badji Mokhtar BP12 Annaba 23000, Algeria)
10. I. Geonea, N. Dumitru, A. Margine, Analytical and numerical study of critical speed for right shafts, in *Acoustics and Vibration of Mechanical Structures-AVMS-2017* (Springer, Cham, 2018), pp. 411–417
11. D. Kong, J.M. Meagher, C. Xu, X. Wu, Y. Wu, Nonlinear contact analysis of gear teeth for malfunction diagnostics (2008)

Dynamical Response of a Beam in a Centrifugal Field Using the Finite Element Method



Eliza Chircan , Maria Luminița Scutaru , and Ana Toderiță 

Abstract In this chapter, we propose a method of analyzing the motion equations in the case of a beam in rotation in plane, in order to determine the domain of instability without actually calculating the eigenvalues or to integrate the obtained equations of motion. This can ease the computational effort needed to solve such a problem. Some examples are studied in the paper.

1 Introduction

The first research in the field of elastic elements with a general rigid motion using numerical methods (especially Finite Element Method) has begun in the 1970s. The first studies were made for a single-beam one-dimensional finite element, using third-degree-shape functions. The complexity of the studied cases increased, and the method was developed for fifth-degree-shape polynomials. The method was used for a plane motion and for the three-dimensional rigid motion of a beam. In all these cases, a one-dimensional finite element was used [1–5]. The first model was a Bernoulli model. Other models, such as the Rayleigh model or Timoshenko model, were studied in [6–11]. Thereafter, the researchers developed two-dimensional and three-dimensional finite elements [12–14]. The developed models created new theoretical problems related to the methods of solving and qualitative analysis of such equations [15, 16]. To study a mechanical system with elastic elements which also involve a previous dynamical analysis, so we use of MBS (multibody models) models. In this paper, we propose to make a study, for a set of geometrical parameters, if the mechanical system is stable or not, in the case of a beam with a rotation around one of the ends. More elaborated models are made in [17–19].

E. Chircan (✉) · M. L. Scutaru · A. Toderiță
Transilvania University, Str. Politehnicii nr. 1, 500024 Brașov, Romania
e-mail: chircan.eliza@unitbv.ro

M. L. Scutaru
e-mail: lscutaru@unitbv.ro

In the study, an analysis is made of the motion equations in the case of a beam in rotation in plane, in order to determine the domain of instability without actually calculating the eigenvalues or to integrate the obtained equations of motion. This problem can be important in the engineering of the multibody with elastic elements.

2 One-Dimensional Finite Element

The problem of the study of a one-dimensional finite element in a centrifugal field was made by many researchers, for a general three-dimensional motion and for a plane motion [12, 14]. In the following, we will use the notation from [4, 5] in order to obtain the motion equations for a single element. We need this approach to apply our proposal concerning the study of such a system. Let's consider a point M of beam and its displacements $[\delta(u, v, w)]$ that can be expressed in terms of nodal displacements at the ends as follows:

$$\{\delta\} = \begin{Bmatrix} u \\ v \\ w \end{Bmatrix} = [N] \{\delta_{e,L}\} = [N] \begin{Bmatrix} \delta_{-1} \\ \delta_{-2} \end{Bmatrix} \quad (1)$$

where we have the vector of nodal displacements $\{\delta_e\}$:

$$\{\delta_{e,L}\} = \begin{Bmatrix} \delta_{-1} \\ \delta_{-2} \end{Bmatrix} = \{\delta_e\} \quad (2)$$

where $\{\delta_e\}$ is the displacement vector for e-th finite element in the local coordinate system, δ_{-1} and δ_{-2} , are, respectively, the displacement vectors of the nodes one and two.

Consider a finite element with a rotational motion around an axis. The nodal coordinates: the displacements of the beam ends in the three directions x , y , and z , the torsion angles at the end, the angles of rotation β and γ of the cross section at ends around the two y and z axes, and the curvatures of the neutral axis in the two xOz and xOy planes at both ends. If we consider the two ends, then the displacements at the ends, the rotations, and the curves are [20]:

$$\begin{aligned} \{f_1\} &= \begin{Bmatrix} u_1 \\ v_1 \\ w_1 \end{Bmatrix}; \quad \{f_2\} = \begin{Bmatrix} u_2 \\ v_2 \\ w_2 \end{Bmatrix}; \quad \{\phi_1\} = \begin{Bmatrix} \alpha_1 \\ \beta_1 \\ \gamma_1 \end{Bmatrix}; \quad \{\phi_2\} = \begin{Bmatrix} \alpha_2 \\ \beta_2 \\ \gamma_2 \end{Bmatrix}; \\ \{m_1\} &= \begin{Bmatrix} m_{xOz1} \\ m_{xOy1} \end{Bmatrix}; \quad \{m_2\} = \begin{Bmatrix} m_{xOz2} \\ m_{xOy2} \end{Bmatrix} \end{aligned} \quad (3)$$

where β_1, γ_1 and β_2, γ_2 are the slopes of the ends of the beam; α_1 and α_2 represent the torsion of the end sections; m_{xOz1}, m_{xOy1} and m_{xOz2}, m_{xOy2} are the curvatures in the corresponding plane.

If v and w are the displacements of a beam point on the directions Oy and Oz , respectively, we shall have the equations known from the continuum mechanics [12]:

$$\beta = -\frac{dw}{dx} \text{ and } \gamma = \frac{dv}{dx}. \tag{4}$$

The matrix $[N]$ contains shape functions. The lines of the matrix $[N]$ correspond to the displacements u, v , and w . We have denoted as $N(u), N(v)$, and $N(w)$:

$$N = \begin{bmatrix} N_{(u)} \\ N_{(v)} \\ N_{(w)} \end{bmatrix} \tag{5}$$

The displacements of the nodes at beam ends (left and right ends) have been named $\{\delta_{-1}\}$ and $\{\delta_{-2}\}$.

For the rotations angles, we have:

$$\begin{Bmatrix} \alpha \\ \beta \\ \gamma \end{Bmatrix} = [N^*]\{\delta_e\}; \quad \begin{Bmatrix} \dot{\alpha} \\ \dot{\beta} \\ \dot{\gamma} \end{Bmatrix} = [N^*]\{\dot{\delta}_e\}; \tag{6}$$

where: $[N^*] = \begin{bmatrix} N_{(\alpha)}^* \\ N_{(\beta)}^* \\ N_{(\gamma)}^* \end{bmatrix}$. Can be noted that: $[N_{(\beta)}^*] = [N'_w]$ and $[N_{(\gamma)}^*] = [N'_v]$.

For axial displacements u linear interpolation polynomials are chosen:

$$u = N_1u_1 + N_2u_2 \tag{7}$$

with:

$$N_1 = 1 - \xi; \quad N_2 = \xi; \quad \text{where: } \xi = \frac{x}{L} \tag{8}$$

Let us consider now the transversal displacements v and w :

$$v = N_3v_1 + N_5\gamma_1 + N_7m_{xOz1} + N_4v_2 + N_6\gamma_2 + N_8m_{xOz2}; \tag{9}$$

$$w = N_3w_1 - N_5\beta - N_7m_{xOy1} + N_4w_2 - N_6\beta_2 - N_8m_{xOy2}, \tag{10}$$

The interpolation polynomials will be chosen as:

$$\begin{aligned}
N_3 &= 1 - 10\zeta^3 + 15\zeta^4 - 6\zeta^5; & N_4 &= 10\zeta^3 - 15\zeta^4 + 6\zeta^5; \\
N_5 &= l(\zeta - 6\zeta^3 + 8\zeta^4 - 3\zeta^5); & N_6 &= l(-4\zeta^3 + 7\zeta^4 - 3\zeta^5); \\
N_7 &= \frac{l^2}{2}(\zeta^2 - 3\zeta^3 + 3\zeta^4 - \zeta^5); & N_8 &= \frac{l^2}{2}(\zeta^3 - 2\zeta^4 + \zeta^5).
\end{aligned} \tag{11}$$

The shape function matrix is:

$$\begin{aligned}
[\mathbf{N}] &= \begin{bmatrix} N_{(u)} \\ N_{(v)} \\ N_{(w)} \end{bmatrix} \\
&= \begin{bmatrix} N_1 & 0 & 0 & 0 & 0 & 0 & 0 & 0 & 0 & N_2 & 0 & 0 & 0 & 0 & 0 & 0 & 0 \\ 0 & N_3 & 0 & 0 & 0 & N_5 & 0 & 0 & N_7 & 0 & N_4 & 0 & 0 & 0 & N_6 & 0 & 0 & N_8 \\ 0 & 0 & N_3 & 0 & -N_5 & 0 & 0 & -N_7 & 0 & 0 & 0 & N_4 & 0 & -N_6 & 0 & 0 & -N_8 & 0 \end{bmatrix}
\end{aligned} \tag{12}$$

The rotations of the beam ends can be obtained as:

$$\beta = -\frac{d}{dx}([N_w]\{\delta_e\}) = -[N'_w]\{\delta_e\}; \quad \gamma = \frac{d}{dx}([N_v]\{\delta_e\}) = [N'_v]\{\delta_e\}; \tag{13}$$

Let's also note:

$$\begin{aligned}
[N^*] &= \begin{bmatrix} N_{(\alpha)}^* \\ N_{(\beta)}^* \\ N_{(\gamma)}^* \end{bmatrix} \\
&= \begin{bmatrix} 0 & 0 & 0 & N_1 & 0 & 0 & 0 & 0 & 0 & 0 & N_2 & 0 & 0 & 0 & 0 & 0 & 0 \\ 0 & 0 & -N'_3 & 0 & N'_5 & 0 & N'_7 & 0 & 0 & 0 & -N'_4 & 0 & N'_6 & 0 & N'_8 & 0 & 0 \\ 0 & N'_3 & 0 & 0 & 0 & N'_5 & 0 & N'_7 & 0 & N'_4 & 0 & 0 & 0 & N'_6 & 0 & N'_8 & 0 \end{bmatrix}
\end{aligned} \tag{14}$$

$$\begin{aligned}
[N^{**}] &= \begin{bmatrix} N_{(z)}^{**} \\ N_{(y)}^{**} \end{bmatrix} \\
&= \begin{bmatrix} 0 & 0 & -N''_3 & 0 & N''_5 & 0 & -N''_7 & 0 & 0 & 0 & -N''_4 & 0 & N''_6 & 0 & -N''_8 & 0 & 0 \\ 0 & N''_3 & 0 & 0 & 0 & N''_5 & 0 & N''_7 & 0 & N'' & 0 & 0 & 0 & N''_6 & 0 & N'' & 0 \end{bmatrix}
\end{aligned} \tag{15}$$

So:

$$\begin{Bmatrix} u \\ v \\ w \\ \alpha \\ \beta \\ \gamma \\ m_{xOz} \\ m_{xOy} \end{Bmatrix} = \begin{bmatrix} N \\ N^* \\ N^{**} \end{bmatrix} \begin{Bmatrix} \delta_1 \\ \delta_2 \end{Bmatrix} \tag{16}$$

The internal energy stored in the beam shall be calculated. The internal energy due to bending is given by the relation:

$$\begin{aligned} E_{pi} &= \frac{1}{2} \int_0^L \left[EI_y \left(\frac{d^2w}{dx^2} \right)^2 + EI_z \left(\frac{d^2v}{dx^2} \right)^2 \right] dx \\ &= \frac{1}{2} \int_0^L [EI_y \beta'^2 + EI_z \gamma'^2] dx \\ &= \frac{1}{2} \{\delta_e\}^T \left[\int_0^L (EI_y [N''_{(w)}]^T [N''_{(w)}] + EI_z [N''_{(v)}]^T [N''_{(v)}]) dx \right] \{\delta_e\} \\ &= \frac{1}{2} \{\delta_e\}^T [k_{eb}] \{\delta_e\} \end{aligned} \tag{17}$$

where E is Young's modulus, I_y and I_z represent the geometrical moment of inertia around the axis Oy and Oz .

The energy due to the tension/compression is:

$$\begin{aligned} E_{pa} &= \frac{1}{2} \int_0^L EA \left(\frac{du}{dx} \right)^2 dx = \frac{1}{2} \{\delta_e\}^T \int_0^L ([N'_u]^T [N'_u] EA dx) \{\delta_e\} \\ &= \frac{1}{2} \{\delta_e\}^T [k_{ea}] \{\delta_e\} \end{aligned} \tag{18}$$

where A is the area of the cross section of the beam.

The axial load P in an axial section of the beam gives the energy if in a first approximation the axial deformations are neglected:

$$E_a = \frac{1}{2} \int_0^L P_{tot} \left[\left(\frac{dv}{dx} \right)^2 + \left(\frac{dw}{dx} \right)^2 \right] dx = \frac{1}{2} \{\delta_e\}^T [k_e^G] \{\delta_e\} \tag{19}$$

where P_{tot} represents the axial force in the beam cross section at distance x . The force components acting at the right beam end considered in the local coordinate system are represented by $P_x, P_y = 0, P_z = 0$. Beside these components, the value of P and the components of the inertia forces acting upon the portion of the beam between x and L are being determined.

The total internal energy is:

$$\begin{aligned} E_p &= \frac{1}{2} \{\delta_e\}^T ([k_{eb}] + [k_{ea}] + [k_{et}] + [k_e^G]) \{\delta_e\} \\ &= \frac{1}{2} \{\delta_e\}^T [k_e] \{\delta_e\} \end{aligned} \quad (20)$$

The external work of distributed loads is:

$$\begin{aligned} W &= \int_0^L (p_x u + p_y v + p_z w + m_x \alpha + m_y \beta + m_z \gamma) dx \\ &= \int_0^L [p_x \ p_y \ p_z \ m_x \ m_y \ m_z] \begin{bmatrix} N \\ N^* \end{bmatrix} \{\delta_e\} dx \\ &= \{q_{eL}^*\}^T \{\delta_e\}, \end{aligned} \quad (21)$$

here the vector $\{q_{eL}^*\}$ contains the three components of the distributed loads and the three components of the distributed moments.

The external work of concentrated loads $\{q_{eL}\}$ in the nodes is:

$$W^c = \{q_{eL}\}^T \{\delta_e\} \quad (22)$$

After deformation, the position vector of point M becomes M' and it is expressed by:

$$\{r_{M',L}\} = \{r_{M,L}\} + \{\delta\} = \{r_{M,L}\} + \begin{Bmatrix} u \\ v \\ w \end{Bmatrix} = \{r_{o,L}\} + \begin{Bmatrix} x + u \\ v \\ w \end{Bmatrix}, \quad (23)$$

or, with respect to the global coordinate system:

$$\begin{aligned} \{r_{M',G}\} &= \{r_{M,G}\} + [R] \begin{Bmatrix} u \\ v \\ w \end{Bmatrix} = \{r_{o,G}\} + [R] \begin{Bmatrix} x \\ 0 \\ 0 \end{Bmatrix} + [R] \begin{Bmatrix} u \\ v \\ w \end{Bmatrix} \\ &= \{r_{o,G}\} + [R] \begin{Bmatrix} x \\ 0 \\ 0 \end{Bmatrix} + [R][N]\{\delta_e\} \end{aligned} \quad (24)$$

where the matrix $[R]$ expresses the change of the component of a vector from the local coordinate system $Oxyz$ to the fixed (global) reference system $O'XYZ$. The velocity is obtained by differentiation:

$$v_{M,G} = \dot{r}_{M',G} = \dot{r}_{o,G} + \dot{R} \begin{Bmatrix} x \\ 0 \\ 0 \end{Bmatrix} + \dot{R}N\delta_e + RN\dot{\delta}_e \quad (25)$$

The kinetic energy expression is:

$$E_c = \frac{1}{2} \int_0^L \rho \left(A \{ \dot{r}_{M',G} \}^T \{ \dot{r}_{M',G} \} + \{ \omega'_L \}^T [I] \{ \omega'_L \} \right) dx \quad (26)$$

where:

$$[I] = \begin{bmatrix} I_x & 0 & 0 \\ 0 & I_y & 0 \\ 0 & 0 & I_z \end{bmatrix} \quad (27)$$

I_{yy} and I_{zz} represent moments of inertia of the beam cross section about coordinate axis Oy and Oz , respectively, of a reference system with its origin in the mass center of the element $dm = \rho A dx$ (ρ -density); I_{xx} is the inertia moment about the co-ordinate axis Ox . We have chosen y and z as principal directions of inertia $I_{yz} = 0$, we have:

$$\{ \omega'_L \} = \begin{Bmatrix} \omega_{1L} \\ \omega_{2L} \\ \omega_{3L} \end{Bmatrix} + \begin{Bmatrix} \dot{\alpha} \\ \dot{\beta} \\ \dot{\gamma} \end{Bmatrix} = \begin{Bmatrix} \omega_{1L} \\ \omega_{2L} \\ \omega_{3L} \end{Bmatrix} + [N^*] \{ \delta_e \} \quad (28)$$

here ω_{1L} , ω_{2L} , ω_{3L} are the components of the vector angular velocity refer to the local coordinate system.

The Lagrangian for one is:

$$L = E_c - E_p - E_a + W + W^c. \quad (29)$$

Applying the Lagrange's equations [21–24]:

$$\frac{d}{dt} \left\{ \frac{\partial L}{\partial \dot{\delta}_e} \right\} - \left\{ \frac{\partial L}{\partial \delta_e} \right\} = 0. \quad (30)$$

the motion equations for a single element in a centrifugal field can be obtained in the form:

$$\begin{aligned}
& ([m_{11}] + [m_{22}])\{\ddot{\delta}_e\} + 2\omega([m_{21}] - [m_{12}])\{\dot{\delta}_e\} \\
& + [k_e] + \varepsilon([m_{21}] - [m_{12}]) - \omega^2([m_{11}] + [m_{22}]) \\
& = \{q_e\} + \{q_e^*\} - \{q_e^i(\varepsilon)\} - \{q_e^i(\omega^2)\} - [m_{Ee}^i][I]\{\varepsilon\}_L \\
& - [m_{oe}][R]^T\{\ddot{r}_o\}
\end{aligned} \tag{31}$$

where:

$$\begin{aligned}
[m_{oe}^i] &= \int_0^L \rho A [N]^T dx; \quad [m_{Ee}^i] = \int_0^L [N]^* dx; \quad [m_{ij}] = \int_0^L [N_i]^T [N_j] \rho A dx \\
& \qquad \qquad \qquad i, j = 1, 2, 3 \\
\{q_e^*\} &= \int_0^L [p_x \ p_y \ p_z \ m_x \ m_y \ m_z] \begin{Bmatrix} N \\ N^* \end{Bmatrix} dx
\end{aligned} \tag{32}$$

3 Eigenvalues and Domain of Stability

In the following, it was studied a beam that is in a centrifugal field, following how the eigenvalues of the system change according to the variation of the beam geometrical parameters. Considering a certain number of finite elements in which the structure is discretized, after assembling, the motion equations will be of the form:

$$[M]\{\ddot{\Delta}\} + [C]\{\dot{\Delta}\} + [K]\{\Delta\} = 0 \tag{33}$$

The matrix $[C]$ is skew-symmetric. If we note:

$$\{X\} = \{\Delta\}; \quad \{Y\} = \{\dot{\Delta}\} \tag{34}$$

The beam is considered clamped to one end and has a rotation motion around this end with variable angular speed ω .

To perform the calculus, we used the soft MATLAB with its classical subroutines (Figs. 1 and 2).

The motion equations become a linear differential system of the form:

$$\begin{Bmatrix} \dot{X} \\ \dot{Y} \end{Bmatrix} = \begin{bmatrix} 0 & E \\ -[M]^{-1}[K] & -[M]^{-1}[C] \end{bmatrix} \begin{Bmatrix} X \\ Y \end{Bmatrix} \tag{35}$$

In a previous paper, it has been shown that the skew-symmetric matrix $[C]$ does not change the nature of the system matrix's eigenvalues (35). The eigenvalues will

Fig. 1 Eigen pulsations for a beam with $L = 0.55$ m (D variable and ω variable)

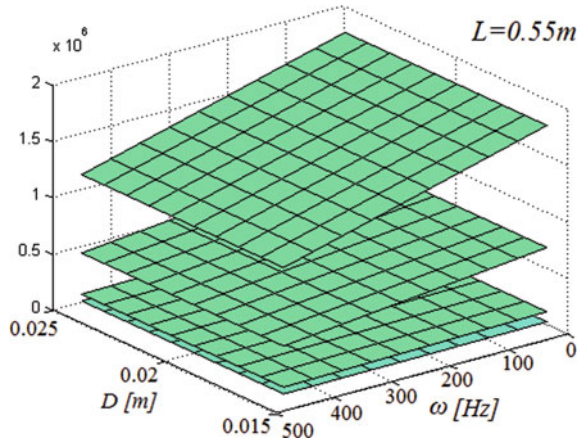
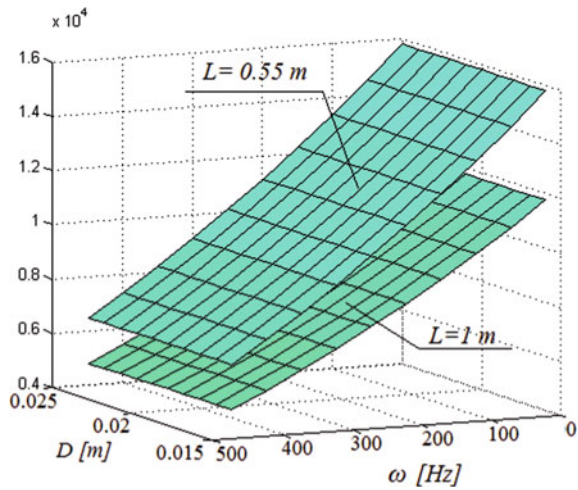


Fig. 2 Eigen pulsations for a beam with $L = 0.55$ m and $L = 1$ m (D variable and ω variable). The first eigenvalue



be complex, without a real part (the Coriolis matrix doesn't introduce damping in the system) (Figs. 3 and 4).

The problem arising in calculating a beam in a centrifugal field is the loss of stability, which happens from a mathematical point of view, when the stiffness matrix becomes negatively defined.

It is virtually impossible to determine analytical expressions to determine the geometric and mass field that ensures the stability of the beam in the centrifugal field. In this case, a numerical analysis can be made to determine the nature of the values.

The numerical calculus of eigenvalues and eigenvectors for a matrix is a difficult operation that consumes time resources. A simpler method is to determine whether the stiffened matrix is positively defined. For a set of defining values for the beam,

Fig. 3 Eigen pulsations for a beam with $L = 0.55 \dots 0.1$ m (D variable and ω variable). The first eigenvalue

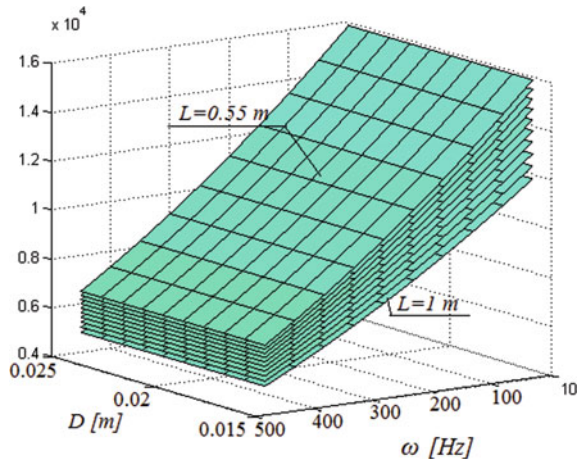
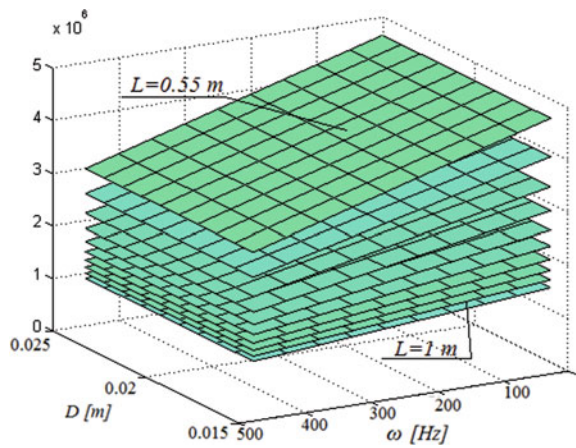


Fig. 4 Eigen pulsations for a beam with $L = 0.55 \dots 0.1$ m (D variable and ω variable). The fifth eigenvalue



it is determined whether the matrix is positively defined. If it is negatively defined then the beam enters into a field of instability. In the paper, the stiffness matrix was analyzed for different sets of beam length, diameter, and angular speeds with which the beam is rotated in a centrifugal field. Figures 5, 6 and 7 show these results. The areas in which we have instability are hatched in the figure.

4 Conclusions

Operation of a machine element that can be modeled as a beam, being in a centrifugal field, can lead to instability phenomena, especially for the reason that the rotations can be found frequently in technical applications. For this reason, it is the question

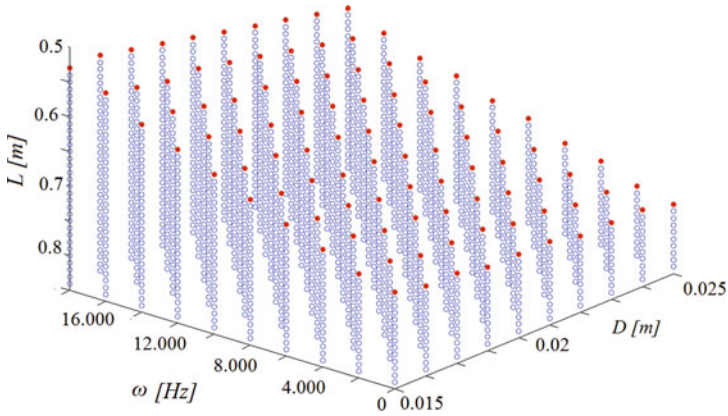


Fig. 5 Domain of instability for D, ω, L variable

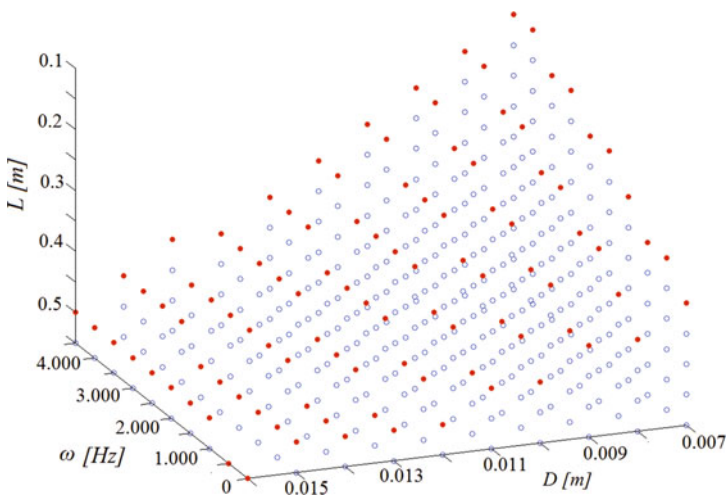


Fig. 6 Domain of instability for D, ω, L variable

of determining the admissible values for geometric and mass elements. Because a theoretical approach is less useful in practical applications, only the numerical approach can provide useful results. In the paper, the motion equations obtained by other authors have been used, in a particular form, for the rotation of a beam around an axis. On the basis of these equations obtained via FEA, it is analyzed for some cases, the domain of values that the geometric and mass parameters can have. The results are presented in graphical form and the method used to determine areas of instability uses the calculation of the positivity of the stiffness matrix, a much easier operation than the calculation of its eigenvalues. Our application is inspired from the practical case of the rotor blade of helicopters, where the use of one-dimensional

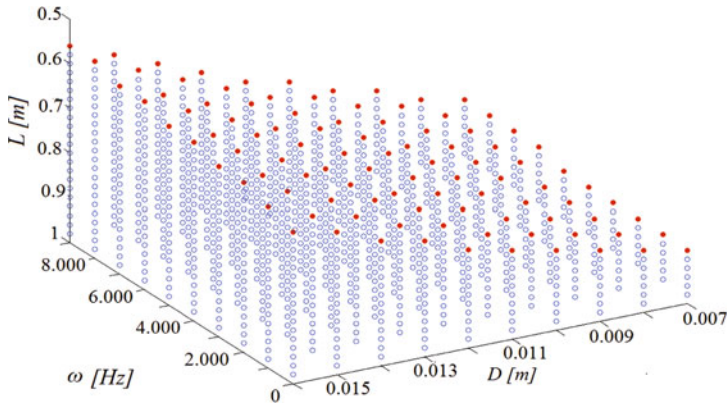


Fig. 7 Domain of instability for D , ω , L variable

finite element has the advantage of simplicity and offers, in the same time, good results. Such kind of problems occurs often in the engineering practice where great operation speed and high loads can lead to instability.

References

1. A.G. Erdman, G.N. Sandor, A. Oakberg, A general method for kineto-elastodynamic analysis and synthesis of mechanisms. *J. Eng. Ind. ASME Trans.* **94**(4), 1193–1203 (1972)
2. P. Fanghella, C. Galletti, G. Torre, An explicit independent-coordinate formulation for equations of motion of flexible multibody systems. *Mech. Mach. Theory* **38**, 417–437 (2003)
3. B.S. Thompson, C.K. Sung, A survey of finite element techniques for mechanism design. *Mech. Mach. Theory* **21**(4), 351–359 (1986)
4. S. Vlase, Finite element analysis of the planar mechanisms: numerical aspects. *Appl. Mech.* **4**, 90–100 (1992)
5. S. Vlase, Dynamical response of a multibody system with flexible element with a general three-dimensional motion. *Rom. J. Phys.* **57**(3–4), 676–693 (2012)
6. J.-F. Deu, A.C. Galucio, R. Ohayon, Dynamic responses of flexible-link mechanisms with passive/active damping treatment. *Comput. Struct.* **86**(35), 258–265 (2008)
7. D. De Falco, E. Pennestri, L. Vita, An investigation of the influence of pseudoinverse matrix calculations on multibody dynamics by means of the Udwadia-Kalaba formulation. *J. Aerosp. Eng.* **22**(4), 365–372 (2009)
8. J. Gerstmayr, J. Schberl, A 3D finite element method for flexible multibody systems. *Multibody Syst. Dyn.* **15**(4), 305–320 (2006)
9. A. Ibrahimbegovic, S. Mamouri, R.L. Taylor, A.J. Chen, Finite element method in dynamics of flexible multibody systems: modeling of holonomic constraints and energy conserving integration schemes. *Multibody Syst. Dyn.* **4**(2–3), 195–223 (2000)
10. N.V. Khang, Kronecker product and a new matrix form of Lagrangian equations with multipliers for constrained multibody systems. *Mech. Res. Commun.* **38**(4), 294–299 (2011)
11. G. Piras, W.L. Cleghorn, J.K. Mills, Dynamic finite-element analysis of a planar high speed, high-precision parallel manipulator with flexible links. *Mech. Mach. Theory* **40**(7), 849–862 (2005)

12. S. Vlase, P.P. Teodorescu, Elasto-dynamics of a solid with a general "Rigid" motion using FEM model part I. Theoretical approach. Rom. J. Phys. **58**(7–8), 872–881 (2013)
13. S. Vlase, P.P. Teodorescu, C. Itu et al., Elasto-dynamics of a solid with a general "Rigid" motion using FEM model part II. Analysis of a double cardan joint. Rom. J. Phys. **58**(7–8), 882–892 (2013)
14. S. Vlase, C. Danasel, M.L. Scutaru, M. Mihalca, Finite element analysis of two-dimensional linear elastic systems with a plane rigid motion. Rom. J. Phys. **59**(5–6), 476–487 (2014)
15. B. Simeon, On Lagrange multipliers in flexible multibody dynamic. Comput. Methods Appl. Mech. Eng. **195**(50–51), 6993–7005 (2006)
16. S. Vlase, M. Marin, A. Öchsner et al., Motion equation for a flexible one-dimensional element used in the dynamical analysis of a multibody system. Continuum Mech. Thermodyn. **31**, 715 (2019). <https://doi.org/10.1007/s00161-018-0722-y>
17. M. Marin, A. Öchsner, The effect of a dipolar structure on the Holder stability in Green-Naghdi thermoelasticity. Continuum Mech. Thermodyn. **29**(6), 1365–1374 (2017)
18. M. Marin, Cesaro means in thermoelasticity of dipolar bodies. Acta Mech. **122**(1–4), 155–168 (1997)
19. M. Marin, A. Öchsner, *Complements of Higher Mathematics* (Springer, Cham, 2018)
20. A. Öchsner, *Computational Statics and Dynamics: An Introduction Based on the Finite Element Method* (Springer, Singapore, 2016)
21. I. Negrean, *New Formulations in Analytical Dynamics of Systems*, Acta Technica Napocensis. Applied Mathematics, Mechanics and Engineering, vol. 60, issue I (2017), pp. 49–56
22. I. Negrean, *Mass Distribution in Analytical Dynamics of Systems*, Acta Technica Napocensis. Applied Mathematics, Mechanics and Engineering, vol. 60, issue II (2017), pp. 175–184
23. I. Negrean, *Generalized Forces in Analytical Dynamics of Systems*, Acta Technica Napocensis. Applied Mathematics, Mechanics and Engineering, vol. 60, issue III (2017), pp. 357–368
24. S. Vlase, A Method of eliminating Lagrangian-Multipliers from the Equation of Motion of Interconnected Mechanical Systems. J. Appl. Mech. Trans. ASME **54**(1), 235–237 (1987)

Environmental and Occupational Noise

Development of Methodologies and Means for Noise Protection of Urban Areas—Project Results



Zlatan Šoškić , Milan Kolarević , Branko Radičević ,
Momir Praščević , and Vladan Grković 

Abstract The paper presents the results of the Serbian national project “Development of methodologies and means for noise protection of urban areas” after eight years of work (2011–2018). Initially designed to last for four years; the project was extended and represented an important contribution to the development of technological basis for creation and implementation of noise protection policies in Serbia. The paper has presented the resources committed to the realization of the project, publications, registered technical achievements, as well as Ph.D. thesis and other results achieved in the course of the project duration. The project impact and a lack of an institutional response up to now are also discussed.

1 Introduction

In 2009, the Government of Republic of Serbia has passed the law on environmental noise protection [1] that addressed subjects in charge for environmental noise protection, means and conditions for environmental noise protection, measurements of environmental noise, access to information about noise surveillance and other topics of relevance for environmental and health protection. Further, directions were defined by respective regulations [2], guidelines [3–7] and standard [8] that are relevant to environmental noise protection and are in line with the Directive 2002/49/EC [9] of European Parliament and The Council of The European Union.

However, majority of the measures prescribed by the regulations were not supported by the existence of relevant accredited institutions, noise protection means available at market and adequate software support. Proposed as a response to a call of the Serbian Ministry for Science and Technology, the project “Development of

Z. Šoškić (✉) · M. Kolarević · B. Radičević · V. Grković
Faculty of Mechanical and Civil Engineering in Kraljevo,
University of Kragujevac, Kragujevac, Serbia
e-mail: soskic.z@mfkv.kg.ac.rs

M. Praščević
Faculty of Occupational Safety, University of Niš, Niš, Serbia

Table 1 Project goals and objectives

Goal	Development of methodologies for estimation of degree of exposition to noise	Development of methods and materials for noise protection	Design of means for active and passive noise protection	Dissemination of the results
Objectives	Study on dominant noise sources in urban environment	Design and testing of reverberation chamber	Methodologies for application of active noise protection	Website of the project
	Database on urban noise sources	Accreditation of laboratory for urban noise measurements	Design of modular noise barriers	Launching of regional journal on noise protection
	Software support to strategic noise mapping	Investigation of acoustic properties of materials	Design of modular cabins for noise protection	Seminars on noise protection
	Methodology for drawing of action plans for noise protection of urban environment	Database on acoustic properties of materials	Implementation of the designed solutions	Monograph on noise protection of urban areas

methodologies and means for noise protection of urban environment” (acronym “urbaNoise”) is aimed to facilitate the solution of these problems and deficiencies. The project was initially proposed to last for four years (2011–2014); but by the decision of the ministries responsible for science and technology development, it was later extended on annual basis, and it is still underway in 2019.

The goals and objectives of the project, and the project plan and the organization were described in a paper published at the start of the project [10]. The structure of the goals and objectives of the product is repeated here in Table 1.

This paper presents an overview of the project resources, activities and main results achieved in the period of 2011–2018. Its main goal is to assess the overall impact of the project. Besides, with reference to the paper it describes the project [10], and this paper should be a useful tool for planning further projects and actions.

2 Concept and Activities

According to the initial project plan, which was realized in the period 2011–2014, the project consisted of six work packages, presented in Fig. 1. The first work package “Theoretical and methodological project preparation” was of a preparatory character and managerial type. The activities of the work package comprised of state-of-the-art analysis, definition of the project aim and structure of the goals, the establishment

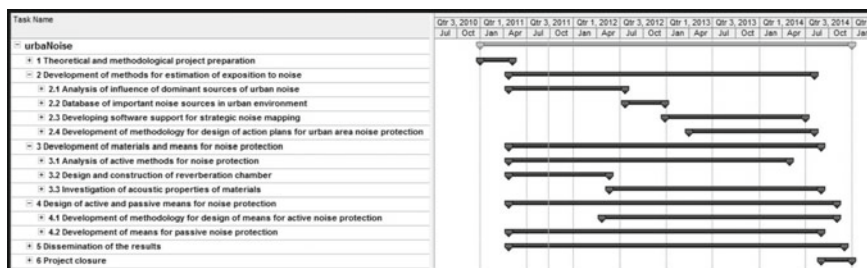


Fig. 1 Gantt chart of the project

of the team and organizational structure of the project, determining the work breakdown structure, resource requests analysis, cost–benefit analysis, determining of the expected results and risk analysis. The work package lasted for four months (January to April 2011), and the results of that activity were later presented in the paper [10].

The activities of the three following work packages, which were carried out simultaneously and independently were of scientific character. The simultaneous flow was possible due to the difference in the required expertise, which enabled avoiding of overlapping between the assignments of team members.

The work package “Development of methods for estimation of exposition to noise” comprised of four activities. The activity “Analysis of influence of dominant sources of urban noise”, primarily scheduled for the period 2011–2012, raised a lot of attention of the project team and, after the completion of the initial project plan in 2014, was turned into a permanent activity in the period of 2015–2018. Within the activity were studied industrial noise sources met in practice of Serbian industry (impact hammers, junkyard presses, fans and other components of ventilation systems) [11–14], traffic noise sources (railway vehicles, buses and helicopters) [15–19] and noise sources of public service companies (construction machinery) [20–22]. The key source of the project results was the activities performed on systematic noise measurements of the road traffic in cities Niš and Kraljevo [23–25]. The obtained results were served as the basis for updating the present [26–28] and the development of new traffic noise models, based on application of the soft computing techniques [29, 30]. The activity “Database of important noise sources in urban environment” was completed in 2012 [31, 32], and the database was made publicly available; but the amount of data in the database is still very limited. The activity “Developing software support for strategic noise mapping” is passed through a change of the initial scope, as it was redirected to develop a software tool for the calculation of noise fields in urban areas. The reason for the change was the presence of complex commercial software packages for strategic noise mapping, which were, on the other hand, not suited for usual applications of development of local noise protection measures. The software package for the local noise mapping became available in 2013 [33, 34] and was later used for evaluating variants of noise protection systems by project team [35, 36]. The activity “Development of methodology for design of action plans for noise protection of urban areas” comprised two groups of actions: analysis and definition of the

descriptors of the influence of the noise to environment [37–39], and the development of procedures for systematic assessment of the level of danger that noise poses to environment [40–44].

Activities of the work package “Development of materials and means for noise protection” were carried out in two directions: the first was the development of the means for characterization of materials for noise protection [45–47] and the second was the development of the materials for noise protection [48–50]. While the initial project plan considered just the construction of the reverberation chamber for the characterization of the noise protection materials, during the project it was found out that the other means for the characterization of noise protection materials are needed, and they were designed and manufactured almost until the end of the initial project lifetime in 2014. Conversely, the activities on the studies of the sound absorption materials were postponed for the project extension in the period of 2014–2018.

The activities of the work package “Design of active and passive means for noise protection” were focused to the application of the methodologies and means developed within the previous two work packages to the construction of the noise protection systems against the industrial [11–13, 51, 52] and traffic [35, 36, 52, 53] noise. Despite the practical aspect of the activity, certain conclusions of general character were drawn [54, 55], which suggest the directions of development and construction of modular components for noise protection.

The whole project was made permanent efforts within the work package “Dissemination of project results” and not only in the form of publication of scientific papers and participation in scientific conferences aimed for researchers, but also through the organization of seminars for noise protection aimed at professionals in environmental protection, as well as by participation in the technical fairs organized in Serbia, aimed at the widest range of general audience.

3 Results

The project results are published in 59 papers in international, as well as in 43 papers in national, peer-reviewed journals; they were also presented in 123 articles in international and 14 articles in national conferences. A list of the references of the selected publications is given in the literature, and a more complete overview may be found at the overview of project results at the website of the project, <http://www.mfkv.kg.ac.rs/urbanoise/pages/ostvareni-rezultati.php>. However, here it will be pointed out some important project results of practical importance that are not visible in the publications, or which are not presented in the publications in a systematic way.

Six project results are registered as original technical accomplishments at national level:

- The reverberation chamber constructed at the Faculty of Mechanical and Civil Engineering in Kraljevo (Fig. 2); the reverberation chamber, with the volume of 203 m³, is the largest reverberation chamber in Serbia.

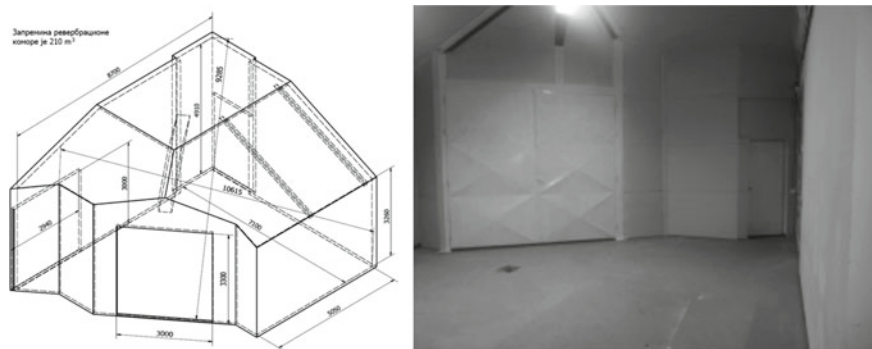


Fig. 2 Drawing and photograph of the reverberation chamber of the Faculty of Mechanical and Civil Engineering in Kraljevo

- The software package for drawing of local noise maps “BelCo” (Fig. 3); the software enables calculation of noise levels according to the ISO 9613-2 standard in a field represented by a 3D rectangular network of points.
- Noise protection system of the “SPIK Ivanjica Fantoni Group” plywood factory close to the residential area of a Serbian town (Ivanjica); the system, which comprises construction of two barriers with height of 6 m and total length of 108 m, as well as sound insulation of the selected noise sources within the factory (Fig. 4), reduced the maximal specific daily noise level in the surrounding settlement from 76 dB(A) to 62 dB(A), which is below the legally allowed 65 dB(A) 52.
- Database on noise sources that enables the description of noise sources by sound power, spectral content and spatial distribution of their noise emission; publicly available at the URL <http://www.mfkv.kg.ac.rs/urbanoise/dbnoise/> the database

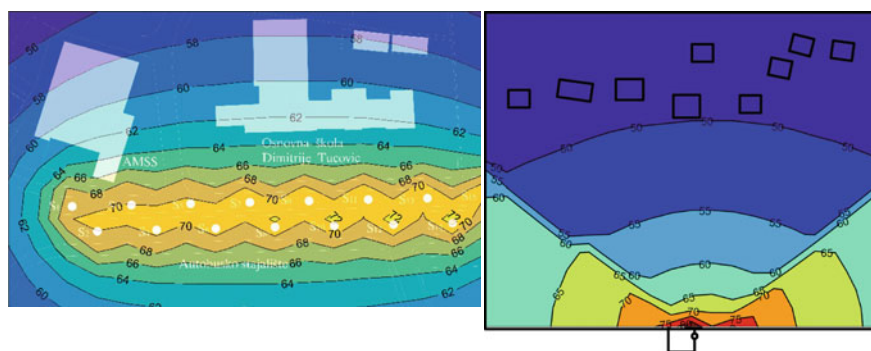


Fig. 3 Noise map of the area around an elementary school located between two crossroads in Kraljevo (left) and a neighbourhood of a car scrapyards (right), calculated by the “BelCo” software package



Fig. 4 Elements of the noise protection system in the “SPIK Ivanjica Fantoni Group” plywood factory

underwent recent reconstruction to be capable of storing various data that arose from measurements of noise emissions [31, 32].

- Acoustic zoning of City of Niš (Fig. 5), as the first and the most comprehensive endeavour of that type in Serbia, which comprised definition of the acoustic zones and limiting values of noise indicators, then calculation and measurement of the indicators, followed by the comparison of the two datasets which allowed the identification of the present level of danger and definition of action plans [41, 42].
- The NAISS model for calculation of the level of traffic noise in urban areas of Serbia; the model enables calculation of the equivalent noise level (L_{eq}) based on the number of the cars, buses and trucks within a period [26, 27].

Apart from that registered technical achievements were also constructed other noise protection systems:

- sound insulation of a small mechanical workshop with eccentric presses is located in a densely populated residential area of a Serbian City (Čačak); starting from the theoretical model of acoustic insulation power of a single solid partition, a complex partition and a multi-layer partition, the acoustic insulation power of the

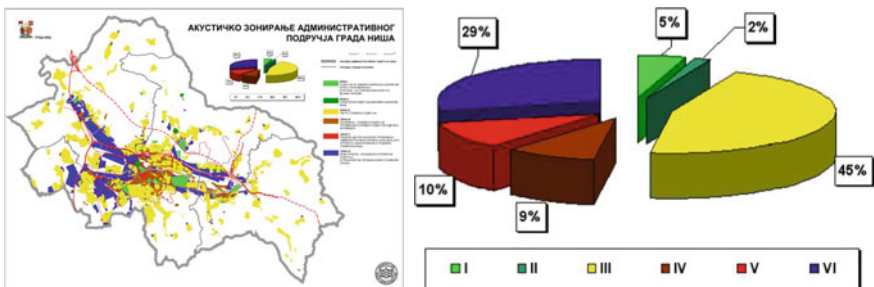


Fig. 5 Graphical representation of acoustic zones in the City of Niš and the distribution of surfaces of the acoustic zones

walls and the ceiling in the workshop were determined so that the noise level of 94 dB(A) in the machine room is reduced to 47 dB(A) in front of the building [12];

- noise protection curtain for a scrapyard with car crushers close to a suburban area of a Serbian City (Užice); application of the noise protection mean reduced the noise level in the control point on the border of the residential area from 53.1 to 51.2 dB(A) and the calculate noise map. Figure 3 shows that the level of the noise within the residential area is less than 50 dB [13];
- acoustic treatment of a mechanical workshop with seven machines that generated cumulative noise levels of 94.4 dB(A); by covering all of the open surfaces of the workshop (walls, floors and ceilings) with sound absorption materials, the noise level was reduced to 87.7 dB(A), which is sufficient to allow permanent exposition to noise in periods less than 6 h [51];

The project was also developed and three measurement systems for the characterization of materials by sound absorption, transmission or emission:

- Device for the measurement of airflow resistance according to the standard SRPS ISO 9053 (Fig. 6); the measurement cell of the device has the inner diameter of 100 mm and length of 300 mm; the air pump enables laminar airflow of 0,4 l/min through the measurement cell; the dynamic range of the pressure difference measurement is 1–200 Pa, and the measurement error of the airflow resistance is less than 7% in the range of 1.5–30 MPa s/m³ [46];
- Laboratory prototype of a photoacoustic system for the characterization of porous materials and biological tissues (Fig. 7); the system employs an open-ended photoacoustic cell configuration and enables photoacoustic excitation by a LED or laser diode light modulated in the frequency range of 10 Hz–10 kHz [47];
- Laboratory prototype of a low-cost noise measurement monitoring station based on a MEMS microphone technology and a Raspberry Pi microcontroller (Fig. 7); after the construction, a communication protocol is developed and tested, and the further development comprises connection of temperature, wind speed and humidity sensors, as well as preparation for networking of similar devices [39];

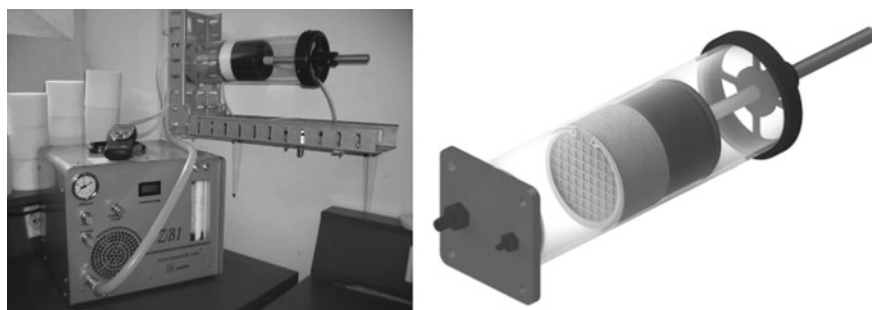


Fig. 6 Device for measurement of the airflow resistance (left) and a model of its cell (right)

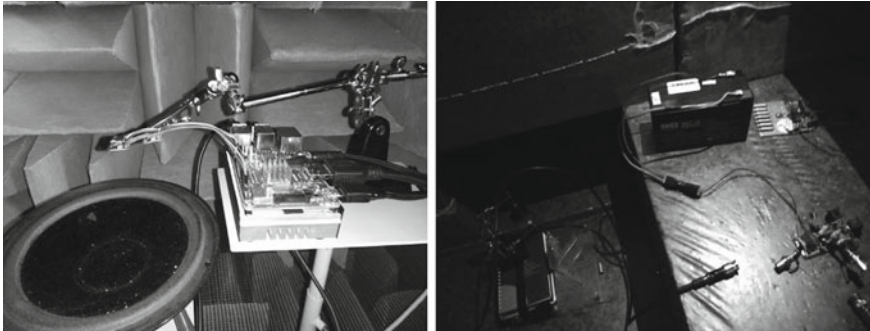


Fig. 7 Laboratory prototypes tests of the low-cost monitoring system (left) and photoacoustic measurements system (right) in an anechoic chamber

Under the auspices of the project were organized four seminars and one lecture for noise protection professionals, mainly the inspectors of the environmental protection departments of local governments. Besides, the project team supported through participation in program committees and organizing committees, organization of eight international conferences (four in Serbia and four in Romania) that dealt with noise and vibration protection.

Finally, the project team members have defended seven Ph.D. theses within the project duration. While three of them had an interdisciplinary character, four had topics directly connected to the subject of project [56–59].

4 Analysis

Since the ultimate goal of the paper is to serve as a tool for planning of future projects, the results should be considered from the aspect of the resources committed to the project.

The research organizations that participated in the projects were three faculties from three major Serbian universities: (1) The Faculty of Mechanical and Civil Engineering in Kraljevo of University of Kragujevac; (2) The Faculty of Occupation Hazard from University of Niš; and (3) The Faculty of Transport and Traffic Engineering of University of Belgrade. The supporting organizations were representative end-users of the project results, two Serbian local governments (City of Niš and City of Kraljevo) and two Serbian companies (“Korali” from Kraljevo and “ABS Mine!” from Mladenovac).

The team consisted both from experienced researchers (full professors, associate professors, assistant professors and research associates) and Ph.D. students (teaching assistants and research assistants). The composition of the project team varied through years from the points of view of the number of project team members, the level of their competences and their work engagement, as shown in Fig. 8. After

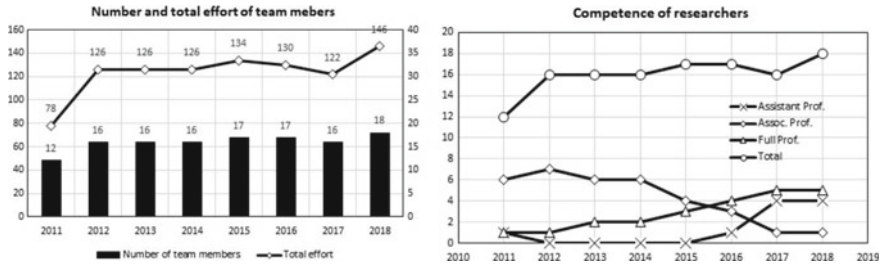


Fig. 8 Number and total effort of team members (left) and competence of the team members (right) in the period of 2011–2018

the start-up phase of the project, the overall research effort and research competence of the project team was kept constant by the replacement of the retired (hence most experienced) researchers by Ph.D. students without previous research experience.

The calculated direct project costs for the period 2011–2018 are close to 585,000 EUR with major part (close to 76%) being the personnel costs (Fig. 9), with the remaining costs being the equipment costs (around 18%), material, travel costs and overheads (in total 6%). However, the project funding may be separated into two distinct phases, the first during the initial project period (2011–2014) and the second in the extended period (2015–2018). While the first phase was characterized by a coherent long-term plan, the extensions of the project were granted as temporary measures, on annual basis. As a consequence, the annual project costs decreased in the extended period (Fig. 9), and, what could be even more important, the structure of the direct costs profoundly differed in the two periods (Fig. 10). The ratio between the personnel costs and equipment costs increased from 2.5 during the initial project period to 11 during the extension of the project lifetime.

For the sake of the analyses, the project output is also very roughly structured on annual basis, providing the results presented in Fig. 11. The distinction between the publication output in two periods is striking: the average number of publications was rising during the initial project period, characterized by long-term planning and

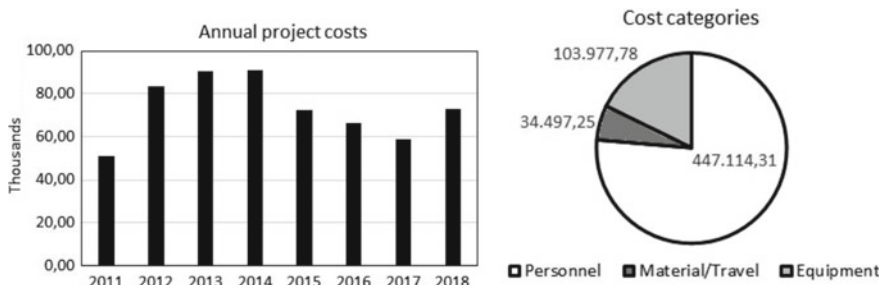


Fig. 9 Annual direct project costs (left) and direct cost distribution over categories (right)

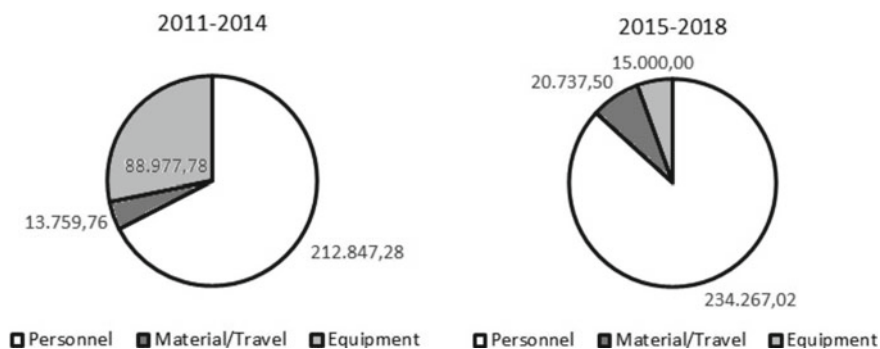


Fig. 10 Distribution of the direct project costs (in EUR) within the initial (left) and the extended (right) project period

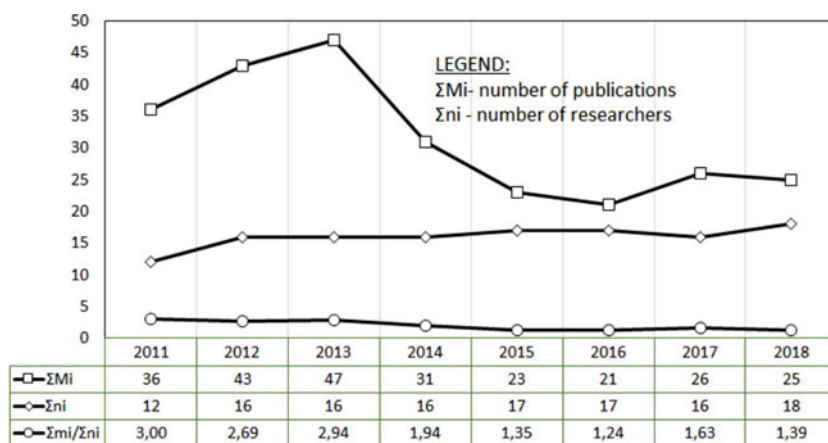


Fig. 11 Annual project output of the project

clear personal goals for each of the researchers and was suddenly halved after the project funding went to short-term arrangements.

Although the publications are not the only output of the project, the results presented in Fig. 11 are certainly worthy of consideration. It is the fact that during the periods of 2015–2018 were written and defended all the seven Ph.D. theses of researchers from project team, and that two more Ph.D. theses are being prepared for 2019; since both the candidates and mentors (who are also the members of the project team) were occupied with the activities during the process, a decline in the number of publications is expected. However, no original technical achievements or patents were registered in the meantime, and since the research effort stayed constant, the decrease of the project output in the period of 2015–2018 should be accepted as a fact.

5 Conclusions

The presented paper describes a national research project on noise protection, which was envisioned as a technical complement to the legislative measures made by the beginning of the decade. From the technical point of view, the project was successful, as it resulted in the establishment of hardware and software tools, procedures and methodologies that were devised to enable implementation of the legal framework. Further, it profoundly expanded the research basis for further studies of the noise abatement measures. Finally, it also established a basis for strengthening of the national education framework on noise and vibrations, as it is evident by the fact that majority of the project team members now participate also in the EU funded education project “Strengthening Educational Capacities by Building Competencies and Cooperation in the Field of Noise and Vibration Engineering—SENVIBE”, which is carried out within the Erasmus Plus program.

However, the project team members believe that the project did not have the expected social impact because of the lack of true interest of the society at large. A very good and modern legal framework is not supported by a strong push towards its implementation. A full decade after the Law on Environmental Noise Protection is passed, no Serbian City really implements a consequent action plan for noise protection, and a majority of the local governments has a rather formal approach to the problem of environmental noise, as it was the case in 2011 [60].

The presented analysis led also to an unintended, but potentially very important conclusion. The research results of the project definitely thrived during the period when the project team carried out a coherent long-term plan. The same project team, under the same management, almost halved the research output during the period of short-term planning, which suggests that, despite frequent assertions that long-term projects do not suit the needs of industry, their beneficial influence to research may not be easily disputed.

Acknowledgements The authors wish to express their gratitude to the Ministry for education, science and technology of the Republic of Serbia for support through the research grant TR37020. The paper is dedicated to the memory of Prof. Dr. Zoran Petrović, who recently passed away, but who envisioned this project, led its development, and participated in it until his retirement in 2015.

References

1. Law on environmental noise protection of Republic of Serbia, Official Gazette of Republic of Serbia, No. 36/2009 (2009)
2. Regulation on noise indicators, limiting values and methods for estimation of noise indicators, annoyance and detrimental effects of noise, Official Gazette of Republic of Serbia, No. 75/2010 (2010)
3. Guidelines on methodology for determination of acoustical zones, Official Gazette of Republic of Serbia, No. 72/2010 (2010)

4. Guidelines on methods for noise measurements, contents and scope of noise measurement report, Official Gazette of Republic of Serbia, No. 72/2010 (2010)
5. Guidelines on methodology for design of action plans, Official Gazette of Republic of Serbia, No. 72/2010 (2010)
6. Guidelines on contents and methods of strategic noise mapping and their public presentation, Official Gazette of Republic of Serbia, No. 80/2010 (2010)
7. Guidelines on conditions and documentation for expert organization for noise measurements, Official Gazette of Republic of Serbia, No. 72/2010 (2010)
8. Serbian standard ISO 1996-1,2, Official Gazette of Republic of Serbia, No. 72/2010 (2010)
9. Directive 2002/49/EC of The European Parliament and The Council of The European Union (2002)
10. M. Kolarević, Z. Šoškić, Z. Petrović, B. Radičević, Noise protection in urban environment—description of a project. *Mech. Transp. Commun.* (3), article No. 0593, IV69–IV78 (2011)
11. B. Radičević, Z. Petrović, S. Todosijević, Z. Petrović, Design of noise protection of industrial plants-case study of a plywood factory, in *Proceedings of the 23rd National and 4th International Conference “Noise and Vibration”*, Niš 17–19 Oct 2012 (2012), pp. 71–75
12. Z. Petrović, B. Radičević, M. Kolarević, V. Grković, Sound insulation of a mechanical workshop, in *Proceedings of the 24th International Conference “Noise and Vibration”*, Niš, 29–31 Oct 2014 (2014), pp. 135–140
13. B. Radičević, M. Kolarević, M. Bjelić, V. Grković, Z. Šoškić, Noise protection of an automobile scrapyard with car crushers—a case study. *Appl. Mech. Mater.* **801**, 71–76 (2015)
14. A. Petrović, M. Rasinac, V. Grković, M. Ivanović, An experimental plan for noise analysis and chatter detection in milling depending on the cutting parameters, in *Proceedings of 26th International Conference Noise Vibration*, Niš, 6–7 Dec 2018 (2018), pp. 41–44
15. B. Tatić, N. Bogojević, Z. Šoškić, Z. Petrović, Railway vehicles as source of noise in urban areas, in *Proceedings of The VII International Triennial Conference “Heavy Machinery-HM 2011”*, Vrnjačka Banja, 29 June–2 July 2011 (2011), pp. 71–80
16. J. Tomić, N. Bogojević, M. Pljakić, Measurements of noise of diesel motor train of series ŽS 711, in *Proceedings of 25th International Conference “Noise and Vibration”*, Tara (2016), pp. 81–85
17. J. Tomić, N. Bogojević, Measurements of noise levels of freight trains on Serbian railways, in *Proceedings of the IX International Conference “Heavy Machinery-HM 2017”* (2017), pp. E71–E76
18. D. Sekulić, V. Dedović, S. Rusov, S. Šalinić, A. Obradović, Analysis of vibration effects on the comfort of intercity bus users by oscillatory model with ten degrees of freedom. *Appl. Math. Model.* **37**(18–19), 8629–8644 (2013)
19. B. Tatić, N. Bogojević, S. Todosijević, Z. Šoškić, Analysis of noise level generated by helicopters with various numbers of blades in the main rotor, in *Proceedings of the 23rd National Conference and 4th International Conference “Noise and Vibrations”*, Niš 17–19 Oct 2012 (2012), pp. 249–253
20. B. Cvetanovic, D. Cvetkovic, M. Ristic, A. Milosevic, Application of 3×3 Matrix Method in the estimating of risk of vibrations generated during the use of agriculture tractors. *J. Environ. Prot. Ecol.* **15**(2), 750–757 (2014)
21. B. Cvetanović, D. Cvetković, M. Prašćević, M. Cvetković, M. Pavlović, An analysis of the impact of agricultural tractor seat cushion materials to the level of exposure to vibration. *J. Low Freq. Noise Vib. Active Control* **36**(2), 116–123 (2017)
22. M. Cvetković, B. Cvetanović, M. Feadto Neto, The evaluation of the whole-body vibration exposure of vibratory roller operators, in *Proceedings of 26th International Conference Noise and Vibration*, Niš, 6–7 Dec 2018 (2018), pp. 151–153
23. M.R. Prascevic, D.I. Mihajlov, D.S. Cvetkovic, Measurement and evaluation of the environmental noise levels in the urban areas of the city of Nis (Serbia). *Environ. Monit. Assess.* **186**(2), 1157–1165 (2014)
24. D.I. Mihajlov, M.R. Prascevic, Permanent and semi-permanent road traffic noise monitoring in the city of Nis (Serbia). *J Low Freq. Noise Vib. Active Control* **34**(3), 251–268 (2015)

25. M. Prašćević, D. Mihajlov, M. Ličanin, Noise monitoring on the territory of the city of Niš—overview of the methodologies and the results, in *Proceedings of the 26th International Conference "Noise and Vibration"*, Niš, Serbia, 6–7 Dec 2018 (2018), pp. 85–92
26. M. Prasecevic, D. Cvetković, D. Mihajlov, NAISS model validation based on measured data of noise monitoring, in *Proceedings of VII International Triennial Conference "Heavy Machinery-HM 2011"*, Vrnjačka Banja, 29 June–2 July 2011, No 6 (2011), pp. 35–38
27. M. Prasecevic, D. Cvetkovic, D. Mihajlov, Z. Petrovic, B. Radicevic, Verification of NAISS model for road traffic noise prediction in urban areas. *Elektron. elektrotehnika* **19**(6), 91–95 (2013)
28. M. Prašćević, A. Gajicki, D. Mihajlov, N. Živković, L. Živković, Application of the prediction model "SCHALL 03" for railway noise calculation in Serbia. *Appl. Mech. Mater.* **430**, 237–243 (2013)
29. J. Tomić, N. Bogojević, M. Pljakić, D. Šumarac-Pavlović, Assessment of traffic noise levels in urban areas using different soft computing techniques. *J. Acoust. Soc. Am.* **140**(4), EL340–EL345 (2016)
30. J. Tomić, N. Bogojević, Z. Šoškić, Application of artificial neural network to prediction of traffic noise levels in the city of Niš, Serbia, in: *Acoustics and Vibration of Mechanical Structures—AVMS-2017*, ed. by N. Herisanu, V. Marinca. Springer Proceedings in Physics, vol 198 (2018), pp. 91–98
31. J. Tomić, N. Bogojević, B. Tatić, Z. Šoškić, Design and implementation of on-line database of noise sources, in *Proceedings of 23rd National and 4th International Conference "Noise and Vibration"*, Niš, 17–19 Oct 2012 (2012), pp. 17–19
32. Z. Šoškić, Design of database of urban noise sources. *Mech. Transp. Commun.* **10**(3/3), article No. 0719, UK7.1–UK7.9 (2012)
33. J.Z. Tomić, Methodology for verification of software for noise attenuation calculation according to ISO 9613-2 standard. *Facta Univ. Ser. Working Living Environ. Prot.* **12**(1), 29–38 (2015)
34. J. Tomić, N. Bogojević, Z. Šoškić, Method for calculation of noise fields in multiple-building environment. *Mech. Transp. Commun.* **14**(3/2), article No. 1372, IX1–IX6 (2016)
35. Z. Petrović, B. Radičević, Z. Petrović, N. Zdravković, Design of noise protection in urban areas—case study of an elementary school. in *Proceedings of the 23rd National and 4th International Conference "Noise and Vibrations"*, Niš 17–19 Oct 2012 (2012), pp. 17–19
36. I. Topalov, B. Radičević, B. Tatić, Z. Šoškić, Noise mapping in area of an urban overpass, in *Proceedings of 35th International Conference on Production Engineering*, Kraljevo-Kopaonik, 25–28 Sept 2013 (2013)
37. D. Cvetković, M. Prašćević, D. Mihajlov, Estimation of uncertainty in environmental noise measurement. *Measurement* **100**, 3 (2011)
38. M. Prašćević, D. Mihajlov, D. Cvetkovic, A. Gajicki, Long-term noise measurements and harmonica index as a way of raising public awareness about traffic noise in the city of Niš. *Facta Univ. Ser. Working Living Environ. Prot.* **14**, 41–51 (2017)
39. M. Ličanin, M. Prašćević, D. Mihajlov, Realization of the low-cost noise measurement monitoring station using MEMS microphone technology and micro PC, in *Proceedings of the 26th International Conference "Noise and Vibration"*, Niš, Serbia, 6–7 Dec 2018 (2018), pp. 133–136
40. M. Prašćević, D. Cvetković, D. Mihajlov, A framework for strategic noise mapping in urban areas, in *Proceedings of XI Symposium "Acoustics and Vibration of Mechanical Structures AMVS 2011"*, 26 May 2011, Timisoara, Romania (2011), pp. 7–22
41. M. Prašćević, D. Cvetković, D. Mihajlov, N. Holeček, The acoustic zoning—a comparison of legislation and experiences in Italy and Serbia, in *23rd National and 4th International Conference "Noise and Vibrations"*, Niš, 17–19 Oct 2012 (2012), pp. 21–28
42. M. Prašćević, D. Mihajlov, A. Gajicki, D. Cvetković, N. Holeček, Acoustic zoning and noise assessment for railway noise calculation in Serbia. *Appl. Mech. Mater.* **430**, 244–250 (2013)
43. D. Mihajlov, M. Prašćević, M. Ličanin, Defining the environmental noise indicators measurement time interval using multi-criteria optimization, in *Proceedings of the 26th International Conference "Noise and Vibration"*, Niš, Serbia, 6–7 Dec 2018 (2018), pp. 99–106

44. D. Mihajlov, M. Praščević, N. Herisanu, Selection of measurement strategy for the assessment of long-term environmental noise indicators using multi-criteria optimization, in *Acoustics and Vibration of Mechanical Structures—AVMS-2017*, ed. by N. Herisanu, V. Marinca. Springer Proceedings in Physics, vol. 198. Springer, Cham (2018)
45. M. Praščević, D. Cvetković, D. Mihajlov, Comparison of prediction and measurement methods for sound insulation of lightweight partitions. *Facta Univ. Ser. Archit. Civ. Eng.* **10**(2), 155–167 (2012)
46. M. Kolarević, B. Radičević, V. Grković, Z. Petrović, One realization of the system for measuring airflow resistance, in *Proceedings of the 24th International Conference Noise and Vibration*, Niš, 29–31 Oct 2014 (2014), pp. 123–128
47. S. Todosijević, D. Ćirić, B. Radičević, Z. Šoškić, Experimental characterization of a photoacoustic measurement system. *Facta Univ. Ser. Working Living Environ. Prot.* **14**(1), 053–060 (2017)
48. M. Kolarević, B. Radičević, N. Herisanu, M. Rajović, V. Grković, Acoustic properties of recycled rubber at normal incidence, in *Proceedings of IX International Triennial Conference “Heavy Machinery—HM17”*, Zlatibor, 28 June–1 July 2017 (2017), pp. F23–F28
49. J. Bojković, B. Radičević, N. Manojlović, M. Bjelić, V. Mandić, S. Marinković, Prediction of acoustical properties of porous building materials, in *Proceedings of IX International Triennial Conference “Heavy Machinery—HM17”*, Zlatibor, 28 June–1 July 2017 (2017), pp. G13–G19
50. B. Radičević, M. Kolarević, N. Herisanu, M. Bjelić, T. Miodragović, Sound absorption of recycled plastic material, in *Proceedings of the 26th International Conference “Noise and Vibration”*, Niš, Serbia, 6–7 Dec 2018 (2018), pp. 29–34
51. D. Mihajlov, M. Praščević, D. Cvetković, Acoustic treatment of machine workroom for staples production, in *Proceedings of XI Symposium “Acoustics and Vibration of Mechanical Structures—AMVS 2011”*, Timisoara, Romania, 26 May 2011 (2011), pp. 37–46
52. N. Herisanu, B. Radičević, Z. Petrović, V. Grković, Sound insulation of a plywood transporter, in *35th International Conference on Production Engineering, Kraljevo-Kopaonik*, 25–28 Sept 2013 (2013)
53. A. Gajicki, M. Praščević, An example of noise abatement measures for railway line, in *Proceedings of 25th International Conference “Noise and Vibration”*, Tara (2016), pp. 75–80 (2016)
54. Z. Petrović, B. Radičević, M. Praščević, Z. Šoškić, Noise protected buildings, in *Proceedings of the VII Triennial International Conference Heavy Machinery HM*, Vrnjačka Banja (2011), pp. 81–86
55. V. Grković, M. Kolarević, Z. Petrović, M. Vukićević, Morphology of modular traffic noise barriers, in *Proceedings of the 23rd National and 4th International Conference “Noise and Vibrations”*, Niš, 17–19 Oct 2012 (2012), pp. 89–94
56. B. Radičević, Development of a decision-making model for the selection of the optimal mixture of sound absorbing materials. Ph.D. thesis, University of Kragujevac, Faculty of Mechanical and Civil Engineering in Kraljevo (2016)
57. S. Todosijević, Development of photoacoustic measurement system for thermal characterisation of thin samples. Ph.D. thesis, University of Belgrade, School of Electrical Engineering (2016)
58. D. Mihajlov, Multi-criteria optimization for selection of measurement strategy for the assessment of the long-term environmental noise indicators. Ph.D. thesis, University of Niš, Faculty of Occupation Hazard (2016)
59. J. Tomić, Application of soft computing techniques in traffic noise prediction. Ph.D. thesis, University of Belgrade, School of Electrical Engineering (2018)
60. M. Pljakić, B. Radičević, J. Tomić, Z. Petrović, Analysis of systematic measurements of noise in cities, in *Proceedings of the 23rd National and 4th International Conference “Noise and Vibration”*, Niš 17–19 Oct 2012 (2012), pp. 59–62

Acoustic Treatment Solution of the Technical Room in Water Pumping Station—Case Study



Darko Mihajlov, Momir Prašćević, Marko Ličanin, and Aleksandar Gajicki

Abstract Among many other noise sources, living environment is often significantly affected by industrial noise. It is very common in cities that many industrial plants are located near residential areas providing citizens with basic living needs. Noise generated by industrial machines within those facilities strongly affect the quality of life in the close proximity. Goal of the research represents one of the possible solutions of noise-level reduction in the environment affected by a water pump station No. 25, located at Mokroluško brdo in Belgrade. Demands and limitations that have been set during the project solution stage were the main factor for the appropriate noise reduction method. Noise generated by centrifugal water pumps has been analyzed, and acoustic treatment of the technical room is chosen as a solution. Results of the research in the paper represents the possibility of successful application of the surface absorbers available on the market, where price and delivery conditions act as the main factors for the choice of acoustic materials.

D. Mihajlov · M. Prašćević · M. Ličanin (✉)
Faculty of Occupational Safety, Čarnojevićeva 10A, Niš, Serbia
e-mail: marko.licanin@znrfak.ni.ac.rs

D. Mihajlov
e-mail: darko.mihajlov@znrfak.ni.ac.rs

M. Prašćević
e-mail: momir.prascevic@znrfak.ni.ac.rs

A. Gajicki
Institute of Transportation CIP, Trg Nikole Pašića 8/A, Belgrade, Serbia
e-mail: agajicki@sicip-trg.com

1 Introduction

Water pumping station represents the facility that extract water from the lower to higher level. In the water supply systems, the main purpose of this facility is the transport of the freshwater from the source wells or rivers, or to create water pressure for filling the water tanks. Depending on the capacity, the facility where water pumps are installed has a technical room in which machines are placed (pumps, electromotors, internal combustion diesel engines, compressors, and cranes) and supports rooms (workshops, boiler rooms, ventilation chambers, transformer rooms, sanitary facilities, resting areas, etc.). In the pumping stations what moves liquid from lower to higher depths, a horizontal single-step centrifugal pumps are often used, while vertical multi-step pumps are needed when extraction water from the higher depths [1].

Pumping stations that are parts of the water supply system are often located in the vicinity of the residential areas, due to the supply demands, terrain configuration, and technical reasons. Even though, traffic noise is considered as highest noise polluter, if this kind of facility is installed in the residential area, it significantly affects the quality of life. Despite the traffic noise, where noise level depends of the traffic frequency during the different parts of the day, some industrial facilities, such as described water pumping stations, emit the constant amount of noise often during the entire day (24 h period). The noise spectra of such facilities can in many cases have a tonal component that significantly adds to the noise disturbance. Having in mind the construction and operation of the rotational machines (turbo machines), tonal components in frequency spectrum of the pumping engines are natural and expected, and thus, it will for certain influence the environment.

Under the assumption that number of machinery and operational regimes are defined, the amount of transmitted noise is influenced by the construction and condition of the building facility where water pumps are installed. Problem of the noise control in the vicinity of the pumping station is related to the following steps.

1. Estimation of the existing noise condition in the water pumping technical room, with analysis of the operation regimes and working loads of different pump engines;
2. Estimation of the existing noise condition at the border of the industrial complex and the neighboring acoustical zone. This is determined by measuring the environmental noise level according to the standard [2, 3] and comparing the measurement results with the following step;
3. Calculation of the relevant (authoritative) equivalent noise level at the border of the industrial complex and adjacent acoustical zone, and comparison of with the limit values of the adjacent acoustical zone [4];
4. Technical idea solution for environmental noise reduction generated by pumping engines in the water pumping station, taking into concern the amount of noise that is above the acoustical zone limits, as well as noise limits related to the safe working conditions inside the facility.

2 Study Case—Problem Analysis

2.1 Noise Source Data

Pumping station No. 25 “Mokroluško brdo” in Belgrade is a facility with a purpose of water supply of a city segment at third and fourth height zone. Facility is shown in Fig. 1—left. The facade of the building where technical room is located can be also seen on Fig. 1. The face pf the facade is looking toward the affected object in the vicinity, which can be seen on Fig. 1—middle.

Inside the technical room, six pumping engines are installed (two groups with three of the same type). The distribution of the machines is shown in Fig. 1—right, while technical characteristic can be seen in Table 1.



Fig. 1 Pumping station No. 25. “Mokroluško brdo” in Belgrade (left), residential building in the nearby the pumping station (middle), and distribution of the water pump engines in the technical room inside pumping station (right)

Table 1 Technical characteristics of the pumping engines

Electric engine—3 peaces				
Group	Manufacturer	Type	P (kW)	n (min^{-1})
I	Sever	OKN 6110/4	200	1472
II	Sever	OKN 6130/4	315	1476
Pump—3 peaces				
Group	Manufacturer	Type	H (m)	Q (l/s)
I	Litostroj	CV9/40-IV-8	146	80
II	Litostroj	5CN9	80	250

2.2 *Noise Level in the Technical Room*

To solve the noise problem, all of six pumps in the operation regime have been considered. After the series of five measurements with a 5 min interval, mean value of the noise level inside technical room has been obtained $L_{A\text{Freq},t=5\text{min}} = 98.4$ dB. Instrument that has been used for measurements is Brüel&Kjær, type 2270, at the height of 1.5 m from the floor of the room.

2.3 *Noise Level at the Receiver*

To determine the amount of noise pollution of the environment, generated by water pump station, series of measurements have been taken at the border of the industrial complex and the adjacent territory defined as the strictly residential area without the traffic noise influence. After taking the five measurements in the 5 min interval, average equivalent background noise level has been obtained $L_{A\text{Freq, res}, t=5\text{min}} = 44.2$ dB. After turning all of the six water pump engines, process has been repeated under the same conditions, and average equivalent noise level obtained $L_{A\text{Freq}, t=5\text{min}} = 68.7$ dB. Measurements has been done without influence of the traffic, due to the fact that traffic frequency is very low during the day and evening, especially during the night.

Results that have been gathered point to the following conclusion

- water pump engines in the absence of traffic represents the dominant noise sources at the given location;
- to reduce the noise level at the given location, it is necessary to undertake certain technical measures to reduce the amount of emitted noise.

3 Study Case—Problem Analysis

3.1 *Choice of the Problem Solving Strategy and Task Definition*

Solution for the excess noise problem at the receiver position can be done in tri ways [5]:

1. Undertake the technical measures at the noise source by applying enclosure around the sources, where it is necessary to provide nominal operational functionality of the machines and enable easy maintenance access. If entire facility where machines are installed is considered as a noise source, then it is possible to apply the acoustic treatment inside the room (walls, ceiling, etc.) by lining

some of the surfaces with acoustic absorption material, or increase the sound insulation of the facade wall.

2. Undertake the technical measures at the noise propagation path, to increase noise attenuation. In the absence of physical space for planting a dense forest trees or building a mounds, acoustical barrier presents the only option.
3. Undertake the noise reduction measures at the receiver position applying the acoustic treatment on the receiver facade increasing the sound insulation.

The choice for determining the best strategy from environmental noise reduction generated by pumping station No. 25 “Mokroluško brdo” in Belgrade has been influenced by following factors:

- Terrain configuration and the spatial placement of the buildings (noise sources and receiver);
- Shape, dimensions, and orientation of the technical room in relation to the nearby residential objects;
- Available financial funds at the investor disposal.

Taking into concern the results that has been gathered by noise-level measurements, to solve a given problem, method of acoustic treatment by applying surface absorbers of the water pumping station technical room has been chosen. Additional reason for this decision is the fact that technical room is equipped with a lifting bridge crane, and due to the lack of the available space, using volume type of absorbers was not possible.

Task is defined in such a way that by using the available resources, acoustic treatment of the technical room will be done to reduce the noise levels, in the condition when all of the water pumps are under the working load. In addition, it was important to present the results of the acoustic treatment and corresponding noise reduction using different types of acoustic absorption materials available on the market, and the economic justification versus results of the selected materials.

3.2 *Realization of the Task*

To realize the given task, following steps has been made [5]:

- By increasing the absorption coefficient value of the sound energy, absorption surface of the partition is being increased:

$$A = S \cdot \alpha \tag{1}$$

where A (m^2) is partition surface absorption, S (m^2) is partition surface, while α is the frequency dependant absorption coefficient of the material.

- By increasing the absorption coefficient at certain frequency bands, absorption surface at those bands is also increased, which results in the noise reduction at the same frequency bands according to equation:

$$\Delta L_{\text{band},i} = 10 \log \frac{A'_{\text{band},i}}{A_{\text{band},i}}, \quad (2)$$

where $\Delta L_{\text{band},i}$ (dB) is the noise reduction in the i th third octave band achieved by acoustic treatment, $A_{\text{band},i}$ (m^2) is the summation of absorption surfaces of all of the partition in the i th third octave band before acoustic treatment, while $A'_{\text{band},i}$ (m^2) is the summation of absorption surfaces of all of the partition in the i th third octave band after the acoustic treatment.

- Noise levels of the i th third octave band after the treatment is then calculated as:

$$L'_{\text{band},i} = L_{\text{band},i} - \Delta L_{\text{band},i}. \quad (3)$$

- Finally, noise level inside the technical room after the treatment is being determined as:

$$L' = 10 \log \sum_{i=1}^n 10^{L'_{\text{band},i}/10}, \quad (4)$$

where i is the number of the third octave band in the range ($i = 1 - n$), $n = 18$ is the total number of third octave bands (100–5000 Hz).

To perform mathematical calculations, following data has been provided:

- Precise dimensions of all of the partitions inside the technical room.
- Values of the absorption coefficient for all of the considered materials based on the available literature [5, 6].

During the problem solving stage, for graphical representation a software package, *Sketchup* has been used. On Fig. 2, in 1:1 scale, graphical representation of the existing condition of the technical room can be seen. All of the surfaces of interests are made of concrete.

According to the availability on the market, as well as price per m^2 , for solving the given problem, following absorption material and construction have been chosen:

1. Polyurethane foam (thickness: 100 mm, density: 25 kg/m^3 , fire resistance: B2) is shown in Fig. 3;
2. Rock wool (thickness: 100 mm, density: 50–60 kg/m^3) is shown in Fig. 4. If rock wool is used, it is necessary to apply the protection acoustic transparent net to prevent material particles to float in the air and protect the acoustical absorber layer (Fig. 5).
3. Metal perforated panels are presented on Fig. 6. Construction elements of the metal perforated panel can be seen on Fig. 7.
 - Panel thickness—100 mm;
 - Perforated plate thickness—5 mm;
 - Hole radius—10 mm;
 - Hole distance—40 mm;

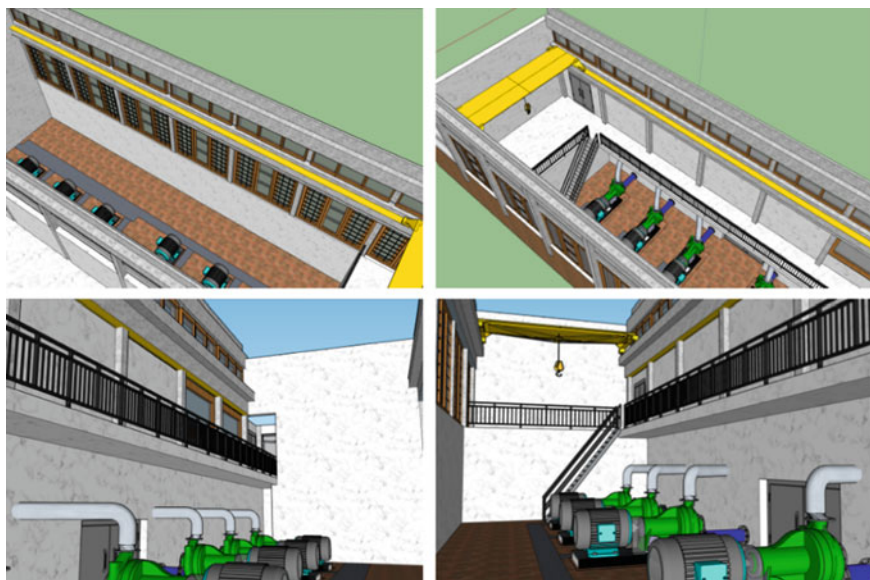


Fig. 2 Graphical representation of the technical room before the acoustic treatment

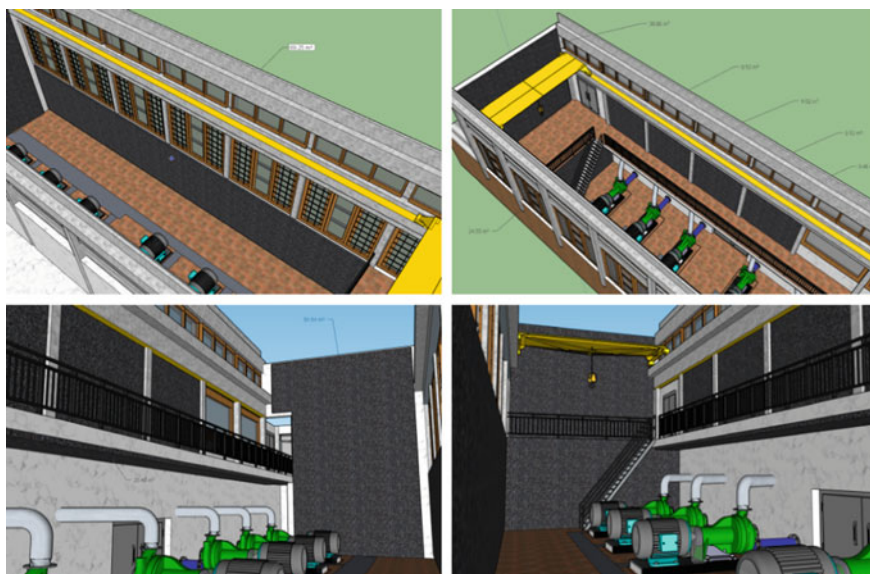


Fig. 3 Graphical representation of the technical room using polyurethane foam for acoustic treatment

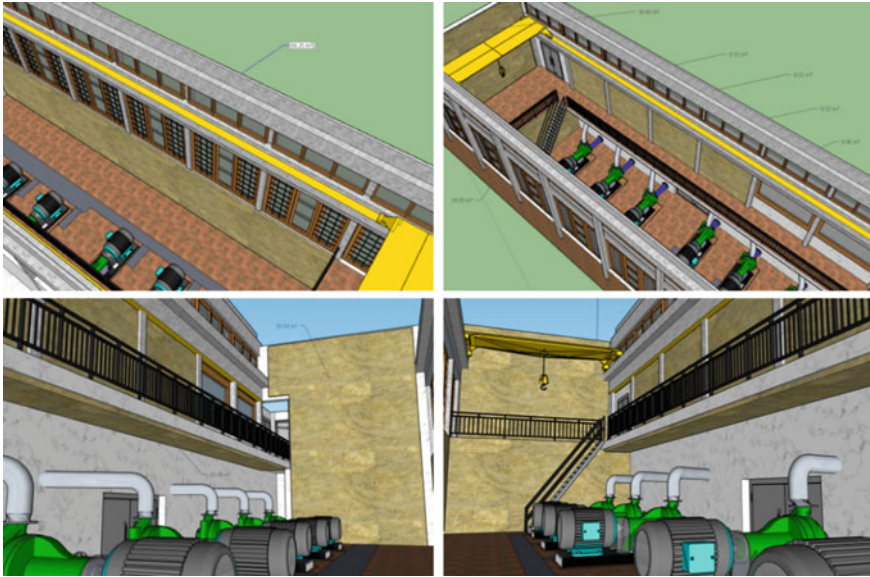
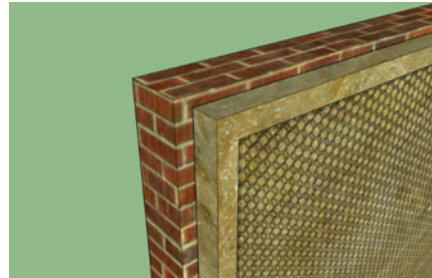


Fig. 4 Graphical representation of the technical room using rock wool for acoustic treatment

Fig. 5 Mounting the rock wool material at the wall surface together with a protection net



- Front plate perforation—19.63%;
- Absorber thickness—75 mm;
- Absorber type—Rock wool with density 50 kg/m^3 or polyurethane foam 30 kg/m^3 ;
- Air gap—25 mm next to the absorber back plate.
If rock wool is used, it is necessary to apply the protection acoustic transparent net.

The values of the absorption coefficient for the observed material can be seen on Fig. 8.

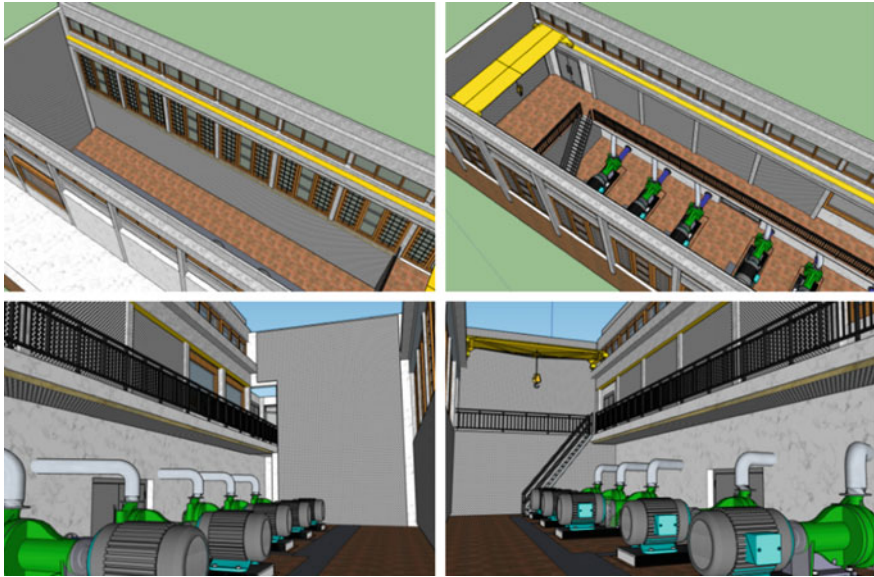


Fig. 6 Graphical representation of the technical room using metal perforated panel for acoustic treatment

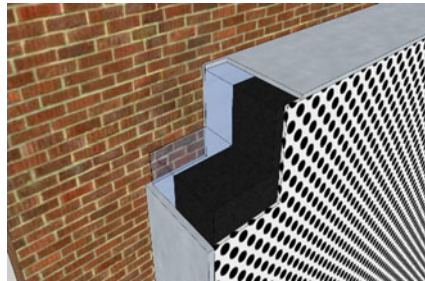


Fig. 7 Cross-section of the metal perforated panel

4 Results of the Research

During the investigation of the optimal solution of the given task (highest noise reduction while using less material), described mathematical approach (2, 3, 4) has been used and applied for cases of surfaces of 240 m², 200 m², 150 m², and 100 m² lined with proposed absorption material. Results of the calculation have been presented in Figs. 9, 10, 11, and 12.

First case—lining surface of 240 m². Reduction of the equivalent noise level for the polyurethane treatment is 5.40 dB, and for the treatment with rock wool it is 5.34 dB, while for the metal perforated panel, it is 5.40 dB. Difference between calculated

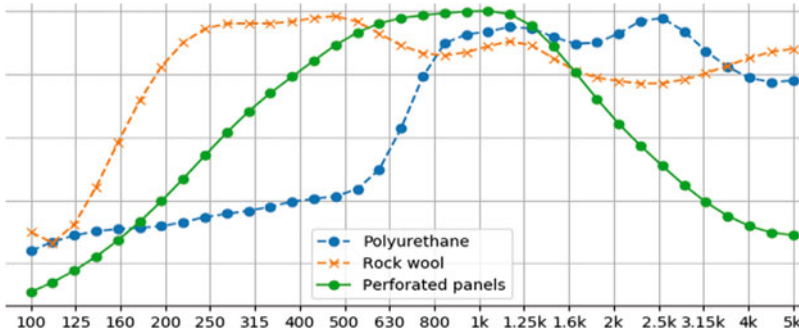


Fig. 8 Absorption coefficient values of the suggested materials (y-axis) at the central frequencies of the third octave bands for frequencies 100–5000 Hz (x-axis)

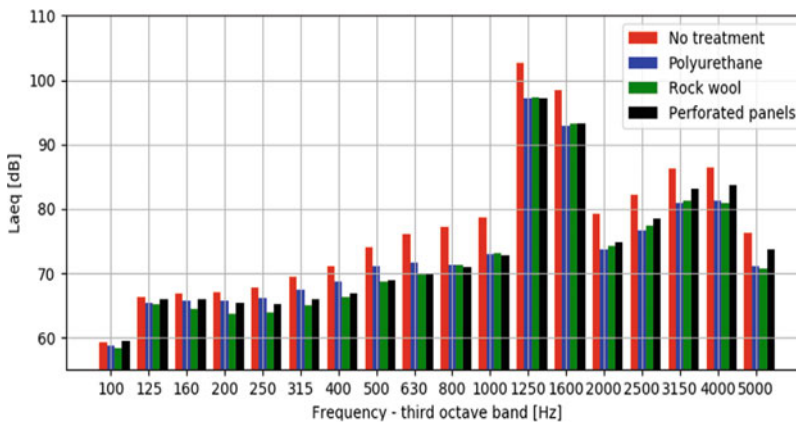


Fig. 9 Results of the noise reduction calculation by applying different acoustic materials with a lining surface 240 m²

noise levels at the central frequencies 1250 Hz and 1600 Hz must not be higher than 5 dB. If there is a larger difference, noise in the technical room would have a tonal component at the 1250 Hz. If polyurethane foam is used, this difference would be 4.18 dB, and if rock wool is used, it will be 4.02 dB, while in the case of perforated metal panel, this difference is 3.78 dB. According to this criteria, it would be best to use metal perforated panels.

Second case—lining surface of 200 m². Reduction of the total noise reduction is 4.46 dB for the case of the polyurethane foam, 4.75 dB if rock wool is used, while 4.86 dB of reduction is gained when using metal perforated panels.

Third case—lining surface of 150 m². Reduction of the total noise reduction is 4.17 dB for the case of the polyurethane foam, 4.00 dB if rock wool is used, while 4.06 dB of reduction is gained when using metal perforated panels.

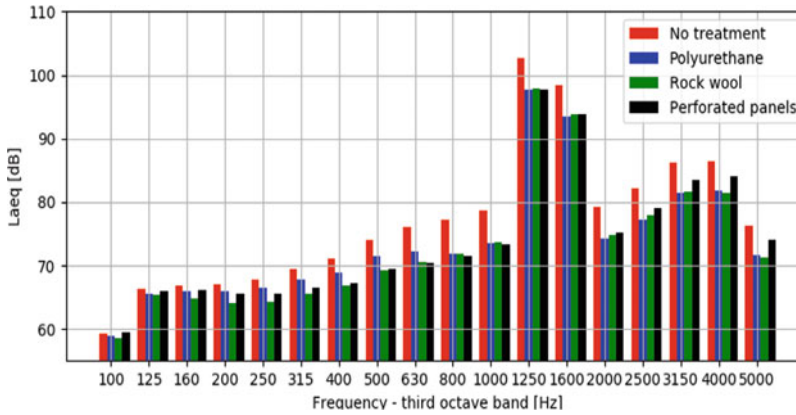


Fig. 10 Results of the noise reduction calculation by applying different acoustic materials with a lining surface 200 m²

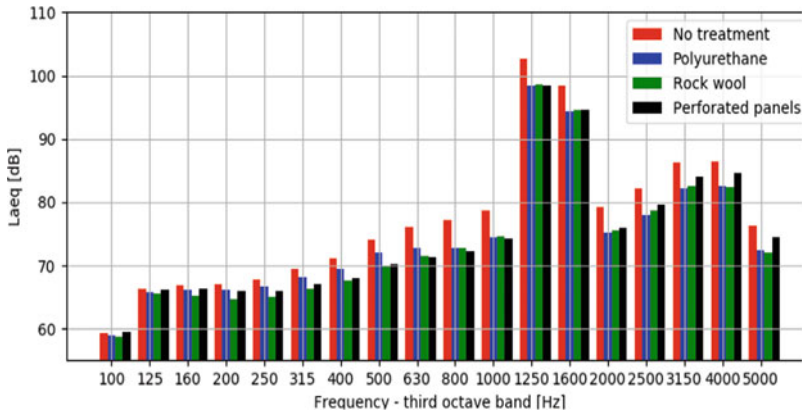


Fig. 11 Results of the noise reduction calculation by applying different acoustic materials with a lining surface 150 m²

Fourth case—lining surface of 100 m². Reduction of the total noise reduction is 3.18 dB for the case of the polyurethane foam, 3.03 dB if rock wool is used, while 3.09 dB of reduction is gained when using metal perforated panels.

Table 2 gives comparative results of the application of different materials in the four listed cases.

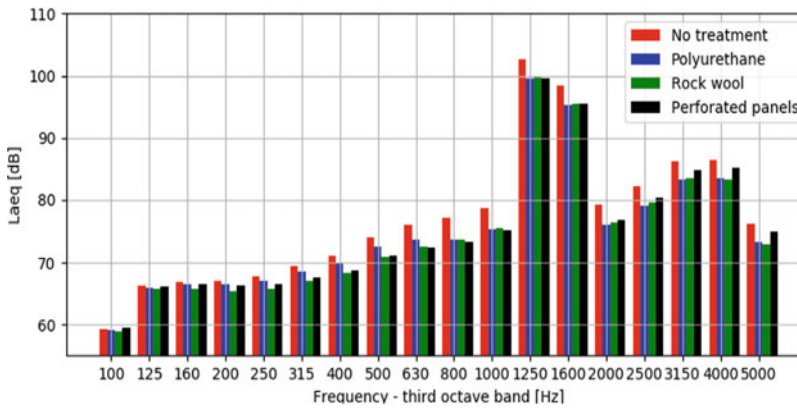


Fig. 12 Results of the noise reduction calculation by applying different acoustic materials with a lining surface 100 m²

Table 2 Results of the noise reduction using different acoustic materials

Surface (m ²)	Reduction of the total noise level ΔL (dB)		
	Polyurethane foam	Rock wool	Perforated metal panel
240	5.54	5.34	5.40
200	4.46	4.75	4.86
150	4.17	4.00	4.06
100	3.18	3.03	3.09

5 Conclusion

Industrial objects especially affect the environment in a negative way if they are in its immediate vicinity. One of the main problems that occurs then is the increased presence of noise.

The case discussed in the paper points to the limited ability to solve the problem, primarily because of the availability of financial resources for taking more serious measures. The results of the research show that acoustic treatment of the technical room of the pump station can achieve a certain reduction in the noise level in the room itself, which would positively affect the noise levels in the immediate vicinity of the pump station. The conceptual solution of the problem is based on market conditions—the possibility of purchasing certain absorption materials and their price, as well as the results (effect) of each of them. The performed mathematical calculation is expected to indicate that the noise-level reduction is directly proportional to the amount of absorption material used for the acoustic treatment of the room, regardless of the material. Bearing in mind the large price difference, it is also shown that the considered construction of perforated metal panels does not have a particular advantage in the concrete case over other materials. Accordingly, depending on the

effect desired, the decision on the type and quantity of materials when solving this kind of problem remains at the investor. Certainly, achieving more serious results is expected by changing the facade construction of the technical room of the pump station and possibly replacing the existing machines with modern quieter machines.

Acknowledgements This paper is presented as a part of the projects “Development of the methodology and means for noise protection in urban areas” (No. TR-037020). Authors would like to express gratitude to the Ministry of education, science and technological development of Republic of Serbia, for the financing support in these research.

References

1. G.M. Jones, *Pumping Station Design*, 3rd edn. (Butterworth-Heinemann, 2008). ISBN: 9781856175135
2. ISO 1996-1:2016, Acoustics—description, measurement and assessment of environmental noise—part 1: basic quantities and assessment procedures
3. ISO 1996-2:2017, Acoustics—description, measurement and assessment of environmental noise—part 2: determination of sound pressure levels
4. Regulation on noise indicators, limit values, methods for assessing noise indicators, disturbance and harmful effects of environmental noise, “Gazette RS” No. 75/2010 (in Serbian)
5. M. Praščević, D. Cvetković, *Environmental Noise*, 1st edn. (Faculty of Occupational Safety, University of Niš, Serbia, 2005). ISBN: 86-80261-53-X
6. F. Fahy, *Foundations of Engineering Acoustics* (Academic Press, 2001). ISBN: 0-12-247665-4

Solution of the Environmental Noise Problem Generated by HVAC Systems—Case Study



Marko Ličanin, Darko Mihajlov, Momir Praščević, Ana Đorđević, Miomir Raos, and Nenad Živković

Abstract Modern buildings, shopping malls, and supermarkets nowadays rely on centralized systems to maintain the optimal air and water temperature. These units often placed in the open areas affect the environment by generating a significant amount of noise which influences acoustical comfort in residential areas, and reduces the productivity of the people working in nearby office buildings. The main engineering challenge in performing the noise control of heating/cooling units is that a significant amount of air has to be provided for its subsystem cooling, while at the same time noise must attenuate. Here, a practical approach based on the simulation is investigated, noise reduction system implemented and results observed. Combination of the custom made adsorption elements and the chosen geometry based on simulations showed the promising results that can be applied to various types of HVAC systems.

M. Ličanin (✉) · D. Mihajlov · M. Praščević · M. Raos · N. Živković
Faculty of Occupational Safety, Čarnojevićeva 10A, Niš, Serbia
e-mail: marko.licanin@zrfak.ni.ac.rs

D. Mihajlov
e-mail: darko.mihajlov@zrfak.ni.ac.rs

M. Praščević
e-mail: momir.prascevic@zrfak.ni.ac.rs

M. Raos
e-mail: miomir.raos@zrfak.ni.ac.rs

N. Živković
e-mail: nenad.zivkovic@zrfak.ni.ac.rs

A. Đorđević
Faculty of Electronic Engineering, Aleksandra Medvedeva 14, Niš, Serbia
e-mail: ana.djordjevic@elfak.rs

1 Introduction

Heated Ventilated Air Conditioning Units (HVAC) are important parts of modern buildings, especially those that have community purposes (offices buildings, supermarkets, shopping malls, hospitals, etc.). Very often, these types of systems are positioned on the rooftops of buildings, where there is enough physical space. To perform with optimal working parameters, air intake and exhausts of the unite should have enough airflow [1]. HVAC (Chiller) units often move a massive amount of air around them, producing a significant amount of noise. This becomes a problem, which is not easy to solve using classical acoustic enclosures, due to the fact that air supply needs to be provided. Generated noise becomes especially prominent during the hot summer days, where people in residential areas and office buildings tend to open windows and balconies for fresh air. Noise problem then becomes one of the biggest environmental disturbances.

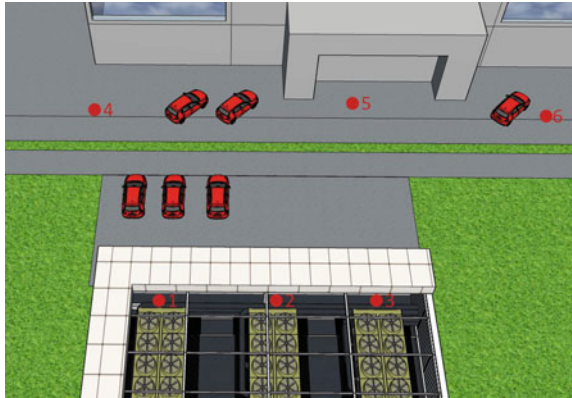
Engineering challenge when performing the noise control of the HVAC systems is to provide the proper noise attenuation [2, 3] while at the same time allow the device sufficient airflow. This paper exploits the possibility of using the special type of segmented barrier as a solution to the noise problem. It also follows the most important steps of the project that was successfully realized at the central office building of one international bank in Belgrade. After identifying the problem at the site location, a series of simulations of the segmented barrier has been performed in COMSOL. Based on the simulation and in situ measurements, this type of barrier has been designed and implemented. In order to visualize the problem, a 1:1 3D model using Sketchup software has been built. After the construction and panel mounting is performed, measurements have been retaken, and results of the practical application observed.

2 Noise Evaluation

Measurements have been taken at positions presented in Fig. 1. Three measurement positions have been chosen at 1 m distance from the each of the noise sources (1, 2, and 3 on Fig. 1), while three positions were chosen on the noise path near the affected building (4, 5, 6 on Fig. 1). Three chillers are positioned on the rooftop of the support technical facility next to the bank office building. Noise is generated towards another office building across the small street, which is considered as a noise receiver.

Measurement interval has been set to 5 min, and measurements were taken three times at each chosen position. HVAC units can be set in different operation modes and under different output loads. For the measurement conditions, all three chillers have been set in high load regime without working regime change during measurements. This allowed that the source can be considered as a stationary noise source. Another way of performing measurements would be to use longer intervals, which will cover all of the working regimes of the noise source [4]. Noise levels of measurement

Fig. 1 Sketchup representation of the noise sources affected office building and noise level measurement positions during the initial evaluation



positions 2 and 5 are presented in Fig. 2 (Top). The resolution of the observed noise levels is in the third-octave bands.

At 1 m distance HVAC units produced noise level between 79.8 dB and 81.8 dB (positions 1, 2, and 3), while near the noise receiver building (positions 4, 5, and 6) measured noise was between 64.3 and 65.2 dB. Once the HVAC units have been

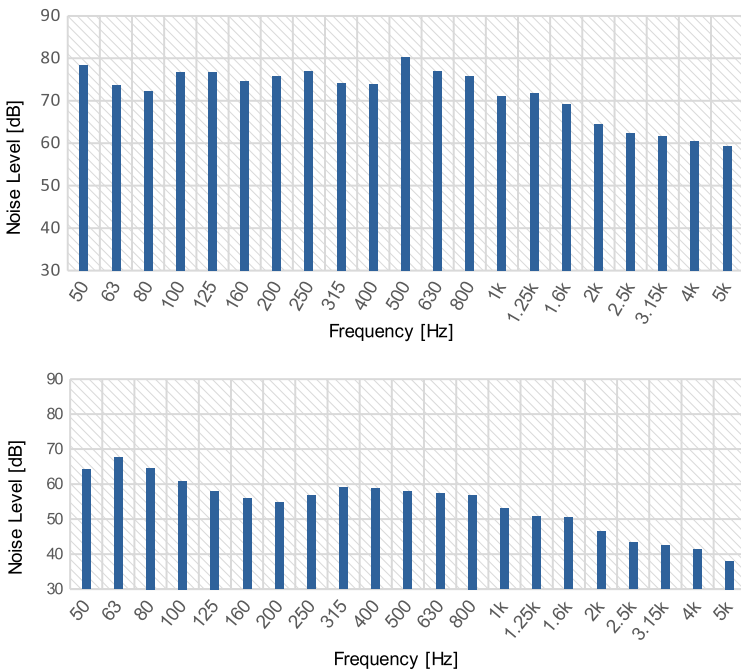


Fig. 2 Noise levels in third-octave band averaged per each band for three repeated measurements at position 2 (Top) and position 5 (bottom)

turned off, the residual noise level at positions 4, 5, and 6 were in the range between 54.6 dB and 55.3 dB. After the analysis of the measurements, a decision has been made that noise control should provide at least 8 dB of noise attenuation and as a result, match the residual noise level. Another reason is the acoustical zoning of the Belgrade, which is an ongoing process. By reducing more than 8 dB of noise, this will satisfy the day noise limits of the most strict acoustical zones [5].

After the noise level evaluation, using the construction blueprint of the technical room, the entire object has been made in 3D in a 1:1 ratio so different engineering solutions can be visually exploited.

3 Simulation of the Acoustic Barrier

Traditional one segment barrier would not satisfy the need of HVAC air supply, and can potentially create the overheating of the units. To solve this problem an investigation of the multi-segment barrier has been considered. During in situ measurements, it has been observed that there is a possibility to redirect some of the noise energy to a longer path. This will naturally attenuate the sound energy without a negative influence on the nearby buildings. Area where noise could be redirected is highly influenced by traffic noise from the nearby busy street. This has been tested in the simulation.

Segmented noise barrier has been analysed in COMSOL Multi-physics. It is composed of absorption metal perforated panels angled at the 25°. Figure 3 shows the simulation results without barrier, and with barrier included.

Results are presented at frequencies of 100 Hz (Fig. 3—top), 500 Hz (Fig. 3—middle), and 1 kHz (Fig. 3—bottom). As can be seen, when the barrier is placed, more noise energy is contained inside the technical room where chillers are placed. This is especially visible at the middle to high frequency.

Besides observation of the sound propagation, another simulation has been performed using the Raytrace method (Fig. 3).

As mention before, some of the noise has to redirect to the longer path and simulation has been used for evaluation of the geometry of the segmented barrier. In Fig. 4, results have been presented in a way that the left portion of the figures represent the case without a segmented barrier (barrier influence is disabled), while on the right side situation with a barrier is shown (barrier is enabled). Simulation length is 120 ms, with four steps 30 ms each. In Fig. 4, the first row is a situation after the first step, where each subsequent row represents another step. As it can be observed, placement of the segmented barrier (Fig. 3—right) truly redirects the sound to a longer path. In combination with the absorption in the metal perforated panels, this has been proved to be a good course of action.

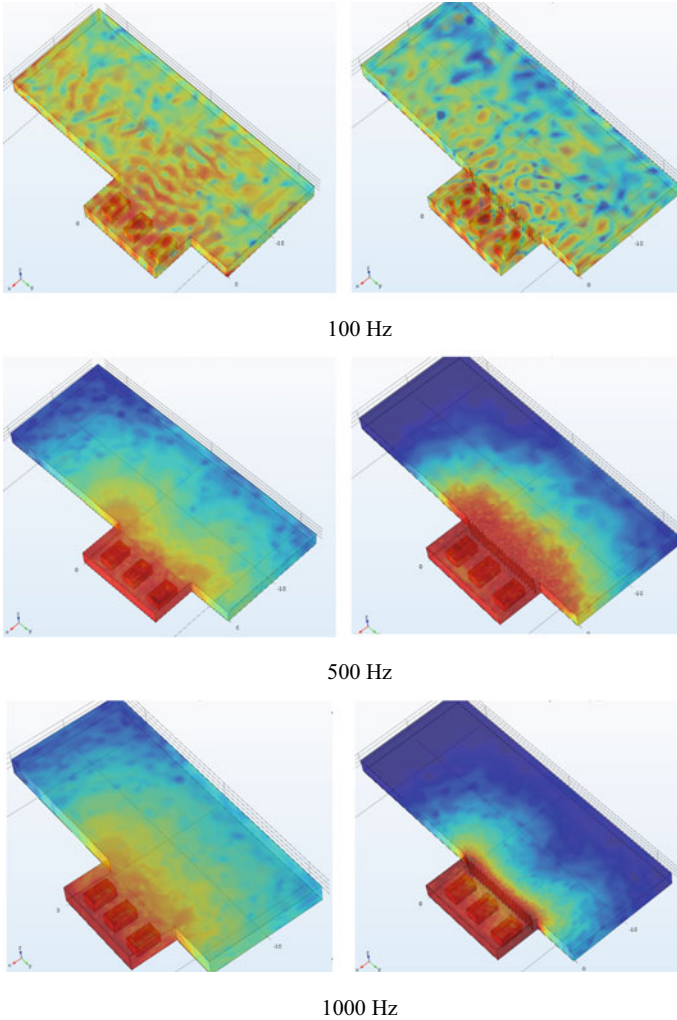


Fig. 3 Simulation results in the sound propagation for different frequencies, without barrier (left) and with barrier (right)

4 Design of the Acoustic Barrier

Simulation has pointed out that using a segmented barrier can be a solution to the given problem. As this barrier is composed of the angled metal perforated panels, the maximum efficiency of the panel, based on the measured noise spectra has been exploited. The process of calculating the absorption coefficient accounts for the front perforated panel thickness, hole repeat distance, hole radius, cavity depth, absorber thickness, air space thickness, and flow resistivity, which is already well established

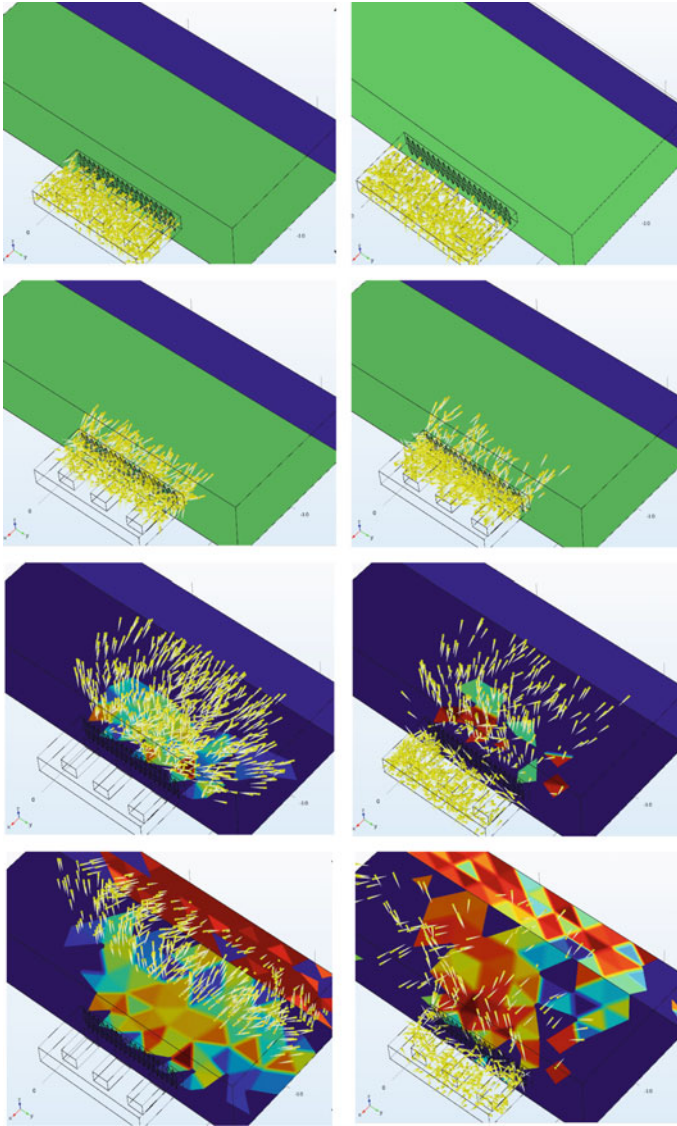


Fig. 4 Simulation results the segmented barrier noise redirection in the case where barrier is disabled in the model (left) and enabled (right). First step (0 ms), second step (60 ms), third step (90 ms), and fourth step (120 ms) shows the flow of the simulation

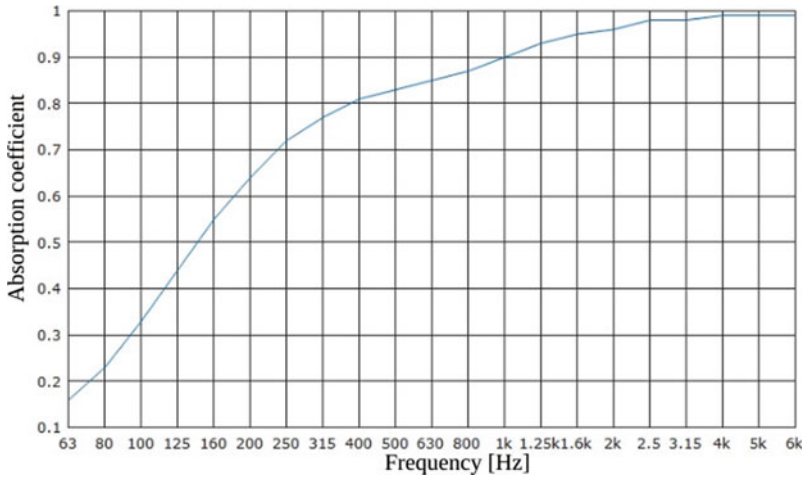


Fig. 5 Designed metal perforated panel absorption coefficient curve

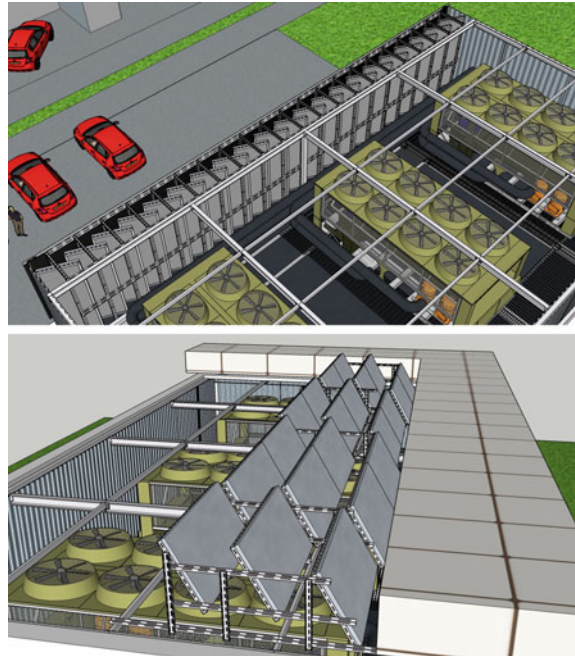
throughout the literature [2, 3, 5]. Calculation has been done for each third-octave band, and frequency-dependent curve fitted to match the noise spectra of the HVAC, which is presented in Fig. 5.

Barrier is composed of connecting multiple panels using the metal construction material to form the rigid cage that will provide sufficient static to the weight of the panels. In the design process, another segmented barrier has been considered. To ensure that noise generated by the fans of the chiller units will not reach the upper floors of the affected building, this additional barrier has been included on the top of the existing metal support beam structure on the site. Besides the absorption effect, it will also redirect the noise towards the sky. Sketchup representation of both of these barriers is presented in Fig. 6. For the easier observation, the rooftop and the upper barrier is removed from the 3D model (Fig. 6—top). The support structure where the upper barrier is placed is also visible in Fig. 6. This metal beam structure is responsible for the static of the entire roof segment.

5 Results

After the mounting process has been done, measurements have been retaken to validate the effectiveness of the project. All of the conditions have been recreated as it was done in the noise evaluation stage. This included the working load of the HVACs, measurement locations (see Fig. 1), measurement interval, etc. The effectiveness of the project has been validated at measurement positions 1, 2, and 3. If the noise level when HVAC devices are working match the residual noise generated by traffic, this would prove that project is successful. The results of the validation process can be

Fig. 6 Graphical representation in 3D of the lower barrier (top) and the barrier above the chiller (bottom)



observed in Table 1. In all of the measurement positions, noise level has been reduced by more than 9 dB. Comparison of the background noise during the first and second measurements (measurement positions 4, 5, and 6), as well as the resulting noise level when units are working, is presented in Table 2. We observe that background noise levels are consistent between measurements, which indicates that there was no significant change in the traffic density. Noise levels after the application of the barrier are within the boundaries of the background noise as well. This is yet another proof that the project has been successful, as the noise level in the measurement positions will be masked by the background traffic noise. In the Fig. 7, several photos of the mounted barriers at the site are presented.

Table 1 Measurement results of the validation

Meas. position	1	2	3	4	5	6
	Noise level [dB]					
Initial phase	81.8	79.8	80.1	64.4	65.2	64.3
Validation phase	71.9	70.1	70.2	54.4	54.8	54.3
Noise reduction	9.6	9.7	9.9	10	10.4	10

Comparison between initial and validation stage of the project

Table 2 Comparison of the background noise between initial stage, validation stage, and noise level when noise source is active

Meas. position	4	5	6
	Noise level [dB]		
Initial phase background noise	55.2	53.2	54.1
Background noise levels	53.8	54.8	54.2
Validation phase noise HVACs are active	54.4	54.8	54.3



Fig. 7 Documented photos during and after the mounting process

6 Conclusion

Design of the noise control solution for the HVAC devices requires multidisciplinary approach. Many of the mechanical aspects of their operation have to be considered. One very important is the airflow that is necessary for the HVAC subsystems to perform as expected. Classical acoustical enclosures can block the airflow creating overheat and unstable conditions of the devices. Noise control engineers then have to turn to the different construction of the barrier that will enable HVAC with sufficient air, while at the same time block and absorb the excess noise. Here, a study case of one of the noise control projects is described from initial steps to the installation and finally validation. Measurements in the first stage have provided useful inputs on the noise level, spectrum of the noise, and constraints related to the HVAC units. In the simulation stage, noise propagation and the behavior of the proposed segmented barrier has been observed. Gather data showed promising results that were used in the following stage of designing the physical barrier and absorption panel. After the material production and mounting stage, the validation process has been performed by measuring noise levels in the same way as in the first stage. Results showed that total noise reduction achieved, at each of the measurement positions, is more than 9 dB. This exceeds the expectation of the project and proves the feasibility of this type of noise control application. In the future, it would be interesting to exploit the use of different barrier geometry that could perhaps provide even better results

Acknowledgements This paper is presented as a part of the projects “Development of the methodology and means for noise protection in urban areas” (No. TR - 037020). Authors would like to express gratitude to the Ministry of education, science, and technological development of Republic of Serbia, for the financing support in this research.

References

1. R. McDowall, *Fundamentals of HVAC systems*, 1st edn. (Elsevier, Burlington, Great USA, 2007)
2. F. Fahy, *Foundations of Engineering Acoustics*, 2nd edn. (Academin Press London, Great Britain, 2003)
3. D.A. Bies, C.H. Hansen, *Engineering Noise Control—Theory and Practice*, 3rd edn. (Spon Press, London, Great Britain, 2003)
4. M. Prašćević, D. Mihajlov, D. Cvetković, Permanent and semi-permanent noise monitoring. *J. Low Freq. Noise Vib. Active Control* **34**(3), 251–268 (2015). (Serbia)
5. G. Licitra, *Noise maps in the EU: Models and procedures*, 1st edn. (USA: CRC Press, New York, 2012)

Coefficient of Sound Absorption of Polyamide PA12 Samples Manufactured by Selective Laser Sintering



Nebojša Bogojević, Branko Radičević, Aleksandar Vranić,
and Snežana Ćirić Kostić

Abstract Selective laser sintering is the additive manufacturing technology that is predominantly used for production of small series of products and prototypes, and the polyamide PA 12 represents the basic material for the technology process. The technology presents a reasonable choice for production of scientific instruments and laboratory equipment, as it is the case with the equipment for material characterization by sound absorption or emission. As the sound absorption by the instruments and equipment may affect interpretation of the obtained results, it is useful to know the frequency dependence of the sound absorption coefficient of the material used for their construction. The paper presents the results of measurements of the sound absorption coefficients of the PA12 samples with thicknesses between 0.7 mm and 2.2 mm in the frequency range between 125 Hz and 2.5 kHz, which is predominantly used in the photoacoustic applications. The measurements were performed according to the method SRPS ISO 9053, using the resistance of the airflow measurements and the Miki model. The obtained results show that the sound absorption coefficient of the PA12 samples manufactured by laser sintering are lower than 0.05 within the frequency range, and that it monotonously increases with frequency, similar to the behaviour of some other studied polymers and composite materials based on polymers.

1 Introduction

In the recent years, the additive manufacturing (AM) has become a mature technology that is, due to the short lead times and high manufacturing costs, predominantly used for production of prototypes and small series of products. For this reason, the AM is increasingly used for construction and reconstruction of scientific instrumentation, especially for configurable and customizable measurement equipment.

N. Bogojević (✉) · B. Radičević · A. Vranić · S. Ć. Kostić
Faculty of Mechanical and Civil Engineering in Kraljevo, University of Kragujevac, Kraljevo,
Serbia
e-mail: bogojevic.n@mfv.kg.ac.rs

The key advantage of the AM technologies is their ability to build products with complex shapes. The ability closes the gap between the theoretical models and experimental verifications for numerous research studies. For example, using a CAD and FEA software package in conjunction with AM technologies, today it is relatively easy to design and study lightweight parts, as well as parts optimized for specific applications. While majority of the AM applications are based on the unique ability of the technologies to build complex shapes, the applications are anyway affected by the properties of the materials that are used to build the products. Since the material properties are, in turn, affected by the production process of the AM technologies, the current decade witnessed extensive studies of the properties of the AM materials.

Among many others, the fitness of the AM technologies for development of various experimental setups attracted attention of those researchers who deal with application of photoacoustic effect [1]. The ability of AM technologies to create small structures with internal spaces could substantially increase sensitivity of the photoacoustic measurement equipment. However, any application of the AM technologies for design of structures for control of sound propagation requires good understanding of sound absorption and reflection properties of the structures [2]. Different researchers started to use AM to build specialized structures—metamaterials, which can be used to control the sound propagation, as demonstrated by Jiang et al. [3] and Liu [4]. In their research, the main focus was put on the geometrical characteristics of the structures produced by AM, and how these geometrical characteristics can influence the coefficient of absorption of the structure. None of the research, however, considered the influence of material to the sound absorption during propagation through the structures.

AM comprises various technologies that differ in basic material and in principle of joining the basic material to build the final product. While majority of AM technologies, such as stereolithography (SLA) and fused deposition modelling (FDM), require specialized support structures to build the parts with overhanging features, the selective laser sintering (SLS) technology does not require these structures, which makes the technology particularly suitable for building the parts with extremely complex shapes and design. The important advantage of the SLS technology is based on use of polyamide PA12 powder as the basic material and laser sintering as the principle of joining the basic material. Due to such concept of the SLS technology, the non-sintered powder acts as the support to the product during building process. Further advantage of the SLS technology is that the sintered PA12 has superior mechanical properties in comparison with other polymer AM materials. Finally, the laser sintered PA12 is stable against impact, chemicals, heat, UV light, water and dirt, and is also a biocompatible material. Due to those advantages, the SLS technology is an optimal choice for production of experimental equipment, and consequently, material properties of the laser sintered PA12 are subject of many studies [5]. This paper presents a study of the coefficient of sound absorption of PA12 samples manufactured by SLS technology, which is of interest for design of equipment used for studies of sound propagation. To the best knowledge of the authors, the measurements of the coefficient of sound absorption of laser sintered polyamide PA12 are not presented in literature.

2 Methods

The coefficient of absorption was determined on the basis of measurements of air flow resistance, which was measured according to SRPS ISO 9053 standard, using steady state air flow method.

2.1 Measurement Setup and Theoretical Background

Air resistance is one of the main non-acoustic parameters that shows the behaviour of porous materials used in sound absorption systems. The standard SRPS ISO 9053 [9] specifies two methods for measuring airflow resistance: a steady state airflow method and an alternating airflow method. The paper presents the results of measurements using the method of constant air flow.

The basic element of the measurement equipment, presented in the Fig. 1, is the measurement cell, which is constructed as a plexiglass tube with 100 mm diameter. The sample, in the form of a thin disc with 100 mm diameter is coaxially positioned in the middle of the measurement cell. Atmospheric pressure acts upon one side of the sample, while the other side of the sample is exposed to the pressure produced by a vacuum pump. The pressure difference between two sides of the sample has to provide air flow with sufficiently small velocity so that the measured air flow resistance does not depend on air flow velocity.

The vacuum pump ZAMBELLI, used in the experimental setup for research presented in this paper, may achieve the maximum air flow of 30 l/min, and produces pressure differences higher than 0.773 bar (580 mmHg). The air flow is controlled by two ball rotameters, with the smaller rotameter controlling the air flow in the range 0.2–6 l/min, and the larger rotameter controlling the air flow in the range 5–30 l/min. The maximum error of the air flow measurement is 2%. The pump provides airflow

Fig. 1 The measuring system for determining the air flow resistance



velocity of 0.4×10^{-3} m/s through the measurement cell, which completely corresponds to the recommendations of the standard SRPS ISO 9053, where the air flow should be below the 0.5×10^{-3} m/s. The difference between the pressures on two sides of the sample has been measured by differential pressure gauge TESTO 512. The measurement range of this instrument is from 0 to 200 Pa, with resolution of 0.1 Pa. Therefore, the experimental setup used for the measurements is capable of measuring the airflow resistances below 60 MPa s/m^3 .

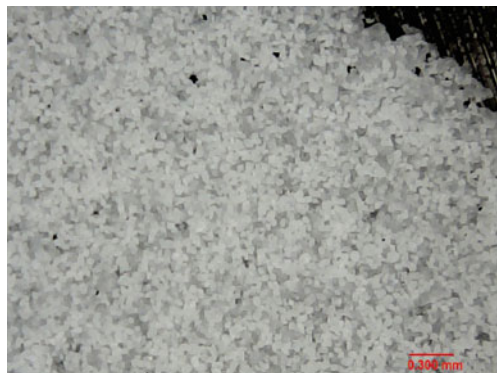
2.2 Specimens

For the purposes of the study, 40 samples were made from PA12 during a single production process using the SLS technology. All specimens are produced using an EOS P100 machine from the PA12 powder with trade name PA2200. As explained in the previous section, the samples had the shape of a disc with diameter of 100 mm.

The thickness of the samples was selected to study the effects of the porosity and layered structure of the material, characteristic for the SLS technology, to its air flow resistance and sound absorption properties. Microscopic analyses revealed that the parts produced by SLS have grainy structure and contain porosities, as it is shown in Fig. 2. According to the specifications of the manufacturer of the PA2200 powder, due to the porosities, the manufactured parts with thicknesses below 1.5 mm are not watertight. As the specimens are built with layer thickness of 0.1 mm, the samples were manufactured with thicknesses 0.7 mm, 1.2 mm, 1.7 mm and 2.2 mm, producing 10 samples for each of the thicknesses.

Previous research [6, 7] have shown that the densities of parts produced by SLS are around 10% smaller than the densities of the parts made by injection moulding. As the density of the PA12 parts manufactured by injection moulding is around 1.01 g/cm^3 [8], the measured density of the samples, which is around 0.93 g/cm^3 , further suggests that the laser sintered PA12 should be considered to be a porous material.

Fig. 2 The porosity of the specimens under the microscope



3 Empirical Model for Estimation of the Acoustic Properties

According to Delany and Bazley [8], the propagation of sound in an isotropic homogeneous material can be represented by the characteristic impedance Z_c and the sound propagation constant γ of the absorption material.

$$Z_c = R + jX \quad (1)$$

$$\gamma = \alpha + j\beta \quad (2)$$

Furthermore, relying on the empirical considerations from the Delany and Bazley research [8], the characteristic impedance and sound propagation coefficients may be calculated using the following relations:

$$R = \rho_0 c_0 \left[1 + C_1 \left(\frac{\rho_0 f}{r} \right)^{-C_2} \right] \quad (3)$$

$$X = -\rho_0 c_0 \left[C_3 \left(\frac{\rho_0 f}{r} \right)^{-C_4} \right] \quad (4)$$

$$\alpha = \left(\frac{2\pi f}{c_0} \right) \left[C_5 \left(\frac{\rho_0 f}{r} \right)^{-C_6} \right] \quad (5)$$

$$\beta = \left(\frac{2\pi f}{c_0} \right) \left[1 + C_7 \left(\frac{\rho_0 f}{r} \right)^{-C_8} \right] \quad (6)$$

where R and X are the real and the imaginary part of the characteristic acoustic impedance Z_c , α and β are the real and imaginary part of the propagation constant γ of the sound in the absorption material, while ρ_0 stands for the air density, f for the sound frequency, c_0 for the sound speed and r for the longitudinal air flow resistance of a sample. The regression coefficients in the (3–6), denoted as C_1 – C_8 , are defined in the Delany and Bazley paper [10] for fibrous materials and in the Miki paper [11] for porous materials.

According to the recommendations of European norm EN 12354-6 [12], the coefficient of sound absorption for porous materials can be calculated using the (7–11). For a diffuse acoustic field, the absorption coefficient α_s can be determined as:

$$\alpha_s = \int_0^{\pi/2} \alpha_\varphi \sin \varphi d\varphi \quad (7)$$

$$\alpha_\varphi = 1 - |r_\varphi| \quad (8)$$

$$r_\varphi = \frac{Z' \cos \varphi + 1}{Z' \cos \varphi - 1} \quad (9)$$

$$Z' = Z'_c \coth \gamma d \quad (10)$$

$$Z'_c = \frac{Z_c}{\rho_0 c_0} \quad (11)$$

with the following designations:

- φ angle of incidence, in radians,
- α_φ the absorption coefficient for a plane sound wave bound to the angle φ ,
- r_φ reflection coefficient for a plane sound wave bound to the angle φ ,
- Z' normalized surface impedance of the sample
- Z'_c normalized characteristic impedance of absorbent material,
- d sample thickness

4 Results and Discussion

The results of the measurements of the air flow resistance of the samples are given in the Table 1.

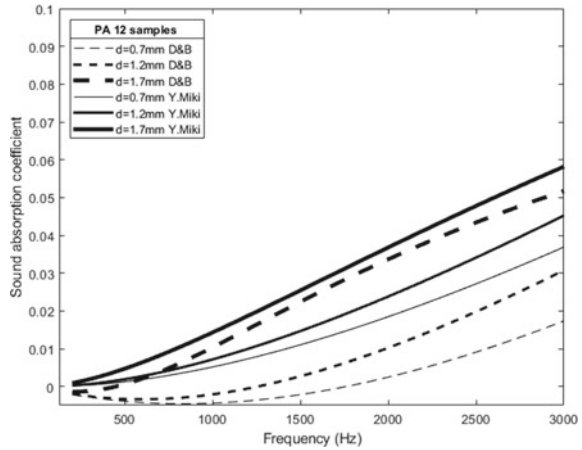
The measurements show high values of the airflow resistance of the samples even for thicknesses below 1.5 mm, where the material of the samples is not watertight. The airflow resistance of the samples with thickness 2.2 mm was higher than the maximal value measurable by the experimental equipment (60 MPa s/m³), and those samples may be considered to be airtight.

On the basis of the obtained measurements, the frequency dependence of the absorption coefficient was calculated in the frequency range 125–2500 Hz, which is predominantly used in the photoacoustic applications. The calculations of the absorption coefficients were performed using the Miki model [11] for porous materials. The results of the calculations are presented by solid lines in the Fig. 3. The results show that the sound absorption coefficient monotonously increases with sound frequency, but that it has values lower than 0.05 within almost the whole studied frequency range.

Table 1 Measurements of the air resistance of the samples under study

d [mm]	Measured air flow resistance		Calculated specific air flow resistance	
	r [MPa s/m ³]	Δr [MPa s/m ³]	ρ [MPa s/m ²]	$\Delta \rho$ [MPa s/m ²]
0.7	6.3	0.65	71	8
1.2	8.3	1.1	54	8
1.7	17.2	2.1	64	8
2.2	–	–	–	–

Fig. 3 Frequency dependence of the coefficient of sound absorption of polyamide PA12 calculated using the Miki model (solid lines) and Delany and Bazley model (dashed lines)



The obtained results may be compared to the scarcely published results for absorption coefficients of polymer materials and composites. A research on acoustic properties of polypropylene composites reinforced with stone groundwood [13] showed specific air flow resistances around 1 MPa s/m^2 , considerably lower than those presented in this paper. The difference in the measured values of the air flow resistance may be explained by the differences in the microstructure of the materials, as the laser sintered PA12 has porous structure and the polypropylene composites reinforced with stone groundwood is a composite material with fibrous structure. The absorption coefficient of the material is close to 0.05 for frequencies up to 1600 Hz, but rapidly increases for higher frequencies. The difference in the high-frequency behaviour observed for two materials may not be easily explained by the difference in their structure because the wavelengths of the sound in the whole studied frequency range are much longer than the characteristic dimensions of the material features, which represent distinction between the microstructures of the materials. However, it may be noticed that the rapid increase of the sound absorption coefficient in the high-frequency range is not discussed in the paper [13].

In literature is frequently used Delany and Bazley model [10] for calculation of the frequency dependence of the sound absorption coefficients of fibrous materials. While the microscopy and density measurements suggest that the laser sintered PA12 has porous structure, the authors nevertheless calculated the frequency dependence of the sound absorption coefficient using the Delany and Bazley model, and the results of calculation are shown in the Fig. 3 by dashed lines. The values of the sound absorption coefficients calculated according Delany & Bazley model are lower than the values calculated by the Miki model, but negative values of the sound absorption coefficients in the range 200–1000 Hz confirm that the Delany and Bazley model is not applicable to the laser sintered PA12, further confirming that the laser sintered PA12 should be considered as a highly reflective porous material for the purposes of sound propagation studies.

5 Conclusion

In the paper are presented the results of experimental measurements of air flow resistance and calculation of the frequency dependence of the sound absorption coefficient of the polyamide PA12 samples produced by selective laser sintering technology. The results have shown that the samples with thickness higher than 2.2 mm may be considered airtight, and that the absorption coefficient of the samples with thicknesses above 0.7 mm are smaller than 0.05 in a wide sound frequency range between 125 and 2500 Hz.

The obtained result means that the products manufactured from polyamide PA12 by the selective laser technology may be considered highly reflective for the purposes of the sound propagation applications, such as design and construction of the measurement equipment based on photoacoustic effect.

Acknowledgements The authors wish to acknowledge the support of European Commission through the project “Advanced design rules for optimal dynamic properties of additive manufacturing products—A_MADAM”, which has received funding from the European Union’s Horizon 2020 research and innovation programme under the Marie Skłodowska-Curie grant agreement No. 734455. The authors also acknowledge the support of the Serbian Ministry of Science, Education and Technology through the grants No. TR36005 and No. TR37020.

References

1. A.C. Tam, Applications of photoacoustic sensing techniques. *Rev. Mod. Phys.* **58**(2), 381 (1986)
2. F. Setaki, M. Tenpierik, A. Timmeren, M. Turrin, New sound absorption materials: using additive manufacturing for compact size, broadband sound absorption at low frequencies, in *Proceedings of the INTER-NOISE 2016 - 45th International Congress and Exposition on Noise Control Engineering: Towards a Quieter Future*, pp. 4073–4078, Hamburg, Germany (2016)
3. C. Jiang, D. Moreau, C. Doolan, Acoustic absorption of porous materials produced by additive manufacturing with varying geometries, in *Proceedings of ACOUSTICS 2017*, P79, pp. 19–22 Nov 2017, Perth, Australia
4. Z. Liu, J. Zhan, M. Fard, J. Davy, Acoustic properties of a porous polycarbonate material produced by additive manufacturing. *Mater. Lett.* **181**, 296–299 (2016)
5. M. Schmid, A. Amado, K. Wegener, Polymer powders for selective laser sintering (SLS), in *AIP Conference proceedings*, vol. 1664, no. 1, p. 160009. AIP Publishing
6. G.V. Salmoria, J.L. Leite, L.F. Vieira, A.T.N. Pires, C.R.M. Roesler, Mechanical properties of PA6/PA12 blend specimens prepared by selective laser sintering. *Polym. Testing* **31**(3), 411–416 (2012)
7. S. Dupin, O. Lame, C. Barrès, J.Y. Charneau, Microstructural origin of physical and mechanical properties of polyamide 12 processed by laser sintering. *Eur. Polymer J.* **48**(9), 1611–1621 (2012)
8. B. Van Hooreweder, D. Moens, R. Boonen, J.P. Kruth, P. Sas, On the difference in material structure and fatigue properties of nylon specimens produced by injection molding and selective laser sintering. *Polym. Testing* **32**(5), 972–981 (2013)
9. ISO 9053: 1991, Acoustics—Materials for acoustical applications—Determination of airflow resistance. International Organisation for Standardization (1991)

10. M.E. Delany, E.N. Bazley, Acoustical properties of fibrous absorbent materials. *Appl. Acoust.* **3**(2), 105–116 (1970)
11. Y. Miki, Acoustical properties of porous materials—modifications of Delany-Bazley models. *J. Acoust. Soc. Jpn.* **11**(1), 19–24 (1990)
12. EN 12354-6: 2003, Building acoustics—Estimation of acoustic performance of buildings from the performance of elements. European Committee for Standardization (2003)
13. J.P. López, N.E. El Mansouri, J. Alba, R. Del Rey, P. Mutjé, F. Vilaseca, Acoustic properties of polypropylene composites reinforced with stone groundwood. *Bio Resour.* **7**(4), 4586–4599 (2012)

Online Database of Industrial Noise Sources



Tanja Miodragović, Mladen Rasinac, Jelena Tomić, and Branko Radičević

Abstract The paper presents concept and structure of relational database for description of noise sources investigated within the framework of the project “Development of methodologies and means for protection from environmental noise.” The database is used for collecting and storing experimental results of industrial noise measurements that were carried out for the purpose of noise mapping and noise protection planning. The database provides information about equivalent noise level and one-third octave noise spectrum in the near field of sound sources. The access to the database is possible through standard SQL queries, which is suitable for software tools used for noise reduction. The rights for submitting data are granted only to the developers, while all collected data are publicly available via the Internet.

1 Introduction

In addition to air, soil and water pollution, the development of industrial and transport capacities causes increase in levels of communal noise which has negative impact on the psycho-physical health and productivity of the population. Industrial noise is a major cause of damaged hearing in millions of working people [1]. The degree of hearing loss depends on sound intensity (the loudness of sound), the duration of exposure, and individual sensitivity to noise. Knowledge and information related to the identification of noise problems play a very important role in developing strategies for noise reduction. With that aim, the European Union adopted Environmental Noise Directive (2002/49/EC) [2] and the corresponding standards. According to the Directive, Member States have to create strategic noise maps, and, based on the noise maps, the stakeholders have to create action plans designed to manage noise issues and contribute to the noise reduction. The FP5 project “Harmonoise” [3], the FP6 project “Imagine” [4] and the FP7 project “Silence” [5] were established for those purposes.

T. Miodragović (✉) · M. Rasinac · J. Tomić · B. Radičević
Faculty of Mechanical and Civil Engineering, Dositejeva 19, 36000 Kraljevo, Serbia
e-mail: miodragovic.t@mfkv.kg.ac.rs

© Springer Nature Switzerland AG 2021

N. Herisanu and V. Marinca (eds.), *Acoustics and Vibration of Mechanical Structures—AVMS 2019*, Springer Proceedings in Physics 251,
https://doi.org/10.1007/978-3-030-54136-1_16

165

As Serbia is in process of European integration, it dedicates particular attention to the environmental protection, especially noise protection. According to the respective policies, the Serbian Ministry of Education and Science funded the project “Development of methodologies and means for noise protection of urban areas” (acronym “urbaNoise”) [6]. The project is realized by three major Serbian state universities, University of Kragujevac, represented by Faculty of Mechanical and Civil Engineering Kraljevo, University of Niš, represented by Faculty of Occupational Safety and University of Belgrade, represented by the Faculty of Traffic Engineering. The project goals are:

- development of national noise assessment methodologies harmonized with EU;
- construction of laboratory facilities for testing of acoustic materials;
- design of modular noise barriers from waste materials;
- development of software tools for local noise mappings;
- development of national database of noise sources.

A database is an excellent tool of sharing data between scientific organizations which collect and interpret data. However, databases about noise sources were not developed in Serbia until this project.

Within the project “urbaNoise,” two databases for collection of data about noise sources are developed. The first database [7] was aimed to be Serbian national database for urban noise sources, intended for purposes of noise mapping [8, 9]. The database presented in this paper is intended to describe the results of noise measurements of industrial and communal sources (presses, compressors, hammers, etc.) that are not performed within the standard systematic environmental noise measurements. During many of these measurements, it was not possible to fulfill the standard requirements for environmental noise assessment, but the acquired results are nevertheless worthy of keeping for future studies.

The second section describes the basic mechanisms of noise sources. The third section of the paper defines requests for creation of the database of industrial noise sources, and the respective structure is described in the fourth section, while the description of the database implementation is given in the fifth section.

2 Industrial Noise Sources

This section describes the basic noise generation mechanisms of industrial noise sources, as well as some examples of the most common machines used in the working environment. Machinery in the industry creates a serious noise problem. It is responsible for intense indoors as well as outdoors noise. This noise is due to machinery of all kinds and generally increases with the power of the machines. The resulting sound pressure level depends on the type of noise source, the distance from the source to the receiver, and the nature of the environment. For a given machine, the sound pressure level is determined by the part of the total mechanical or electrical energy that is transformed into acoustical energy.

Sound fields at the workplace are usually complex because of the involvement of many sources in the process of sound generation, propagation and absorption: propagation through air, propagation through solid matter, reflection from the floors, walls, ceilings and machinery surfaces, absorption on the surfaces, etc. The noise control measures should be performed only after an appropriate study of noise sources. The basic mechanisms of noise generation can be due to mechanical noise, fluid noise and/or electromagnetic noise.

Noise produced from electrical equipment such as motors and generators is generally low-frequency noise. Electrical motors convert electrical energy to magnetic energy then to the mechanical energy. Since part of the transformed energy is converted to heat energy, the electric machines should be supplied with cooling systems, quite often fan systems that generate noise.

Air-moving equipment tends also to generate noise with a wide frequency range. Air turbulence and vortices generate noise, especially at high air flow velocities. Turbulence may be generated by moving or rotating solid objects, such as the blade tips of a ventilator fan. Therefore, care must be taken to reduce flow velocity, reduce turbulence flow by using diffusers and removing obstacles to the flow.

For mechanical sound sources, care must be taken to reduce the vibrating surfaces and to reduce the vibration velocity. Reduction of the vibration velocity can be carried out by using damping materials at resonance frequencies and by blocking the induced forced vibration. Reducing the vibrating areas can be carried out by separating a large area into small areas, using flexible joints.

Due to the needs of industry and economic development, there is an increasing demand for cost-effective consumer goods. For the machine manufacturer, this generally means offering products with a low space, material, energy and production time requirement. Increased production and productivity are often accompanied by an increase in noise levels. The staff are then exposed to higher noise levels than before, despite the noise reduction measures taken in the design of the machine. Noise is a common occupational hazard in workplaces such as the industries of steel and iron, crushing mills, foundries, sawmills, airports and aircraft maintenance workshops, textile mills, among many others.

3 Request

The database of noise sources is intended to describe industrial noise source. Noise emitted by industrial sources may depend on many factors, but the database should be simple and practical to use and should contain minimal number of data that describe noise sources. Since the main reason for design of the database was statistical analyses, the relevant data that describe the results of measurements of industrial noise sources are:

- name of the noise source;
- description of noise source and/or measurement conditions;

- distance between the noise source and microphone;
- measured equivalent noise level;
- spectral distribution of noise.

The database is not intended to be used only by participants of project “urbaNoise,” but also to permit public access to reading collected data, so the third parties could use data as input in software tools for noise mapping. It should be accessible over Internet and should respond to standard SQL queries.

4 Database Structure

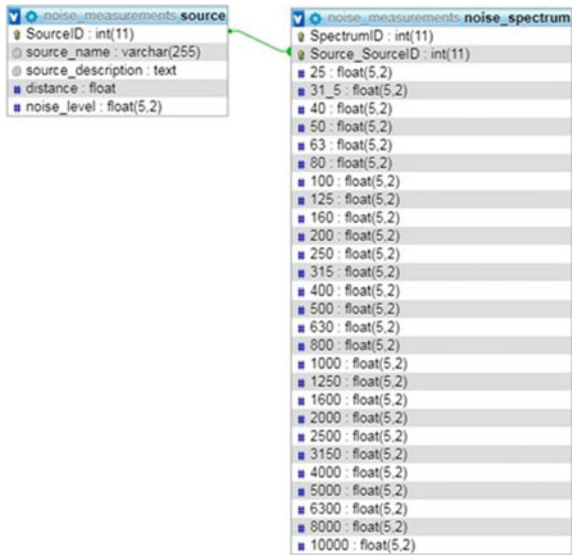
Entity–relationship (ER) diagrams are often used in design of relational database. An ER diagram is a flowchart that illustrates the logical structure of a database by defining its entities, their attributes and relationships. Database entity is an object about which data are stored in the form of table. The properties of an entity are defined by its attributes. Primary key represents an attribute or set of attributes that uniquely identifies a particular entity. Foreign keys are attributes that define relationships between the entities. The attributes of a foreign key in one table are the attributes of a primary key in another table. Relationships between the entities can be “1-to-1” or “1-to-many”. “1-to-1” relationship between two tables indicates that each record in the first table corresponds to one, and only one, record in the second table. “1-to-many” relationship indicates that each record in the first table corresponds to one or more records in the second table, but each record in the second table corresponds to only one record in the first table.

The entity–relationship diagram of the database structure is shown in Fig. 1. A noise source is represented by the table *source*, which contains the following attributes (columns):

- *SourceID*—the primary key of the table;
- *source_name*—the name of the source;
- *source_description*—the textual description of the noise source;
- *distance*—microphone distance from the noise source during measurement;
- *noise_level*—measured equivalent A-weighted noise level

The table *noise_spectrum* is linked by “1 – to – 1” relationship to the table *source* by the key *source_SourceID*. This table contains information about third octave noise spectrum, which is described by sound level for each third octave frequency range, as shown in Fig. 1.

Fig. 1 EER diagram of the database of industrial noise sources



5 Implementation

The database was created using MySQL database engine, and it is running under Linux operating system on the Web server of the Faculty of Mechanical and Civil Engineering in Kraljevo. The user interface to the database is developed using PHP programming language which enables generation of HTML pages. The graphical user interface has been developed in order to provide a user-friendly solution for interaction with the database and data manipulation. The designed user interface enables data insertion, modification, and deletion, as well as a preview of already submitted information. Collected data are publicly available on the Internet address www.mfkv.kg.ac.rs/urbanoise/measurements. Due to safety and security reasons, data manipulation is granted only to the developer team and project participants.

Data exchange between the database and the third-party software tools may be realized through SQL query. Structured Query Language (SQL) is a domain-specific language designed for accessing and manipulating databases. SQL queries perform data retrieval, submitting and updating, as well as creation of data objects such as SQL databases and SQL tables. As submitted data should be publicly accessible, SQL query will be the basic tool for obtaining data from developed database.

On the next figure is given example of input data about noise sources (Fig. 2).

If input of information about spectral content of the sound is selected, a new form for input of sound level data for each of the frequency ranges is opened.

The entered data may be sorted and searched, and an example of the noise spectrum of noise source is shown in Fig. 3.

urbaNoise

Database of noise sources

Development of methodologies and means for protection from enviromental noise

Source name:
Source 1

Source description:
Smoke ventilator K4

Distance from the source [m]:
0.5

Measured noise level [dBA]:
90.2

Select one of the following and then press "Next":
 input information about the spectral content of the sound
 end of input

Next

Fig. 2 Example of input data of noise source

Fig. 3 Noise source octave spectrum

Frequency [Hz]	Sound Level [dBA]
25	0,00
31,5	0,00
40	0,00
50	0,00
63	59,10
80	0,00
100	0,00
125	67,10
160	0,00
200	0,00
250	74,70
315	0,00
400	0,00
500	80,20
630	0,00
800	0,00
1000	80,30
1250	0,00
1600	0,00
2000	75,90
2500	0,00
3150	0,00
4000	69,70
5000	0,00
6300	0,00
8000	59,60
10000	0,00



The database was available by the beginning of March 2019 and has at the moment 49 entries including description of noise measurements for 10 transporters, seven fans, three mills, two dryers, two hammers and two turbo engines.

6 Conclusion

The database presented in this paper was developed for collecting and storing data that describe industrial noise sources. The main purpose of database is statistical analyses of the data that may reveal relations between source parameters and emitted sound power. Using an SQL query or XML, the third-party software tools for noise mapping may read the data from the database.

Acknowledgements The authors wish to express their gratitude to Serbian Ministry of Education and Science for support through project TR37020.

References

1. A. Lie, M. Skogstad, H.A. Johannessen, T. Tynes, I.S. Mehlum, K.C. Nordby, K. Tambs, Occupational noise exposure and hearing: a systematic review. *Int. Arch. Occup. Environ. Health* **89**(3), 351–372 (2016)
2. Directive 2002/49/EC of the European Parliament and the Council of June 2002. *Official J. Eur. Communities*
3. http://cordis.europa.eu/fetch?ACTION=D&CALLER=PROJ_IST&QM_EP_RCN_A=57829
4. <http://www.imagine-project.org>
5. <http://www.silence-ip.org>
6. <http://www.mfkv.rs/urbaNoise/>
7. <http://www.mfkv.kg.ac.rs/urbanoise/dbnoise/>
8. Z. Soskic, Design of database of urban noise sources. *Transport*, **10**(3/3) (2012)
9. J. Tomic, N. Bogojevic, B. Tatic, Z. Soskic, Design and implementation of on–line database of noise sources, in *Proceedings of the 23rd National and 4th International Conference “Noise and Vibrations”*, Niš 17–19 Oct 2012. pp. 225–228

Studies on the Experimental Validation of the Theoretical Static Noise Field in the Neighbourhood of Agricultural Tractors



Petru Cardei, Cristian Sorica, Valentin Vladut, and Mihai Matache

Abstract The article presents results on the measurement and modelling of the field of noise generated by agricultural tractors in aggregate with agricultural machines operated by human operators. The data required to construct the field level noise level in the vicinity of the tractors at work are obtained by measurement. The results, both the measured and the theoretical ones, are finally used to verify the compliance with the occupational safety standards, taking into account the specific activities carried out by the staff working on the trailed agricultural machines. The field of noise intensity level is also worthwhile in the design of agricultural machinery and in the estimation of the level of noise received by human personnel working on other equipment trailed by the tractor under consideration, other than those appearing in this article. Also, important references are made to the expression of the logarithmic term, which generally characterizes the variation of the noise intensity level based on the distance to the source.

1 Introduction

Among the ways of approaching the problem of the propagation of acoustic waves in space and their effects on the environment, from the engineering point of view and from the theoretical point of view, there are, at least apparently, quite large differences. This issue has been addressed in previous papers, [1–5].

In general, traction noise measurement standards focus on effects on the tractor driver. The effects of the tractor's noise on the environment are considered to be minor, given the working regime of the tractor, which is generally in continuous movement. In this way, the impact of an environmental objective takes place for a relatively negligible time relative to the allowable times in the standards for the noise intensities caused by these machines.

P. Cardei (✉) · C. Sorica · V. Vladut · M. Matache
INMA, Bucharest 013813, Romania
e-mail: petru_cardei@yahoo.com

© Springer Nature Switzerland AG 2021
N. Herisanu and V. Marinca (eds.), *Acoustics and Vibration of Mechanical Structures—AVMS 2019*, Springer Proceedings in Physics 251,
https://doi.org/10.1007/978-3-030-54136-1_17

In the model described above, there are neglected a number of cases where the environment (and especially human beings) are subjected to noise of constantly high intensity in relation to the values admitted in the standard. We refer here to those agricultural machines that agricultural workers work and the effects of noise on them. Such machines are, for example: forestry for seedlings equipment, MPF1, Fig. 1, [6], miscanthus planting machine, MPM4, Fig. 2, [7], the cucumber harvest machine patented in the Republic of Moldova, Fig. 3, planter seedling machine, Fig. 4, [8], planter seedlings machine, made by Avenue SRL Caransebes, [9], Ferrari FPA manual planting machines, [10].

Staff working on the above-mentioned agricultural machines or other machines of the same type is suspected of being subject to a complex regime of demands that are part of the pollution category: noise, noxiousness, vibrations, plus working positions, often hard to bear and which accentuates the action of pollution factors. In this context, it is important to estimate the effects of each factor that affects the personnel involved in such work processes and, possibly, the increase of protection



Fig. 1 MPF1 forest seedlings planting



Fig. 2 Miscanthus planting machine, MPM4

Fig. 3 Cucumber harvester



Fig. 4 Akpil machine for seedlings planting



by limiting working time or additional isolation protection conditions to factors such as those mentioned above. Estimation of the noise pollution of personnel working on agricultural machinery has as its main source the tractor (mainly engine and transmission). Controlling the noise intensity in the neighbourhood of tractors is a first action that can be applied for this purpose. Direct measurement for each machine is a solution. Considering the fact that the agricultural machines with human staff are very numerous and that they are trailed or driven by tractors of various types and with various exploitation times, it is useful to create a simulation tool for the purpose of forecasting the noise intensity. The noise intensity forecast is useful in the design or improvement of trailed agricultural machines serviced by agricultural workers. Such a noise simulator is the one proposed in this article.

2 Methodology

2.1 The Measurement of Noise on Agricultural Machinery with Human Staff

The noise level measurement was done using an 80 hp New Holland TD80D tractor, aggregated with the miscanthus planting machine and the forest seedlings planting machine. Figure 5 shows four images of the noise measurement activity in the neighbourhood of the tractor. Also, in Fig. 5, it shows the position of the referential system fixed to the tractor (do with the machine). The background noise level was 53.2 dB.



Fig. 5 Measurements made for model calibration and the referencing in space

The origin of the tractor reference system is at the centre of the parallelepiped that modelling the motor block, with the dimensions of $1.0 \times 0.45 \times 0.87$ m.

2.2 Creating the Mathematical Model

To create the noise level simulation tool in the vicinity of the tractor, we starting from a simple formula suggested and used by [11] and also applied in [1]. The start formula contains three parameters, the power of the source, L_w and the model parameters, a, b :

$$L_{eq}(\xi_1, \xi_2, \xi_3, x_1, x_2, x_3, L_w, a, b) = L_w - a \ln \sqrt{\frac{(\xi_1 - x_1)^2 + (\xi_2 - x_2)^2 + (\xi_3 - x_3)^2}{S}} - b \quad (1)$$

where (ξ_1, ξ_2, ξ_3) is a point where a source (point source) is located, (x_1, x_2, x_3) is the current point in the three-dimensional space, L_{eq} is the noise intensity level, and S is the external surface of the source (thus, the argument of the logarithmic function becomes dimensionless and there are no dimensional problems). The introducing of the constant S was made to satisfy the requirements expressed in [12] and [13]. Therefore, with respect to reference models, based on a point source, this model uses a spatially distributed source on the surface of a three-dimensional body. By hypothesis, we assume that the considered noise source is evenly distributed on a parallelepiped that includes, at the limit, the tractor block. We consider the origin of the Cartesian axis system at the centre of this parallelepiped and the dimensions of the parallelepiped given after the measurement, $-X_{min} = X_{max} = \frac{l}{2}$, $-Y_{min} = Y_{max} = \frac{l}{2}$, $-Z_{min} = Z_{max} = \frac{h}{2}$, where $L = 1.0$ m, $l = 0.45$ m, $h = 0.87$ m. Taking into account the above considerations, the total noise level results on each plane portion that is a face of the parallelepiped by summing, for example, the face $x_3 = Z_{max}$:

$$L_{eqZ_{max}}(x_1, x_2, x_3, L_w, a, b) = 10 \cdot \log \left(\int_{V_{min}}^{Y_{max}} \int_{X_{min}}^{X_{max}} 10^{\frac{L_{eq}(\xi_1, \xi_2, Z_{max}, x_1, x_2, x_3, L_w, a, b)}{10}} d\xi_1 d\xi_2 \right) \quad (2)$$

Similarly, the level of noise generated by distributed sources is uniformly distributed over the other five faces of the parallelepiped. The noise level of the source distributed on the six faces of the parallelepiped has the expression:

$$\begin{aligned}
& L_{eq}(x_1, x_2, x_3, L_w, a, b) \\
&= 10 \cdot \log \left(10^{\frac{L_{eqZ_{max}}(x_1, x_2, x_3, L_w, a, b)}{10}} + 10^{\frac{L_{eqZ_{min}}(x_1, x_2, x_3, L_w, a, b)}{10}} + 10^{\frac{L_{eqX_{max}}(x_1, x_2, x_3, L_w, a, b)}{10}} \right. \\
&\quad \left. + 10^{\frac{L_{eqX_{min}}(x_1, x_2, x_3, L_w, a, b)}{10}} + 10^{\frac{L_{eqY_{max}}(x_1, x_2, x_3, L_w, a, b)}{10}} + 10^{\frac{L_{eqY_{min}}(x_1, x_2, x_3, L_w, a, b)}{10}} \right) \quad (3)
\end{aligned}$$

The noise level given by the expression (3) is a three-dimensional static field (variables x_1, x_2, x_3), dependent on three parameters (L_w, a, b). The three parameters will be determined by minimizing the function built according to the method of least squares, using the measurements made (a procedure for calibration of the formula (3) for a certain machine). For the measurement data (see Table 1), the following values of the noise level parameters are obtained: $L_w = 100.000$ dB, $a = 15.725$ dB, $b = 17.000$ dB. In order to obtain these values, the next functional was minimized:

Table 1 Measurement results for the acoustic field generated by the tractor

x_1 (m)	x_2 (m)	x_3 (m)	Leq (dB)	Observations
0.50	0.22	0.00	93.50	Tractor engine
0.00	0.22	0.00	99.10	Tractor engine
-0.50	0.22	0.00	100.50	Tractor engine
0.00	0.23	0.71	93.50	Exhaust pipe, mid
-2.30	0.32	1.30	91.80	Exhaust pipe, up
-2.30	0.00	0.00	83.70	Rear tractor, centre
-1.30	0.15	1.40	73.40	Driver's ear
11.50	0.00	1.25	69.40	Front tractor
-12.50	0.00	1.25	64.40	Rear tractor
0.00	6.00	1.25	73.60	Right side tractor
0.00	6.00	1.25	75.00	Left side tractor
-3.77	2.00	-0.58	74.60	Worker level ear ^a
-3.77	0.00	-0.58	75.90	Worker level ear ^a
-3.77	-2.00	-0.58	78.40	Worker level ear ^a
-3.80	2.00	0.76	73.80	Worker level ear ^b
-3.80	1.00	0.76	75.60	Worker level ear ^b
-3.80	-1.00	0.76	76.20	Worker level ear ^b
-3.80	-2.00	0.76	74.20	Worker level ear ^b
-3.35	0.75	0.76	75.30	Worker level ear ^c
-3.35	-0.75	0.76	74.90	Worker level ear ^c

^aCucumber harvester

^bMPM 4

^cMPF1

$$\Psi(L_w, a, b) = \sum_k^N (L_{\text{eq}}(x_{1k}, x_{2k}, x_{3k}, L_w, a, b) - L_{\text{eq exp } k})^2 \quad (4)$$

with the next restrictions:

$$100.0 \leq L_w \leq 140.0, 10.0 \leq a \leq 30.0, 0 \leq b \leq 17.0. \quad (5)$$

Because we have not studied in detail in qualitatively terms the functional (4), we have limited to obtain relative minima (including the ends of the interval) only aiming to achieve a value as close as the measured value at the smallest distance from the engine.

2.3 Results

The distribution of the noise level around the tractor is the main result of this article. The function minimization calculation (4), guided to the best approximation of the maximum and minimum measured values, leads to the following values of the function parameters (3): $L_w = 90$ dB, $a = 18.307$ dB, $b = 12.786$ dB. There are only two values in the twenties that deviate over 10% from the mean value of experimental data. The remaining 18 differences between experimental and theoretical data are below 5.5% of the mean value of experimental data. Under these conditions, the interpolation approximation (3), with the values of the parameters given above, is considered satisfactory.

Using the interpolated noise level (3), to better understand its behaviour, is given the graphical representations of Figs. 6, 7, and 8. The noise level function (3) is a function of three real variables. The representation of the function as the surface of Figs. 6 and 7 is made for constant values of the vertical coordinate, x_3 . The noise level distribution in Fig. 6 corresponds to the most likely vertical coordinate of the human operator's ear which works on the sowing plant or on the miscanthus planting machine. The vertical coordinate corresponding to the noise distribution in Fig. 7 is most likely for the ears of agricultural workers from the cucumber or strawberry harvest machine.

The variation of the noise level in the direction of the trajectory, for various heights and values of the coordinate in the normal direction to the trajectory, is given in Fig. 8. The horizontal area of the continuous curve $x_2 = 0.227$ m, $x_3 = 0.000$ m in Fig. 8 corresponds to the length of the parallelepiped that borders the engine. Noise level attenuation is observed, and is in accordance with scientific experience, and measurement.

The values of the noise level at the ears of operators of trailed agricultural machines are given in Table 2. The experimental and theoretical values can be used as arguments and considerations regarding the labour protection in the field of agricultural machinery exploitation.

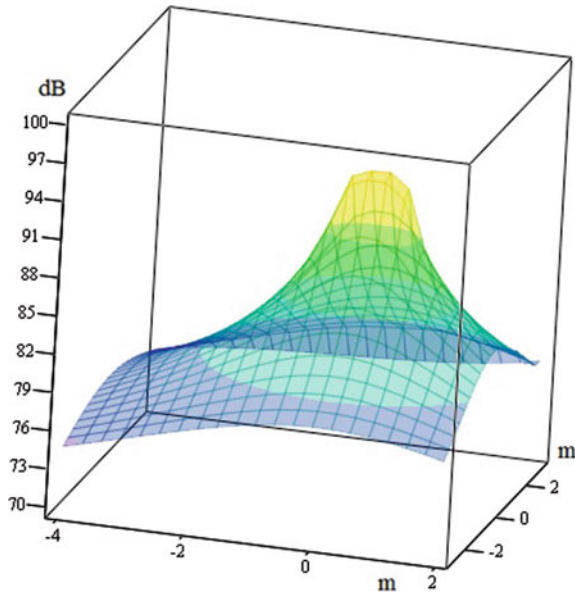


Fig. 6 Distribution of the noise level at 0.45 m from the engine centre (1.385 m from the ground)

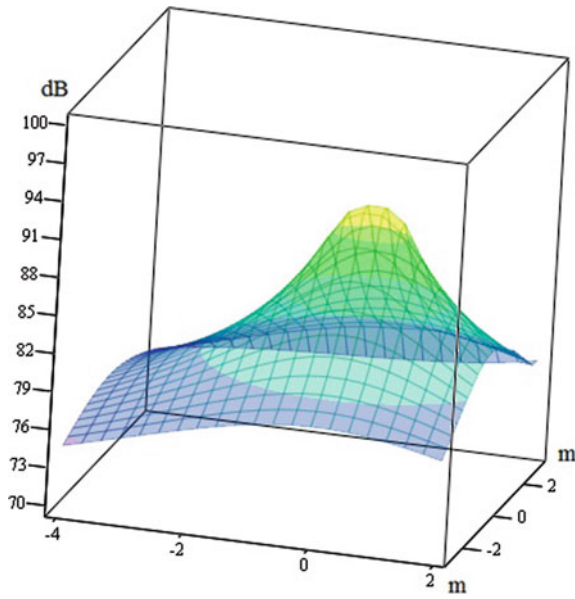


Fig. 7 Distribution of the noise level at 0.585 m from the engine centre (0.35 m from the ground)

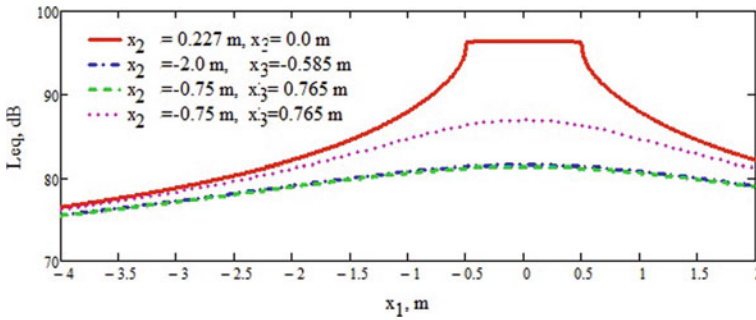


Fig. 8 Distribution of the noise level along the direction of movement of the machine, for the certain coordinates in the transverse direction to the displacement and vertical, specified

Table 2 Noise level comparative, experimental and theoretical values at the level of the ear of human operators working on trailed agricultural machines

x_1 (m)	x_1 (m)	x_1 (m)	L_{eq}^* (dB)	L_{eq}^{**} (dB)	Observations
-3.770	2.00	-0.585	74.60	75.87	Worker level ear ^a
-3.770	0.00	-0.585	75.90	76.86	Worker level ear ^a
-3.770	-2.00	-0.585	78.40	75.87	Worker level ear ^a
-3.800	2.00	0.765	73.80	75.77	Worker level ear ^b
-3.800	1.00	0.765	75.60	76.47	Worker level ear ^b
-3.800	-1.00	0.765	76.20	76.47	Worker level ear ²
-3.800	-2.00	0.765	74.20	75.77	Worker level ear ²
-3.350	0.75	0.765	75.30	77.51	Worker level ear ^c
-3.350	-0.75	0.765	74.90	77.51	Worker level ear ^c

*Experimental, **Theoretical

^aCucumber harvester

^bMPM

^cMPF1

It can be seen from the practice that the workplaces for which the noise level has been measured and calculated are very supplicant for human operators: physical and psychic. They are working in rather awkward positions and the operator is required to pay attention to a quality work (high rhythm), but also to avoid some work accidents, some possibly quite serious. The jobs on the agricultural machines considered in this paper reach or exceed in complexity the works mentioned in Table 15 from the Article 598 [14], where the allowed noise level is 75 dB. As a result, even working with a relatively new generation tractor (New Holland TD80D), the noise level is at the permissible limit to facilitate work with increased neuro-psychic and psycho-sensory demands. The time limitation of the working time for human staff working under the conditions specified above occurs only if the noise level intensity pass from 80 to 90 dB [15, 16].

3 Conclusions

From the scientific point of view, the presented results show that the methodology followed is an efficient one: the measurement and the interpolation of the experimental results by classical and nonstandard distance functions. The accuracy of calculation of theoretical models is appropriate and increases with the distance from the source.

It is useful to consider the dependence of the logarithmic term in the expression of the noise intensity level, by the more complicated terms than the distance, because the reformulation of the logarithm function argument regulates its dimensional condition and, furthermore, it can also highlight other parameters of the model. We believe that this methodology can also contribute to efforts to eliminate singularities in the acoustic wave propagation equations. However, it is proven that experimental and theoretical-empirical research can achieve the satisfactory precision required in practical applications, even considering slightly different terms in the propagation equations, in relation to the theoretical solution.

The immediate application of experimental and theoretical research described in the article is to increase the level of noise protection for human staff working on the agricultural machines trailed by tractors. Even in the specific case of the tractor under consideration, the noise field has values that fall within the hours of exposure for 8–10 h of daily work, however, it is estimated that in a dynamic regime, the noise can increase by 2–5 dB, thus, that its estimation enters somewhere in the questionable area, which imposes the limitation of working time. The discussion is more complicated if account is taken of the frequencies of noise propagation, but especially if there are other sources of pollution: traction engine emissions, vibrations, difficult jobs. These are arguments for a comprehensive multidisciplinary study. In addition, as shown in [4], for example, tractors of older or used generations can produce more intense noise levels.

Acknowledgements This work was supported by a grant of the Romanian Research and Innovation Ministry, through Programme 1—Development of the national research-development system, subprogram 1.2—Institutional performance—Projects for financing excellence in RDI, contract No. 16PFE.

References

1. P. Cardei, M. Ludig, M. Matache, R. Sfiru, Mathematical modeling and use in acoustics applications in agriculture. *Sci. J. Agric. Eng.* **2**, 81–89 (2014)
2. P. Cardei, Some proposal for the improvement of the simulations of the acoustic noise propagation. *Int. J. Math. Models Methods Appl. Sci.* 285–293 (2008)
3. E. Sorica, V. Vladut, P. Cardei, C. Sorica, C. Bracacescu, Comparative analysis of the noise and vibration transmitted to the operator by a brush cutter, in *Acoustics and Vibration of Mechanical Structures—AVMS-2017*, (Springer, Cham 2018), pp. 165–172

4. P. Cardei, A. Atanasov, V. Muraru, Acoustic comparative analysis for tractors. https://www.researchgate.net/publication/332415044_Acoustic_comparative_analysis_for_tractors. 16 Apr 2019
5. E. Postelnicu, V. Vladut, C. Sorica, P. Cardei, I. Grigore, Analysis of the sound power level emitted by portable electric generators (outdoor powered equipment) depending on location and measuring surface. *Appl. Mech. Mater.* **430**, 266–275 (2013)
6. I. Pirna, Provocari si solutii tehnice pentru dezvoltarea mecanizarii si automatizarii in agricultura. *Market Watch*, nr. **173** (2015)
7. G. Voicu, I.C. Poenaru, G. Paraschiv, M.N. Dinca, V. Vladut, Theoretical modelling of working process of covering devices to miscanthus rhizomes planters, in *Symposium "Actual Tasks on Agriculture Engineering"*, Opatija (2014)
8. Simpalexim, Utilaje Agricole, <https://www.utilajeagricole-buchin.ro/utilaje-agricole-echipamente-agricole/>. Last accessed 16 Apr 2019
9. Avenue, <https://www.utilajemasiniagricole.ro/>. Last accessed 16 Apr 2019
10. Ferrari, <https://ferrariostruzioni.com/en/film-planters/25-fpa-evolution-transplanter.html>. Last accessed 16 Apr 2019
11. Canarina, Environmental Software. <http://www.canarina.com/acousticcontrol.htm>. Last accessed 13 Apr 2019
12. P. Cardei, The dimensional analysis of the U Sle—musle soil erosion model. *Proc. Roum. Acad. Serie B* **3**, 249–253 (2010)
13. P. Cardei, I. Gageanu, A critical analysis of empirical formulas describing the phenomenon of compaction of the powders. *J. Modern. Technol. Eng.* **2**(1), 1–20 (2017)
14. M. Ministerul Muncii si Solidaritatii Sociale, Norma de protectie a muncii din 20.11.2002, Bucuresti: Monitorul Oficial al Romaniei, <https://www.iprotectiamuncii.ro/norme/norme-generale-protectia-muncii.pdf>. Last accessed 2019/04/13
15. A.P.G. Peterson, *Handbook of Noise Measurement* (Gen Rad Inc., Concord, Massachuttes, 1980)
16. A.S. Pasca, M. Arghir, Psychoacoustic effects of structural noise issued for machine-tools, in *XI-a Conferinta Nationala multidisciplinara "Profesorul Dorin Pavel—fondatorul energeticii romanesti"*, Sebes (2011)

An Analysis of How Physical and Social Factors Influence the Efficiency of Crew Members of a Ship Running on the Danube



Laurentiu Picu, Eugen Rusu, and Mihaela Picu

Abstract This paper analyzes how physical factors (vibrations, noise and meteorological parameters), social factors (work and living in enclosed spaces, resting area, sleep time, staff cut downs) and factors related to each individual (physical characteristics, age, experience, alcohol consumption, smoking, stress resistance) induce fatigue and degradation of mental effort, leading to a general decrease in human performance. The paper is divided into two parts: (a) measuring physical parameters and (b) assessment of performance decline. In order to achieve this objective, it was analyzed the reaction of a ship's 6 people crew members under different stressors. The ship traveled on the Tulcea—Calarasi route, in January 2017. The vibrations transmitted to the subjects in the control room exceeded, on average, by 28.95% for exposure action value EAV, to 180.32% for exposure limit value ELV, indicated in ISO 2631:2018 and Directive 2002/44/EC. Also, the noise levels were 41.25% (lower exposure) higher than what is indicated in Directive 2003/10/EC. To determine the effectiveness of crew members exposed to vibration and noise, they were asked to resolve the Purdue Pegboard test. There was a decrease in performance while increasing fatigue. Under heavy winter conditions, work on a ship running on the Danube is very harsh. In addition to physical measurable values, fatigue occurs which leads to a decrease in seafarer efficiency.

L. Picu (✉) · E. Rusu · M. Picu
Dunarea de Jos, Galati University, Galati, Romania
e-mail: constantin.picu@ugal.ro

E. Rusu
e-mail: eugen.rusu@ugal.ro

M. Picu
e-mail: Mihaela.Picu@ugal.ro

1 Introduction

There is a continuing concern that onboard ships and crew work and live in the best conditions in order to have good professional results. Unfortunately, these studies refer only to seagoing vessels and not to river ones [1, 2]. There are also a number of regulations regarding habilitation conditions onboard of seagoing vessels; as far as river vessels are concerned, these rules are fewer and less restrictive.

Apart from the complexity of imposed rules, apart from the new ship technology (or rather because of their age), the human factor is a very important part in navigation. Under the current conditions, when technology tends to take most of the ship's activity, the number of crew members decreases; also, on the river ships, the crew is aging. The interaction between man and technology depends on many factors: experience, age, health condition, fatigue, etc.; it also depends on the workspace, vibrations, noise, temperature, resting time and sleeping schedule, and other stressors.

Another very important factor is that all operations are performed on a platform in motion; this continuous movement can cause adverse effects. For all these reasons, it is necessary to pay more attention to the human factor in order to ensure the health, safety and work efficiency. In critical situations, when all crew members are required to be present at their posts, emerges the great problem of seafarer personnel reduction. Also, working on a moving platform, exposure to vibrations and under very high noise conditions reduces the people's movement ability (both gross and fine movements). These physical limitations cause the interruption of any task when local movements cause slipping or loss of balance and are called motion-induced interruptions [3].

In 2000, ISO 6954, a standard which refers to habitability on ships, has been issued. In 2002, the European Commission issued Directive 2002/44/EC, on the minimum health and safety requirements regarding the exposure of workers to the risks arising from physical agents (vibration) [4].

Since these two regulations were not in agreement to properly assess the habitability conditions, ISO has replaced the standard with ISO 20283-5:2016—Mechanical vibration—Measurement of vibration on ships—Part 5: Guidelines for measurement, evaluation and reporting of vibration with regard to habitability on passenger and merchant ships [5].

Also, different classification societies have found it necessary to reduce vibration and noise on ships: DNV GL, LR, ABS [6–8].

In recent years, due to growth freedom of movement and globalization, transport activities have radically increased.

Thus, pollution has increased (especially noise pollution), even around cities. For this reason, new regulations are needed to ensure noise reduction, not only for the comfort and performance of crew members.

In order to achieve this, but also because of the high costs, the stationing time for loading/unloading of a ship was reduced to the minimum [9].

Lately, there is a trend to reduce the number of crew members on ships. At the same time, the operational requirements are increasing. These produce stress and

fatigue, which along with environmental factors affect the comfort and performance of the crew. Among the environmental factors that act on sailors, vessel motions and noise are the most important [10]. Large waves can prevent sailors from maintaining their balance and carrying out their tasks [11]. Dobie also said that “a mix of people and technology interact you will find human factors; a branch of engineering in which the primary emphasis is on the human input” [11].

An important factor that greatly influences the habilitation and performance of crews and passengers (in the case of cruise ships) is the temperature. A special situation is the work in the engine room. There were studied the temperature and the awkward working postures [12]. Another factor, in the comfort and performance of a crew, is the number of days spent on the ship [13].

Vibrations act on humans in many ways. They are transmitted to the entire body: through whole-body surface simultaneously when laying a bed, through the feet when standing and buttocks when seated (WBV), through hands when in contact with vibrating equipment (HAV) and indirectly when objects in the field of vision move, causing blurring of vision and difficulties of interpretation data [11]. Whole-body vibration from 2 to 12 Hz can have affected human performance [14]. Low frequencies can lead to fatigue, decreased performance, accidents or health hazards.

The limits of vibrations set out in the regulations are not intended to respect single spectrum components, but refer to its global characteristic value.

This value is obtained by weighing the sum of the components of one-third octave with a suitable curve (named as “combined frequency weighting curve”), as defined in ISO 2631-2 Rule [15], in the range 1–80 Hz, called “overall frequency-weighted r.m.s. value.” For this parameter, marked with A_w , and measured in m/s^2 , we have the following relation:

$$A_w = \left[\sum_{j=1}^n (W_j \cdot a_j)^2 \right]^{1/2}$$

where a_j is the acceleration measured in the one-third octave band in m/s^2 , and W_j is the weighting factor for the one-third octave band [16].

The purpose of this paper is to make an analysis of vibration (WBV and HAV) and the noise transmitted to seafaring personnel on a river vessel running on the Romanian Danube sector. Experimental determinations were performed in the control room and in the engine room.

2 Materials and Methods

The analysis was made on a 1000 HP pushboat, for 6 days in January 2017:

- (a) The vibrations transmitted to the subjects were measured with Maestro 01 dB; the noise was measured with the BlueSolo sonometer, and the meteorological

parameters were measured with the Kestrel 5000 Portable Weather Station. All parameters were measured in the control room and in the engine room.

- (b) To assess the decrease in subjects' efficiency, they were asked to perform the Purdue Pegboard specific test. The results of the test were related to the vibration and noise level at the site of the last activities.
- (c) The external temperature was between -17 and -18 °C during the night and -2 – -3 °C during the day. The Danube was partially frozen ≈ 70 – 75% , and the wind was very strong and gusty (9 on the Beaufort scale). It was extremely difficult to travel: The average speed was 2–3 km/h; the work shifts were 4 h. The crew consisted of six people: one captain, one coxswain, one mechanic, three sailors.

Measurements were made simultaneously in the control room and inside the engine room, in four situations: ship starts from the shore, ship's running, in mooring maneuver and idle with the generator.

According to ISO 20283-5:2016, ISO 8041-1:2017 [17], ISO 2631-2:2018 and to the Guide to crew habitability on ships: 2016, only WBV acceleration values are considered. In this paper, we will consider, in addition to whole-body vibration (WBV), the hand-arm vibrations (HAV) and the noise, as these factors also contribute to decreasing the performance of people's work.

2.1 Measurement of Whole-Body Vibration (WBV)

Whole-body accelerations were measured according to ISO 2631-1 [18] and were calculated: partial vibration dose value (VDV), partial (daily) exposure A(8), time to reach exposure action value EAV (VDV option) $9.1 \text{ m/s}^{1.75}$, time to reach EAV (A(8) option) 0.5 m/s^2 , time to reach exposure limit value ELV (A(8) option only) 1.15 m/s^2 , total daily exposure A(8), and total VDV. The calculations were made with Vibration Calculator—HSE. Measurements were made with vibrometer Maestro from 01 dB-Stell with SEAT pad underfoot (Fig. 1).

2.2 Measurement of Hand-arm Vibration (HAV)

Hand-arm accelerations were made with vibrometer Maestro and finger support for triaxial accelerometers (Fig. 2). The accelerometers were 356A16-PCB Piezotronics, from 01 dB-Stell. With Vibration Calculator—HSE were calculated: exposure points per hour, time to reach exposure action value T_{EAV} (A(8) option) 2.5 m/s^2 , time to reach exposure limit value T_{ELV} (A(8) option only) 5 m/s^2 , partial exposure A(8), partial exposure points, daily exposure and total exposure points (<http://www.hse.gov.uk/vibration/hav/readyreckoner.htm>).



Fig. 1 SEAT pad underfoot



Fig. 2 The triaxial accelerometer in finger support

2.3 Measurement of Noise Level

The sound level was measured with the BlueSolo sonometer (Fig. 3) according to Directive 2003/10/EC, on the minimum health and safety requirements regarding the exposure of workers to the risks arising from physical agents (noise) [19], and

Fig. 3 Measurement of noise with BlueSolo sonometer



using Noise Exposure Calculator—HSE was calculated daily noise exposure (LEP,d), exposure points (job/task) and exposure points per hour.

Using the dBFA 3.2 software, the results of the measurements were processed, and the results of the measurements were presented suggestively in the form of sonograms, spectral distributions and time-history graphics to obtain comparative information.

A sonogram describes the noise characteristics at the location where the determination was made and shows the sound level distribution on frequency, at a given point in time. This helps find the frequencies that contribute most to the high noise level.

2.4 Characteristics of the Subjects

From Table 1, it is seen that the crew is aging, subject no. 1 is obese, subjects 2, 3 and 4 are overweight and subjects 5 and 6 have a normal weight. Of all, only one person does not smoke, and half of them drink more than two glasses of wine/day. Also, half of them said they have cardiovascular problems and they all have personal problems.

Table 1 Subject's features

Subject	BMI ^a	Age (years)	Smoker	Drinker ^b	Seniority (years)	Cardiovascular problems	Personal problems
1	30.2	49	Yes	–	25	–	x
2	26.4	52	Yes	–	29	x	x
3	25.8	47	Yes	–	22	–	x
4	32.4	57	–	Yes	34	–	x
5	24.8	51	Yes	Yes	33	x	x
6	24.5	50	Yes	Yes	31	x	x

^aOverweight = 25–29.9; Obesity = 30 or greater

^bMore than two glasses of wine/day (when not on the ship)

These subjects work in difficult conditions: multiple tasks due to numerical reduced crew, limited space for rest and recreation, a work schedule which is not respected, not enough sleep (frequently interrupted), etc., factors that lead to lower performance that they would have had under normal working conditions (8 h schedule).

2.5 Method for Determining a Efficiency of Crew Members of a Ship Running on the Danube

The subjects solved the Purdue Pegboard test, under the same types of vibration and noise exposure. The Purdue Pegboard test uses a board with two parallel rows, each with 25 holes into which the examinee places cylindrical metal nails. There is a short briefing at the beginning of the test. The subsets for preferred, non-preferred and both hands require the subject to place the pins in the holes as quickly as possible, and the score is the number of pins placed in 30 s. The test was repeated three times in three different days: day 1, day 4 and day 6 [20].

3 Results and Discussions

For all cases were calculated the averages of the values obtained from at least five measurements.

Table 2 Requirements of ISO 2631:2018

Exposure action value (EAV)	Exposure limit value (ELV)
0.5 m/s ² A(8) r.m.s.	1.15 m/s ² A(8) r.m.s.
9.1 m/s ^{1.75} VDV	21 m/s ^{1.75} VDV

3.1 Measurement of Whole-Body Vibration (WBV)

Assuming that we only refer to the HAB criteria (not HAB+ and HAB++), the maximum RMS level must be below 0.214 m/s² (Guide for crew habitability on ships: 2016). The whole analysis of vibrations transmitted to the human body was made in relation to the requirements of ISO 2631:2018 which state that (Table 2).

From the measurements and calculations made for WBV, HAV and noise level in the four cases (starts from the shore, ship's running, mooring maneuver, idle with generator), the following values were obtained (Tables 3, 4, 5, 6, 7 and 8):

In the case of whole-body vibration, analyzing time to reach EAV (A(8) option) for all situations, it is found that they have equally sensitive values in the control room and inside the engine room, for all the four cases of motion of the ship (Tables 3 and 4). On the other hand, for the time to reach ELV (A(8) option), there are significant differences between the values calculated for the control room and the engine room: If the ship starts from the shore, the T_{ELV} for the engine room is 2.9% higher than T_{ELV} for the control room. When the ship is running T_{ELV} is 44.4% higher than T_{ELV} for the control room, during the mooring maneuver is 36% higher and while idling with the generator is 18.4% higher (Fig. 4). These values show that work on the engine room is more harmful in terms of vibrations than the inside control room.

3.2 Measurement of Hand-arm Vibration (HAV)

Vibrations transmitted to the arm system were measured in the same four cases: ship starts from the shore, ship is running, mooring maneuver and idle with generator turned on, in the control room and engine room (Tables 5 and 6).

In the case of hand-arm vibrations (Fig. 5), analyzing the time to reach EAV (A(8) option) for all situations, they are almost double inside the engine room relative to the control room (except idle with generator). On the other hand, for time to reach ELV (A(8) option), the values are equal to or greater than 24 h (except for the mooring maneuver where it is 17 h). These values show that work inside the engine room is more dangerous in terms of vibrations than on the control room. Besides, in the case of engine room, the computer has given then warning on exceeding of the limit values.

Table 3 Measurement of whole-body vibration in the control room


		Vibration magnitude r.m.s.		Exposure duration		Partial VDV	Partial exposure A(8)	Time to reach EAV VDV option 9.1 m/s ^{1.75}		Time to reach EAV A(8) option 0.5 m/s ²		Time to reach ELV A(8) option 1.15 m/s ²		
		(m/s ²)	(h)	(min)	(h)			(h)	(min)	(h)	(min)	(h)	(min)	
Control room														
Starts from the shore		3.025	0	30	0	27.6	0.76	0	10	0	13	1	9	
Ship is running		3.417	17	0	0	75.2	4.98	0	0	0	10	0	54	
Mooring maneuver		3.568	0	30	0	32.5	0.89	0	0	0	9	0	50	
Idle with generator		2.885	6	0	0	49.0	2.50	0	0	0	14	1	16	
Results		Total exposure A(8) = 79.277009 m/s ²											Total VDV = 5.693967 m/s ^{1.75}	

Table 4 Measurement of whole-body vibration in the engine room


	 Engine room	Vibration magnitude r.m.s. (m/s ²)	Exposure duration		Partial VDV (m/s ^{1.75})	Partial exposure A(8) (m/s ²)	Time to reach VDV option 9.1 m/s ^{1.75}		Time to reach EAV A(8) option 0.5 m/s ²		Time to reach ELV A(8) option 1.15 m/s ²		
			(h)	(min)			(h)	(min)	(h)	(min)	(h)	(min)	
Starts from the shore		2.996	0	30	27.3	0.75	0	10	0	13	1	11	
Ship is Running		2.857	17	0	62.9	4.16	0	0	0	15	1	18	
Mooring maneuver		3.054	0	30	27.8	0.76	0	0	0	13	1	8	
Idle with generator		2.663	6	0	45.2	2.31	0	1	0	17	1	30	
Results	Total exposure A(8) = 67.69 296 m/s ²											Total VDV = 4.879325 m/s ^{1.75}	

Table 5 Measurement of hand-arm vibration in the control room



	Control room	Vibration magnitude r.m.s.	Exposure points per hour	Time to reach EAV A(8) option 2.5 m/s ²		Time to reach ELV A(8) option only 5 m/s ²		Exposure duration		Partial exposure m/s ² -A(8)	Partial exposure points
				(h)	(min)	(h)	(min)	(h)	(min)		
	Starts from the shore	3.145	20	5	3	20	13	0	30	0.8	10
	Ship is running	2.887	17	5	60	23	60	17	0	2.9	133
	Mooring maneuver	3.419	23	4	17	17	7	0	30	0.9	12
	Idle with generator	1.556	5	20	39	>24	0	6	0	0.8	10
Results	Daily exposure A(8) = 3.2 m/s ²										
Total exposure points = 165											
Warning: Exposure at or above 2.5 m/s ² -A(8) EAV (100 points)											

Table 6 Measurement of hand-arm vibration in the engine room

	Vibration magnitude r.m.s.		Exposure points per hour	Time to reach EAV A(8) option 2.5 m/s ²		Time to reach ELV A(8) option only 5 m/s ²		Exposure duration		Partial exposure m/s ² -A(8)	Partial exposure points	
	(h)	(min)		(h)	(min)	(h)	(min)	(h)	(min)			
Engine room												
Starts from the shore	2.141		9	10	54	>24	-	0	30	0.5	5	
Ship is running	2.106		9	11	16	>24	-	17	0	2.1	71	
Mooring maneuver	2.413		12	8	35	>24	-	0	30	0.6	6	
Idle with generator	1.558		5	20	36	>24	-	6	0	0.8	10	
Results	Daily exposure A(8) = 2.4 m/s ²			Total exposure points = 92								

Warning: Exposure at or above 2.5 m/s²-A(8) EAV (100 points)

Table 7 Measurement noise level in control room



	Control room	Noise level (L_{Aeq} dB)	Exposure duration (h)	Exposure points (job/task)	Exposure points per hour
	Starts from the shore	95	0.5	63	125
	Ship is running	90	17	672	40
	Mooring maneuver	99	0.5	157	314
	Idle with generator	87	6	119	20
	Total		24 h	1011 points	499 points
	Daily noise exposure ($L_{EP,d}$)		95 dB		

Table 8 Measurement noise level inside the engine room

	Engine room	Noise Level (L_{Aeq} dB)	Exposure duration (h)	Exposure points (job/task)	Exposure points per hour
	Starts from the shore	110	0.5	1976	3953
	Ship is running	108	17	42,399	2494
	Mooring maneuver	109	0.5	1570	3140
	Idle with generator	107	6	11,887	1981
	Total		24 h	57,832 points	11,568 points
	Daily noise exposure ($L_{EP,d}$)		113 dB		

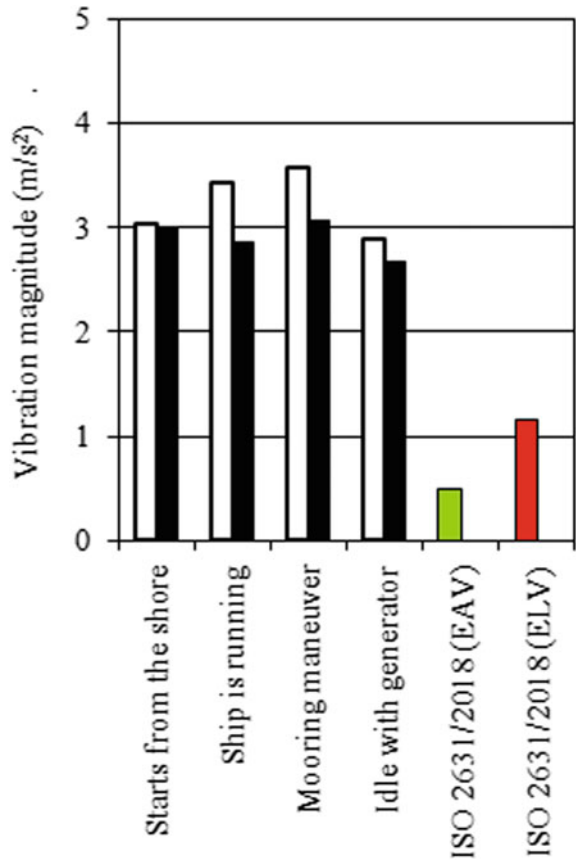
3.3 Measurement of Noise

Simultaneously with vibration measurement, noise measurements were made with the BlueSolo sonometer. The noise analysis was carried out in relation to the requirements of Directive 2003/10/EC, which state that: (a) exposure limit values: $L_{EX,8h} = 87$ dB(A); (b) upper exposure action values: $L_{EX,8h} = 85$ dB(A); (c) lower exposure action values: $L_{EX,8h} = 80$ dB(A).

Figure 6 shows an example of noise measured in the engines room. In the sonogram (top right), the cursors are placed at 280.616 Hz and at 4 min 49 s (96.76 dB (A)). For the moment of 4 min 49 s, the spectrum (top left) shows a maximum of 96.76 dB (A) at 315 Hz. The L_{eq} sound level has a maximum of 98.96 dB (A) at 6 min 57 s in the time history (lower right) for 280.616 Hz.

The lower exposure action value (an $L_{EP,d}$ of 80 dB) is represented by 32 exposure points, the upper exposure action value ($L_{EP,d}$ of 85 dB) by 100 points. In all cases, the noise levels exceed the values indicated by the Directive 2003/10/EC by 18.75% and 11.76% (95 dB vs. 80 dB and 85 dB) for the control room (Table 7). For the

Fig. 4 Comparison between WBV (□)—in control room; (■)—in engine room



engine room, the value of 113 dB (from Table 8) is higher with 41.25% and 32.94% than the provisions of the Directive.

In Fig. 7 and Table 9, it can be seen that there is not a great difference between the sound levels in the control room and those inside the engine room; but these values surpass not only the lower exposure action value but also the upper exposure action value.

Table 9 is presented the analysis of the sound level average for each day of the journey in both cases. The overall average does not differ much (99.5 dB in the control room compared to 107.66 dB in the engine room), but its distribution is interesting (Fig. 8): If for engine room there is some uniformity around 107 dB, for control room, this distribution has a more sinusoidal shape, depending on how hard the engine was forced, which in turn depends on the specific weather conditions of each day.

Fig. 5 Comparison between HAV (□)—in control room; (■)—in engine room

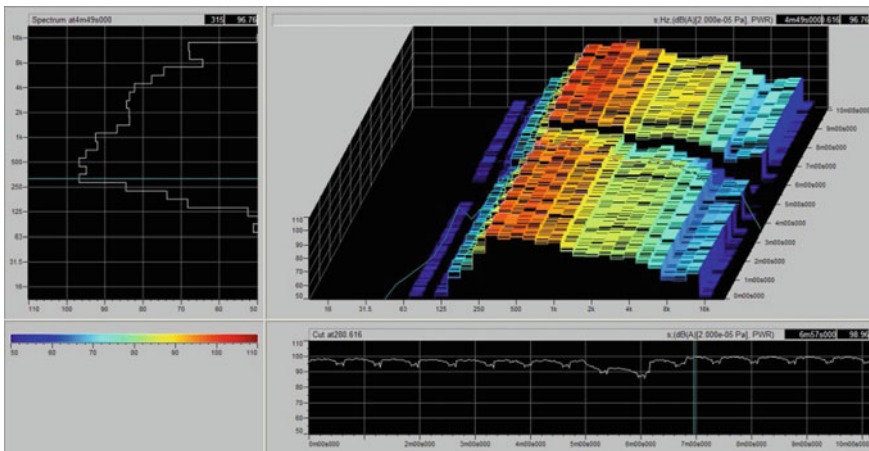
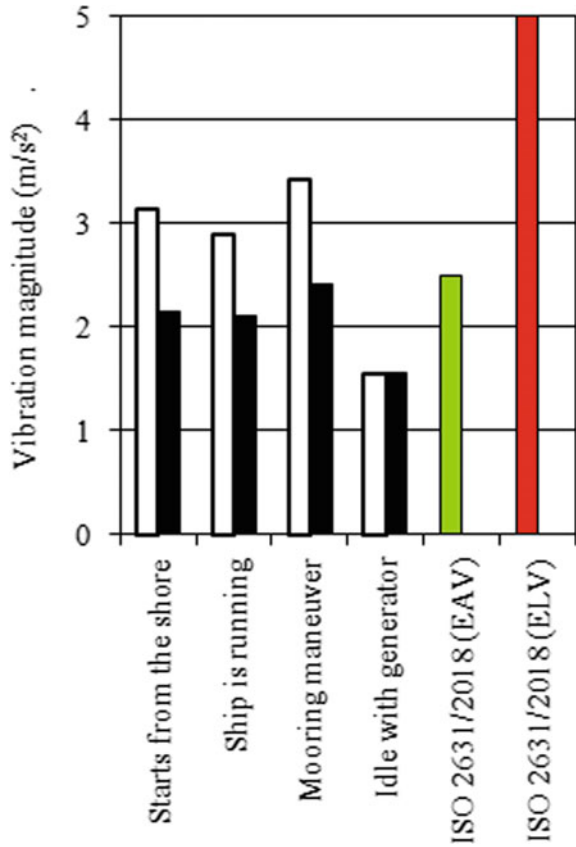


Fig. 6 Sonogram of the noise measured in the engines room

Fig. 7 Comparison between noise levels (□)—in control room; (■)—in engine room

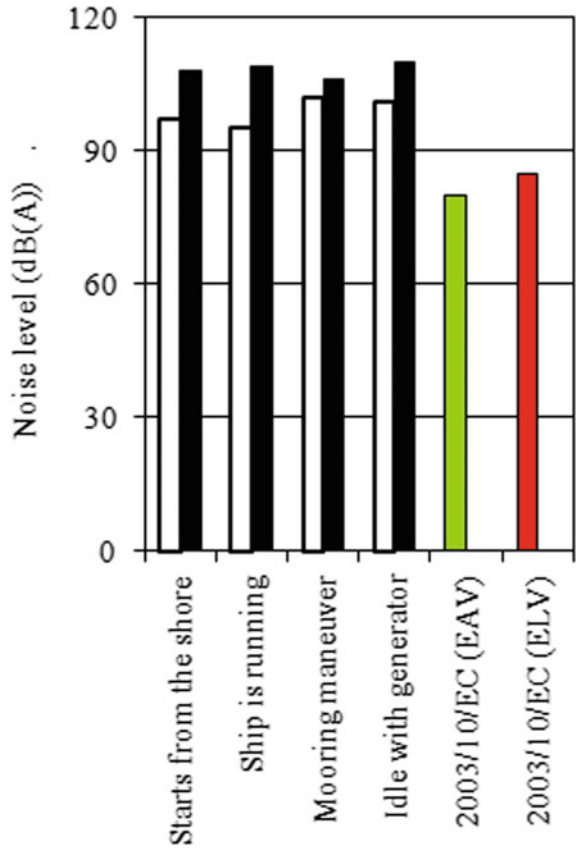


Table 9 Weekly noise exposure calculator


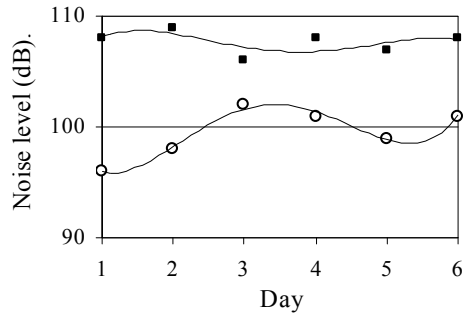
	Daily exposure ($L_{EP,d}$ dB)	
	Control room	Engine room
Day 1	96	108
Day 2	98	109
Day 3	102	106
Day 4	101	108
Day 5	99	107
Day 6	101	108
$L_{EP,w}$	99.5 dB	107.66 dB

Fig. 8 Daily sound level distribution (o)—control room; (■)—engine room



3.4 Measurement of Crew Members Efficiency

Each subject was asked to complete the Purdue Pegboard test. They were explained what to do, and they were told they could leave the test anytime they wanted. Using this test, under the same types of vibration and noise exposure, the following results were obtained (Fig. 9):

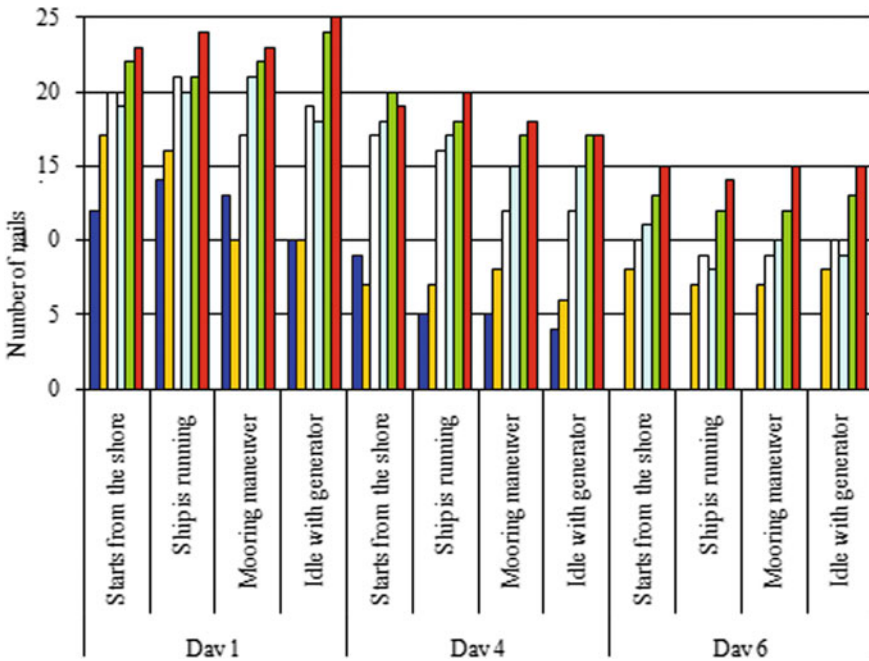


Fig. 9 Number of correct placed nails: (■)—Subject 1; (■)—Subject 2; (□)—Subject 3; (■)—Subject 4; (■)—Subject 5; (■)—Subject 6

From Fig. 9, the dependence of the number of nails correct placed inside the holes decreases over time, with the fatigue onset.

The best results obtained by Subject 6, with 76% correctly placed pins, followed by Subject 5 with 70.33%. Subjects 3 and 4 had close outcomes: 57.3% and 60.3%, respectively. Subject 2 had only 37%, and Subject 1 refused to participate in the experiment on the last day. All tests were carried out at the workplace of each subject.

It results that the performance of the subjects decreases, as the days pass and fatigue accumulates; so if on the first day more than 20 correct placed nails were obtained, on the last day, their number was less than 15. Also, worse results were obtained by the subjects who are overweight or obese (who get tired faster) as well as by those who have a lower seniority in work, so they are less accustomed to stress. Also, the age of the subjects has a great influence on efficiency; the crew is aging, and half of the subjects said they have health problems. Smoking is a very important factor when it comes to dexterity, consequently on the ability to solve a test that highlights the subject's handiness. If all these add to the totally unfavorable weather conditions, there is an accumulation of risk factors that lead to modest results in terms of subjects' efficiency.

4 Conclusions

From the measurements made for WBV, it was surprising that T_{EAV} and T_{ELV} for control room were higher than T_{EAV} , or T_{ELV} , for the engine room. Similar results were obtained with HAV measurements.

This may be explained by the fact that the ship is quite old and that the vibrations are more pronounced at the higher structures.

Also, the situation is serious in the case of daily noise exposure ($L_{EP,d}$) whose average is 99.5 dB inside the control room and 107.6 dB for the engine room, so it is exceeded by 17/26.6% compared to the Directive 2003/10/EC requirements.

As far as the effectiveness of crew members is concerned, it is reflected in the old age of the subjects and the fact that among them are smokers and drinkers. Some of these subjects have also several cardiovascular problems. It is also found that the effectiveness of crew members decreases toward the end of the voyage because, in addition to the fatigue accumulated during the journey, the other stressors: noise and vibrations interfere. It is clear that engine room workers have lower performances than those who worked in the control room.

All problems of the subjects (age and personal problems) are contributing to the poor health caused by vibrations and noises; if to this are added irregular work schedule, living on a boat for 2–3 weeks, extreme weather work, etc., it can be said that it is necessary to create better working conditions for the crew: newer ships, shorter work shifts by increasing staff numbers, etc.

Obviously, this study on an only six people crew and a single ship cannot be so conclusive, but it is a starting point for future research.

Acknowledgements This work was carried out in the framework of the research project REMARC (Renewable Energy extraction in MARine environment and its Coastal impact), supported by the Romanian Executive Agency for Higher Education, Research, Development and Innovation Funding—UEFISCDI, grant number PN-III-P4-IDPCE-2016-0017.

References

1. L. Picu, M. Picu, E.V.C. Rusu, Evaluation of human exposure to whole-body vibration - verification method of Stevens's power law, in *Proceedings 18th International Multidisciplinary Scientific GeoConference, SGEM 2018*, vol. 18, no. (5.2). (Albena, Bulgaria (2018), pp. 413–420
2. L. Picu, E.V.C. Rusu, Multiple physical stress exposures of sailors on several ships—a longitudinal study. *Annals of Dunarea de Jos University, Fascicle II—Mathematics, Physics, Theoretical Mechanics, Year X(XLI), No. 1, (2018), pp. 84–93*
3. A.E. Baitis, F.D. Holcombe, S.L., Conwell, P. Crossland, J. Colwell, J.H. Pattison, 1991–1992 Motion induced interruptions (MII) and motion induced fatigue (MIF) experiments at the Naval Biodynamics Laboratory. Technical Report CRDKNSWC-HD1423011. (Bethesda, MD: Naval Surface Warfare Center, Carderock Division 1995)
4. European Parliament and the Council, Directive 2002/44/EC, on the minimum health and safety requirements regarding the exposure of workers to the risks arising from physical agents (vibration) (2002)
5. ISO 20283-5:2016, Mechanical vibration—measurement of vibration on ships—Part 5: guidelines for measurement, evaluation and reporting of vibration with regard to habitability on passenger and merchant ships, International Standard Organization (2016)
6. DNV-GL, Criteria for handling of excessive noise and vibration levels, DNVGL-CG-0493 (2016)
7. Lloyd's Register, Ship Vibration and Noise, Guidance notes (2006)
8. ABS, Guide for Crew Habitability on Ships (2016)
9. M. Oldenburg, H. Jensen, Merchant seafaring: a changing and hazardous occupation. *Occup. Environ. Med.* **69**(9), 685–688 (2012)
10. R.E. Kurt, H. Khalid, O. Turan, M. Houben, J. Bos, I.H. Helvacioğlu, Towards human-oriented norms: considering the effects of noise exposure on board ships. *Ocean Eng.* **120**, 101–107 (2016)
11. T.G. Dobie, Critical significance of human factors in ship design. Presented to 2003 RVOC Meeting, Large Lakes Observatory, University of Minnesota (2003)
12. M. Lundh, M. Lützhöft, L. Rydstedt, J. Dahlman, Working conditions in the engine department—A qualitative study among engine room personnel on board Swedish merchant ships. *Appl. Ergon.* **42**(2), 384–390 (2011)
13. D.K. Brown, The value of reducing ship motions. *Naval Eng. J.* **97**(3), 41–46 (1985)
14. H.E. von Gierke, K. McCloskey, W.B. Albery, Military performance in sustained acceleration and vibration environments, in *Handbook of Military Psychology*, ed. by R. Gal, A.D. Mangelsdorff (Wiley, New York, 1991), pp. 352–364
15. ISO 2631-2:2003, Mechanical vibration and shock—evaluation of human exposure to whole-body vibration—Part 2: vibration in buildings (1–80 Hz) (2003)
16. M. Biot, F. De Lorenzo, Noise and vibrations on board cruise ships: are new standards effective? in *2nd International Conference on Marine Research and Transportation, ICMRT '07*, Ischia (Naples), Italy (2007)
17. ISO 8041-1:2017, Human response to vibration—measuring instrumentation—Part 1: General purpose vibration meters (2017)

18. ISO 2631-1:1997, Mechanical vibration and shock—evaluation of human exposure to whole-body vibration—Part 1: General requirements (1997)
19. European Parliament and of the Council, Directive 2003/10/EC, on the minimum health and safety requirements regarding the exposure of workers to the risks arising from physical agents (noise) (2003)
20. M. Picu, Multi-stress and human performance: a refutation of inverted-u hypothesis. *J. Multi. Eng. Sci. Technol.* **2**(9), 2542–2552 (2015)

Mitigating Noise Pollution Level When Loading Useful Mineral Substances in CFR Wagons in Order to Increase Acoustic Comfort in Neighbouring Areas



Sorin Simion, Daniel Pupăzan, Angelica Călămar, Cristian Nicolescu, and Izabella Kovacs

Abstract Directive 2002/49/EC on ambient air noise assessment and management represents an indication of constant concerns regarding reducing noise related discomfort, which generates numerous physiological, psychological and social implications. Environmental noise, which is one of the most important discomfort factors for residents in areas adjacent to industrial premises, spreads both in urban areas and in rural areas. It is omnipresent, cannot be avoided, and much of the population is influenced by its presence. In this respect, the paper presents a case study, of industrial activity generating high levels of noise, affecting neighbourhoods, noise pollution being above limits allowed by national/international legislation. The current paper analyses the manner in which noise generated by technological process of loading useful mineral substances in vehicular and CFR transport influences areas adjacent to the industrial site, establishing necessary measures to reduce effects of noise on neighbourhoods. In order to quantify noise pollution level generated by human activity, it was necessary to establish noise levels in several representative points so that, after analysing the results, we could establish the area with the highest noise level to suggest optimal noise pollution reduction measures.

1 Introduction

Because of its specificity, loading and transporting useful mineral substances (UMS) in auto and CFR means of transport are a noise-generating activity.

The main activities performed during loading/transporting/unloading USM are

- USM transport on conveyor belts;
- Loading of silos with USM (concrete platforms for loading in auto means of transport);

S. Simion (✉) · D. Pupăzan · A. Călămar · C. Nicolescu · I. Kovacs
INCD INSEMEX Petroșani, Petroșani, Romania
e-mail: sorin.simion@insemex.ro

© Springer Nature Switzerland AG 2021

N. Herisanu and V. Marinca (eds.), *Acoustics and Vibration of Mechanical Structures—AVMS 2019*, Springer Proceedings in Physics 251,
https://doi.org/10.1007/978-3-030-54136-1_19

205

- Loading of convoy wagons by free fall from silos in CFR wagons;
- Frontal loading USM in auto trucks.

Because of increased production capacity, supplementation of transport capacity of industrial railway with auto transportation was necessary, leading to an increase in noise level generated in the environment affecting neighbourhoods. Part of the UMSs from quarries is stored in siloes according to their grading, and other part is stored in piles on the ground for auto transport by dumpers. This loading/unloading activity generates an intense noise level that can affect both workers and neighbourhoods (households) [1].

In order to quantify effects and reduce the level of noise pollution, noise audit is performed, which involves the following steps:

- Measurement of noise level produced by the economic activity at points of interest by sonometric measurements performed according to applicable standards;
- Identifying major noise sources and the contribution each has to noise levels;
- Evaluating the level of noise from analysed activity by comparison with maximum admissible values according to applicable national legislation and in force standards;
- Suggesting works and measures to reduce noise level;
- Evaluating the effectiveness of different suggested or predicted technical variants to reduce noise level for workers at reception points considered sensitive.

In order to identify sites liable to be exposed to noise levels above allowed limits at functional area limit, the SR 10009: 2017 standard limits were used, also performing spectrograms of workplaces where it was considered necessary to apply a complex of measures to reduce noise. The successive implementation of these measures will achieve the ultimate goal of reducing exposure to noise, respectively, that workers are not affected by noise.

2 Working Instruments

For measuring noise levels, Bruel & Kjaer type 2250 Danish construction integrated sonometers equipped with 1 octave and/or 1/3 octave bandwidth filters, Bruel & Kjaer type 4231 calibrators and the BZ 5503 measurement visualization software were used. In order to ensure quality of measurement results, the sonometers and calibrators used have been subjected to metrological verification, following requirements of current legislation [2].

The 2250 type noise analyser (Fig. 1) is used to perform individual measurements or measurement series for laboratory and field analysis.

The acoustic calibrator (Fig. 1) is used to check the sonometers used for measurements, to obtain high accuracy results (checking is performed both before and after a series of measurements).

Fig. 1 Bruel & Kjaer type 2250 analyser and 4231 type acoustic calibrator



The 4231 type acoustic calibrator was used to perform acoustic calibration. It provides a stable sound pressure at 1 kHz and is least influenced by environmental factors.

If the calibration differs by more than $\pm 1, 5$ dB from the initial one, then the sonometer used is checked to see if it is appropriate in terms of standards.

In reporting the measurement results, an estimate of the overall measurement uncertainty was included, taking into account influence of factors such as:

- measuring apparatus;
- microphone location;
- number of measurements;
- variation in time and space of noise source.

3 Case Study

Within research activities carried out by INCD INSEMEX Petroşani, a series of measurements were performed on economic operators active in loading of useful mineral substances (UMS) in means of transport and CFR wagons according to national legislation in force [3].

In order to meet requirements of noise audit, noise level measurements have been performed taking into account location of main noise-generating equipment. Spectral analysis was necessary to obtain data on characteristics of noise generated by the equipment for choosing sound absorbing/soundproofing materials compatible with particularities of analysed noise. Assessment of the efficiency of various technical variants suggested or predicted to reduce noise level for workers at reception points considered sensitive was performed by taking into account noise characteristics (noise level by frequency) [4].

In order to quantify noise level for establishing necessary technical and organizational measures, noise level measurements were performed according to SR 10009: 2017.

Table 1 Measuring point and activity deployed

Measuring point	Activity deployed
1	Loading small limestone in convoy trains (next to car scales)
2	Loading bulky limestone in convoy trains (next to car scales)
3	Auto access gate area
4	Loading silo
5	Loading silo
6	Transporting conveyer belt area
7	Loading trucks with front loader behind the silo
8	Loading trucks with front loader behind the silo

During noise level measurements at the limestone loading point, the activity was carried out normally, i.e. the loading wagons of limestone by free fall from the silo, loading trucks with a front loader (Table 1).

The table below shows the values of noise level for each measurement point (LAeq dB (A)), the Cz curves and noise level analysis for each frequency (12.5 Hz ÷ 16 kHz), measured at loading UMS in auto transportation and CFR wagons.

Spectral analysis for each measurement point is shown below, noise levels dB (A) being noted on the ordinate and frequencies corresponding to each noise level (Hz) on the abscissa (Fig. 2).

According to SR 10009: 2017 on permissible limits of noise level in the environment is max 65 dB (A). Exceedances of noise level with values between 4.4 dB (A) and 27 dB (A) were found. It can be noticed (Table 2) that the noisiest activity is UMS free fall from silo into CFR wagons (Fig. 3).

Noise measurements show that industrial activity of loading mineral useful substances in automotive and CFR means of transportation influences areas adjacent to the industrial enclosure generates a high noise level. This leads to occurrence of a pollution source, an extension of noise discomfort generated by technological process being present, the complexity of effects justifying the name of “ecological discomfort”.

Sound pollution can create discomfort, disturb sleep, affect cognitive functions, cause physiological stress reactions, this type of pollution affecting practically the whole population not exposed to professional noise (children, elders, housewives) [5]. The presence of this extraprofessional noise pollution in the recuperation and rest period of active population, frequently exposed to occupational noise, accentuates the harmful impact of occupational noise by prolonging exposure to this noxae, diminishing normal possibilities for restoring work capacity in the absence of extraprofessional noise pollution. Population is physiologically and psychologically

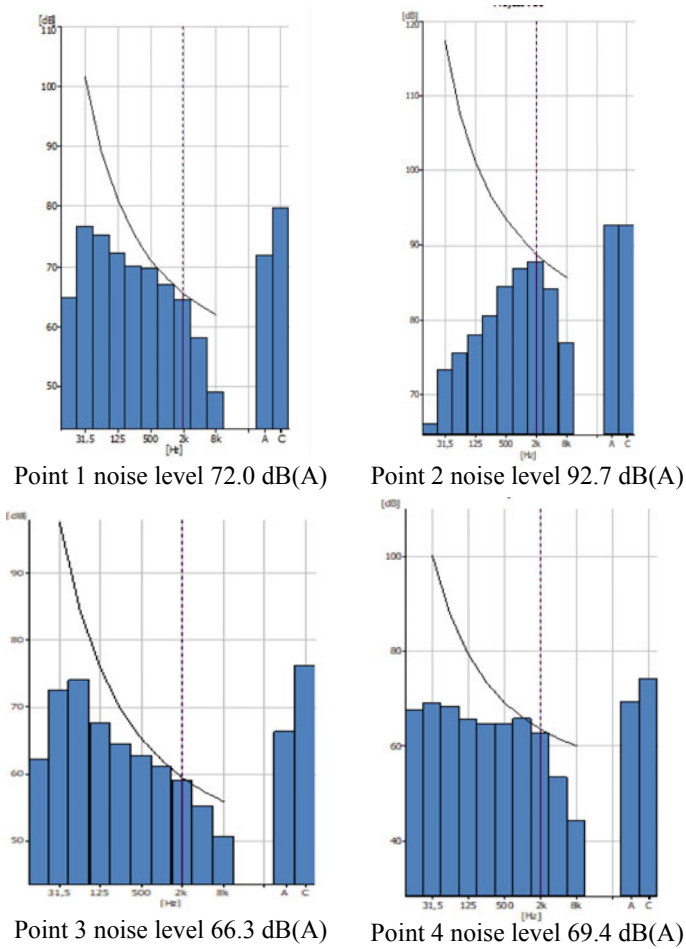


Fig. 2 Noise frequency analysis

impaired, noise affecting basic activities such as sleep, rest, study and communication. Although these effects on human health have long been known, recent research shows that noise has effects on humans at lower levels than previously thought [6].

4 Sound Reduction Solutions Using Sound Absorbing and Soundproofing Panels

The analysis of noise sources in technological processes resulted that the most suitable noise reduction solutions consist of

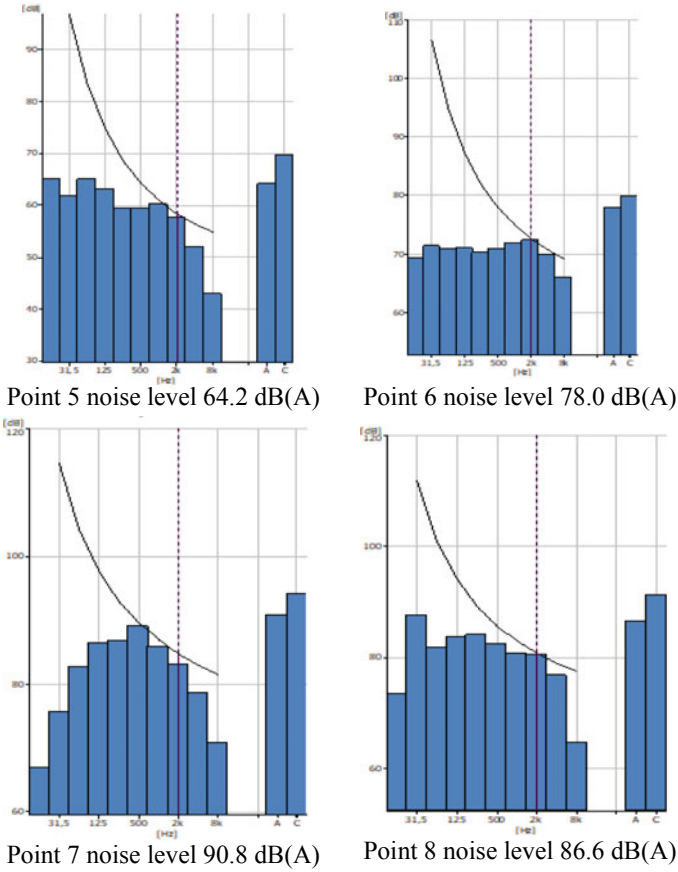


Fig. 2 (continued)

- placement of sound insulating panels/screens close to the limestone loading lines or bordering the limits of UMS silo area;
- treating wagon generating a load noise level of up to 92 dB (A) with sound absorbing materials;
- lowering limestone dropping heights when loading wagons using adjustable troughs to reduce the drop height from 1.5 to 0.50 m.

These solutions can be achieved using measures suggested in the following synthetic plan:

- placement of sound insulating panels/screens close to the limestone loading lines or to premises limits in the UMS silo area;
- acoustic treatment of wagons (use of sound absorbing paints or fitting rubber terries under wagons, their placement in the wagon being not viable because of

Table 2 Frequency noise centralizer

No.	Noise level dB(A) LAeq	Noise curves Cz	Frequencies										
			16 Hz	31.5 Hz	63 Hz	125 Hz	250 Hz	500 Hz	1 kHz	2 kHz	4 kHz	8 kHz	16 kHz
1	72.0	68	64.92	76.6	89.2	81.14	70.01	69.68	67.04	64.43	58.09	49.03	42.81
2	92.7	91	66.12	73.37	75.64	78.08	80.64	84.57	86.92	87.88	84.18	77.03	64.68
3	66.3	62	62.17	72.6	74.06	67.57	64.45	62.72	61.24	59.12	55.13	50.68	43.46
4	69.4	66	67.56	69.18	68.35	65.68	64.73	64.83	65.85	62.88	53.44	44.19	28.32
5	64.2	61	65.24	61.95	65.07	63.25	59.47	59.5	60.28	57.61	52.06	42.95	29.63
6	78.0	75	69.39	71.42	70.99	71.05	70.30	70.93	71.9	72.45	69.97	65.96	52.72
7	90.8	87	66.95	75.8	82.85	86.62	87.00	89.56	86.00	83.23	78.66	70.98	59.44
8	86.6	83	73.46	87.7	81.83	83.75	84.1	82.49	80.68	80.5	76.86	64.8	52.3

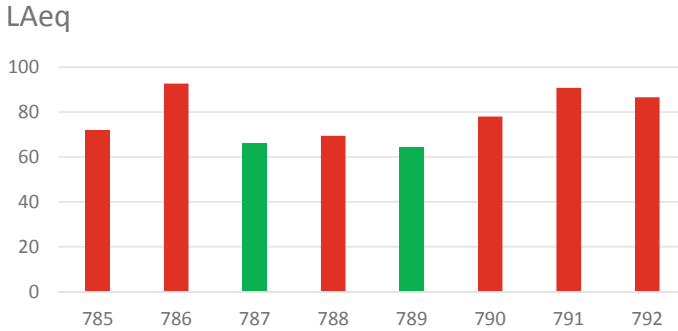


Fig. 3 Noise level chart

transported UMS hardness, which would rapidly destroy this protective terry for damping impact noise at loading);

- lowering limestone dropping height when loading wagons using adjustable troughs;
- use of individual hearing protection (internal or external antiphons for workers);
- limiting operator’s exposure time to noise.

The measurement of noise emitted by vehicles running on rails and of noise emitted by road traffic vehicles and equipment requires the measurement of the noise spectral composition to identify the acoustic characteristics to be met by sound absorbing/sound insulating panels in order to reduce noise level.

In determination of spectral composition for machinery and equipment listed above, reference is made to test methodology and sampling manner of signals specified by standards:

- SR EN ISO 3095: 2006 “Railway applications. Acoustics. Measuring noise emitted by vehicles circulating on rails”;
- SR EN ISO 11200: 2010 “Acoustics. Noise from machines and equipment. Guide to the use of basic standards for measurement of sound pressure levels of emissions at work and other specified positions”;
- SR ISO 1996-1: 2008 “Acoustics. Description, measurement and assessment of environmental noise. Part 1: Fundamental dimensions and evaluation methods”;
- SR ISO 1996-1: 2008 “Acoustics. Description, measurement and assessment of environmental noise. Part 2: Measurement of ambient noise levels” and related standards.

Account will also be taken of the provisions of Directive 2002/49/EC of 25 June 2002 on the assessment and management of environmental noise. In order to identify the noise spectrum and identify resonance frequencies specific to road traffic vehicles, specific methods of spectral analysis of noise signals will be presented.

Sound absorbing panels are used to mitigate noise pollution in transport infrastructure, along railways and other fixed noise sources.

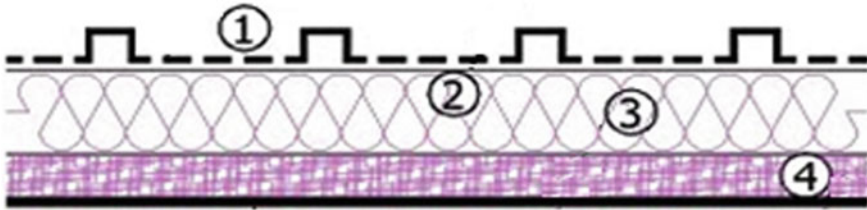


Fig. 4 Example of sound panel [7]

To reduce noise, an obstacle is interposed between the source and the receiver, which by absorption, reflection, diffraction reduces level of noise reaching the receiver. Traffic noise is minimized by fitting such obstacles commonly referred to as noise barriers.

The noise barrier refers to a structure that blocks or dims noise level of a sound source. Depending on their surface type, these barriers may partially or totally reflect incident noise.

The term “phono absorbent barrier” is used when referring to a structure containing phono absorbent components, and “noise barrier” term is used for any type of structure that has the role of screening noise.

Acoustic Panels (Fig. 4): the part facing the noise source is made of corrugated perforated sheet (1), followed by a polyester wool moisture protection (2), a layer of sound absorbing material (3) and a layer of acoustic soundproofing material (4), and the outside (5) is made of galvanized steel sheet. The acoustic materials are non-flammable and are fitted between the supporting elements of the panel. All elements are combined into a sandwich panel with the use of a shear-resistant polyurethane adhesive.

Frequently used soundproofing panels are vertical screens (walls).

Depending on their height, the following categories are distinguished:

- high screens—over 6 m;
- medium height screens—with values ranging from 2 to 6 m;
- low screens—less than 2 m.

Depending on the acoustic characteristics, the screens include

- absorbent screens;
- reflective screens;
- ground unevenness or mixed solutions “screens plus unevenness”;
- total or partial coatings of noise sources;
- protective devices fitted on the edge of railways (Figs. 5 and 6).

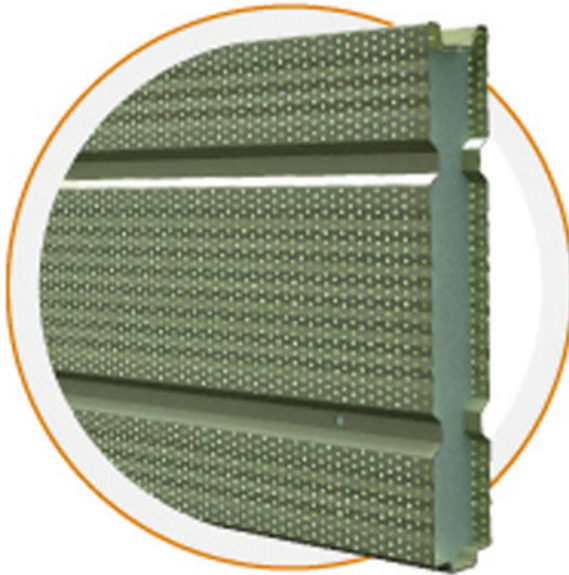


Fig. 5 Soundproofing rampant. 100 AL /AC PE modular sound absorbing panels [8]



Fig. 6 Herifon phono absorbent panel [9]

5 Conclusions

After analysing noise level generated by industrial activity of charging useful mineral substances in auto and CFR transportation means, the following conclusions were drawn

- Analysis of noise measurements carried out when loading useful mineral substances in automotive and CFR vehicles, noise exposure level was between 64.9 and 93 dB (A) exceeding the 87 dB occupational exposure limit (A) when loading wagons. In this case, spectrograms have also been measured to assess the exceeding over frequencies in order to establish optimal noise reduction solutions.
- Measured acoustic pressures show exceeding of 1.3–27 dB, compared to legal limits for noise level at industrial premises limit (max 65 dB (A)).
- Spectrogram analysis showed exceeding medium and high frequency bands considered dangerous, with values between 0.1 and 9 dB, taking technical and organizational measures being mandatory.

Considering that noise reduction is a complex problem, the purpose of reducing noise is to achieve acoustic comfort at an acceptable price; the primary variables of the system are acoustic characteristics and costs. The concept of noise reduction system is generally a compromise between acoustic performance and costs.

In conclusion, application of soundproofing barriers at the point of loading useful mineral substances in auto and CFR transportation means will reduce the impact of industrial activities on neighbours (lowering below 65 dB (A) at industrial premises limit) in accordance with the technical data provided by the manufacturer of sound absorbing/sound insulating panels [7].

References

1. A. Draghici, M. Kovacs, L. Toth, Occupational health and safety regarding the exposure to noxious of workers from the steel industry. *Metal Int* **18**(2), 147–153 (2013)
2. *** Law 319/2006 Law on Safety and Health at Work
3. *** Directive 2002/49/EC of the European Parliament and of the Council of 25 June 2002 relating to the assessment and management of environmental noise
4. G.D. Vasilescu, A.N. Draghici, C. Baci, Methods for analysis and evaluation of occupational accidents and diseases risks. *Environmental Engineering and Management Journal* **7**(4), 443–446 (2008)
5. S. Sorin, V. Ciprian, K. Marius, in *Exposure of workers to noise in mining industry*, ed. by N. Herisanu, V. Marinca, 12th International Symposium Acoustics and Vibration of Mechanical Structures (AVMS 2013), Timisoara (2013)
6. S. Simion, S. Simion, Prevention and reduction of noise emissions from industrial mining processes, (INSEMEX Publishing House, Petroşani, 2008). ISBN: 978-973-88753-0-2
7. Acoustic Design Homepage, <https://sites.google.com/site/controlzgomot/solutii-acustice/panouri-acustice>. Last accessed 2019/02/02
8. Marcegaglia Homepage. http://www.marcegaglia.ro/marcegaglia_product/parapete-antifonice-de-siguranta-integrate-panouri-fonoabsorbante-100-al-pe/. Last accessed 2019/02/02
9. Hericon Homepage. http://hericon.ro/panouri_sandwich/panou_fonoizolante.html. Last accessed 2019/02/02

Research on Speech Changes Due to Environmental Noise



Diana Cotoros, Ionel Șerban, Corneliu Drugă, and Anca Stanciu

Abstract People are tending to be more focused upon their own preoccupations and unable to divide their attention to several stimuli around them. This phenomenon increasingly occurs when they find themselves in a situation requiring to listen to a lecture, a conference or a speech for a certain amount of time. There usually occurs an environmental sound due to furniture creaking, people coughing or whispering, and even the audio tools may provide some unexpected noises, or some construction site may work nearby, etc. The speaker has the tendency of changing his way of speaking in order to instinctively challenge these environmental disturbances (Lombard's effect). The paper is presenting some experiments done with the participation of several subjects with different ages, meant to observe and analyze the speech changes in various environmental disturbances in order to raise awareness upon the stress induced by environmental noise in professions requiring speeches in front of a large audience (actors, teachers, politicians, etc.).

1 Introduction

Modern life provides a setting for a regularly noisy environment of our daily activities and communications, the result being, besides the well-known noise pollution shortcomings, some changes in the communication behavior that are meant to help human beings to adjust to the environmental challenges. Some people in some professions are more challenged than others, so people talking in front of a large audience are more exposed than those whose jobs do not assume such kind of human interactions.

More than 100 years ago, the French otolaryngologist Etienne Lombard stumbled upon an interesting effect occurred when people need to speak in a noisy environment, while he was trying to study hearing loss and its simulation [1]. Since then, researchers determined new ways of using Lombard's findings and apply them in various domains where speech takes place in noisy conditions [2, 3].

D. Cotoros (✉) · I. Șerban · C. Drugă · A. Stanciu
University Transilvania of Brasov, Brasov, Romania
e-mail: dcotoros@unitbv.ro

Several explanations were provided starting with physiological reflex or willing compensation, analysis of the starting point, and probably most important the influence on speech recognition [4, 5].

There are controversies regarding the adaptation of the people to communication in noisy environments, some researchers consider there is no active adaptation, and people just speak louder but others tried to find proofs that there are significant involuntary changes not only in the sound intensity but also in the fundamental frequencies, higher emphasis on vowels, etc [6].

Some interesting approaches aim at creating some systems able to manipulate natural speech into Lombard's speech in order to enhance intelligibility [7] or studying the effect of outside noises upon the communicative phenomenon [8], even improving speech recognition with forensic purposes.

2 Materials and Methods

The experiment was performed due to the involvement of several persons, aged between 25 and 60 years old, three males and seven females, with no reported issues regarding hearing loss or speech problems. They are all native Romanian speakers, and eight of them have no clue regarding Lombard's effect. Only two of the subjects are vaguely aware of the phenomenon, but the purpose of the experiment was revealed only after the recording.

The subjects were asked to read a short text (around 300 words) from a book review, while wearing headphones. They were subjected to four possible disturbances:

- Quiet headphones—the headphones are used only to camouflage any environmental sound and create a silent area.
- White noise—It is created by a continuum of frequencies equally distributed over the whole hearing range. In healthcare applications, white noise is used to treat increased sensitivity to normal environmental sounds, or to camouflage the annoyance caused by tinnitus.
- Construction site noise.
- Pop music.

A Shure SM7B microphone was used to record them while reading. This type of microphone was selected as it is a microphone that focuses on capturing a clean recording of a single sound source, while filtering out everything else, making this polar pattern perfect for clearly recording a subject's voice, while being surrounded by progressively more excessive background noise [9] (see Fig. 1).

The experimental setup also includes a pair of Audio-Technica ATH-M50 X headphones with a closed back, keeping the sounds playing back to the subject from bleeding into the microphone, allowing for a clear recording. Everything was recorded into a program called REAPER, a digital audio workstation (DAW)-type

Fig. 1 Shure SM7B microphone used for recordings



software which digitally emulates a multi-track tape recorded, allowing for simultaneous playback and recording on multiple tracks. This made it possible to play different types of sounds to the subjects, while also recording them on separate tracks. The sound samples played were either music bought from Bandcamp, with permission from the artist to use said music for this study, or downloaded from Freesound.org, a site which provides a large library of free royalty sound samples.

The recordings were made in the research laboratory of the Advanced Mechatronics Systems at the university research institute, in a quiet environment far away from the crowded city, so there was no outside influence.

The results were then analyzed using a sound spectrum analyzer, and statistical processing of the data leads us to final conclusions.

3 Results and Analysis

The sound spectrum analyzer offers the connection between the speech sound frequencies (Hz) and the sound pressure level (SPL) (dB) in real time while the recording is played. Some examples are presented in the following figures, for all the studied conditions (Figs. 2, 3, 4 and 5).

The gray areas in the diagrams are due to the “peak hold” option of the software allowing the highlighting of the maximum SPL values corresponding to the measured frequencies, while the yellow areas represent the current measurements.

The subjective feedback after talking to the subjects revealed that they all considered music the most disturbing element; they felt the need of shouting in order to hear themselves speaking. This result is supported by the spectral analysis as it was

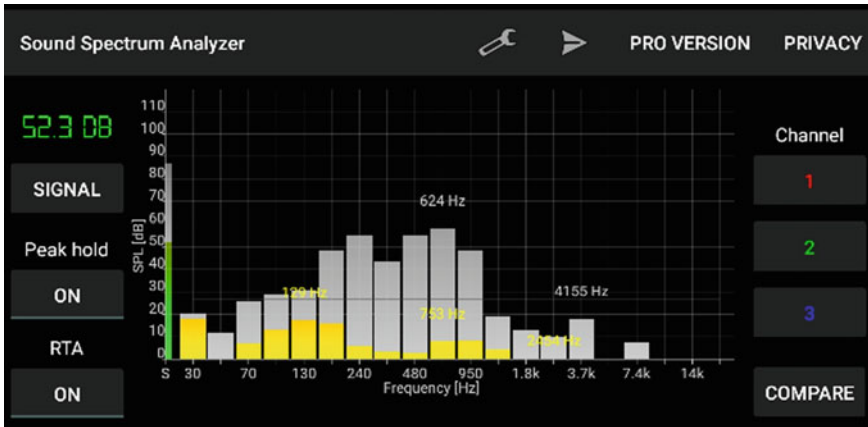


Fig. 2 Spectral analysis for female subject reading in quiet conditions

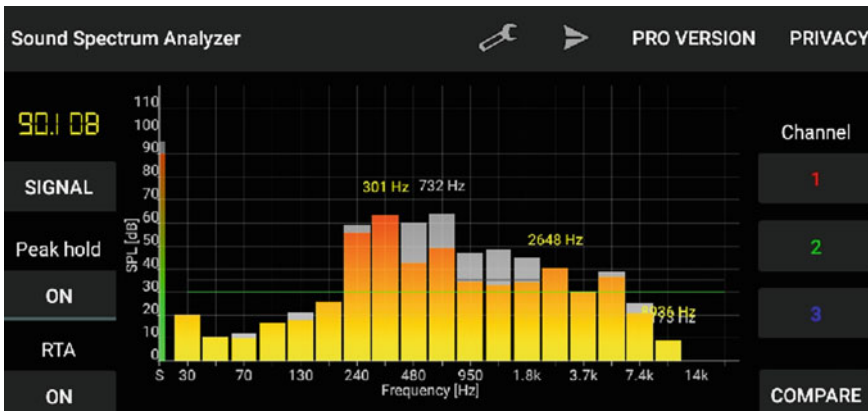


Fig. 3 Spectral analysis for female subject reading while listening pop music

determined that the sound intensity of their speech was increased with over 40% when listening to pop music.

Surprisingly, the construction site noises did not lead to very high levels of the intensity, nor the white noise. For both, a growth of less than 10% was recorded. In Fig. 6, the values of the average sound pressure for each of the ten subjects in all four conditions were represented.

By analyzing the diagram, it becomes obvious that all the subjects slightly increased their speech intensity with construction site and white noise, but the growth is more dramatic in case of the pop music (purple columns). The reason might be the fact that human mind tends to listen when hearing another human voice, to a much greater extent than hearing another type of sound. It is much easier for a person to filter random unpleasant noises than human voices. For this reason, reading on

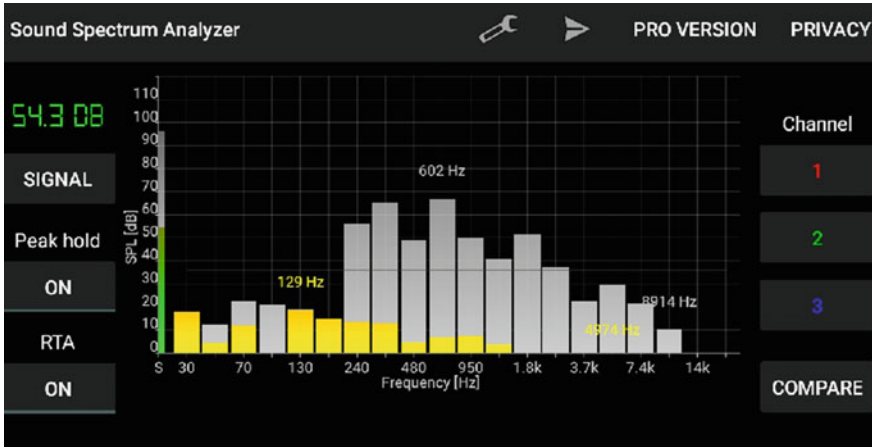


Fig. 4 Spectral analysis for female subject reading with construction site noises

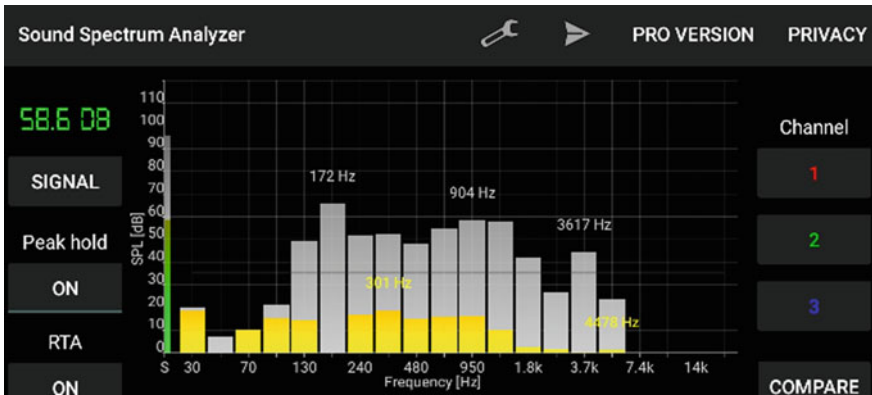


Fig. 5 Spectral analysis for female subject with white noise

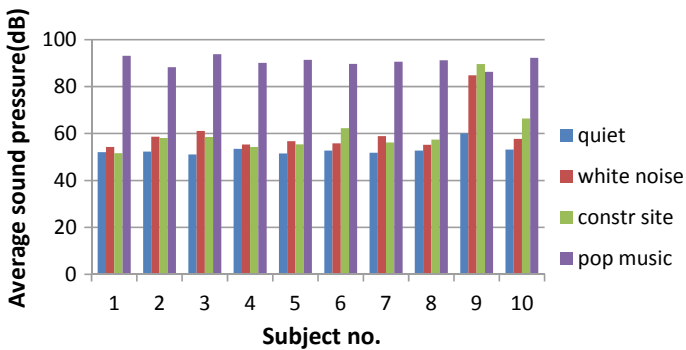


Fig. 6 Average sound pressure for all subjects

construction site noises or white noise is less annoying and leads to a small number of mistakes while reading on pop music is rather a challenge, involving many mistakes and higher intensity.

As far as frequency is concerned, human voice is of course not a pure sound; the sound spectrum shows a larger range of values. The fundamental frequency for men's voice is usually between 85 and 180 Hz, while for women, it gets to 165–255 Hz, but many harmonic series will be present and the impression of hearing the fundamental tone. In fact, the usable voice frequency band ranges between 300 and 3400 Hz.

The investigated subjects started from a fundamental frequency of 172 Hz—the male subjects and 210–258 Hz the female subjects. A 20% growth in frequency was recorded when the subjects were asked to read with construction site and white noise. The frequency increased up to 50% during reading with pop music.

4 Conclusions

There are many situations in real life when people need to speak to an audience in a noisy environment due to faulty technical devices, large or bored audience, construction sites or maintenance work nearby, traffic, music, etc. Human voice will involuntarily change its characteristics when subjected to a noisy environment, and this paper analyzed the characteristics during four different types of environments. The results showed that all the subjects regardless if they had any knowledge about Lombard's effect displayed dramatic growth in both intensity and frequency of speech when the perturbation involved pop music with human voice. Also the number of reading mistakes was considerably higher.

As for the other types of sounds, construction site and white noise, a slightly higher intensity and frequency were obtained and also just a few reading mistakes as the subjects declared that impersonal noises are easier to be filtered by their minds than noises involving human voices. We intend to further analyze the subject involving discussion between two or more people in order to determine the influence of human voice as a disturbing speech factor.

References

1. H. Brumm, S.A. Zollinger, The evolution of the Lombard effect: 100 years of psychoacoustic research. *Behaviour* **148**, 1173–1198 (2011)
2. D. Vljaj, Z. Kacic, *The Influence of Lombard Effect on Speech Recognition* (Speech Technologies, Maribor, Slovenia, 2011), pp. 151–168
3. V.S. Varadarajan, J.H.L. Hansen, Analysis of Lombard effect under different types and levels of noise with application to In-set speaker ID systems, in *INTERSPEECH 2006-ICSLP*, Pittsburgh, Pennsylvania (2006), pp. 937–940
4. P. Bottalico, I.I. Passione, S. Graetzer, E. Hunter, Evaluation of the starting point of the Lombard effect. *Acta Acust. Unit. Acust.* **103**(1), 169–172(4) (2017)

5. L. Folk, F. Schiel, The Lombard effect in spontaneous dialog speech, in *INTERSPEECH 2011*, Florence, Italy (2011), pp. 2701–2704
6. M. Garnier, N. Henrich, How does the Lombard effect improve acoustic contrasts between speech and ambient noise. *Comput. Speech Lang.* **28**, 580–597 (2014)
7. D.Y. Huang, S. Rahardja, E. Ong, Lombard effect mimicking (2010). https://www.researchgate.net/publication/267545252_Lombard_Effect_Mimicking. Last accessed 2019/05/02
8. P. Lau, The Lombard effect as a communicative phenomenon (UC Berkeley Phonology Lab Annual Report, 2008)
9. B. Owsinski, *The recording engineer's handbook*, 3rd edn. (Cengage Learning, Boston USA, 2014)

Biomechanics and Bioacoustics

Angular Momentum About the Total Body Center of Mass Computed at Different Speeds



Dan Ioan Stoia, Cosmina Vigaru, Andreea Nicoara, and Nicolae Herisanu

Abstract Dynamical parameters of human walking are required in robotic researches. These provide essential information for development of control possibilities and joint activation. The study starts with kinematical recordings of the over-ground walking at self-selected velocity and imposed velocity of one subject. Taking into account the kinematical data and the length measurements of body elements and total body mass, a computational model for determining the angular momentum was created. The masses of individual segments and inertia were approximated as percentages to the total body mass and radius of gyration, relying on the literature data. In order to identify the differences in angular momentum at different speeds, mean absolute difference and correlation coefficient were computed.

1 Introduction

The determination of human kinetic parameters starting from kinematical data represents a permanent concern among authors [1–4].

The angular momentum is a kinetic parameter which can be computed relying on kinematical data and on mass distribution in the body. Some researches' concern is on computing the angular momentum during walking respecting the ground

D. I. Stoia (✉) · C. Vigaru · A. Nicoara · N. Herisanu
Department of Mechanics and Strength of Materials, Politehnica University Timisoara, Timisoara, Romania
e-mail: dan.stoia@upt.ro

C. Vigaru
e-mail: cosmina.vigaru@upt.ro

A. Nicoara
e-mail: andreean9@yahoo.com

N. Herisanu
e-mail: nicolae_herisanu@yahoo.com

contact point. However, in order to develop control strategies in robotics, the angular momentum should be computed about the total body center of mass (CoM) [5–7].

Respecting to CoM, the angular momentum during walking is conserved as long as no external torque acts upon the body, according to Newton's second law for rotational motion. Angular momentum is composed of two quantities: rotational angular momentum and translational angular momentum [8].

Rotational angular momentum (spin) reflects the angular momentum of a segment computed about its center of mass [9]. Translational angular momentum (orbital) represents the angular momentum of the center of mass of a segment about a chosen point.

The kinematic data can be measured using motion analyzing systems [10–12], while the body mass and inertia are computed based on ratios to the total body mass [13].

Independently on the type of gait investigation (overground movement or on a treadmill) [14, 15], the kinematical parameters are comparable.

The study reflects the measurements of kinematic gait parameters together with calculus of masses and inertia of segments according to the existing literature and aims to establish an analytic model for computing the total angular momentum of the lower limb. The results, together with spatial and temporal parameters of gait [16, 17], can be used in development of prediction systems for human locomotion apparatus [18, 19].

2 Materials and Methods

2.1 *Experimental Approach*

The kinematic measurements have been measured in the Motion Analysis Laboratory within Politehnica University of Timisoara. As the paper aims to establish a computational model, and not a statistical approach, only one healthy feminine subject was involved in the study.

After a set of 10 min training, the subject has been equipped with ultrasound markers which were placed on the tights and on top of the feet.

Prior to recording, the anatomical landmarks have been pointed. This pointing serves to identifying the joints of the lower limb. The spatial coordinates of these points are defined relatively to the tights and feet ultrasound markers.

The subject has accomplished three trials of walking, counting between 4 and 5 steps on each. The first trial was performed at a self-selected velocity of the subject, followed by an increase of twice the velocity. After 3 trials at high velocity, the subject was asked to walk with a decrease of half of the self-selected velocity.

The set of kinematical parameters corresponding to each walking velocity has been exported for further data processing. The kinematic data recorded were: all

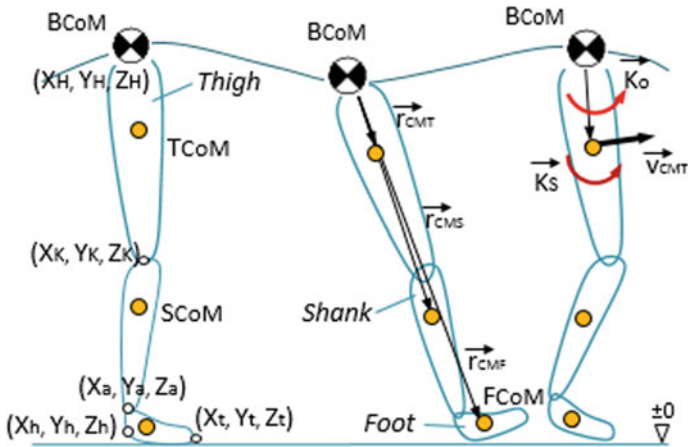


Fig. 1 Analytical model representation

angles of the lower limbs as time series and the spatial coordinates of every joint, heel and toe.

2.2 Analytical Approach

The developed model serves only for the determination of angular momentum in sagittal plane and does not contain frontal or transversal plane parameters. However, while walking, the dominant movements, velocities and accelerations occur in sagittal plane. In this plane, the progression of the body center of mass (B_{CoM}) is produced (Fig. 1). The angular momentum will be computed in respect to B_{CoM}.

Our study will be based on the three segments that build the lower limb: thigh, shank and foot. For each of these, the spin component K_S and orbital component K_O of angular momentum will be computed. In computation, the definitions of total angular momentum and its components are used (1–3) [5, 8, 9].

$$\{K_o\} = m_s \cdot \{r_{CM}\} \times \{v_{CM}\} \tag{1}$$

$$\{K_s\} = [J_s] \cdot \{\omega_{CM}\} \tag{2}$$

$$\{K_{seg}\} = \{K_o\} + \{K_s\} \tag{3}$$

$$J_s = \begin{bmatrix} m_s \cdot \rho_s^2 & 0 & 0 \\ 0 & m_s \cdot \rho_l^2 & 0 \\ 0 & 0 & m_s \cdot \rho_f^2 \end{bmatrix} \tag{4}$$

The elements of the inertia tensor (4) were computed using the radius of gyration in concordance to the axis of rotation. The gyration radii were computed using the Dempster's percentages for every axis (frontal, sagittal and longitudinal) applied to the total length of each segment [13].

The mass of each segment and its center were determined using the same approach (Dempster), as percentages of body mass and segment length. The length of each segment was determined from measurements, using the joint coordinates.

The position vectors were determined using the joint and CoM coordinates, while the linear velocity was computed as numerical derivative of those.

The angular displacements were provided by the system, while the angular velocity was computed as numerical derivative.

3 Results and Discussions

In Fig. 2, one kinematic (flexion-extension angle) and two kinetic parameters (spin and orbital angular momentum) of shank are presented. The representations were drawn in a gait cycle by normalizing the time series. In this way, representation of one parameter measured or computed for three or more velocities is possible without showing large frequency differences.

In every graphic (Fig. 2a–d), the series *vel-1* represents the lowest velocity of movement, the *vel-3* represents the largest velocity and *vel-2* the middle velocity.

As expected, larger amplitudes in both kinematic and kinetic parameters are recorded when the velocity of movement increases. The orbital angular momentum, computed in respect to the body center of mass, is four times larger than the spin angular momentum due to the segmental mass position according to the two rotation axes. Lower values of spin angular momentum are associated with low angular velocity of the segment and vice versa. The orbital component shows a dramatic decreasing when the limb passes through the midstance position.

By adding the series of orbital component by the series of spin component, the variation of total (segmental) angular momentum was determined. It represents the kinetic characteristic of a body segment that is varying along the gait cycle due to the muscular actions. It displays the highest peaks during the segment acceleration periods.

In the same manner, the thigh parameters are presented in the Fig. 3. Larger amplitudes are also associated with larger velocities. Due to the proximity of this segment to the B_{CoM} , the orbital angular momentum is less large comparing to shank case. Also, less evident tendency is recorded. The spin component is as for the shank, proportional to the angular velocity. The total (segmental) angular momentum is highly influenced by the orbital component, and therefore, their variations look very similar (Fig. 3c, d).

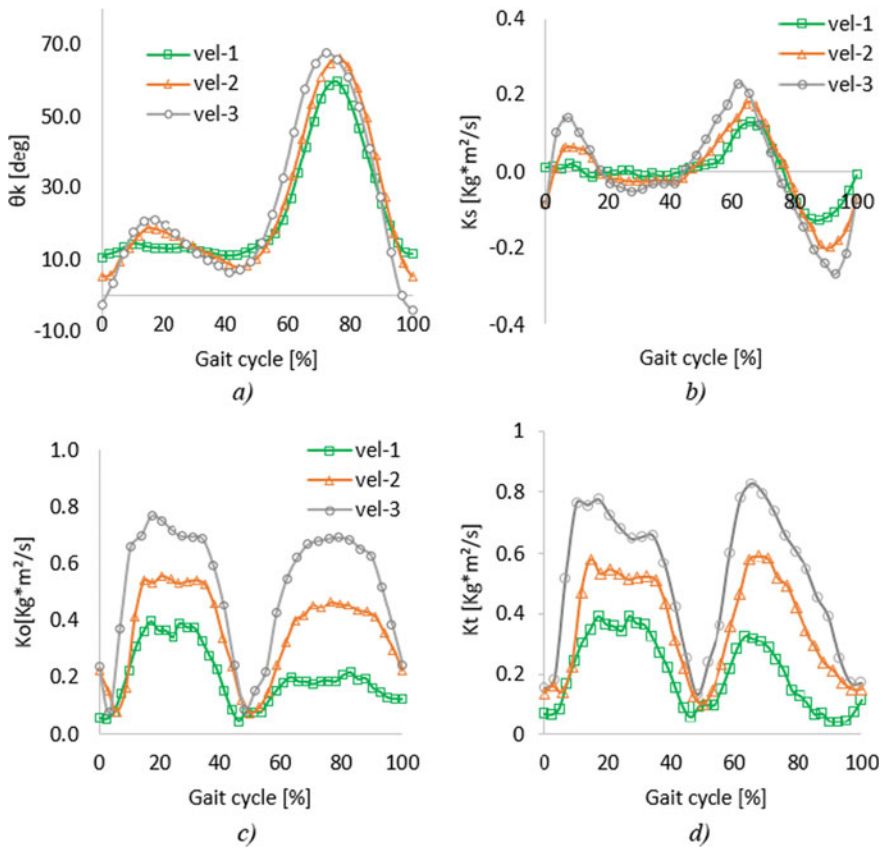


Fig. 2 Shank kinematic and kinetic parameters: **a** flexion angle; **b** spin angular momentum; **c** orbital angular momentum; **d** segmental angular momentum

4 Conclusions

In this paper, results of kinematic measurements and kinetic parameters obtained using an analytical model are presented. The measurements were conducted for three movement velocities, and the results are presented accordingly.

As the velocity increases, larger amplitudes are obtained for every parameter, due to the body inertia. Also, the movement frequency increases.

The orbital angular momentum is superior in value to the spin component. The spin component is always proportional to the angular velocity around the segment center of mass. In midstance phase of gait, the orbital component exhibits the lowest values.

The segmental angular momentum computed as sum of orbital and spin components is proportional to the accelerations of the body segments and is controlled by the action of muscles, according to the gait cycle events.

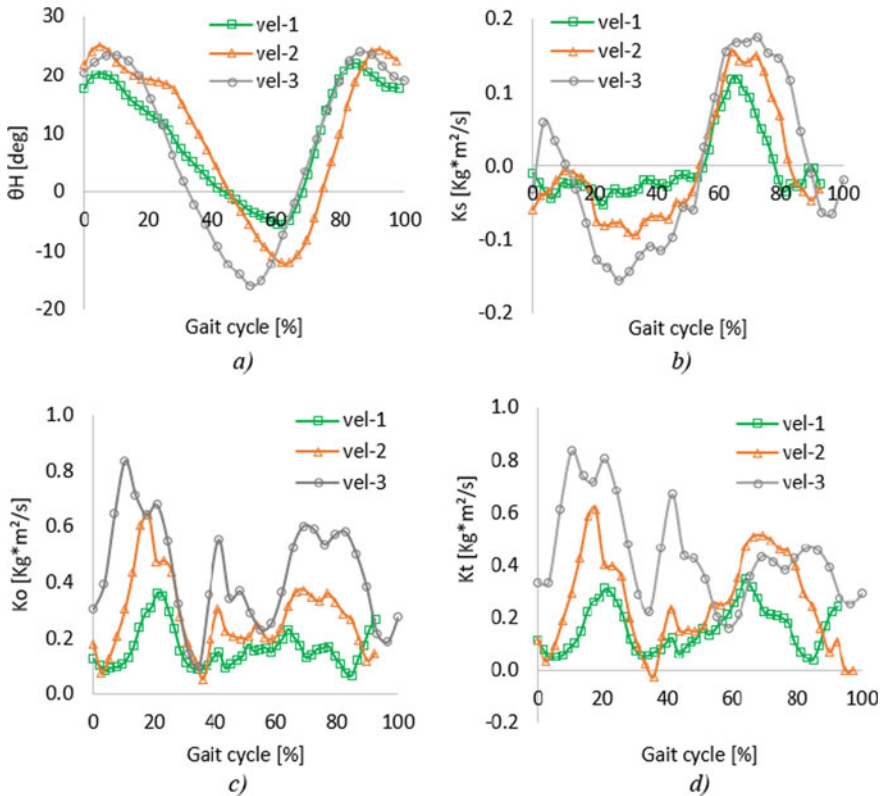


Fig. 3 Thigh kinematic and kinetic parameters: **a** flexion angle; **b** spin angular momentum; **c** orbital angular momentum; **d** segmental angular momentum

Acknowledgements This work was supported (in part) by research grant GNaC2018-ARUT, No. 1363/01.02.2019, financed by Politehnica University of Timisoara.

References

1. C.A. Fukuchi, R.K. Fukuchi, M. Duarte, A public dataset of overground and treadmill walking kinematics and kinetics in healthy individuals. *Peer J* **6**, e4640 (2018)
2. D. Dragulescu, V. Perdereau, M. Drouin, L. Ungureanu, K. Menyhardt, 3D active workspace of human hand anatomical model. *Biomed Eng. Online* **6**, 15 (2007)
3. D. Tarnita, M. Georgescu, D.N. Tarnita, Applications of nonlinear dynamics to gait analysis on plane & inclined treadmill. *New Trends Med. Serv. Rob.* **39**, 59–73 (2016)
4. D. Tarnita, M. Catana, D.N. Tarnita, Nonlinear analysis of normal human gait for different activities with application to bipedal locomotion. *Rom. J. Techn. Sci. Appl. Mech.* **58**(1–2), 177–192 (2013)
5. B.C. Bennett, S.D. Russell, P. Sheth, M.F. Abel, Angular momentum of walking at different speeds. *Hum. Mov. Sci.* **29**, 114–124 (2010)

6. J. Hamill, K.M. Knutzen, Biomechanical basics of human movement, 2nd edn. (Lippincott Williams &Wilkins, 2003)
7. D. Dragulescu, L. Ungureanu, K. Menyhardt, A. Stanciu, 3D active workspace of the human hand shaped end effector, in *Proceedings of the 13th IASTED International Conference on Robotics and Applications*, Wurzbug, Germany (2007)
8. B.M.M. Gaffney, C.L. Christiansen, A.M. Murray, A.K. Silverman, B.S. Davidson, Separation of rotational and translational segmental momentum to assess movement coordination during walking. *Hum. Mov. Sci.* **51**, 99–111 (2017)
9. N.J. Kasdin, D.A. Paley, *Engineering Dynamics: A Comprehensive Introduction* (Princeton University Press, 2011)
10. J. Sun, Y. Wang, J. Li, W. Wan, D. Cheng, H. Zhang, View-invariant gait recognition based on kinect skeleton feature. *Multimed. Tools Appl.* **77**(295) (2018)
11. R. Luca, S.-I. Bejinariu, Classification method for human locomotion, in *Proceedings of the 10th International Conference on Electronics, Computers and Artificial Intelligence, ECAI 2018*, Iasi, Romania (2019)
12. M.I. Baritz, D. Cotoros, Oscillatory movements analysis at knee level. *Appl. Mech. Mater.* **436**, 271–276 (2013)
13. W.T. Dempster, *Space Requirements of the Seated Operator: Geometrical, Kinematic, and Mechanical Aspects of the Body, with Special Reference to the Limbs* (Wilfrid Taylor, 1955)
14. R. Luca, Statistical analysis of some parameters describing human locomotion, in *Proceedings of 5th IEEE International Conference on E-Health and Bioengineering* (2015)
15. S. Focke Martinez, O. Kuzmicheva, A. Gräser, Prediction of characteristic points of hip and knee joint trajectories during overground walking using IMUs and artificial neural networks, in *IEEE International Symposium on Medical Measurements and Applications (MeMeA)* (2016)
16. A.J.J. Smith, E.D. Lemaire, Temporal-spatial gait parameter models of very slow walking. *Gait Posture* **61**, 125–129 (2018)
17. M. Toth-Tascau, D.I. Stoia, Influence of treadmill velocity on spatio-temporal parameters of human gait, in *Published in E-Health and Bioengineering Conference (EHB)* (2011), pp. 1–4
18. D. Santra, S. Sadhukhan, S.K. Basu, S. Das, S. Sinha, S. Goswami, Scheme for unstructured knowledge representation in medical expert system for low back pain management. *Smart Innov. Syst. Technol.* **105**, 33–41 (2019)
19. A. Alionescu, I.S. Herban, C.-B. Vilceanu, C.C. Muşat, Mathematic interpolation methods—support for an efficient 3D modeling of landslides in the context of displacements monitoring, in *AIP Conference Proceedings ICNAAM* (2014)

Analysis of Oscillatory Eye Movements as a Nystagmus, Manifested in the Visual System



Mihaela Ioana Baritz and Alexandra Maria Lazar

Abstract The state of normality of the oculomotor equilibrium is determined by the characteristics of eye movements that are analyzed from the point of view of kinematic and dynamic dimensions. A great deal of research has highlighted and identified the connections between eye movements and the mode of action of stimuli in the environment. Depending on the degree of action of these stimuli, the reaction in the visual system may allow the identification of functional, neuromotor or normal physiological abnormalities. The first part of the paper analyzes the types of eye movements that the visual system can perform both monocular and binocular and the normal and abnormal physiological limits are identified. Of all these, the emphasis was placed on the oscillatory movements of the eyeball to highlight the importance of binocular balance on the stability of the formation of the corresponded retinal images. In the second part of the paper, we present the experimental system designed and built to record these continuous and/or oscillatory movements in order to compare the ideal trajectory with that performed by each ocular globe. In the final part of the paper, the results of image processing of the eyeball movements and the conclusions regarding the influence of external stimuli on oculomotor balance are presented.

1 Introduction

Eye movement is considered an essential element in defining the normality state of the visual system and how binocular vision is achieved and eye balance maintained.

The human visual system is characterized by a series of movements that it develops in the form of reflexes or conscious movements, programmed and controlled by the

M. I. Baritz (✉) · A. M. Lazar

Product Design, Mechatronics and Environment Department, Transilvania University from Brasov, b-ul Eroilor nr.29, 500036 Brasov, Brasov, Romania

e-mail: mbaritz@unitbv.ro

A. M. Lazar

e-mail: ale.lazar@yahoo.com

© Springer Nature Switzerland AG 2021

N. Herisanu and V. Marinca (eds.), *Acoustics and Vibration of Mechanical*

Structures—AVMS 2019, Springer Proceedings in Physics 251,

https://doi.org/10.1007/978-3-030-54136-1_22

central nervous system. The main types of eye movements are: nystagmus, saccade, miniature, pursuit, smooth, compensatory and vergence.

Nystagmus is a condition of involuntary movement acquired in the first years of life or maybe even later. This form of eye movement results in a reduced or even limited view of the axes of the visual system. These moves are even more evident when the head rotates around an axis and the remote images of the visual system are supported by turning the eyes in a direction opposite to the movement of the head to compensate for the rotation.

From a functional point of view, there are two forms of manifestation of the nystagmus: physiological and pathological, presenting, within each group, other variants of manifestation. Forms of interest for oculographic computational analysis are represented by physiological nystagmus, the pathological one requiring a medical approach of ophthalmological and neurological specialty. The forms of nystagmus may be determined by a variety of causes, such as nervous system disorders, congenital disorders, acquired disorders, toxicity and medication. As mentioned in many research papers, physiological nystagmus is a form of involuntary eye movement that is part of the vestibulo-ocular reflex (VOR), characterized by alternating smooth pursuit in one direction and saccadic movement in the other direction [1]. In turn, the physiological nystagmus presents the following forms of manifestation: downbeat nystagmus, upbeat nystagmus, seesaw nystagmus, periodically alternating nystagmus.

Other forms of manifestation of physiological nystagmus, which are of interest for studies on biomechanical posture, dynamical or static behavior of the human body, are the form of opto-kinetic and post-trophic nystagmus, respectively. The form of opto-kinetic nystagmus is induced by the pursuit of visual stimuli (vertical or horizontal), the post-trophic form is determined by the rotation motion of the body around the vertical axis, and the rapid phase of the nystagmus is performed in the opposite direction of this rotation, trying to compensate some internal physiological manifestations (Fig. 1).

Another form of movement determined in each ocular globe is saccade movement, a rapid eye movement, conjugated and performed under voluntary control from the central cortex (visual cortex). Generally, the purpose of these oscillatory movements is to form the images of the surrounding space in the foveal area; therefore, the saccade oscillations are considered as an important mechanism for characterization of selective visual attention.

In the case of saccade movements, an important problem was identified, which is to analyze how the visual system works during these movements (whether or not images are formed on the retina to be transmitted to the visual cortex). Thus, it is stated in the literature that in fact visual information, in this case, is obtained as sequential images and interrupted by fixation processes, a phenomenon aware of the subject with this form of eye movement [2]. Fixation periods last up to 200–300 ms, and the fixation sequence is related to the sampling rate of the eye movement recording technique that has been used. Saccade movements are very rapid, resulting in a phenomenon of sacred suppression, a phenomenon during which visual perception is not completely eliminated but only substantially reduced. From the experimental point of view, the

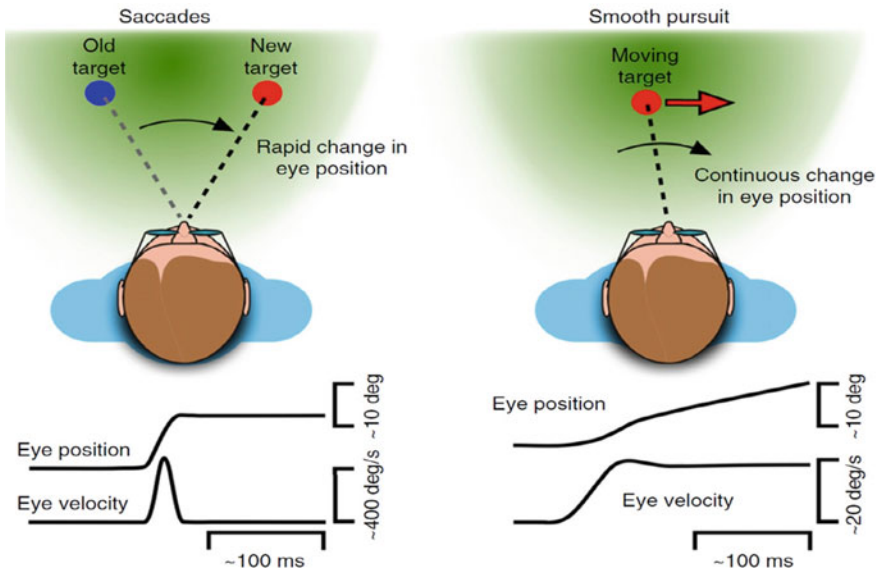


Fig. 1 Eye movements that redirect gaze and saccades change the line of sight to place the retinal image of visual targets onto the fovea [8]

saccade movements are pre-programmed movements such that during fusing, both foveal and peripheral information help to guide to the associated fixation site and respectively the occurrence of the next saccade movement. Eye tracking movements are conjugated, and they easily track objects that move slowly in the field of vision that the eye fixes. Their primary purpose is to stabilize objects' movements on the retina, allowing the subject to perceive the details of the object. Compensatory ocular movements are related to tracking movements and act to compensate for the movement of the head or body in order to partially stabilize the image of an object on the retina. For the evaluation of ocular movements, different techniques of real-time recording of ocular microscopes are used in order to highlight the normal, physiological or possibly existing state of eye pathologies.

Eye tracking technology offers the ability to measure eye movements of users, allowing you to identify the areas in the field of view frequently viewed and the time when your eyes move from one fixation point to another. For example, the use of eye tracking technology in measuring online interactivity can confirm the results obtained by using other methods or can be directly applied in evaluating the proposed interactivity attributes for evaluation [3].

There are various techniques for eye movement monitoring, including dual Purkinje image, electro-oculography, search coils, known as scleral contact lens or search coil, photo-oculography and video-oculography. Photo-oculography or video-oculography is a technique that involves measuring the characteristics of the moving eye. The technique is the most used today and consists in mounting an infrared camera either at the bottom of the monitor or at the base of the laptop screen, or on

the frame of a special eyewear designed for this activity. This camera, equipped with image processing software, locates and identifies the reflection of the cornea and the center of the pupil to be able to analyze the eyeball trajectory and evaluate the preferences of visual interest in site images [4, 5]. The optical and video means used in the visual system analysis are the myGaze device, along with the related software.

MyGaze-n system is designed to be used with the myGaze software SDK and to create applications based on the visual system and its motor features but is limited to laptop or display attachment systems and cannot be used wirelessly, mobile on a glasses frame [6].

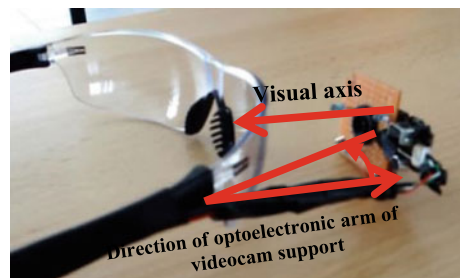
2 Experimental Setup

The experimental system designed to analyze the eyeball oscillatory movements in the convergence-fixation process is based on the use of captured images with a video camera mounted on a special pair of spectacles, and on the processing of images through specialized acquisition and processing software. Also, eyeball motion analysis is performed on the basis of a dynamic nonlinear and predictive model of saccadic system. The study of the control of eye movement and oculomotor disorders was based on theoretical control concepts. This model analyzes the displacements through a set of equations that correlate the velocities and positions of the eye globes, obtained from the quantitative investigations of the physical movements of the eyes. Another aspect as important as defining the analysis model of nystagmus moves determines the set of fixation time ranges, from the initial position to the final position [7] (Fig. 2).

A complementary approach based on the theory of nonlinear dynamic systems, presented in the paper [7], allows development by using a nonlinear dynamical model of the saccadic system, comprising a symmetrical, linear and uniform system consisting of six autonomous differential equations. A first result of the modeling showed that, besides generating the normal saccades, it could also simulate random, oscillating instability.

Therefore, an experimental system that highlights these saccadic movements must allow the acquisition of positional data and the oscillation velocity of the eyeball to

Fig. 2 Optoelectronic device to record ocular movements



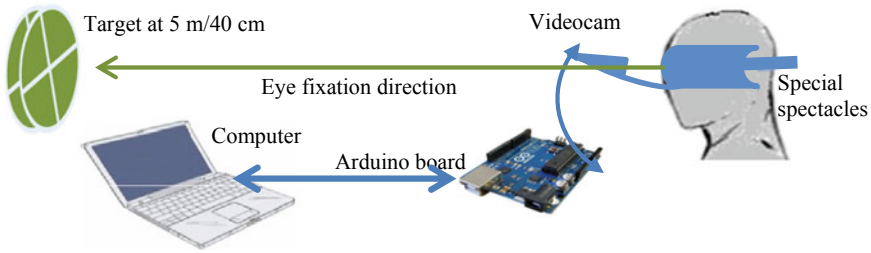


Fig. 3 Experimental setup

model the dynamics of normal jaws and random jaws. This system is made up of an assembly of images based on a autofocus videocam (30 frames/s) and a special eye glasses. The optoelectronic image acquisition system at the eye level, fixed on the right side of spectacles, has the ability to position at different distances (10–15 cm) and angles (0–30°) from the subject visual system axis (see Fig. 3).

3 Results and Conclusions

With this system, macro-eye and micro-eye movements can be tracked when the subject is shown a certain visual behavior (fixation at a fixed point at a distance of 5 m or fixation at a distance of 40 cm in front of it). The subject was every time in the bipedal postural position, with no biomechanical motion in the body, with the hands next to the body and with the convergent visual system, accommodated at the analysis distances (see Fig. 4). The video-captured images of eye movements were processed by image processing and analyzed dimensionally, after calibration procedure (see Fig. 5).

The ideal trajectory taken into account was to perform eyeball movements corresponding to the eight initial analysis positions and without any influences of postural movements. The analysis of horizontal and vertical displacements, as well as the velocity variation graph for a subject without a nystagmus, shows variations of μm , respectively $\mu\text{m/s}$ (see Fig. 6), and the number of micro-oscillations made by the eyeball is approximately 300 for 10.5 s recorded. For a subject with saccade eye movement, variations on both directions are much higher, and the speed chart highlights the peaks of movement in successive saccade. Variations in oscillations of



Fig. 4 Image processing to evaluate eye dimensions

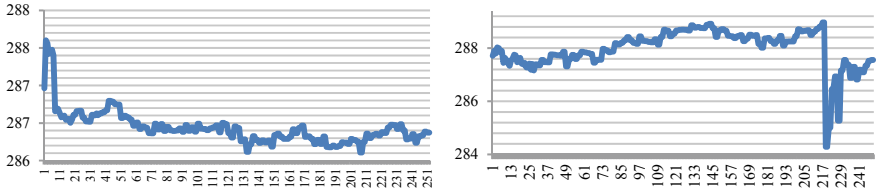


Fig. 5 Displacements [μm] on X-direction without nystagmus (left) and with nystagmus movements (right) (in abscise are no. of samples)

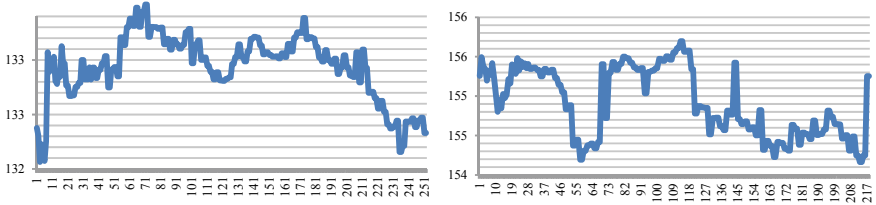


Fig. 6 Displacements [μm] on Y-direction without nystagmus (left) and with nystagmus oscillations (right) (in abscise are no. of samples)

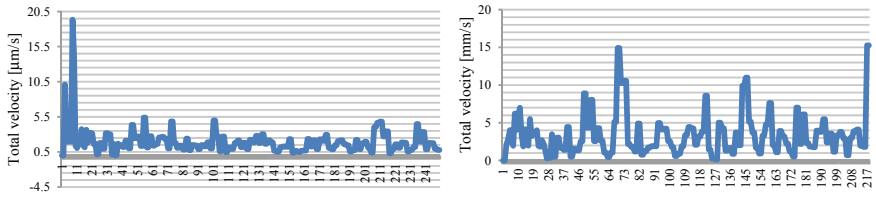


Fig. 7 Total velocity [$\mu\text{m/s}$] measured for eye without nystagmus (left) and with nystagmus oscillations (right) (in abscise are no. of samples)

the nystagmus eye movements exceed with 26% the variation limits in the case of a physiological (functional) nystagmus, values were determined in the same conditions for subjects with and without the emphasis of the saccade movements. These variations may indicate a form of visual stress and may be monitored over longer periods to identify the cause of the oscillations changes in the eyeball and the possibilities to rehabilitation if the saccade movements are only physiological. Immediate applications of this recording system can be developed by taking into account several parameters of the state and functioning of the visual system to track the evolution of nystagmus over time (Fig. 7).

Acknowledgements In these experiments, we have developed the investigations with equipment from *Advanced Mechatronic Systems Research Center—C04* and *Applied optometry Laboratory* at University Transylvania of Brasov, in Ph.D. school Program.

References

1. P. Cernea, Ocular physiology, in *Fiziologie Oculara* (Medicala, 1986)
2. Types of Eye Movements, Applied Vision Research Unit, Institute of Behavior Sciences, <https://lecerveau.mcgill.ca/flash/capsules>
3. Eye Tracking, <https://www.usability.gov/how-to-and-tools/methods/eye-tracking.html>. Accessed 19 February 2019
4. A.E. Robu, *Utilizarea tehnologiei "eye tracking" pentru a măsura interactivitatea online: un cadru teoretic* (Alexandru Ioan Cuza University of Iași, Iași, Romania, 2017)
5. D. Salvucci, J. Goldberg, Identifying fixations and saccades in eye-tracking protocols, in *Proceedings of the Eye Tracking Research and Applications Symposium* (2000), pp. 71–78
6. B. Mihaela, Eye movement analysis system in relation to biomechanical perturbations, in *Proceedings of the 15th International Scientific Conference eLearning and Software for Education Bucharest* (2019)
7. O.E. Akman, D.S. Broomhead, R.V. Abadi, R.A. Clement, Eye movement instabilities and nystagmus can be predicted by a nonlinear dynamics model of the saccadic system, Report, University of Manchester (2005). ISSN 1749-9097
8. R.J. Krauzlis, Eye movements (Chap. 32), *Fundamental Neuroscience*, 4th edn (2013)

Visual Aids Based on Ultrasonic Sensors to Increase Mobility of Patient with Blindness or Low Vision



Mihaela Ioana Baritz and Mirela Gabriela Apostoaie

Abstract Manifestations of ocular pathologies in the visual perception often induce visual impairment, but also discomfort, which motivates the creation of dedicated help. Analyzing the manifestations of different ocular pathologies that occur at birth or with aging, the idea of creating a system for increasing the mobility of patients with low vision or blindness has been outlined. In the first part of the paper, there are presented general aspects related to the changes of the posture and the mobility of the subjects in relation to the decrease of the visual function. In the second part of the paper, there are presented the main aspects of visual aids device designing to increase the mobility of subjects with low vision. These devices are based on ultrasonic sensors to measure distances to the obstacles a patient with blindness or low vision may encounter in his gait or mobility activity for different actions. In the final part of the paper, there are presented the results highlighted in the procedure for evaluating the mobility in gait and the conclusions regarding the method and construction of the devices.

1 Introduction

Low vision status for patients with ocular pathologies may occur over a longer period of time (order of years) or shorter (weekly). This condition is usually painless, but with specific manifestations such as the contrast, the need for more light radiation in the environment, visual field loss, the dramatic decrease in visual acuity, and the poor perception of colors. The condition of blindness is the final phase of evolution in the process of diminishing patient vision and has a very strong behavioral, medical, social, and even an economic impact on their ability to reintegrate and re-adapt to the

M. I. Baritz (✉) · M. G. Apostoaie
Product Design, Mechatronics and Environment Department, Transilvania University Brasov,
B-ul Eroilor Nr. 29, 500036 Brasov, Romania
e-mail: mbaritz@unitbv.ro

M. G. Apostoaie
e-mail: mirela.apostoaie@gmail.com

new situation. The partial or total loss of vision is for patients a loss of up to 80% of the environmental information acquisition capacity, adaptation to the environment based on the other senses that will cover over 20% of the amount of information needed of adaptability.

On the other hand, visual function is considered to be a part of the mechanism of locomotion, therefore, a diminution or loss of the visual system characteristics will cause substantial changes in posture (balance and equilibrium) and walking cycle, respectively. Patients who lose their vision will soon present a multitude of problems related to the mobility of the entire loco-motor system, joint blockages, static equilibrium changes, and the dynamics of activities. At the same time, patients with low vision or blindness accentuate the use of other senses (if not affected) by trying to “transform” the optical information into audio, tactile, smelling, or even tasteful information. In the case of subjects with visual dysfunctions, neural processes are more involved in using the information stored in the long-term memory (if disability is installed at maturity) and correlating them, through much wider connections, with those obtained in real time from other senses. As shown in [1], the sensory substitution is taken up by the regions of the visual sensory cortex and “sensory substitution (SS) is therefore intrinsically cross-modal and has a unique type of cross-modal plasticity between multimodal and uni-modal cortical regions.”

The mechanism of adaptation by substitution of human sensorial features is intended to become a visual aid and recovery method for patients with low vision or blindness and to render their functionalities to the fullest extent possible. This substitution mechanism is naturally developed for patients who acquired low vision or blindness, but at the same time, it can be stimulated to integrate quickly through different constructive forms, but also through the training and rehabilitation procedures that patients can under the guidance and control of the specialist [1].

In some researches on procedures to reinvent the perception of the environment, some patients report intense emotional states (enthusiasm and positive emotions) with physiological changes in the blood circulation system. Most of the time, when describing the perception of objects in the environment, they relate to the status and denomination of view even if the acquisition of information is made on another sensory system [2].

The development of the sensory supportive capacity associated with the increase of the loco-motor abilities through specific training represents the solution for the reintegration of patients with blindness or low vision into activities and social environment, respectively. Through these processes, patients with blindness or low vision are motivated and able to train, recover, or restore sensory perceptions and, through the involvement of more organizations, can reduce the social pressure on the national health system.

2 Theoretical Aspects of Patient Mobility with Low Vision

After losing the ability to perceive information in the environment, the mobility of patients with low vision or blindness is mostly affected and poses a major disadvantage to them in the development of rehabilitation procedures. The cycle of walking, posture, its stability and balance components, other dynamic activities (running, climbing/descending steps) are altered, altered by the lack of the fixation point of the visual system and the binoculars used in the binocular view. Patients with visual impairments require visual aids to improve their posture, gait, or other activities involving the locomotive system, and they are designed and developed each time in relation to anthropometric dimensions and patient needs. In general, continuous adaptation with additional energy and effort to distances or performing dynamic activities was observed in subjects with visual disabilities [3]. As shown in experimental research systems based on “the touch-walking model of human can be described by the following formulas:

$$\begin{cases} J\ddot{\beta} = M + M_d \\ M = K_1 \cdot u_c \\ M_d = -K_2 \cdot \dot{\beta} \end{cases} \quad (1)$$

where J is the moment of inertia of the blind along the yaw axis, M the kinetic moment that the blind applied to himself when turning, M_d damping torque on the yaw degrees of freedom, β the angle of the traveling direction of the blind, u_c the controlled quantity that output by controller, K_1 the scale factor between the kinetic moment and the controlled quantity, K_2 the damping factor” [4]. In this system, the transfer function is computed between the input u_c and output intakes, represented by the angle β of the direction of displacement of the patient and is respectively expressed by the relationship (2) according to the same experimental determinations [4].

$$G(s) = \frac{\beta(s)}{u_c(s)} \quad (2)$$

Also, in order to be able to analyze the data gathered from the registration modules, it is indicated the use of the sigmoid function which presents an important characteristic, especially for studies on the stability of the human body. Thus, the movement of the human body around its equilibrium position can be described by a linear variation, and outside its function the function has a nonlinear argument and a variance that tends exponentially toward a unitary value (see Fig. 1) [5].

The posture of patients with low vision will change from the posture of a person with a good view, but will show a personalized variation in relation to the body mass center (COM), the only difference being the longer duration of the required distance [6]. What is remarkable is the fact that from the experimental research it was

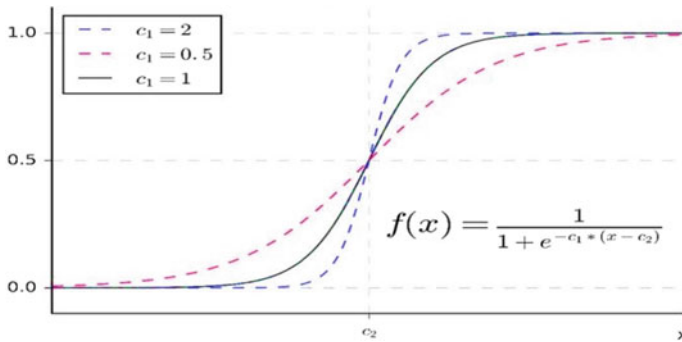


Fig. 1 Basic sigmoid function with two parameters (c_1 and c_2) [5]

found useful the implementation of the sigmoid function, even in these situations of postural changes.

3 Experimental Setup

The experimental system used in this research is based on the construction of sensory modules mounted on the patient's body with low vision or blindness in major areas that are important and easy to handle. Systems so mounted help to guide the patient's movement, to get a tactile and auditory sensory signal to which it has a motor response. Thus, the positioning of sensors is determined by the height of the patient, the type of activity they perform (walking normally or fast, stepping) and, last but not least, the level of visual dysfunction.

Experimental modules are designed to be as easy to use and carry as it will be attached to the subject in two essential points: at the waist, belt, and foot of the subject through a detachable gripping system (see Fig. 2).

Also, the two sensor modules work independently but controlled by the same data acquisition and processing system and solve a problem of orientation and perception of obstacles in the xoz plane. These systems will alert the user if they have an obstacle, from the legs to the hip (and slightly above). The two fastening systems are adjustable for any person and can be worn over any kind of clothing (see Fig. 3). In modular construction, two of the ultrasound sensors (hips and knees) scans the environment and sends signals to the Arduino Uno board, it processes the received data and when an obstacle encounters, and a signal is sent to the buzzer to warn the user.

The third ultrasonic sensor (mounted in the same housing as the knee) detects the presence of the travel surface (within a set distance within the customized parameters), and when it is no longer detected, the buzzer will emit a tone specific to the situation one step is met. The entire system is compact, low weight, ergonomic, and easy to use for patients with low vision or blindness. The system is assembled into

Fig. 2 Positioning sensory modules on the human body [7]

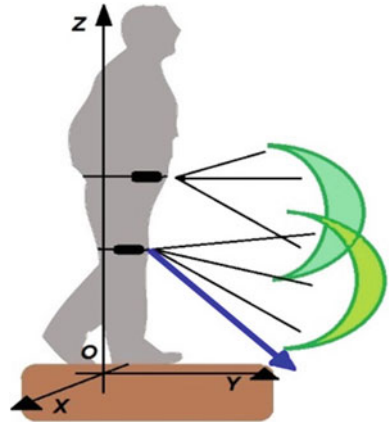


Fig. 3 Using the system on subjects with low vision and blindness simulation [7]

Catia V5 R19 design software and exported to Cura 3.2.1, a 3D printer-compatible software that has built-in housings and caps in a compact system (see Fig. 4).

Fig. 4 Modules construction with the three sensors and buzzer [7]



Table 1 Calibration values of ultrasonic sensors in wearable modules

No. measures	Sensor 1 for 300 cm	Sensor 2 for 100 cm	Sensor 3 for 65 cm
1.	298.723	81.93	64.95
2.	288.911	70.77	64.11
3.	266.801	96.99	65.03
4.	299.404	99.59	66.19
5.	296.093	102.93	65.55
6.	300.423	99.22	65.69

4 Results and Conclusions

The sensors introduced into the portable modules were initially calibrated and checked to obtain a response corresponding to the distance they are intended for (Table 1).

Thus, the three sensors were placed at different distances from the calibration obstacles (corresponding to the anthropometric dimensions used and the type of motor-drive action) and a series of measurements were made to determine the sensing sensitivity of the sensors and the sound response of the sensors them. Sensors indicate specified distances with increasingly precision, taking into account the subjects' ability to interpret sound signals and react [7]. Subjects who tested this device quickly adapted to the lack of information and the test runs became more and more secure on the move, and more certain on the go, even if they encountered obstacles they did not know. At this stage, the device is designed to sense only the fixed obstacles at the heights above the hip and at varying distances on the trajectory of the person with low vision or blindness. In another variant, we will consider the way of differentiation of the two parts (left/right) of movement and also the level of the ambient noise [8].

The device was used in open spaces where there were many other random noises, but the alert signal sounded good. The system in the prototype phase can be improved by adding elements of communication with a smartphone and using a headphone for too intense sound signals.

Acknowledgements In these experiments, we have developed the investigations with equipment from *Advanced Mechatronic Systems Research Center—C04* and *Applied optometry Laboratory* at University Transylvania of Brasov, in Ph.D. school Program.

References

1. N.R.B. Stiles, S. Shimojo, *Sensory Substitution: A New Perceptual Experience*, ed. by J. Wagemans (Oxford Handbook of Perceptual Organization, Oxford University Press, 2018)

2. D.-R. Chebat, V. Harrar, R. Kupers, S. Maidenbaum, A. Amedi, M. Ptito, Sensory substitution and the neural correlates of navigation in blindness, in *Mobility in Visually Impaired People* (Springer International Publishing, AG, 2017)
3. M.S. Sharifi, Analysis and modeling of pedestrian walking behaviors involving individuals with disabilities, Thesis, Utah State University Logan, Utah, 2016
4. W. Tong, Z. Lin, Continuous closed-loop control method based on intelligent adaptive PID algorithm in the walking guidance system for the blind, in *The 6th Annual IEEE International Conference on Cyber Technology in Automation, Control and Intelligent Systems*, Chengdu, China, (2016), pp. 518–523
5. T. Leibovich-Raveh, D.J. Lewis, S.A.-R. Kadhim, D. Ansari, A new method for calculating individual subitizing ranges, Project, The University of Haifa, Israel, 2018
6. T.-N. Nguyen, H.-H. Huynh, J. Meunier, Measurement of human gait symmetry using body surface normals extracted from depth maps. *Sensors* **19**(4), 891 (2019)
7. A. Mirela, B. Mihaela, 3D printing procedure applied in the design of portable devices for visual aid, in *Conference POLCOM*, Bucharest (2018)
8. F. Reynard, P. Terrier, Role of visual input in the control of dynamic balance: variability and instability of gait in treadmill walking while blindfolded. *Exp. Brain Res.* **233**, 1031–1040 (2015)

Numerical Investigation of an Idealized Overlapping Coronary Stents Configuration



Alin Totorean, Iuliana-Claudia Totorean, Sandor Bernad, and Dan Gaita

Abstract Overlapping stents is a common occurrence during percutaneous coronary interventions, the need for multiple stents frequently emerging from the complexity of coronary lesions. Stent overlap has been associated with increased risk for stent thrombosis and restenosis, irrespective of stent type. Altered hemodynamics at the site of overlap has been linked to delayed stent endothelialization, incomplete strut coverage or altered drug distribution, which trigger both thrombosis and restenosis. This paper aims to describe to near-wall flow behavior in case of overlapping stents for an idealized 2D stented coronary model, by analyzing the associated hemodynamic parameters: WSS distribution and recirculation zones and pressure distribution.

1 Introduction

Stent overlap is a relatively frequent technique used during percutaneous coronary interventions (PCI) and stent placement, with up to 30% of the patients that undergo PCI being treated with overlapping stents [1, 2].

Stent overlap has been defined as the use of ≥ 2 stents for a single coronary lesion, with a minimum 1 mm zone with overlapping stent struts. Reasons for using this technique may include: excessive lesion length, incomplete lesion coverage, proximal or distal dissection following stent implantation [1, 2].

A. Totorean

Politehnica University of Timisoara, No 1 Mihai Viteazul Street, 300222 Timisoara, Romania

I.-C. Totorean (✉) · D. Gaita

University of Medicine and Pharmacy Victor Babes Timisoara, No 2 Eftimie Murgu Square, Timisoara, Romania

e-mail: claudia_hudrea@yahoo.com

Cardiology Department, Institute for Cardiovascular Diseases, Timisoara, Romania

S. Bernad

Romanian Academy—Timisoara Branch, No 24 Mihai Viteazul Street, 300223 Timisoara, Romania

© Springer Nature Switzerland AG 2021

N. Herisanu and V. Marinca (eds.), *Acoustics and Vibration of Mechanical*

Structures—AVMS 2019, Springer Proceedings in Physics 251,

https://doi.org/10.1007/978-3-030-54136-1_24

Stent overlap is associated with impaired clinical and angiographic outcomes at follow-up, regardless of stent type and overlap pattern. Stent thrombosis and restenosis rates proved to be higher than in the case of single stent implantation for both bare metal stents (BMS) and drug eluting stents (DES) and studies report the following mechanisms as major determinants: incomplete or delayed endothelialization, incomplete strut coverage, increased vascular injury and inflammation, or stent fracture. The impact of these phenomena translates clinically into increased risk of repeat revascularization, myocardial infarction and even death [1, 2].

Wall Shear Stress (WSS) has been widely recognized as a key factor in both atherogenesis and thrombosis processes [3]. Regions along the arteries walls associated with low WSS are prone to atherosclerotic plaque formation and neointimal hyperplasia leading to in-stent restenosis, whereas high WSS seems to modulate stent thrombosis [3–5].

Investigating the hemodynamic environment within a vascular segment is possible using computational fluid dynamics (CFD) techniques. These methods permit the analysis and description of near-wall flow patterns, WSS distribution, recirculation zones, etc., for either native or stented coronary arteries [3–5].

Previous studies used CFD to investigate the hemodynamics associated with overlapping stents. These studies showed that the regions within the vessel exposed to the overlapping segments are subjected to development of extended recirculation zones, which associate increased size areas of low WSS, compared to the proximal or distal parts of the stents not affected by overlap. These hemodynamic disturbances affect drug distribution, concentration and drug wall uptake for drug eluting stents, delay endothelial healing, promote platelet deposition and chronic inflammation regardless of stent type, and lead to increased risk for either stent thrombosis or in-stent restenosis and lumen loss [6, 7].

The aim of this paper to investigate the near-wall flow behavior in case of overlapping stents for an idealized 2D stented coronary model by analyzing and describing the associated WSS distribution and recirculation zones, but also further hemodynamic parameters like pressure distribution, using CFD.

2 Vascular Model

A 2D idealized coronary artery model was used for the purpose of flow analysis using CFD techniques. Two adjacent stents of $L_{\text{stent } 1} = 22$ mm and $L_{\text{stent } 2} = 12$ mm in length were inserted within the model, with a region with two overlapped struts (Fig. 1). The main characteristics of both coronary model and stents were chosen according to data extracted from the literature.

Details associated with the stent overlapping region are shown in Fig. 2.

The artery diameter D is considered to be 3 mm. The geometrical details associated to the stents are: strut width $w = 100$ μm , strut height $h = 100$ μm and distance between struts is $L_{\text{interstrut}} = 1$ mm.

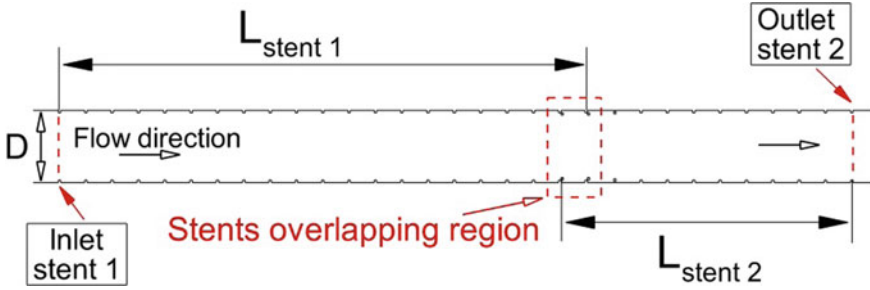


Fig. 1 General view of the 2D idealized stented artery configuration

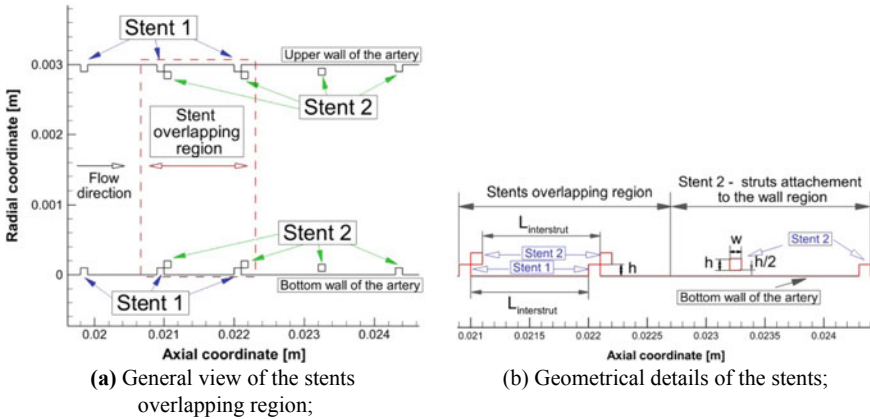


Fig. 2 Geometrical details of the stent overlapping region

The inlet and outlet of the model were extended each with the length $6D$ (equivalent to the length of the diameter multiplied by six times), so that the flow through the stented region, which is the segment of interest, will not be affected.

A structured mesh configuration with 533.856 cells was used.

3 Boundary Conditions

The boundary conditions set in the analysis were:

- Inlet: a real cardiac cycle, described by Banerjee et al. [8] was used as input velocity (Fig. 3);
- Outlet: outlet pressure 0 Pa;
- Walls: rigid, nonslip, considering that vascular stented region suffer very small deformations under cardiac cycle pressure due to the stents rigid conformation;

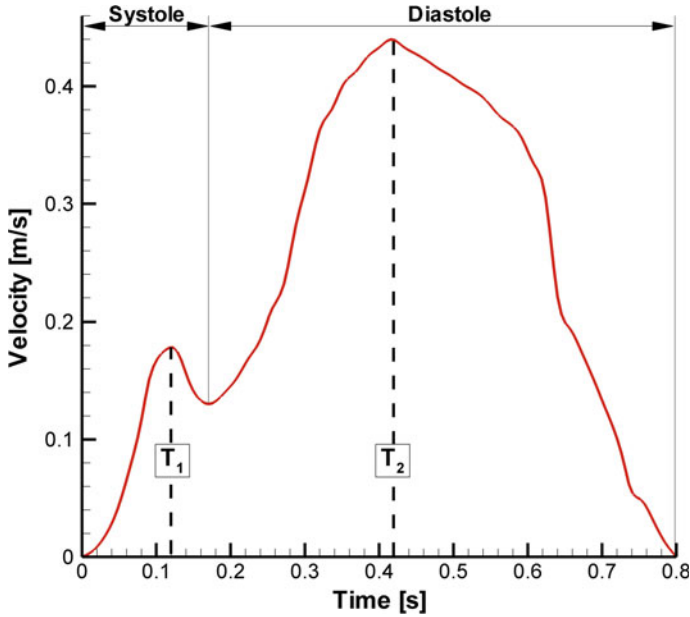


Fig. 3 Cardiac cycle used as inlet velocity [8]

- Fluid is assumed to be homogenous, incompressible, similar to blood, with dynamic viscosity of 0.00368 kg/ms and density of 1050 kg/m^3 . [9]

The physical properties were assumed to remain constant, and the gravitational effects were negligible during the analysis.

The numerical simulation was performed under unsteady-state conditions, considering the k - ω SST turbulence model, using the commercial CFD software Fluent 6.3 [10].

4 Results

For a better understanding of the flow phenomena, we may define the following regions:

- The proximal region of the first stent;
- The stent overlapping region;
- The region with the second stent struts attachment to the wall;
- The distal region of the second stent.

The hemodynamic parameters were analyzed associated with two significant time steps of the cardiac cycle: T_1 associated with the systolic peak and T_2 associated with the diastolic peak.

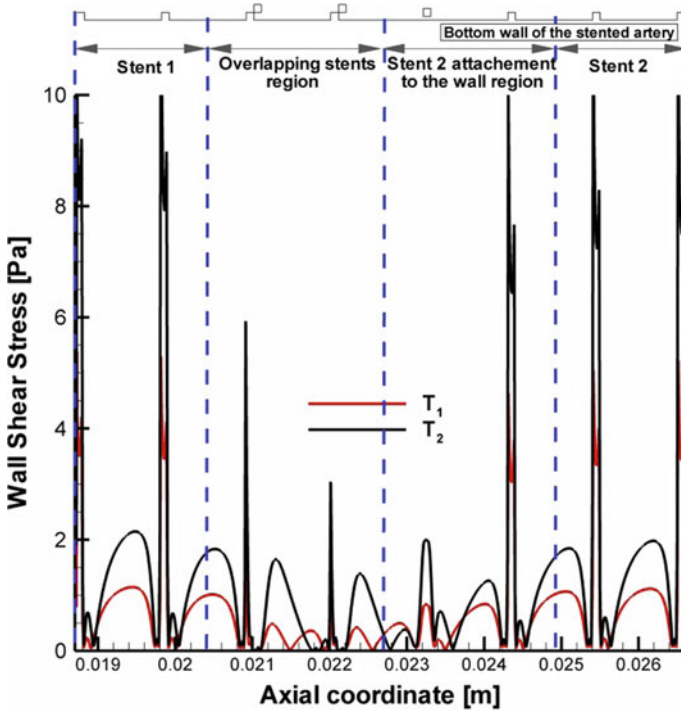


Fig. 4 Wall Shear Stress distribution along the bottom wall of the vascular model associated with the stent overlapping region

Wall Shear Stress (WSS) was computed along the bottom wall of the stent overlapping region (Fig. 4).

High values of WSS are associated with the upper wall of the strut, whereas low values of WSS are associated upstream and downstream of each strut, where recirculation regions develop. The presence of the overlapped struts is characterized by significant decrease of WSS values and larger regions with low WSS downstream each overlapped pair of struts. The variation of WSS along the stented arterial wall is similar in both time steps analyzed, but the highest WSS values are associated with the T_2 diastolic peak time step.

Low values of WSS are associated with recirculation regions, which develop upstream and downstream of each strut, being larger in the overlapping region (Figs. 5 and 6). The length of recirculation regions is higher in case of T_2 time step compared to the T_1 systolic peak.

Pressure distribution along the stented artery centerline is shown in Fig. 7. It can be observed that in the proximal region of the first stent, the pressure is constantly decreasing, whereas in the overlapping region a sudden decrease and a high pressure drop occur, induced by the overlapped struts which act as a resistance to the flow. The pressure suffers a small recovery in the region where the struts of the second stent

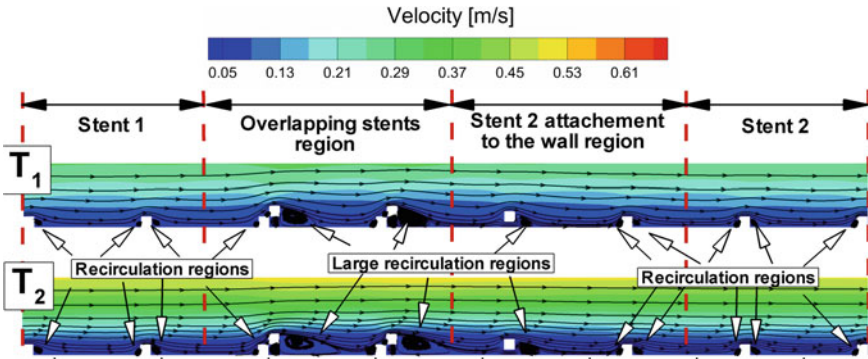


Fig. 5 Velocity field and streamlines representation in the vicinity of the stented arterial wall, associated with the stent overlapped regions for T_1 and T_2 time steps

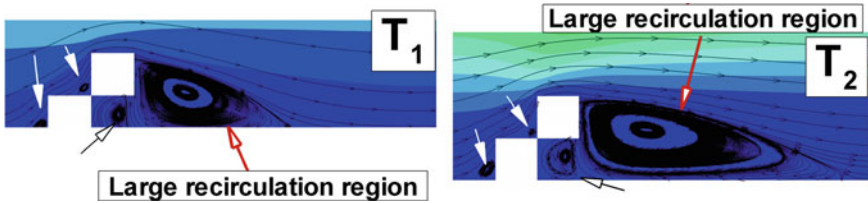
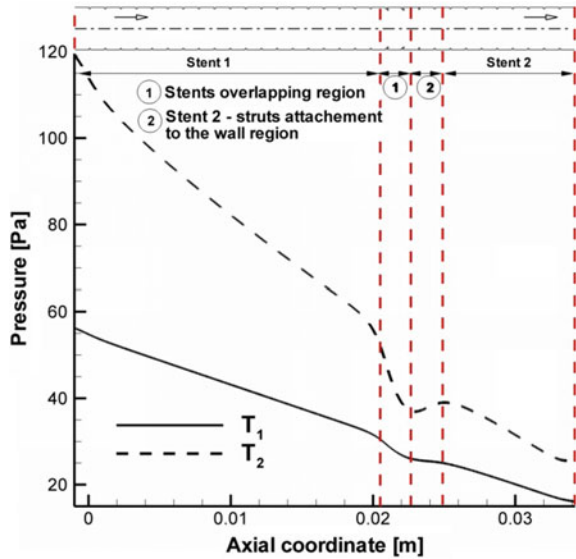


Fig. 6 Streamlines representation and recirculation regions in the vicinity of the first pair of overlapping struts, white arrows showing the multiple recirculation regions, associated with T_1 and T_2 time steps

Fig. 7 Pressure distribution along the stented artery centerline



reattach to the wall, and in the distal part of the second strut, the pressure constantly continues to decrease. The highest values and the most significant variations are associated with the diastolic peak (T_2).

5 Conclusions

Stent overlap leads to important modifications of the hemodynamic parameters and significantly alters the flow in the vicinity of the wall, resulting in extended regions with low WSS, large recirculation regions and high pressure variation. This type of hemodynamic alterations may account for increased risk of stent thrombosis, as previously described in various studies.

This paper has obvious limitations due to the idealized 2D features that do not account for all anatomical and physiological characteristics of a real stented coronary segment, requiring more complex patient-specific 3D model for validation and further analyses. However, these findings enhance the knowledge regarding the impact of overlapping stents on the near-wall hemodynamics and provide useful information that could potentially help improve future stent deployment techniques and stent designs.

References

1. L. Räber, P. Jüni, L. Löffel, S. Wandel, S. Cook, P. Wenaweser, M. Togni, R. Vogel, C. Seiler, F. Eberli, Th. Lüscher, B. Meier, S. Windecker, Impact of stent overlap on angiographic and long-term clinical outcome in patients undergoing drug-eluting stent implantation. *J. Am. Coll. Cardiol.* **55**(12), 1178–1188 (2010)
2. C.J. O’Sullivan, G.G. Stefanini, L. Räber, D. Heg, M. Taniwaki, B. Kalesan, T. Pilgrim, T. Zanchin, A. Moschovitis, L. Büllsfeld, A.A. Khattab, B. Meier, P. Wenaweser, P. Jüni, S. Windecker, Impact of stent overlap on long-term clinical outcomes in patients treated with newer-generation drug-eluting stents. *EuroIntervention* **9**(9), 1076–1084 (2014)
3. N. DePaola, M.A. Gimbrone Jr, P.F. Davies, P.F. Dewey Jr, Vascular endothelium responds to fluid shear stress gradients. *Arterioscler. Thromb.* **12**(11), 1254–7 (1992)
4. J. Ng, Chr. Bourantas, R. Torii, et al., Local hemodynamic forces after stenting implications on restenosis and thrombosis. *Arterioscler. Thromb. Vasc. Biol.* **37**, 2231–2242 (2017)
5. K. Kolandaivelu, R. Swaminathan, W.J. Gibson, V.B. Kolachalama, K.L. Nguyen-Ehrenreich, V.L. Giddings, L. Coleman, G.K. Wong, E.R. Edelman, Stent thrombogenicity early in high-risk interventional settings is driven by stent design and deployment and protected by polymer-drug coatings. *Circulation* **123**, 1400–1409 (2011)
6. F. Rikhtegar, C. Wyss, K.S. Stok, D. Poulidakos, R. Müller, V. Kurtcuoglu, Hemodynamics in coronary arteries with overlapping stents. *J. Biomech.* **47**, 505–511 (2014)
7. F. Rikhtegar, E.R. Edelman, U. Olgac, D. Poulidakos, V. Kurtcuoglu, Drug deposition in coronary arteries with overlapping drug-eluting stents. *J Control Release* **28**(238), 1–9 (2016)

8. R.K. Banerjee, L.H. Back, M.R. Back, Y.I. Cho, Physiological flow simulation in residual human stenoses after coronary angioplasty. *ASME J. Biomech. Eng.* **122**(4), 310–320 (2000)
9. I.C. Hudrea, A.F. Totorean, D. Gaita, Computational fluid dynamics analysis of coronary stent malapposition, in *IFMBE Proceedings 68/1* (2019)
10. FLUENT 6.3 User's Guide, ANSYS-Fluent Incorporated (2006)

Biomechanical Evaluation of Medical Rehabilitation for a Patient with Ankle Fracture



Madalina Lupsa, Alin Totorean, Dan Ioan Stoia, and Alina Totorean

Abstract Ankle fracture is one of the most common fractures of the lower limb having as effect changes of equilibrium, stability and joint mobility. The total recovery of the patient is quite difficult to achieve, but the results may be favorable as long as the therapeutically rehabilitation plan is followed. The efficiency of kinetherapeutic recovery procedures applied to a patient with ankle fracture could be evaluated by analyzing the plantar pressure distribution and kinematic parameters associated with the patient's gait cycle using experimental techniques. Correlating the plantar pressure and the angles associated to the ankle joint, the biomechanical efficiency of the recovery plan applied to the patient is assessed. As soon as the recovery plan is completed, the affected ankle mobility is recovered, plantar loading is relatively similar for both feet, and the kinematic parameters of the affected joint improved, compared to the results associated with the first steps of the recovery period.

1 Introduction

Ankle joint is responsible for maintaining body balance and posture during both static and dynamic activities [1]. At the level of the ankle joint, movements of the plantar and dorsal flexion of the foot are performed. The lateral mobility of the ankle has the role of helping us to walk on uneven surfaces and maintain balance in a complex range of movements (such as walking, running, jumping) [2].

The most common diseases that occur in the ankle are: sprains, fractures, gout, septic arthritis, psoriatic arthritis, ankle arthritis, rheumatoid arthritis. Ankle fracture

M. Lupsa · A. Totorean (✉) · D. I. Stoia
Politehnica University of Timisoara Romania, No 1 Mihai Viteazul Street, 300222 Timisoara,
Romania
e-mail: alin.totorean@upt.ro

A. Totorean
University of Medicine and Pharmacy “Victor Babes”, No 2 Eftimie Murgu Square, 300041
Timisoara, Romania

© Springer Nature Switzerland AG 2021

N. Herisanu and V. Marinca (eds.), *Acoustics and Vibration of Mechanical Structures—AVMS 2019*, Springer Proceedings in Physics 251,
https://doi.org/10.1007/978-3-030-54136-1_25

259

is one of the most common fractures of the lower limb in adult population. The most common causes of malleolus fracture are: twisting, kinking or ankle rotation (over the joint), accidents which have an impact on the ankle [3].

The total recovery of the patient and the return to the normal functioning level before the lesion are quite difficult to achieve, but the results may be favorable as long as the principles of recovery are respected [4, 5].

Depending on the location of the fracture line at the malleolus, the ankle fractures can be classified as incomplete and complete fractures. Complete fractures may have a traverse, an oblique trajectory, a spiroid tract or a longitudinal tract. An incomplete fracture occurs when the bone bends and crack but does not completely break. They may be in the form of a greenstick fracture, with clogging, trabecular ruptures. Depending on the location and the severity of the fracture, the treatment of ankle fractures can be surgical, consisting in immobilizing the segment by surgically implanting plaques, rods or conservatory by applying the gypsum immobilization. In the case of gypsum immobilization, the callus formation and bone consolidation may take between 4 and 6 weeks, while the affected lower limb weight-bearing is progressive [6–8].

Once the orthopedic treatment was applied, the most important aspect of patient recovery is medical recovery initiation as soon as possible. The recovery therapy is followed in order to combat inflammation and pain, restore joint mobility, restore balance and joint stability, restore the planting vault (if necessary), restore the leg alignment, gain a correct attitude of the affected body and affected limb [8].

The aim of this paper is to evaluate the efficiency of kinetotherapeutic recovery procedures applied to a patient with malleolus fracture, by using experimental techniques for biomechanical investigation of plantar pressure and kinematic parameters associated with the patient's walking cycle.

2 Materials and Methods

The patient investigated in this study is a 51-year-old female with the following diagnosis: comminuted fracture with displacement and intra-articular tracheal right jaw, minimal right fractured malleolus fracture. After medical imaging investigations (Fig. 1), gypsum immobilization was recommended for 6 weeks.

The medical rehabilitation started after the gypsum was removed, and it included physiotherapy procedures (TENS, iontophoresis with Ca chloride and iontophoresis procedure with dexamethasone) and physical therapy procedures [9, 10].

Physical therapy procedures were performed to recover the affected segment, swollen, tonus and muscle strength, improving coordination, fighting redness and muscle contractions, and increasing the amplitude of the movement [8].

The rehabilitation protocol with respect to the ankle fracture treatment guidelines was followed, and it consisted in:

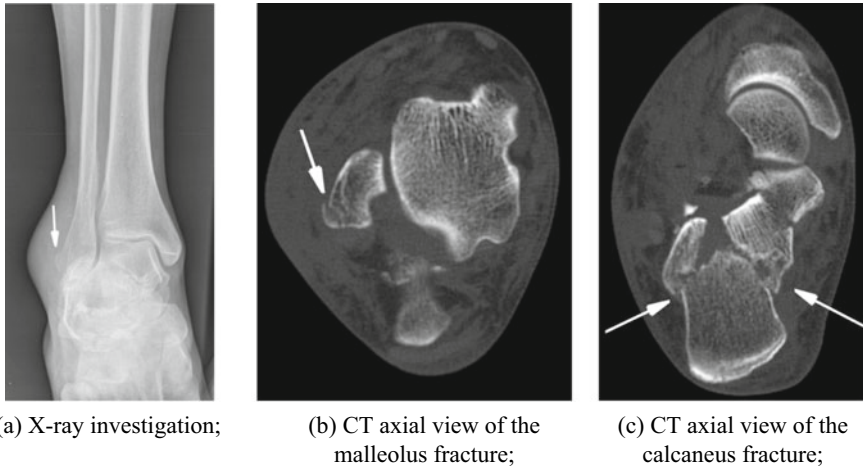


Fig. 1 Medical investigations (X-ray and CT scans) showing with white arrows the fracture lines

- Phase 1 (weeks 0–6) the initial phase: isometric exercises, frame exercises, crutches, lifting movements of the lower limb;
- Phase 2 (weeks 6–8) mobilization exercises phase: exercises of plantar flexion, dorsal flexion, inversion, eversion, muscle strengthening exercises, weight loading, bicycle, transition to the baton;
- Phase 3 (starting from the 8th week): toning program, strength, proprioceptive exercises phase, bilateral, semi-wedge, stretching, unilateral balancing exercises [11].

To evaluate the efficiency of the medical rehabilitation plan, two experimental measurements were performed at different time-steps during the recovery period:

- The first was performed at the week 8, when the patient started to walk unassisted by other device,
- The second was performed at the end of the rehabilitation period.

The experimental measurements were performed using the Zebris pressure sensor platform and the Zebris motion analysis system. The parameters considered for evaluation were the plantar pressure (foot loading) and kinematic parameters associated with the gait cycle (ankle flexion and foot rotation angles) [11–15].

The Zebris pressure sensor platform was used to assess the loading associated to both feet, patient being in orthostatic position. Five trials for stance balance were performed for each of the two measurements.

The Zebris motion analysis system was used to assess the kinematic parameters associated with gait cycle. Patient was placed between two ultrasound emitters, and anatomical landmarks were positioned on the lower limbs as described in Fig. 2. The equipment registered the kinematical parameters associated with gait cycle while patient walked between the ultrasound emitters. Five trials consisting in 4–5 steps

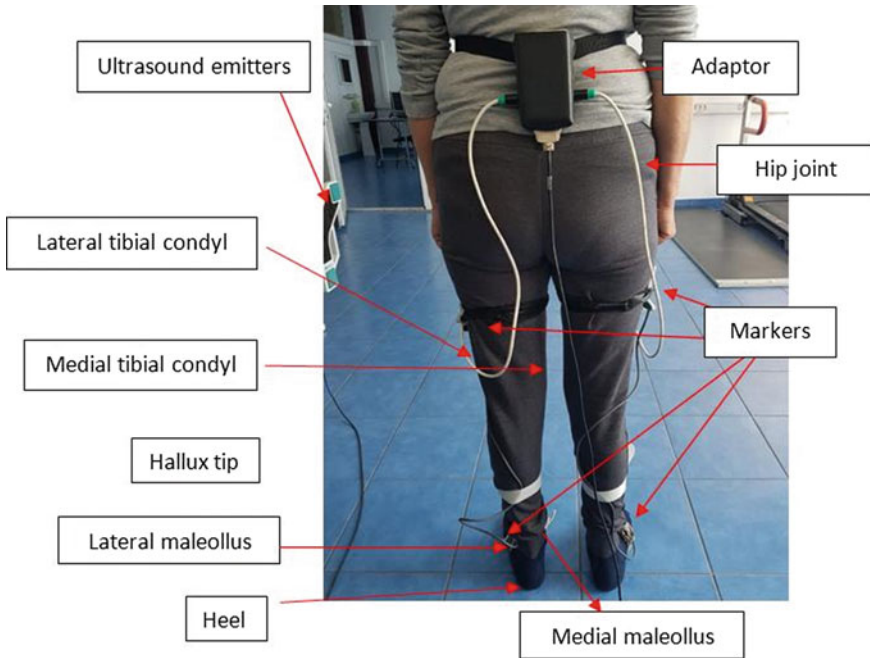


Fig. 2 General view of the experimental setup and landmark position

were performed for each measurement session. The recording system sample rate was set to 25 Hz, a sufficiently high frequency for the patient’s condition and velocity [15].

The kinematical parameters (ankle flexion and foot rotation angles) were recorded as described in Fig. 3 [15].

3 Results

Plantar pressure measurements associated with stance analysis were performed, and foot loading data were processed, as described in Table 1.

At week 8, the foot loading was 72% associated with the left foot, whereas the right foot was only 28% loaded. At the end of the rehabilitation period, the right foot loading improved to the value of 42% being relatively close to the value associated with the left foot.

Right ankle flexion angles during a gait cycle were recorded, as shown in Fig. 4. Low values of the flexion angle are associated with the stance gait cycle phase, whereas the swing phase is characterized by high values. It can be observed that during the first measurement, the values are lower than those corresponding to the end of the rehabilitation period, showing that the ankle joint mobility improved and

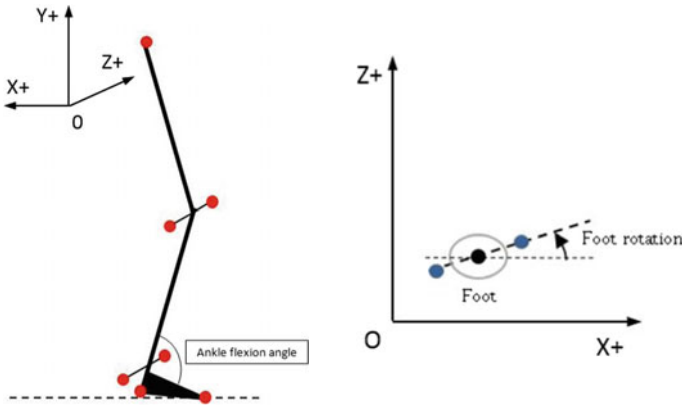
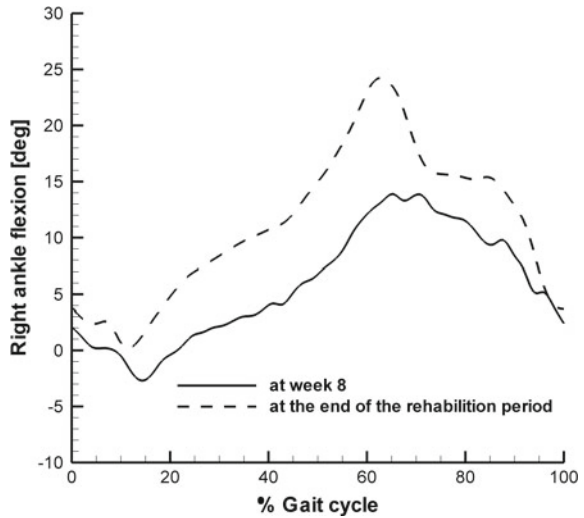


Fig. 3 Kinematical parameters representation: **left** the scheme of the upper limb with the markers' positions and the ankle flexion angle, **right** the general view of the foot rotation angle

Table 1 Foot loading associated with stance analysis

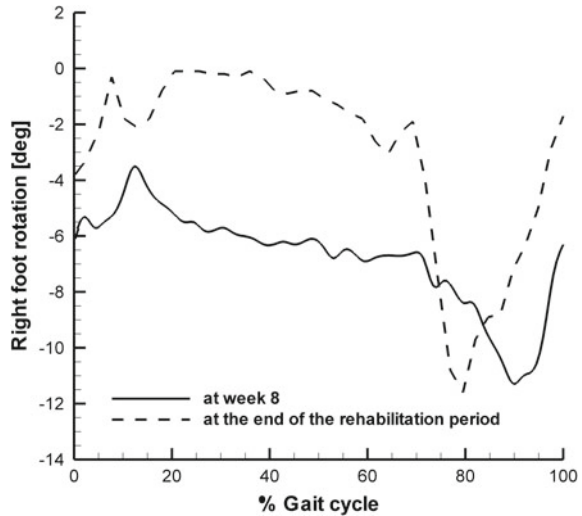
	Left foot	Right foot
At week 8 (%)	72	28
At the end of the rehabilitation period (%)	58	42

Fig. 4 Right ankle flexion angles variation along a gait cycle measured at week 8 and at the end of the rehabilitation period



the amplitude of the movements increased. Figure 4 presents consecutive constant values that could be associated with the stance phase to patient's hesitation due to joint mobility limitation and pain.

Fig. 5 Right foot rotation angles variation along a gait cycle measured at week 8 and at the end of the rehabilitation period



The right foot rotation angles are represented in Fig. 5, showing that the highest values were recorded at the time step associated with the end of the rehabilitation period. The amplitude differences are associated with a higher range of motion for this joint. Also, a higher walking frequency recorded at the end of the rehabilitation period proves the confidence of the patient in her lower limb.

4 Conclusions

Patient with ankle conditions undergoing medical rehabilitation procedures could be biomechanically evaluated by analyzing the kinematical parameters associated with the ankle joint region, such as ankle flexion and foot rotation. The results shown in this paper are particularly associated with a patient with ankle fracture who followed the medical rehabilitation procedures for more than 8 weeks.

The recovery plan improved the joint mobility and increased the ankle flexion and foot rotation angles which are approximately in accordance to those presented in literature [16]. This paper does not intend to show general results and conclusions associated with ankle joint fracture, but aims to particularly describe the measured biomechanical parameters associated with one patient with specific conditions. On the other hand, the results may be influenced by the patient measurements' daily behavior due to pain level or other subjective and individual situations patient may had encountered through the medical rehabilitation period which were not taken into consideration in this paper.

References

1. M. Tile, Fractures of the ankle, in *The Rationale of Operative Fracture Care*, 3rd edn., ed. by J. Schatzker, M. Tile (Springer, Berlin, 2005), pp. 551–590
2. P. Golanó, M. Dalmau-Pastor, J. Vega, J.P. Batista, Anatomy of the ankle, in *The ankle in Football*, 1st edn. (Springer, Paris, 2014)
3. H. Juto, H. Nilsson, P. Morberg, Epidemiology of adult ankle fractures: 1756 cases identified in Norrbotten County during 2009–2013 and classified according to AO/OTA. *BMC Musculoskelet. Disord.* **19**(1), 441 (2018)
4. A.M. Moseley, P.R. Beckenkamp, M. Haas, R.D. Herbert, C.W. Lin, EXACT team: rehabilitation after immobilization for ankle fracture: the EXACT randomised clinical trial. *JAMA* **314**(13), 1376–1385 (2015)
5. P. Yufit, D. Seligson, Malleolar ankle fractures, a guide to evaluation and treatment. *Orthop. Trauma* **24**(4), 286–297 (2010)
6. V. Lampridis, N. Gougoulias, A. Sakellariou, Stability in ankle fractures: diagnosis and treatment. *EFORT Open Rev.* **3**(5), 294–303 (2018)
7. A. Totorean, O. Suciu, R. Onofrei, A. Nita, Functional assessment in posttraumatic ankle osteoarthritis. *Osteoporos. Int.* **25**, S419–S419 (2014)
8. C. Lin, N. Donkers, K. Refshauge, P.R. Beckenkamp, K. Khera, A.M. Moseley, Rehabilitation for ankle fractures in adults. *Cochrane Database Syst. Rev.* **11**, CD005595 (2014)
9. K.A. Suka, D. Walsh, Transcutaneous electrical nerve stimulation: Basic science mechanisms and clinical effectiveness. *J. Pain* **4**(3), 109–121 (2003)
10. A. Joshi, G. Stagni, A. Cleary, K. Patel, D.S. Weiss, M. Hagins, Iontophoresis successfully delivers dexamethasone sodium phosphate to dermis as measured by microdialysis. *J. Pharm. Sci.* **103**(1), 191–196 (2014)
11. J.K. Lowry, *Ankle Fracture Treatment Guidelines* (Arlington Orthopedic Associates, 2012)
12. A.H.A. Razak, A. Zayegh, R.K. Begg, Y. Wahab, Foot plantar pressure measurement system: a review. *Sensors (Basel)* **12**(7), 9884–9912 (2012)
13. S. Aminiaghdam, R. Blickhan, R. Muller, C. Rode, Posture alteration as a measure to accommodate uneven ground in able-bodied gait. *PLoS ONE* **12**(12), e0190135 (2012)
14. I. Hetsroni, M. Nyska, D. Ben-Sira, Y. Arnson, C. Buksbaum, E. Aliev, G. Mann, S. Massarwe, G. Rozenfeld, M. Ayalon, Analysis of foot and ankle kinematics after operative reduction of high-grade intra-articular fractures of the calcaneus. *J. Trauma-injury Infect. Crit. Care* **70**(5), 1234–1240 (2011)
15. D.I. Stoia, C. Vigar, L. Rusu, Relative and absolute angles computed from pathologic gait data. *Springer Proc. Phys.* **198**, 201–206 (2018)
16. J. Dichary, Kinematics and kinetics of gait: from lab to clinic. *Clin. Sports Med.* **29**(3), 347–364 (2010)

New Medical Rehabilitation System



**Cristian-Gabriel Alionte, Daniel-Constantin Comeagă,
and Liviu-Marian Ungureanu**

Abstract In the paper, a new type of a rehabilitation system for knee and ankle is represented that integrates a vibration system which allows a faster recovery and has a beneficial action on the bones, muscle and nerves, which is a well-known treatment. The system will be used as an ambulatory system for home use and must be cheaper and easy to manufacture. The system has a special design using tubes connected hydraulically. Two main possibilities were considered to transmit the vibration to the leg. The first is based on filling the tubes with a liquid, and using vibration transmission through liquid the vibration energy is transmitted to an elastic part of the frame, supporting the leg. The second method is using a vibration-exciting additional device, using an electrodynamic exciter to transmit the vibration.

1 Introduction

There are numerous experimental evidences made on both animal models and people demonstrating that mechanical vibrations increase the regenerative potential of muscle tissue [1–3].

In this paper, we present a new medical rehabilitation system for knee and ankle in which we can integrate a vibration system, at the final element, that is designed to shorten the time of recovery of users or for other medical purposes. This system is mobile and can be used both outdoor and in personal dwellings. Numerous medical clinical trials [4–7] have shown that the inclusion of vibrations in the process of medical recovery shorts the period of rehabilitation, but their vast majority is focused

C.-G. Alionte · D.-C. Comeagă

Mechatronics and Precision Mechanics Department, University Politehnica of Bucharest, Splaiul Independentei, No.313, 060042 Bucharest, Romania

L.-M. Ungureanu (✉)

Theory of Mechanisms and Robots Department, University Politehnica of Bucharest, Splaiul Independentei, No.313, 060042 Bucharest, Romania

e-mail: ungureanu.liviu.marian@gmail.com

© Springer Nature Switzerland AG 2021

N. Herisanu and V. Marinca (eds.), *Acoustics and Vibration of Mechanical*

Structures—AVMS 2019, Springer Proceedings in Physics 251,

https://doi.org/10.1007/978-3-030-54136-1_26

Table 1 Values of the vibration frequency and applications [10]

Frequency (Hz)	Target
30–50	Muscle relaxation
50	Delayed onset muscle soreness
80–100	Improvement of proprioception
100	Pyramidal spasticity
120	Muscle relaxation
100–120	Pain
200	Strengthening of slow muscle fibers
300	Strengthening of fast muscle fibers

on the inclusion of the entire whole-body vibration (WBV), and the studies are not focused on a particular zone on the human lower limb.

The first vibration system proposed is located within the mechanical structure either by introducing liquid into the structure or by placing a system of excitation at the level of the calf or sole. Performing dynamic combined exercises with vibration compared to the static position exercises could be beneficial for the musculature.

The combined vibrations and the movement of the lower limb offered by the new medical recovery system can help the stimulation of the local muscle mass or can have other purposes as can be seen in Table 1. Information on vibration frequency and amplitude for the whole-body vibration has also been analyzed in more clinical studies and applications in treating various health problems [8–12].

2 First Version of the Medical Rehabilitation System

The first system has three control independent systems, as can be seen in Fig. 1a:

1. system 1 for tibia and fibula support which will have a rotation on the knee zone (D, C, B frame);

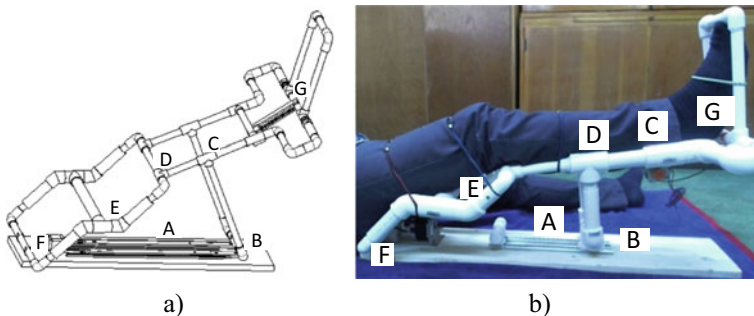


Fig. 1 First version of the medical rehabilitation system: **a** 3D model; **b** physical prototype

2. system 2 for forefoot support which will have a rotation on the ankle zone (G frame);
3. system 3 for vibration excitation of the muscles, especially for forefoot (on G frame).

The first system consists of one stepper motor, which is moving through a belt a frame on which the leg is fastened. The motor is a stepper one, so the control is very easy to implement.

The motion is transmitted to an L-frame, which has a linear guide on the bottom and is connected on a parallelogram system in the upper part. Also, this frame is sustaining the system 2 which only has a rotational movement of the patient foot. The movement is generated using a second stepper motor.

The simulation software is using the D'Alemberts principle, and considering a continuous structure with a discretization in finite elements the analysis considers the equation function of time, t [13]:

$$M \cdot \ddot{u} + C \cdot \dot{u} + K \cdot u = f(t) \tag{1}$$

where

- M is the structural mass,
- C is the damping,
- K is the stiffness matrices,
- u is the vector of displacement,
- \dot{u} is the vector of velocity,
- \ddot{u} is the vector of acceleration,
- $f(t)$ is the vector of applied forces.

All the parameters which are necessary for the simulation have been obtained from the 3D model using an automated mixed meshing with 74,807 nodes and 38,507 elements where each element is tetrahedral and considering as material DuPont Delrin 127UV NC010 which is acetal resin and the structure is filled with water [15].

Using a 3D simulation software, we focus on the forefoot frame, we have analyzed the modal behavior, and we obtain the frequencies of the first four deformation modes, as can be seen in Fig. 2 which has low frequencies because the material and the structure geometry introduce a high stiffness, and the forefoot frame is filled with water. Also, the solver used Direct Sparse solver has the tendency to over-stiffen the model, resulting extremely low-frequency values.

The kinematic model and the vibration analyses were made in other papers and permit us to conclude that the structure has some advantages: It is cheap and easy to build, and it is portable and has a very low natural frequency. But it has some disadvantages, it is not stable, and the motion of the tibia frame is very slow. Therefore, we analyze a second system which is made from steel and has fewer elements.

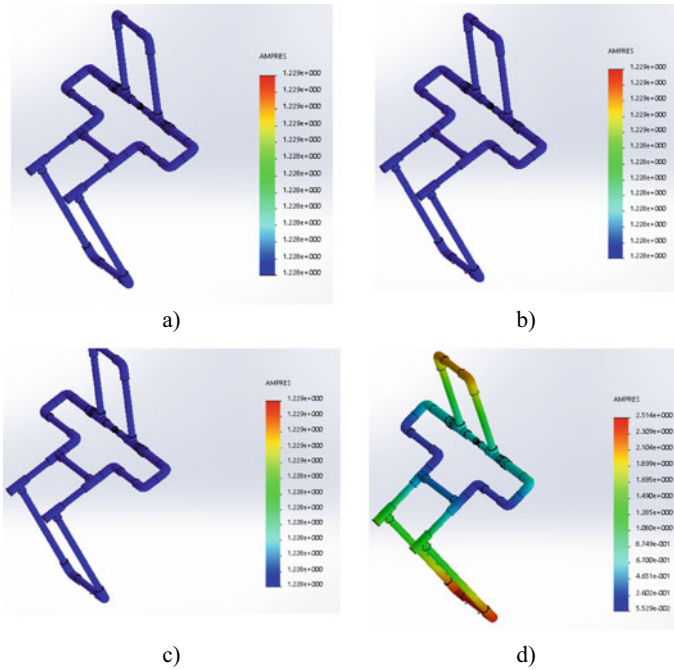


Fig. 2 Modal analysis of the first system: **a** first deformation shape frequency—1.2 Hz; **b** second deformation shape frequency—40 Hz; **c** third deformation shape frequency—58.94 Hz; **d** fourth deformation shape frequency—69.51 Hz

3 Second Version of the Medical Rehabilitation System

The second system is simpler than first system and is made only with six elements and seven joints, as can be seen in Fig. 3.

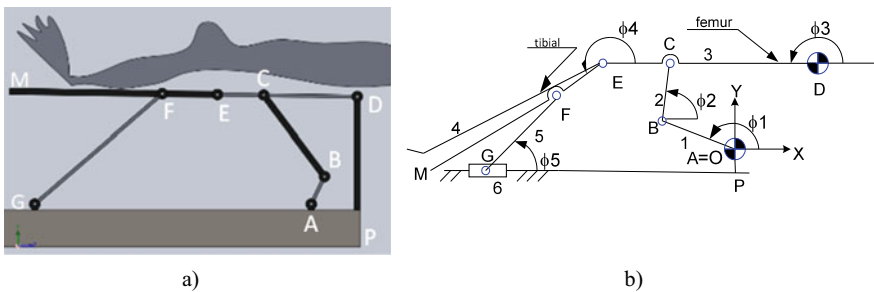


Fig. 3 Second version of the medical rehabilitation system: **a** 3D model of the second system; **b** kinematic model analysis of the second system

From a structural point of view, the rehabilitation mechanism consists of six movable elements and one element fixed (respectively 7), with four rotations and one translation. We applied the (2) for calculating mobility

$$M = 6n - \sum_{m=1}^5 m * C_m \tag{2}$$

where

- n represents the number of mobile elements,
- C_m is the number of pair elements,
- m is the number of constraints.

The degree of mobility is (2) and highlights the number of independent elements that define the status parameters of the mechanism. We will consider two distinct solutions, one where the elements (3) and (4) are parallel and another solution when we have a knee rotation in point E .

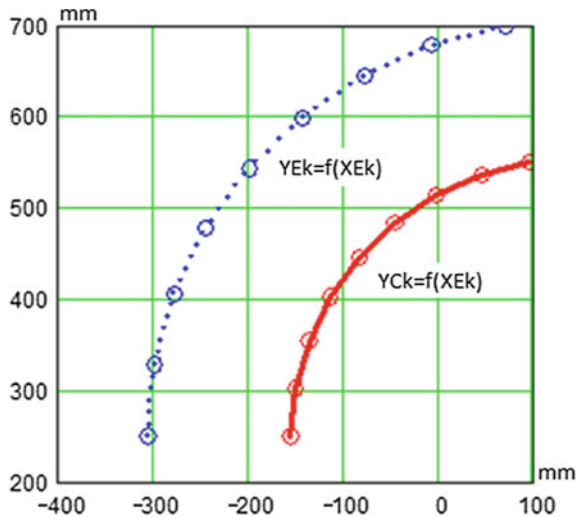
The contour equalization can be rewritten using Fig. 3b:

$$\overline{AB} + \overline{BC} + \overline{CD} + \overline{DA} = 0 \tag{3}$$

$$\overline{AB} + \overline{BC} + \overline{CE} + \overline{EF} + \overline{FG} = \overline{AP} + \overline{PG} \tag{4}$$

We used the software SciLab to model the system, considering numerical approach where each step k means time in seconds and we obtain the displacement of point E , which correspond with the knee joint (presented in Fig. 4).

Fig. 4 Displacement of the elements in point C and E for vertical displacement (mm) in function of horizontal displacement (mm) for each step k (s)



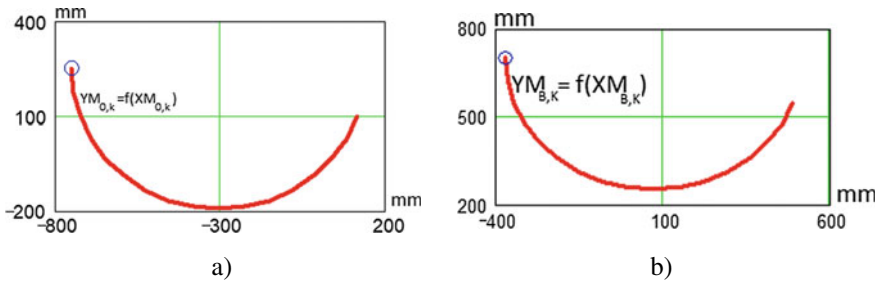


Fig. 5 Displacement of the elements in point *M* for vertical displacement (mm) in function of horizontal displacement (mm) for each step *k* (sec): **a** at the minimum position of *G*; **b** at the maximum position *G*

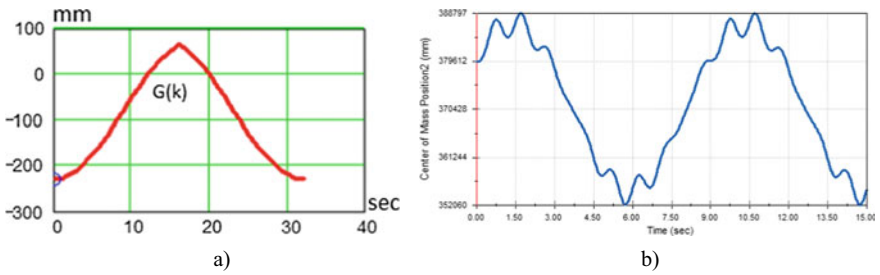


Fig. 6 Displacement of the final element where the leg is fastened: **a** calculation result for vertical displacement (mm) in function of horizontal displacement (mm) for each step *k* (s); **b** 3D simulation result

If in (3) and (4) we consider the projections on the *X*-axes and *Y*-axes, we obtain the displacement of the point *M*. This point has the rotation in joint *E*, where the knee is positioned (presented in Fig. 5) and has a maximum or a minimum curve according to the displacement of the leg frame *G* for each step *k* (presented in Fig. 6a).

We also made a simulation in the 3D software, presented in Fig. 6b where we can see that at the peaks the form is not ideal as in Fig. 6a because of the clearances in joints.

Using the same 3D simulation software, as in the case of the first system, we focus on the tibia frame, we have analyzed the modal behavior, and we obtain the frequencies of the first four deformation modes, as can be seen in Fig. 7. We consider that the tibia frame is filled with water. On the tibia frame, we consider a bar for the forefoot which transmits the vibration of the system.

In the last analyses, we wanted to test the system behavior at a sinusoidal load of 10 N placed on the direction of the tibia element as the vibration system will have action (Fig. 8). Also, considering a static load of 100 N working perpendicularly on the tibia element, we obtain the results presented in Fig. 9. The deformations are small, and we can say that the system will resist on this mechanical stress.

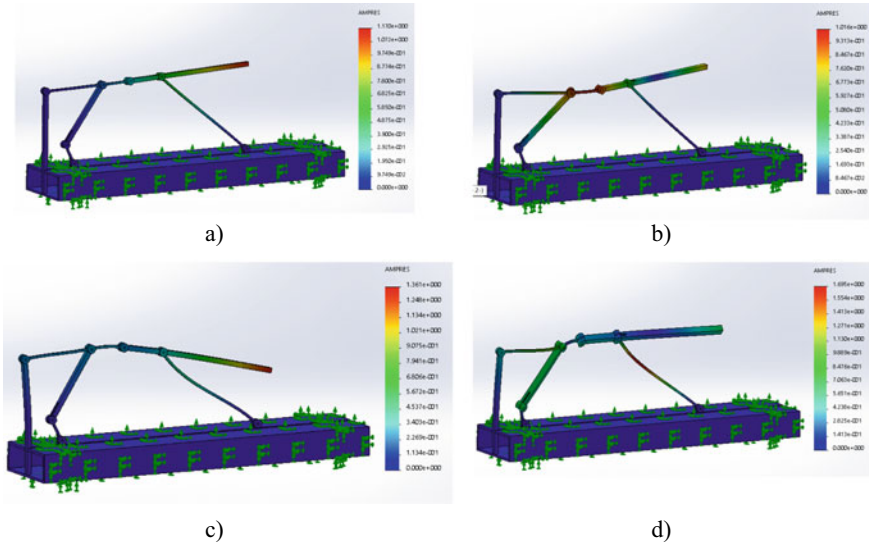


Fig. 7 Modal analysis of the first system: **a** first deformation shape frequency—5.7839 Hz; **b** second deformation shape frequency—17.966 Hz; **c** third deformation shape frequency—23.329 Hz; **d** fourth deformation shape frequency—75.955 Hz

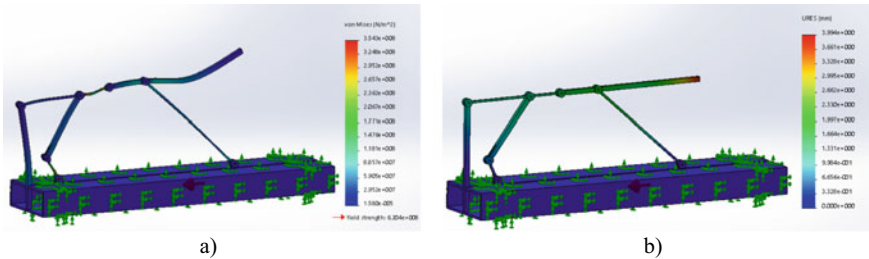


Fig. 8 Dynamic analysis of the second model: **a** mechanical stress; **b** mechanical deformation

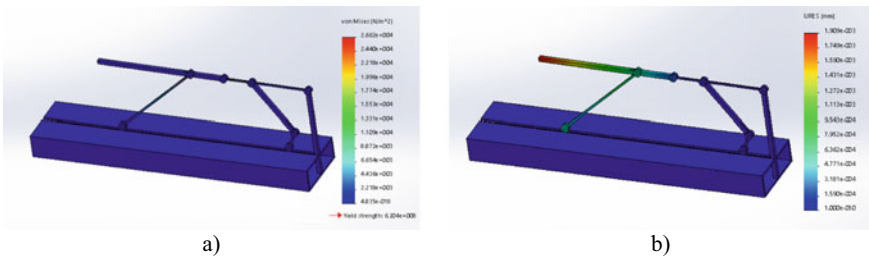


Fig. 9 Static analysis of the second model: **a** mechanical stress; **b** mechanical displacement

All the parameters, which are necessary for the simulation, have been obtained from the 3D model using an automated mixed meshing with 23,974 nodes and 11,984 elements each types of elements are tetrahedral.

4 Excitation Systems

We imagine two kinds of systems; one is hydraulic and the second is electrical. The first is based on a membrane which transmits the vibration generated by a piezo fastened on the membrane to a liquid. As can be seen in Fig. 10, the vibration is transmitted by liquid using flexible conducts to an end element which can be formed by using a foam and injected into a hole made in forefoot frame (the first version of the rehabilitation system) ore in tibia element (second version of the rehabilitation system).

This system has the advantage that the vibration can be placed on any location on the frames or on the elements, does not add any mass, the mechanical load is distributed, but it is too complex to be analyzed in this paper.

The second system is much simpler and consists of a DC motor, a ball bearing and a system to connect to the element of the system. The disadvantage is that a mass is added to the fastened element and is modifying the vibration mode. The vibration is generated by the following [14]:

- fundamental train frequency— ftf

$$ftf = f \cdot \frac{1}{2} \left(1 - \frac{D_b}{D_m} \cos \theta \right) \tag{5}$$

- ball passing frequency inner race— fir

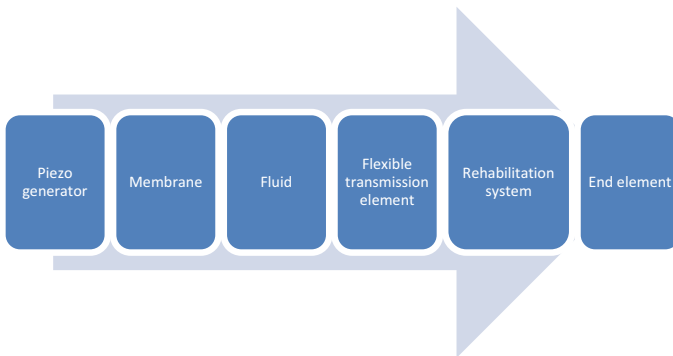


Fig. 10 Principle of vibration generation and transmission of the vibration

$$f_{ir} = f \cdot \frac{Z}{2} \left(1 + \frac{D_b}{D_m} \cos \theta \right) \quad (6)$$

- ball passing frequency outer race— f_o

$$f_o = f \cdot \frac{Z}{2} \left(1 - \frac{D_b}{D_m} \cos \theta \right) \quad (7)$$

- ball spin frequency— f_s

$$f_s = f \cdot \frac{D_m}{2D_b} \left[1 - \left(\frac{D_b}{D_m} \cos \theta \right)^2 \right] \quad (8)$$

In (5–8), we used the following annotation:

f is the rotation frequency of the shaft,

Z is the number of balls,

θ is the contact angle,

D_m is the pitch diameter (the average diameter of the bearing), and

D_b is the balls diameter.

In conclusion, the biggest advantage in our case is that the control of the vibration is much simpler because it's has only the DC motor speed as variable.

5 Conclusion

We presented in this paper two versions of a rehabilitation system with two kinds of vibration generation systems: one hydraulic and electrical. The first version is simply to build cheap, but it is very slow, the second one is made from steel bars, is simpler than the first one but it is more expensive. Both systems are reliable and resist up to 100 N.

References

1. J. Bush, G. Blog, J. Kang, A. Faigenbaum, N. Ratamess, The effects of quadriceps strength following static and dynamic whole body vibration exercise. *J. Strength Conditioning Res.* **29**(5), 1367–1377 (2015)
2. C. Mustafa, B. Ceyhun, Y. Sertac, S. Turker, A. Cihan, Effects of whole body vibration training on isokinetic muscular performance, pain, function, and quality of life in female patients with patellofemoral pain: a randomized controlled trial. *J. Musculoskelet. Neuronal. Interact.* **18**(4), 473–484 (2018)

3. A. Hernández-Vicente, A. Santos-Lozano, R. Bailón, C. Mayolas-Pi, P.J. Marín, N. Garatachea, Effects of the type of exercise performed on the vibration delivered during whole-body vibration exercises. *J. VibroEng.* **20**(3), 1522–1529 (2018)
4. M. Stania, P. Król, G. Sobota, A. Polak, B. Bacik, G. Juras, The effect of the training with the different combinations of frequency and peak-to-peak vibration displacement of whole-body vibration on the strength of knee flexors and extensors. *Biol. Sport J.* **34**(2), 127–136 (2017)
5. S.S. Colson, S. Roffino, M. Mutin-Carnino, A. Carnino, P.-D. Petit, The effect of dynamic whole-body vibration warm-up on lower extremity performance. *Sci. Sports J.* **31**(1), 19–26 (2016)
6. V. Cazás-Moreno, J. Gdovin, C. Williams, C. Allen, Y.-C. Fu, L. Brown, J. Garner III, Influence of whole body vibration and specific warm-ups on force during an isometric mid-thigh pull. *Int. J. Kinesiol. Sports Sci.* **3**(4), 31–39 (2015)
7. S. Esmaeilzadeh, M. Akpınar, S. Polat, A. Yildiz, A. Oral, The effects of two different frequencies of whole-body vibration on knee extensors strength in healthy young volunteers: a randomized trial. *J. Musculoskelet. Neuronal. Interact.* **15**(4), 333–340 (2015)
8. P. Iodice, R.G. Bellomo, G. Gialluca, G. Fanò, R. Saggini, Acute and cumulative effects of focused high-frequency vibrations on the endocrine system and muscle strength, mechanical vibration in rehabilitation: state of the art. *Eur. J. Appl. Physiol.* **111**(6), 897–904 (2011)
9. N. Wei, M.Y. Pang, S.S. Ng, G.Y. Ng, Optimal frequency/time combination of whole-body vibration training for improving muscle size and strength of people with age-related muscle loss (sarcopenia): a randomized controlled trial. *Geriatr. Gerontol. Int.* **17**(10), 1313–1321 (2017)
10. R. Saggini, S.M. Carmignano, T. Palermo, R.G. Bellomo, Mechanical vibration in rehabilitation: state of the art. *J. Novel Physiotherapies* **6**(6), 1–4 (2016)
11. A. Salvarani, M. Agosti, A. Zanrè, A. Ampollini, L. Montagna, M. Franceschini, Mechanical vibration in the rehabilitation of patients with reconstructed anterior cruciate ligament. *Europa Medicophysica* **39**(1), 19–25 (2003)
12. D. Poenaru, D. Cinteza, I. Petrusca, L. Cioc, D. Dumitrascu, Local application of vibration in motor rehabilitation—scientific and practical considerations. *Maedica (Buchar)* **11**(3), 227–231 (2016)
13. E. Wang, T. Nelson, *Structural Dynamic Capabilities of ANSYS* (CADFEM GmbH, Munich, Germany, 2012)
14. C. Carp-Ciocârdia, A. Dragomirescu, C.A. Safta, M. Schiaua, I. Magheti, *Acta Technica Napocensis Series Appl. Math. Eng.* **60**, 545 (2017)
15. Material properties of DuPont Delrin 127UV NC010. http://www.gc.co.th/upload/datasheet/pom_delrin_127_uv_nc_010.pdf (visited 2017)

Designing and Creating a Smart Audiometer Using an Arduino Platform



Corneliu Drugă, Ionel Șerban , Antonio Serbănescu, and Diana Cotoros

Abstract This paper presents an audiometer prototype that aims to improve the development of hearing systems, especially in the field of telemedicine, by making a better link between medicine device and the physician, the transmission of data between the audiometer and another medical device being much easier to achieve. The system uses an Arduino Mega 2560 development board to provide a host of features such as data transmission without the use of connection cables or communication with devices such as desktop computers, laptops, tablets, or smartphones via wireless. The system also includes an LM386 audio amplifier to amplify the signal to deliver the sounds to the required parameters, a headphone jack to connect headphones, a 2004 (or Arduino 2560 compatible TFT display) to display parameters and data, an I2C adapter and a micro SD and micro SDHC (high speed card) adapter module where pure sounds at specific frequencies are stored. The audiometer is designed to be portable audiometer, compact, lightweight and works with an external 9 V battery. During the test, the results are displayed on the LCD screen, so the audiogram can be built with the test, or the results can be transferred to your computer or smartphone to make a printable audiogram. The audiometer offers the possibility of saving the results and integrating them into a database of patients, diversifying audiometric testing (automatic, vocal testing).

1 Introduction

People can hear sound waves only when the frequency is between approximately 20 and 20 kHz. Sounds over 20 kHz are called ultrasounds and are not perceptible to humans. Sound waves below 20 Hz are known as infrasound and are not perceptible [1].

C. Drugă · I. Șerban (✉) · A. Serbănescu · D. Cotoros
Transylvania University, Brașov, Romania
e-mail: Ionel.serban@unitbv.ro

© Springer Nature Switzerland AG 2021
N. Herisanu and V. Marinca (eds.), *Acoustics and Vibration of Mechanical Structures—AVMS 2019*, Springer Proceedings in Physics 251,
https://doi.org/10.1007/978-3-030-54136-1_27

277

Sound features of which the most important are:

- **Frequency** or pitch, this is the fundamental frequency and is measured in Hertz (Hz), unit of measurement illustrating the number of cycles or waves produced in one second.
- **Amplitude** or grit, this is the power of sound, that is, the way we perceive a sound: weaker or louder. It is measured in decibels (dB).
- **Timber** represents the harmonic spectrum made from higher than fundamental sounds also called harmonics [1].

The simplest type of sound wave is sinusoidal wave. Sinusoidal pure waves rarely exist in nature, but they are useful because all other sounds can be divided into combinations of sinusoidal waves [2]. Human ears are remarkably sensitive to vibration in the air. The human hearing threshold is about 20 micro pascal (μPa), which is an extremely small amount of atmospheric pressure. At the other extreme, the strongest sound that a person can withstand without pain or ear damage is about 120 dB (20 Pa) [2]. Hearing or hearing perception is the ability to perceive sound by detecting vibrations and environmental pressures over time through an organ such as the ear [3]. Thus, vibrations in the environment are received by the ear and transformed into nerve impulses that reach the brain and are decoded, resulting in hearing sensation.

Hearing serves a range of functions such as: speaking, alerting you to potentially dangerous events that appear outside of the field of vision, and serving an esthetic function such as appreciation of music or nature. Loss of hearing is when your ability to hear is low, it is also known as hearing or hearing impairment. The wider impact of hearing loss can therefore be profound, with consequences on the social, functional and psychological well-being of the person [4].

Audiology is the field and branch of medicine that studies hearing, balance, and pathological conditions that can affect them. As a health care profession, audiology refers to all ages, from children to the elderly, and to the evaluation, management, and therapeutic rehabilitation of those with hearing problems, balance problems, or those with tinnitus [5]. The modern audiology industry dates back to the end of the Second World War, when the loss of hearing-related fights was widespread. Acoustic trauma from high-intensity artillery and the noise of firearms have been common causes of hearing loss [6]. Audiometry is a branch of audiology and is the science of measuring auditory acuity for variations in intensity, pitch, and purity, involving different thresholds and frequencies. Typically, audiometric tests determine the audible level of the subject with an audiometer, but it can also measure the ability to discern different sound intensities, recognize pitch, or distinguish between background noise and noise. Acoustic reflexes and rotational emissions can also be measured. The results of audiometric tests are used to diagnose hearing loss or ear disease and often use an audiogram [7]. A pure tone audiometry test measures the smallest or least audible sound a person can hear. During the test, you will wear earphones, and you will hear a series of sounds directed at each ear. The amplitude of the sound is measured in decibels (dB). A whisper is about 20 dB, strong music varies between 80 and 120 dB, and a response engine is about 180 dB. The tone

of the sound is measured in frequencies (Hz). Low bass tones vary between 50 and 60 Hz, and high tones vary between 10,000 Hz and over. The normal listening range is 125 and 8000 Hz at an interval between 20 μ Pa and 200 Pa [8].

2 Materials and Methods

The design of this audiometer has as its starting point an Arduino MEGA 2560 development board (Fig. 1), because it offers a number of facilities such as the ease with which various devices can be attached (Wi-Fi module, Bluetooth, display LCD, or TFT, etc.), power can be made from an external source (9 V battery), reduced gauge, ease of programming low cost, and data storage (Fig. 1). The system is built in such a way that, if necessary, the data obtained can also be transmitted via a USB cable (Fig. 1).

The system also includes an LM386 audio amplifier that amplified the signal to output the sound to the required parameters, a headphone jack to connect the headphones, a 2004 LCD screen for displaying parameters and data, an I2C adapter, and an adapter module for microSD cards and micro SDHC (high speed card) where pure sounds are stored at specific frequencies.

The audiometer is designed to be portable audiometer, compact, lightweight and works with an external 9 V battery. During the test, the results are displayed on the LCD screen, so the audiogram can be built with the test, or the results can be transferred to your computer or smartphone to make a printable audiogram. The audiometer works according to the electrical diagram below. For this purpose, it was used a PCB board, the Arduino MEGA 2560 development board, the Wireless module, the LCD screen 2004, the I2C adapter, the LM386 audio amplifier, the card

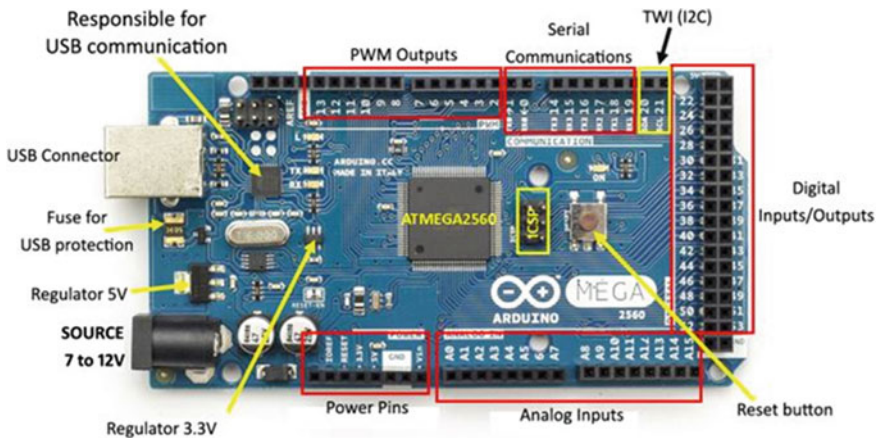


Fig. 1 Configuration of the Arduino MEGA 2560 board [9]

reader module, two push buttons, a three-way button, a potentiometer 1kOhm, a DPDT ON/OFF button, an RGB led, a headphone jack, 9 V external battery, connection cables, and a ribbon cable with IDC connectors. The electrical scheme was made using the Fritzing program (Fig. 2). The LM386 amplifier is a very popular and widely used audio amplifier that allows a user to amplify the sound. The LM386 chip is made up of eight pins, where pin 1 and 8 represent amplification control (Fig. 3) [10]. The LM386M-1 and LM386MX-1 are power amplifiers designed for use in low-voltage consumer applications. The gain is internally set to 20 to keep external part count low, but the addition of an external resistor and capacitor between pins 1 and 8 will increase the gain to any value from 20 to 200. The inputs are ground referenced while the output automatically biases to one-half the supply voltage. The quiescent power drain is only 24 mW when operating from a 6-V supply, making the LM386M-1 and LM386MX-1 ideal for battery operation (Fig. 3).

This micro SD card is used for transferring data to and from a standard SD card. The pin out is directly compatible with Arduino and also can be used with other microcontrollers. It allow us to add mass storage and data logging to our project. A liquid-crystal display (LCD) is a flat panel display, electronic visual display, or video display that uses the light modulating properties of liquid crystals (Fig. 4). In this case, we are going to use a monochromatic 20 × 4 alphanumeric LCD. 20 × 4 means that 20 characters can be displayed in each of the 4 rows of the 20 × 4 LCD, thus a total of 80 characters can be displayed at any instance of time (Fig. 4).

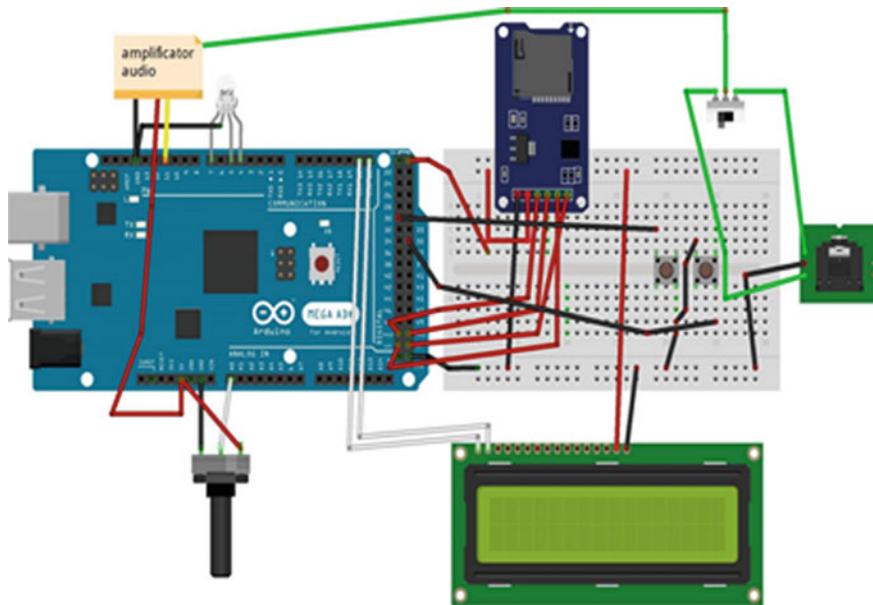


Fig. 2 Electrical circuit of the audiometer

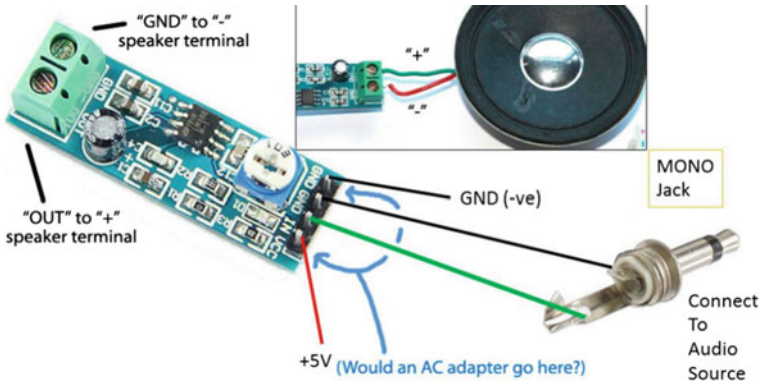


Fig. 3 LM386 audio amplifier



Fig. 4 a 2004 LCD display; b I2C adapter circuit

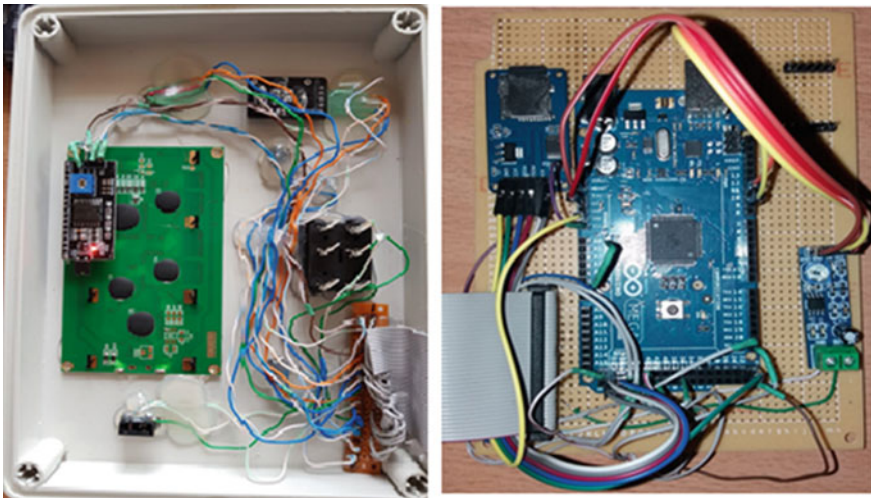


Fig. 5 Hardware part of the audiometer



Fig. 6 Massive synthesizer



Fig. 7 Sound amplification with 10 dB

The I2C LCD adapter reduces the number of pins 16 to 4, and it can be connected to a compatible 16×2 or 20×4 character display module that supports the 4-bit mode [11]. This card has an I2C PCF8574 chip that converts I2C series data to parallel data for the LCD display. The I2C address is $0 \times 3F$ by default, but this can be changed by three soldering jumpers provided on the board. This allows up to three LCD displays to be controlled via a single I2C bus (giving each of their own addresses) [11]. To make it more ergonomic and more esthetical, a ribbon cable with IDC connectors was used to connect the central panel and the development board to the rest of the PCB board components. This connects the headphone jack with the

three-way button and then with the audio amplifier to make the test on the left ear or right ear (Fig. 5).

After the electrical part has been started, the code is written to program the audiometer, so that the LCD will display the current frequency and intensity, the push buttons will be used to give PLAY the sound, and the second STOP” to stop the test at the desired frequency and intensity. The potentiometer is programmed to change the frequency or intensity by rotating it. The LM386 audio amplifier has amplified your signal until it reaches the appropriate level to emit the sounds through the headphones at the specified level. The microSD card reader module was used to read the microSD card used as a flash memory, and the sounds were memorized.

Programming the microcontroller to perform automatic testing and wireless module programming was the second major step in the source code because it gives us the opportunity to escape the multitude of wires and cables and at the same time gives us the opportunity to connect the audiometer to other devices or to connect other peripheral components to the system. Thus, after the code was created in the C++ program, it was stored on the Arduino MEGA 2560 development board. An audiometer is capable of delivering tones between 125 and 16,000 Hz, the test frequency being 125, 250, 500, 1000, 2000, 4000, 8000, 16,000 Hz, and the intensity is amplified from 5 to 5 dB or 10 in 10 dB. In this sense, sounds were created using the FL Studio software (a virtual studio to create music), using a native instruments massive synthesizer with three oscillators with over 40 wave forms, filters, stamp modulator, frequency, etc (Fig. 6).

In this case, a single oscillator was used to generate the sinusoidal waveform, since this is the basic form in acoustics, by the overlapping of the sinusoidal waves the other signal forms are formed. During the tests, using a digital equalizer with a visual panel, it has been found that the useful frequencies are somewhere between Si (246.94 Hz *B*) and Do (261.63 Hz *C*), but closer to the Si basic frequency. In this case, a single oscillator was used to generate the sinusoidal waveform, since this is the basic form in acoustics, by the overlapping of the sinusoidal waves the other signal forms are formed (Fig. 7).

The frequency was isolated using a more precise equalizer post using the “Peak band” filter characteristic that is, leaving only the input frequency to pass. After the desired frequency isolation, by removing the harmonics by leaving only the base frequency to pass, pure tone was created, which was exported as a WAV audio file at the 44.100 Hz sampling rate and 12-bit depth. To amplify the frequencies at the required intensities (-10, 0, 10, 20 ... 110 dB), Ozone 7 masked program from Izotop was used. So, the audio files were loaded with the necessary frequencies, and the equalizer was used to amplify or reduce the sound by 10 dB.

3 Results and Discussion

The audiometer features MP3 player-like features, where the sounds created in FL Studio are loaded onto a microSD card. With the card reader module, Arduino MEGA 2560 will play the sounds loaded on the card through the headphones each time we

press the play button or the test will start automatically after the first press of the Play button. Headphones connected to the headphone jack will play pure-specific tones at different intensities and frequencies. The subject will be instructed to raise his hand whenever he hears or he seems to hear the sound.

The desired frequency can be selected by means of the linear potentiometer, rotating to the right to increase the frequency and turning to the left to decrease the frequency, and the intensity will be automatically played by the audiometer until the Stop button is pressed or the potentiometer is rotated to move to the next frequency. The RGB led will change color according to the frequency that we are changing. The test can be stopped every time you press the “Stop” button to record the data or send the data to the desired device (PC, laptop, smartphone, Iphone, etc.) via the USB cable or the connection wireless. This will generate a server on a local wireless network where the desired device will need to connect. Performing the test on the desired ear is done very easily by pressing the left three-way button to the left for the left ear or to the right for the right ear.

This device was built as a portable audiometer and can run for up to 12 h; after unloading the batteries, you can rename a microSD. Test results are displayed on an audiogram (Fig. 8). An audiogram is a graph showing the weakest sounds that a person can hear at different degrees or frequencies. Where the patient’s results are on the audiogram, indicate the different degrees of hearing loss (Fig. 8). The audiogram

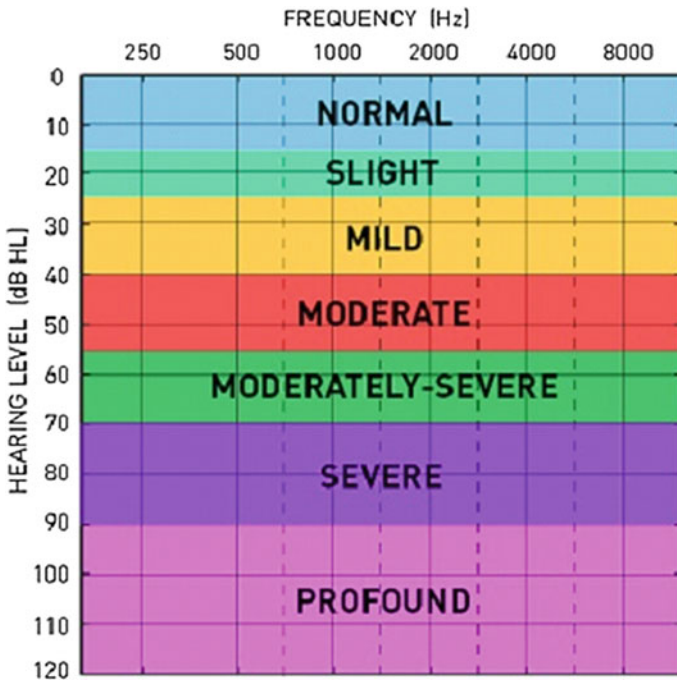


Fig. 8 Audiogram [12]

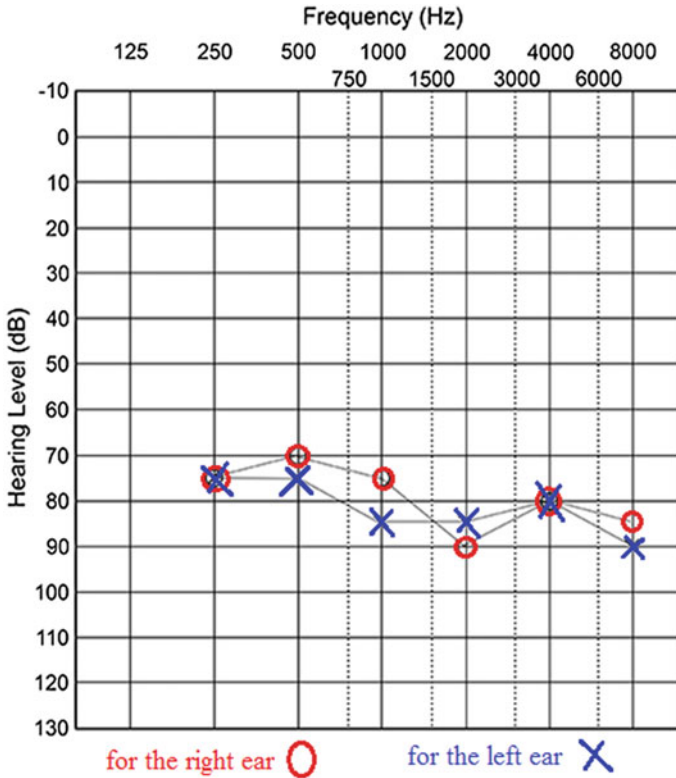


Fig. 9 Audiogram with severe hearing loss [12]

below shows the different degrees of hearing loss. Generally, a red color “O” is often used to represent right ear answers, and a “X” written in the blue color is used to represent left ear responses. Frequency is measured horizontally from left to right, and the intensity is measured at the top left of the top left [13]. Figure 9 shows an audiogram with an example of severe hearing loss, and Fig. 10 shows an example with normal hearing.

4 Conclusion

Although this audiometer is an experimental one, it is used in the Medical Engineering Laboratory of the Faculty of Product and Environment Design (Transylvania University of Brasov).

This audiometer, although used only for didactic purposes within specialized laboratories (construction and maintenance of medical devices, medical electronics,

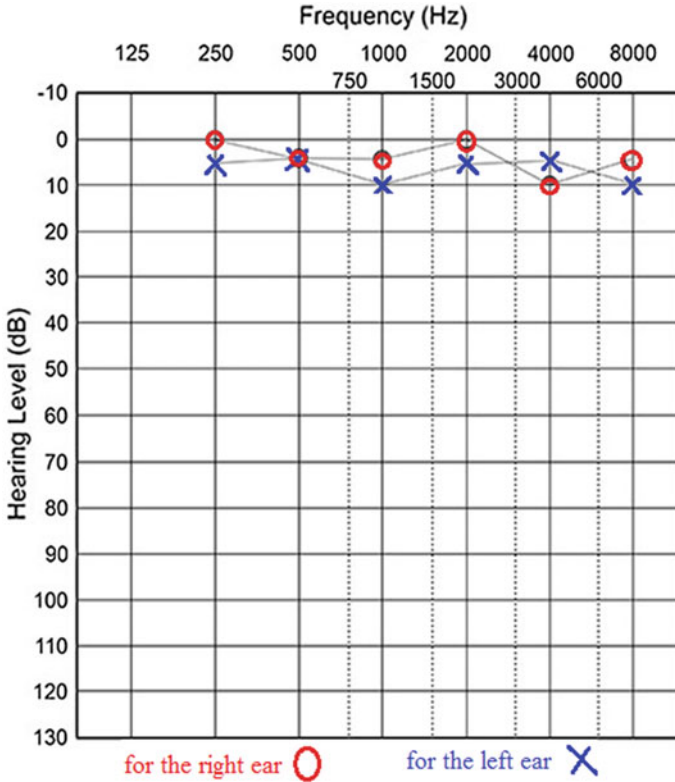


Fig. 10 Audiogram with normal hearing [12]

protective engineering, microcontroller programming, etc.), has a number of advantages, such as: low cost, use and easy maintenance and can support a number of improvements (hardware and software).

Acknowledgements Practical realization of this project was made possible thanks to funding received in a competition held in the Transylvania University of Braşov as HCA nr.20/01.03.2017 (Annex 3).

References

1. <https://en.wikipedia.org/wiki/Sound>. Accessed on 26.07.2018
2. https://www.cdc.gov/nceh/hearing_loss/what_noises_cause_hearing_loss.html. Accessed on 12.07.2019
3. <https://documentation.apple.com/en/soundtrackpro/usermanual/index.html#chapter=B%26section=1%26tasks=true>. Accessed on 27.07.2018
4. <https://en.wikipedia.org/wiki/Hearing>. Accessed on 27.07.2018

5. <https://www.hiddenhearing.co.uk/hearing-information/hearing-loss/age-related-hearing-loss>. Accessed on 27.07.2018
6. <https://www.embracehearing.com/blogs/hearingaidsnews/5903159-a-brief-history-of-hearing-aids-part-i-the-audiometer>. Accessed on 28.07.2018
7. <https://en.wikipedia.org/wiki/Audiometry>. Accessed on 28.07.2018
8. <http://www.mayfieldclinic.com/PE-hearing.htm>. Accessed on 28.07.2018
9. https://www.researchgate.net/figure/Block-Diagram-1-ArduinoMEGA2560-The-Arduino-Mega-2560-is-a-type-of-microcontroller_fig5_281538436. Accessed on 12.07.2019
10. LM386 Audio Amplifier Circuit and its Applications. [online] Buy Electronics & Electrical Projects in India. Available on <https://www.edgefx.in/lm386-audio-amplifier-circuit/>. Accessed on 29.07.2018
11. LM386 Audio Amplifier Module 200 times gain amplifier module audio amplifier! Arduino Robots & electronics component in kabulafghanistan. [online]. Nooraziz.com. Available on <http://www.nooraziz.com/product/lm386-audio-amplifier-module-200-times-gain-amplifier-module-audio-amplifier/>. Accessed on 29.07.2018
12. Babyhearing.org. What is an Audiogram? – Understanding Hearing Test Results! Babyhearing.org (2018). [online]. Available at <https://www.babyhearing.org/what-is-an-audiogram>. Accessed on 29.07.2018
13. <https://www.babyhearing.org/what-is-an-audiogram>. Accessed on 29.07.2018

Influence of Whole Body Vibration Machines, for Sport Exercises, on the Human Balance and Stability



Corneliu Drugă, Ionel Șerban , Diana Cotoros, and Angela Repanovici

Abstract Shock and vibration are present in all areas of our daily lives. It may be transmitted and generated by machine-tools, turbines, motor, towers, bridges, and even by the human body. Vibration and shock also may be desirable, disturbing and even destructive. It depends on the place and what type of source of vibration that occurs. This paper presents a case study of the influences of vibration machine, used in sport exercises, on the human balance and stability. The equipment used is a vibration machine Insportline, a force platform Kistler and four subjects (mean age 23 ± 1 years; mean weight 75 ± 3 kg; mean height 1.78 ± 0.4 m). The subjects were analyzed, on the Kistler platform, in three situations: with eyes open, with eyes closed, and after 1 min of standing on the vibration machine. The analyses consist of a 30 s stand still on the force platform in an orthostatic position. The parameter taken into account is the center of pressure of the foot. The results indicate that there is a slight influence of the vibrations on the balance and stability of the subjects indicated by the variation of the center of pressure on a 2D plane.

1 Introduction

Vibration machines are said to help lose weight up to three times more quickly than a regular fitness trainer. Because they transfer vibrations to muscles, and they present a true revolution in exercising. Nowadays, these machines can be used at home. It is said that a vibration machine helps you better exercise your muscles, improve your agility and flexibility, improve your blood circulation, and stimulate the cardiovascular system [1].

Several studies are centered on the influence of whole body vibrations on the human balance, equilibrium, stability, locomotion, and so on. These studies have shown various results [2–8]. Taking them into account, this study is oriented to detect some new results.

C. Drugă · I. Șerban (✉) · D. Cotoros · A. Repanovici
Transylvania University, Brașov, Romania
e-mail: Ionel.serban@unitbv.ro

Besides, all these studies, there are a lot of studies that are oriented on the influence of environmental parameters on human balance and locomotion. The environmental parameters that might need an evaluation are the ones that directly affect the human body equilibrium systems (vestibular, visual and proprioception systems), these being: vibrations, sound, light, and surface of the support. Of course, there are other environmental parameters like temperature, humidity, obstacles, chemicals that influence human comfort and might have an influence on human equilibrium and balance.

The hypothesis of this study is that whole body vibrations affect the center of pressure of the human body.

2 Materials and Methods

Using the Kistler force plate, the experimental stages of the foot support on the ground and the dynamic parameters (forces and reaction moments) specific to these phases can be determined. Thus, a mechatronic system is used, namely the Kistler system (Fig. 1), consisting of a force platform (four piezoelectric sensors), an electric signal amplifier, two analog-digital acquisition boards, and a user interface program, BioWare, and a laptop (acquisition system).

The whole body vibration system used is an Insportline equipment (Fig. 2) that might be used at home for specific exercises.

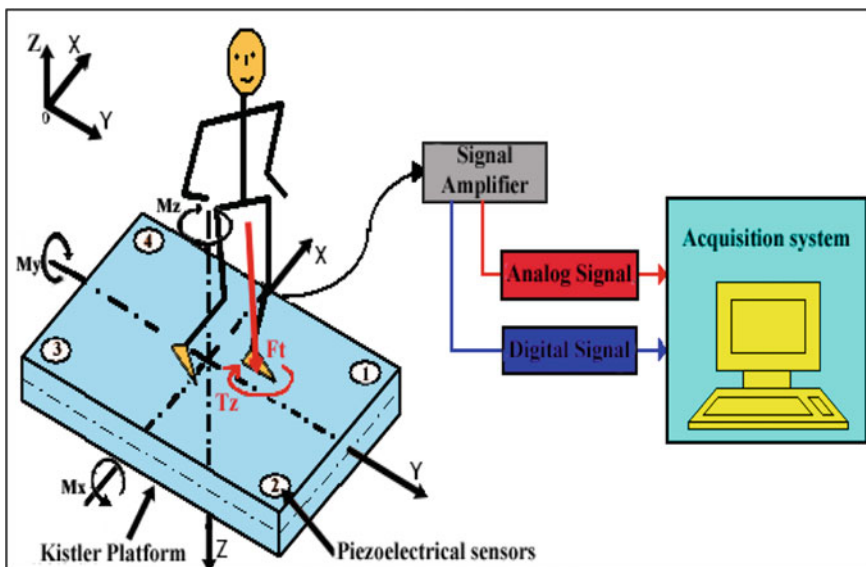


Fig. 1 General setup that was used to determine the coordinates of the center of pressure [9]

Fig. 2 Whole body vibration system [10]



The parameter pursued within the measurements was the center of pressure. The measurements consist of three steps: first orthostatic posture with eyes opened (EO), second orthostatic posture with eyes closed (EC), and third orthostatic posture with eyes open after 1 min of standing (orthostatic posture) on the whole body vibration (WBV) system. The study was done on a group of four subjects, which have given their approval. The measurements on the Kistler platform consist of a 30 s standing according to the steps explained before. The acquisition of this data was done through the BIOWARE software, with the help of which we could generate a series of graphs in which we were able to notice the smallest changes in the movements of the four subjects participating in the study. All values were analyzed in excel.

3 Results and Discussion

The next step was to create a graph for each type of measurement (Table 1) to track the amplitude variation of the center of pressure. In the table below, we can see the amplitudes for each type of measurement and each subject.

According to other studies [9], in an orthostatic position, the center of pressure varies in an anterior–posterior direction considering the base of support, but this study shows a greater variance in the left–right direction possibly due to the way the vibrations were sent to the body in the frontal plane, not in the sagittal plane.

The results (Figs. 3 and 4) indicate that each subject has a personal evolution although we tried to find a normalized group of subject (this reflects in the small number of subjects taken into account). Amplitude was measured between the maximum and the minimum value on the X -axis and the Y -axis of the center of pressure. In the figures below, it can be seen the dispersion of these values. The values of the center of pressure are obtained from the software in two columns X and Y relative to time.

The most important ratio of the center of pressure dispersion (Figs. 5 and 6) can be seen in the case of subject 2, in frontal plane, Y -axis, where the amplitude increases for EC and after WBV in relation to EO situation.

Table 1 Amplitude of center of pressure on X -axis (Anterior–posterior direction) and Y -axis (Left–right direction) for every subject and experimental step

Experimental steps	Subject	Amplitude	Amplitude
		X[m]-Antero-posterior	Y[m] Left-right
With EO	1	0.037	0.028
	2	0.021	0.012
	3	0.025	0.012
	4	0.028	0.0128
With EC	1	0.013	0.014
	2	0.0155	0.0175
	3	0.025	0.0165
	4	0.031	0.013
After exposure to WBV	1	0.028	0.03
	2	0.02	0.034
	3	0.031	0.021
	4	0.043	0.021

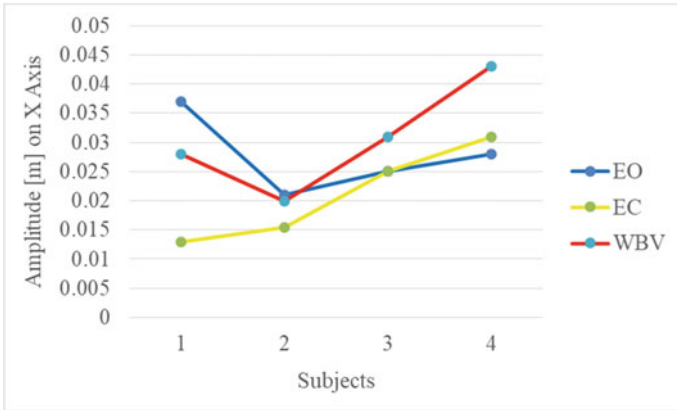


Fig. 3 Amplitude of the center of pressure on anterior–direction posterior direction-X-axis, sagittal plane

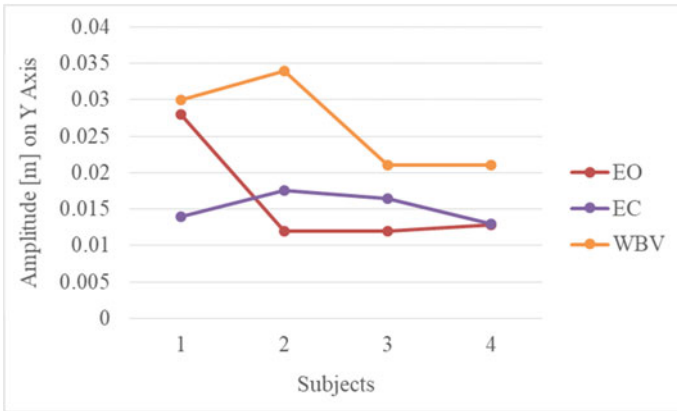


Fig. 4 Amplitude of the center of pressure on left–right direction-Y-axis, frontal plane

4 Conclusion

According to the results presented above and taking into consideration some of the results of other studies, it can be concluded that WBV affects the center of pressure (mostly on left–right direction, than on anterior–posterior direction) of the human body.

The results also indicate that for EC situation, the amplitude of the center of pressure decreases on anterior–posterior direction. These results indicate the need for further analyses on a larger set of subjects.

Considering the small number of subjects, implicated in these experiments, it cannot be generalized but it sets a goal for further studies.

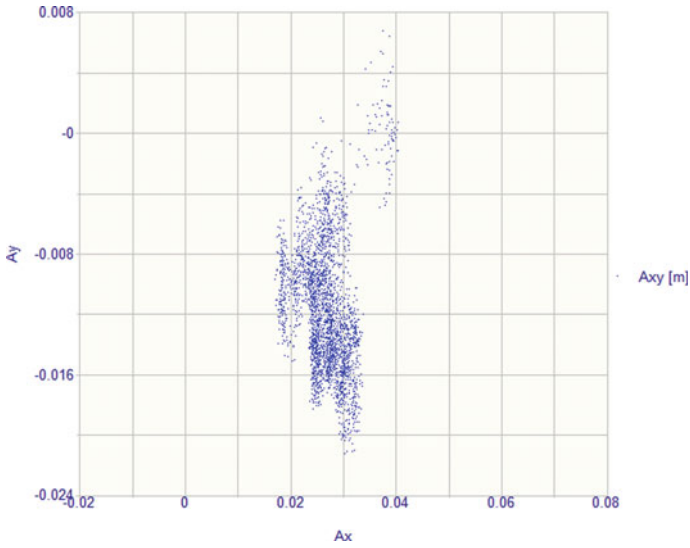


Fig. 5 Dispersion of the center of pressure, subject 2 with EO

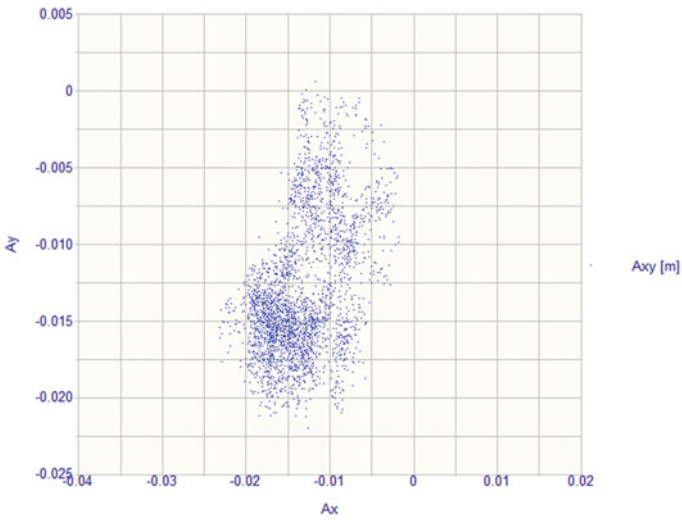


Fig. 6 Dispersion of the center of pressure, subject 2 after WBV

Acknowledgements Practical realization of this project was made possible thanks to funding received in a competition held in the Transylvania University of Braşov as HCA nr.20/01.03.2017 (Annex 3).

References

1. <https://www.insportline.eu/vibration-machines>. Accessed on 18.02.2019
2. C. Lachance, P. Weir, K. Kenno, S. Horton, Is whole-body vibration beneficial for seniors. *Eur Rev Aging Phys Act* **9**, 51 (2012). <https://doi.org/10.1007/s11556-011-0094-9>
3. L. Lanitia, C. Edelle, Whole-body vibration improves walking function in individuals with spinal cord injury: a pilot study. *Gait Posture* **30**(4), 436–440 (2009). <https://doi.org/10.1016/j.gaitpost.2009.06.016>
4. H. Liang, M. Beerse, X. Ke, J. Wu, Effect of whole-body vibration on center-of-mass movement during standing in children and young adults. *Gait Posture* **54**, 148–153 (2017). <https://doi.org/10.1016/j.gaitpost.2017.03.005>
5. I. Șerban, Gait and balance analysis in people with meniscal tear, in *6th International Conference Computational Mechanics and Virtual Engineering COMEC*, 15–16 October 2015 (Brasov, Romania, 2015), pp. 417–420
6. C. Druga, I. Șerban, D. Cotoros, Vibration measurement system with mems accelerometers based on arduino, in *7th International Conference on Computational Mechanics and Virtual Engineering, COMEC 2017*, Brasov, ROMANIA, 16–17 November 2017, pp 136–139
7. M. Baritz, Comparative analysis of walking typologies in relation to lower limb joints lock, in *Proceedings of 2015 International Conference Computational Mechanics and Virtual Engineering (COMEC)*, Brașov, Romania, 15–16 October 2015, pp. 361–366
8. Drugă, C., Șerban, I. Study of foot pressure- sole pressure sensor (2017), *the 7th International Conference on Computational Mechanics and Virtual Engineering COMEC 2017* Brasov, ROMANIA, 16–17 November 2017, pp 132-135
9. I. Șerban, I.C. Roșca, M. Baritz, Influence of sound frequency on human body stability. *EEMJ* **15**(2), 375–380 (2016)
10. <https://icdt.unitbv.ro/centre-de-cercetare/sisteme-mecatronice-avansate/infrastructur>. Accessed on 18.02.2019

Human Factor Balance Under the Influence of Variable Sound Frequency and Orientation



Diana Cotoros, Ionel Șerban, Corneliu Drugă, and Anca Stanciu

Abstract Our modern world is inevitably a permanent source of sounds of different physical characteristics, some of them beneficial for the human factor, even with healing properties, and some becoming part of the growing environmental stress, better known as noise pollution. Besides the usual negative effects like hearing problems, neurological diseases, or psychological issues, some types of noise may lead to sudden loss of stability according to their wave length, frequency, distance from the human factor, location, etc. The present paper aims at illustrating by practical experiments, using healthy subjects in a controlled environment, the influence of sounds with variable frequency, occurred in different locations in a random manner, upon the stability of human factor. Loss of stability during various activities interrupted by random and variable noise may endanger the health or even the life of the affected person. In order to determine the degree of stability loss and the types of sounds inducing a higher influence upon the human body, an experimental setup was accomplished at the Advanced Mechatronic Systems Laboratory, consisting mainly of a Kistler force platform, laptop for data acquisition, and a sound generator with speakers. The acquired data were analyzed and conclusions drawn to be able to prevent work accidents or other unfortunate situations that might lead to health endangerment.

1 Introduction

People are subjected to various types of sounds every second of their lives, especially due to the recent technological progress. Sounds may come either from nature (wind, thunderstorms, waterfalls, animal noise, etc.) or they are produced by human activities (industry, medical devices, explosions, transport, and so on). Some of these sounds may have a beneficial influence upon human health (music, sea waves, and

D. Cotoros (✉) · I. Șerban · C. Drugă · A. Stanciu
University Transilvania of Brasov, Brasov, Romania
e-mail: dcotoros@unitbv.ro

© Springer Nature Switzerland AG 2021
N. Herisanu and V. Marinca (eds.), *Acoustics and Vibration of Mechanical Structures—AVMS 2019*, Springer Proceedings in Physics 251,
https://doi.org/10.1007/978-3-030-54136-1_29

297

birds chirping) but they may also produce negative effects like hearing troubles, circulatory problems, balance loss, and many other symptoms, subjective or not [1].

The present study was concerned with the fact that most lethal accidents at work places are due to falls as a result of balance loss, which may often happen during exposure to certain types of sounds [2].

Previous studies focused upon the influence of low frequency sounds (frequency sounds below 0.5 kHz) upon laboratory mice [3] but also of ultrasonic sounds (high frequency over 20 kHz) on people with various age [4] or gender [5], proving that there is no doubt that low and high frequency sounds will affect to a certain extent the posture control of the investigated subjects. There are also authors who found there are no significant changes in postural stability during quiet standing if subjected to auditory stimuli [6].

There are different opinions on the subject mainly because there are so many physical parameters of sound that may influence at a certain extent human postural balance (frequency, intensity, type, duration, location, etc.), so things are insufficiently researched.

Our team focused not only upon changing frequency but also on producing sounds coming unexpectedly from different locations because the intermittence of sound may be a stressful factor affecting suddenly the postural balance.

2 Materials and Methods

In order to perform the tests, a number of 48 students (37 females and 11 males) were involved. They are young with ages between 20 and 26 and declared they had no previous health issues; also their age offered some assurance that hearing was not yet affected by aging and normal hearing frequencies would not be a problem. Their height is between 1.57 and 1.93 m and their weight between 46 and 87 kg. The subjects were carefully briefed at a certain extent about their contribution. The experiments were performed within the Advanced Mechatronic System Laboratory of Transilvania University Research Center. The building is situated in a quiet area with no traffic sounds or other interfering noises which might affect the results of our experiment. The students were called at different times, one by one and remained in the laboratory after the experiment so that communication was avoided and allowed to surprise them with the sounds.

For producing sounds of variable intensity and frequency, a free sound generator software on mobile phone was used and also a small speaker in order to be able to change rapidly the sound location without catching the subject's attention. The software offers the possibility of producing sine wave sounds (basic isolated sound with no harmonic or inharmonic sounds), square wave sounds (contains odd harmonics besides the basic sound), sawtooth wave sounds (contains all harmonics), or triangle wave sounds (fundamental frequencies plus odd harmonics) with different intensities and frequencies [7].

Fig. 1 Student subjected to a noise coming from behind



A Kistler force platform was used to determine the area of stability by representing the positions of the body COP (center of pressure). The platform was connected to a laptop and we used Bioware for graphical representations and statistical results.

The subjects were instructed to stand relaxed for 30 s on the force platform in order to determine a reference stability area. Then, without warning, they were subjected to sudden noises coming from different directions, as shown in Fig. 1. Frequencies, types of sounds, and intensities were also changed in order to determine which will produce stronger reactions by loss of balance.

Results were recorded and analyzed using the dedicated software, as mentioned before (Bioware).

3 Results and Discussions

In order to have a reference for the stability area, all subjects were first required to stand on the force platform and assume a relaxed position for 30 s. The stability areas were in most situations compact and sways on axis O_x (lateral) and O_y (antero-posterior) were below 0.025 m, like in the example shown in Fig. 2.

The test subjects were divided into four groups; some of them being exposed to sounds coming from front, some of them from behind and some from left side or right side. Also the types of the waves were changed, without telling them, into

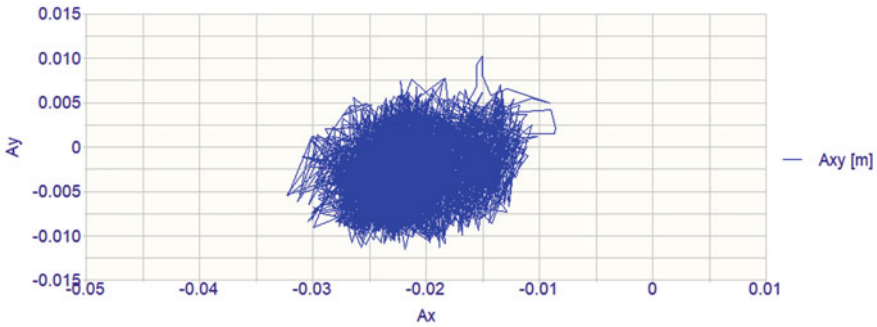


Fig. 2 Stability area in quiet standing position

sine, triangle, square, or sawtooth wave sounds. The sound intensity was maintained around 100 dB which is the highest limit accepted by ergonomic standards at workplaces.

In the following representations, some of the most eloquent results obtained for different combinations between sound locations and types were selected.

Thus, Figs. 3 and 4 will show the stability area for a sine wave which was sent from different directions. Sine waves are the shape of basic sounds with no harmonics and they are usually relatively pleasant for the hearing.

By analyzing the changes occurred in the stability area representation, it was found that the sudden occurrence of a sine wave sound from a certain direction would surprise the subject and he/she will have the tendency of “protecting” themselves from the sound and sway toward the opposite direction from where the sound was coming (increased sway on Oy means lateral sway). Thus, for the sounds coming from front and from behind, we determined an increased antero-posterior sway of about 0.036 m and a lateral sway slightly increased up to 0.03 m for sounds coming from sides.

Another interesting observation was made about the forces values on all axes but especially on axis Oz (perpendicular to the platform). The graphical representations

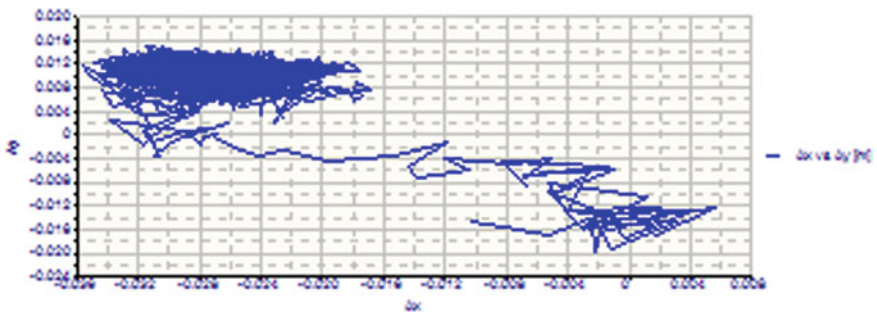


Fig. 3 Stability area for sine wave sound coming from front

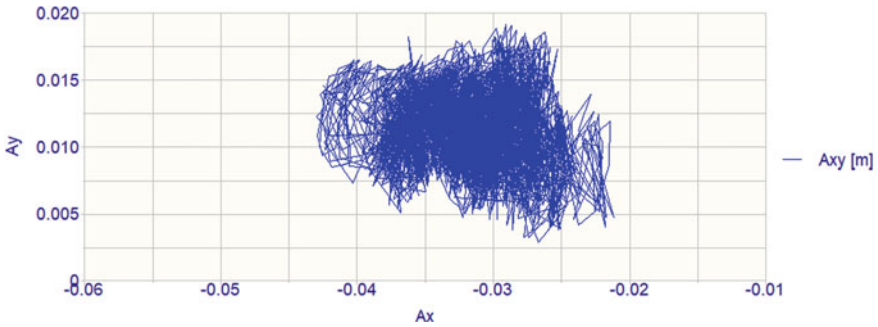


Fig. 4 Stability area for sine wave coming from one side

show very clearly higher values of the forces occurring at the exact moment when the sound was released (second 12 and second 27) proving the physiological reaction due to the small shock of surprise by the sudden noise. (Fig. 5)

Also it can be noticed that the reaction to the repeated sound was not so powerful as to the initial sound because the subject was already prepared at a certain extent that some sound may occur and stayed focused.

Similar reactions were obtained for triangle wave and square wave sounds, the sway was a little higher and also the values for the force F_z .

A special attention was paid to the sawtooth wave sound, as it includes all harmonics besides the fundamental frequency. This type of sound waves is the most disturbing one, it happens, for example, during explosions and earthquakes, so as it was expected, the reactions were proportional.

Some of the most representative results are presented in Figs. 6, 7 and 8.

The “protection” instinct is very obvious in this diagram; the stability area is spread along the lateral axis Oy and the sway reaches 0.064 m.

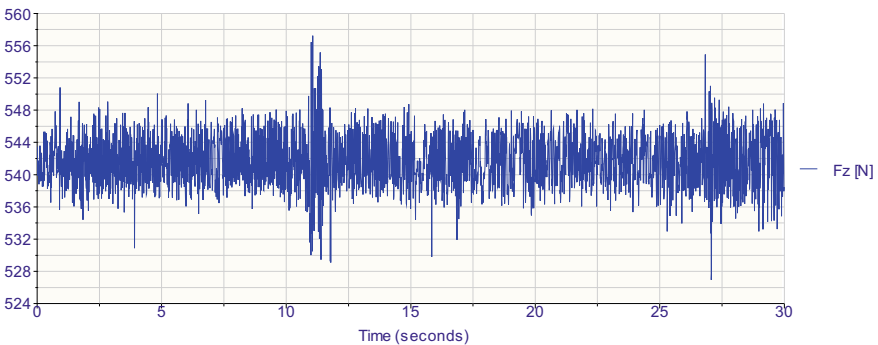


Fig. 5 Variation of reaction force F_z during the sine wave experiment

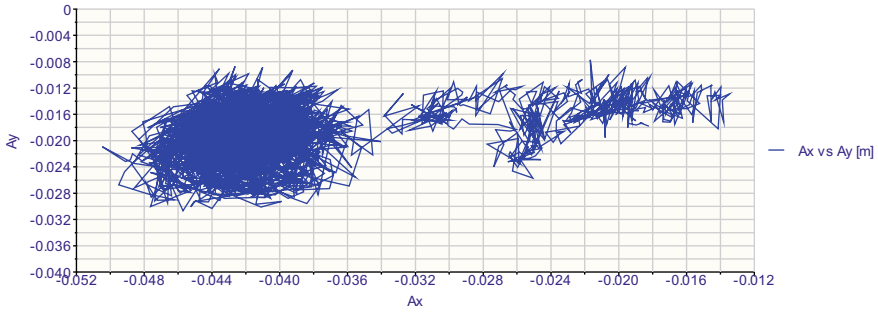


Fig. 6 Stability area for sawtooth sound wave coming from the side

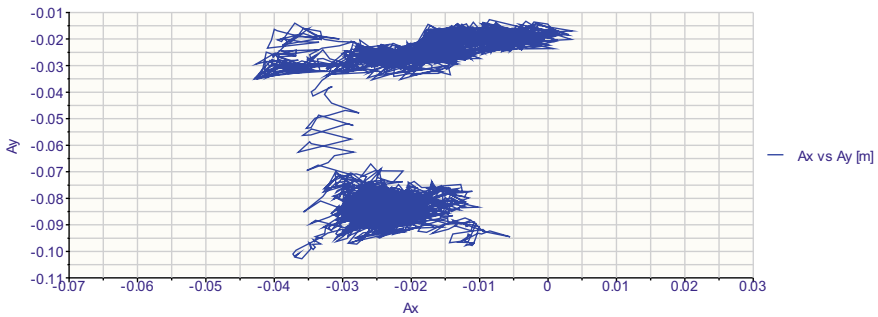


Fig. 7 Stability area for sawtooth wave coming from behind

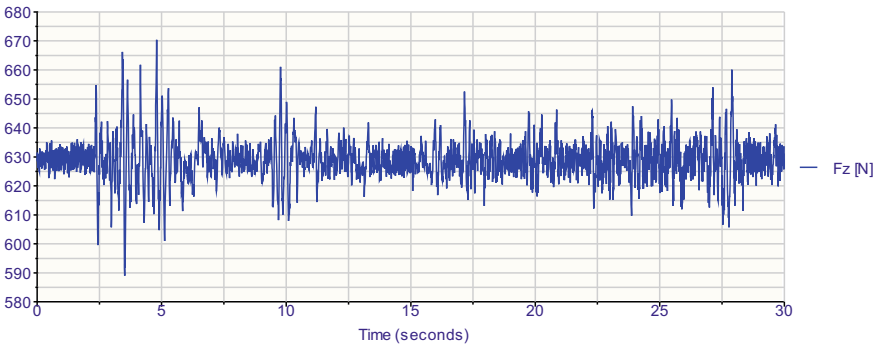


Fig. 8 Variation of reaction force Fz for sawtooth sound wave

The loss of balance takes place according to Fig. 7 in antero-posterior plane showing that the subject is strongly affected by the sound. There is also a significant sway on lateral direction proving that the stress was very powerful and totally imbalanced the subject.

The reaction force shows again a peak at second 3 when the sound occurred but this time, the subject is unable to rebalance as fast as in case of sine waves and unusual peaks continue to appear even after the sound stopped.

4 Conclusions

Based upon the experimental studies performed, the team found that the direction the sound is coming from influences loss of stability in basically the same manner, regardless of the sound direction. People have the tendency of getting away or “protecting” themselves from the noise especially when it is unexpected (they sway to the front when the sound comes from the back, etc.). This might lead to loss of balance and even fall, resulting in severe trauma or even death at certain workplaces.

It is known that frequencies affect the person’s balance in different ways but if several harmonics are involved changing the wave shape, major influences are witnessed. By comparing the types of sound waves, it was found that sawtooth sound wave, which includes all harmonics, has the most powerful influence upon losing stability. Of course, people react to sudden sounds at different extents, some display minor loss of stability and some suffer significant changes of the stability area. Also, after the first shock of surprise, their reaction is not so powerful if another disturbing sound occurs a little later, the body being already alerted.

In order to avoid accidental falls due to occurrence of unexpected disturbing sounds, people working in dangerous conditions might be checked following the above procedure, thus identifying the persons who can be in danger at their workplace and direct them to safer jobs or at least provide them with suitable safety equipment, even if the noise is not permanent.

References

1. B. Smagowska, M.P. Luszczinska, Effects of ultrasonic noise on the human body—a bibliographic review. *Int. J. Occup. Saf. Ergonomics* **2**(19), 195–202 (2013)
2. S.H. Park, K. Lee, T. Lockhart, S. Kim, Effects of sound on postural stability during quiet standing. *J. Neuroeng. Rehabil.* **8**(67) (2011)
3. H. Tamura, N. Ohgami, et al., Chronic exposure to low frequency noise at moderate levels causes impaired balance in mice. *PLOS ONE* **7**(6) (2012)
4. T. Tanaka, S. Kojima, H. Takeda, The influence of moving auditory stimuli on standing balance in healthy young adults and the elderly. *Ergonomics* **44**(15), 1403–1412 (2001)
5. B. Siedlecka, M. Sobera, A. Sikora, I. Drzewowska, The influence of sounds on posture control. *Acta of Bioengineering and Biomechanics* **3**(17), 95–102 (2015)
6. M.R.M. Mainenti, L.F. De Oliveira, T. De Melo et al., Stabilometric signal analysis in tests with sound stimuli. *Exp. Brain Res.* **181**, 229–236 (2007)
7. <https://en.audiodanzine.com/getting-started/editorial/articles/in-search-of-the-perfect-wave.html>. Accessed July 2018

The Effect of Vibration Exposure on Posterior Lower Limbs Skin Temperature During the Warm-up Process of Athletes



Daniel Vlădaia, Adela Neamțu Popescu, Steliana Stanciu, Dorin Simoiu, and Liviu Bereteu

Abstract Warming up before physical activity is a stage of transition between rest and effort, necessary to progressively move the joints, muscles, cardio-respiratory system, and of course on the psyche. Over the last decade, numerous studies have postulated that the whole-body vibration (WBV) exercise, for short periods of time, could be used as a warm-up procedure. In this paper, it is looking at the dynamic behavior of a viscoelastic model of posterior lower limbs muscle, an analysis of how the energy dissipation takes place based on the model used, as well as the increase in the limbs skin temperature thereof. Harmonic-type vibrations are generated by a Power Plate that moves in a precisely controlled manner, producing comfortable vibratory stimulus, constantly changed when passing from one motion to the next. For temperature measurement of skin, a forward-looking infrared camera (FLIR) also called thermal imaging camera or infrared thermograph is used. The temperature variation according to the frequency, amplitude and vibration exposure time is analyzed.

D. Vlădaia · A. N. Popescu · S. Stanciu · D. Simoiu · L. Bereteu (✉)
Mechanics and Materials Strength Department, Politehnica University of Timișoara, Bd. Mihai
Viteazul, Nr. 1, 300222 Timișoara, Romania
e-mail: liviu.bereteu@upt.ro

D. Vlădaia
e-mail: vladaiadaniel@gmail.com

A. N. Popescu
e-mail: adelaneamtu@yahoo.com

S. Stanciu
e-mail: stelly_nov@yahoo.com

D. Simoiu
e-mail: dorin.simoiu@upt.ro

© Springer Nature Switzerland AG 2021

N. Herisanu and V. Marinca (eds.), *Acoustics and Vibration of Mechanical Structures—AVMS 2019*, Springer Proceedings in Physics 251,
https://doi.org/10.1007/978-3-030-54136-1_30

1 Introduction

The training of any athlete takes place in three distinct phases: warming, proper training and relaxation after effort. Warming consists of all measures that allow for an optimal state of physical and mental training before a training or competition. A first effect of warming is the increase in the temperature of the internal organs, which ensures good tissues irrigation, a decrease in the psychic tension and an increase in the attention, coordination and precision of the movements. Another effect of warming is the increase in the temperature of the muscles, skin and joints, providing an increase in muscle elasticity and viscosity, and an increase in synovial fluid at the joints. Warming is a stage of transition between rest and effort, playing an important role in preventing injuries. In addition to classical warm-up exercises: light running, fanders, step added, stretching, shoulder rotation, squatting, push-ups, and more, running lane or body exposure to vibrations for short time is used more and more often.

For a long time, only the negative effects of human body exposure to high frequency vibrations and/or large amplitudes were observed, which made the human body subject to accelerations, several times greater than gravitational acceleration. This, noting the obvious possibility of the resonance of some internal organs, made the joints subject to shocks we can say some kind of internal impacts, which in time led to their destruction.

Over the last decade, many studies have postulated that the whole-body vibration exercise (WBV) can be used as a warm-up procedure. The lack of consistent reports and the lack of standardized protocols make this warm-up method full of contradictions between those who have developed the scientific literature.

The warm-up phase of training and of competitions is essential to maximize the athletes' muscle performance [1], and the investigation of new warm-up procedures is of great interest. This type of warm-up, using the WBV method, has become very common and has been promoted as an active warm-up procedure [2, 3], mainly based on its effectiveness to rapidly improve muscular performance, even if there are many skeptics [4, 5].

The WBV heating exercise consists in placing the body, generally in a vertical position, on a vibrant platform from which the mechanical energy is transferred to the body through the heels of the feet. The viscoelastic behavior of tendons and lower limb muscles, mainly the elastic component, causes this mechanical oscillation to induce changes in their length, also causing reflex muscle contractions [6]. As a result of these contractions, the electromyographic activity of lower limb muscles is higher than if the body is at rest [7, 8]. On the other hand, the viscos component generates damping, which results in the release of heat by friction the muscle fibers [9]. As opposed to passive and active procedures, this method causes metabolic and cardiovascular changes resulting in increased muscle and joint temperature [10]. The effects of vibrations on ankle spasticity, balance and walking ability in patients with incomplete spinal cord injury at cervical level were investigated [11] and led to improved posture and gait of patients who had fractures [12, 13] and also to the performance of football players [14].

The aim of this paper is to analyze the dynamic behavior of a viscoelastic model, for the lower leg muscles when exposed to vibrations. The energy dissipation mode, based on the model used, as well as the temperature increase of the skin, is followed.

2 Dynamic Behavior of Viscoelastic Model

The simplest mechanical model, which besides the accumulation of potential deformation energy also describes energy dissipation, is the Kelvin–Voigt model. Although this rheology model has a number of disadvantages, which it will not insist on here, its simplicity, but above all its linear behavior, makes the Kelvin–Voigt model, especially used to explain the phenomenon of energy dissipation by vibration. The mechanical behavior of the limbs muscle can be considered as a superposition of the elastic property, as a spring, over the viscous flow property as a dashpot (Fig. 1). The Kelvin–Voigt model consists of a spring having the elastic constant k and a dashpot having the damping constant c , connected in parallel.

If a harmonic deformation is imposed for the model, as it can be thought to be transmitted cinematically from the vibratory platform [15].

$$X(t) = X_0 \cos \omega t = X_0 \cos 2\pi f t, \tag{1}$$

where $X(t)$ is the steady-state deformation as a time t function, X_o is the amplitude of deformation, ω is the circular frequency and f is the frequency of the harmonic deformation. Then, the model responds with a force

$$F(t) = kX_0 \cos \omega t - c\omega X_0 \sin \omega t = F_0 \cos(\omega t + \varphi), \tag{2}$$

where

$$F_0 = X_0 \sqrt{k^2 + \omega^2 c^2}, \quad \text{and} \quad \tan \varphi = \frac{\omega c}{k} = \delta. \tag{3}$$

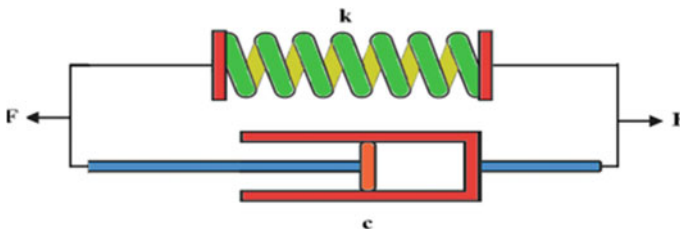


Fig. 1 Rheological model Kelvin–Voigt

In the three relations, (3) were defined the force F_0 amplitude, the phase φ of the deformation and the response force of the model, as well as the internal friction coefficient, δ . The (1) and (2) are the parametric equations for an ellipse. By eliminating the time between two above equations, a family of ellipses was obtained having δ or φ as a parameter.

$$\left(\frac{F}{F_0}\right)^2 + \left(\frac{X}{X_0}\right)^2 - 2\left(\frac{F}{F_0}\right)\left(\frac{X}{X_0}\right)\cos\varphi = \sin^2\varphi. \quad (4)$$

The area inside this loop is the energy dissipated during a cycle of vibration motion in a volume unit, and it is equal to the work done by the force (2) acting on the displacement (1). The mechanical energy dissipated in a cycle is denoted by W_d and much transformed into heat. Therefore, it can be written

$$W_d = \oint F dX = \int_0^{\frac{2\pi}{\omega}} F \dot{X} dt = \omega F_0 X_0 \int_0^{2\pi} \cos(\omega t + \varphi) \sin \omega t dt = \pi F_0 X_0 \sin \varphi. \quad (5)$$

Using the two relations of (3), the expression of dissipation energy over a whole cycle of a harmonic vibration becomes

$$W_d = 2cf\pi^2 X_0^2. \quad (6)$$

To better suggest that the energy dissipated on a cycle by viscous damping is dependent on the internal friction denoted by δ a family of six ellipses for different values of this coefficient were represented in Fig. 2. The area, therefore, the energy dissipated on the cycle is as small as the coefficient δ is smaller. For $\delta = 0$, the ellipse turns into a right, so the behavior would be purely elastic.

Total energy dissipated in the rheological model over exposed time t of a harmonic vibration, denoted by W_{dt} can also be put into the form

$$W_{dt} = 2c\pi^2 f^2 X_0^2 t. \quad (7)$$

Most of the dissipated energy will come in the form of heat in the leg muscles and will do into increasing the temperature of the skin. It can be seen that the energy dissipated in a time t , by viscous damping, is directly proportional to the square of the excitation frequency, to the square of the transmitted vibration amplitude, to the vibration exposure time and to the damping constant.

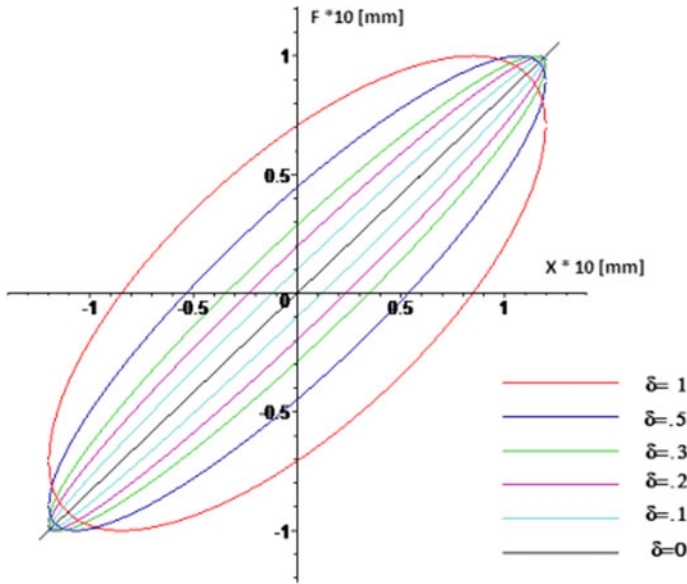


Fig. 2 Elliptical figures for a different internal friction coefficient

3 Materials and Experiment

The measurements were carried out within the Vibration Laboratory of the Polytechnic University of Timisoara, during the period 9–10 May 2019, in which a controlled ambient temperature of $(24 \pm 0.43) \text{ }^\circ\text{C}$ and a relative humidity of $(45 \pm 3.12)\%$ was ensured. Determination of lower limb skin temperatures was performed with a FLIR infrared thermographic camera. An experienced 25-year-old sportsman with a 68 kg body mass and a height of 168 cm was taken for experiment. To accommodate with the environment, he had an acclimatization period of 30 min. He is not a smoker or drinker of coffee or alcohol. For the warm-up of the athlete, a Power Plate body vibration platform (Power Plate North America Inc., Northbrook, IL) was used (Fig. 3).

The measurements were made on an experienced athlete, therefore, the three components of the lower limbs: calves, knees and thighs are very physically demanding in sports activity (Fig. 4). That is why knowing how the athlete’s warm-up process is done, through this WBV technique, is important in setting up his training program.

In these experiments, the FLIR T530 infrared camera was used which has the characteristics required for professional measurements. With a platform equipped with 180° rotating lenses and a 4-inch screen, the thermographic camera is designed to help users diagnose hard-to-reach components in any environment, ensuring high image quality. Thermographic infrared cameras provide temperature measurement without contact with the observed body.

Fig. 3 Vibratory plate



Fig. 4 Posterior parts of the lower limbs measured skin



The infrared camera FLIR T530 is equipped with software that can measure the temperature of any point in the analyzed area. It can also specify the position of the maximum temperature point. For the analysis to be selected for calves, knees and thighs, in all experiments, the maximum temperature points on the right skin limb. This is marked by a triangle in the two representative figures (Figs. 5 and 6).

Fig. 5 Skin temperature in the calf area

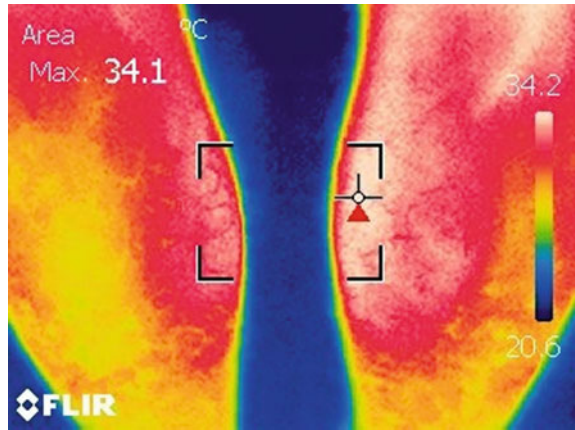
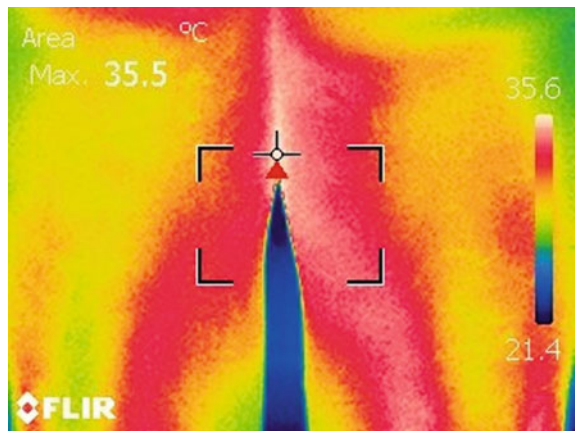


Fig. 6 Skin temperature in the thigh area



4 Results

In order to track the way the lower limb skin temperature changes as a result of acute exposure to vibration within a short time of less than 100 s, a protocol has been established.

The first experiment was achieved by maintaining a constant frequency of 50 Hz and constant amplitude of 2 mm, peak to peak, and the exposure time changed from 40 s to 100 s in a 20 s step. For each experiment, the maximum temperature on the calf skin, knee and thigh skin of the lower right limb was recorded. These results are plotted as shown in Fig. 7. It is found that the skin temperature of the three components of the lower limb increases with the increase in vibration exposure time. The most pronounced increase of the temperature is seen on the thigh skin.

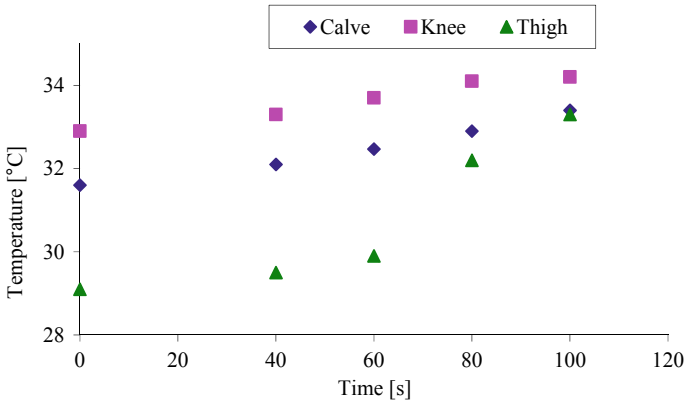


Fig. 7 Temperature variation of the posterior lower limb skin depending on the time exposure

In the second experiment, the amplitude of 2 mm was maintained, peak to peak, constant, and duration of exposure to vibration was also maintained constant, i.e., 100 s.

From a medical point of view, the size of the vibration amplitude is not a limited parameter, unlike the frequency and time of exposure which have limited values. A benefit of lower limb exposure through a vibrating platform is that muscles can be performing quickly and efficiently, making them able to provide more strength.

In this case, the vibration frequency from 20 to 50 Hz is changed at a rate of 10 Hz. As a result of this experiment, it can see that the maximum skin temperature points on the calves, knees and thighs increase with the frequency of vibrations. The results of the measurements are presented graphically in Fig. 8.

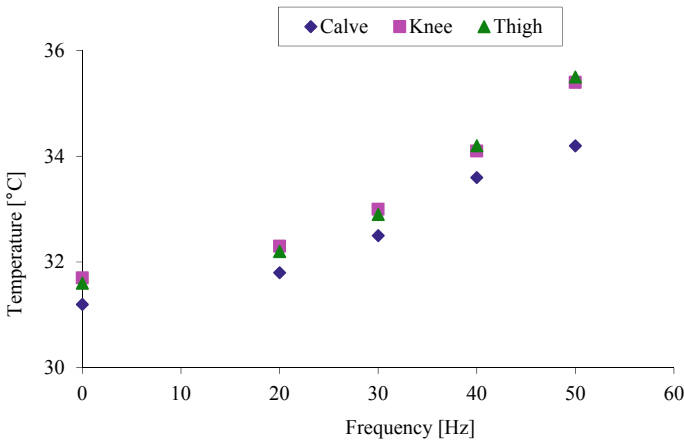


Fig. 8 Temperature variation of the posterior lower limb skin depending on the frequency

5 Conclusions

A first conclusion that can be drawn is that to the detriment of other work, which states that the temperature of the skin decreases [16, 17], following the acute exposure to vibrations of the lower limbs, and in this experiment, it is found that this is denied. It is necessary to carry out research on a larger lot and a statistical analysis is required. Another conclusion from exposure to vibration for a time of 100 s with different frequencies has as effect on the posterior region of lower limbs the increase in temperature, as can be seen from Figs. 7 and 8. Certainly, research in this area must be continued to remove the inconsistencies.

References

1. D. Bishop, Warm up I: potential mechanisms and the effects of passive warm up on exercise performance. *Sports Med.* **33**(6), 439–454 (2003)
2. D.J. Cochrane, The sports performance application of vibration exercise for warm-up, flexibility and sprint speed. *Eur. J. Sport Sci.* **13**(3), 256–271 (2013)
3. S.S. Colsona, S. Roffino, M. Mutin-Carninoa, A. Carninoa, P.D. Petit, The effect of dynamic whole-body vibration warm-up on lower extremity performance. *Sci. Sports* **31**(1), 1–8 (2015)
4. W.J. Armstrong, D.C. Grinnell, G.S. Warren, The acute effect of whole-body vibration on the vertical jump height. *J. Strength Cond. Res.* **24**(10), 2838–2839 (2010)
5. A. Gerodimos, V. Zafeiridis, K. Karatrantou, T. Vasilopoulou, K. Chanou, E. Pispirikou, The acute effects of different whole-body vibration amplitudes and frequencies on flexibility and vertical jumping performance. *J. Sci. Med. Sport* **13**(4), 438–443 (2010)
6. D.J. Cochrane, I.D. Loram, S.R. Stannard, J. Rittweger, Changes in joint angle, muscle-tendon complex length, muscle contractile tissue displacement, and modulation of EMG activity during acute whole-body vibration. *Muscle Nerve* **40**(3), 420–429 (2009)
7. K. Lienhard, A. Cabasson, O. Meste, S.S. Colson, sEMG during whole-body vibration contains motion artifacts and reflex activity. *J. Sports Sci. Med.* **14**(1), 54–61 (2015)
8. R.D. Pollock, R.C. Woledge, F.C. Martin, D.J. Newham, Effects of whole body vibration on motor unit recruitment and threshold. *J. Appl. Physiol.* **112**(3), 388–395 (2012)
9. J.M. Wakeling, B.M. Nigg, A.I. Rozitis, Muscle activity damps the soft tissue resonance that occurs in response to pulsed and continuous vibrations. *J. Appl. Physiol.* **93**(3), 1093–1103 (2002)
10. J. Rittweger, G. Beller, D. Felsenberg, Acute physiological effects of exhaustive whole-body vibration exercise in man. *Clin. Physiol.* **20**(2), 134–142 (2000)
11. T. In, K. Jung, M.G. Lee, H.Y. Cho, Whole-body vibration improves ankle spasticity, balance, and walking ability in individuals with incomplete cervical spinal cord injury. *Neuro Rehabil.* **42**, 491–497 (2018)
12. O. Suci, R.R. Onofrei, A.D. Totorean, S.C. Suci, E.C. Amaricai, Gait analysis and functional outcomes after twelve-week rehabilitation in patients with surgically treated ankle fractures. *Gait Posture* **49**, 184–189 (2016)
13. O. Suci, L. Bereteu, G. Draganescu, T. Ioanovici, Determination of the elastic modulus of hydroxiapatite doped with magnesium through nondestructive testing, in *Advanced Materials Research*, vol. 814 (Timisoara, Romania, 2013), pp. 115–122
14. R.R. Onofrei, E.C. Amaricai, R. Petroman, D. Surducan, O. Suci, Preseason dynamic balance performance in healthy elite male soccer players. *Am. J. Mens Health* **13**(1), 1–7 (2019)
15. M. Radeş, *Mechanical Vibrations* (Editura Printech, Bucharest, Romania, 2006)

16. D.J. Cochrane, S.R. Stannard, A.J. Sargeant, J. Rittweger, The rate of muscle temperature increase during acute whole-body vibration exercise. *Eur. J. Appl. Physiol.* **103**, 441–448 (2008)
17. A. Seixas, R. Vardasca, J. Gabriele, The effect of different vibration frequencies in the skin temperature in healthy subjects, in *2014 IEEE International Symposium on Medical Measurements and Applications (MeMeA)* (2014), pp. 1–5

Modeling and Simulation of Mechanical Behavior of Spinal Ligaments with Applications in Traction Therapy



Adela Neamțu Popescu, Lucian Rusu, Ion Crăștiu, Alexandru Pavăl,
and Liviu Bereteu

Abstract Traction is a mechanical action and refers to forces applied to the body with the purpose of stretching a certain part or separating two or more parts. This physiotherapeutic method has been known since antiquity, and its use is generally limited to the cervical and lumbar spine, with the aim of relieving pain in or coming from this area. The purpose of this paper is to model the viscoelastic behavior of the spine ligaments through a Burgers rheological model, respectively, to simulate this behavior in Simulink by highlighting the two phases of the stretching process: creep and creep recovery. The practical physiotherapeutic effects of the ligament elongation process are analyzed. The elongation process is determined by a traction force that can be controlled computerized, both in size and shape.

1 Introduction

The vertebral column is the most important segment of the locomotor system and forms the axial skeleton of the trunk, providing spinal cord protection, orthostatic positioning of the body, as well as a biomechanical role in the transmission of large movements. To ensure the resistance and mobility of the spine, bone elements called vertebrae are joined by fibrous connective elements called ligaments and between two vertebrae there is an intervertebral disk.

A. Neamțu Popescu · L. Rusu · I. Crăștiu · A. Pavăl · L. Bereteu (✉)
Mechanics and Materials Strength Department, Politehnica University of Timișoara, Bd. Mihai
Viteazul, Nr. 1, 300222 Timișoara, Romania
e-mail: liviu.bereteu@upt.ro

A. Neamțu Popescu
e-mail: adelaneamtu@yahoo.com

L. Rusu
e-mail: lucian.rusu@upt.ro

I. Crăștiu
e-mail: ion_crastiu@yahoo.com

Elongation or stretching is a process that applies to the various regions of the spine that create a decrease in intervertebral pressure. A first mechanism by which stretching works is the elongation of the ligaments of the vertebral column leading to the dislocation of the disco-vertebral segments and the creation of space for the volume increase of the intervertebral disk. Another mechanism of the stretching process is to create a vacuum or negative pressure effect within the intervertebral disks, an effect that will help the disks to hydrate, providing a good environment for healing. At the same time, the decompression of the spine and the hydration of the disk lead to the height of the intervertebral space.

Cervical traction is used for various types of vertebral lesions such as cervical herniated nucleus pulposus, strains and myofascial pain [1]. The effect of traction can provide beneficial effects on posture and lumbar movement [2]. Improving the amplitude of the hip and pelvis movement helps reduce back pain and is achieved by stretching the broad facial tensor [3]. Static and dynamic stretching has an effect on increasing spine movement in patients with low back pain [4]. The acute effects of the tract of stretching in the thorax and lumbar curves and the pelvic inclination were determined in the paper [5]. The effect of stretching exercises leads to the correction of the posture and walking of patients who have had fractures [6, 7], but also to the performance of soccer players [8].

The purpose of this paper is to model the viscoelastic behavior of the spine ligaments, to simulate this behavior in Simulink by highlighting the two phases of the stretching process: creep and stress relaxation. The effects of the stretching process in which the traction force can be given by the body's own weight by sliding on an inclined plane, by means of counterweights or by means of straps, in which case a controlled computerized force command is provided.

2 Viscoelastic Modeling of Spinal Ligaments

The mechanical behavior of the ligaments can be considered as a superposition of the elastic property, as a spring, over the viscous flow property as a dashpot. The Burgers model is the result of connecting two units in a series, one unit representing a Maxwell model and the other unit representing a Kelvin model (Fig. 1).

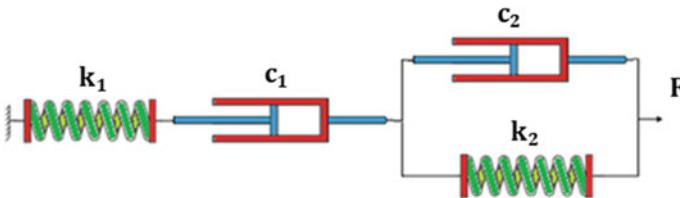


Fig. 1 Burgers rheological model

It is well known that other simple models such as Kelvin and Maxwell have a viscoelastic behavior but do not show the relaxation phenomenon. This is the reason why the Burgers model was chosen to simulate the biomechanical behavior of the spinal ligaments in traction. In the Maxwell model the two constituent elements connected in series are characterized by the elasticity given by the stiffness coefficient k_1 and by an amortization given by the damping coefficient, c_1 . The Kelvin model, consists of two parallel elements, is characterized by the elasticity given by the stiffness coefficient k_2 and by an amortization given by the damping coefficient, c_2 .

To obtain the constitutive equation of the Burgers model, the total elongation, given by the action of a force F , is taken as the sum of three elongations corresponding to the three elements connected in series, the spring, the dashpot and the Kelvin model

$$d = d_1 + d_2 + d_3, \tag{1}$$

where d_1 is the elongation of the spring

$$d_1 = \frac{F}{k_1}, \tag{2}$$

where d_2 is the elongation of the dashpot

$$\dot{d}_2 = \frac{F}{c_1}, \tag{3}$$

and d_3 is the elongation of the Kelvin unit

$$\dot{d}_3 + \frac{k_2}{c_2}d_3 = \frac{F}{c_2}. \tag{4}$$

The internal variables, d_1 , d_2 and d_3 can be eliminated in the above equations to obtain the constitutive equation of the Burgers model in the external variables F and d

$$F + \left(\frac{c_1}{k_1} + \frac{c_1}{k_2} + \frac{c_2}{k_2} \right) \dot{F} + \frac{c_1 c_2}{k_1 k_2} \ddot{F} = c_1 \dot{d} + \frac{c_1 c_2}{k_2} \ddot{d}. \tag{5}$$

In order to obtain the creep behavior of the Burgers model in (5), it will be assumed that at the initial moment the applied force is the constant F_0 and the initial conditions result from the instantaneous elongation of the spring k_1 and the elongation velocity are

$$d = d_1 = \frac{F_0}{k_1}, \quad d_2 = d_3 = 0, \quad t = 0 \tag{6}$$

$$\dot{d} = \frac{F_0}{c_1} + \frac{F_0}{c_2}, \quad t = 0. \tag{7}$$

Creep diagrams can be simulated using the Simulink model in MATLAB, and the constitutive equation is

$$\frac{c_1 c_2}{k_2} \ddot{d} + c_1 \dot{d} = F_0, \quad t < t_1. \quad (8)$$

If the force F_0 is removed at time t_1 the constitutive equation of the recovery behavior of the Burgers model can be obtained from (8)

$$\frac{c_1 c_2}{k_2} \ddot{d} + c_1 \dot{d} = 0, \quad t > t_1 \quad (9)$$

3 Numerical Analysis of Creep and Creep Recovery

The simulation of spinal ligament behavior and the acquisition of creep and creep recovery after traction are performed using the numerical analysis software given by the SIMULINK module in MATLAB. Two cases are analyzed. In the first case the constant force is applied in a time t_1 interval, after which the traction force is removed for a relaxation phase for a time t_2 higher than t_1 time. The total creep time and creep recovery time is 40 s. In the second case the traction force is applied for a short time t_1 , after which for a shorter time t the traction force is removed. Then this cycle is restarted. Intermittent drive of the traction force is obtained, and a certain number of creep and creep recovery cycles are obtained.

The scheme for simulating creep and creep recovery behavior of the Burgers model is done by following (8) and (9) and is shown in Fig. 2.

The elastic behavior of the ligaments causes them to return to their initial length after the force is removed. Therefore, in the simulation, it was intended to observe how the two elements that characterize the damping influence on the remanent length of the ligament after the removal of the force. For this purpose, four curves were obtained with the applied force, the elasticity and the damping constants were the input elements and the elongation of the ligament was the output.

In the paper [9] the biomechanical properties of six types of human lumbar spine ligaments were determined. Based on these results, the following data were considered for simulations:

- for curve 1 (cyan line): $F = 10 \text{ N}$, $k_1 = 1 \text{ N/mm}$, $c_1 = 20 \text{ Ns/mm}$, $k_2 = 10 \text{ N/mm}$, $c_2 = 40 \text{ Ns/mm}$;
- for curve 2 (red line): $F = 10 \text{ N}$, $k_1 = 10 \text{ N/mm}$, $c_1 = 30 \text{ Ns/mm}$, $k_2 = 10 \text{ N/mm}$, $c_2 = 30 \text{ Ns/mm}$;
- for curve 3 (green line): $F = 10 \text{ N}$, $k_1 = 10 \text{ N/mm}$, $c_1 = 35 \text{ Ns/mm}$, $k_2 = 10 \text{ N/mm}$, $c_2 = 45 \text{ Ns/mm}$;
- for curve 4 (blue line) $F = 10 \text{ N}$, $k_1 = 10 \text{ N/mm}$, $c_1 = 50 \text{ Ns/mm}$, $k_2 = 10 \text{ N/mm}$, $c_2 = 50 \text{ Ns/mm}$.

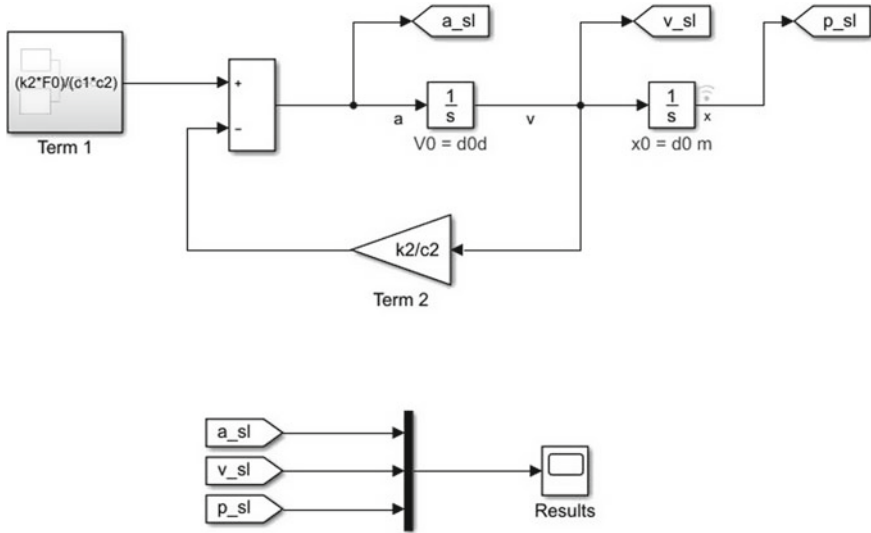


Fig. 2 Simulink scheme to simulate creep and creep recovery of the Burgers model

For all cases, it is considered that the force acts on a single ligament and is applied for 8 s, after which it is removed, and the evolution of the elongation is followed for another 32 s.

Following the application of force in the ligaments, due to the elastic behavior, an instantaneous elongation of 1 mm occurs, in the case considered. Then, on the time of force application, elongation increases. At the moment of force interruption, also due to elastic behavior, there is an instantaneous decrease of the elongation, also by 1 mm. After this moment the decrease of the elongation is slowly, asymptotically, toward a constant value which depends on the amount of the damping. In conclusion, the residual elongation of the ligament depends on its viscosity level. For high values of damping coefficient, smaller residual elongations are obtained. See curves 1–4 of Fig. 3.

4 Traction System and Method

Creating a satisfactory intervertebral space is only possible through a relatively severe traction, but the over-stretching of the ligament should be avoided. For these reasons, intermittent traction is usual applied. This means that the traction force remains constant only for a short time, after which it is reduced or eliminated completely. There is a relaxation phase, after which the force can grow again.

This type of force applied intermittently should be maintained throughout the treatment. Spinal traction is a method that is used with confidence due to the age

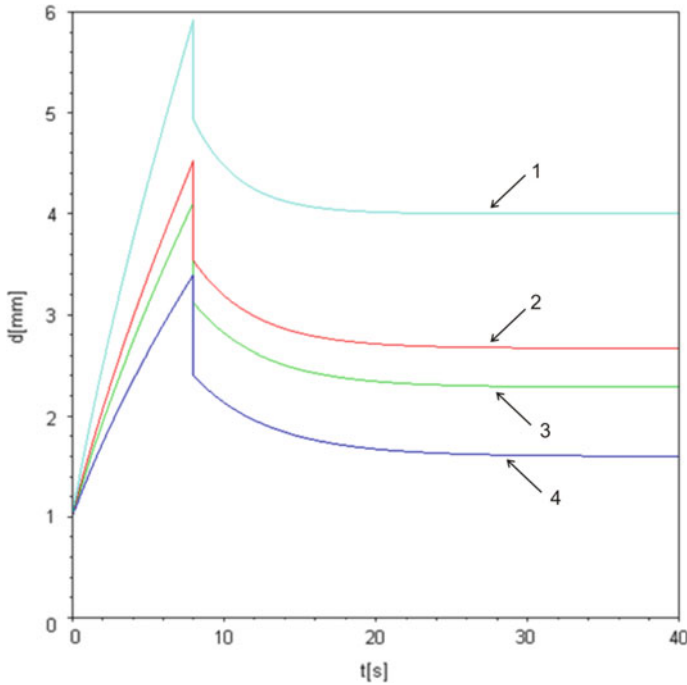


Fig. 3 Creep and creep recovery for viscoelastic Burgers model

of its application over time for the treatment of disk prominence, degenerative disk disease and joint dysfunction. Treatment is not always effective and is not easy to administer, as pain may recur. There are many variations of traction techniques, some of which are questionable. It should be stressed that spinal traction is only part of the total treatment regimen, which should include other forms of therapy.

Without this type of program, spinal traction, like many other methods, only remains valid for a long time rather than long term. Spinal cord traction therapy is an important component in the treatment of most of its diseases, including osteochondrosis, scoliosis and intervertebral hernia. Traction as a therapeutic effect aims at eliminating muscle spasms, reducing intra-disk pressure, reducing disk herniations, eliminating painful pathological impulses in the spinal spinal-motor segment. For spinal traction therapy (cervical traction and lumbar spine), the BTL-16 Plus (UK production) was used (Fig. 4). BTL-16 Plus is a microprocessor-controlled traction device designed for continuous and intermittent cervical and lumbar therapy. Traction therapy is a common treatment option used for back and neck pain [10].

The patient claims pain in the lumbar region. Following MRI investigations, it was found that pain was caused by L5-S1 lumbar discopathy, and a somatoscopic examination showed a musculoskeletal disorder. The lumbar traction was applied for 15 min per session, and traction-relaxation cycle lasted for 40 s. In the first session, the patient accuses a pain with an index of 8 on a pain scale from 0 to 10. For

Fig. 4 Exercise from the sitting position, keeping the heels on the platform



the 0 index, it is considered non-existent pain and for the index 10 it is considered unbearable pain. After the 10 treatment sessions the pain reached index 2, appearing only in certain patient positions.

In future research, a patient group will be tracked so that a statistical analysis of the results can be made. It will also be sought to find a method for measuring the dimensions of the intervertebral disks in order to validate the simulations given by the curves in Fig. 3.

5 Conclusions

The results of the numerical simulation represented by the diagrams in Fig. 3 show that human spine ligaments, under traction forces, can be modeled with a viscoelastic behavior as the Burgers model, with a remanent elongation. It is found that after applying the traction and then eliminating the force the ligaments remain with a remanent elongation, which means that it allows the intervertebral disks to be hydrated, to return to shapes closer to the initial form and thereby eliminate their pressures on the nerves. From the curved family, it can be concluded that these remanent stretches also

depend on the viscous nature of the ligaments. For elderly people these depreciation values are higher and consequently the residual elongations diminish.

Although traction therapy is very useful, especially in the US, this technique has some inconsistencies both in terms of explaining the biomechanical behavior of the body to this type of mechanical stress as well as in terms of results [9]. Statistical analyzes by groups of subjects are necessary and simulation development on nonlinear viscoelastic models.

References

1. J. Cyriax, G. Russell, *Textbook of Orthopaedic Medicine*, vol 2, 10th edn. (Bailliere, Tindall & Cassell Ltd, London, 1980)
2. Y. Li, P. McClure, N. Pratt, The effect of hamstring muscle stretching on standing posture and on lumbar and hip motions during forward bending. *Phys. Ther.* **76**(8), 836–845 (1996)
3. H.I. Bae, D.Y. Kim, Y.H. Sung, Effects of a static stretch using a load on low back pain patients with shortened tensor fascia lata. *J. Exerc. Rehabil.* **13**(2), 227–231 (2017)
4. H.R.D. Ray, T.A. Firmansah, S. Giriwijoyo, The effect of static and dynamic stretching techniques to increase spine range of movement (ROM) on low back pain (LBP) patients. *J. Eng. Sci. Technol. Special Issue on AASEC'2016*, 23–33 (2017)
5. P.A. López-Miñarro, J.M. Muyor, F. Belmonte, F. Alacid, Acute effects of hamstring stretching on sagittal spinal curvatures and pelvic tilt. *J. Hum. Kinet.* **31**, 69–78 (2012)
6. O. Suci, R.R. Onofrei, A.D. Totorean, S.C. Suci, E.C. Amaricai, Gait analysis and functional outcomes after twelve-week rehabilitation in patients with surgically treated ankle fractures. *Gait Posture* **49**, 184–189 (2016)
7. O. Suci, L. Bereteu, G. Draganescu, T. Ioanovici, Determination of the elastic modulus of hydroxyapatite doped with magnesium through nondestructive testing, in *Advanced Materials Research*, vol. 814 (Timisoara, Romania, 2013), pp. 115–122
8. R.R. Onofrei, E. Amaricai, R. Petroman, D. Surducun, O. Suci, Preseason dynamic balance performance in healthy elite male soccer players. *Am. J. Mens. Health* **13**(1), 1–7 (2019)
9. F.A. Pinter, N. Yoganandan, T. Myers, A. Elhagediab, A. Sances Jr., Biomechanical properties of human lumbar spine ligaments. *J. Biomech.* **25**(11), 1351–1356 (1992)
10. I.A. Young, L.A. Michener, J.A. Cleland, A.J. Aguilera, A.R. Snyder, Manual therapy, exercise and traction for patients with cervical radiculopathy: a randomized clinical trial. *Phys. Ther.* **89**(7), 632–642 (2009)

Parameter Optimization for Biocompatible Polyamide Used in Selective Laser Sintering (SLS)



Dan Ioan Stoia, Liviu Marsavina, Alexandru Cosa, and Andreea Nicoara

Abstract One of the major issues in additive manufacturing concerns the geometrical and mechanical properties of its products. Selective laser sintering uses a laser beam that binds together the biocompatible polyamide powder, having as results rigid parts that can be used for mechanical constructions. The biocompatibility of the material makes the construction appropriate to interact with human body. Optimization of manufacturing parameters was conducted using Taguchi's method considering three parameters: energy density, temperature of the building environment, and part orientation taken at three levels (L9, 3×3 orthogonal array). The output parameter considered for computing the signal-to-noise (SN) ratio (using maximization criterion) was the tensile strength of the samples. The optimal parameter plan for acquiring the highest mechanical strength will further be used on the machine for developing a surgical, single use, osteotomy guide.

1 Introduction

The reliability of the additive manufacturing process can be evaluated by the quality of its products. These had to meet geometrical tolerances, anticipated shape and mechanical properties all together [1–3]. None of the additive technologies available on market produce parts that are free of errors. However, the endless possibilities in

D. I. Stoia (✉) · L. Marsavina · A. Cosa · A. Nicoara
Politehnica University Timisoara, Mihai Viteazul no. 1, Timisoara, Romania
e-mail: dan.stoia@upt.ro

L. Marsavina
e-mail: liviu.marsavina@upt.ro

A. Cosa
e-mail: alex_cosa@yahoo.com

A. Nicoara
e-mail: andreean9@yahoo.com

achieving complex geometrical shapes that can be used in a variety of applications [4–7] make this class of technologies very attractive.

According to the technology type, the process variables are different. In selective laser sintering (SLS), the main process parameters that directly influence the quality of the products are: chamber temperatures, exposure parameters, layer thickness, geometry of the part, position and orientation, material type, and quality [8–10].

Taking into account the number of variables that influence the quality of the final product, and the fact that they can be set within a range of values, process optimization using design of experiments (DOE) can be used [11, 12].

Taguchi's approach is an effective tool used by engineers in all classes of manufacturing processes [13, 14]. Efforts in optimizing additive manufacturing processes using Taguchi's design method have been made in the past, showing that the quality of a product can be quantified based on noise and signal factors. Maximizing the signal-to-noise ratio will lead most of the times to an optimal parameter setup [15, 16].

The purpose of the paper is to use the Taguchi method as an optimization tool toward the goal of achieving the highest mechanical strength of polyamide PA2200 samples, manufactured by SLS.

2 Materials and Methods

2.1 Sample Design and Fabrication

Sample design was accomplished in SolidWorks 2015 according to the regulations of ISO 527-1:2012 standard for tensile testing of plastics [17]. The shape and size of the sample can be observed in Fig. 1.

The material used was polyamide PA2200 in powder form. It possesses relatively high strength and stiffness, good chemical stability, high geometric resolution, and biocompatibility according to EN ISO 10993-1 [18]. The general properties provided

Fig. 1 3D design of tensile sample according to ISO 527-1:2012

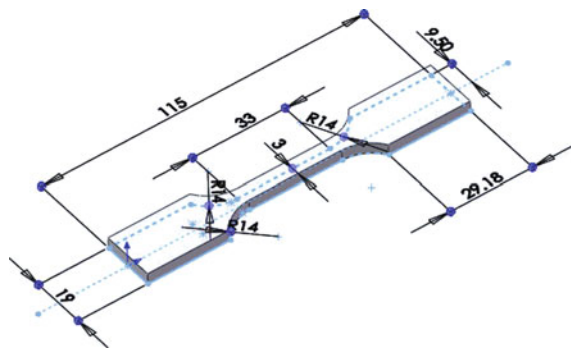


Table 1 Manufacturing parameters and levels

Control factors	Symbol	Level/value		
		0	1	2
Energy density (J/mm ²)	<i>E</i>	0.0732	0.0502	0.0346
Orientation (deg)	<i>θ</i>	0	30	45
Temperature (°C)	<i>T</i>	169.5	170.0	170.5

Table 2 Experiment orthogonal (L9) array

Experiment	Factor/level		
	<i>E</i>	<i>θ</i>	<i>T</i>
First	0	0	0
Second	0	1	1
Third	0	2	2
Fourth	1	0	1
Fifth	1	1	2
Sixth	1	2	0
Seventh	2	0	2
Eighth	2	1	0
Ninth	2	2	1

by the manufacturer are: average grain size 56 μm; density of 0.45 g/cm³; melting point 172–180 °C; tensile strength 48 MPa.

The manufacturing process was conducted on EOS Formiga P100 machine that uses selective laser sintering for bonding layer by layer the powder material to a solid compact form. The powder is heated up using an electrical heater, while additional energy required for sinterization is provided by a 30 W CO₂ laser.

For evidencing the influence of energy density, orientation angle, and building temperature on tensile strength of the samples, the manufacturing process was conducted nine times by setting up the factor’s level according to Table 1. For every manufacturing process (described in Table 2), three parts were built, resulting a total number of 27 parts.

At the end of the building process, the parts were cooled down for 5 h inside of the machine, and air blasted for cleaning after.

2.2 Geometric Evaluation and Mechanical Testing

Geometrical evaluation was done before the mechanical testing by measuring the dimensions of every sample using a digital caliper. The samples were also weighted using a digital balance in order to compute the density of each individual sample.

The mechanical testing runs on a tensile testing machine, setting up the displacement velocity to 5 mm/min. The tests were all conducted to the breaking point. The force displacement diagrams were then used to extract the maximum force and to compute the corresponding stress value, taking into consideration the real cross-sectional area of samples.

2.3 Taguchi Design

The main goal in Taguchi design is to improve the quality of the products by determining which individual factor has more or less influence in the process results. According to Taguchi’s approach based on control factors, L9 is an appropriate orthogonal array that reduces the number of experiments from 27 to 9 (Table 2) saving the time and costs and producing accurate results.

Because the goal parameter is the tensile strength and this should be as high as possible, the maximization criterion was used. In larger is better approach, the signal-to-noise ratio is computed using (1) [14], where x_i represents the mechanical strength.

$$SN = -10 \times \log_{10} \left(\frac{1}{n} \cdot \sum_{i=1}^n \frac{1}{x_i^2} \right) \tag{1}$$

3 Results and Discussions

In Table 3, the results of computed SN ratio along with control factor levels are presented.

Table 3 DOE table and tensile strength vales

Exp	E	θ	T	σ_m values (MPa)			av. σ_m (MPa)	S/N
First	0	0	0	29.619	31.281	29.988	30.296 ± 0.873	29.621
Second	0	1	1	32.018	32.224	31.483	31.908 ± 0.382	30.077
Third	0	2	2	32.130	31.281	31.010	31.474 ± 0.584	29.956
Fourth	1	0	1	12.728	13.410	11.843	12.660 ± 0.786	22.015
Fifth	1	1	2	16.938	18.077	17.142	17.386 ± 0.608	24.793
Sixth	1	2	0	14.348	13.089	15.585	14.341 ± 1.248	23.065
Seventh	2	0	2	9.476	9.370	9.165	9.337 ± 0.158	19.402
Eighth	2	1	0	11.366	11.479	10.789	11.211 ± 0.370	20.983
Nineth	2	2	1	10.180	9.967	11.232	10.460 ± 0.677	20.355

Here, σ_m values represent the values obtained for tensile strength according to the process parameters and $av.\sigma_m$ stance for its average value and standard deviation. The values of SN ratio computed by maximization criterion are also presented.

The corresponding SN values for every factor and each level were then selected and averaged. The computation result is denoted by *Average S/N* and is presented in Table 4.

The relative difference (*Rel.dif*) is computed by subtracting the lowest SN value from the highest one (Table 4). The highest rank (I) is attributed to the highest relative difference taken without sign. It signifies which of the control factors is generating a higher influence on the goal parameters. As it can be observed, the energy density plays the main role.

The optimal level for each factor was is also presented in Table 4. The highest average SN ratio taken without sign for every factor represents the optimum value for a high mechanical strength.

Table 4 Results of SN ratio and average analysis

Parameter	Level	Value	Average S/N	Rel. dif.	Rank	Optimal
<i>E</i>	0	0.073	29.884	9.638	I	<i>E</i> 0
	1	0.050	23.291			
	2	0.035	20.247			
θ	0	0.0	23.679	1.605	II	θ 1
	1	30.0	25.285			
	2	45.0	24.459			
<i>T</i>	0	169.5	24.556	0.568	III	<i>T</i> 2
	1	170.0	24.149			
	2	170.5	24.717			

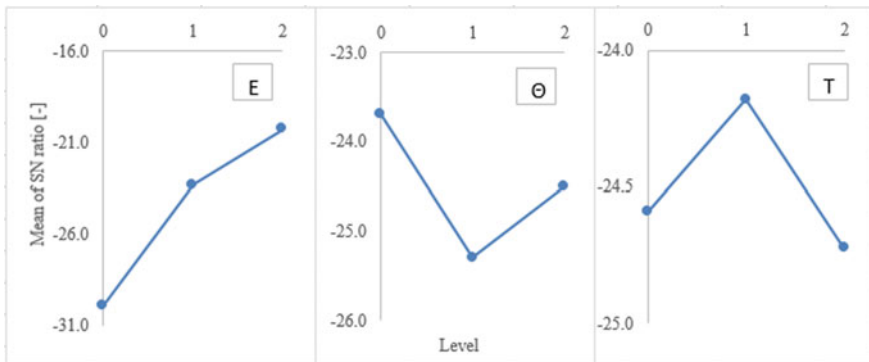


Fig. 2 Representations of signal-to-noise ratio according to *E*, θ and *T* factors at three levels

The SN ratio was graphically presented in Fig. 2, showing the influence of each control factors taken at every level on the mechanical strength of PA2200 samples. The values used for representation are averages.

4 Conclusions

The paper presents an optimization work conducted using Taguchi's design. It starts with modeling the standard sample, continuing with the additive manufacturing process according to the experiment table, and finally conducting the tensile testing.

The main role in tensile strength of PA2200 obtained by SLS is played by the energy density of the laser beam followed by the orientation angle and the chamber temperature.

The optimum level obtained for each control factors was achieved: $E = 0$, $\theta = 1$ and $T = 2$. Using this parameter setup, optimal (from the perspective of mechanical strength) polyamide parts can be obtained by SLS. The greatest influence of the three factors considered in the study belongs to the energy density. It plays an essential role both in mechanical strength and stiffness of the SLS manufactured parts.

Acknowledgements This work was supported (in part) by research grant GNaC2018-ARUT, no.1363/01.02.2019, financed by Politehnica University of Timisoara.

References

1. C.K. Chua, C.H. Wong, W.Y. Yeong, Standards, Quality Control, and Measurement Sciences in 3D Printing and Additive Manufacturing (Elsevier Inc., 2017)
2. D.I. Stoia, E. Linul, L. Marsavina, Influence of manufacturing parameters on mechanical properties of porous materials by selective laser sintering. *Materials* **12**, 871 (2019)
3. A. Rajic, E. Desnica, S. Stojadinovic, D. Nedelcu, Numerical simulation and additive manufacturing technology in design of knee implant patterns. *J. Optoelectron. Adv. Mater.* **16**(9–10), 1180–1190 (2014)
4. A. Marin, K. Menyhardt, A.M. Marin, R. Nagy, M. Poenaru, Prototype device for mastoid obliteration in pediatric cholesteatoma patients, in *AVMS 2017, Springer Proceedings in Physics*, vol. 198 (Springer, 2018)
5. C. Cosma, N. Balc, M. Moldovan, L. Morovic, P. Gogola, C. Miron-Borzan, Post-processing of customized implants made by laser beam melting from pure Titanium. *J. Optoelectron. Adv. Mater.* **19**(11–12), 738–747 (2017)
6. D. Vermesan, I. Trocan, R. Prejbeanu, D.V. Poenaru, H. Haragus, D. Gratian, M. Marrelli, F. Inchingolo, M. Caprio, R. Cagiano, M. Tatullo, Reduced operating time but not blood loss with cruciate retaining total knee arthroplasty. *J Clin Med Res.* **7**(3), 171–5 (2015)
7. R. Nagy, R.S. Maruta, K. Menyhardt, Active vibration control of test equipment through feedback algorithm, in *AVMS-2017, Springer Proceedings in Physics*, vol. 198 (Springer, Berlin, 2018)
8. K. Zhang, G. Fu, P. Zhang, Z. Ma, Z. Mao, D.Z. Zhang, Study on the geometric design of supports for overhanging structures fabricated by selective laser melting. *Materials* **12**, 27 (2019)

9. W.Y. Yeong, C.K. Chua, Implementing additive manufacturing for medical devices: a quality perspective, in *6th International Conference on Advanced Research in Virtual and Physical Prototyping* (VRatP, Portugal, 2014)
10. B. Song, X. Zhao, S. Li, C.J. Han, Q.S. Wei, S.F. Wen, J. Liu, Y.S. Shi, Differences in microstructure and properties between selective laser melting and traditional manufacturing for fabrication of metal parts: a review. *Frontiers Mech Eng* **10**(2), 111–125 (2015)
11. A. Wegner, G. Witt, Correlation of process parameters and part properties in laser sintering using response surface modeling. *Phys Procedia* **39**, 480–490 (2012)
12. V.D. Sagias, K.I. Giannakopoulos, C. Stergiou, Mechanical properties of 3D printed polymer specimens. *Procedia Struct Integrity* **10**, 85–90 (2018)
13. K.R. Ranjit, *Design of Experiments Using the Taguchi Approach* (John Wiley & Sons, New York, 2001)
14. G. Taguchi, S. Chowdhury, Y. Wu, *Taguchi's Quality Engineering Handbook* (Wiley, New Jersey, 2005)
15. I.F. Ituarte, E. Coatanea, M. Salmi, J. Tuomi, J. Partanen, Additive manufacturing in production: a study case applying technical requirements. *Phys Procedia* **78**, 357–366 (2015)
16. N. Kumar, H. Kumar, J.S. Khurmi, Experimental investigation of process parameters for rapid prototyping technique (selective laser sintering) to enhance the part quality of prototype by Taguchi method. *Procedia Technol* **23**, 352–360 (2016)
17. ISO 527-1. Plastics-Determination of tensile properties—Part 1: general principles, in *International Organization for Standardization* (1214 Vernier, Geneva, Switzerland, 2012), pp. 23
18. ISO 10993-1. Biological evaluation of medical devices—Part 1: evaluation and testing within a risk management process, in *International Organization for Standardization* (1214 Vernier, Geneva, Switzerland, 2018), pp. 41

Vibration Problems in Industrial Processes

Experimental Analysis of Noise and Chatter Detection in Milling Depending on the Cutting Parameters



Mladen Rasinac, Aleksandra Petrović, Branko Radičević, Vladan Grković, and Marina Ivanović

Abstract The aim of this paper was to experimentally analyse the generated noise and detect the appearance of self-excited vibrations, i.e. chatter vibrations during milling. There were performed three different types of experiments, based on the plan proposed in ([1]). In the first experiment, we measured sound pressure level—SPL [dBA] in dependence of cutting parameters, in second we measured SPL [dBA] induced by chatter vibrations and the stability lobes diagram is machined into workpiece while in the third experiment is also measured SPL [dBA] in dependence of radial depth of cut that increases linearly. Material of the workpiece was carbon steel and we used milling cutter with carbide inserts. Vertical machining centre was used for milling and noise was measured with microphone. Purpose of those experiments was to see how different cutting parameters influence on a generation of noise and vibrations. Also, in that way, we can select cutting parameters that will not lead us to unstable regions. The experimental results obtained can be used for future investigations in this field.

1 Introduction

Improving the performance of cutting operations has led to an increase in noise levels, especially during milling. The main sources of noise during milling are self-excited vibrations, i.e. chatter vibrations. In the literature, it is usual to compare noise levels with respect to the spindle speed, feed rate, axial and radial depth of the cut. Purpose of those comparisons is to gain insight into the effects of cutting parameters on the occurrence of noise and vibrations [1, 2, 3, 4].

In [1] are given detailed explanations of an experimental plan to study the noise emission during the milling process. The experimental plan consists of three experiments and this paper presents the results of the experiments carried out on the basis of the experimental plan.

M. Rasinac (✉) · A. Petrović · B. Radičević · V. Grković · M. Ivanović
Faculty of Mechanical and Civil Engineering, University of Kragujevac, Kraljevo, Serbia
e-mail: rasinac.m@mfkv.kg.ac.rs

2 Experiment

In this section are presented setups of the conducted experiments. The equipment consists of: (1) the machine CHARNOA CNC SYSTEMS (vertical milling machine), (2) the milling cutter with proper diameter and APKT inserts and 3) tool holder SANDVIK (Fig. 1). A microphone Bruel & Kjaer 2270 was used for measurements of the sound pressure level (SPL). The distance between the centre of the cutter and the microphone was 200 mm for the first set of experiments, 100 mm for the second set of experiments and 100 mm for the third set of experiments [5].

The samples—workpieces had pre-defined shapes and dimensions, shown in Fig. 2.

For the first and the third set of experiments, the material of the workpieces was carbon steel S355, and the diameter of the cutter was 40 mm with four inserts. For the second set of the experiments material of the workpiece was carbon steel 1C45, while the diameter of the cutter was 20 mm.

2.1 The First Set of Experiments

The first set of experiments comprises measurements dependence of maximum sound pressure level $L_{F_{max}}$ [dBA] and the equivalent sound pressure level L_{eq} [dBA] on cutting parameters (axial depth of cut, feed rate, spindle speed and radial depth of cut).

Table 1 presents the values of cutting parameters for each of the experiments of the first set. The shaded table fields indicate the cutting parameter that was varied during an experiment, while the three remaining parameters were kept constant.

Figure 3 shows individual cuts that arise due to passes of the cutter during each of the experiments of the first set of experiments.

Fig. 1 The machine, tool and the microphone used for the experiments

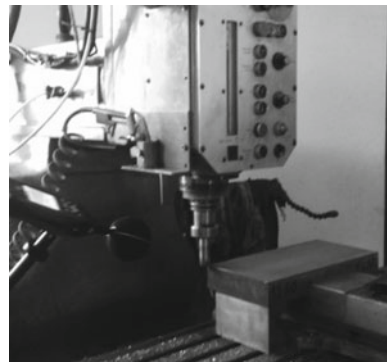


Table 1 Values of cutting parameters in first set of experiments

Cutting parameters				
Experiment no.	Axial depth (mm)	Feed rate (mm/min)	Spindle speed (rpm)	Radial depth (mm)
1.1	0.5–3	150	800	5
1.2	1	375–900	1000	5
1.3	1	300	600–1300	5
1.4	1	150	1000	5–40

2.2 The Second Experiment

The second type of experiment is based on experiments performed in [6]. The sample for this experiment is shown in the bottom-left part of Fig. 2, while the bottom right part of the Fig. 2 indicated the position on the sample where the passes of the cutter started.

The methodology for identifying the stability lobes diagram (SLD) is based on an empirical test where the workpiece has an inclined surface, with a gradual increase of the axial depth of cut in the feed direction. Axial depth of cut is shown in the ordinate of the SLD, while the spindle speed is shown in the abscissa. The cutting process is stopped when the chatter is detected by an operator. In this way, the SLD is physically machined on the workpiece [1, 2, 6, 7]. The simultaneous measurement of the SPL generated by the chatter vibrations reveals the dependence on the level of noise on spindle speed and axial depth of cut.

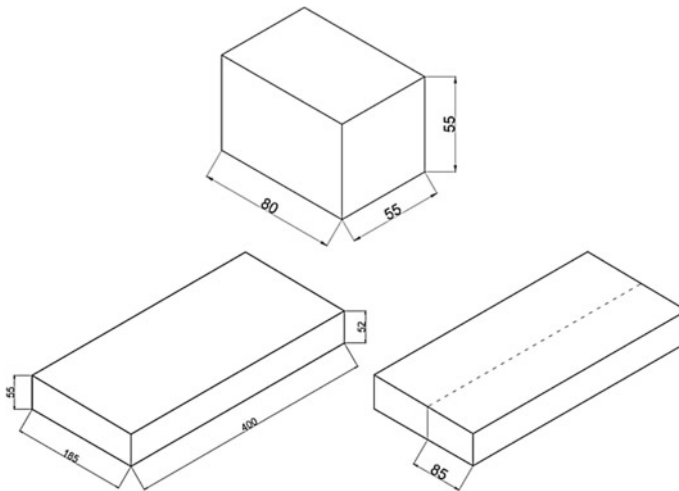


Fig. 2 Dimensions of the samples for the first and the third set of experiments (top row) and the second set of experiments (bottom row)

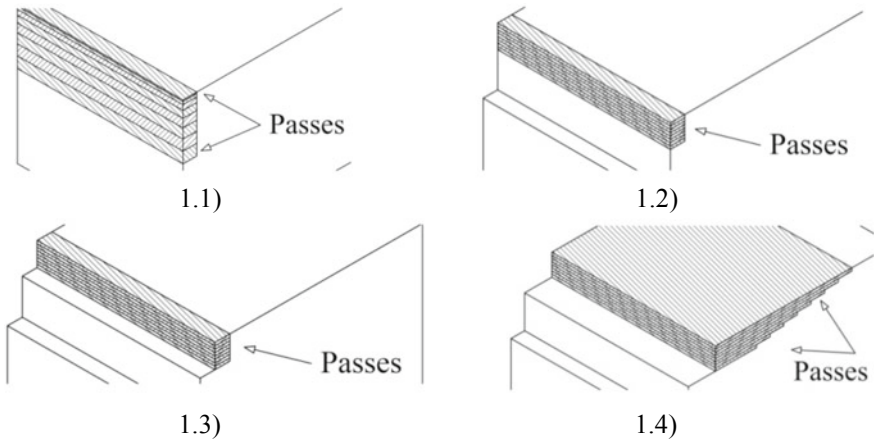


Fig. 3 Schematic representation of eight passes at each experiment. [1]

Table 2 Values of cutting parameters in second experiment

Cutting parameters			
Axial depth of cut (mm)	Feed rate (mm/min)	Spindle speed (rpm)	Radial depth of cut (mm)
0–1.62	150	900–2000	20

Table 2 shows the cutting parameters during the second experiment. It may be seen that the axial depth of cut varied between 0 and 1.62 mm, while the spindle speed was changed between 900 and 2000 rpm with a step of 100 rpm.

2.3 Third Experiment

In the third experiment (Fig. 4), the aim was to study the dependence of the emitted noise level on the radial depth of cut, which was increased linearly from 0 to 40 mm (the diameter of the cutter).

While the performed experiment revealed the dependence of the SPL on the radial depth of cut for one selected spindle speed, it is possible in general (similar to the second experiment) to construct the SLD by plotting the values of radial depth of cut versus spindle speed [7].

Table 3 shows the values of the cutting parameters during the third experiment.

Fig. 4 The third experiment

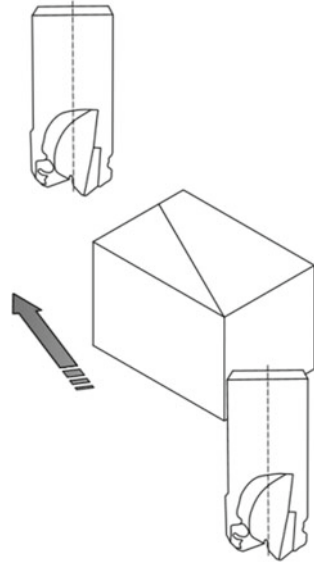


Table 3 Values of cutting parameters in third experiment

Cutting parameters			
Axial depth of cut (mm)	Feed rate (mm/min)	Spindle speed (rpm)	Radial depth of cut (mm)
1	150	1000	0–40

3 Results and Discussions

3.1 The First Set of Experiments

The first set of experiments reveals the dependence of the noise emission of milling on the selected cutting parameters. As an illustration, Fig. 5 shows in the top part the workpiece after the first set of the experiments, while in the bottom part shows the time variations of the L_{eq} [dBA] during the first passes of the cutter in the experiments 1.1. and 1.4.

In Tables 4, 5, 6 and 7 are given the values of maximum sound pressure level and equivalent sound pressure level during each pass of the first set of experiments.

The results show that, in general, the SPL increases by increasing the value of all of the cutting parameters, except for the dependence of the SPL on the feed rate, which shows an apparent maximal SPL around 675 mm/min. The variations of the SPL were highest with the changes of the axial and radial depth of the cut (more than 10 dB within the studied range), while the variation of the SPL on the spindle speed was substantially lower (less than 5 dB within the studied range).

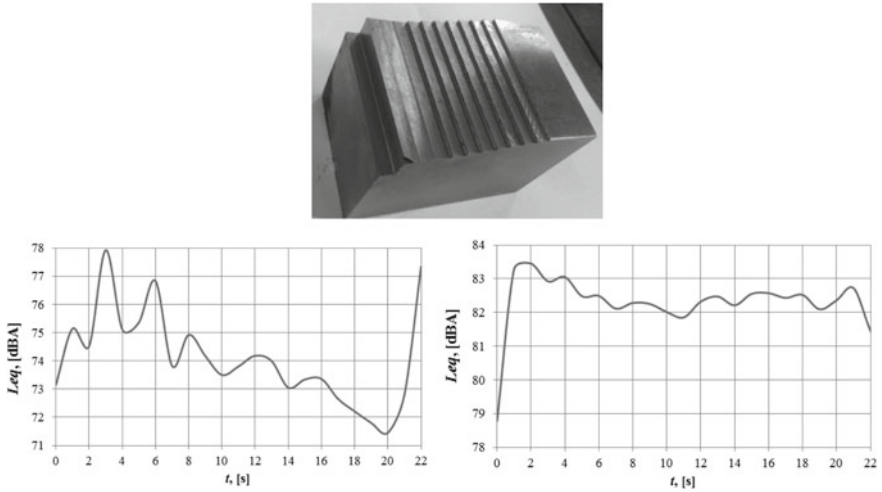


Fig. 5 The machined workpiece (top) and the time variations of L_{eq} [dBA] during the first pass of the cutter in experiment 1.1 (bottom-left) and the experiment 1.4 (bottom right)

Table 4 The results of experiment 1.1

First experiment								
Pass	1	2	3	4	5	6	7	8
Axial depth [mm]	0.5	1.0	1.8	2.0	2.2	2.5	2.8	3.0
L_{Fmax} [dBA]	80.3	80.9	86.6	86.7	87.6	88.4	89.5	90.1
L_{eq} [dBA]	74.4	78.8	83.6	84.8	85.5	86.7	87.8	87.7

Table 5 The results of experiment 1.2

Second experiment								
Pass	1	2	3	4	5	6	7	8
Feed rate [mm/min]	375	450	525	600	675	750	825	900
L_{Fmax} [dBA]	85.7	86.6	87.7	89.7	89.1	87.4	86.3	85.7
L_{eq} [dBA]	82.6	80.9	82.9	84.8	85.9	84.6	82.8	83.7

The largest influence to noise emission during the measurements had the radial depth of the cut, which led to the highest measured SPL of 97.7 dBA. The SPL was reduced when the cutter was cutting by entire diameter during the last pass.

Table 6 The results of experiment 1.3

Third experiment								
No.	1	2	3	4	5	6	7	8
Spindle speed [rpm]	600	700	800	900	1000	1100	1200	1300
L_{Fmax} [dBA]	84.8	89.8	85.0	85.4	85.1	86.9	85.8	86.5
L_{eq} [dBA]	82.2	84.6	83.2	84.0	83.1	84.7	83.9	84.7

Table 7 The results of experiment 1.4

Fourth experiment								
No.	1	2	3	4	5	6	7	8
Radial depth [mm]	5	10	15	20	25	30	35	40
L_{Fmax} [dBA]	84.2	86.1	88.2	89.1	91.9	97.4	97.7	95.4
L_{eq} [dBA]	82.3	84.6	84.8	85.4	89.6	94.9	96.2	93.7

3.2 The Second Experiment

The second experiment enabled the construction of the SLD (Fig. 6).

Table 8 presents the values of the L_{eq} [dBA] and L_{Fmax} [dBA] measured during each of the passes of the cutter, while Fig. 7 shows the time variation of the L_{eq} during the first pass and the last pass.

Table 8 shows the values of L_{eq} increased during each of the passes but had a substantial dip between the 6th and the 7th pass of the cutter.

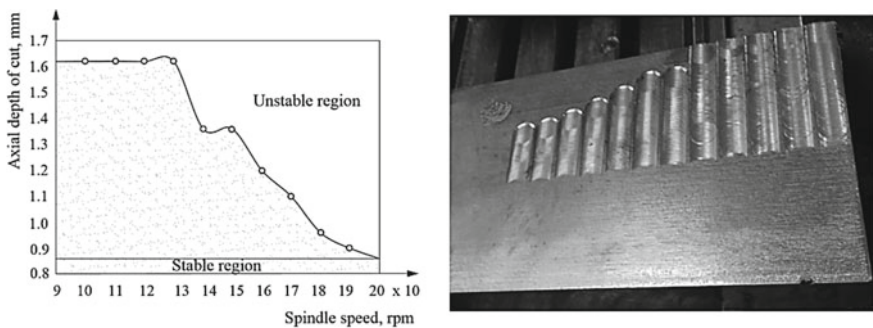


Fig. 6 The SLD on the graph (left) and its mirrored image machined into the workpiece (right)

Table 8 The results of the second experiment

Pass	L_{eq} [dBA]	L_{Fmax} [dBA]
1	80.8	84.4
2	81.9	85.5
3	82.7	87.9
4	84.2	89.8
5	85.4	93.0
6	92.0	106.8
7	88.1	98.9
8	88.2	93.8
9	88.2	93.6
10	89.4	93.4
11	89.3	97.0
12	88.4	96.6

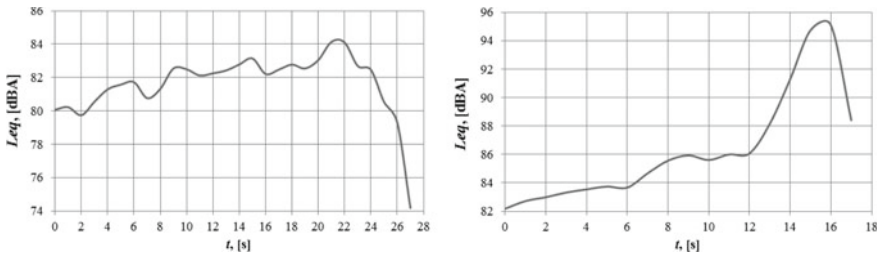


Fig. 7 The time variations of L_{eq} [dBA] during the first (left) and the last (right) pass of the cutter in the second experiment

3.3 The Third Experiment

The third experiment considered dependence of the noise emission on the radial depth of the cut. The machined workpiece and the SPL during the experiment are presented in Fig. 8.

The diagram of the time variation shows that the highest level of noise was emitted while the cutter was approximately half inside the cut. The maximal measured value of the sound pressure level (L_{Fmax}) was 94.56 dBA. Later in the process, when the cutter was inside the cut by the entire diameter, the SPL showed a substantial drop.

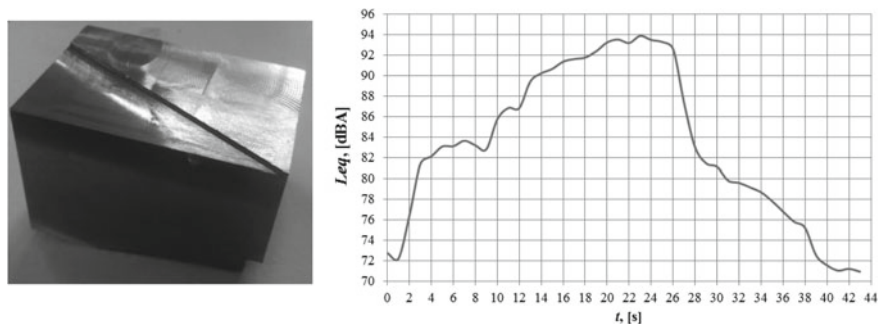


Fig. 8 The machined workpiece (left) and the time variation of the L_{eq} [dBA] during the third experiment

4 Conclusions

Measurements of noise reveal the maximum and equivalent values of sound pressure level, allowing studies of the influence of the cutting parameter to the generated noise. The measurements performed in this study have shown that the measurement of the emitted noise enables control of the cutting process by proper selection of the cutting parameters, with the aim to make it stable (without extreme values of noise and chatter).

In this paper are presented and discussed three different types of experiments to measure noise level and study its relationship with chatter vibrations. In the first experiment was measured dependence of the SPL on the cutting parameters, in the second experiment was measured the noise level induced by chatter vibrations, and the idea of the third experiment was to study the dependence of the noise emission on the radial depth of the cut, which was discovered to have the strongest influence to the noise emission during the first experiment. The common aim of the three types of experiments was to determine the regions of stable regimes of the cutting process. The results presented in this paper can be used for further investigations in that direction.

After the obtained results, the radial and axial depth of the cut have the critical influence to chatter vibrations, and they could be adjusted to avoid the high level of noise emission during the process of milling in practical application. The next step of the research will be further experiments that should be performed with different types of material and various cutters, and the use of accelerometers to study the correlation of the vibrations and noise emission.

Acknowledgements The authors express their gratitude to the Ministry of Education, Science and Technological Development of the Republic of Serbia for the support of this research through the project TR37020.

References

1. A. Petrović, M. Rasinac, V. Grković, M. Ivanović, An experimental plan for noise analysis and chatter detection in milling depending on the cutting parameters, in 26th International Conference Noise And Vibration 2018, University of Niš, Faculty of Occupational safety, Niš (2018), pp. 41–44
2. G. Quintana, J. Ciurana, Chatter in machining process: a review. *Int. J. Mach. Tools Manuf* **51**, 363–376 (2011)
3. J. Rech, F. Dumont, A. Le Bot, P.J. Arrazola, Reduction of noise during milling operations. *CIRP J. Manufact. Sci. Technol.* **18**, 39–44 (2017)
4. Y. Altintas, *Manufacturing Automation—Metal Cutting Mechanics, Machine Tool Vibrations and CNC Design*, 2nd edn. (Cambridge University Press, New York, USA, 2012)
5. K. Sampath, S.G. Kapoor, R.E. DeVor, Modeling and analysis of aerodynamic noise in milling cutters. *J. Manuf. Sci. Eng.* **129**, 5–11 (2007)
6. G. Quintana, J. Ciurana, D. Teixidor, A new experimental methodology for identification of stability lobes diagram in milling operations. *Int. J. Mach. Tools Manuf* **48**, 1637–1645 (2008)
7. A. Petrović, Optimization of the path of milling cutter at high-speed contour milling, Ph. D. thesis, University of Kragujevac, Faculty of mechanical and civil engineering, Kraljevo, 2016

Modal Analysis of a Gearbox Housing in Order to Avoid Resonance Frequencies



Attila Geroacs, Zoltan Korka, Vasile Cojocaru, and Calin-Octavian Miclosina

Abstract Housings, as essential parts of gearboxes, surround the inner parts—the gears, support the bearings and ensure protection both to the inner parts in contrast to the environment, and the working ambience against pollution with lubricant. Housings also transfer to the environment the vibrations produced during the gears engagement process, which, in case of resonance, become a source of the noise. Therefore, the decrease of noise radiated by gear transmissions is an important factor in the control of environmental pollution. In this study, the natural frequencies of a gear housing are established, both by Experimental Modal Analysis (EMA) and by finite element analysis (FEA), using two different software. Finally, for mapping the resonance frequencies, the Campbell diagram is used.

1 Introduction

It is well known that the gearbox housing is one of the most important components of the gear system and plays an important role in vibration and noise emission. As its weight typically represents about 50% of the gearbox weight, optimizations of shape and weight are of particular importance, leading to significant material and cost savings. Furthermore, the vibration generated by the gear mesh is transmitted through shafts and bearings to the housing. The vibration of the housing is perceived as noise.

Optimization of the housing design is necessary in order to lower noise emission, decreasing weight, reducing complexity, and subsequently the manufacturing costs. By using the Finite Element Method (FEM), previous researches [1, 2] have investigated the possibilities to improve the housing dimensions and shape, focusing on the

A. Geroacs · Z. Korka (✉) · V. Cojocaru · C.-O. Miclosina
Department of Engineering Sciences, “Eftimie Murgu” University of Resita, Traian Vuia Square,
No. 1-4, 320085 Resita, Romania
e-mail: z.korka@uem.ro

analysis of displacement and stress distribution. The obtained results show real opportunities regarding both weight reduction and optimization of material consumption and costs.

Other researches [3, 4] have studied the possibilities to reduce the gearbox radiated noise by increasing the housing stiffness. This measure can be applied by placing ribs, in particular positions, on the housing surface. Research results have shown that by placing stiffening ribs along the connection lines between the bearing shells and the nearest fixed point of the gearbox it is possible to obtain good results regarding the reduction of noise [5, 6].

Modal analysis has recently become a powerful tool in the design and optimization of various mechanical components [7, 8], being constantly employed, principally in the primary stages of the product design [9, 10].

Currently, there are available a lot of researches [11, 12] concerning modal analysis performed on gearboxes, but seeing the complexity of the subject, the topic supports favorable circumstances for alternative investigations.

The objective of this work is to perform an FEA on an existent gearbox housing, by using two different software, in order to prevent undesired resonance in real operating circumstances. Furthermore, the numerical results are validated by experimental data.

2 Case Study

The study presented here is concerned with the determination of the natural frequencies of the housing being part of a single helical gearbox. The fundamental technical data of the gearbox and the main dimensions of the housing are presented in Table 1, while Fig. 1 provides a 3D-view of the bottom housing and upper housing.

In the first stage of this study, an Experimental Modal Analysis (EMA) of the housing was accomplished. The first six natural frequencies have been established

Table 1 Fundamental technical data of the gearbox and main dimensions of the housing

Data	Symbol (M.U.)	Value
Maximum power	P (kW)	2.5
Range of input speed	n_1 (rpm)	1000–1500
Centre distance	A (mm)	125
Module	m_n (mm)	4
Number of teeth	z_1/z_2 (–)	17/43
Gear width	b (mm)	40
Helix angle	β (°)	11
Housing main dimensions	$L \times B \times H$ (mm \times mm \times mm)	439 \times 251 \times 280

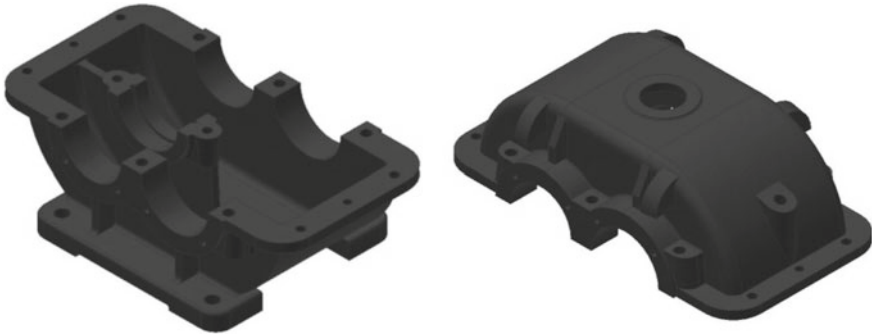


Fig. 1 3D model of bottom housing and upper housing

in order to find out the presence of any critical speed in the operating range of the gearbox.

Thereupon, using SolidWorks facilities, the 3D model of the housing was build and an FEA was performed in order to determine the first six natural frequencies and the corresponding mode shapes. Supplementary, the Inventor software was employed to determine the mode shapes and the natural frequencies of the housing. The experimentally obtained eigenfrequencies were compared with the FEA results acquired with the two different software utilities.

3 Experimental Modal Analysis

In this study, the EMA results were used to calibrate the FEA and to validate the underlying presumptions (boundary conditions and material properties).

For determining the natural frequencies of the gearbox housing using EMA, the test rig, shown in Fig. 2, was organized. To simulate real operating conditions, the housing (1) was rigidly fixed on a frame (2). For impacting the structure, a PCB

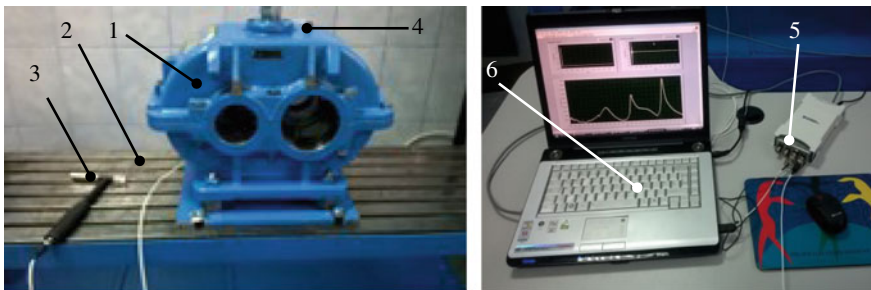


Fig. 2 Views of the test rig

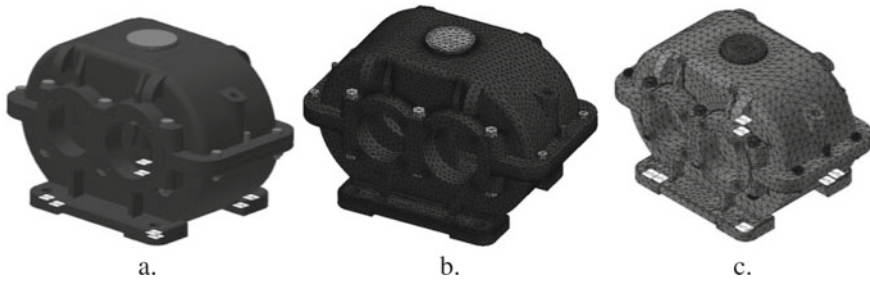


Fig. 3 Boundary conditions (a) and mesh applied in SolidWorks (b) and Inventor (c)

Piezotronics hammer (3) of type 086C01 was used, while for collecting the vibrations, a Kistler 8772 accelerometer (4) was employed. The hardware of the test rig was completed by the signal acquisition module with four channels, of type NI 9234 (5). The natural frequencies were computed with a custom application developed in LabView software which was running on a laptop (6). The accelerometer was placed in 10 different points on the gearbox surface, for each measurement point being recorded 5 impacts. The frequency response was obtained as an average of the measured frequencies.

4 Modal Analysis Using Finite Element Method

For the purposes of this work, the frequency analysis module of SolidWorks and Inventor was used. For simulating real operating conditions, the housing was fixed at its bottom part (the gearbox base) and on the foundation fastening holes. The upper and bottom parts of the housing were connected by screws and nuts, the contact between the two elements being set as bonded type.

Figure 3a depicts the boundary conditions which were set for the simulation (fixed constraints for the bottom surface of the housing base). In order to obtain trustworthy results, in SolidWorks was applied a high-quality mesh of 126,364 solid tetrahedral elements and 210,270 nodes, 89.4% of these elements having an aspect ratio smaller than 3, while in Inventor was used a mesh of 3,091,677 finite elements and 4,466,504 nodes. Figure 3b, c show the meshes which were applied to the housing in SolidWorks and Inventor software.

5 Results and Discussion

Table 2 presents the values of the first six natural frequencies of the gearbox housing acquired by EMA and FEA performed with SolidWorks, respective Inventor. Figure 4 presents the six vibration modes obtained from FEM in Inventor. As it can be noticed,

Table 2 Comparison of natural frequencies (EMA data with FEA results)

Mode no.	Natural frequency (Hz)/deviation to EMA (%)				
	EMA	Feasolidworks		FEA-Inventor	
1	584	571.4	-2.16	564.18	-3.39
2	608	633.4	4.17	618.63	1.75
3	728	752.4	3.35	745.60	2.42
4	1115	1136.9	1.96	1112.96	-0.18
5	1242	1208.8	-2.67	1178.73	-5.09
6	1410	1447.6	2.67	1431.30	1.51

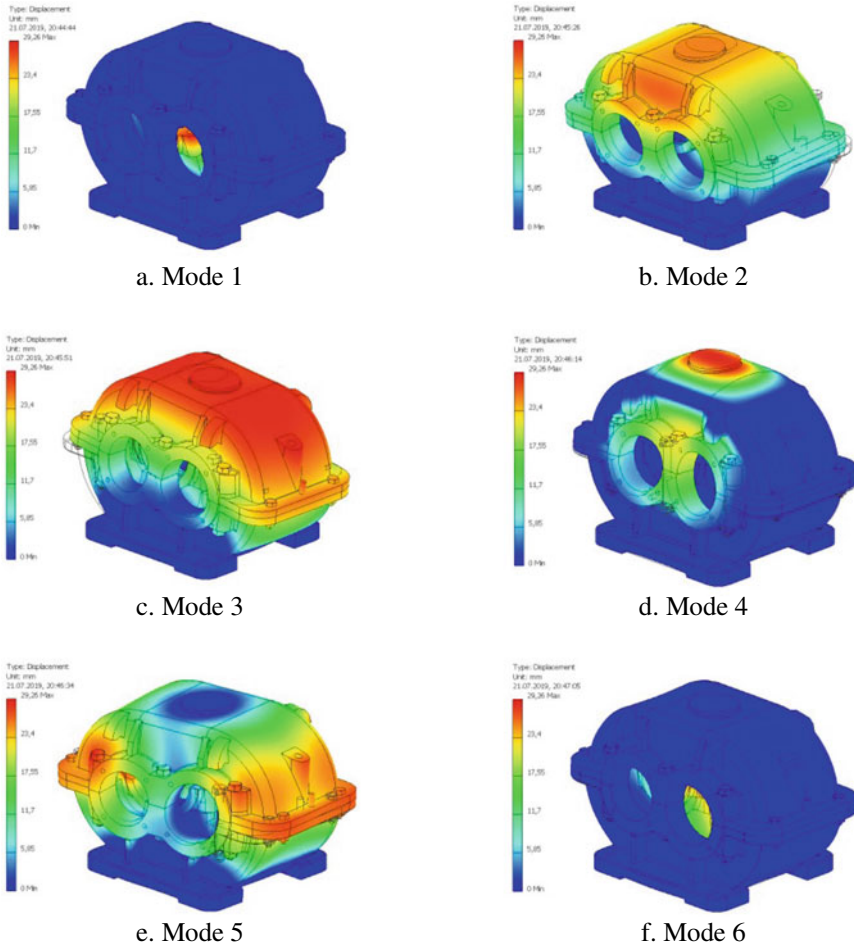


Fig. 4 First six vibration modes obtained from FEM in Inventor

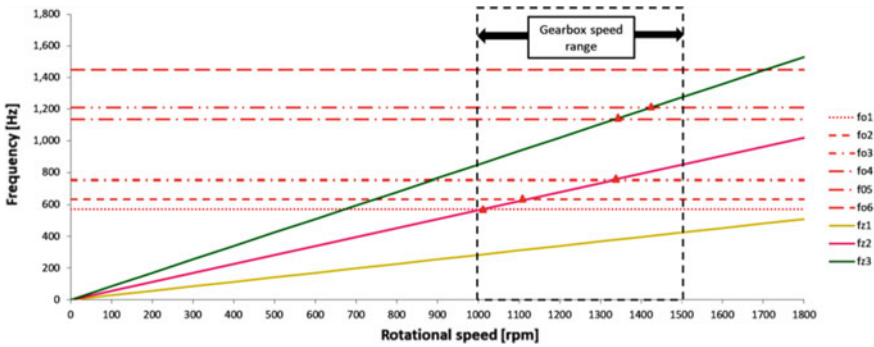


Fig. 5 Campbell diagram

the difference between the experimental and computed results does not exceed 6%. This confirms that the 3D model, the assumed material properties and the boundary conditions were correct set, as the simulation results are validated by comparing them with the experimental data.

The differences between the eigenfrequencies obtained by experimentation and FEA may be generated by some differences between the material properties, primarily mass density, Poisson’s ratio and elastic modulus, ahead with mass differences caused by the geometrical irregularities of the real housing.

Finally, the Campbell diagram was employed for localizing and mapping the resonant frequencies of the housing. Being a mathematically constructed graph, the Campbell diagram is an important tool in assessing the dynamic behavior of rotating machines. It plots frequency versus rotational speed and is used to check coincidence of natural frequencies with vibration sources. Thus, critical speed may be identified if the natural frequency line intersects the exciting frequency (in case of gear systems the teeth engagement frequency) line. If there are intersections of these lines in the Campbell diagram, they lead to resonance, a phenomenon that must be avoided.

Figure 5 presents the Campbell diagram for the investigated housing. With horizontal lines are plotted the first six natural frequencies ($f_{o1}, f_{o2}, \dots, f_{o6}$), while the inclined lines show the variation of the first three harmonics of the teeth engagement frequencies (f_{z1}, f_{z2} and f_{z3}) depending on the gearbox driving speed.

As it can be observed, in the operation speed range of the gearbox ($n_1 = 1000 - 1500$ rpm—see Table 1), which is delimited in the diagram by a rectangle drawn with dashed black lines, some converging points marked with red color triangles appear at the intersections between the natural frequency lines and the excitation frequency lines. There were identified five critical speeds.

Commonly, not all diagnosed critical speeds are equally alarming. A reason for this is the fact that probably some natural frequencies of the higher modes do not occur as compelling vibrational peaks in the system. Furthermore, the situation may arise, when more critical speeds are detected in the Campbell diagram, but they don’t

appear in the real system. A possible explanation for this phenomenon might be that some modes are substantially damped and thus, the amplitudes are not amplified at these modes.

6 Conclusion

In this study, the natural frequencies of a gear housing are determined by the Experimental Modal Analysis. The experimental results are compared with those obtained by using finite element analysis, performed by two different software programs, as seen in Table 2. Thus, it can be observed that the experimental results are close to the results obtained by FEA, some frequency mode maps being presented in Fig. 4. Additionally, the Campbell diagram was employed to detect the occurrence of critical speeds, which have to be avoided to prevent resonance.

As further research, the influence of the material type and the size of different geometrical elements of the housing on its natural frequencies are proposed to be analyzed.

References

1. V. Cojocar, Z.I. Korca, C.O. Miclosina, Influence of the mesh parameters on stresses and strains in FEM analysis of a gear housing. *Ann. "Eftimie Murgu" Univ. Resita* **XX**(2), 47–52 (2013)
2. V. Cojocar, Z.I. Korca, C.O. Miclosina, Stress analysis and optimal design of the housing of a two-stage gear reducer. *Appl. Mech. Mater.* **658**, 183–188 (2014)
3. Z. Jianxing, W. Sun, Q. Tao, Gearbox low-noise design method based on panel acoustic contribution, *Math. Probl. Eng.* **850549**, 10 (2014)
4. J.P. Wang, G. Chang, G. Liu, Effects of rib arrangements on radiated noise of gearboxes, in *Proceedings of the International Gear Conference 2014*, Lyon, 26–28 August (2014), pp. 190–199
5. A.K. Nandy, C.S. Jog, Optimization of vibrating structures to reduce radiated noise. *Struc. Multi. Optim.* **45**(5), 717–728 (2012)
6. E. Tanaka, H. Houjou, D. Motoh, Vibration and sound-radiation analysis for designing a low-noise gearbox with a multi-stage helical gear system. *JSME Int J. Ser. C* **46**(3), 1178–1185 (2003)
7. W. Yang, X.L. Tang, Modelling and modal analysis of a hoist equipped with two-stage planetary gear transmission system. *Proc. Inst. Mech. Eng. Part K-J. Multi-Body Dyn.* **231**(4), 739–749 (2017)
8. P.X. Yi, P. Huang, T.L. Shi, Numerical analysis and experimental investigation of modal properties for the gearbox in wind turbine. *Front. Mech. Eng.* **11**(7), 388–402 (2016)
9. P.G. Catera, F. Gagliardi, D. Mundo, L. De Napoli, A. Mateeva, L. Farkas, Multi-scale modeling of triaxial braided composites for FE-based modal analysis of hybrid metal-composite gears. *Compos. Struct.* **182**, 116–123 (2017)
10. M. Tufoi, G.R. Gillich, Z.I. Praisach, Z.I. Korca, Modal analysis of a butterfly valve with different stiffening elements. *Rom. J. Acoust. Vibr.* **13**(1), 11–15 (2016)

11. Z.I. Korka, N. Gillich, Modal analysis of helical gear pairs with various ratios and helix angles. *Rom. J. Acoust. Vibr.* **14**(2), 91–96 (2017)
12. Z.I. Korka, V. Cojocaru, C.O. Miclosina, Shape improvement of a gearbox housing using modal analysis. *Rom. J. Acoust. Vibr.* **15**(1), 47–52 (2018)

Dependence Between the Percussion Centre and the Uniformity of the Rotor Movement



Mircea Fenchea 

Abstract In the study of the working mill, insufficiently treated is the problem of the hammer construction, the main working organs of the mill, which have a decisive influence on the working regime. The paper emphasized the effects of the construction of hammer and it is underlined the necessity to respect the existence of one centre of percussion. The vibration measurements show the connection between the centre of percussion and the vibration level.

1 Introduction

There are a lot of studies concerning the influence of the different factors, which can contribute to the bettering of the operation indexes of the mills with hammers. The problem of the hammers construction, (the main working organs of mill), which have a decisive influence on the working regime it is insufficiently treated.

The main working organ of the mill is the hammer and its constructive form determines the quality of the crushing and the specific consumption of energy.

The main working part of hammer crusher is rotors with hammer. The rotor consists of main shaft, disk, pin shaft and hammers. Materials enter the crusher through the feed opening and are stricken, impacted and cut by the high-speed hammers to small size. The material is ground by repeated contact with these hammers, contact with the walls of the grinding chamber, and particle to particle contact. The size of the final product can be adjusted by changing the screening plate under the rotor [1]. The percussion interactions between the hammer and material produce additional perturbations, generating irregularities during the work [2, 3].

The process of crumbling, in the mills with hammers are determined by the percussive interactions between the hammers and the material. Each hammer is bind at the rotor by a plane articulation so that it executes a relative rotation motion in relation to the fixed axis of the rotor [4].

M. Fenchea (✉)

“Politehnica” University of Timișoara, B-dul Mihai Viteazul, nr.1, 1900 Timișoara, Romania

e-mail: mircea.fenchea@upt.ro

© Springer Nature Switzerland AG 2021

N. Herisanu and V. Marinca (eds.), *Acoustics and Vibration of Mechanical*

Structures—AVMS 2019, Springer Proceedings in Physics 251,

https://doi.org/10.1007/978-3-030-54136-1_35

Because of the percussion interactions between the hammer and material, unbalances appear even if the rotor, from the dynamic point of view, is considered as balanced. Obviously, this situation does not appear if the percussion is applied to the hammer so that it annuls the percussion in the articulation [5]. This thing leads to the considerations of the percussion centre through which the percussions in the articulation are eliminated and so the work of the machine is not disturbed [6].

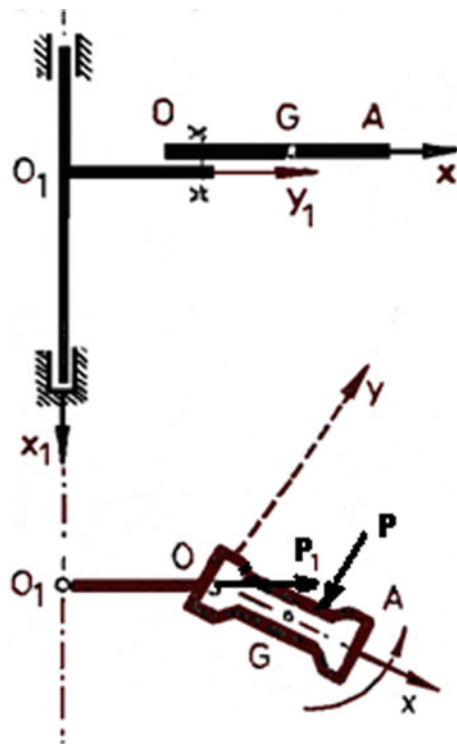
2 Percussion Centre of Hammer

The joint between the hammer and rotor is made through a plane articulation so that the hammer makes a relative rotation motion in relation to the axis of the articulation.

It is supposed that on the articulated hammer in O, the percussion \vec{P} acts in point A, due to the collision with the material particle. As a result, in O the joint percussions \vec{P}_1 appear (see Fig. 1).

If $\Delta\vec{H}$ and $\Delta\vec{K}_o$ are the variations of the impulse and of kinetic moment in relation to the articulation O, the laws of the collision [6] will be

Fig. 1 Percussive interactions



$$\Delta \vec{H} = \vec{P} + \vec{P}_1 \quad (1)$$

and

$$\Delta \vec{K}_o = \vec{r}_A \times \vec{P} \quad (2)$$

The axis system O_{xyz} , attached to the hammer has the axis O_z even as the rotation axis in O , and the axis O_x , so that the plan Oxz to contain the centre of gravity G .

Obviously, the impulse of the hammer is

$$\vec{H} = m\vec{v}_G = m(\vec{v}_0 + \vec{\omega} \times \vec{r}_G) \quad (3)$$

where m is the mass of the hammer. Consequently, the variation of the impulse $\Delta \vec{H}$ during the collision is

$$\Delta \vec{H} = mx_G \Delta \omega \vec{j} \quad (4)$$

where $\Delta \omega$ is the variation of the angular velocity of the hammer.

Analogously, the variation of kinetic moment of the hammer in relation to the point O results

$$\Delta \vec{K}_0 = (-J_{xz} \vec{i} - J_{yz} \vec{j} + J_z \vec{k}) \Delta \omega \quad (5)$$

It must be established the conditions so that the joining percussions to be null. It means that in the (1) and (2) it must be taken $\vec{P}_1 = 0$; it results:

$$\Delta \vec{H} = \vec{P} \quad (6)$$

and

$$\Delta \vec{K} = \vec{r}_A \times \vec{P} \quad (7)$$

From the (4) and (6), it remarks that the percussion \vec{P} must be orientated along the axis O_y , what practically can be supposed as realized because the hammer can be considered radially placed in the moment of collision.

If the percussion \vec{P} is removed in the (6) and (7), it results:

$$\Delta \vec{K}_o = \vec{r}_A \times \Delta \vec{H} \quad (8)$$

and

$$\Delta \vec{K}_0 = mx_G (-z_A \vec{i} + x_A \vec{k}) \Delta \omega \quad (9)$$

If the expression (5) and (9) are equalized, it is obtained the existence conditions

$$J_{yz} = 0 \quad (10)$$

and the equations of the support of percussion

$$x_A = \frac{J_Z}{mx_G} \quad (11)$$

and

$$z_A = \frac{J_{xz}}{mx_G} \quad (12)$$

which define the centre of percussion [6].

Particular, the usual case of the hammer in the form of a plane which presents the axis of longitudinal symmetry can be taken $J_{xz} = 0$ and $J_{yz} = 0$. This thing shows the existence of a centre of percussion, and $z_A = 0$.

Consequently, for the joint percussions to be null, it is sufficient to be verified the (11).

3 Experimental Determinations

The accelerometer KD 35 (piezoelectric transducer), mounted of the bearings of the mill, put in evidence the perturbations of the rotor as a result of the unbalances. Transducer receives these perturbations, which generate a tension signal, proportional to the acceleration.

If the rotor is considered well-balanced, the signal in the time domain was sinusoidal (see Fig. 2), and the frequency spectrum is shown in Fig. 3.

For put in evidence, the dependence between different tips of hammer and well-balanced rotor, it's made experimental determinations with two tips of hammer where the differences between the values of the real parameter of the hammer used for determinations and the calculated ones for the same types of hammers (x_A) are:

- Hammer set 1: 1,9290 mm (see Figs. 4 and 5)
- Hammer set 2: 15,7411 mm (see Figs. 6 and 7).

4 Conclusions

In practice, the existence conditions of the percussion centre are not always satisfied. In consequence, unbalances depending on the connection percussions appear, having as effect supplementary perturbations in the mills with hammers.

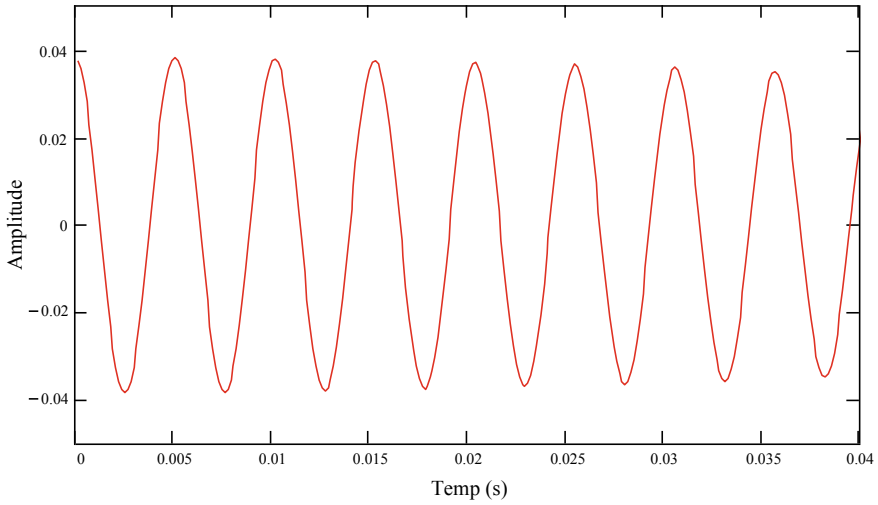


Fig. 2 Signal in the time domain. Well-balanced rotor

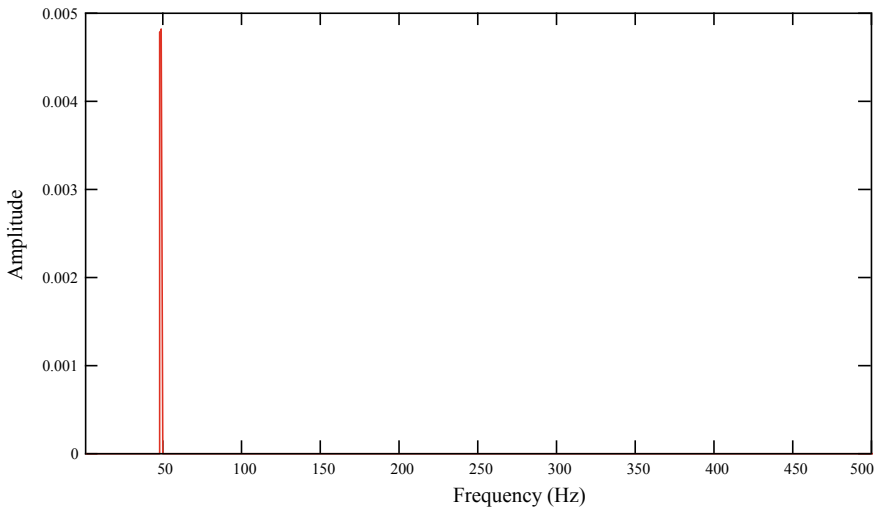


Fig. 3 Frequency spectrum. Well-balanced rotor

In the case of the hammers mill, it is unavoidable the rapid wear of the hammers, case appearing difficult problems of balance.

If the rotor, from the dynamic point of view, is considered balanced, because of the percussion interactions between hammer and material, the rotor becomes unbalanced (it does not respect the percussive centre).

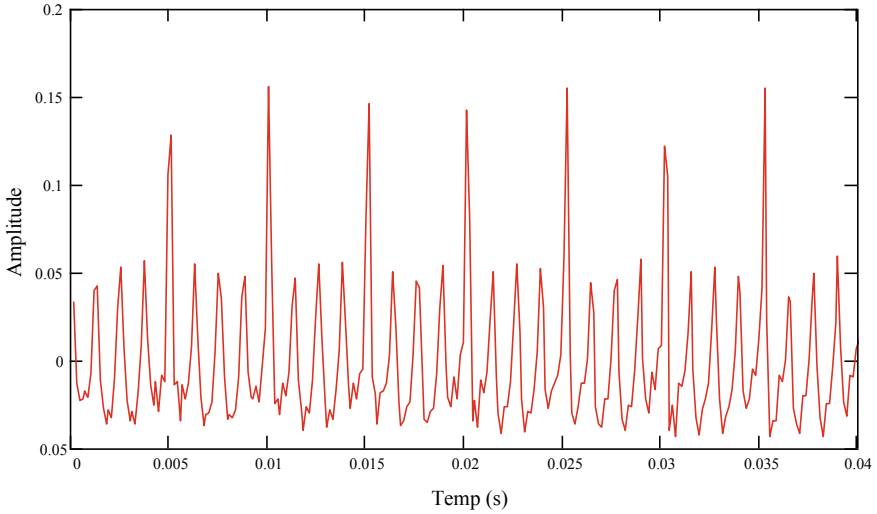


Fig. 4 Signal in the time domain. Hammer set 1

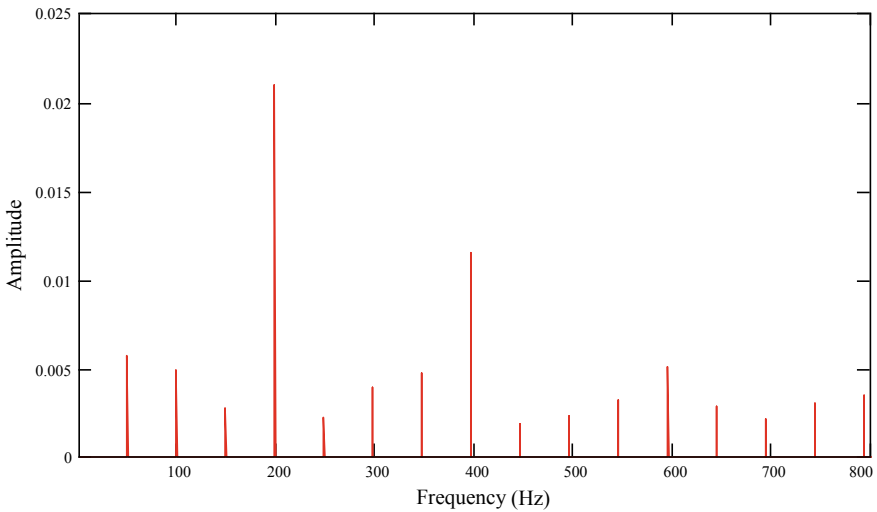


Fig. 5 Frequency spectrum. Hammer set 1

The vibration measurements show that when the parameters that show the value of percussion centre have great value (15,7411 mm), the signals in the frequency domain are great and when the parameters that show the value of percussion centre have small value (19,290 mm), the signal in the frequency domain are small. This fact puts in direct correspondence the dependence between percussion centre of the hammer and the uniformity of rotor movement.

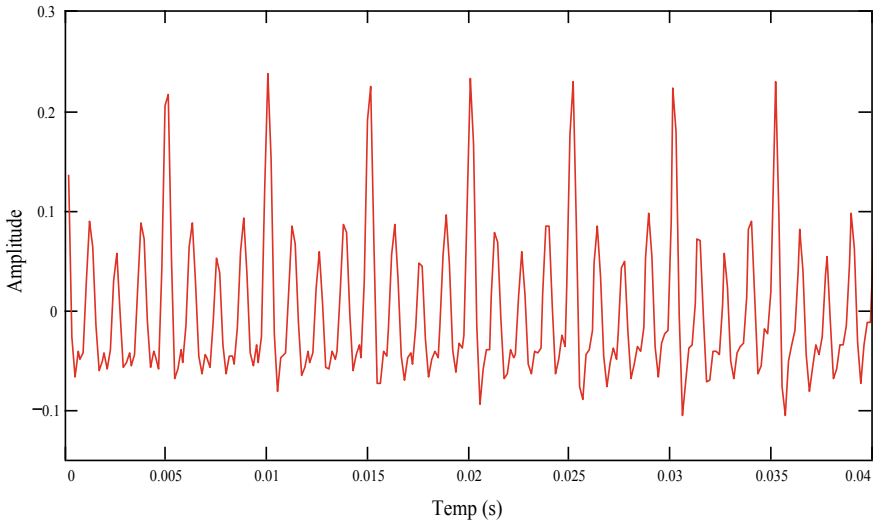


Fig. 6 Signal in the time domain. Hammer set 2

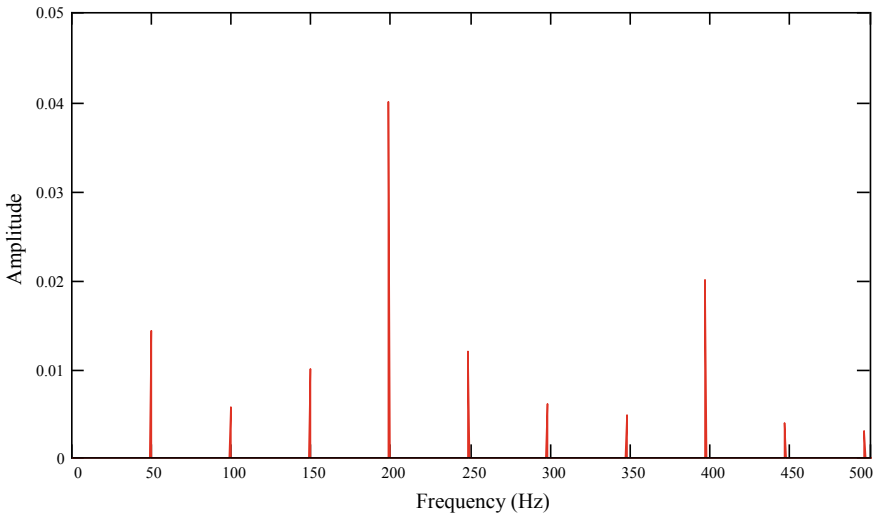


Fig. 7 Frequency spectrum. Hammer set 2

References

1. N.C. Princewill, Development and performance evaluation of improved hammer mill. *J. Sci. Eng. Res.* **4**(8), 159–164 (2017)
2. T.H. Mohamed, H.A. Radwan, A.O. Elashhab, N.Y. Adly, Design and evaluate of a small hammer mill. *Egypt J. Agric. Res.* **93**(5) (2015)

3. N. Yancey, C.T. Wright, T. Westover, Optimizing hammer mill performance through screen selection and hammer design. *Biofuels* 85–94 (2014)
4. M. Smits, E. Kronbergs, Determination Centre Of Percussion For Hammer Mill Hammers. *Eng. Rural Dev.* 364–368 (2017)
5. V. Kosse, J. Mathew, Design of hammer mills for optimum performance. *Proc. Inst. Mech. Eng. Part C J. Mech. Eng. Sci.* **215**(1), 203–210 (2001)
6. M. Fenchea, Design of hammer mills for optimum performance. *J. Vib. Control* **19**(14), 2100–2108 (2013)

Comparative Analysis of the Voigt–Kelvin and Maxwell Models in the Compaction by Vibration Process



Cornelia-Florentina Dobrescu

Abstract The dynamic compaction of the soil is made with cylindrical vibratory equipment called vibratory compact rollers. The compaction process consists of transmitting the static force corresponding to the weight of the roll as well as the dynamic force generated by a vibrator placed inside the roller. By the combined effect of static pressure and simultaneous transmission of the dynamic force on the soil, it is achieved the compaction of the soil layers over their entire height. The final effect of the compaction process consists of the increase in the soil density and reduce the reduction of the holes so that the conditions for increasing the mechanical strength and the stability of the foundation of the road construction are created. In this context, the variety of the physical and mechanical parameters of soil requires the analysis of the compatibility of the significant rheological models with the dynamic action capacity of the vibratory rollers.

1 Introduction

The specified problematics can be addressed by the comparative analysis of soil behavior at compaction on the basis of two significant models, namely the Voigt–Kelvin model and the Maxwell model [1–5]. These models describe two distinct behaviors such as the predominantly elastic character with reduced viscosity represented by the Voigt–Kelvin rheological scheme or the predominantly viscous character with reduced elasticity represented by the Maxwell rheological schematization [6–8].

As a result of the researches made, this article will present the results of the dynamic behavior modeling exemplified by the evaluation of the maximum dynamic force transmitted to the land for the two significant rheological models [9–11].

C.-F. Dobrescu (✉)
INCD URBAN-INCERC, Sos. Pantelimon, 266, Bucharest, Romania
e-mail: corneliadobrescu@yahoo.com

2 The Parametric Analysis of the Compaction Process for the Vibratory-Field Roller System

Based on experimental and numerical, research, on the rheological modeling and the dynamic capability of vibratory rollers, there can be used, in a first approach, the viscoelastic linear models made of a viscoelastic resort-bumper system with the series connection.

2.1 The Dynamic Model with Voigt–Kelvin Schematics

The linear viscous-elastic dynamic model composed of a Voigt–Kelvin linear rheologic system with k , elasticity, c amortization and m mass of the compactor vibrating roller, inertially excited with an m_0 eccentric mass with the r rotary radius, with ω angular velocity, is represented in Fig. 1 [12–14].

The differential movement equation of mass m , formulated in the complex is

$$m\ddot{\tilde{x}} + c\dot{\tilde{x}} + k\tilde{x} = F_0e^{j\omega t} \tag{1}$$

where $\tilde{x} = \tilde{X}e^{j\omega t}$; $\tilde{X} = X_0e^{-j\varphi}$, $F_0 = m_0r\omega^2$

As $\ddot{\tilde{x}} = j\omega\dot{\tilde{x}}$ și $\dot{\tilde{x}} = -\omega^2\tilde{X}e^{j\omega t}$ in relation (1) we obtain

$$-m\omega^2\tilde{X} + jc\omega\tilde{X} + k\tilde{X} = F_0 \tag{2}$$

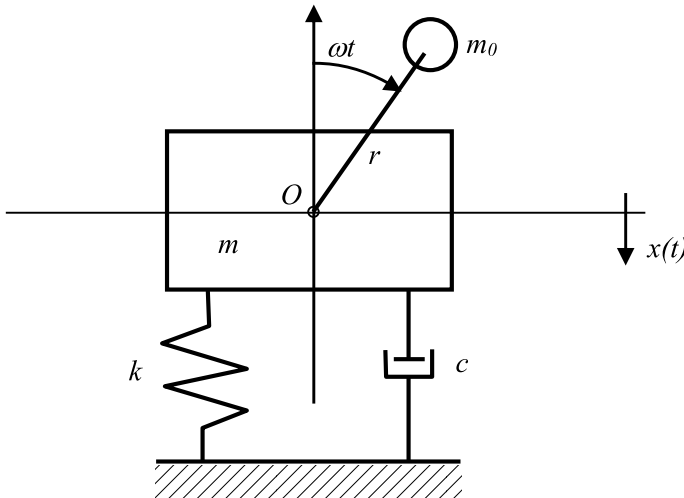


Fig. 1 Voigt–Kelvin dynamic model

from where we have

$$\tilde{X} = \frac{F_0}{(k - m\omega^2) + jc\omega} \quad (3)$$

The amplitude of the vibration of the vibratory roll with mass m emerges from (3) as

$$X_0^{V-K} = \frac{m_0 r \omega^2}{\sqrt{(k - m\omega^2)^2 + c^2 \omega^2}} \quad (4)$$

The dynamic force transmitted to the soil, formal in the complex is given by the relation

$$\tilde{Q} = k\tilde{x} + c\dot{\tilde{x}}$$

or

$$\tilde{Q} = (k + jc\omega)\tilde{X}e^{j\omega t} \quad (5)$$

Taking into account the relation (3), we have

$$\tilde{Q} = F_0 \frac{k + jc\omega}{(k - m\omega^2) + jc\omega} \quad (6)$$

The amplitude of the force transmitted (maximum transmitted force) to the soil in the process of dynamic compaction emerges as

$$Q_0^{V-K} = m_0 r \omega^2 \sqrt{\frac{k^2 + c^2 \omega^2}{(k - m\omega^2)^2 + c^2 \omega^2}} \quad (7)$$

It is found that for $\omega \gg \omega_n$, where $\omega_n = \sqrt{\frac{k}{m}}$, that is for the after-resonance are of technological functioning, it may be passed to the limit with $\omega \rightarrow \infty$, in which case we have

$$(a) \quad X_0^{K-V} = \frac{m_0 r}{m}$$

The amplitude remains constant regardless of the variation of the excitation pulse ω , when $\omega \gg \omega_n$.

$$(b) \quad Q_0^{K-V} = \frac{m_0 r}{m} c \omega$$

The maximum transmitted force linearly varies with the variation of the excitation pulse ω .

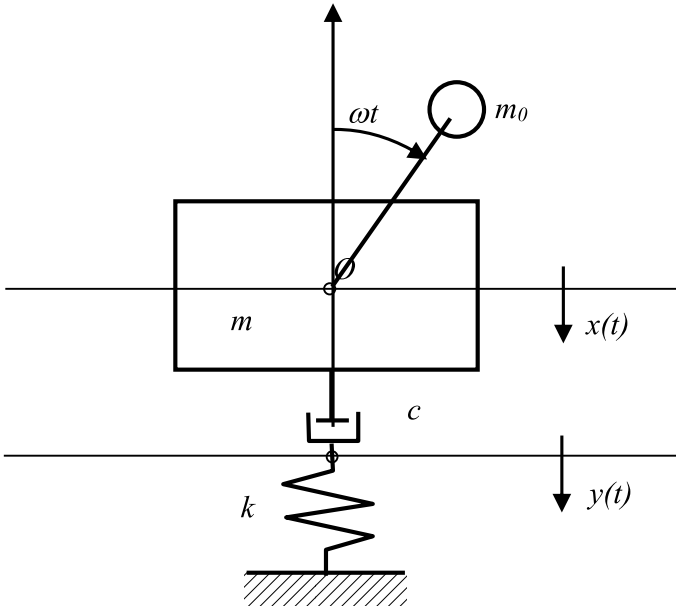


Fig. 2 Maxwell dynamic model (m, c, k)

2.2 The Dynamic Model with the Maxwell Schematization

The Maxwell linear schematization with m mass, c bumper and k resort is presented in Fig. 2.

The differential movement equations in complex are as follows:

$$\begin{cases} m\ddot{\tilde{x}} + k\tilde{y} = F_0 e^{j\omega t} \\ c(\dot{\tilde{x}} - \dot{\tilde{y}}) = k\tilde{y} \end{cases} \tag{8}$$

where $\tilde{x} = \tilde{X}e^{j\omega t}$, $\tilde{X} = X_0e^{-j\varphi}$, $\tilde{y} = \tilde{Y}e^{j\omega t}$, $\tilde{y} = Y_0e^{-j\theta}$, $F_0 = m_0r\omega^2$.

Consequently, system (8) may be written down as follows

$$\begin{cases} -m\omega^2\tilde{X} + k\tilde{Y} = F_0 \\ jc\omega\tilde{X} = (k + jc\omega)\tilde{Y} \end{cases} \tag{9}$$

from where we have

$$\tilde{X} = \tilde{X}(\omega) = F_0 \frac{k + jc\omega}{-m\omega^2k + jc\omega(k - m\omega^2)} \tag{10}$$

$$\tilde{Y} = \tilde{Y}(\omega) = F_0 \frac{j c \omega}{-m\omega^2k + jc\omega(k - m\omega^2)} \tag{11}$$

The amplitude of the vibrations of the compactor roller with mass m from the relation (10) emerges as

$$X_0^M = \frac{m_0 r \omega^2 c}{\sqrt{m^2 \omega^2 k^2 + c^2 (k - m \omega^2)^2}} \quad (12)$$

The transmitted force may be written down as follows:

$$\tilde{Q}(t) = k \tilde{Y} e^{j \omega t}$$

or taking into account relation (11) we have

$$\tilde{Q}(t) = \frac{j c \omega k F_0 e^{j \omega t}}{-m \omega^2 k + j c \omega (k - m \omega^2)} \quad (13)$$

The amplitude of the transmitted force (maximum force) emerges as

$$Q_0^M = \frac{m_0 r \omega^2 c k}{\sqrt{m^2 \omega^2 k^2 + c^2 (k - m \omega^2)^2}} \quad (14)$$

It is noticed that for the functioning technologically established in after-resonance, that is for $\omega \rightarrow \infty$, we have

$$X_0^M = \frac{m_0 r}{m}$$

Amplitude remains steady regardless of the variation of the excitation pulse ω , for $\omega \gg \omega_n$.

$$Q_0^M = \frac{m_0 r}{m} k$$

The maximum force transmitted remains steady regardless of the variation of the excitation pulse ω , for $\omega \gg \omega_n$ [15, 16].

3 The Comparative Analysis of the Dynamic Behavior for the Linear Voigt–Kelvin and Maxwell Rheological Models

For the comparative analysis, the parametric values for an experimental system of dynamic vibratory-soil roller system were established. Thus, for the continuous variation of the excitation pulse $\omega = 0 \dots 900$ rad/s and of the discrete variation of the

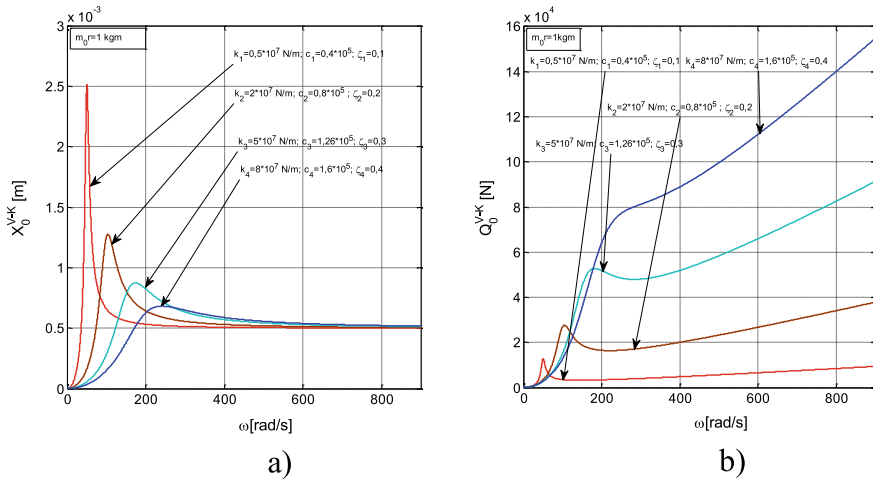


Fig. 3 The dynamic response for the Voigt–Kelvin rheologic model: **a** variation of amplitude depending on pulse ω and rigidity k ; **b** variation of the force transmitted to the soil

k_i stiffness and the c_i amortization corresponding to each passing i with $i = 1, 2, 3, 4$, parametric variation curves were taken X_0^{K-V} , X_0^M , Q_0^{K-V} and Q_0^M .

Thus, based on the experimental data and the analysis of the typologies of the compaction processes, the following initial parametric values were established: $m_0r = 1$ kg; $m = 2000$ kg; $k_1 = 0.5 \times 10^7$ N/m; $k_2 = 2 \times 10^7$ N/m; $k_3 = 5 \times 10^7$ N/m; $k_4 = 8 \times 10^7$ N/m; $\zeta_i = (0.1; 0.2; 0.3; 0.4)$; $c_i = 2\zeta_i \sqrt{mk_i}$, $i = 1, 2, 3, 4$.

Figures 3 and 4 present the families of curves of the parametric response units for both rheological models [13, 14].

4 Conclusions

In the case of the soil made of clay mix with natural aggregates (sand, mineral aggregates, clay) the compaction ability is given by natural humidity and water addition when put into operation. For the research conducted, two categories of soil were used, consisting of the following components:

- soil with 20% sand, 50% river mineral aggregates and 30% clay, whose predominantly elastic behavior can be Voigt–Kelvin modeled;
- soil with 30% sand, 10% river mineral aggregates and 60% clay, with predominantly viscous behavior, and Maxwell modeling.

Based on the experimental results performed with a vibratory roller whose excitation pulse $\omega = 400$ rad/s and four successive passes on the same soil layer, the

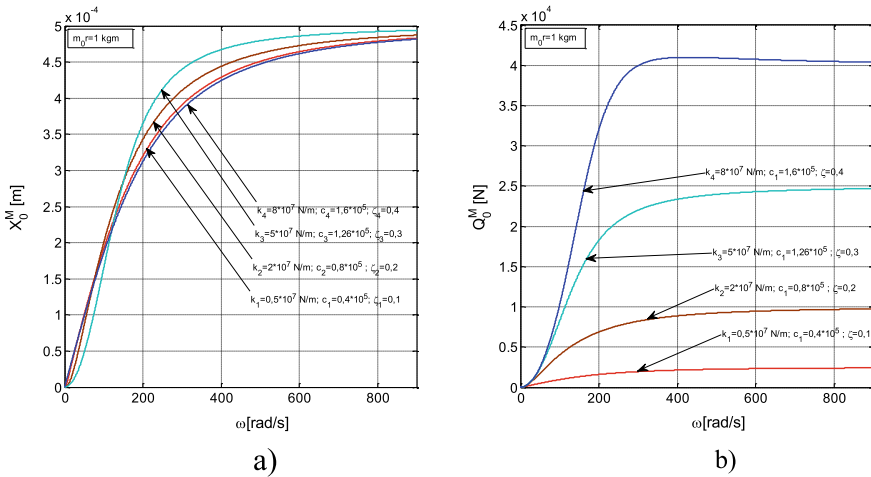


Fig. 4 The dynamic response for the Maxwell model: **a** variation of amplitude depending on pulse ω and rigidity k ; **b** variation of the force transmitted to the soil

characteristic curves for the variation of amplitude and of force transmitted to the soil were raised under conditions of continuous variation of the pulsation [17, 18].

It is noted that the fact that at the pulse of 400 rad/s the following results can be synthesized:

- (a) for the Voigt–Kelvin model compaction, the amplitude of the vibrations changes after each pass from 0.50 to 0.52 mm and the transmitted force for each pass increases from 5 to 85 kN [10, 11];
- (b) for the Maxwell model compaction, the amplitude of the vibrations changes after each pass from 0.425 to 0.47 mm and the transmitted force for each pass increases from 2.5 to 41 kN [10, 11];

In this case, it is found that the compaction efficiency corresponds to the soils that have the Voigt–Kelvin rheological behavior. For this reason, it is necessary starting with the laboratory tests, to be able to establish the predominantly elastic or viscous character so that in the field there may be achieved soil improvement works by correcting the mineral aggregate dosages, that is switching from the Maxwell rheological behavior to the Voigt–Kelvin rheological behavior [10, 17, 18].

References

1. D. Adam, F. Kopf, *Theoretical Analysis of Dynamically Loaded Soils, European Workshop: Compaction of Soils and Granular Materials* (ETC11 of ISSMGE, France, Paris, 2000)
2. S. Bejan, *Analysis of Dynamic Vibration Compaction Process Performance for Road Structures*. Ph.D. thesis, “Dunarea de Jos” University of Galati, 2015

3. P. Bratu, The behavior of nonlinear viscoelastic systems subjected to harmonic dynamic excitation, in The 9th International Congress on Sound and Vibration, University of Central Florida Orlando, Florida, 8–11 July (2002)
4. P. Bratu, Dynamic response of nonlinear systems under stationary harmonic excitation, nonlinear acoustics and vibration, in 11th International Congress on Sound and Vibration, St. Petersburg, 5–8 July, (2004), pp. 2767–2770
5. P. Bratu, Dynamic analysis in case of compaction vibrating rollers intended for road works, in the 17th International Congress on Sound & Vibration, ICSV, Cairo, 18–22 July (2010)
6. P. Bratu, C. Debeleac, The analysis of vibratory roller motion, in *Proceedings of the VII International Triennial Conference Heavy Machinery—HM 2011, Session Earth-moving and transportation machinery*, Vrnjačka Banja, Serbia, 29 June–2 July, pp. 23–26 (2011). ISBN 978-86-82631-58-3
7. P. Bratu, A. Stuparu, S. Popa, N. Iacob, O. Voicu, The assessment of the dynamic response to seismic excitation for constructions equipped with base isolation systems according to the Newton-Voigt-Kelvin model. *Acta Tehnica Napocensis seria Appl. Math. Eng.* **60**(IV), 459–464 (2017)
8. P. Bratu, A. Stuparu, A. Leopa, S. Popa, The dynamic analysis of a construction with the base insulation consisting in anti-seismic devices modeled as a Hooke-Voigt-Kelvin linear rheological system. *Acta Tehnica Napocensis seria Appl. Math. Eng.* **60**(IV), 465–472 (2018)
9. P. Bratu, A. Stuparu, S. Popa, N. Iacob, O. Voicu, G. Spanu, The dynamic isolation performances analysis of the vibrating equipment with elastic links to a fixed base. *Acta Tehnica Napocensis, seria Appl. Math. Eng.* **61**(I), pp. 23–28 (2018)
10. C.F. Dobrescu, Highlighting the change of the dynamic response to discrete variation of soil stiffness in the process of dynamic compaction with roller compactors based on linear rheological modeling, in ed. by N. Herisanu, V. Marinca *Acoustics & Vibration of Mechanical Structures II* (vol. 801, 2015), 350 p. (ISBN 978–3-03835-628-8), pp. 242–248, [ISI Web of Science (WoS)], disponibil la. [10.4028/www.scientific.net/AMM.801.242](https://doi.org/10.4028/www.scientific.net/AMM.801.242)
11. C.F. Dobrescu, E. Brăguță Optimization of vibro-compaction technological process considering rheological properties, in *Proceedings of the 14th AVMS Conference*, Timisoara, Romania, May 25–26, 2017, Springer Proceedings in Physics (vol. 198, 2017) ed. by N. Herisanu, V. Marinca, pp. 287–293. ISSN 0930-8989. ISSN 1867-4941 (electronic). Springer Proceedings in Physics ISBN 978-3-319-69822-9. ISBN 978-3-319-69823-6 (eBook). <https://doi.org/10.1007/978-3-319-69823-6>
12. A. Leopa, C. Debeleac, S. Năstac, Simulation of vibration effects on ground produced by technological equipments, in 12th International Multidisciplinary Scientific GeoConference SGEM2012, Conference Proceedings, vol. 55, pp. 743–750 (2012). ISSN 1314-2704
13. P. Bratu, Evaluation of the dissipated energy in viscoelastic or hysteretic seismic isolators. *Rom. J. Acoust. Vib.* **9**(1), 53–56 (2012)
14. P. Bratu, Dynamic stress dissipated energy rating of materials with maxwell rheological behavior. *Appl. Mech. Mater.* **801**, 115–121. [10.4028/www.scientific.net/AMM.801.115](https://doi.org/10.4028/www.scientific.net/AMM.801.115) (2015)
15. R.M. Morariu-Gligor, A.V. Crisan, F.M. Șerdean, Optimal design of an one-way plate compactor. *Acta Technica Napocensis Ser. Appl. Math. Mech. Eng.* **60**(IV), 557–564 (2017)
16. R. Pințoi, R. Bordoș, E. Braguța, Vibration effects in the process of dynamic compaction of fresh concrete and stabilized earth. *J. Vib. Eng. Technol.* **5**. ISSN 2321–3558 (2017)
17. M.A. Mooney, R.V. Rinehart, Field monitoring of roller vibration during compaction of subgrade soil. *J. Geotech. Geoenviron. Eng. ASCE* **133**(3), 257–265 (2007)
18. M.A. Mooney, R.V. Rinehart, In-situ soil response to vibratory loading and its relationship to roller-measured soil stiffness. *J. Geotech. Geoenviron. Eng. ASCE* **135**(8), 1022–1031 (2009)

Parametric Analysis of Dynamic Insulation in the Action of the Seismic Movements of the Base-Insulated Buildings



Polidor Bratu, Cristina Oprețescu, Amalia Țârdea, Ovidiu Voicu,
and Adrian Ciocodeiu

Abstract Buildings protection against seismic actions has, in recent times, led to an intense emulation of innovative solutions for the insulation of the base. Thus, under the new conditions of industrial development of antiseismic devices, at high and guaranteed performance level, dynamic isolation systems can be achieved resulting from assembling in various configurations of simple devices. In this context, the designers have, on the basis of the elastomeric antiseismic devices and the fluid dissipators, constructed individual units in a modular system. These, by installation-mounting in a sufficiently large number, are designed to provide the degree of dynamic isolation. In the present paper we present a modular $E/(E - V)$ type Zener model, consisting of two elastomeric devices and a viscous damping fluidized dissipator. In order to isolate a building, a sufficient number of modules must be used to define in a unitary isolation system the base for a given building. Consequently, the paper will include the dynamic model based on Zener schematization of the entire isolation system and the specific parameters for calculating and evaluating the dynamic isolation level.

1 Introduction

The Zener complex rheologic model for the entire dynamic base insulation system is equivalent to the assembly of the insulation modules, each of them being made of a Zener rheological element, individualized by two parallel Hooke and Maxwell connections. In this case, individual rigidity and amortizations, by properly

P. Bratu (✉) · C. Oprețescu · A. Țârdea
ICECON SA, Bucharest, Romania
e-mail: icecon@icecon.ro

P. Bratu
Faculty of Engineering and Agronomy, “Dunărea de Jos” University of Galați, Brăila, Romania

O. Voicu · A. Ciocodeiu
Institute of Solid Mechanics, Romanian Academy, Bucharest, România

combining the rheological elements, ensures the equivalent rigidities and equivalent amortizations of the insulation system for the entire building.

The kinematic excitation of the seismic movement is represented by the instantaneous displacement of the first vibratory motion mode from the earthquake spectral composition. Thus, the fundamental component, that is the first mode of movement, is the spectral displacement $x_0 = X_0 \sin \omega t$ or $\tilde{x}_0 = X_0 e^{j\omega t}$, where (ω, X_0) represents the pulse and respectively, the amplitude of the first spectral mode with the period $T_0 = \frac{2\pi}{\omega}$ [1, 2].

The dynamic response of the building is represented by the instantaneous displacement $x = x(t) = A \sin(\omega t + \varphi_1)$ or $\tilde{x} = \tilde{A} e^{j\omega t}$, where $\tilde{A} = A e^{j\varphi_1}$. Also, the instantaneous coordinate of the serial link point between the elastic element and the viscous element, noted with B, is $y = y(t) = B \sin(\omega t + \varphi_2)$ sau $\tilde{y} = \tilde{B} e^{j\omega t}$, where $\tilde{B} = B e^{j\varphi_2}$. The imaginary unit was denoted by $j = \sqrt{-1}$. Essentially, the work highlights the dynamic response, the force transmitted by the earthquake to the building through the dynamic insulation system, as well as the dissipate energy on the viscous fluid amortization device [3, 4].

The paper highlights the possibility to model the dynamical isolation system of the base using the Zener rheological schematics, for a building under a significant seismic action for Romania, with $\omega = 4\pi$ rad/s or $T_0 = 0.5$ s and a corresponding displacement $X_0 = 0.3$ m, on the fundamental excitation mode. The input data for such an seism are adopted according the map containing the zones of high seismic risk and the requirements of the Romanian Technical Regulation P 100/2004. For the case under consideration, the favorable technical solution for a transmissibility $T = 0.05$, or a dynamic isolation degree $I = 95\%$ is the adoption of the Zener mode. This is achieved by appropriately associating the elastomeric antiseismic and viscous fluid dissipation devices in combinations of favorable connections so that the schematic can be a Zener equivalent model. For the case of study for a building in Romania, based on the technical data mentioned above, in this paper are characteristic the following parameters: the actual pulse of the mass on the horizontal axis $\omega_n = 1.6$ rad/s the excitation pulse for the fundamental mode of the seism $\omega = 4\pi$ rad/s, equivalent damping $\zeta = \zeta_{eq} = 5\%$ and relative pulse $\Omega = \frac{\omega}{\omega_n} = 7.8$.

For the dynamic isolation calculation of the base it is used the fundamental mode of excitation, according to the structural calculation regulations for constructions under seismic action. Consequently, it is studied the dynamic response to fundamental excitation, using linear viscoelastic modeling for the isolation systems of the base, which can be modeled, in this way. The results are based on the researches and design solutions developed by ICECON SA (Research Institute for Construction Equipment and Technology from Bucharest, Romania) for some buildings in Romania that have the basis isolated, that are confidential data.

2 Dynamic Response

Figure 1 presents the Zener equivalent dynamic model, where rigidity k and amortization c represent equivalent measures for the entire dynamic insulation system as a whole where N was inserted as real and positive multiplication factor.

Taking into account that $x_0 > x$ and $y > x$, by hypothesis, the movement equations, in complex formalism, are

$$\begin{cases} m\ddot{x} - k(\tilde{x}_0 - \tilde{x}) - c(\dot{y} - \dot{x}) = 0 \\ c(\dot{y} - \dot{x}) - Nk(\tilde{x}_0 - \tilde{y}) = 0 \end{cases} \tag{1}$$

The solutions of system (1) are $\tilde{x} = \tilde{A}e^{j\omega t}$, with $\tilde{A} = Ae^{j\varphi_1}$ and $\tilde{y} = \tilde{B}e^{j\omega t}$, with $\tilde{B} = Be^{j\varphi_2}$, which must verify the equation system. Thus, amplitudes A and B are obtained as

$$A = X_0 \sqrt{\frac{N^2k^4 + c^2\omega^2k^2(1 + N)^2}{D}} \tag{2}$$

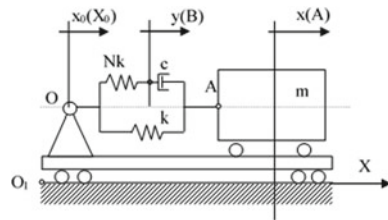
$$B = X_0 \sqrt{\frac{N^2k^2(k - m\omega^2)^2 + c^2\omega^2k^2(1 + N)^2}{D}} \tag{3}$$

where D has the expression

$$D = N^2k^2(k - m\omega^2)^2 + c^2\omega^2[(k - m\omega^2) + Nk]^2 \tag{4}$$

The initial data of a case in work are as follows: $m = 3$ Mkg, $k = 8$ MN/m, $X_0 = 0.3$ m, $N = 10$. $c = (1, 2, 3, 4, 5)$ MNs/m enabled the analytical calculation and the representation of the curve families for A and B , in Fig. 2.

Fig. 1 The Zener base insulation model



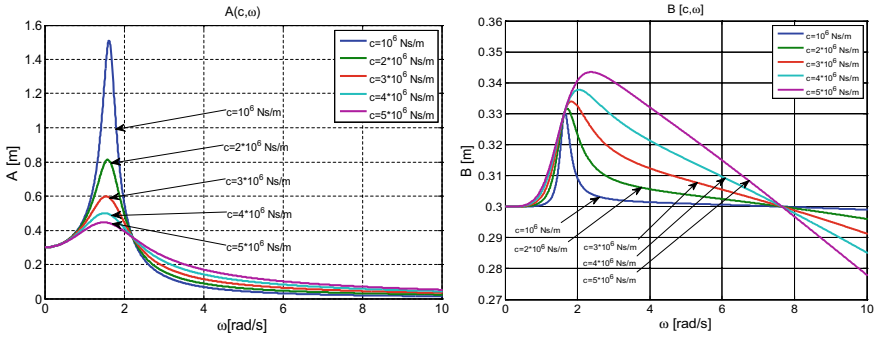


Fig. 2 The family of curves A and B

3 Transmitted Force

Based on the scheme in Fig. 1 the instantaneous deformation $z_v = z_v(t)$ of the viscous shock absorber may be expressed as

$$\tilde{z}_v = \tilde{z}_v(t) = \tilde{y} - \tilde{x} \tag{5}$$

where $\tilde{z}_v = \tilde{Z}_v e^{j\omega t}$, with $\tilde{Z}_v = Z_{0v} e^{j\varphi}$ in which φ is the phase shift between deformation \tilde{z}_v and the instantaneous displacement \tilde{y} .

Replacing in relation (5) the expressions of the complex measures $\tilde{z}_v, \tilde{y}, \tilde{x}$, we obtain

$$\tilde{Z}_v = \tilde{B} - \tilde{A} \tag{6}$$

and based on previous relations for A and B it emerges amplitude Z_{0v} in analytical form as follows

$$Z_{0v} = X_0 \frac{mk\omega^2 N}{\sqrt{D}} \tag{7}$$

The maximum transmitted force $\tilde{Q}_T = \tilde{Q} e^{j\omega t}$, where $\tilde{Q} = Q_0 e^{j\theta}$, in which θ is the phase shift between \tilde{Q}_T and \tilde{x}_0 , may be expressed as follows

$$\tilde{Q} = \tilde{Q}_1 + \tilde{Q}_2 \tag{8}$$

Forces \tilde{Q}_1 and \tilde{Q}_2 of the Maxwell model branch and respectively from Hooke branch are as

$$\begin{cases} \tilde{Q}_1 = c\omega\tilde{Z}_v \\ \tilde{Q}_2 = k(X_0 - \tilde{A}) \end{cases} \tag{9}$$

Carrying out all operational calculations based on relations (8) and (9) it is obtained the amplitude of the force transmitted as

$$Q_0 = \frac{X_0}{D} \sqrt{R^2 + I^2} \tag{10}$$

where we have

$$\begin{cases} R = -N^2k^2m\omega^2(k + c\omega)(k - m\omega^2) - kmc^2\omega^4(k + kN - m\omega^2) \\ I = Nkmc\omega^3[c\omega(k - m\omega^2) + Nk(k + c\omega)] \end{cases} \tag{11}$$

4 Transmissibility Displacement

By definition transmissibility T of movement is given by relation

$$T = \frac{A}{X_0} \tag{12}$$

or taking into account the expression of A , we have

$$T(c, \omega) = \sqrt{\frac{N^2k^4 + c^2\omega^2k^2(1 + N)^2}{D}} \tag{13}$$

with the representation in Fig. 4 [1, 5].

5 The Linear Viscous Dissipated Energy

The energy dissipated in the composed amortization system with the equivalent constant c is given by the relation

$$W_d = \pi c\omega Z_{0v}^2 \tag{14}$$

In relation (14) we insert relation (7) and we obtain

$$W_d(c, \omega) = \pi X_0^2 \frac{m^2k^2c\omega^5N}{D} \tag{15}$$

with representation in Fig. 5.

6 Conclusions

Systems made up of HDRB (High Damping Rubber Bearing), LRB (Lead Rubber Bearing), elastomeric antiseismic devices in connection with FVD (fluid viscous damper) dissipative antiseismic devices can be plotted as a Zener equivalent model based on the following methods of analysis and evaluation:

- (a) identifying the size and distribution of mass elements, the geometric configuration and rigid behavior of the building to be isolated at the base;
- (b) maximum acceleration level and spectral component (fundamental) for earthquakes from the seismic zoning of the building site;
- (c) conceiving the system of supporting and lateral displacement of the building placed on the insulation system at the base;
- (d) the Zener connection specifying all elastic and viscous stiffnesses as an equivalent model;
- (e) analytical calculation of the dynamic response and evaluation of the dynamic isolation parameters.

Computational relationships can be used for dynamic optimization of base isolation so that the transmissibility must be no more than 20–30%, as a critical and significant condition for Zener model performance, [1, 2, 6–9].

On the basis of Figs. 2, 3, 4, and 5, the efficiency of the base isolation system can be evaluated, using the Zener model, because the families of curves offer the possibility for comparative appreciation of the parameters, depending to the relative pulse Ω , the fraction of equivalent critical damping ζ , or the viscous damping c , or the excitation pulse ω .

Thus, for the case of study, with $\omega = 4\pi$ rad/s, $c = 10^6$ Ns/m, $\zeta = 5\%$, $\omega_n = 1.6$ rad/s, $\omega = 12.56$ rad/s the following parameters are obtained: $A = 0.05$ m, $B = 0.295$ m, $Q = 4000$ kN, $W = 1000$ kJ, $T = 0.05$ ş $I = 95\%$, %, resulting a very good dynamic isolation, meaning an efficient isolation system of the base.

Fig. 3 Maximum transmitted force $Q_0(\zeta, \Omega)$

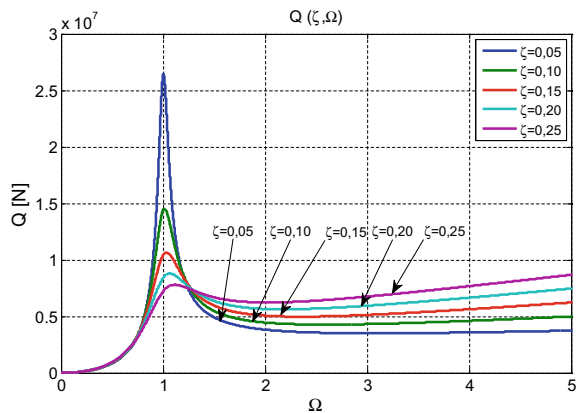


Fig. 4 Variation of transmissibility according to Ω and ζ

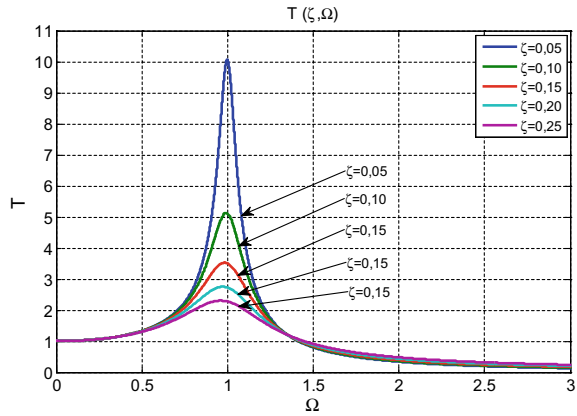
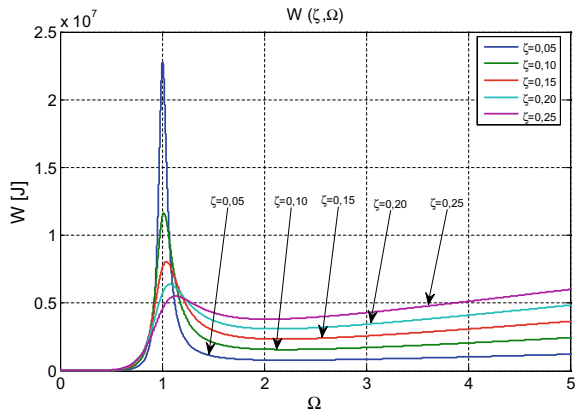


Fig. 5 Variation of dissipated energy $W_d(\zeta, \Omega)$



References

1. Y.-P. Wang, Fundamentals of Seismic Base Isolation (International training programs for seismic design of building structures hosted by National Center of Research on Earthquake Engineering, Taiwan, 2002)
2. P. Bratu, Evaluation of the dissipated energy in viscoelastic or hysteretic seismic isolators. Rom. J. Acoust. Vib. **9**(1), 53–56 (2012)
3. T. Sireteanu, Smart suspension systems. Rom. J. Acoust. Vibration **13**(1), 2 (2016)
4. N.D. Stanescu, Vibrations of a shell with clearances, neo-Hookean stiffness, and harmonic excitations. Rom. J. Acoust. Vib. **13**(2), 104–111 (2016)
5. O. Vasile, Active vibration control for viscoelastic damping systems under the action of inertial forces. Rom. J. Acoust. Vib. **14**(1), 54–58 (2017)
6. E.A. Johnson, J.C. Ramallo, B.F. Spencer, M.K. Sain, Intelligent base isolation systems, in 2nd World Conference on Structural Control, Kyoto, Japan (1998)
7. A.M. Mitu, T. Sireteanu, G. Ghita, Passive and semi-active bracing systems for seismic protection: a comparative study. Rom. J. Acoust. Vib. **12**(1), 49–56 (2015)

8. C. Dobrescu, The rheological behaviour of stabilized bioactive soils during the vibration compaction process for road structures, in 22th International Congress on Sound and Vibration, Florence, Italy, 12–16.07 (2015)
9. P. Bratu, Dynamic stress dissipated energy rating of materials with maxwell rheological behavior. *Appl. Mech. Mater.* **801**, 115–121 (2015). 10.4028/www.scientific.net/AMM.801.115

Vibration of Fixing Device of the Reaction Chamber for Gamma-Ray Beam in the Project ELIADE



Sorin Vlase, Călin Itu, Paul Nicolae Borza, Gabriel Suliman, Cristian Petcu, and Maria Luminița Scutaru

Abstract The ELI-NP Array of Detectors (ELIADE) is a project dedicated to be the main experimental setups in order to use in practical applications the gamma-ray beam. The project is developed at ELI-NP Bucharest. The reaction chamber for ELIADE array with all their devices are the goal of this research team. The level off the research activities in ELI Institute imposes to obtain high precision of the experiments. The study of the small deformation and the vibration of the equipment becomes important. All the parts of the reaction chamber, to a greater or lesser extent, consist of elastic elements. In the experiment, conducted by the Institute of Atomic Physics, in connection with the ELIADE project, precision is so important that it requires extremely small or undetected vibration of the device. Finite Element Method is used to model the system and the sensitive element, the fixing device of the target has been studied.

1 Introduction

Previous studies [1, 2] have analyzed the possibility of modeling the interaction chamber and the influence of constructive parameters on system vibrations. To accomplish this, a previous dynamic analysis [3–5] was made to determine to what extent the rigid motion of the system influences the response to vibrations. In the present paper, vibration analysis of the system as a whole and of the target fixing rod is performed. This element has been shown to present vulnerabilities from the point of view of design, resulting in a pronounced amplification of an external excitation for certain frequency ranges. The interaction chamber is clamped on two plans where two actuators assure the movement of the interaction chamber on gamma beam direction. The kinematics of the acting system was designed and simulated. In order

S. Vlase (✉) · C. Itu · P. N. Borza · M. L. Scutaru
Transilvania University of Brasov, Brașov, Romania
e-mail: svlase@yahoo.com

G. Suliman · C. Petcu
Institute of Atomic Physics, Bucharest, Romania

© Springer Nature Switzerland AG 2021

N. Herisanu and V. Marinca (eds.), *Acoustics and Vibration of Mechanical Structures—AVMS 2019*, Springer Proceedings in Physics 251,
https://doi.org/10.1007/978-3-030-54136-1_38

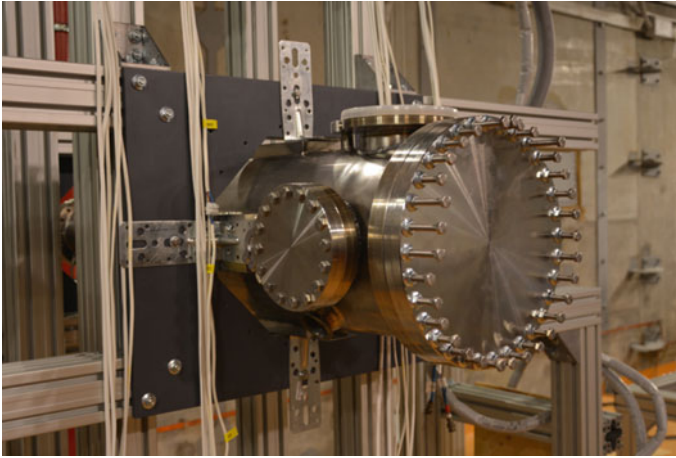


Fig. 1 Interaction chamber

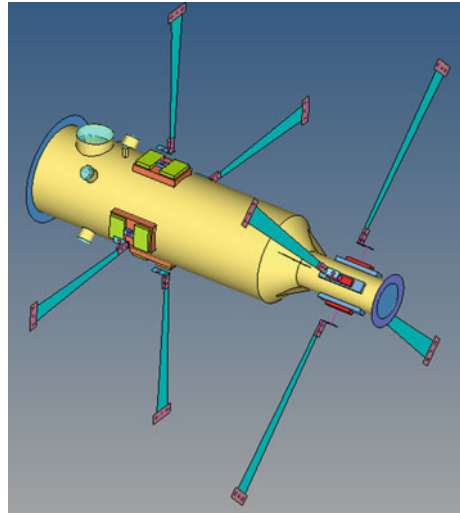
to have an initial “reference position” a laser visible beam, independent alignment system will be used. This will assure the raw alignment of the interaction chamber and the designed system will take this point as a reference for all future alignment commands done on actuators. The system design and also the functions necessary to assure the implementation of the alignment system were developed. The actual stage of the interaction chamber is illustrated in Fig. 1. We already take correction measure in order to resynchronize the initial plan (schedule) take into account the real situation. Practically, the focus was on development of the tracking system’ firmware including important features as the development of testing and calibration procedures necessary to proof the quality of whole tracking system (individual and serial precision in the positioning of sample holder inside interaction chamber and determination of time constant of the whole “close loop” controlling system).

In order to assure the precision for the alignment system, it is necessary to know the response of the system to an external step load and the vibration of the lever where is situated the target (in this area must to act the gamma beam). For this, previous works have been used [6–9].

2 Vibration Analysis

In Fig. 2 is presented the model used in FEA analysis [2]. The element that presents interest for us is the lever with the target at the end. This element is elastic and can have great transmissibility. This can decrease the precision of the command system. The target is a material body (can be solid, liquid or gaseous) being hit by a gamma beam; it is necessary to provide inside the interaction chamber a vacuum environment

Fig. 2 FEM model of the interaction chamber



at the level 10–3 mbar; it is necessary to provide a mechanical alignment with the gamma beam in the experimental area (Gamma Beam Transportation System).

In Fig. 3, there are shown some eigenmodes of the whole interaction chamber (presented in Table 1). For example, the modes 5, 23, 24 involve camera body vibration. The modes 12–15 and 19, 20. An excitation at a frequency close to resonance can lead to unwanted effects. But since the part involved in this eigenmode

Table 1 The first 15 eigenpulsation for the whole structure

No	Frequency (Hz)
1	15,15
2	19,24
3	40,48
4	64,28
5	71,01
6	80,14
7	84,58
8	85,69
9	95,22
10	119,95
11	152,89
12	183,92
13	184,22
14	199,73
15	204,31

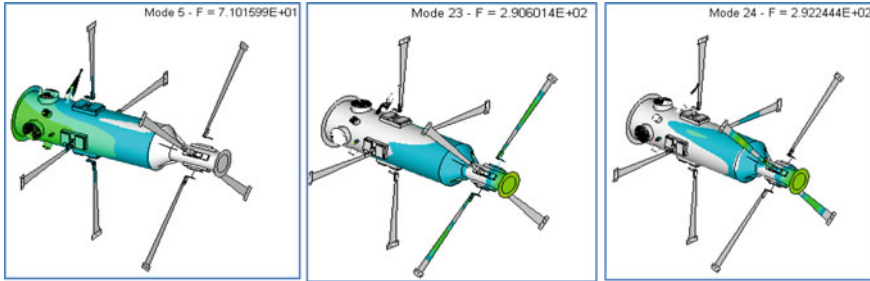


Fig. 3 Eigenmodes of vibration of the whole chamber (modes 5, 23, 24)

is well defined, it is possible to avoid unwanted effects and to modify the eigenfrequency by acting on the geometry and elasticity of the significant, highlighted parts in the corresponding eigenmode.

3 Clamping Lever Analysis

A study of the lever with the target is imposed due to the elasticity of this element. A finite element analysis to study the eigenvalues and eigenvectors are made. In Fig. 4, the lever into the interaction chamber and alone is presented.

The first ten eigenmodes of vibration of the fixing device are presented below (Fig. 5a–e). The stiffness of the rest of the structure over the clamping device is large and the influence of the target bar motion on the rest of the elastic structure is small. At least for the small eigenfrequencies, an independent study of the fixing device is warranted.

The rigidity of this device, compared to that of the rest of the interaction chamber, is small and, as a result, it is expected that in the case of external excitations this device will have vibrations with high amplitudes. It is, therefore, useful to make

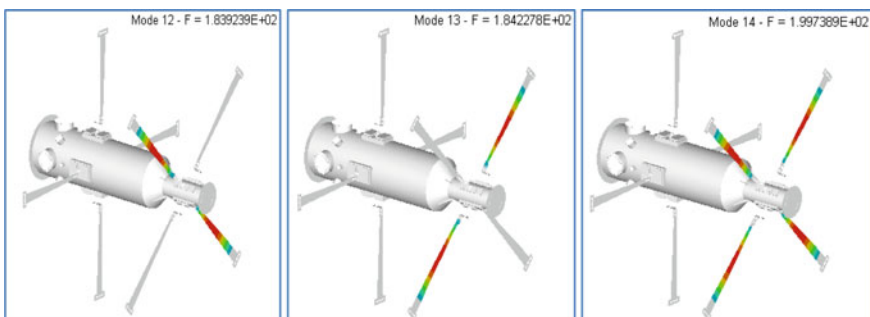


Fig. 4 Eigenmodes of vibration of the whole chamber (modes 12, 13, 14)

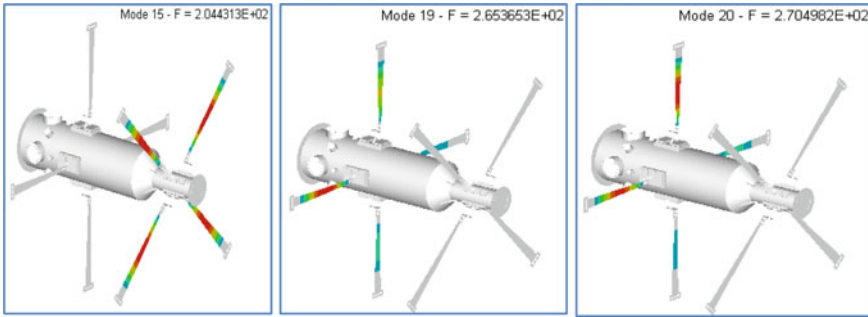


Fig. 5 Eigenmodes of vibration of the whole chamber (modes 15, 19, 20)

an analysis of the transmissibility of displacement of the ground to the target fixed at the end of the clamping lever. To achieve this, we imposed a unit displacement of the amplitude of the harmonic vibration of the ground and to study how big the amplitude of the target vibrations, in this case, would be. The obtained graph represents the transmissibility of the displacement (Fig. 6). This representation is obtained in the following manner: the ground is excited with a unitary amplitude, for different frequencies, from 0 to 5000 Hz. This excitation determines an amplitude of the target having 13 units, for the frequency 800 Hz, or having 2 units for a frequency 490 Hz. Making this calculus for all the frequencies between 0 and 5.000 Hz, it is possible to obtain Fig. 6. It can be seen that for some frequencies the magnitude of the amplitude can increase even 13 times. So the vibrations of the interactive chamber’s mount base amplify. In this case, there are two paths to follow: to avoid operating in the vibration amplification area and redesign the target clamping device in such a way that it becomes stiffer (Figs. 7, 8, 9, 10, 11 and 12).

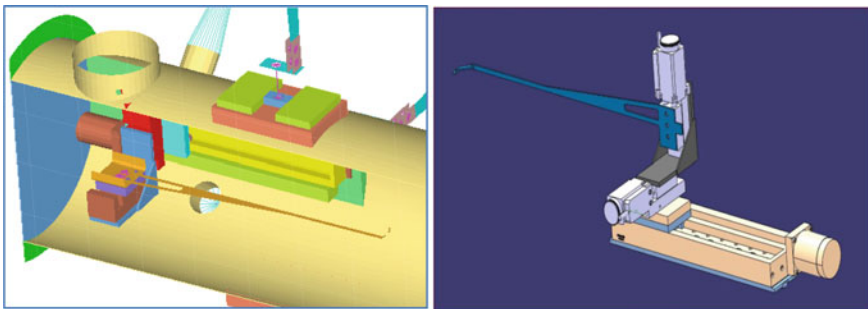


Fig. 6 The lever with the target [1]

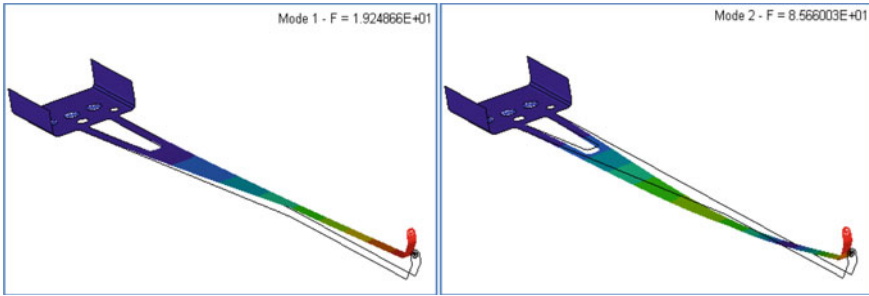


Fig. 7 Eigenmodes of vibration (modes 1 and 2)

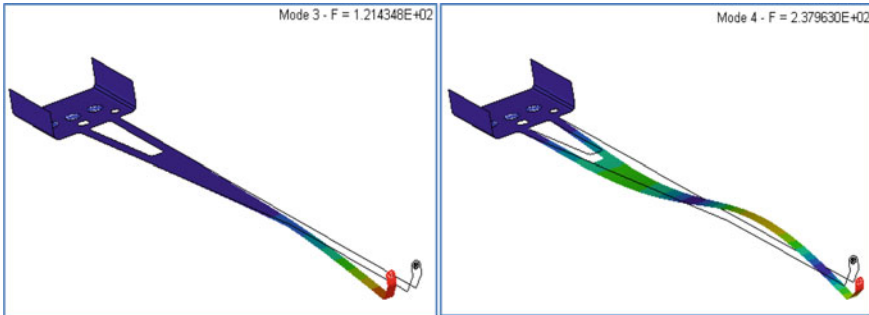


Fig. 8 Eigenmodes of vibration (modes 3 and 4)

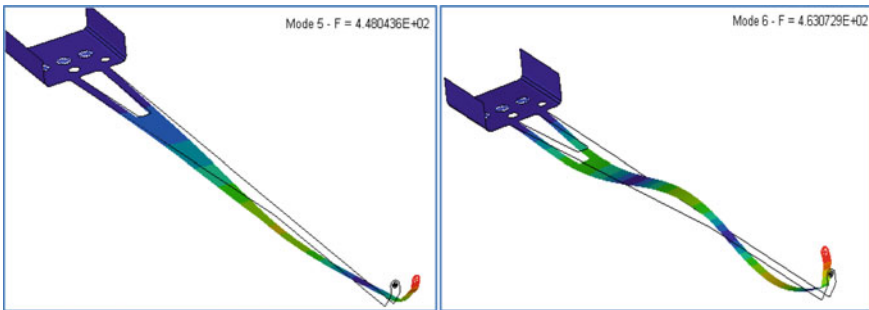


Fig. 9 Eigenmodes of vibration (modes 5 and 6)

4 Conclusion

The study of the vibration of the system and the transmissibility from the ground to the target is made in the paper. The change of the material and a redesign of its shape so as to ensure less transmissibility of the amplitude of vibration it is imposed. The foundation of the laboratory is specially built to provide good isolation to vibration.

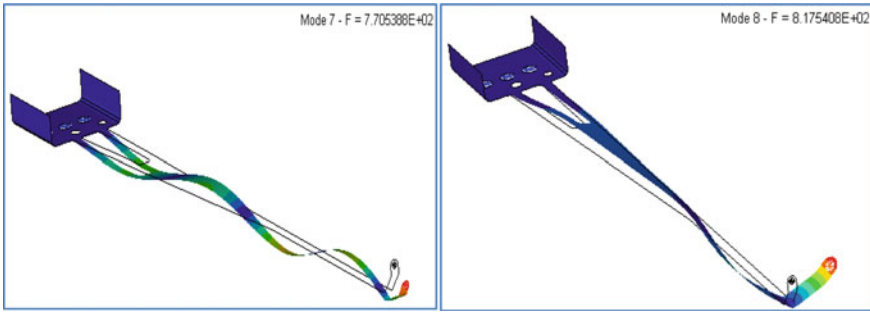


Fig. 10 Eigenmodes of vibration (modes 7 and 8)

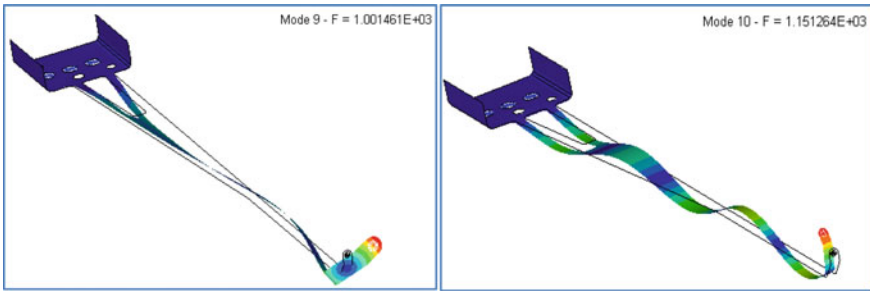


Fig. 11 Eigenmodes of vibration (modes 9 and 10)

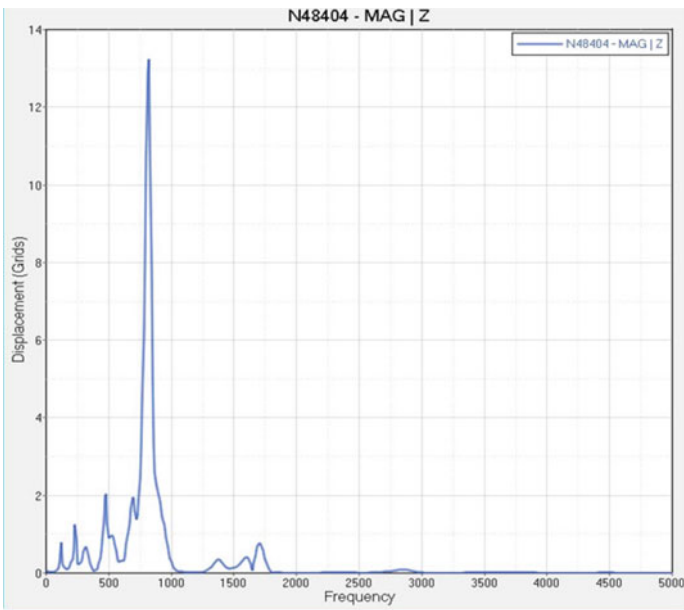


Fig. 12 Transmissibility of the displacement

As unpredictable excitations may occur, however, it is a problem to perform a correct design of the interaction chamber and the bar on which the target is fixed. Based on the analysis, it has been found that, from a theoretical point of view, it is possible that a unitary amplitude of the vibration of the ground in one direction may result in vibration with 13 times greater amplitude of the target in the same direction. This is because, in this version, this bar has too low stiffness. It is necessary to redesign this clamping device so that the transmissibility of the displacement decreases. This is the next objective of the joint research team.

References

1. S. Vlase, A. Crişan, C. Itu, M.L. Scutaru, FE analysis of the interaction chamber for the ELI-NP array of detectors (ELIADE). *Acta Tech. Napoc. Ser.: Appl. Math. Mech. Eng.* **62**(I) (2019)
2. S. Vlase et al., Optical analysis of the reaction chamber for the ELIADE array. *Procedia Manuf.* **22**, 215–220 (2018)
3. A. Öchsner, *Computational Statics and Dynamics: An Introduction Based on the Finite Element Method* (Springer, Singapore, 2016)
4. S. Vlase, P.P. Teodorescu, Elasto-dynamics of a solid with a general “rigid” motion using FEM model part I. *Theor. Approach. Rom. J. Phys.* **58**(7–8), 872–881 (2013)
5. S. Vlase, M. Marin, A. Öchsner, et al., Motion equation for a flexible one-dimensional element used in the dynamical analysis of a multibody system. *Continuum Mech. Thermodyn.* **31**, 715 (2019). <https://doi.org/10.1007/s00161-018-0722-y>
6. A.G. Erdman, G.N. Sandor, A. Oakberg, A general method for kineto-elastodynamic analysis and synthesis of mechanisms. *J. Eng. Ind. ASME Trans.* **94**(4), 1193–1203 (1972)
7. J. Gerstmayr, J. Schberl, A 3D finite element method for flexible multibody systems. *Multibody Syst. Dyn.* **15**(4), 305–320 (2006)
8. B. Simeon, On lagrange multipliers in flexible multibody dynamic. *Comput. Methods Appl. Mech. Eng.* **195**(50–51), 6993–7005 (2006)
9. S. Vlase, Dynamical response of a multibody system with flexible element with a general three-dimensional motion. *Rom. J. Phys.* **57**(3–4), 676–693 (2012)

ANN Samples Generation Using 2D Dynamic FEM for Predicting Machining Vibrations



Andrei-Ionuț Berariu, Iulia-Maria Prodan, Cosmin-Ioan Niță,
and Tudor Deaconescu

Abstract Cutting operations are difficult to predict in terms of dynamic behavior and prove to be equally difficult to control. The productivity and quality of the generated surface are influenced directly by phenomena like chatter, adhesion and wear, which left undetected can be destructive and cost-intensive. The paper presents and discusses a 2D finite element method that can be used to simulate and extract the cutting forces frequency components for various milling operations. The proposed method represents an effective approach to predicting such nonlinear behavior and entails unwrapping the analytical chip section and running of plane stress simulations using a linear kinematic trajectory. The results are rewrapped according to the geometry of the tool, which is used to generate the overall dynamic behavior in the machine coordinate system. The paper concludes with considerations concerning future directions in deep learning in milling operations and the necessary effort for creating high-end control algorithms.

1 Introduction

One of the most used surface—generating process in the industry is milling. The productivity of this process is strongly related to the development of new technologies for the machine tools, cutting tools, materials and computer science advances, the latest being more and more present in the field. In order to optimize the milling

A.-I. Berariu (✉) · I.-M. Prodan · C.-I. Niță · T. Deaconescu
Transilvania University of Brasov, B-dul Eroilor nr. 29, Braşov, Romania
e-mail: andrei-ionut.berariu@unitbv.ro

I.-M. Prodan
e-mail: iulia-maria.prodan@unitbv.ro

C.-I. Niță
e-mail: nita.cosmin.ioan@unitbv.ro

T. Deaconescu
e-mail: tdeacon@unitbv.ro

productivity, the process itself needs to be modeled with regards to the material properties, cutting mechanics, tool geometry, process kinematics and structural dynamics in order to predict the forces, torque, power, form errors and vibrations during the metal cutting operations.

One of the main issues that process engineers will encounter while trying to optimize the MRR (Material Removal Rate) is the apparition of chatter. The current understating of this phenomena leads to the conclusion that there are three types of chatter: frictional chatter, mode coupling chatter and regenerative chatter. In their research [1], the authors concluded that in order to control the milling stability it is mandatory to know the cutting force coefficients, the model parameters in term of cutting system, the dynamics characteristics of the workpiece, the damping effect of the process, the tool runout and the gyroscopic effect. One of the most recent works in the field [2] treats the frictional chatter separately. The team highlighted a sweet spot where all vibrations are reduced suggesting a transient phase dependent on the cutting velocities.

The authors of [3] managed to create a unified cutting force model that proved to be precise where the geometric, kinematic and mechanic parameters are used to predict the forces for turning, milling, boring and drilling operations.

The usage of Artificial Neural Network (ANN) is now largely available due to the increasing efficiency in computation and has reached a point where it is feasible to be applied also in the manufacturing field. In [4], the research team managed to train an ANN to predict the cutting forces in all three directions F_x , F_y and F_z for turning operations. The database contained 96 samples and using this setup, the team managed to validate the ANN model and the results showed a good correlation between predicted forces and experimental forces.

In order to maximize the precision of the ANN model or to extend the dimensions (add more variables like new materials, cutting parameters, etc.) the number of “training” samples needs to be increased exponentially. There are two ways to generate samples, the first one is through experiments and the second is to use different mathematical models. The first one is usually more expensive than the second, but it offers high precision. The second uses various analytical models or numerical models like Finite Element Method (FEM) that are able to simulate the physics with sufficient precision at a fraction of the cost.

The proposed method is centered on shoulder milling for proof of concept. The shoulder milling operations include: shoulder/face milling, edging peripheral milling and shoulder milling of thin deflecting walls. Also, the radial depth a_c and axial depth a_p (Fig. 1) are considered constant for this method. The method is verified using one cutting scenario where the Al6061_Machining material is used with the aim of obtaining one sample that will become the input for a machine/deep learning algorithm.

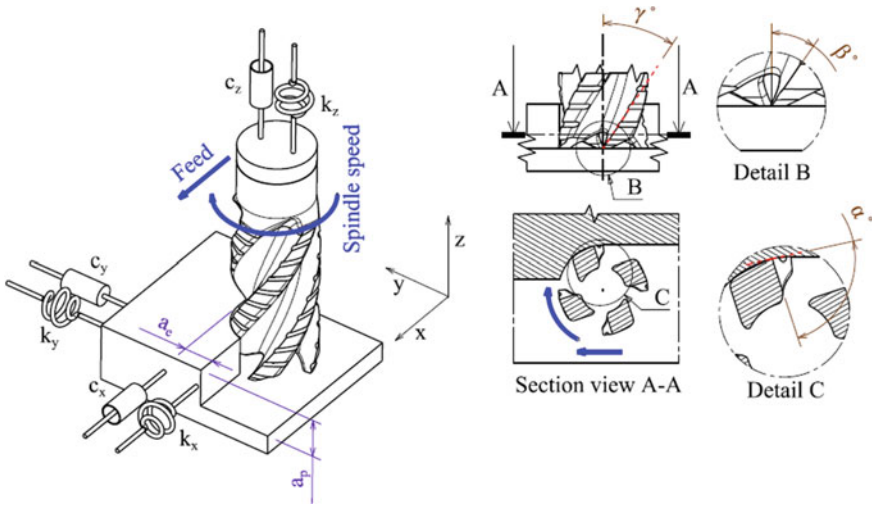


Fig. 1 Shoulder milling, main: kinematic, dynamic and cutting—geometry parameters

2 Milling Dynamics

A common practice is the use of Kelvin—Voigt approach when the dynamics of a system needs to be modeled generating pairs of $c_i - k_i$ (where c represents the damping and k the stiffness) for each of the considered axes (Fig. 1).

The main kinematic parameters in case of shoulder milling are Feed V_{fm} [mm/min] and Spindle speed N [rpm]. The cutting speed V_c [m/min] can be obtained with the cutting diameter D_c [mm]. The parameters of the chip geometry are dependent on the axial depth a_p [mm], radial depth a_c [mm] and the helix angle γ [°]. The last component involved in the cutting process is the cutting-edge which has two important parameters: rake angle and relief angle. Shoulder milling generates two faces simultaneously, which requires peripheral milling in combination with face milling, thus resulting in two cutting edges. Further, only the face milling component for which the rake angle is noted with α [°] will be taken into account and the relief angle will be ignored. For more clarity, the rake angle for the peripheral milling was introduced in figure β [°] (Fig. 1).

The actual path of any point of the cutter edge during milling is cycloidal in nature. The chip width \tilde{x} is strongly dependent on the axial depth of the cut a_p and the helix angle γ :

$$\tilde{x} = \frac{a_p}{\cos(\gamma)} [\text{mm}] \tag{1}$$

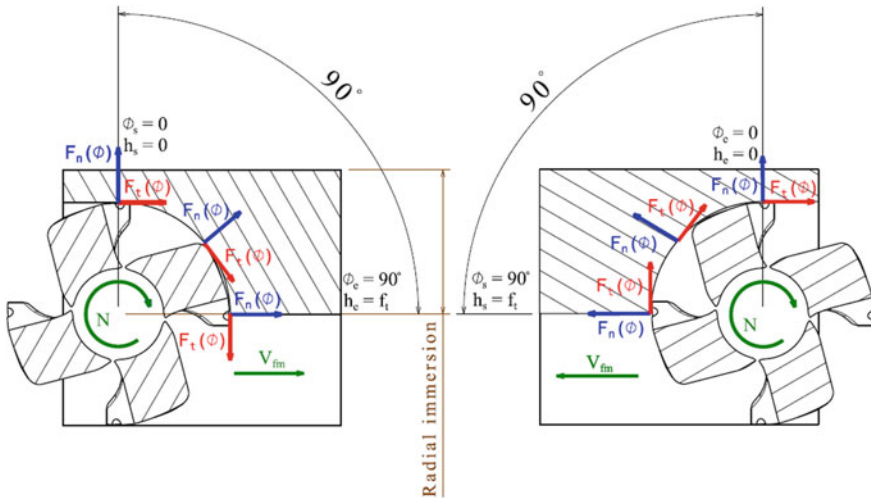


Fig. 2 Start/Exit angle geometry for up (left) and down (right) milling with 50% radial immersion

Usually, for analytical calculation, this influence is neglected ($\tilde{x} = a_p \rightarrow \gamma = 0^\circ$) but this approximation can be applied only when the axial depth a_p is small, otherwise, the F_z component will be mistakenly considered 0.

There are two ways to remove material from the workpiece in milling, up milling (conventional milling) (Fig. 2 left) and down milling (climb milling) (Fig. 2 right).

In order to obtain a good surface quality in milling, the aim is for thick chips (h_s) on entry and thin chips (h_e) on exit (down milling) but this is not always possible.

The chip thickness increases during the up milling and decreases in down milling. For up milling, the entry, or the start, angle is $\phi_s = 0 [^\circ]$ while the exit angle, ϕ_e , is dependent on the radial immersion, a_e , and tool radius (Fig. 2).

The transition from a purely kinematic model to a cutting force prediction model is done using the specific force coefficients K_s . This empirical coefficient is referred to as the specific (per unit chip area) force and depends on the workpiece material, tool geometry and chip thickness. In order to express the resulting cutting forces as a function of the angle, all the important variables like the entry angle, ϕ_s , and the exit angle, ϕ_e need to be taken into account. Adding the instantaneously chip section using the normal and tangential forces determined in polar coordinate (F_n, F_t) completes the picture so that:

$$F_x(\phi) = k_t \cdot a_p \cdot h \cdot \cos(\phi) + k_n \cdot a_p \cdot h \cdot \sin(\phi)[N] \tag{2}$$

$$F_y(\phi) = k_t \cdot a_p \cdot h \cdot \sin(\phi) + k_n \cdot a_p \cdot h \cdot \cos(\phi)[N] \tag{3}$$

where k_t and k_n are the tangential and normal components of the specific force K_s , θ [°] is the angle between F_n and the resulting total force and h [mm] is the chip thickness.

The number of teeth, Z , will directly influence the periodic impulses train caused by partial immersion (up and down milling). The number of teeth dictates the passing frequency that can be easily associated with the same phenomena for one tooth but with a Z -dependent phase shift. The aim is to extract the harmonics caused by the tooth passing frequency, using the Spindle speed N in order to apply the Fourier transformation, that can be used later to validate the method. Normally, these frequencies should be confirmed in the obtained spectrum alongside other frequencies caused by various nonlinear phenomena related to chip formation [5].

3 3D to 2D Conversion of Milling Dynamics

Obtaining the unwrapped chip of two consecutive teeth A novelty method which computes the chip thickness value as a function of angle $h(\phi)$ [mm] is presented in this chapter, allowing the unwrapping of the complicated polar cutting problem for a more simple 2D linear problem. The method is geometric in nature and Python™ is used as the programming language of choice.

The first step is determining the trajectories of two consecutive teeth during cutting (Fig. 3) by using the kinematic parameters from the milling process. The following variables are considered: Cutting diameter D_c [mm], Feed per tooth V_z [mm] and number of teeth, Z [integer].

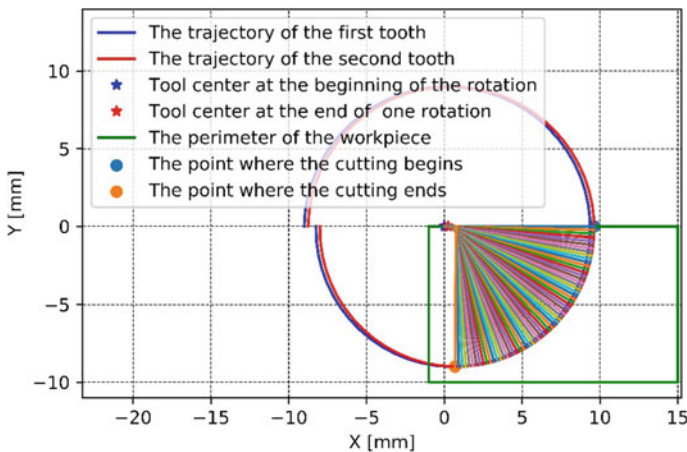


Fig. 3 The cycloidal trajectories of two consecutive teeth, workpiece perimeter with the start/end points and the instantaneous section generation

A real cutting case is used, where the same material (Al6061_Machining) is pre-machined with the following cutting values: cutting speed $V_c = 588$ [m/min], feed per tooth $V_z = 0.25$ [mm], cutting diameter $D_c = 18$ [mm] and clockwise rotation.

Next step is defining the workpiece perimeter (boundary definition vs. trajectories) in order to detect the locations where the cutting tool will start cutting, ϕ_s [°], and where it will exit the cutting ϕ_e [°] (Fig. 3).

Worth mentioning is that for the definition of the start/end points, the intersections between the workpiece boundary and the trajectory of the second tooth will be used, the reason being that this curve will be used as a base for the unwrapping process and each section of the chip will be defined based on this curve and the first. Also, this method is applicable only for the cases where the chip length is constant (stationary phase where the same chip geometry is removed by each tooth).

The final phase for the unwrapping process is the chip sectioning. The sectioning lines as a function of ϕ [°] need to be defined. The reason is that the radial origin needs to move while rotating (Fig. 3) and connect each position with the correct point of reference located on the second tooth trajectory (the one that will become the base for the unwrapping).

After the sections are defined, the last step is to intersect the new lines with the first trajectory (first tooth) and measure the distances for each pair of points. The distances $h(\phi)$ [mm] together with ϕ_s [°] and ϕ_e [°] can be used to calculate the chip length and map the thicknesses (Fig. 4 right).

An XY coordinate system can be defined in preparation for the chip deformation simulation in FEM in which the $P_s(0, 0)$ point represents the point where the cutting begins and the $P_e(x_{\max_unwrapped}, 0)$ where it ends (Fig. 4 right). Points P_s and P_e

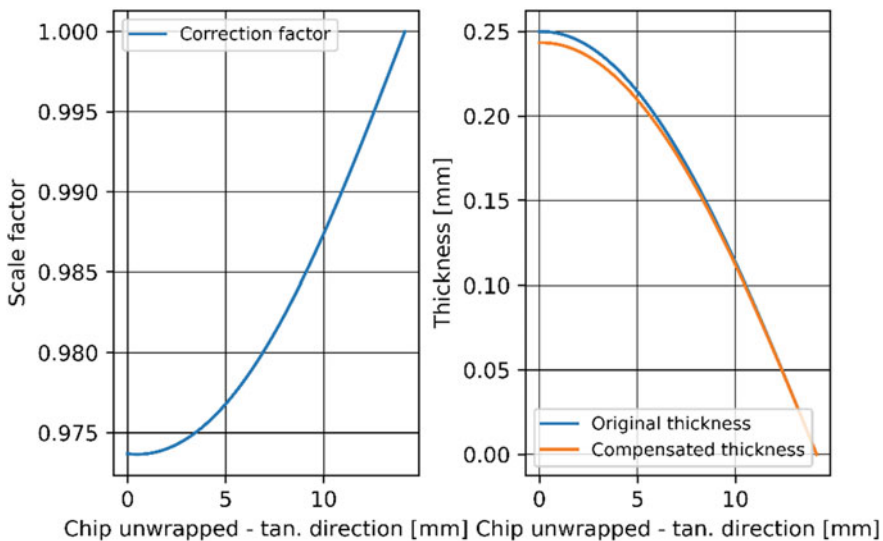


Fig. 4 Curve correction factor (left), the original and the compensated thickness (right)

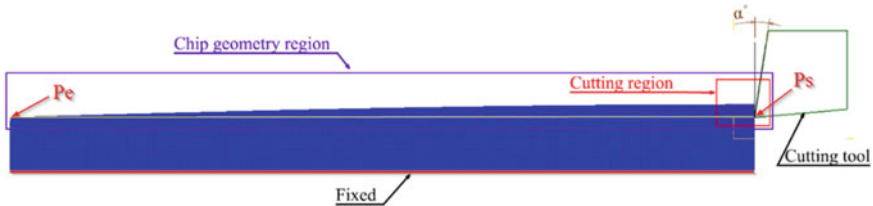


Fig. 5 Orthogonal cutting simulation for chip formation

(Fig. 5) will become the base for the reconstruction and will be remapped as a function which uses the two angles, ϕ_s [°] and ϕ_e [°].

The polar thicknesses are mapped directly on the arc length of the chip without taking into account the curvature of the base trajectory. Although this influence can be neglected (as for the analytical model) because the thickness of the chip is relatively small compared with chip length, in some particular cases where the radial immersion has the same order of magnitude as the thickness, this can become a problem in term of precision.

One solution that can help with this problem is the usage of a correction factor based on the linear velocity of the cutting tip (Fig. 4 left).

The linear velocity uses the cycloidal trajectory points and the central tool positions associated with the first points to determine the speed variation. Although this parameter is not necessarily part of the proposed cutting model, for the present case, the ratio (Fig. 4 left) between the speed of the first trajectory and the second can be used to correct the thickness values.

Running the 2D dynamic simulation for the cutting process Cutting parameters like cutting speed V_c [m/min], workpiece material, rank angle α [°], nose radius r [mm], will make sense for the simulation. Other important parameters like coefficient of friction $\mu = 0.4$ (shear-type—default value for Aluminum in Deform™) and simplification assumptions are added as well. The cutting tool is considered rigid. The second assumption is that the nose radius r will be considered 0. This is because it has a great influence on important phases of the chip formation like start/end angles ϕ_s [°], ϕ_e [°] and the chip thickness h [mm].

In this particular case, the frequency content of the process besides the deformation process is of interest. Deform™ uses triangle and quadrangle elements to mesh the 2D problems and offers a good solution to control the size of the elements by creating parametric mesh regions (Fig. 5). In the current application, there are two important areas where the mesh needs to be controlled. The first region is where the cutting-edge cuts through the material. In order to have a good simulation of this complex process, the mesh density needs to be adapted constantly and a good rule of thumb is to have the element size equal to 1/2 of the displacement step (~0.002 mm). Furthermore, this region can be attached to any geometry such that it follows the cutting tool through the complete process and maintains the mesh density and the quality of the deformation. The second region is the chip geometry. As seen in Fig. 5,

in order to correctly simulate the material cutting some thickness needs to be added. To complete the mechanical system the bottom part is fixed representing the material continuum. The last assumption used is the dry cutting condition.

There are important phases in the chip formation process that help extract the frequency component. First one (Fig. 6—top left and right) is the tool–workpiece contact. In this phase, depending on the milling type (up or down milling plus the radial immersion), the friction and the chip thickness the first force jump is induced. Another important phase is the chip separation (Fig. 6—bottom left). Depending on the material and the cutting regime, the material separation might happen discontinuously with a frequency component. The last phase to mention is when/if the deformed chip section comes back and contacts the workpiece surface again with a frequency component that might be important (Fig. 6—bottom right).

The total runtime of the simulation was 1.5 days with the results: tangential force F_t [N] and normal force F_n [N] (Fig. 7) being presented.

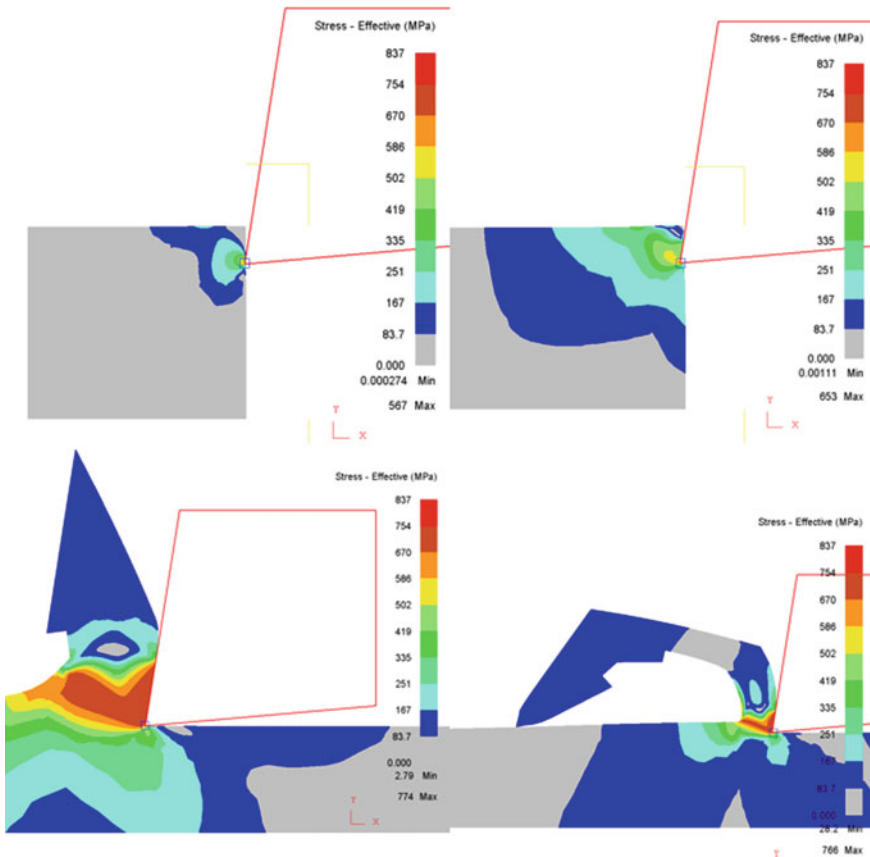


Fig. 6 Important stages in chip formation

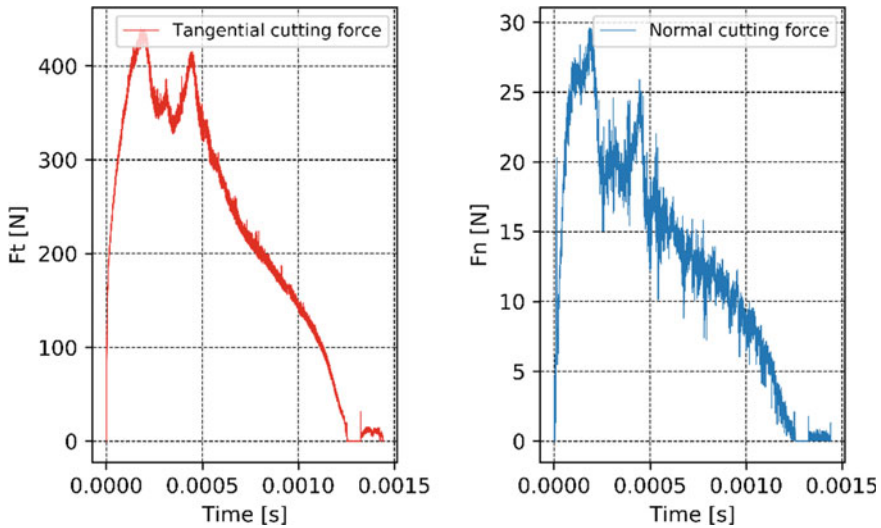


Fig. 7 Normal and tangential cutting force prediction

At this stage, the overall dynamic behavior of the cutting process can be reconstructed in order to get the three force components F_x , F_y and F_z in time-domain.

Reconstructing the overall 3D cutting behavior of the milling operation All the kinematic variables used for the chip geometry calculation are expressed as function of ϕ [°]. As already mentioned, ϕ_s [°] and ϕ_e [°] are mapped into the unwrapped geometry space as P_s and P_e thus the geometric polar connection between the XYZ frame (machine tool coordinate system) is maintained. Taken into account is also the helix angle γ [°], to extract the Z force component from F_t . The time base could be calculated from the cutting parameters, but in this paper, the computed time from the FEM simulation will be used for better precision. The obtained time signals need to be recomposed to add all the teeth into the process using the phase delay given by the total number of teeth Z. Also, the simulation time steps are interpolated in order to have a constant Δt [s] for the discrete-time Fourier Transformation (DTFT) that we will be applied. Python™ already contains DTFT libraries that are used to convert the time-domain cutting forces into frequencies-domain.

4 Results

As mentioned in Chap. 2, in order to validate the fact that this method is able to catch the dynamic behavior of the cutting process correctly, the tooth passing frequency value can be used.

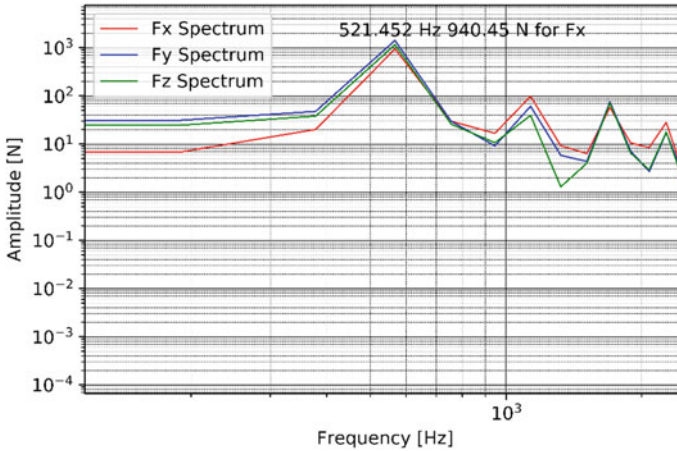


Fig. 8 Frequency components of each force

It can be calculated based on the kinematic parameters and confirm that it is part of the obtained spectrum. Having known the number of teeth $Z = 3$, and the Spindle speed $N = 10,400$ [rpm], then the first harmonic $1f_{\text{tooth}} = 520$ [Hz], and the second $2f_{\text{tooth}} = 1040$ [Hz], etc. can be calculated. The first peak (Fig. 8) is at the expected frequency of $1f_{\text{tooth}}$ confirming that at least this component is correctly modeled.

The ideal case is to have in this spectrum components that are not only caused by the tooth passing frequency. The complexity of the obtained spectrum depends on many variables like kinematic resolution, cutting case, workpiece material, cutting geometry, FEM precision, etc., incorporating many complex aspects of this problem. Unfortunately, in order to obtain realistic results, all steps involved require heavy fine-tuning but we can consider that as a proof of concept the method has real prospects.

5 Conclusions

This paper responds to the growing demand of introducing ANN technology in the manufacturing field of engineering. The scope of this paper is to present a quick and efficient method that can reduce the computational cost of sample generation especially for new material type applications [4]. For the presented example, this cost was reduced by an estimated 90% from the original 21 days of 3D simulation to 1.5 days of 2D simulation.

Starting from the kinematic parameters of the milling process (shoulder milling), the unwrapped chip geometry was generated using a program developed in PythonTM. The cutting process was simulated using DeformTM with Arbitrary Lagrangian–Eulerian (ALE) formulation. The 3D simulation computed the F_x , F_y and F_z forces directly while the 2D simulation computed the F_t and F_n from which the F_x , F_y

and F_z components were extracted. For both cases, the cutting tool was considered a rigid body and the nose radius 0.

The final part reconstructed the overall dynamic behavior of the milling process and converted the results from forces expressed in polar coordinates system into cartesian coordinate system which are usually associated with the machine tool.

Depending on the application for which it is used, the method offers the possibility of using the cutting forces or the force's spectrum directly as input. This situation can be found in a wide range of applications like deflection predictions, frequency response cases or a combination of the two having known the tool point frequency response functions (FRF).

The results are conclusive, although no emphasis has been placed on numerical validation in this paper, the proof of concept has been made and the results obtained have suggested that this method is scalable and shows realistic prospects for future research.

Acknowledgements This research was supported by Siemens Industry Software România.

References

1. C. Yue, H. Gao, X. Liu, S.Y. Liang, L. Wang, A review of chatter vibration research in milling. *Chin. J. Aeronaut.* **32**(2), 215–242 (2019). <https://doi.org/10.1016/j.cja.2018.11.007>
2. A. Wang, W. Jin, W. Chen, R. Feng, C. Xu, Bifurcation and chaotic vibration of frictional chatter in turning process. *Adv. Mech. Eng.* **10**(4), 1–8 (2018). <https://doi.org/10.1177/1687814018771262>
3. M. Kaymakci, Z.M. Kilic, Y. Altintas, Unified cutting force model for turning, boring, drilling and milling operations. *Int. J. Mach. Tools Manuf.* **54–55**, 34–45 (2012). <https://doi.org/10.1016/j.ijmachtools.2011.12.008>
4. G. Özden, F. Mata, M.Ö. Öteyaka, Artificial neural network modeling for prediction of cutting forces in turning unreinforced and reinforced polyamide. *J. Thermoplast. Compos. Mater.* (2019). <https://doi.org/10.1177/0892705719845712>
5. T.L. Schmitz, K. Scott Smith, in *Machining Dynamics*. 2nd edn. Springer, Switzerland (2019). <https://doi.org/10.1007/978-3-319-93707-6>

Improved Model of a Vibrating Sieve



Maria Dragomir, Alina Ovanisof, and Roxana Alexandra Petre

Abstract Various mechanical devices use vibrations in order to produce useful effects. Such an example can be found in vibrating sieves, used to separate certain particles out of a mix of small seeds. The particles move on the surface of the sieve under the action of the gravity, as well as of the effect induced by longitudinal vibrations. During the process, the mix stratifies, the heavy and small particles tending to accumulate in the lower layer. A simplified model of such a device was proposed and analyzed by the first author of the present paper in a previous publication. This model is now improved, by taking into account certain characteristics previously neglected. The free and the forced vibrations induced by an exciter with an eccentric rotating mass are studied. The optimal location of the exciter is determined, in order to maximize the separation, as well as to avoid secondary adverse effects. The study is illustrated by a numerical example based on the experimental device used in the previous publication. Calculated values of certain quantities are compared with those calculated on the simplified model, as well as with the measured ones. The results can be used by mechanical engineers involved in the design of vibrating sieves.

1 Introduction

The motion generated by the vibrations of a system is used, in practice, in various fields of activity, including agriculture and food industry. Among the use of such motions, as described above, are the separation and sorting of the material consisting of a mixture of seeds and impurities, as well as sorting the seeds by size, with devices equipped with sieves acted mechanically in order to induce a relative movement of the material with respect to the sieve.

Aspects regarding vibrating sieves were studied by various authors. Thus, numerical simulations of the process were presented in [1, 2]. A three degree of freedom

M. Dragomir · A. Ovanisof (✉) · R. A. Petre
University Politehnica of Bucharest, Bucharest, Romania
e-mail: alinaovanisof@yahoo.com

model was proposed in [3]. Optimization of vibrating devices has been analyzed in [4–6].

Deducing exact mathematical equations that describe this complex process is often difficult and, therefore, most of the equations proposed by researchers in the literature are based on several simplifying assumptions that make these calculations easier. These can lead to more or less relevant results, with respect to the real phenomenon.

This paper studies a system consisting of three oscillating sieves used to strain a seed mixture. A model with a finite number of degrees of freedom is considered [7–9] which improves the simplified model presented in a previous paper [10].

2 Model of the System

The model in Fig. 1 is considered, consisting of the masses m_1 , m_2 and m_3 , hinged on two vertical elastic blades, which are clamped on the base.

In order to study the vibrations transmitted to the system (Fig. 1), a perturbing force $F_p = F_o \cos \Omega t$ was introduced on the mass m_1 , by using an excitation system with eccentric mass.

The differential equations of the vibrating system in matrix form are [11]

$$[M]\{\ddot{x}\} + [C]\{\dot{x}\} + [K]\{x\} = \{F_o\} \cos \Omega t. \tag{1}$$

It is shown in the literature [11] that the stiffness matrix $[K]$ is the inverse of the matrix of the influence coefficients $[\delta]$:

$$[K] = [\delta]^{-1} \tag{2}$$

For one blade, clamped at the lower end,

Fig. 1 The system with two rigidly embedded vertical elastic lamellas

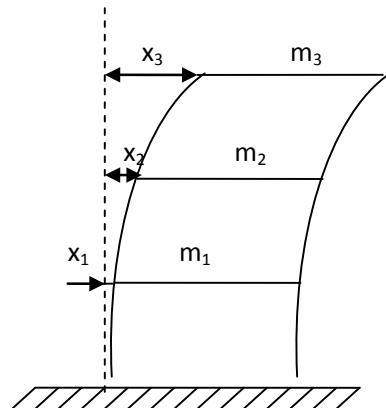
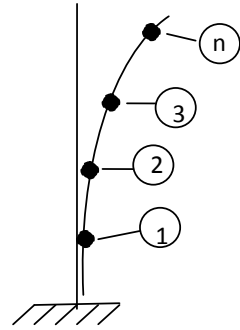


Fig. 2 The elastic bars of the system



$$\delta_{ij} = \frac{x_i^2(3x_j - x_i)}{6EI} \tag{3}$$

where δ_{ij} represents the deformation occurred in section i when a force equal to the unit is applied in section j , E denotes the Young modulus and I is the moment of inertia of the cross-section, with respect to the neutral axis, x_i is the abscissa of section i , while j is the abscissa of section j .

The elastic bars are discretized by replacing the mass m , which is uniformly distributed, with n concentrated masses equal to $\frac{m}{n}$, arranged equidistantly along the bar [7, 8] (Fig. 2).

By discretizing the bar in n elements, the mass matrix has the form:

$$[M] = \begin{bmatrix} m_{11} & \cdots & 0 \\ \vdots & \ddots & \vdots \\ 0 & \cdots & m_{nn} \end{bmatrix}, \tag{4}$$

where, for an arbitrary section

$$m_{ii} = 2\frac{m}{n}, \tag{5}$$

while for the sections where the sieves are hinged,

$$m_{ii} = 2\frac{m}{n} + m_s, \tag{6}$$

where m_s is the mass of the sieve.

For the studied system, the damping matrix has the expression:

$$[C] = \chi[K] = \chi[\delta]^{-1}, \tag{7}$$

where χ denotes a viscosity coefficient

$$\chi = \tilde{x}l^2 \sqrt{\frac{\rho A}{EI}}. \quad (8)$$

By replacing (2) and (7), the differential equations of the forced, damped vibrations become:

$$[M]\{\ddot{x}\} + \chi[\delta]^{-1}\{\dot{x}\} + [\delta]^{-1}\{x\} = \{F_o\} \cos \Omega t. \quad (9)$$

By multiplying the above equation with the matrix $[\delta]$, system (9) takes the form

$$[\delta][M]\{\ddot{x}\} + \chi\{\dot{x}\} + \{x\} = [\delta]\{F_o\} \cos \Omega t. \quad (10)$$

In order to simplify the equations, the following notations are used:

$$[\delta][M] = [D], \quad (11)$$

$$[\delta]\{F_o\} = \{f_o\}. \quad (12)$$

Thus, by replacing (12) and (11) in the system (10), the following form results:

$$[D]\{\ddot{x}\} + \chi\{\dot{x}\} + \{x\} = \{f_o\} \cos \Omega t. \quad (13)$$

The steady solution of the damped, forced vibrations is

$$\{x\} = \{A\} \cos \Omega t + \{B\} \sin \Omega t, \quad (14)$$

where the n -dimensional column matrices $\{A\}$ and $\{B\}$ can be determined by substituting (14) in (13).

By remarking that

$$\{\dot{x}\} = -\Omega\{A\} \sin \Omega t + \Omega\{B\} \cos \Omega t, \quad (15)$$

$$\{\ddot{x}\} = -\Omega^2\{A\} \cos \Omega t - \Omega^2\{B\} \sin \Omega t, \quad (16)$$

it follows successively:

$$\begin{aligned} & -\Omega^2[D]\{\{A\} \cos \Omega t + \{B\} \sin \Omega t\} \\ & + \chi\{-\Omega\{A\} \sin \Omega t + \Omega\{B\} \cos \Omega t\} \\ & + \{A\} \cos \Omega t + \{B\} \sin \Omega t = \{f_o\} \cos \Omega t, \end{aligned} \quad (17)$$

$$\begin{cases} -\Omega^2[D]\{A\} + \mu\Omega\{B\} + \{A\} = \{f_o\} \\ -\Omega^2[D]\{B\} - \mu\Omega\{A\} + \{B\} = \{0\} \end{cases}, \quad (18)$$

$$\begin{cases} [I] - \Omega^2[D]\{A\} + \mu\Omega[I]\{B\} = \{f_0\} \\ -\mu\Omega[I]\{A\} + [I] - \Omega^2[D]\{B\} = \{0\} \end{cases}, \tag{19}$$

$$\begin{bmatrix} [I] - \Omega^2[D] & \mu\Omega[I] \\ -\mu\Omega[I] & [I] - \Omega^2[D] \end{bmatrix} \begin{Bmatrix} \{A\} \\ \{B\} \end{Bmatrix} = \begin{Bmatrix} \{f_0\} \\ \{0\} \end{Bmatrix}. \tag{20}$$

By solving the above algebraic system, vectors $\{A\}$, $\{B\}$ are obtained.

3 Numerical Analysis

For the numerical application, the following values were considered: the mass of the sieve $m_s = 3902$ kg, the mass of the sieve with exciter 5105 kg, the length of the blades 45 cm long, Young’s modulus $E = 2.1 \cdot 10^{11}$ N/m² and the moment of inertia of the cross-section $I = 2 \cdot I_0 = 2 \cdot \frac{b \cdot h^3}{12}$ where $b = 60$ mm and $h = 2$ mm.

Two values were considered for the damping: $\tilde{x} = 0.01$ and $\tilde{x} = 0.02$, and three positions for the exciter: 1 on the lower sieve, 2 on the middle sieve and 3 on the top sieve.

The circular eigenfrequencies obtained for the system are presented in Table 1.

The resulting deformation functions are represented in Figs. 3, 4 and 5.

Table 1 The values obtained for each study case

Study case	ω [rad/s]
position 1 of the exciter	10.313
	64.306
	167.526
	2913.716
position 2 of the exciter	10.019
	63.661
	174.808
	2909.629
position 3 of the exciter	9.320
	65.782
	180.807
	2913.217

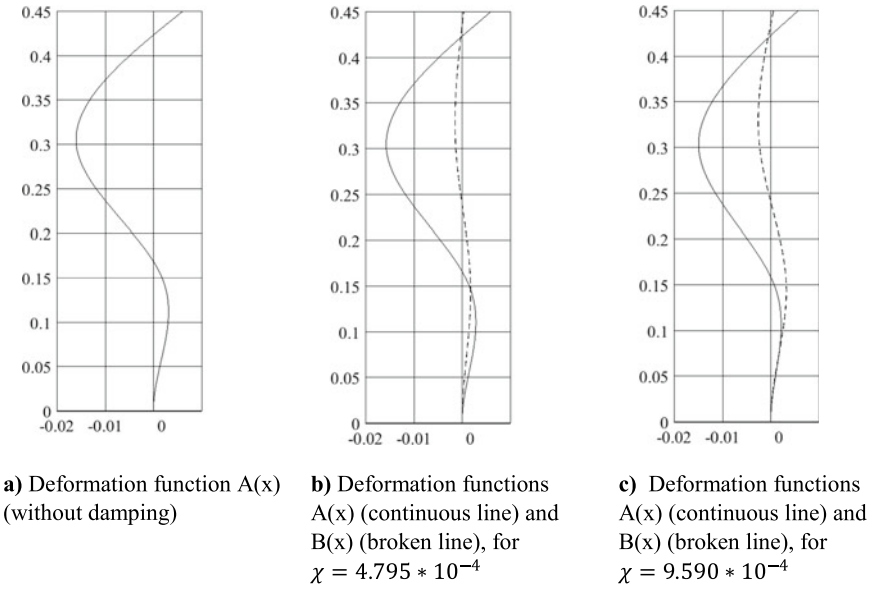


Fig. 3 Deformation functions for position 1 of the exciter

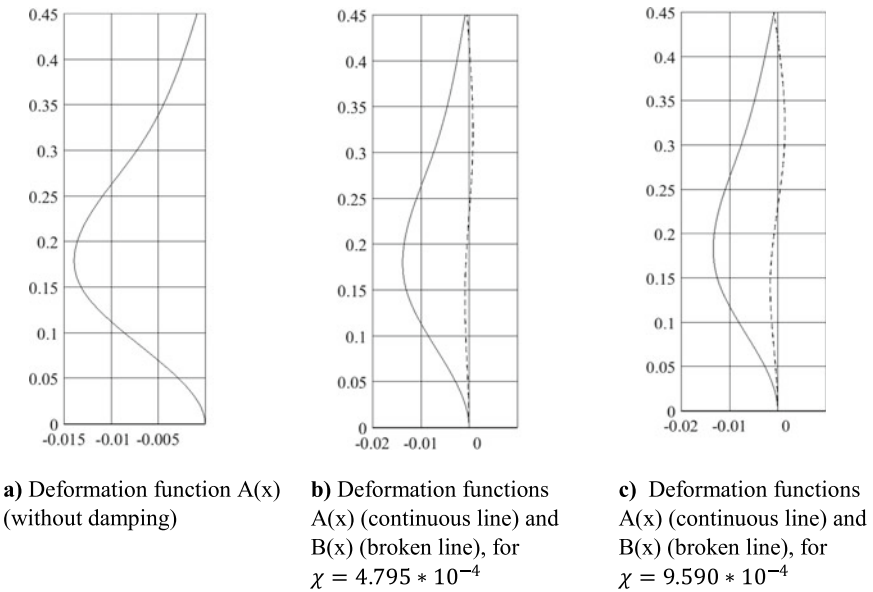
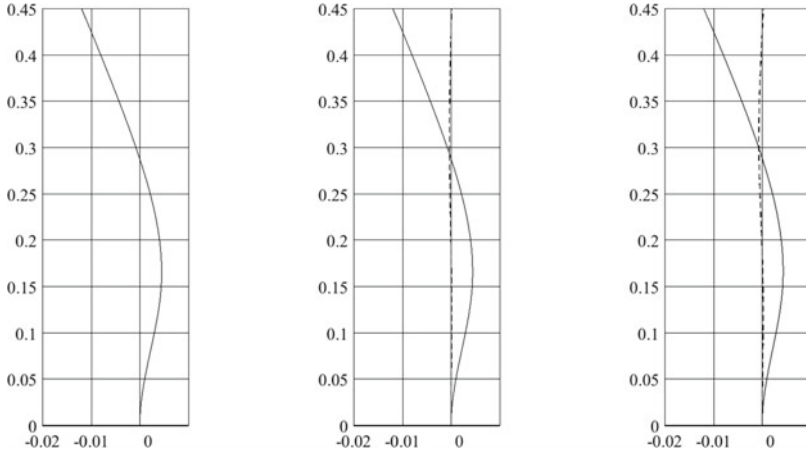


Fig. 4 Deformation functions for position 2 of the exciter



a) Deformation function $A(x)$ (without damping) **b)** Deformation functions $A(x)$ (continuous line) and $B(x)$ (broken line), for $\chi = 4.795 \cdot 10^{-4}$ **c)** Deformation functions $A(x)$ (continuous line) and $B(x)$ (broken line), for $\chi = 9.590 \cdot 10^{-4}$

Fig. 5 Deformation functions for position 3 of the exciter

4 Conclusions

The study leads to the following conclusions:

- (1) the first three circular eigenfrequencies are close to the corresponding ones obtained for a model with three degrees of freedom [10];
- (2) the higher order circular eigenfrequencies are greater with one magnitude order, compared to the first three ones;
- (3) for the considered values, the forced vibrations the sieves have amplitudes of the order of one centimeter, which ensures an efficient straining of the seed mixture;
- (4) for the first position of the excitator, the maximum amplitude is 16 mm for sieve 2, for the second position the maximum amplitude is 14 mm on sieve 3 and for the third position the amplitude is 12 mm on sieve 1;
- (5) since the coarse mixture is on the top sieve, (sieve number 3), it is convenient to maximize the amplitude on this sieve, therefore the optimal configuration is the one with the exciter on the top sieve.

References

1. G.W. Delaney, P.W. Cleary, M. Hilden, R.D. Morrison, Testing the validity of the spherical DEM model in simulating real granular screening processes. *Chem. Eng. Sci.* **68**(1), 215–226 (2012)
2. H.C. Li, Y.M. Li, Z. Tang, Numerical simulation and analysis of vibration screening based on EDEM. *Trans. Chin. Soc. Agric. Eng.* **27**(5), 117–121 (2011)
3. S. Danuta, Analysis of vibrations of three degree of freedom, dynamical systems with SMA spring. In: 9th Brazilian Conference on Dynamics, Control and their Applications, June 7–10 (2010)
4. V. Grozubinsky, E. Sultanovitch, I.J. Lin, Efficiency of solid particle screening as a function of screen slot size, particle size, and duration of screening. *Int. J. Miner. Process.* **52**(4), 261–272 (1998)
5. Y.H. Chen, X. Tong, Modeling screening efficiency with vibrational parameters based on DEM 3D simulation. *Min. Sci. Technol.* **20**(4), 615–620 (2010)
6. E. Jiaqiang, C. Qian, T. Liu, G. Liu, Research on the vibration characteristics of the new type of passive super static vibratory platform based on the multiobjective parameter optimization. *Adv. Mech. Eng.* **2014**, 1–8 (2014). Article ID 569289
7. N. Orășanu, A. Craifaleanu, Theoretical and experimental analysis of the vibrations of an elastic beam with four concentrated masses. In: Proceedings of the Annual Symposium of the Institute of Solid Mechanics (SISOM 2011, Bucharest, 2011) pp. 471–480
8. N. Orășanu, A. Craifaleanu, Experimental study of the forced vibrations of a system with distributed mass and four concentrated masses, in Proceedings of the Annual Symposium of the Institute of Solid Mechanics (SISOM 2012, Bucharest 2012), pp. 200–205
9. A. Ovanisof, O. Vasile, M. Dragomir, Analysis of human whole body vibration exposure on a U650 tractor, in ATAE (2018). ISSN: 1848-4425
10. M. Dragomir, V. Ovidiu, Theoretical and experimental analysis for determining the eigen-frequencies of mechanical system with three masses. *Sci. Bull. UPB* **77**(4) (2015). ISSN: 1454-2358
11. L. Meirovitch, in *Fundamentals of Vibrations* (McGraw-Hill, New York, 2001)

Vibration Analysis of High-Pressure Pneumatic Compressor



Ramona Nagy, Remus Stefan Maruta, and Karoly Menyhardt

Abstract Pressure generators are machines used to compress atmospheric air to the desired ratio suitable for various applications. Seldom these pressure values rise above 12–16 bars, but in such cases, special devices must be used, with single or dual-stage compressor chambers. A high-pressure pneumatic compressor (over 60 bar) was commissioned to fill rubber hoses for various mechanical tests. Due to the design of the compressor, a series of unwanted vibrations occurred from the compression room, actuator, transmission, and forced cooling system. The analysis and correlation of these vibrations are presented in the following paper.

1 Introduction

Pneumatic compressors are readily available devices that can pump air at 8–10 bars. Above these values, commercial offers have a steep drop. Most compressors have a single-stage compressor chamber to create the required pressure but, for higher values, a second stage compression chamber is required. Compressors can have multiple number of stages, delivering a maximum pressure proportional with this number [1]. Normally, maximum compression ratio of 5 is realized in single-stage compressors for pressures bellow 5 bar. For compression ratio of more than 5, multistage compressors are used.

In the case of compressors, vibrations are undesirable, wasting energy, destroying equipment, and creating unwanted sound. Such vibrations are caused by imbalances in the rotating parts, friction, meshing of gear teeth, or resonance. Forced vibration

R. Nagy · R. S. Maruta · K. Menyhardt (✉)
Politehnica University Timisoara, Timisoara, Romania
e-mail: karoly.menyhardt@upt.ro

R. Nagy
e-mail: ramona.nagy@upt.ro

R. S. Maruta
e-mail: remus.maruta@upt.ro

due to time-varying disturbances (load, material stiffness, or damping) are applied to an entire mechanical system and can be used to determine overall health of the equipment.

The frequency of the steady-state vibration response resulting from the application of a periodic, harmonic input should be equal to the frequency of the applied force or motion, with the response magnitude being dependent on the actual mechanical system.

Vibration analysis applied in an industrial or maintenance environment aims to reduce maintenance costs and equipment downtime by detecting equipment faults and can be used as predictive maintenance [2].

In this paper, we present the vibration response of custom made high-pressure compressor under various pressure loads (10, 20, 30, 40 bar) with 1 or 2 charging stages and the necessary time needed to attain the desired pressure.

2 Background

In the context of a multidimensional material testing of mechanical properties (force, displacement, pressure, temperature), a high-pressure pneumatic source was required to operate and supply compressed air in sufficient quantity and pressure to suit the capacity of the tested elastic materials. The operational reliability and service life of the pneumatic system depend to a large extent on the preparation of the compressed air, but also on the vibrations that occur internally, due to loose connection and elastic elements and cooling [3, 4]. Switching the compressors on and off, pressure fluctuations occur which have an unfavorable effect on the functioning of the system.

In order to obtain a pressure of above 40 bar, a cylindrical compressor has been developed and built (Fig. 1). Its principle of operation is based on a positive displacement compressor, mainly the compression is realized by displacement of a solid boundary and preventing fluid by solid boundary from flowing back in the direction of pressure gradient. It employs a piston-cylinder arrangement where displacement of

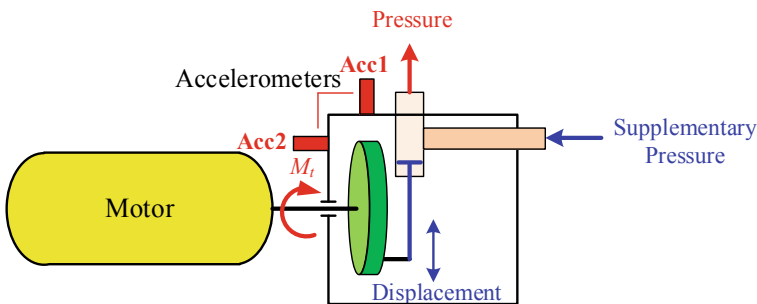


Fig. 1 Compressor schematics as single or dual-stage (added supplementary pressure)

piston in cylinder causes rise in pressure and temperature. Reciprocating compressors are capable of giving large pressure ratios but the mass handling capacity is limited or small, often ending in destroying an undersized actuator or transmission.

During the development of our high-pressure compressor, a number of failures occurred: some due to undersized actuators, some to poorly treated transmission systems. Overcoming these, there was still the problem of destruction of parts inside the compressor case: piston-cylinder assembly and piping. Throughout the life of the compressor, these elements are subjected to fatigue at a high ratio, thus prompting us to perform overall vibration analysis.

For the analysis of the compressor, it was tested at pressures of 10 through 40 bar, both in single-stage mode and overcharged (two stages) from an external compressor at 2 bar. This relatively safe value of 2 bar was set in order to limit the intake pressure inside the primary compressors housing which acted as a buffer chamber and was used as a multiplier for the system produced pressure.

3 Data Acquisition

The acquisition system used was a Bruel & Kjaer PULSE Machine Diagnostics Toolbox Type 9727 and the two accelerometers were Type 4513. These have a wide frequency range, low noise-to-signal ratio, and sensitivity from 1 to 50 mV/m/s². The Type 4513 accelerometer is a piezoelectric Shear accelerometer with integral electronics. The transducers have a high resolution, giving an excellent signal-to-noise ratio.

Accelerometer Acc1 was magnetically positioned with its axis perpendicular to the actuator, while accelerometer Acc2 had its axis parallel with the actuator (Fig. 2).

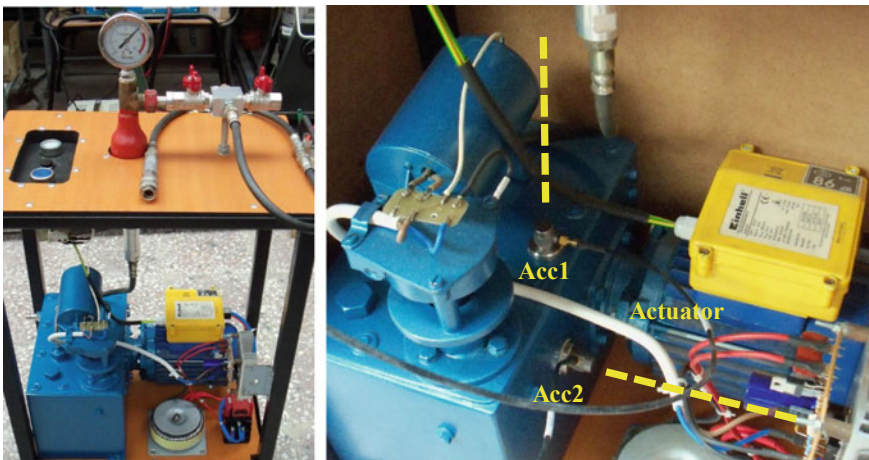


Fig. 2 Accelerometer setup on the high-pressure compressor

Data collected from accelerometers were done at 10, 20, 30, and 40 bar using single-stage compression and dual-stage compression. Because the actuator was an electric motor of 3000 rpm 0.6 kW, the recorded interval was of 250 ms considering the repetitive nature of the electric motor. The sampling frequency of the acquisition system was set to 4096 Hz for an in-depth analysis [5].

The compressor was fixed to a rigid chassis without rubber dampers, and measurements were repeated 3 times in order to validate the repeatability of the measured data, through ulterior comparison of the average root mean square acceleration (a_{rms}). Due to the direct nature of the measurement system, the error from the human factor was excluded.

4 Vibration Analysis

The measured accelerations were imported into Octave and their Fast Fourier Transform (FFT) was computed for each direction (Figs. 3, 4, 5, 6, 7, 8, 9, and 10) at various loading conditions.

Although the system has an electric motor as an actuator, having a cyclical nature, due to the eccentricities and plays, fluid pressure variation, and flow in the internal assemblies, the vibration response is pseudo-periodical. Thus, an Acceleration Spectral Density (ASD) evaluation was considered to correlate the measurements.

In order to calculate the root mean acceleration [6], it was necessary to first determine the acceleration spectral density (ASD) as a function of frequency and then calculate the area under each segment of the pseudo-periodical vibration.

$$a_{rms} = \sqrt{10 \log(2) \frac{ASD_H}{10 \log(2) + m} \left[F_H - F_L \left(\frac{F_L}{F_H} \right)^{m/10 \log(2)} \right]} \tag{1}$$

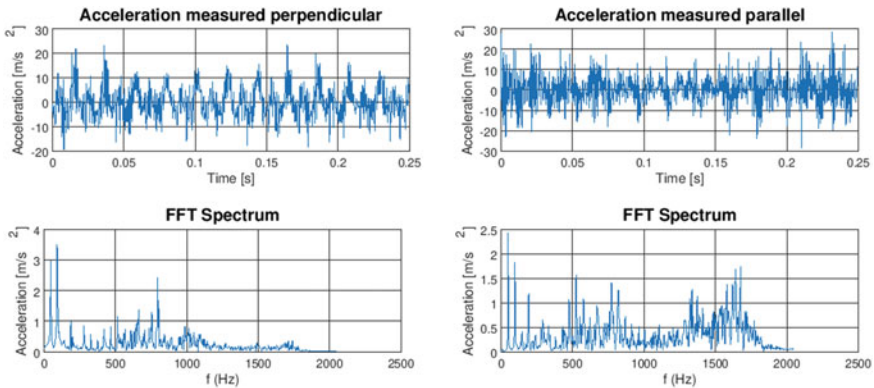


Fig. 3 Acceleration and FFT using one-stage compression at 10 bar

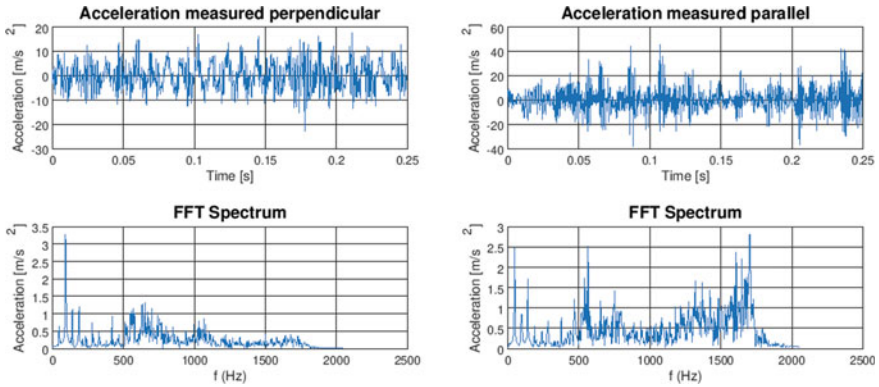


Fig. 4 Acceleration and FFT using two-stage compression at 10 bar

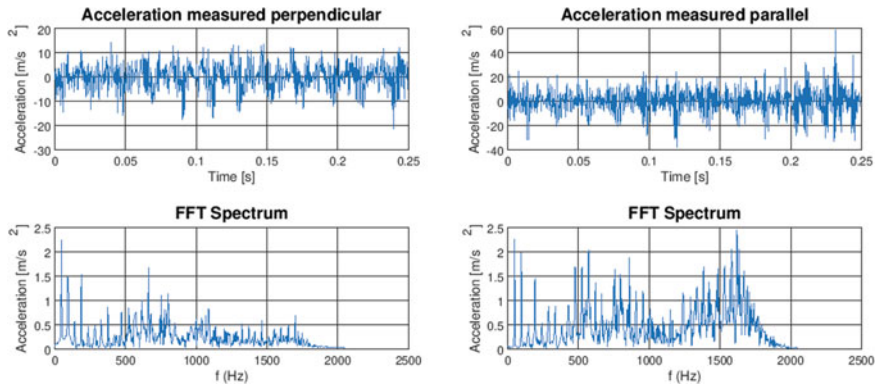


Fig. 5 Acceleration and FFT using one-stage compression at 20 bar

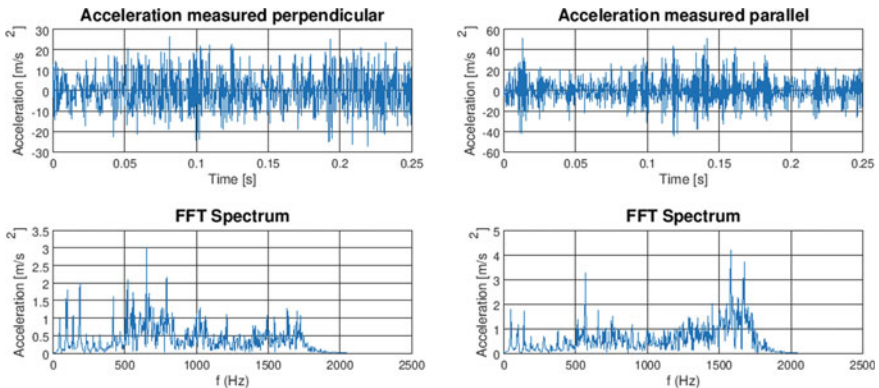


Fig. 6 Acceleration and FFT using two-stage compression at 20 bar

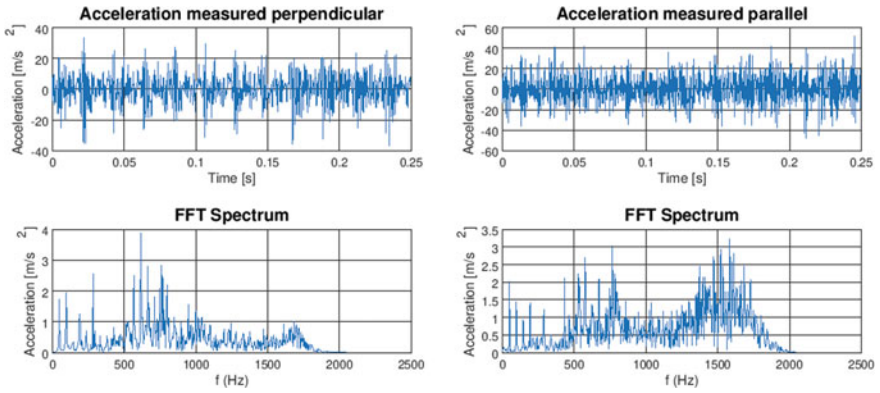


Fig. 7 Acceleration and FFT using one-stage compression at 30 bar

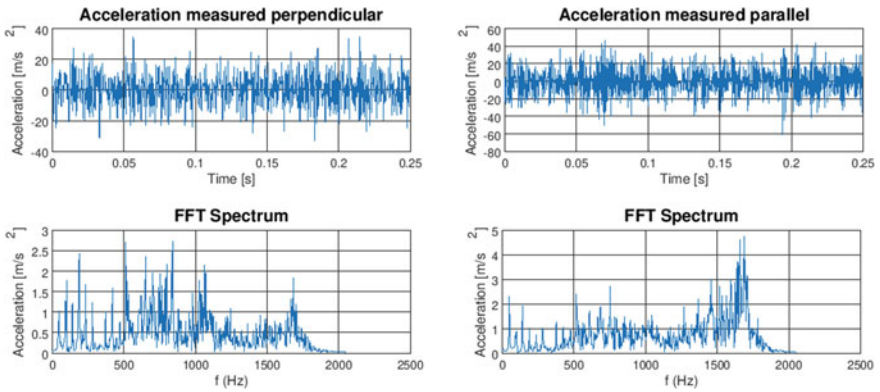


Fig. 8 Acceleration and FFT using two-stage compression at 30 bar

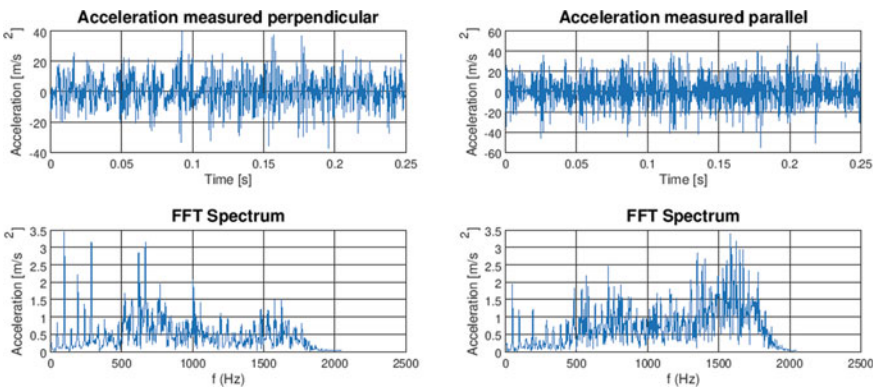


Fig. 9 Acceleration and FFT using one-stage compression at 40 bar

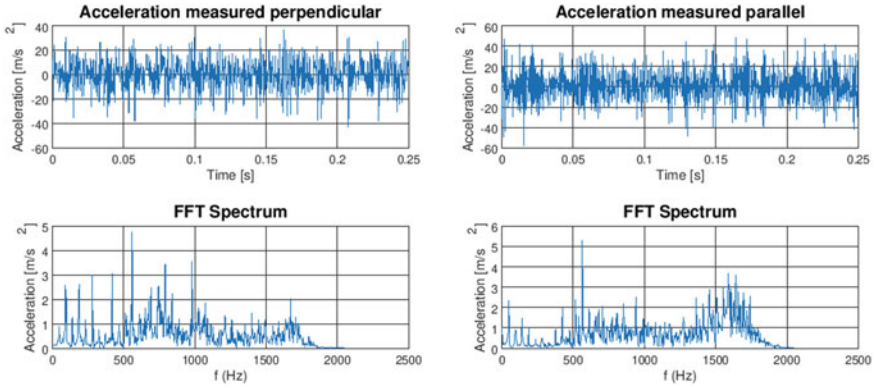


Fig. 10 Acceleration and FFT using two-stage compression at 40 bar

where

- ASD_H is the highest value on the ASD (frequency) chart for each frequency segment
- m is the slope

$$m = \frac{10 \log\left(\frac{ASD_H}{ASD_L}\right)}{\frac{\log\left(\frac{F_H}{F_L}\right)}{\log(2)}} \tag{2}$$

- ASD_L is the lowest value on the ASD(frequency) chart for each frequency segment
- F_H highest frequency for each considered segment
- F_L lowest frequency for each considered segment

Having a random vibrations the ASD calculus was done numerically in GNU Octave computing environment. Previously gathered data (Fig. 11) was dumped into a custom parser to calculate the acceleration spectral density and evaluate the a_{rms} accelerations, taking into account the obtained pressure and number of compression stages used.

Measurements performed with accelerometer Acc1 (Fig. 1) were reading values on an axis perpendicular to the actuators shaft being parallel with the compressor cylinder. Measurements made with accelerometer Acc2 were reading values on an axis parallel with the actuators shaft being perpendicular to the compressor cylinder (Table 1).

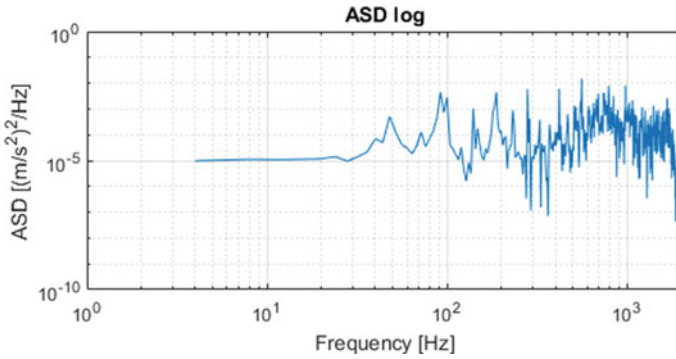


Fig. 11 Example ASD chart for two-stage compression at 40 bar

Table 1 Average of three measured root mean squared accelerations

Accelerometer	Stages	a_{rms} [m/s ²] at 10 bar	a_{rms} [m/s ²] at 20 bar	a_{rms} [m/s ²] at 30 bar	a_{rms} [m/s ²] at 40 bar
Acc1	1	6.4	5.3	9.7	10.5
	2	5.7	8.6	10.3	12.2
Acc2	1	7.4	9.9	14.9	15.1
	2	10.0	12.6	15.8	15.7

5 Conclusions

Using a single-stage compression chamber the equipment is able to easily reach a pressure of 40 bar although throughout the literature this is recommended for pressures below 10 bar.

As expected, the amplitude of the vibration increases with generated pressure. From the measurement data it was possible to observe that vibrations are greater in the case of two-stage compression, even though the first stage was exterior to the compressor and was not inducing direct mechanical vibrations or pulsing pressure.

Using two-stage compression will produce the same desired pressure (0–40 bar) in a smaller amount of time as in the case of one-stage, but at a higher cost in vibrations and wear (Table 2).

The FFT charts show that the major amplitudes are not necessarily due to actuator rotation with a frequency of 50 Hz, but rather to plays, eccentricities, and fluid flow.

Table 2 Time needed to reach nominal pressure

Pressure	10 bar	20 bar	30 bar	40 bar
1 stage	11 s	25 s	46 s	104 s
2 stage	4 s	8 s	12 s	17 s

The discrete gathered data show the current level of vibrations as a function of component wear and cannot predict the life of the equipment under normal load conditions. Considering this, continuous measurement or at well-defined time intervals can lead to an evaluation of the overall health of the compressor, thus avoiding major failures during prolong functioning as in the case of particular fatigue tests.

References

1. NPTEL homepage. <https://nptel.ac.in/courses/112106175/Module%204/Lecture%2034.pdf>. Last accessed 2019/05/12
2. M. Ahmed, F. Gu, A.D. Ball, Fault detection and diagnosis using principal component analysis of vibration data from a reciprocating compressor, in 18th International Conference on Automation and Computing (ICAC), (IEEE Cardiff UK, 2012), pp. 461–466
3. W. Soedel, in *Sound and Vibration of Positive Displacement Compressors* (CRC Press, Boca Raton 2006)
4. K. Imaichi, M. Fukushima, S. Muramitsu, N. Ishii, Vibration analysis of rotary compressors, in International Compressor Engineering Conference, paper 407 (1982)
5. M. Toth-Tascau, D.I. Stoia, F. Balanean, Influence of the sampling rate on the measurement of the upper limb movement, in Proceeding of the 14th Symposium on Experimental Stress Analysis and Material Testing, pp. 163–166 (2014)
6. FEMCI <https://femci.gsfc.nasa.gov/random/randomgrms.html>. Last accessed 2019/04/18

Structural Vibration

Vibroacoustic Diagnostics Based on the Experimental and Numerical Approach



Roman Zajac , Václav Otipka , Aleš Prokop , and Kamil Řehák 

Abstract During the last decade, many developers in the engineering industry are focusing on diagnostics and effective eliminating of the vibration and noise. The vibration and acoustic emissions are directly related to each other. Based on this fact, it is important to take into consideration the original vibration sources (engine, gearbox), but also the radiated noise to the environment. Current time brings unprecedented possibilities in the field of laboratory measurements and computational simulations in terms of hardware and software. In the issue of vibroacoustic diagnostics, the combination of these two approaches is very often required. In the first phase, the modal properties of the structure are usually examined, and the material properties are defined according to the mutual validation from both approaches. Subsequently, the amplitudes in structural (normal acceleration of the surface) and acoustic domain (sound power level—SWL, sound pressure level—SPL) are monitored during the operating conditions. In laboratory conditions, the structure is often excited by a mode exciter. In this case, the maximum amplitudes at the specific locations are primarily recorded on the structure. This article systematically describes the vibroacoustic diagnostics of the rectangular plate. Two approaches are explained in the paper: experimental and computational—based on the finite element method (FEM). In the text below, the individual procedures of the two methodologies are described. The obtained results from modal and harmonic response analyses are validated and compared with each other.

R. Zajac (✉) · V. Otipka · A. Prokop · K. Řehák
Faculty of Mechanical Engineering, Brno University of Technology, Technická 2896/2, 61669
Brno, Czech Republic
e-mail: Roman.Zajac@vutbr.cz

© Springer Nature Switzerland AG 2021
N. Herisanu and V. Marinca (eds.), *Acoustics and Vibration of Mechanical Structures—AVMS 2019*, Springer Proceedings in Physics 251,
https://doi.org/10.1007/978-3-030-54136-1_42

1 Introduction

The vibration sensing is a current trend in every industry. Primarily, the modal properties and the acceleration amplitudes at structurally critical places are examined on the vibrating structure. However, the issues of vibration and noise are mutually connected, the sound power levels and sound pressure levels of the oscillating structure are often evaluated at the final stage [1].

In this paper, a comprehensive vibroacoustic diagnosis is briefly described. This is from the perspective of using computer simulations as well as compiling technical measurements.

2 Technical Measurement

As outlined above, a technical experiment was applied on the simple rectangular plate made of gray cast iron. The vibration testing was divided into two main parts: modal and harmonic analysis.

Individual measurements were preceded by validation of main dimensions, weighting, and pre-preparation of the structure, calibration of the used sensors (acceleration sensors, microphones, etc.).

2.1 *Geometrical and Mechanical Characteristics of the Rectangular Plate*

The basic dimensions of the plate were further considered in the calculation models: the geometry dimensions were measured very precisely to increase the accuracy of numerical simulation, length approx. $a = 200$ mm; width $b = 160$ mm and thickness $t = 9$ mm. The density of the plate was determined from the real weight of the shell.

As mentioned above, the material of the rectangular plate was gray cast iron. These material properties were taken into consideration in the computational model: density $\rho = 6880$ kg m⁻³, Young's modulus $E = 169$ GPa and Poisson's ratio $\nu = 0.285$.

2.2 *Modal Analysis Measurement Process*

Free support was applied as the constraint boundary condition—structure was placed on the low—rigidity foam.

Pulse excitation by a modal hammer was performed—applying a shock pulse at marked points on the structure (see Fig. 1). The response scanning was mediated

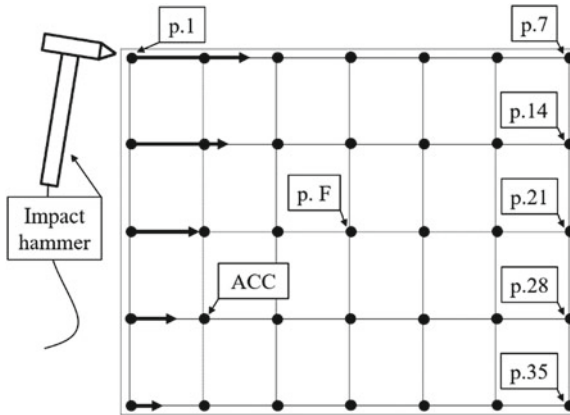


Fig. 1 Points grid

through a uniaxial acceleration sensor, which was stuck to the structure (see the position ACC in Fig. 1).

At the analyzer, two active channels were used. In the first channel, the impact hammer was applied and on the second channel, the ACC sensor was involved. The recording of the transfer functions at marked points and subsequent evaluation of modal properties were followed.

2.3 Harmonic Analysis Measurement Process

Measurement was performed in a fully anechoic chamber—examination of the acoustic features. The whole measuring stand is shown schematically in Fig. 2 with positions of important parts of the measuring chain according to [2, 3].

The structure was hung by silk lines (position e.5)—free boundary condition assumption.

The structure excitation via a modal vibration exciter (e.1)—the exciter was firmly attached to the lodge. The modal exciter was wrapped with a special sound-absorbing material (e.2). The transmission of the excitation signal to the structure was performed via the excitation rod (e.3). It was structurally connected through a force transducer (e.4) that was glued to the structure. A harmonic signal of the specified amplitude and frequency was transmitted to the structure.

There were considered two types of response sensors. In terms of the structural domain, the normal surface accelerations were recorded by a laser vibrometer (e.6). From the acoustic point of view, two condenser microphones (e.7) were used, placed 500 mm away from the vibrating structure in a defined position.

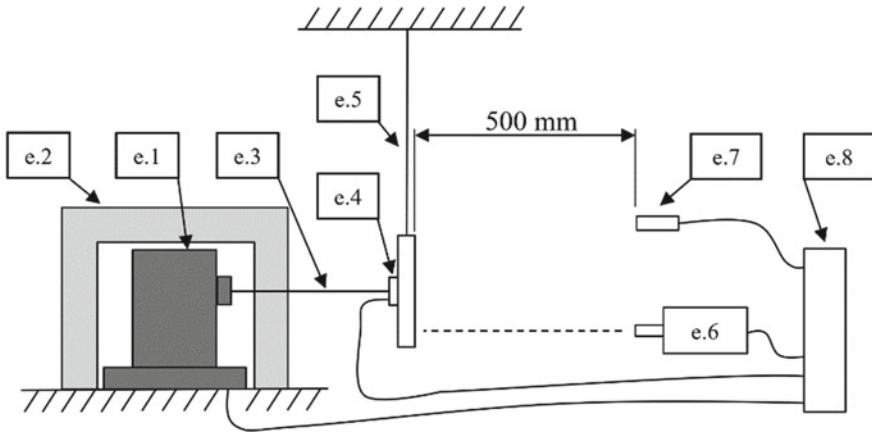


Fig. 2 Measurement set up

In this technical measurement, five channels were on: force sensor, excitation signal, two microphones, and laser vibrometer. In Fig. 2 is shown the position (e.8)—the analyzer, it is one of the most important parts of the measuring chain. Generally, the analyzer communicates between the hardware and the software part of the measuring apparatus. It mediates the measured signals and delivers them in digital form to the evaluation software.

BK CONNECT software from Brüel & Kjaer mediated the whole measurement, recording, and post-processing of the data.

3 Computational Approach

In parallel with the experiment, a computational model was created in FEM-based software. In the software environment, a CAD model with validated dimensions was initially created. In the calculations, the material properties of the given structure were considered, which were partially modified in the initial phase by comparing the modal shapes from the measurement, measuring of dimensions, and mass. Further, the computational modal analysis was followed by a harmonic analysis in the structural and acoustic domains. The numerical models were created based on boundary conditions considered from a technical experiment [4].

3.1 Harmonic Response in Structural Domain

At the very beginning, the modal and harmonic analysis was interconnected in the computational model. A modal superposition method could be used during the solution process.

The finite element model was created by using the solid186 and solid187 elements. Based on the sensitivity analysis, two elements were considered through the thickness of the plate. The final discretized geometry model contained approx. 3200 elements in the structural analysis.

The structure in the analyses was not bound by any constraints—free boundary condition. The force load was applied—the force by which the structure was excited was used from the laboratory testing. See position p . F in Fig. 1, where the force transducer was placed in technical measurement and in parallel the location where the force was applied in the numerical model. The damping parameter was also applied from the modal experimental analysis. The damping ratio was included in the computational model.

Evaluation of the normal acceleration in points based on a technical experiment was given.

3.2 Harmonic Response in Acoustic Domain

The structure-acoustic analysis linking approach was chosen when creating the acoustic model. Creating a 3D model—the rectangular plate model has been cut into the sphere volume that formed the acoustic space. Furthermore, only the acoustic space was used in whole analysis. Creation of FE mesh—in the model discretization, the minimum element size L_{\min} [mm] was chosen in acoustic model according to (1) from [5]:

$$L_{\min} = \lambda/5 = c/(5 * f_{\max}), \quad (1)$$

where λ [m] is wavelength,

c [m/s] is the speed of sound,

f_{\max} [Hz] is considered frequency maximum in analysis.

In the acoustic analysis, the fluid220 and the fluid221 elements were used, which are a high order 3-D solid elements that exhibit quadratic pressure behavior. The final discretized model contained approx. 93,500 elements in the acoustic analysis.

Boundary conditions—in Fig. 3 are shown the boundary conditions used in the acoustic numerical model. On the left side of the picture, the import of surface normal velocities from structural harmonic analysis is depicted. In the middle part of the model, a specific envelope was applied. From this surface area, the acoustic features outside of the FEM model were approximated. An important boundary condition of the “Infinite elements” was applied to the outside surface of the acoustic space. In

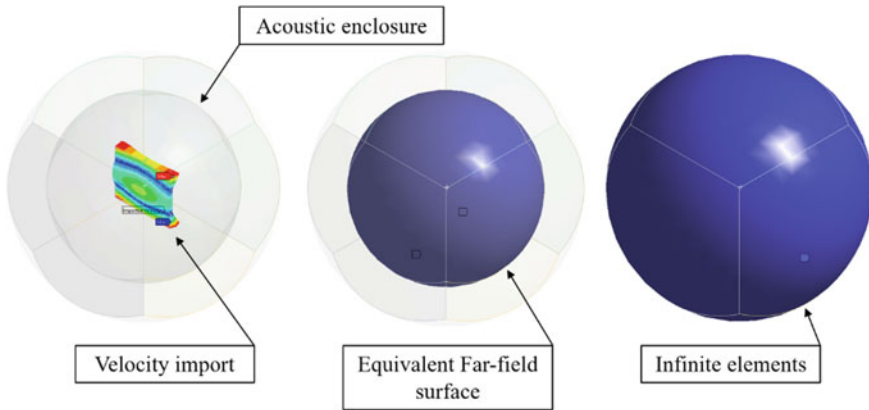


Fig. 3 The acoustic computational model

this way, free propagation of acoustic waves into space was ensured—simulation of fully anechoic chamber.

The microphones were placed according to the experimental measurement.

4 Evaluation of the Results

Through both approaches: by technical experiment and numerical model, it is possible to compare and validate results among themselves.

By the modal analysis, the eigenmodes of the structure were defined. This means its eigenfrequencies, eigen shapes, and modal damping (from lab measurement). In Table 1, two eigen shapes are compared. According to the pictures, it is possible to define and assign a custom shape from experiment and numerical calculation based on color scaling. The percentage difference in own frequencies did not exceed half a percent, which can be considered as very accurate compatibility.

After the evaluation of modal properties, the harmonic analysis was performed. At specified points on the vibrating structure, normal acceleration values were recorded and evaluated. In Table 2, the acceleration amplitudes are compared. From the acoustic point of view, the sound pressure levels (SPL's) were recorded by two microphones in a technical measurement. These values were subsequently validated by a computational model. A comparison of SPL's values is shown in Fig. 4. On the radar chart, the different curves of SPL's are shown around the structure. From the FEM model is possible to compare sound pressure in planes to see the maximum values depending on the eigen shape. In Table 3, the acoustic pressure in two different planes is compared.

Table 1 Eigen frequencies

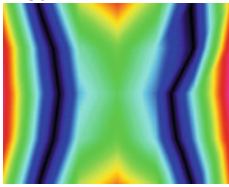
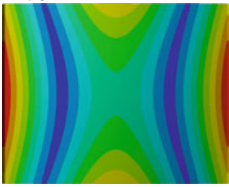
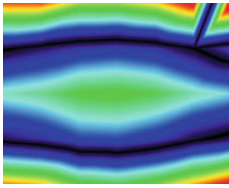
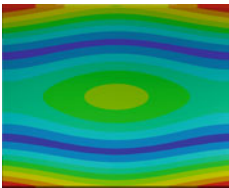
Mode	Experiment	Ansys	Difference
2	1180 Hz 	1178 Hz 	-0,17%
3	1926 Hz 	1920 Hz 	-0,31%

Table 2 Frequency response in the structural domain at selected points for 2nd and 3rd mode shape

Frequency response [$m\ s^{-2}$]													
1178	Point	p1	p2	p3	p4	p8	p9	p10	p11	p15	p16	p17	p18
	Exp	26.3	0.6	21.8	29	33.1	8.48	12.9	20.4	36.6	11.8	9.16	17.1
	FEM	29.6	0.2	23.6	32.6	37.5	8.5	13.9	22.5	40.8	11.8	10.5	18.9
	Diff (%)	12.6	-63.5	8.2	12.5	13.4	0.0	8.1	10.2	11.4	-0.1	14.2	10.7
1920	Point	p1	p2	p3	p4	p8	p9	p10	p11	p15	p16	p17	p18
	Exp	38.5	31.2	25	22.3	0.285	2.21	6.79	9.09	16.4	18.8	23.2	25.7
	FEM	37.9	32.7	27.1	27.1	1.4	3.0	7.6	9.8	16.8	19.1	23.4	25.4
	Diff (%)	-1.7	4.7	8.5	21.6	390.5	35.7	12.3	7.3	2.7	1.6	0.9	-1.0

5 Conclusion

The vibroacoustic properties of the simple structure were analyzed by technical measurement and numerical simulation. Modal properties were evaluated in the first phase. Based on the comparison of results from two approaches, the material model was partially modified. In the subsequent phases, the frequency responses of the structure in the structural and acoustic domains were evaluated in precisely specified locations. The results from numerical simulations were mainly influenced by load condition and damping factor, which was obtained from modal measurement. The differences between technical measurement and FEM model were compared in percent in this paper. Based on the results the numerical method can be used to

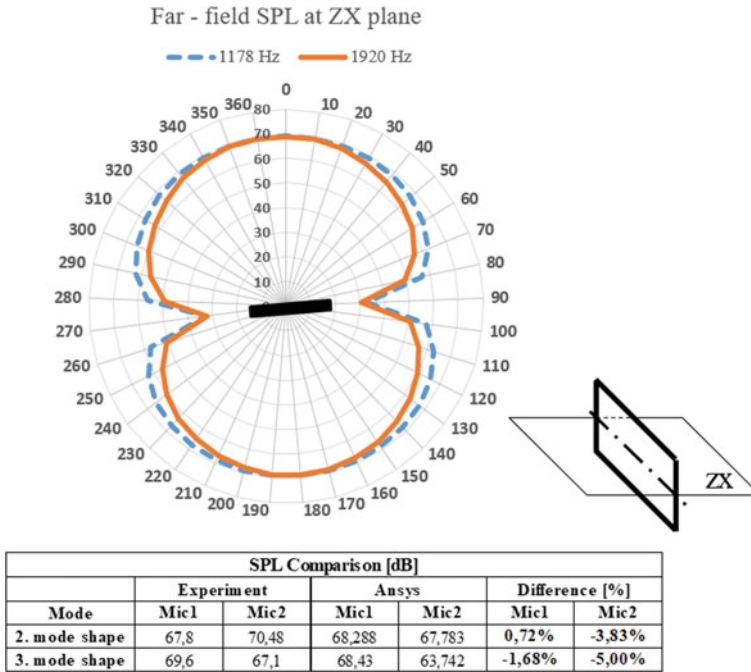
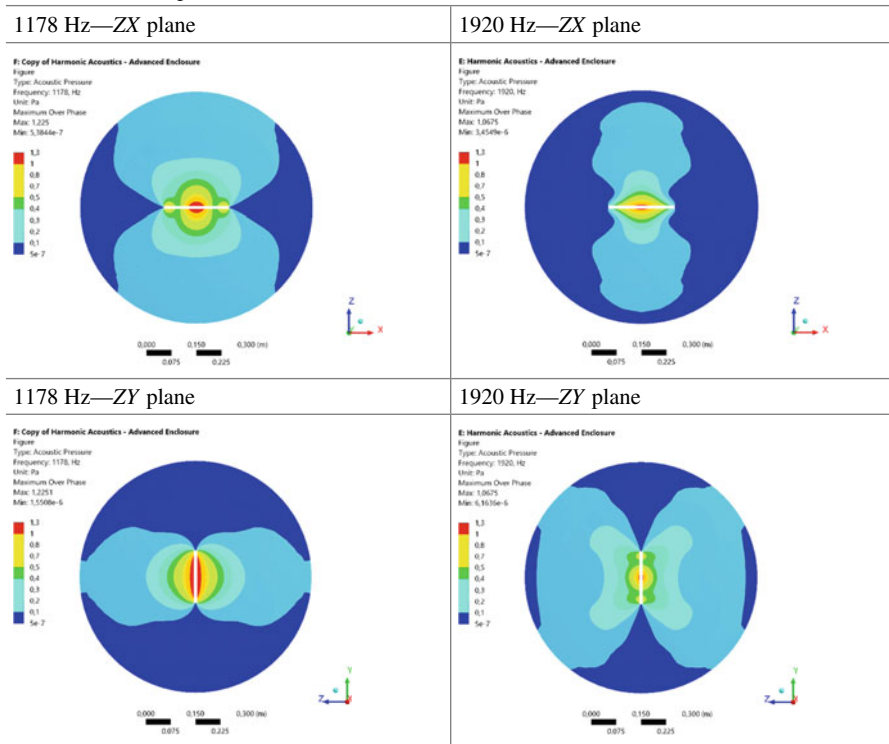


Fig. 4 Sound pressure level

evaluate the acoustic behavior of structure after correlation with technical experiment. Without validation of process, the numerical simulation can show the benefit of change, but without correct values.

Compared to [4], some modifications were applied in acoustic computational model to increase the accuracy. Greater emphasis was placed on the creation of the FE “mesh” based on the size of the element relative to the investigated frequency range. Another change was the boundary condition “Equivalent Far-field Surface”, which more effectively and more accurately determines the SPL’s outside the “acoustic mesh”. This methodology will be used for other structures, which is more complex [6].

Table 3 Acoustic pressure



Acknowledgements The research leading to these results has received funding from the project FV 18-56 granted by specific university research of the Brno University of Technology, Faculty of Mechanical engineering. The authors gratefully acknowledge this support.

References

1. V. Misun, in *Vibrate a Hluk*. (Academic Publishing House CERM, s. r. o., Brno, 2005). ISBN: 80-214-3060-5
2. D.J. Ewins, in *Modal Testing: Theory and Practice*. (Research studies Press, Letchworth, England, 1984)
3. R. Nový, *Hluk a chvění*, České vysoké učení technické, Praha (2009)
4. R. Zajac, K. Řehák, A. Prokop, Investigation of the harmonic response on the simple structure in structural and acoustic domain by experimental and numerical approach, in *Transport Means 2018*. Transport Means. (University of Technology, Kaunas, 2018), pp. 669–672. ISSN: 1822-296X

5. R.D. Blewins, in *Formulas for Natural Frequency and Mode Shape*. (Krieger Publishing Company, USA, 2001). ISBN: 9781575241845
6. J. Tůma, Transmission and gearbox noise and vibration prediction and control, in *The Sixteenth International Congress on Sound and Vibration* (Krakow, 2009)

Gear Shift Investigation Using Virtual Prototype



Aleš Prokop , Kamil Rehak , Roman Zajac , and Václav Otipka 

Abstract The presented paper deals with the prediction of vibroacoustic behaviour of heavy-duty transmission concept by application of virtual prototype. The methodology was developed by a combination of both, numerical and experimental approaches on single-stage gearbox. The results from both approaches were compared to validate computational simulation for the purpose to use numerical model for assembly with a higher level of complexity. The whole methodology is applied to heavy-duty transmission concept. For the purpose of easy application to different gearbox concept, the more complex model is written as open code. This enables to include gear shift option tuning, which can significantly affect vehicle comfort. This paper is mainly focused on the investigation of different gear shift process influence the surface normal velocity which is evaluated on the gearbox housing and is related to acoustic behaviour. The different combination of clutch activation and deactivation profile at different torque is investigated and evaluated by the surface normal velocity at most sensitive locations. Based on the results, the multibody model can be used at designing and optimization phase from the vibroacoustic point of view.

1 Introduction

The developing phase of gearbox consists of designing, manufacturing and verification of technical parameters. The presented trend of transmission development requires optimization in terms of increasing efficiency and passengers' comfort. For that reason, the numerical simulations take a place in the development phase. The design can be modified to decrease weight or optimize stiffness at the same or even higher technical parameters of the final product. The important factors of the key components are strength, vibration and emitted noise during whole operation

A. Prokop (✉) · K. Rehak · R. Zajac · V. Otipka
Faculty of Mechanical Engineering, Brno University of Technology, Technická 2896/2, Brno
61669, Czech Republic
e-mail: prokop.a@fme.vutbr.cz

© Springer Nature Switzerland AG 2021
N. Herisanu and V. Marinca (eds.), *Acoustics and Vibration of Mechanical Structures—AVMS 2019*, Springer Proceedings in Physics 251,
https://doi.org/10.1007/978-3-030-54136-1_43

conditions. Also, at transmission, the gear shift significantly affects the passenger's comfort. This phenomenon is also solved for electric vehicles [1], where the overall sound pressure level of the key sources is significantly lower. At manual transmission, the driver is responsible for the shifting smoothness, in case of automatic transmission this role is moved to gearbox development team. The setting of clutch activation and deactivation at direct shift gearbox can be modelled and debugged by using numerical simulation and afterward by testing at test rig or at whole car prototype. During the developing phase, several modifications are investigated, but the prototype parts are very expensive; thus the experimental approach is dominantly used only for final modification to verify the required parameters. This leads to placing high demands on used numerical simulations. On the other side, the numerical approach and the numerical model have to be validated to be able to use it several times. For that reason, it is appropriate to use the simplified structure first to minimize possibilities of inaccuracies, decrease time and costs demands. The used numerical approach for prediction of dynamic behaviour is developed and validated on the single-stage gearbox, the detail about the whole development process and validation of this numerical approach is described in [2]. Several sensitivity studies were performed afterward.

2 Methods

The determination of dynamic behaviour can be done by three different levels of modelling. The modal analysis is widely used at concept design to find all potential critical operation modes. The second level, the harmonic analysis, is mostly used when the character of excitation is known. Based on the excitation in a given frequency range the optimization of design can be performed. To determine the dynamic behaviour of gearboxes at transition state can be simulated by multibody simulation. Because the accuracy of this simulation depends on the accuracy of all inputs data, the modal analysis and harmonic analysis should be also performed.

2.1 Modal Analysis

The modal analysis of gearbox was performed in frequency range $0 \div 3000$ Hz, which is typical for such applications, the similar frequency range is used for truck transmission in [3]. The results of numerical simulations and technical experiments were compared. The difference in eigen frequency is up to 4%. The results are shown in Fig. 1.

The highest level of numerical model consists of gearbox with other surrounding components, which can affect modal properties. For that reason, the modal analysis of whole complex structure was performed, and the Craig Bampton modal reduction was used to create flexible bodies for the next analysis.

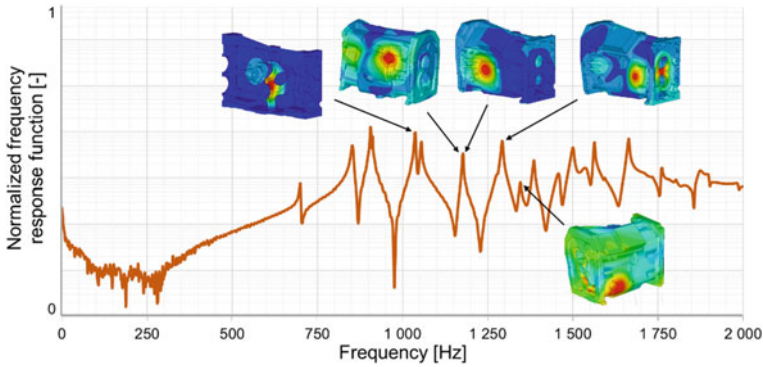


Fig. 1 Selected results in frequency range up to 2 kHz, data obtained from the technical experiment, eigenmode shapes from numerical simulations

2.2 Harmonic Analysis

Based on the results from modal analysis the critical location was determined and the response on the harmonic excitation was evaluated. The excitation of the structure was performed by modal exciter placed in bearing location. The force direction was determined based on the gear contact, the force amplitude is constant with increasing frequency. For that reason, the results are usable for comparative study. The results of harmonic analysis are shown in Fig. 2 for different frequencies.

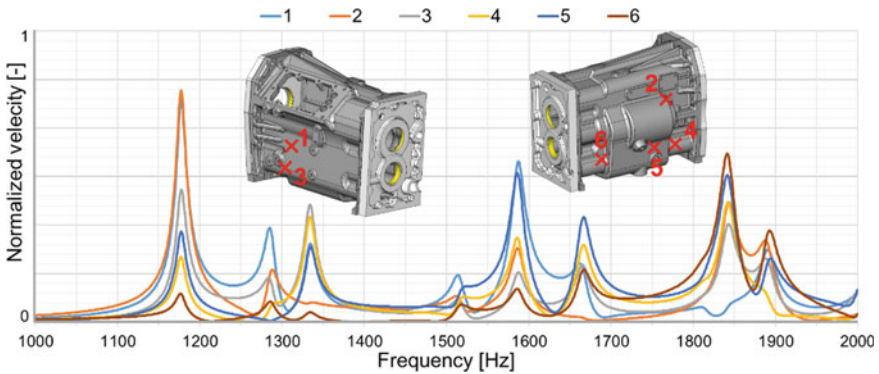


Fig. 2 Results of harmonic analysis in the determined location in range 1 ÷ 2 kHz

2.3 *Multibody Simulation*

First, the virtual prototype of the heavy-duty gearbox was created. The parametrical open code written in ADAMS was modified to use for complex structure and the script was extended for shift application. The virtual prototype includes flexible bodies of key component, stiffness and damping representation of bearings [4], variable gear mesh stiffness [5], backlash influence, clutch activation function and variable input speed, based on the functional principle of the combustion engine [6].

The numerical simulation of whole transmission was performed for run-up simulations at given gears. The technical experiment on the prototype equipment was performed for steady-state at the given gears. The loading and engine speed was monitored in detail. The results were compared, see Fig. 3.

3 Results

In this paper, the influence of clutch activation and deactivation on dual-clutch gearbox dynamic behaviour is investigated. Based on the functional principle of the dual-clutch gearbox, the time of activation and deactivation for the sensitivity study purposes is set between 0.1 and 0.3 s. All combinations are simulated, see Fig. 4. The simulations were performed for the carried torque range 100 and 200 Nm.

When the time between maximal value of the activation and deactivation function is decreasing, the clutch carried torque is increasing. During the transient shift phase, both clutches are partially engaged. The main goal during tuning of the gear shift is to find a good balance between carried torque of the clutch 1 and 2. The carried torque before and after shift process must correspond to the gear ratio between two gears, in this case, $i = 0.63$, see Fig. 5. The maximal value of torque oscillation during gear shift is changing based on the simulated variant. With decreasing of shifting time the higher peaks of the carried torque occur, see Fig. 6. Another sensitivity study is performed for different values of loading torque. Results in Fig. 7 show, that with increasing loading torque through the whole gearbox the peaks in clutch carried torque are decreasing.

The difference from the NVH point of view can be observed in the Multispectrum diagram, where the critical locations are usable for comparison. Short shifting time significantly affects the surface normal velocity, due to mentioned higher peaks of the carried torque and thus of the structure excitation as well. This impact-like character of excitation causes wide frequency range vibration, see Fig. 8, (time 2 ÷ 2.3 s).

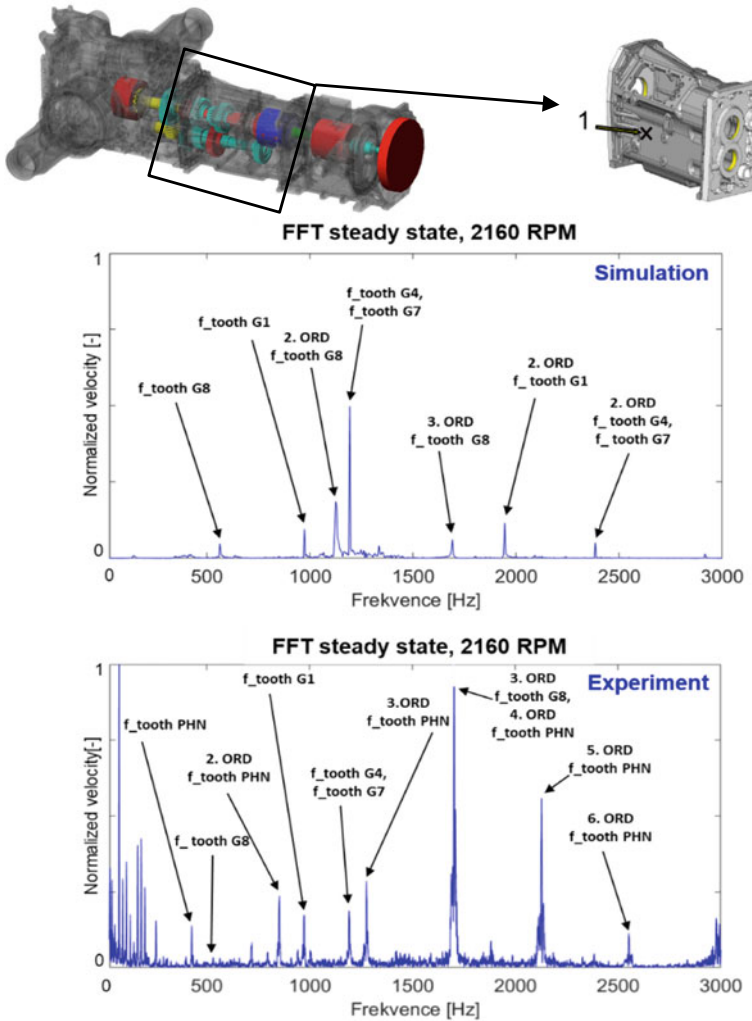


Fig. 3 Comparison of FFT from technical experiment and numerical simulation for fourth gear, the engine speed 2160 RPM and torque 1027 Nm

4 Conclusion

With the increasing complexity of investigated structure, it is necessary to determine the level of modelling with considering the results influencing the accuracy. The study is dominantly focused on the gearbox, but other components are incorporated. The presented paper deals with the investigation of gear shifting influence on the surface normal velocity. The clutch activation and deactivation function were changed, where the torque on shaft and surface normal velocity was evaluated. Based on the results

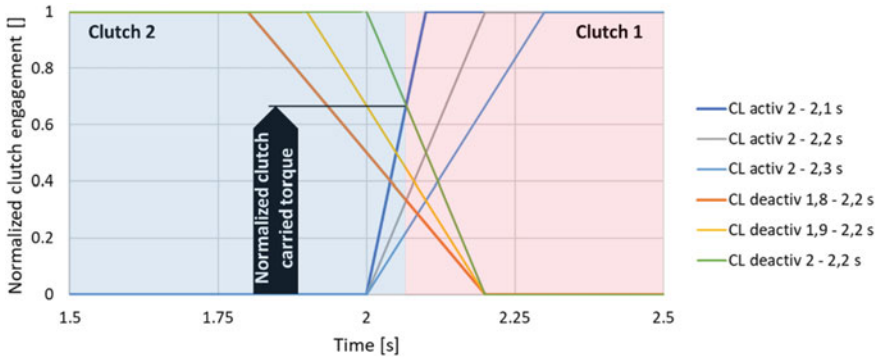


Fig. 4 Clutch activation and deactivation profiles

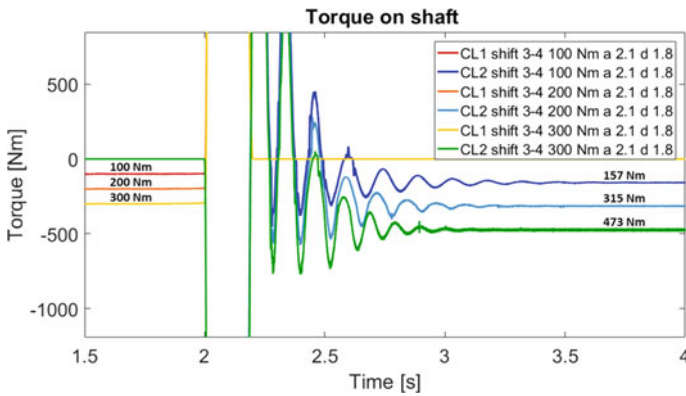


Fig. 5 Clutch carried torque course

comparison it is obvious, that the surface normal velocity level is dependent on the gear shift time, trends are described in the results chapter. Based on the presented results, the virtual prototype can be used for the prediction of dynamic behaviour during gear shifting.

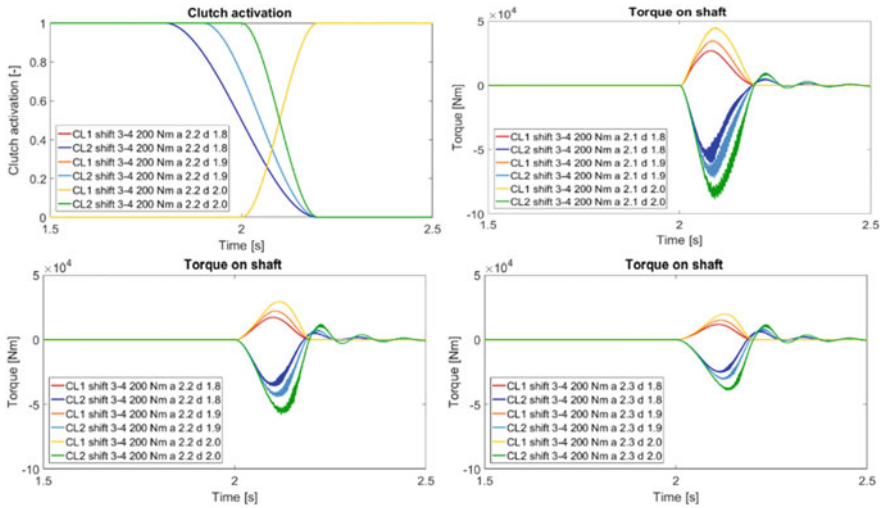


Fig. 6 Shift time influence to the clutch carried torque

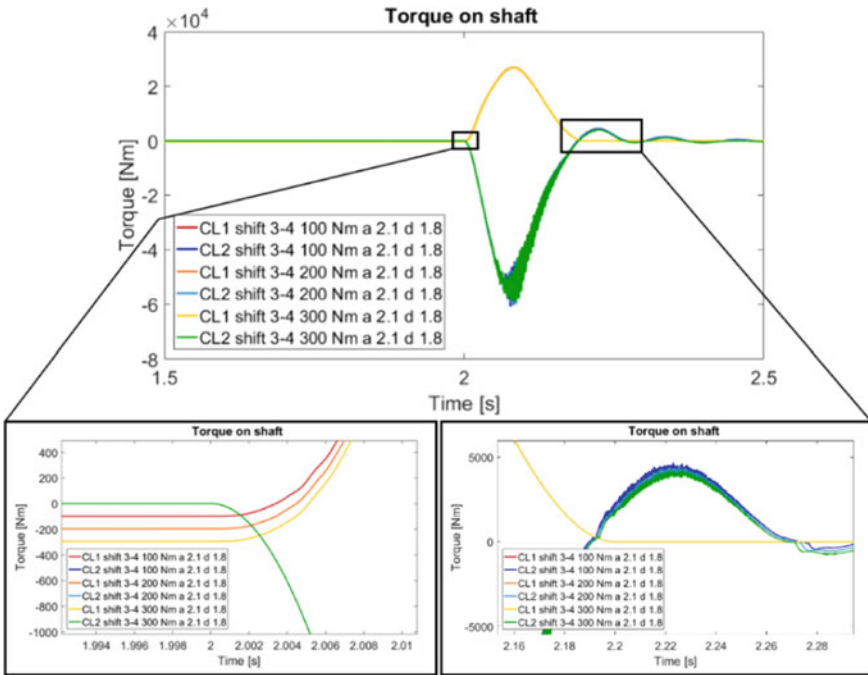


Fig. 7 Clutch carried torque course for different gearbox loading torques

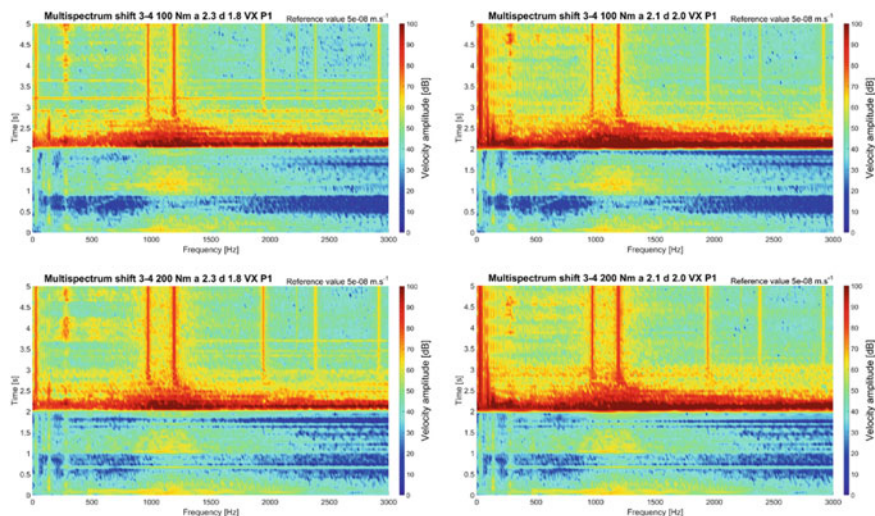


Fig. 8 Multispectrum diagram of the surface normal velocity in investigated point P1

Acknowledgements The research leading to these results has received funding from the project FSI-S-17-4104 granted by specific university research of the Brno University of Technology. The authors gratefully acknowledge this support.

References

1. M. Roozegar, J. Angeles, The optimal gear-shifting for a multi-spe.ed transmission system for electric vehicles. *Mech. Mach. Theory* **116**, 1–13 (2017)
2. M. Zubik, A. Prokop, K. Rehak, P. Novotny, The effect of the gear parameters to the noise of transmission, in *Vibroengineering PROCEDIA*. Vibroengineering Procedia. Kaunas (JVE International Ltd., Lithuania, 2015), pp. 357–362. ISSN: 2345-0533
3. A. Kumar, H. Jaiswal, R. Jain, P.P. Patil, free vibration and material mechanical properties influence based frequency and mode shape analysis of transmission gearbox. *Procedia Eng.* **97**, 1097–1106 (2014)
4. M. Razpotnik, T.M. Bischof, M. Boltežar, The influence of bearing stiffness on the vibration properties of statically overdetermined gearboxes. *J. Sound Vibrat.* (351), 221–235 (2015)
5. T. Kiekbush, D. Sappok, S. Bernd, H. Ian, Calculation of the combined torsional stiffness of spur gears with two- and three-dimensional parametrical FE models. *J. Mech. Eng.* **57**, 810–818 (2011)
6. L. Drápal, L. Šopík, Influence of crankshaft counterweights upon engine block load, in *Transport Means 2016—Proceedings of the International Conference*, pp. 809–814 (2016)

Numerical Dynamic Analysis of Gearbox Behaviour



Václav Otipka , Roman Zajac , Kamil Rehak , and Aleš Prokop 

Abstract This paper is focused on the description of the dynamic behaviour of a single-stage gearbox when changing the operating load using numerical approach. The numerical model, which is further discussed in the paper, combines FEM and MBS approach in the commercial software Ansys Workbench and Adams with plugin GearAT. The key components are represented by flexible structures—modally reduced bodies. The mesh conditions in the model can include the elastic behaviour of the gear rim, backlash and the influence of lubrication in the contact area. At the very beginning used approach was developed on a simple experimental gearbox. Subsequently, this methodology was applied to a complex train gearbox with the aim of optimizing its gearbox housing geometry. In a multi-body system, a series of operating simulations were performed on a virtual test rig. Based on the evaluation of normal surface velocity at selected points, the gearbox housing geometry was optimized.

1 Introduction

Numerical simulations are widely used today in terms of optimizing the vibro-acoustic parameters of transmission systems. The computational models enable predicting the gearbox behaviour during the operation. In case of experimental development many physical prototypes need to be manufactured and subsequently tested. On the other side, the usage of numerical simulations enables to find any problems at the design phase, thus significantly saves total cost and speed up the developing process of new products. This approach is amplified by increasing trend of the modern computing power [1–4].

In this paper, one of these advanced approaches to development using virtual prototype is introduced. The presented computational model was designed primarily

V. Otipka (✉) · R. Zajac · K. Rehak · A. Prokop
Faculty of Mechanical Engineering, Brno University of Technology, Technická 2896/2, 616 69
Brno, Czech Republic
e-mail: vaclav.otipka@vutbr.cz

to evaluate the acoustic performance of transmissions. This model can be used to observe and compare the normal surface velocities at any location.

Transmission noise is the consequence of excited vibration of large transmission walls. The most important source of excitation remains the forces generated by the gears meshing [5]. In principle, during the gear mesh, the stiffness of teeth in contact is changing. This causes deviations from the ideal kinematics between co-engaging gears—transmission error (TE) [6]. Teeth engage in a non-ideal position cause shocks and vibrations. Excitation frequencies are dependent on operating conditions. Generally, these are wide frequency bands, which is necessary to deal with.

2 Methods

The main part of the model is created in multi-body software Adams with including plugin GearAT, while finite element software Ansys Workbench is used to obtain some input data, like modal properties and bearing stiffness. In this case, the same principle as in this paper [7] is used to obtain necessary input data from finite element software.

The computational model is presented on a heavy loaded train gearbox, which could be used also in high-speed application. See Fig. 1.

All key components of transmission are represented by flexible bodies. A shaft including a gear wheel and pinion are inserted into the main housing section. The

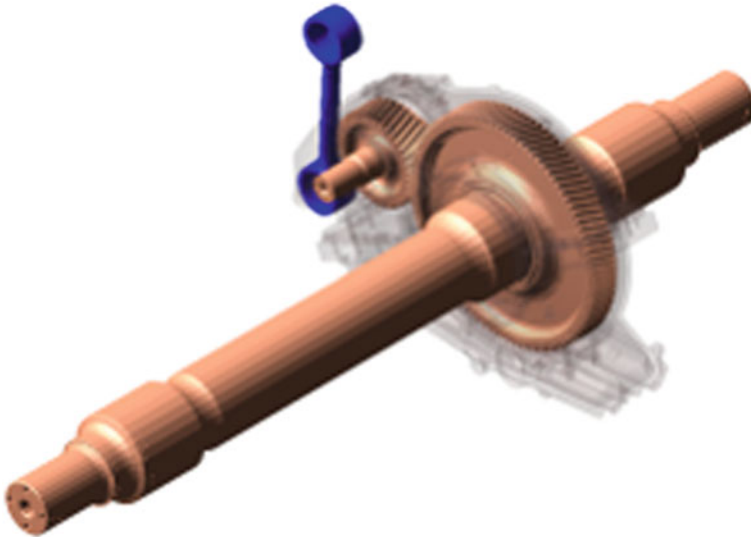


Fig. 1 Model of used train gearbox

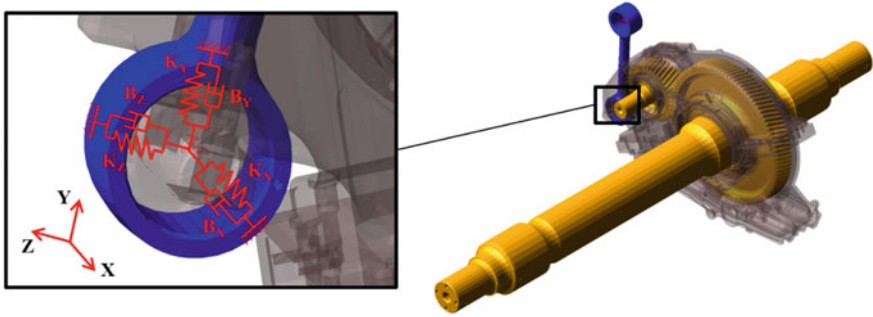


Fig. 2 Principle scheme of replacement rubber silentblock

reaction forces are captured by the reaction rod at the front of the housing. Shaft and pinion bearings are replaced by 6-component force elements in the model. Force interaction is derived by the size and speed of mutual deformation of specific components according to the basic dynamic equation of motion (1)

$$M\ddot{q} + B\dot{q} + Kq = F, \tag{1}$$

where M is the square matrix of mass, B the square matrix of damping, K the square matrix of stiffness, F the column matrix of load and q represents the column matrix of generalized coordinates.

The same procedure is followed for the reaction rod because the gearbox and reaction rod connection is made through rubber silentblock. The principle scheme of replacement by 6-component force element is shown in Fig. 2. The directional characteristics of the rubber silent block stiffness were determined experimentally.

The calculations by using FEM were performed to get directional stiffness characteristics of all used bearings. These values were applied in a virtual prototype afterwards.

Modelling of the gearbox dynamic behaviour is not possible without information about the gear mesh stiffness. In the presented approach the gear mesh stiffness calculation does not take place directly at the tooth flank contact in the main (transient) simulation. The stiffness is pre-calculated by implemented Nastran solver from user-defined teeth shape geometry. The similar approach was used in [8], where the stiffness dependency on carried torque was pre-calculated. Precise definition of the tooth shape is a prerequisite for obtaining corresponding simulation results. The model allows to include both macro and micro geometry, including modifications, tolerances and deviations. The influence of oil layer and friction is also included in the conditions of the gear mesh. In this way it is possible to optimize the geometry of the gears shape in terms of interference with the gearbox housing which is dominant from the NVH point of view.

Simulations that include two basic operating modes of the gearbox were performed—traction and braking mode. In both cases, the pinion was rotated from

zero speed to operating speed according to a defined curve. The total spin time was 64 s. The curve is shown in Fig. 3.

The main difference between the two load conditions is in the different torque characteristics for the traction and braking mode, which are determined based on the motor operation conditions. The defined torque curve for the simulation is shown in Fig. 4.

In the simulations, two design variants of the housing were used, see Fig. 5. Design of housing was gradually developed with the help of modal analysis results. Large walls of first design version were extended with reinforcing ribs. First design version (original) thus presents a housing with a smooth design. Second design version (reinforced) is reinforced by ribs at critical locations.

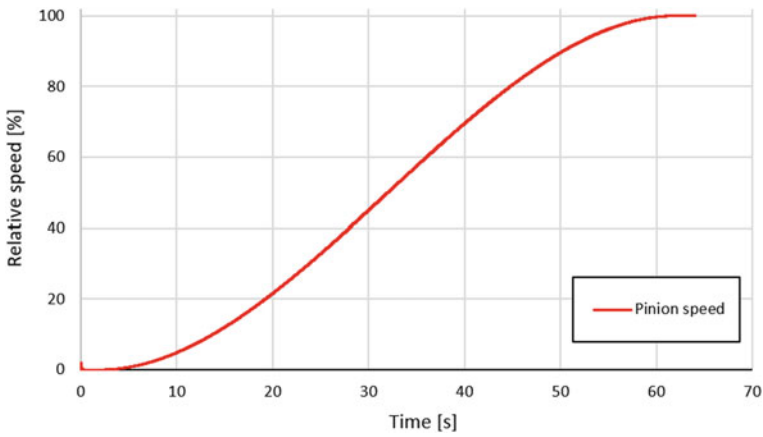


Fig. 3 Pinion RPM curve

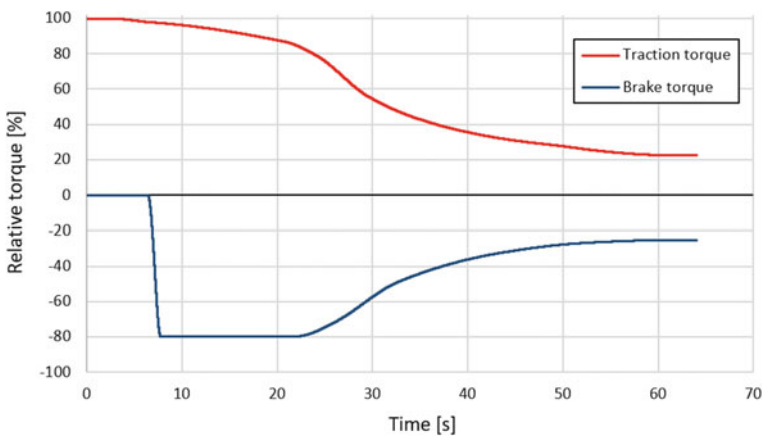


Fig. 4 Motor torque curve



Fig. 5 Two design versions of housing

As a benchmark for the gearbox optimization, surface normal velocities were monitored at specified points. The position of these points was defined based on the results of the housing modal analysis. In addition to the surface normal velocity in the time domain, a multispectrum diagram was also processed using FFT analysis from the obtained data at the given points.

3 Results

By analysing the results obtained from all surface points, the highest velocity values were found in the area of the housing side walls. Due to the symmetry of the gearbox, the surface normal velocities of both right and left sides are very similar. In this paper, the results of two points with highest amplitude will be presented. The location of these points is evident from Fig. 6. In parallel, other areas have been investigated,

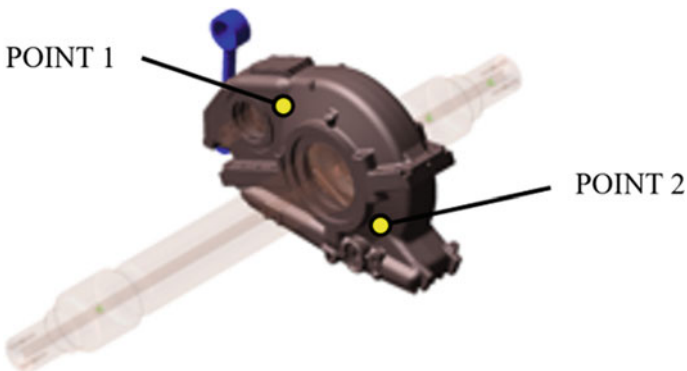


Fig. 6 Location of measuring points on the housing

but the values of surface normal velocity are lower compared to the aforementioned side walls of the housing.

The time domain data of the surface normal velocity and transmission error during braking simulation are shown in Fig. 7. There are highlighted areas where the biggest increasing of amplitudes occurs. The largest increasing of amplitudes occurs between 36 and 42 s. This time range is accompanied by an increasing of the transmission error. The amplitudes of surface normal velocity at both points and peak-to-peak values of transmission error are shown in Table 1.

During the second operating mode, which is based on traction, there are two significant areas where is visible a large increasing of amplitudes. See Fig. 8. The first occurs in the same area as in the first operating mode which is between 36

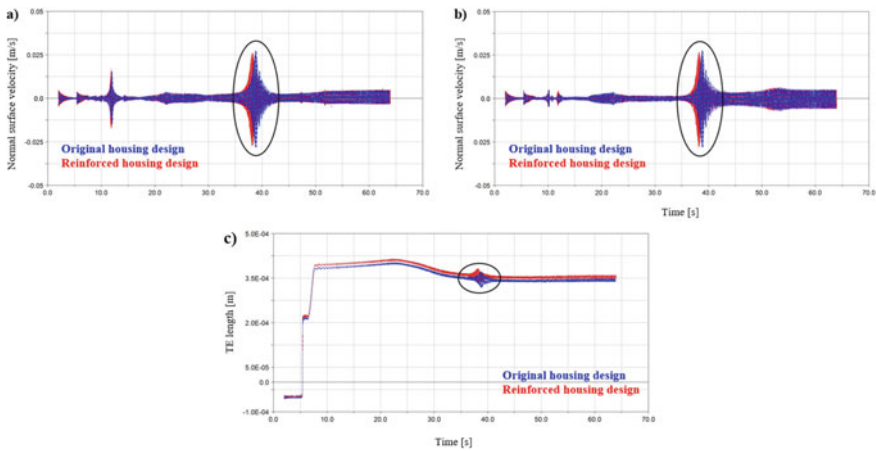


Fig. 7 Surface normal velocity amplitudes and transmission error during braking simulation. **a** Data for point number 1. **b** Data for point number 2. **c** Transmission error diagram

Table 1 Overview of surface normal velocity and transmission error amplitudes for both design versions of housing

Variant		Original housing	Reinforced housing
Braking 36–42 s	Velocity amplitude (point 1) [m s ⁻¹]	0.0273	0.0269
	Velocity amplitude (point 2) [m s ⁻¹]	0.0276	0.0268
	Peak-to-peak TE [mm]	0.0520	0.0510
Traction 36–42 s	Velocity amplitude (point 1) [m s ⁻¹]	0.0290	0.0278
	Velocity amplitude (point 2) [m s ⁻¹]	0.0292	0.0284
	Peak-to-peak TE [mm]	0.0540	0.0532
Traction 53–56 s	Velocity amplitude (point 1) [m s ⁻¹]	0.0484	0.0328
	Velocity amplitude (point 2) [m s ⁻¹]	0.0496	0.0384
	Peak-to-peak TE [mm]	0.355	0.323

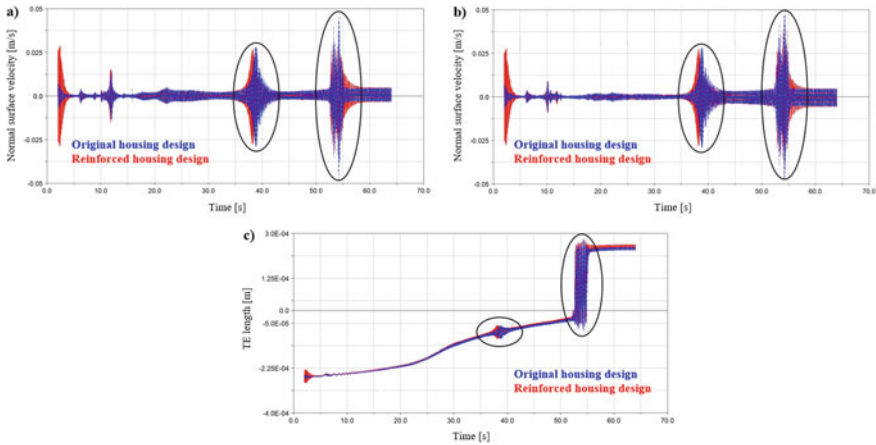


Fig. 8 Surface normal velocity amplitudes and transmission error during traction simulation. **a** Data for point number 1. **b** Data for point number 2. **c** Transmission error diagram

and 42 s. At the time between 53 and 56 s the next increasing of amplitude occurs, which is more pronounced. Peak-to-peak value of transmission error at second area reaches value of backlash (0339 mm)—gear rattle occurs. Specific values are shown in Table 1. Gear rattle is accompanied by impacts, which cause wide band excitation. During gear rattle, the contact pairs of the tooth flanks are continually changed, which is associated with the generation of shocks and vibrations [9]. Gear rattle can be observed especially in less loaded operating conditions of gearboxes, during torsional oscillation of systems.

The consequences of gear rattle are visible in the multispectrum diagram in Fig. 9. This multispectrum diagram was obtained for point 1 of reinforced design housing

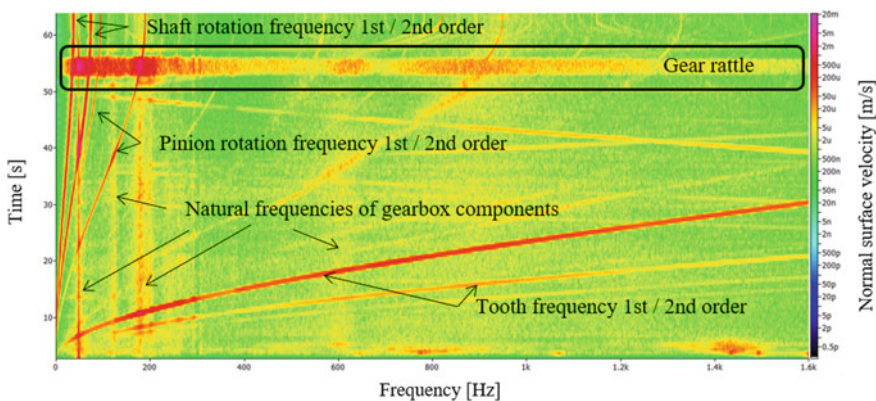


Fig. 9 Multispectrum diagram for point number 1 of reinforced design housing during traction mode simulation

during traction mode simulation. Gear rattle manifests itself in a narrow time area where a wide band of frequencies are excited. Basic components of the signal can also be recognized on the multispectrum diagram—shaft and pinion rotary frequency, tooth frequency and their harmonic orders. Other areas of increased amplitudes are caused by the intersection of excitation frequencies and the natural frequencies of the individual components of the transmission.

4 Conclusion

As already mentioned, optimizing gearboxes in terms of vibro-acoustics is a complex issue. In this paper, the approach of changing the gearbox geometry to surface vibration was presented.

The greatest increase in gearbox surface vibration in a presented configuration during operation occurs due to gear rattle effect. The design changes were intended to reduce amplitudes of surface normal velocities in areas of interest. Only due to design optimization of the housing, the amplitudes in these areas were reduced by more than 20%.

Further reduction of vibration could be achieved by optimizing the modal properties of all components included in the model to minimize intersections of their natural frequencies. It is also possible, for example, to optimize the macro and micro geometry of the gears or to use a lubricant with different parameters.

This computational model is a suitable tool for the initial prediction of the dynamic behaviour of the transmission. However, the level of the presented model can still be increased by including new influences. For example, including the moments of inertia from the entire drive chain, it is also possible to cover the input speed character or to include in-service shocks.

The results have not been validated by propriety experiment yet. Several technical experiments are going to be performed to obtain corresponding data about vibrations and transmission error. Real measured data are very useful for verification of computational model, because the results obtained from computational model are highly dependent on the input parameters from the user.

Acknowledgements The research leading to these results has received funding from the project FSI-S-17-4104 granted by specific university research of Brno University of Technology and Project TH02010725 granted by Technology Agency of the Czech Republic. The authors gratefully acknowledge this support.

References

1. M. Sopouch, T. Resch, P. Herster, Analysis of gearbox acoustics with AVL EXCITE (2011)
2. J. Neher, B. Graf, S. Falkenberger, B. Wender, Sound radiation simulation methods for gearboxes—with a special focus on ribs, vol. 5, pp. 3989–4003 (2012)
3. F. Vanhollebeke, J. Helsen, J. Peeters, D. Vandepitte, W. Desmet, Combining multibody and acoustic simulation models for wind turbine gearbox NVH optimization, vol. 6, pp 4463–4477 (2012)
4. P. Fołęga, R. Burdzik, G. Wojnar, The optimization of the ribbing of gear transmission housing used in transportation machines. *J. Vibroeng.* **18**(4), 2372–2383 (2016). <https://doi.org/10.21595/jve.2016.17168>
5. P. Geradts, B. Christian, L. Christoph, K. Marcel, Reduction of the tonality of gear noise by application of topography scattering. *Appl. Acoust.* **148**, 344–359 (2019)
6. A. Palermo, B. Laurent, J. Karl, M. Domenico, D. Wim, The measurement of Gear Transmission Error as an NVH indicator: Theoretical discussion and industrial application via low-cost digital encoders to an all-electric vehicle gearbox: Theoretical discussion and industrial application via low-cost digital encoders to an all-electric vehicle gearbox. *Mech. Sys. Sig. Process.* **110**, 368–389 (2018)
7. K. Řehák, B. Kopečková, A. Prokop, Gear drive system simulation with different model of input speed, in *Acoustics and Vibration of Mechanical Structures—AVMS-2017. Springer Proceedings in Physics*, vol. 1. (Springer, Cham, 2017), pp. 331–339
8. A. Prokop, P. Kučera, K. Řehák, Heavy-duty transmission gear shift investigation by virtual prototypes. *Vibroeng. PROCEDIA*. Kaunas, Lithuania: JVE International, 226–230 (2018) ISSN: 2345-0533
9. M. Barthod, B. Hayne, J.-L. Tébec, J.-C. Pin, Experimental study of gear rattle excited by a multi-harmonic excitation. *Appl. Acoust.* **68**(9), 1003–1025 (2007)

Acoustic and Vibration Response Analysis of Heavy-Duty Gearbox



Kamil Rehak , Aleš Prokop , Roman Zajac , and Václav Otipka 

Abstract The presented paper deals with determination of acoustic and vibration response of heavy-duty gearbox housing on the defined force excitation. The analysis is performed by both, numerical and experimental approach. The results from both approaches are compared to validate numerical approach for the purpose to use numerical model for design optimization and further for multibody simulations. The excitation is applied to the area of bearing to simulate the real character of the excitation, which is transmitted from the gear mesh contact stiffness, which is changing due to actual geometry of teeth in contact, via gears and shafts to bearings and further to the housing. The same boundary conditions are applied for both approaches. Because the vibrations and the acoustic emissions are directly related to each other, the surface normal acceleration in critical locations is compared first. When the surface normal acceleration is compared, the sound pressure level in defined locations is evaluated. This article systematically describes the prediction of vibro-acoustics behavior of heavy-duty gearbox housing by using two different levels of approach, which can be used for design optimization afterward. The technical experiment with optimized housing has not been performed yet.

1 Introduction

The rail transport is very often used for the reason of independence from traffic jams, easy traveling for long distance, safety, but the increasing of passenger comfort in public rail transport is one of the key points to increase the frequency of their usage even, e.g., for short distance. The manufacturers of public transport vehicles intensively deal with the increasing demands of customers and passengers on driving comfort, ergonomics, thermal comfort and finally on vibration and noise comfort. The reduction of noise and vibration is very complex task, because of increasing

K. Rehak (✉) · A. Prokop · R. Zajac · V. Otipka
Faculty of Mechanical Engineering, Brno University of Technology, Technická 2896/2, 616 69
Brno, Czech Republic
e-mail: rehak@fme.vutbr.cz

demands on transmitted torque, higher rotational speed, smaller build-in dimension and reduction of used material because of efficiency [1].

Commonly, the transmissions are designed for the purpose of transfer the rotation speed and power from input, where source can be engine or electric motor, to the defined rotation and torque on the output. For that purpose, it is necessary to design gears, shafts, bearings, housing for given operation conditions. In case of single stage gearbox, the input shaft is connected to the input gear, which is in contact with the output gear. The torque is transferred from one gear to second gear trough teeth in contact, which is changing in dependence on the type and dimensions of gears and number of teeth. The dependency between input and output rotation and torque is not constant, but it is dependent on the stiffness of teeth variability. The changes of gear mesh stiffness can be evaluated by using static transmission error (TE) [2, 3]. In this parameter there is included also the stiffness of the shafts, bearings and gearbox housing. The TE can be measured from experiment or calculated by computational modeling. The gear mesh stiffness, which corresponds the TE, can be calculated by using Finite element method (FEM) [4].

The excitation of whole gearbox can occur due to several causes, but the main source of gearbox excitation is the variability of gears contact [5, 6]. The amplitude of force excitation is changing based on the type and geometry of the gears. The shape of the gears included macro and micro geometry is designed to minimalist it, but the frequency is still dependent on the rotation speed and number of teeth. The excitation force at given frequency is transferred through shafts and bearings (transfer path) to the gearbox housing. The gearbox housing is the biggest component with large areas, where the excitation can cause high level of vibration and noise. The housing is designed to determine the bearing position, thus shaft axis. In the most cases, the stiffness in this direction is higher than in rest of housing, where the purpose of housing is dominantly to cover the gears, protect parts and to allow using of oil. To decrease the total weight, this part of housing is subject of design optimization. On the other side significant reducing of stiffness can affect the modal properties, vibration and emitted noise.

2 Methods

There are several approaches to determine the dynamic behavior of gearboxes, which can be divided into three different levels based on the complexity. The first one is the modal analysis, which is very often used at designing phase to find, if the operation conditions across eigen frequencies of designed structure [7]. In case of gearbox it is necessary to take into account all components, which are closely connected, thus they can affect each other.

The second level is harmonic analysis, which is also solved in frequency domain. The excitation of structure is necessary to know.

The most complex approach is based on the multibody simulation (MBS), which is solved in time domain. To get results with high level of accuracy needs to incorporate the modal and harmonic analysis including validation of them by technical experiment [8]. In the presented paper the modal and harmonic analysis is described including the acoustics part.

2.1 Modal Analysis

The gearbox housing from the single stage gearbox for application in train is used. The dimensions of gearbox are in max approx. length 980 mm, width 770 mm, depth 180 mm. First the modal analysis by using FEM was performed in software Ansys Workbench. The CAD data and material properties based on the material list were used. The free boundary conditions were applied on the model. The model of bolts was simplified and the pretension corresponding to the tightening moment was applied at first step. Afterward, the modal analysis was performed in frequency range up to 3 kHz.

Subsequently the experiment was performed also with the free boundary conditions. This was simulated by hang up the gearbox housing on the flexible rope. The excitation was performed by using modal hammer and the response was measured by triaxial accelerometer. The accelerometer was placed in the exterior part of housing into locations, which were determined based on the results from numerical simulation. For each side the location was changed. The excitation force was applied into other location based on the grid, which was 60–70 mm, see Fig. 1. The force and response were recorded by using analyzer from Brüel & Kjaer company, where four channels were occupied (impact hammer and three for ACC sensor). The geometry model was simplified to create structure for visualization in software to determine the corresponded eigen shape.

2.2 Harmonic Analysis

For the purpose to get accurate excitation force the experiment of structure harmonic analysis was performed first. The measurement was performed in a fully anechoic chamber, because the measurement of acoustic response by microphones. The housing was hung by rope similar to the modal harmonic. The excitation of structure was performed by modal vibration exciter, which was connected to the support. The thin rod with low stiffness in radial direction was screwed on the output of exciter, see Fig. 2. The modal exciter was encapsulated to minimize noise, which is not connected to the gearbox housing. The force sensor was placed on second end of rod and screwed into one hole of housing close to the bearing location. The harmonic signal of the specified amplitude and frequency was transmitted to the structure.

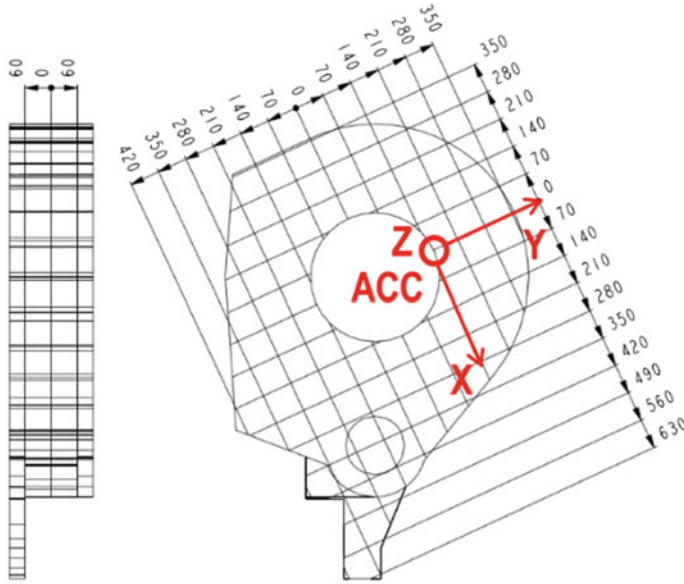


Fig. 1 The grid for application of excitation during the experimental modal analysis

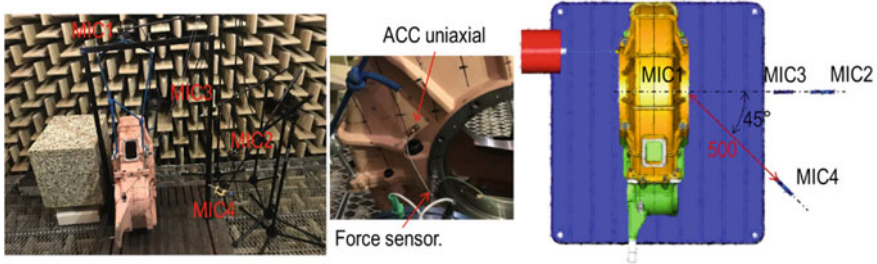


Fig. 2 The harmonic measurement set up in full anechoic chamber, detail of force application and measurement by uniaxial accelerometer, location of microphones

The response was measured by using four uniaxial accelerometers and two triaxial accelerometers. The position for response measurement was defined based on the results from modal analysis to the location, where the movement was significant. The location of accelerometers was changing for different excitation frequency. The response was recorded by using analyzer from Brüel & Kjaer company, where 15 channels were occupied (4 microphones, 4 uniaxial accelerometers, 2 triaxial accelerometers, force sensor).

The boundary condition in numerical simulation was set based on the technical experiment to get comparable results. The free boundary conditions were applied.

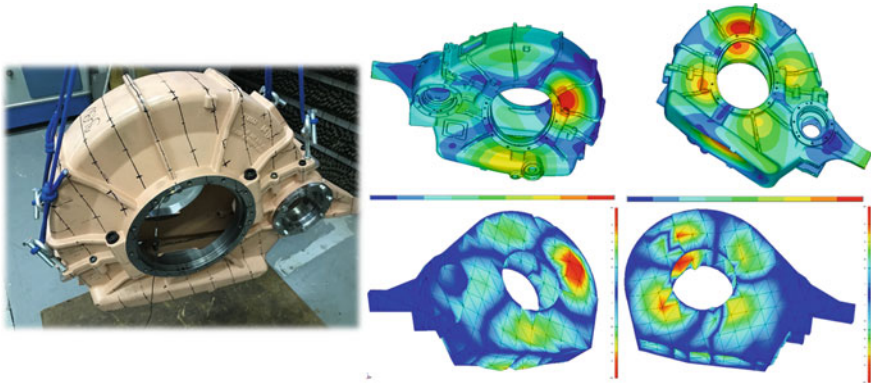


Fig. 3 Comparison of eigen shape from the numeric simulation (top) and experiment (below)

The direction and magnitude of force in given frequency was applied to the identical hole like in experiment. The simulation was performed with the force value from technical experiment in frequency range 20 Hz around each eigen frequency. The acoustic mesh was created around whole gearbox housing to evaluate acoustic response. The sensitivity study of damping was performed.

3 Results

3.1 Modal Analysis

Based on the difference of results comparison, the input parameters should be modified to increase an accuracy of numerical simulation. The 3D scanning equipment was used to increase the geometry model accuracy. The method of reverse engineering was used to get whole geometry of gearbox housing. Based on the volume and the mass, the density was also modified. Approximately 60 eigen frequencies in frequency range up to 3 kHz. Based on this approach the difference was reduced to max 2.73% and average difference 1.05%. The comparison of numerical and experimental eigen shape is shown in Fig. 3.

3.2 Harmonic Analysis

The results from experiment were evaluated for each measurement at given frequency separately. The measurement was performed 3 times to increase the accuracy. The data were evaluated in time and frequency domain. The example of evaluation is

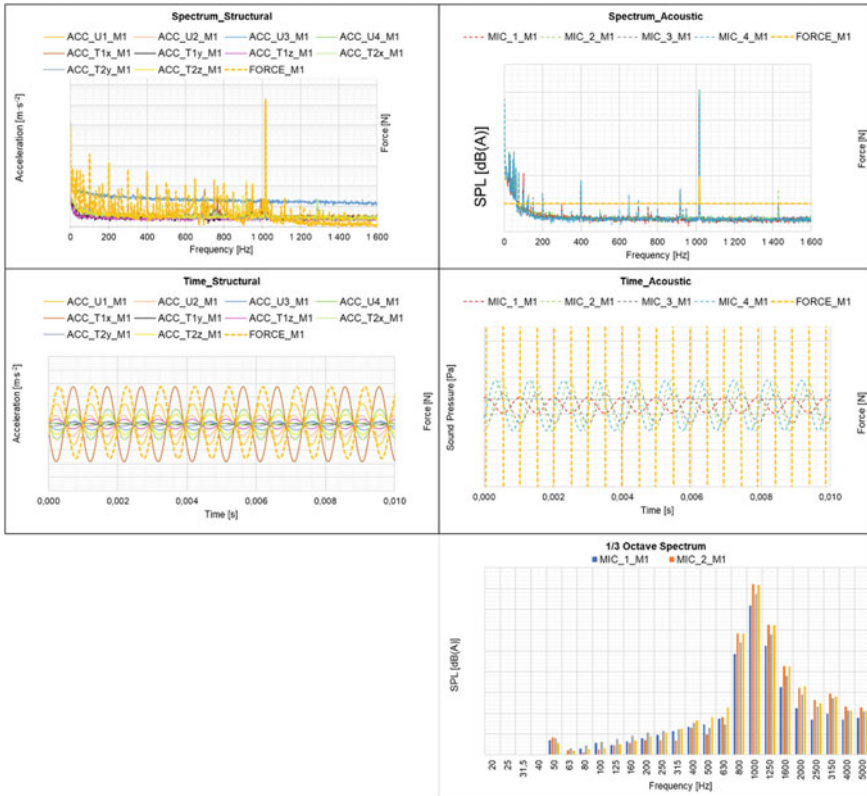


Fig. 4 Data in frequency (top) and time (below) domain; the sound pressure level A weighting

shown in Fig. 4. From the acoustic point of view the results were evaluated in 1/3 octave spectrum up to 5 kHz with A weighting.

The damping coefficient is one of the key parameters of numerical harmonic analysis. The value of damping coefficient was evaluated based on the experimental part of modal analysis for each eigen frequency. The sensitivity study of damping coefficient and investigation of the effect on the amplitude of surface normal acceleration was performed. The damping coefficient from modal analysis was multiplied $1\times$, $2\times$, $3\times$, $8\times$. The amplitude of surface normal acceleration for different eigen frequency from numerical simulation and experiment were compared at each position of accelerometer. The example of comparison is shown in Fig. 5.

The frequency from numerical simulation and experiment is slightly different, thus the harmonic analysis was performed for the frequency determined from corresponding modal analysis. Based on the results from sensitivity study, it is obvious, that the damping coefficient has significant effect on the amplitude of surface normal acceleration. In some frequencies the results from numerical simulations with the damping coefficient determined from experimental modal analysis provides similar structure response on given excitation. But in another frequency, where the damping

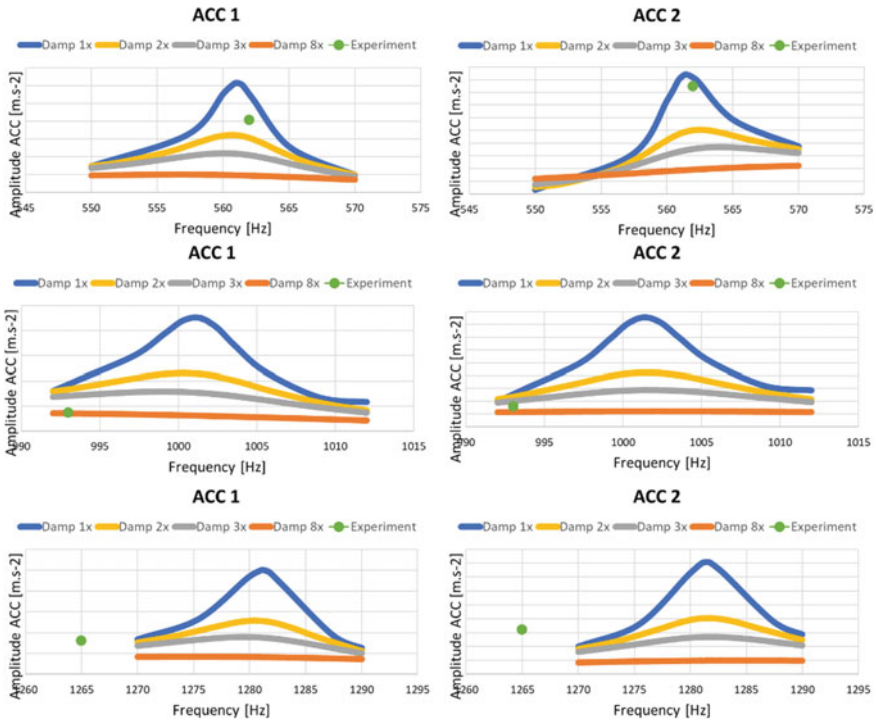


Fig. 5 The comparison of amplitude of surface normal acceleration for different eigen frequency

coefficient from experiment was used, the response was overestimated. In case of multiplying of damping coefficient several times the acceleration starts corresponded to data from experiment.

The numerical simulation was also used for prediction of sound pressure level (SPL); the distribution of SPL is shown in Fig. 6. The SPL can be evaluated in the plane in given distance. The distribution can be helpful for design optimization.

4 Conclusion

The dynamic behavior of the gearbox housing was investigated by using modal and harmonic analysis. There were used numerical and experimental approaches, which were simultaneously compared to each other. For that reason, there were used the same boundary conditions. The computational modal analysis was refined by using measured density and model of geometry created by using 3D scanning and reverse engineering. By using this computational model, the difference to the experimental approach was up to 2.73%. The damping coefficient was determined

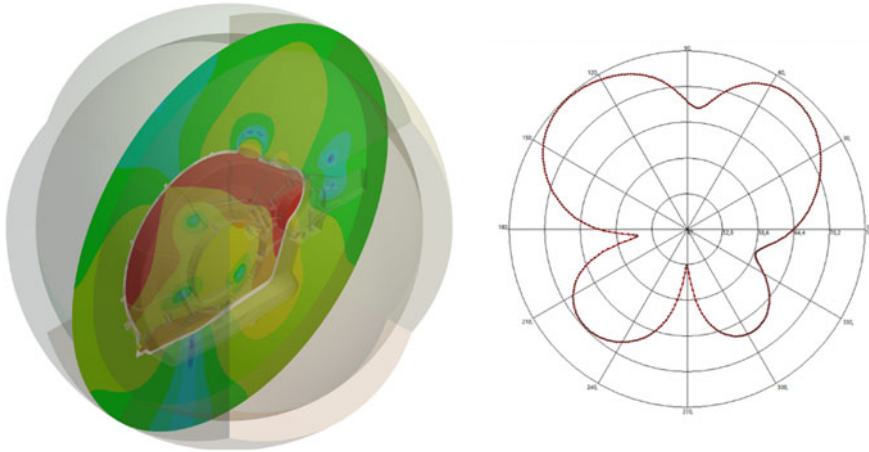


Fig. 6 Sound pressure distribution in cross-section area (left) and the sound pressure distribution in 1 m from the center of gearbox housing (right)

from experimental modal analysis, which was used for further numerical analysis afterward.

The harmonic analysis was performed in fully anechoic chamber to evaluate structure and acoustic response. The numerical approach used the same boundary conditions and excitation force like in experiment. The sensitivity study of damping coefficient was performed, and the response was compared to the experiment. Based on the results, the usage of the damping coefficient from experimental modal analysis can overestimate the response of the structure for given excitation in some cases. Because the acoustic response is closely connected to the surface normal velocity, it is necessary to increase the accuracy of response on the surface first. For that reason, the harmonic acoustic analysis can be helpful tool for design optimization from the acoustic point of view, but it is necessary to be taken into account, that the value of sound pressure level does not corresponds to the measured value from experiment in some frequencies.

Both described approaches can be used at design optimization phase but based on the modal analysis it is very difficult to determine the real behavior during whole range of operation conditions. The harmonic analysis can be used to compare two different housing and determine the response at given excitation, which has to be well known. Based on that, the harmonic analysis can be used at the well-known application, where, for example, measurement were performed; otherwise, the approach with higher level of complexity has to be used.

Acknowledgements The research leading to these results has received funding from the project FSI-S-17-4104 granted by specific university research of Brno University of Technology and Project TH02010725 granted by Technology Agency of the Czech Republic. The authors gratefully acknowledge this support.

References

1. H. Weigang, L. Zhiming, L. Dekun, H. Xue, Failure fatigue analysis of high speed train gearbox housing. *Eng. Fail. Anal.* **73**, 57–71 (2017)
2. P. Sungho, K. Seokgoo, C. Joo-Ho, Gear fault diagnosis using transmission error and ensemble empirical mode decomposition. *Mech. Syst. Signal Process.* **108**, 262–275 (2018)
3. P. Kucera, V. Pistek, K. Rehak, A. Prokop, Transmission error analysis of the gearbox, in *Transport Means 2018 Proceedings. Transport Means*, vol. 1 (Kaunas University of Technology, Kaunas, 2018), pp. 705–708
4. D. Bartosova, V. Otipka, K. Rehak, Determination of transmission error in spur gear by numerical approach. *Vibroeng. PROCEDIA* **19**, 284–288 (2018)
5. C. Brecher, C. Lopenhaus, M. Schroers, Analysis of dynamic excitation behavior of two stage spur gearbox. *Procedia CIRP* **62**, 369–374 (2017)
6. A. Prokop, B. Kopeckova, K. Rehak, Gear drive system simulation of input parameters effect on rattle, in *Acoustics and Vibration of Mechanical Structure. Springer Proceedings in Physics*, (Springer, Cham, 2017), pp. 381–388
7. A. Kumar, H. Jaiswal, R. Jain, P.P. Patil, Dynamic vibration characteristics analysis of truck transmission gearbox casing with fixed constraint of vehicle frame based on FEA. *Procedia Eng.* **97**, 1107–1115 (2014)
8. W. Hao, W. Pingbo, L. Fannsong, S. Huailong, X. Kai, Fatigue analysis of the gearbox housing in high-speed trains under wheel polygonization using a multibody dynamics algorithm. *Eng. Fail. Anal.* **100**, 351–364 (2019)

Application of Friction Pendulum Bearings in Multistory Buildings



Irena Gołębiowska and Maciej Dutkiewicz

Abstract In the paper the analysis of selected sliding base isolation bearings is presented. The second part is the example of the experimental results of the frame building equipped with friction pendulum bearing located on the vibration table. The analysis covers the acceleration response of the frame in time domain for shaking table's horizontal excitation movement.

1 Introduction

Seismic and wind loads pose a design and construction challenge for civil engineers. Passive attenuators, along with other methods, enable vibration reduction. Depending on the dynamic characteristics of the structure, as well as the specifics of excitation, the appropriate type of passive isolation systems, and elasticity and damping parameters are selected.

Liquid dampers have found widespread use in the field of passive isolation systems. Interesting conclusions regarding experimental research on this type of dampers were presented by Aydin et al. [1]. Efficiency of passive dampers for different types of civil engineering structures were presented in [2–4].

Passive bearings were presented, among others in [5]. Such isolation systems are used in particular for seismic excitations [6]. The effectiveness of passive bearings is associated with their relatively simple construction. Tsai [7] presented the concept of friction pendulum bearings with finite element formulations, Fenz and Constantinou [8] described the behavior of the double concave friction pendulum bearing, Tsai et al. [9] presented the results of experimental research for multiple friction pendulum bearings. Barone et al. [10] presented the results of their experimental research in the field of spherical friction-based isolation devices. Some development of issues of friction in sliding isolation bearing was performed by Kumar et al. [11].

I. Gołębiowska · M. Dutkiewicz (✉)

Faculty of Civil, Architecture and Environmental Engineering and Architecture, University of Science and Technology in Bydgoszcz, Al. Prof. S. Kaliskiego 7, 85-796 Bydgoszcz, Poland
e-mail: macdut@utp.edu.pl

© Springer Nature Switzerland AG 2021

N. Herisanu and V. Marinca (eds.), *Acoustics and Vibration of Mechanical Structures—AVMS 2019*, Springer Proceedings in Physics 251,
https://doi.org/10.1007/978-3-030-54136-1_46

453

The problem of designing of effective devices to reduce vibration caused by seismic impacts lies in the unique and difficulties in description of the nature of such excitations. Hence, an important role is played by the probabilistic description, in particular the probabilistic approach to excitation variability. Bucher [12] developed the probability-based optimization of friction damping devices.

Isolation bearings are used in engineering structures of various types, e.g., in buildings, bridges, tanks, industrial facilities. Elastomeric and sliding bearings are the two main groups of insulation devices. Rubber used to isolate structures against vibrations from the ground is used in elastomeric bearings, while low rigidity and friction at the joint, mainly between stainless steel and Teflon are the features that characterize sliding bearings. High axial stiffness for transferring vertical loads without excessive deformation, sufficiently low horizontal stiffness, so that the first natural frequency of the isolated structure is significantly lower than the dominant frequency of the expected ground movement, an effective energy dissipation mechanism, contributing to the reduction of excessive horizontal (lateral) displacements seismic isolation against variable permanent load are the features that seismic isolation devices have.

The paper discusses friction pendulum bearings, taking into account the criterion of energy dissipation efficiency in engineering facilities. In addition, the example of the experiment is the valuable enrichment of this review.

2 Friction Pendulum Bearing Supports

The analyzed group of devices includes isolation bearings defined as Pure-Friction (PF) and the Friction Pendulum (FP) bearing. In a PF bearing, two horizontal flat stainless steel plates slide on top of each other. During an earthquake, the structure moves on the upper insulator plate. This type of insulator will not experience resonance frequency. The second isolation device is Friction Pendulum (FP) proposed by Zayas [13].

The base-plate and the slider covered by the composite material are the basic elements of FP bearing, which uses the mechanism of pendulum and the frictional sliding. A restraining rim around the edge of the sliding surface is a solution to limit the displacement (Fig. 1).

There are two design methods using friction pendulum. The P-D effect transfer downward to the structure below the isolation system or upward to the elements of the superstructure.

Soong and Constantinou [14] propose the formula:

$$F = W \left[\frac{x}{R} + \mu \operatorname{sgn}(\dot{x}) \right], \quad (1)$$

where W —isolator's normal force, R —the spherical curvature's radius, x —horizontal displacement of the slider's pivot, \dot{x} —velocity of sliding, μ —coefficient of friction.

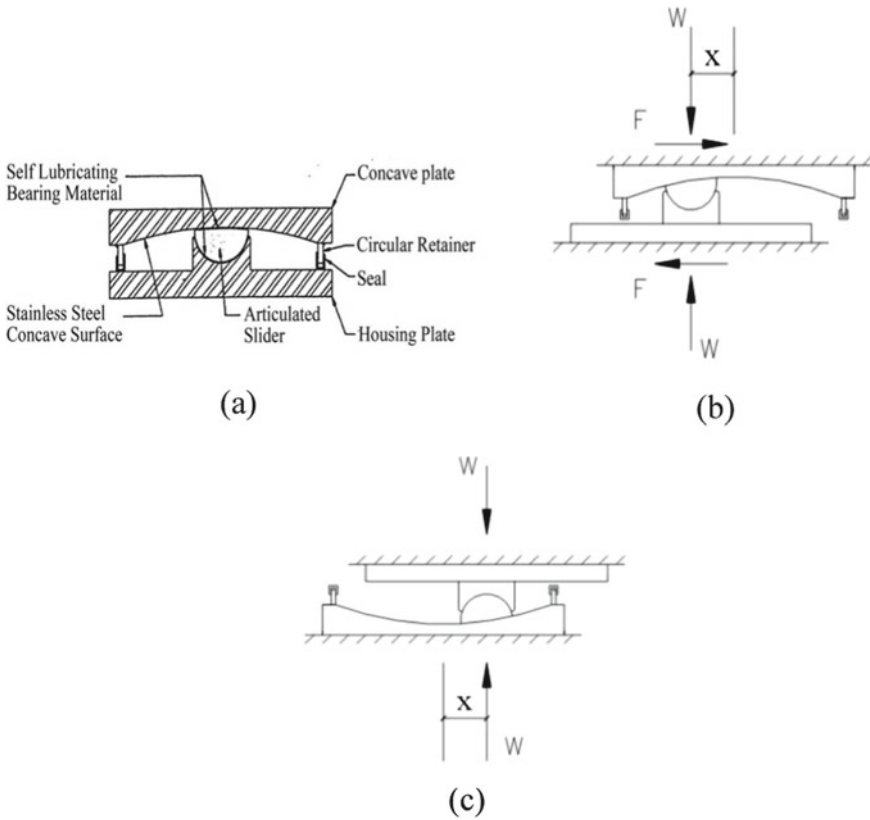


Fig. 1 Friction pendulum system **a** general idea, **b** modeling of FP bearing in upward position, and **c** downward position [13]

An important element of FB is the lateral restoring parameters, such as force, which is provided through spherical shape of the system and stiffness. Hysteretic relationship loop of FP is rigid plastic with post yielding hardening and stick-slip effect at the breakaway as it shown in Fig. 2, for two covering slider materials: polyamide (PA) and polyethylene (PE).

Kumar et al. [11] noticed that the sliding velocity, axial pressure and the temperature on the slip surface have the influence on the sliding friction coefficient as shown in Fig. 3.

In the analysis [11], $\mu = 0.6$ is the coefficient at a bearing pressure $p_o = 10$ MPa when $T_o = 20$ °C is the temperature at the sliding surface. The authors also marked that friction coefficient increases considerably at high speeds and decreases with increase of temperature.

Dynamic excitation is accompanied by the states of predominant periods of ground motions, dangerous from the point of resonance. Increased search for optimal friction bearings prompted the search for adaptive solutions. Depending on the displacement

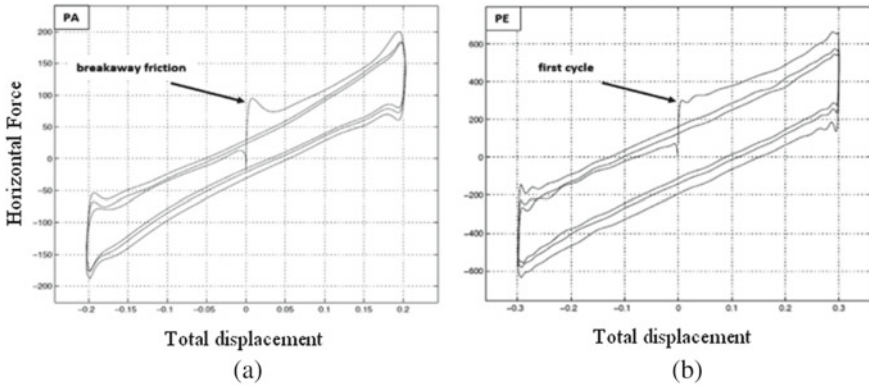


Fig. 2 Force-displacement hysteresis responses for a PA, and b PE based FP bearing [10]

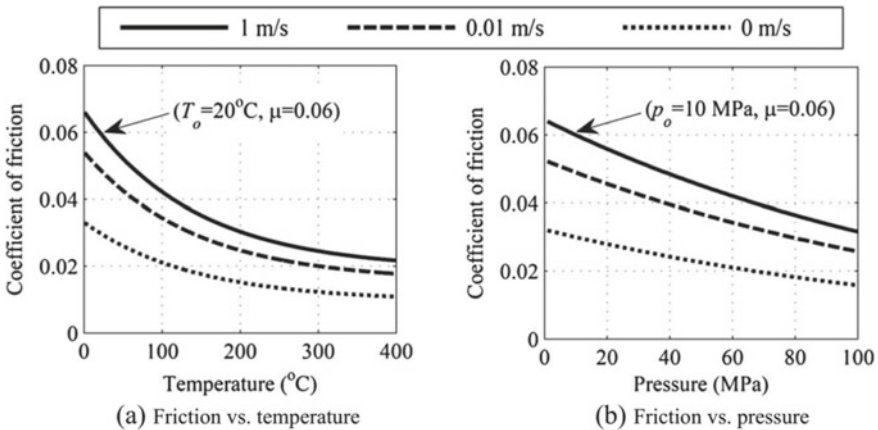


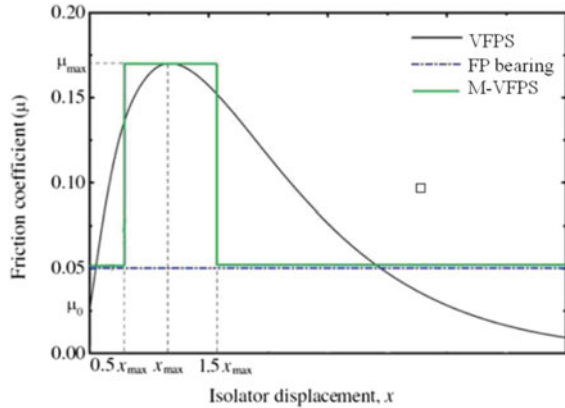
Fig. 3 Variation in the coefficient of sliding friction with sliding velocity a temperature, and b pressure at the sliding surface [11]

level, passive adaptive FP bearings have different hysteretic properties, the example are: sliding isolators with multiple sliding surfaces (SIMSS) [15–17], sliding isolators with variable curvature (SIVC) [18–24], sliding isolators with variable friction (SIVF) [25, 26].

Multi-concave FP bearings are characterized by high efficiency of vibration reduction. This is: double concave friction pendulum (DCFP) bearings, triple concave friction pendulum (TCFP) bearings, and quintuple concave friction pendulum (QCFP) bearings.

Further modifications of FB are proposal of the Variable Friction Pendulum System (VFPS) of Tsai et al. [26] and Shaikhzadeh and Karamoddin who described Modified Variable Friction Pendulum System (m-VFPS) [27, 28]. Comparison of friction coefficients due to isolator displacements is presented in Fig. 4.

Fig. 4 Comparison between friction coefficient of FP bearing, VFPS and M-VFPS [26]



3 Experimental Study

The purpose of this analysis is to present the experimental model of the steel frame equipped with friction pendulum bearings under the dynamical excitation. The response of the frame is measured using the accelerometer attached to the top of the structure. The analysis was performed for different accelerations of lateral excitation, coming from the shaking table.

As seen in Fig. 5, six-story building frame with FPB, which is used for experiment setup, is made of S235JR steel. It was used the following parameters of the system: frame weight 500 gr, each story height 24 cm, frame column steel angle dimensions 2.5×2.5 cm, thickness = 0.1 cm, frame beam steel angle dimensions 2.5×2.5 cm, thickness = 0.1 cm, frame floor dimensions 22×34 cm, dimensions of FPD $8.5 \times 8.5 \times 0.5$ cm, radius R_1 of friction pendulum bearing 350 mm, radius slider R_2 of friction pendulum bearing 10 mm. The shaking table used in this experiment has a compact shape and its dimensions are 40×50 cm and $h = 100$ cm. Shaking table can produce one dimensional horizontal vibrations that can produce desired number and range (1–10 Hz) of frequency and its amplitude changes in between -50 mm to $+50$ mm at maximal range.

National Instruments NI-9172 data acquisition (DAQ) system is applied which combines signal connectors, integrated signal conditioning and converters. DAQ system delivers high accuracy measurements by eliminating error-prone cabling and connectors and reducing the number of components in a measurement system. The LabVIEW software is used to meet the requirements of I/O modules, buses and chassis of hardware system. Two accelerometers, one attached to the table and one to the structure, are connected to the DAQ system.

The measurements were made for 11 steps of excitations which corresponds to the values of accelerations in the range of $\langle 0.1, 2.9 \rangle$ m/s^2 .

In the Fig. 6 accelerations of the shaking table and top of the frame in time domain for selected steps excitation is shown. Sliding surface curvature radius is $R_1 = 0.35$

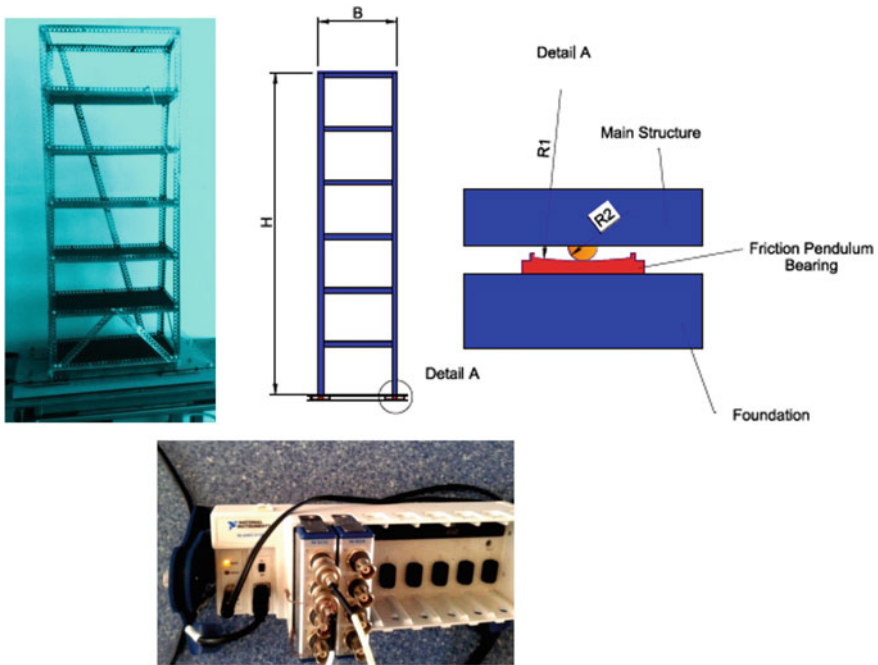


Fig. 5 Analyzed frame with friction pendulum bearing and acquisition system

and friction coefficient is $\mu = 0.12$. Following the measurements, as for the example for the step 5.5, the amplitudes of acceleration increase from the 1.49 m/s^2 for the frame and 2.90 m/s^2 for table.

Figure 7 presents power acceleration spectrum (PAS) for the step 5.5. The highest value of power amplitude spectrum is for frequency 1.8 Hz.

Figure 8 presents summary of PAS of acceleration of top of the frame for steps 0.5–5.5.

Based on the analysis, with the increase of excitation, the frame accelerations increase. In the step excitation range from 0.5 to 2.0, the acceleration increase of table and frame is at the similar level. Significant differences in acceleration increase of table and frame are observed from the step 2.5 and higher.

4 Conclusions

The paper presents the review of the most important friction sliding bearings used in engineering objects exposed to seismic influences, in the context of their effectiveness are presented.

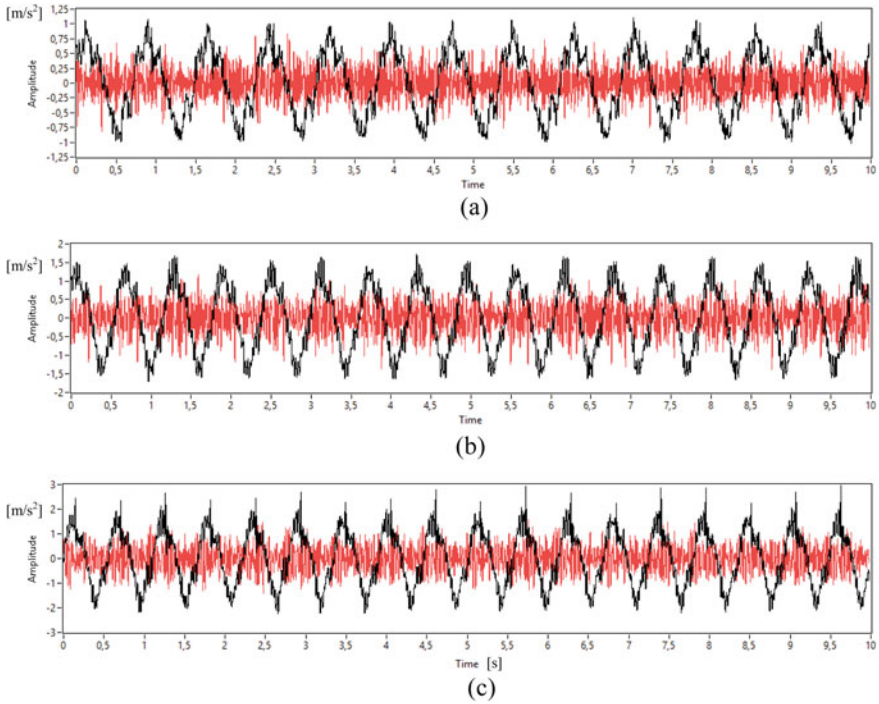


Fig. 6 Acceleration of top of the frame (red line) and the table (black line) in time domain for selected steps of excitations: **a** step 4.5, **b** step 5.0, and **c** step 5.5

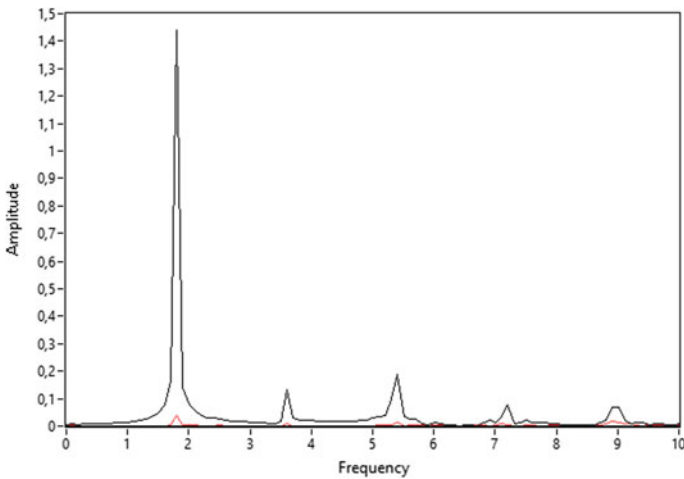


Fig. 7 FFT of acceleration of top of the frame for step 5.5, black line–table, red line–frame

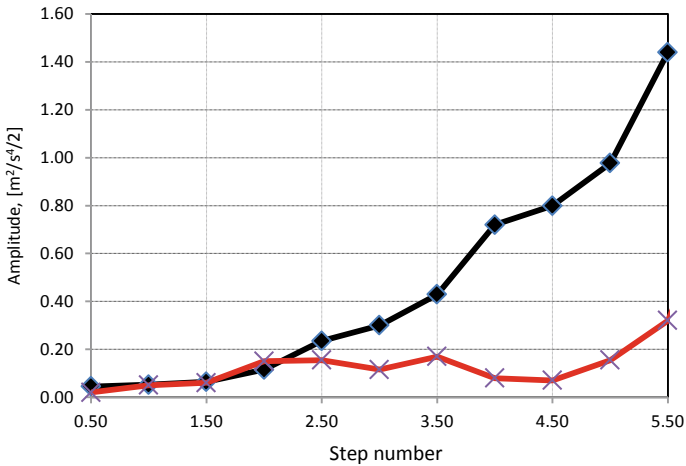


Fig. 8 FFT of acceleration of top of the frame for steps 0.5–5.5, black line–table, red line–frame

The experimental result of the frame building equipped with friction pendulum bearing located on the shaking table was studied. The analysis covers the acceleration response of the frame in time for shaking table's horizontal excitation movement. The high effectiveness of used friction pendulum bearing is confirmed for the fixed parameters of the system.

In the next part of the analysis which is under the preparation, the numerical model of the frame with different friction pendulum bearings will be compared to the results from the laboratory tests and from literature.

References

1. E. Aydin, B. Öztürk, M. Dutkiewicz, H. Çetin, O. Okay, U. Ohancan, Y.E. Şirin, Experiments of tuned liquid damper (TLD) on the reduced shear frame model under harmonic loads, in *EPJ Web of Conferences*, vol. 143 (EDP Sciences, 2017), pp. 02001. WOS:000407743800003
2. E. Aydin, B. Öztürk, M. Dutkiewicz, Optimal passive control of shear buildings, in *Proceedings of 23th International Conference on Engineering Mechanics* (Svratka, Czech Republic, 2017), pp. 98–101. WOS: 000411657600014
3. E. Aydin, B. Öztürk, M. Dutkiewicz, Determination of optimal elastic springs for cantilever beams supported by elastic foundation, in *Proceedings of 24th International Conference on Engineering Mechanics 2018, Web of Knowledge & Scopus, ISI Thomson Reuters* (Svratka, Czech Republic, 2018)
4. E. Aydin, B. Öztürk, M. Dutkiewicz, Analysis of efficiency of passive dampers in multistorey buildings. *J. Sound Vib.* **439**, 17–28 (2019)
5. T.T. Soong, G.F. Dargush, *Passive Energy Dissipation Systems in Structural Engineering* (John & Sons Ltd, Chichester, 1997)
6. R.I. Skinner, W.H. Robinson, G.H. McVerry, *An Introduction to Seismic Isolation* (Wiley, Chichester, England, 1993)

7. C.S. Tsai, Finite element formulations for friction pendulum seismic isolation bearings. *Int. J. Numer. Meth. Eng.* **40**, 29–49 (1997)
8. D.M. Fenz, M.C. Constantinou, Behaviour of the double concave friction pendulum bearing. *Earthquake Eng. Struct. Dyn.* **35**, 1403–1424 (2006)
9. C.S. Tsai, W.S. Chen, T.C. Chiang, B.J. Chen, Component and shaking table tests for full-scale multiple friction pendulum system. *Earthquake Eng. Struct. Dyn.* **35**, 1653–1675 (2006)
10. S. Barone, G.M. Calvi, A. Pavese, Experimental dynamic response of spherical friction-based isolation devices. *J. Earthquake Eng.* (2017)
11. M. Kumar, A.S. Whittaker, M.C. Constantinou, Characterizing friction in sliding isolation bearing. *Earthquake Eng. Struct. Dyn.* (2014)
12. C. Bucher, Probability-based optimization of friction damping devices. *Struct. Saf.* **31**, 500–507 (2009)
13. V.A. Zayas, S.S. Low, S.A. Mahin, The FPS earthquake resisting system experimental report. Tech. Rep. UBC/EERC-87/01 (1987)
14. T.T. Soong, M.C. Constantinou, *Passive and Active Structural Vibration Control in Civil Engineering* (Springer, CISM Courses and Lectures, 1994)
15. D.M. Fenz, M.C. Constantinou, Behavior of the double concave friction pendulum bearing. *Earthquake Eng. Struct. Dyn.* **35**(11), 1403–1424 (2006)
16. D.M. Fenz, M.C. Constantinou, Spherical sliding isolation bearings with adaptive behavior: theory. *Earthquake Eng. Struct. Dyn.* **37**(2), 163–183 (2008)
17. D.M. Fenz, M.C. Constantinou, Modeling triple friction pendulum bearings for response history analysis. *Earthquake Spectra* **24**(4), 1011–1028 (2008)
18. M. Pranesh, R. Sinha, VFPI: an isolation device for a seismic design. *Earthquake Eng. Struct. Dyn.* **29**, 603–627 (2000)
19. A. Krishnamoorthy, Variable curvature pendulum isolator and viscous fluid damper for seismic isolation of structures. *J. Vib. Control* **17**, 1779–1790 (2010)
20. A. Krishnamoorthy, Seismic control of continuous bridges using variable radius friction pendulum systems and viscous fluid dampers. *Int. J. Acoust. Vib.* **20**(1), 24–35 (2015)
21. C.T. Malin, D. Nedelcu, G.R. Gillich, A. Petrica, I. Padurean, Comparison of the performance of friction pendulums with uniform and variable radii. *Vibroeng. PROCEDIA.* **23**, 81–86 (2019) <https://www.jvejournal.com/article/20667/pdf>
22. L.Y. Lu, M.H. Shih, C.Y. Wu, Near fault seismic isolation using sliding bearing with variable curvatures, in *Processing of 13th World Conference on Earthquake Engineering*, Paper No. 3264. 38 (2004)
23. L.Y. Lu, T.Y. Lee, S. Juang, S. Yeh, Polynomial friction pendulum isolators (PFPIs) for building floor isolation: an experimental and theoretical study. *Eng. Struct.* **56**, 970–982 (2013)
24. L.Y. Lu, T.Y. Lee, S.W. Yeh, Theory and experimental study for sliding isolators with variable curvature. *Earthquake Eng. Struct. Dyn.* **2011**(40), 1609–1627 (2011)
25. V.R. Panchal, R.S. Jangid, Variable friction pendulum system for seismic isolation of liquid storage tanks. *Nucl. Eng. Des.* **238**(6), 1304–1315 (2008)
26. C.S. Tsai, T.C. Chiang, B.J. Chen, Finite element formulations and theoretical study for variable curvature friction pendulum system. *Eng. Struct.* **25**, 1719–1730 (2003)
27. A.A. Shaikhzadeh, A Karamoddin, Effectiveness of sliding isolators with variable curvature in near-fault ground motions. *Struct. Des. Tall Spec. Build.* (2015)
28. A.A. Shaikhzadeh, A. Karamoddin, Behavior of sliding isolators with variable friction under near-fault earthquakes, in *7th International Conference on Seismology & Earthquake Engineering* (Tehran, Iran, 2015)

Spectral Element Analysis of Non-stationary Wind Acting on Overhead Transmission Line



Maciej Dutkiewicz and Marcela R. Machado

Abstract In the paper, the issue of vibrations of the transmission line under the impact of non-stationary wind is analysed. Analysis is performed for the ACSR high-voltage transmission line with the span of 213.0 m. Analysis is made for natural and wind excited vibrations. The numerical model is prepared using the spectral element method.

1 Introduction

Non-stationary wind action on structures has the short and transient characteristics so it is difficult to use direct correlation and spectral analysis.

Overhead transmission lines are constantly subjected to variable wind loads which may gradually lead to the impairment of their durability, resulting in the shortened service life.

This is very important to develop the easy and fast methodology for design, taking into consideration all loads and uncertainties acting on the overhead transmission lines. Nowadays, we see the wide development of new materials and solutions to raise the conductivity; but at the same time, we observe that conductors' durability is changed and required the permanent update analysis. Spectral element method seems to be such fast and easy tool which fulfils these requirements.

Many researchers investigate the vibrations of the overhead transmission lines [1–5]. The following cable vibrations occur: aeolian vibrations, galloping and wake-induced vibrations [6–9].

In most cases, galloping is caused by sustained wind of an average and high speed ($V > 15$ m/s), blowing on an asymmetrically loaded (e.g. with ice or wet snow)

M. Dutkiewicz (✉)

Faculty of Civil, Architecture and Environmental Engineering and Architecture, University of Science and Technology in Bydgoszcz, Al. Prof. S. Kaliskiego 7, 85-796 Bydgoszcz, Poland
e-mail: macdut@utp.edu.pl

M. R. Machado

Department of Mechanical Engineering, University of Brasilia, Brasilia 70910-900, Brazil

© Springer Nature Switzerland AG 2021

N. Herisanu and V. Marinca (eds.), *Acoustics and Vibration of Mechanical Structures—AVMS 2019*, Springer Proceedings in Physics 251,
https://doi.org/10.1007/978-3-030-54136-1_47

463

conductor. High amplitudes are observed in the vertical plane, whereas the frequencies depend on the type of a conductor and vibrations [4, 10]. Galloping is a typical instability caused by the coupling of aerodynamic forces which affect the conductor with its vibrations. Conductor vibrations change the wind angle of attack on a periodic basis. The change of the angle of attack results in a change of aerodynamic forces affecting the conductor, which consequently changes the conductor response. The first, simplified criterion (if a single degree-of-freedom system is applied) pertaining to the instability connected with galloping was presented by Den Hartog [11] and developed by other researchers [10]. A precondition for galloping (on the basis of the quasi-steady theory) is the presence of negative aero-elastic damping in the system. A conductor of a circular section cannot gallop due to its geometrical symmetry ($dCL/d\alpha = 0$), unless this section is changed. Icing of a conductor changes its cross section; thus, it leads to its aerodynamic instability [10]. Research works carried out by Den Hartog indicate that the aerodynamic instability is the main reason for the galloping phenomenon. Further research proved that the torsion motion is an integral part of the galloping phenomenon. The effect of a coupled torsion–translational motion plays a crucial role in most cases of progressing galloping [12].

These extremely important phenomena described above have mobilized the authors of the article to look for transmission line vibration solutions using numerical methods. Spectral element method (SEM) proved to be such a method, where the exact dynamic shape functions are used in the solution. The use of SEM is very wide: in composites [13, 14] and in damage detection [15–18].

2 Mathematical Model of Overhead Transmission Line

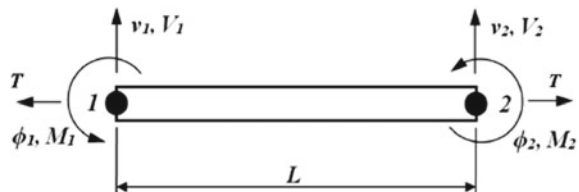
The cable model meets the differential equation presented in the form [19–21]

$$EI \frac{\partial^4 v(x, t)}{\partial x^4} - T \frac{\partial^2 v(x, t)}{\partial x^2} + \rho A \frac{\partial^2 v(x, t)}{\partial t^2} = 0 \tag{1}$$

where ρA —mass per unit length, EI —the uniform bending rigidity, T is tension force, $v(x, t)$ —the cable displacement.

It is applied an elastic two-node element (Fig. 1). Young’s modulus is taken in the form $E = E(1 + i\eta)$, where $i = \sqrt{-1}$ and η are the hysteretic structural loss factor.

Fig. 1 Spectral element



By considering a constant coefficient, a displacement solution can be assumed of the form:

$$v(x, t) = v_0 e^{-i(kx - \omega t)} \quad (2)$$

where v_0 is a amplitude, ω is the frequency and k is the wavenumber.

There are two distinct wave modes in the positive direction (k^2), which is positive-going waves with wavenumbers given as:

$$k_1 = \sqrt{-\frac{T}{2EI} + \sqrt{\left(\frac{T}{2EI}\right)^2 + \frac{\rho A \omega^2}{EI}}} \quad (3)$$

$$k_2 = -\sqrt{-\frac{T}{2EI} - \sqrt{\left(\frac{T}{2EI}\right)^2 + \frac{\rho A \omega^2}{EI}}} \quad (4)$$

The solution for the spectral element subjected to axial load of length L can be expressed in the form:

$$v(x, \omega) = a_1 e^{-ikx} + a_2 e^{-kx} + a_3 e^{-ik(L-x)} + a_4 e^{-k(L-x)} = \mathbf{s}(x, \omega) \mathbf{a} \quad (5)$$

where

$$\mathbf{s}(x, \omega) = \{e^{-ikx}, e^{-kx}, e^{-ik(L-x)}, e^{-k(L-x)}\} \quad (6)$$

$$\mathbf{a}(x, \omega) = \{a_1, a_2, a_3, a_4\}^T \quad (7)$$

The spectral nodal displacements and slopes of the beam element are related to the displacement field at node 1 ($x = 0$) and node 2 ($x = L$), by

$$\mathbf{d} = \begin{bmatrix} v_1 \\ \phi_2 \\ v_2 \\ \phi_2 \end{bmatrix} = \begin{bmatrix} v(0) \\ v'(0) \\ v(L) \\ v'(L) \end{bmatrix} \quad (8)$$

Substituting (5) into the right-hand side of (8) and written in a matrix form gives

$$\mathbf{d} = \begin{bmatrix} s(0, \omega) \\ s'(0, \omega) \\ s(L, \omega) \\ s'(L, \omega) \end{bmatrix} \mathbf{a} = \mathbf{G}(\omega) \mathbf{a} \quad (9)$$

where

$$\mathbf{G}(\omega) = \begin{bmatrix} 1 & 1 & e^{-ikL} & e^{-kL} \\ -ik & -k & ike^{-ikL} & ke^{-kL} \\ e^{-ikL} & e^{-kL} & 1 & 1 \\ -ike^{-ikL} & -ke^{-kL} & ik & k \end{bmatrix} \quad (10)$$

The dynamic stiffness matrix for the spectral beam element under axial tension can be determined as:

$$\mathbf{S}(\omega) = \mathbf{K}(\omega) - \omega^2 \mathbf{M}(\omega) \quad (11)$$

where

$$\mathbf{K}(\omega) = \int_0^L (EI \mathbf{g}''(x)^T \mathbf{g}''(x) + T \mathbf{g}'(x)^T \mathbf{g}'(x)) dx \quad (12)$$

$$\mathbf{M}(\omega) = \rho A \int_0^L \mathbf{g}(x)^T \mathbf{g}(x) dx \quad (13)$$

where ' express the spatial partial derivative. By solving the integral, the dynamic stiffness matrix is:

$$\mathbf{S}(\omega) = \frac{EI}{\Delta} \begin{bmatrix} s_{11} & s_{12} & s_{13} & s_{14} \\ & s_{22} & s_{23} & s_{24} \\ & & s_{33} & s_{34} \\ \text{sym} & & & s_{44} \end{bmatrix} \quad (14)$$

where $\Delta = \cos(kL) \cosh(kL) - 1$ and the components of element matrix (14) are given as

$$s_{11} = -k^3 (\cos(kL) \sinh(kL) + \sin(kL) \cosh(kL))$$

$$s_{12} = -k^2 \sin(kL) \sinh(kL)$$

$$s_{13} = k^3 (\sin(kL) + \sinh(kL))$$

$$s_{14} = k^2 (\cos(kL) - \cosh(kL))$$

$$s_{22} = k (\cos(kL) \sinh(kL) - \sin(kL) \cosh(kL))$$

$$s_{23} = k^2 (\cosh(kL) - \cos(kL))$$

$$s_{24} = k (\sin(kL) - \sinh(kL))$$

$$s_{33} = -k^3 (\cos(kL) \sinh(kL) + \sin(kL) \cosh(kL))$$

$$s_{34} = k^2 \sin(kL) \sinh(kL)$$

$$s_{44} = k(\cos(kL) \sinh(kL) - \sin(kL) \cosh(kL)) \quad (15)$$

Using SEM for beam elements, very accurate results are obtained [22–24]. As in FEM [25], local matrices form a global matrix.

3 Numerical Analysis

Experiments were performed in situ, during the maintenance period of the transmission line. The conductor was aluminium conductor steel reinforced type (ACSR), and according to technical data sheet, it had weight per unit length $m = 0.707 \text{ kg/m}$ and nominal diameter $D = 22 \text{ mm}$. The span length of the conductor is 213 m. The elasticity module was $E = 74 \text{ GPa}$ and density $\rho = 2700 \text{ kg/m}^3$.

3.1 Natural Vibrations

On the basis of the formulas presented in (11–15), it is possible to obtain the frequency response function (FRF) of the overhead transmission conductor. For the numerical tests, it is assumed a pinned–pinned boundary condition.

Once, the structure is excited with a unitary force we can expect that the resonance picks are close to the natural frequency of the system. Figure 2a, b shows the FRF for simulations measured at point $L_1 = 33 \text{ m}$ from the node. For the purpose of the numerical simulation, it is assumed the circular area of the conductor $A = 262 \text{ mm}^2$ and tension force of $T = 100 \text{ kN}$. The zoom image at 0–20 Hz frequency band to better visualization of the firsts resonance pick is shown in Fig. 2b. Time history natural vibration is shown in Fig. 2c.

3.2 Wind Vibrations

In the spectral analysis, the wind force acting on the overhead transmission line is determined by the expression:

$$F = \frac{1}{2} \rho V^2 A_{\text{ref}} C \quad (16)$$

where $\rho = 1.25 \text{ kg/m}^3$, V is the wind speed, A_{ref} is the reference area of the transmission line (diameter \times length), C is the aerodynamic coefficient, equal to 2, according to Eurocode 1: Wind actions on structures, EN 1991-1-4 [26]. The wind speed signal, numerically generated with maximal amplitudes measured in the laboratory tests performed in the wind tunnel, is shown in Fig. 3.

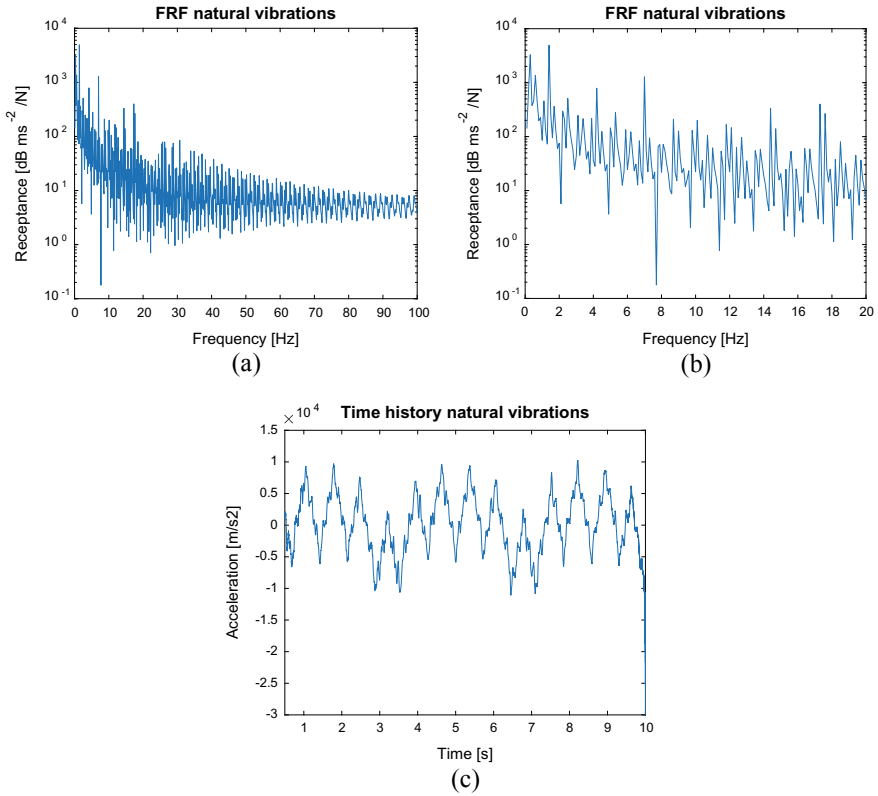
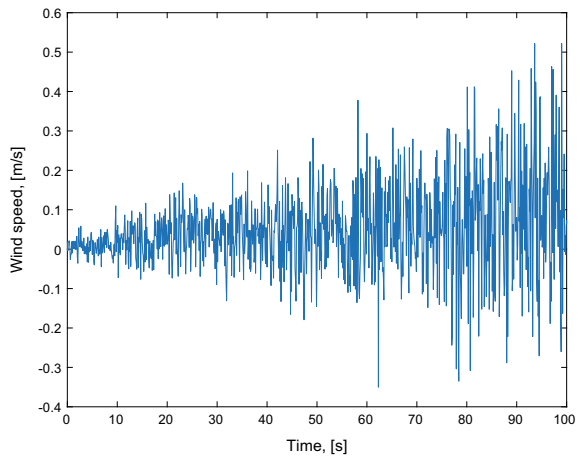


Fig. 2 FRF and time history natural vibrations, **a** FRF from simulation for $A = 262 \text{ mm}^2$, tension force $T = 100 \text{ kN}$, **b** zoom image in 0–20 Hz frequency band, **c** time history vibrations in the range from 0 to 10 s

Fig. 3 Non-stationary wind speed signal used for simulation



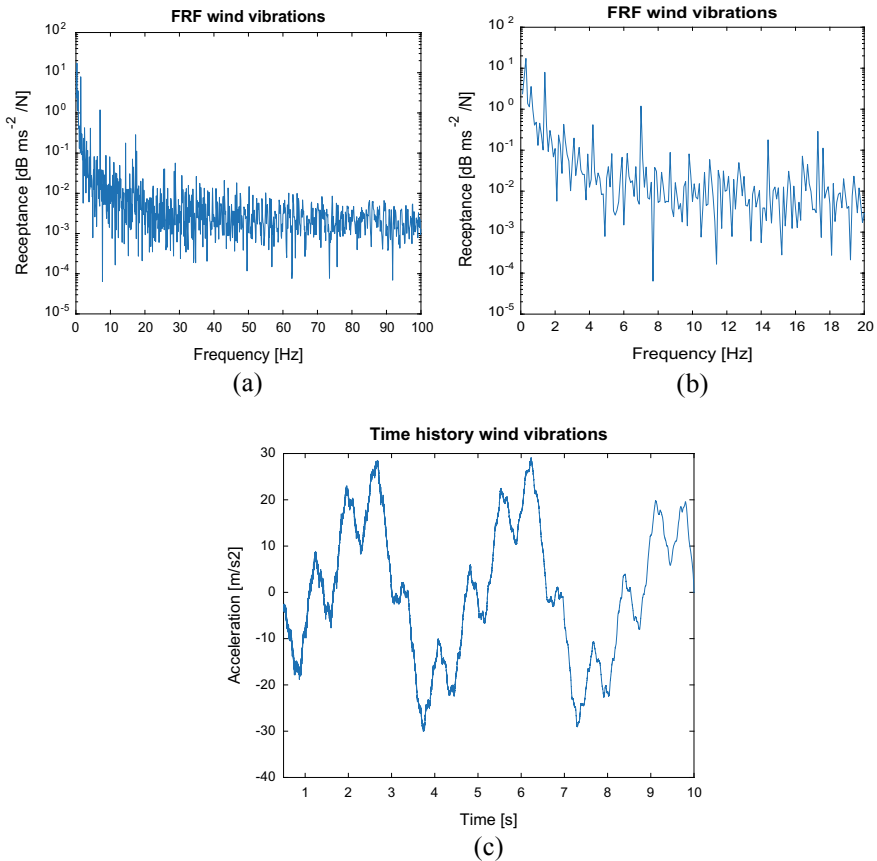


Fig. 4 FRF and time history forced vibrations, **a** FRF from simulation for $A = 262 \text{ mm}^2$, tension force $T = 100 \text{ kN}$, **b** zoom image in 0–20 Hz frequency band, **c** time history vibrations in the range from 0 to 10 s

Figure 4a, b shows the FRF for non-stationary wind excitation. The zoom image at 0–20 Hz frequency band to better visualization of the first resonance peak is shown in Fig. 4b. Time history forced vibration is shown in Fig. 4c.

4 Conclusions

In the paper, the vibrations of the power transmission line under the non-stationary wind with application of spectral method are performed. Simulations were carried out for ACSR high-voltage transmission line with the span of 213.0 m.

In the spectral model, for parameter of stiffness, damping and tension force, the system response was analysed. The next aspect constituting the purpose of this

article was to present the wide possibilities of modelling and simulation of slender conductors using the spectral element method.

In the literature, there are not too many studies on modern constructions of high-voltage transmission lines under real working conditions. It is worth noting that the presented results bring closer the producers and users of power transmission lines for the application of more durable cables than those currently used and more resistant to fatigue damage being the main cause of cable breakages and transmission infrastructure.

References

1. M. Dutkiewicz, Experimental measurements of dynamical wind load acting on the overhead transmission line, in *Anul XXIV*, vol. 1, ISSN 1453 – 7397, pp. 88–100
2. J. Vecchiarelli, I.G. Curie, D.G. Havard, Computational analysis of aeolian conductor vibration with a stockbridge-type damper. *J. Fluids Struct.* **14**, 489–509 (2000)
3. S. Meynen, H. Verma, P. Hagedorn, M. Schäfer, On the numerical simulation of vortex-induced vibrations of oscillating conductors. *J. Fluids Struct.* **21**(1), 41–48 (2005)
4. I. Gołębiowska, M. Dutkiewicz, B. Usewicz, Methods of damping of overhead transmission lines. *TTS* **12**(5), 2544–2548 (2015)
5. H.Q. Wang, J.C. Miao, J.H. Luo, F. Huang, L.G. Wang, The free vibration of long-span transmission line conductors with dampers. *J. Sound Vibr.* **208**(4), 501 (1997)
6. I. Gołębiowska, M. Dutkiewicz, The effectiveness of vibration damper attached to the cable due to wind action, in *International Conference Experimental Fluid Mechanics*, pp. 209–213, Czech Republic (2016)
7. M. Dutkiewicz, Interaction of bridge cables and wake behind in the vortex induced vibrations, in *14th International Conference Dynamical Systems—Theory and Applications*, Łódź, Poland (2017)
8. I. Gołębiowska, M. Dutkiewicz, Vortex induced vibration and wind flow around bridge cables, in *Proceedings of 14th International Conference on Acoustics and Vibration of Mechanical Structures*, Springer Proceedings in Physics, pp. 307–314, Timisoara, Romania (2017)
9. I. Gołębiowska, M. Dutkiewicz, Analysis of wind flow around the bridge cable, in *Proceedings of 2th International Symposium on World Multidisciplinary Civil Engineering, Architecture and Urban Planning*, IOP Conf. Series: Materials Science and Engineering, vol. 245, p. 032066, Prague, Czech Republic (2017)
10. I. Gołębiowska, M. Dutkiewicz, Galloping of overhead power lines conductors, in *Proceedings of 24th International Conference on Engineering Mechanics*, pp. 257–260, Svratka, Czech Republic (2018)
11. J.P. Den Hartog, Transmission line vibration due to sleet. *Trans. Am. Inst. Electr. Eng.* **51**(4), 1074–1076 (1932)
12. A. Luongo, D. Zulli, G. Piccardo, On the effect of twist angle on nonlinear galloping of suspended cables. *Comput. Struct.* **87**(15–16), 1003–1014 (2009)
13. U. Lee, *Spectral Element Method in Structural Dynamics* (Wiley, Singapore, 2009)
14. S. Gopalakrishnan, A. Chakraborty, D.R. Mahapatra, (2007): *Spectral Finite Element Method* (Springer Verlag, New York, 2007)
15. A.T. Fabro, T.G. Ritto, R. Sampaio, J.R.F. Arruda, Stochastic analysis of a cracked rod modeled via the spectral element method. *Mech. Res. Commun.* **37**, 326–331 (2010)
16. E.B. Flynn, M. Todd, J. Croxford, B. Drinkwater, P. Wilcox, Enhanced detection through low order stochastic modeling for guided-wave structural health monitoring. *Struct. Health Monit.* **1**, 1–12 (2011)

17. M.R. Machado, J. Santos, Reliability analysis of damaged beam spectral element with parameter uncertainties, in *Shock and Vibration* (2015)
18. M. Machado, S. Adhikari, J. Santos, A spectral approach for damage quantification in stochastic dynamic systems. *Mech. Syst. Signal Process.* **88**, 253–278 (2017)
19. R. Clough, J. Penzien, *Dynamics of Structures* (McGraw Hill, New York, 1993)
20. B.Y.J. Yu, M. Soliman, Estimation of cable tension force independent of complex boundary conditions. *ASCE J. Eng. Mech.* **60**, 1–8 (2014)
21. S.S. Rao, *Mechanical Vibration* (Person Prentice-Hall, 2008)
22. J.F. Doyle, *Wave Propagation in Structures: Spectral Analysis Using Fast Discrete Fourier Transforms*, 2nd edn., Mechanical engineering (Springer New York, Inc., New York, 1997)
23. M. Dutkiewicz, M.R. Machado, Spectral approach in vibrations of overhead transmission lines. *IOP Conf. Ser. Mater. Sci. Eng.* **471**, 052029 (2019). <https://doi.org/10.1088/1757-899x/471/5/052029>
24. M. Dutkiewicz, M.R. Machado, Dynamical response of overhead transmission line in turbulent wind flow with application of the spectral element method. *IOP Conf. Ser. Mater. Sci. Eng.* **471**, 052031 (2019). <https://doi.org/10.1088/1757-899x/471/5/052031>
25. O.C. Zienkiewicz, R.L. Taylor, *The Finite Element Method*, 4th edn. (McGraw-Hill, London, 1991)
26. Eurocode 1: Wind actions on structures, EN 1991-1-4

Composed Isolation System Concept for Vibration Effects Mitigation on Bridge Structures



Fanel Scheaua

Abstract A bridge structure represents an important infrastructure component capable of withstanding considerable efforts from traffic, wind, or seismic actions. To meet the stability requirements, these structures are designed to cope with the most unfavorable static and dynamic loading situations. At present, isolation solutions are available for these structures types by adding auxiliary mechanical systems to the bridge structure base so that the structure's response is modified when considerable external forces requesting the resistance structure occur. These systems are considered as isolation, and energy dissipation devices being increasingly used in building practice at present. In this paper, a composed isolation system is presented that combines the insulator role of pendulum sliding bearing with the dissipation role of viscous fluid systems. For better isolation results of the composed system, elastomeric elements have been added to the base of the sliding bearing so that these elements have the ability to attenuate vibrations from different dynamic actions. There are presented modeling elements and results of numerical analyzes made for the pendulum sliding isolating system model. By combining the action of the composite system elements, a complete insulation of a bridge structure can be achieved against the effects of intense and varied vibratory actions having advantage over the use of a single type of protective system meant to isolate the bridge structure.

1 Introduction

The use of dampers against forced vibration actions acting on buildings is current all over the world today. Anchor protection systems are based on specially designed mechanical devices that have the possibility to enter into operation when an earthquake occurs and to protect the building against structural degradation or collapse.

F. Scheaua (✉)

"Dunarea de Jos" University of Galati, Engineering and Agronomy Faculty of Braila, MECMET Research Center, Galati, Romania
e-mail: fanel.scheaua@ugal.ro

© Springer Nature Switzerland AG 2021

N. Herisanu and V. Marinca (eds.), *Acoustics and Vibration of Mechanical Structures—AVMS 2019*, Springer Proceedings in Physics 251,
https://doi.org/10.1007/978-3-030-54136-1_48

473

Depending on the constructive principle, insulation or energy dissipation systems may be used at structures in order to reduce the efforts vertical transfer from the ground foundation to the superstructure that must remain stable during an earthquake, or to consume an energy amount that is induced into the structure by seismic movement.

Insulation systems positioned at the base of the structure (between the foundation and the superstructure) are considered as base insulation systems or dissipative systems that are typically positioned between two distinct structural frames in order to minimize relative displacements between them when a seismic motion occurs.

A composite insulation and dissipation system are presented for use in bridges or viaducts structural isolation against the effects of seismic action.

It is a constructive solution that combines the isolation effect of the pendulum systems that use the sliding movement positioned on a set of elastomeric elements.

The viscous fluid anchor system is additionally used for achieving superstructure protection for dangerous displacements that would exceed the sliding bearings limit, thereby endangering the superstructure stability [1, 2].

2 Constructive Details for the Composed Isolation Model Assembly

Ensuring an improved behavior for a bridge structure during seismic movements is a major requirement and must be taken into consideration the conditions in which the efforts are transmitted vertically to the superstructure during the ground seismic motion.

It is necessary to partially disconnect the superstructure from the foundation so that the foundation is able to move with the ground while the superstructure remains in a relative equilibrium position.

In order to achieve this, a base insulation system is installed between the two structural elements (foundation and superstructure).

Due to the fact that the base insulation system introduces freedom of movement of the superstructure; over many moving directions, there is the danger that at a certain point in time when a high magnitude earthquake occurs, the superstructure tends to overcome the constructive limit of the isolation system.

The solution for preventing this danger is represented by the use of the viscous fluid dissipative system as anchor device ensuring the limiting of relative displacements between the two structural elements of the bridge (foundation and superstructure) and to complement the action of the pendulum insulation system at the structure base [3].

The composed seismic protection system is made up of sliding pendulum system supported on elastomeric material and viscous fluid dissipative systems used to limit dangerous displacements on supports up to the breaking limit of the isolation system.

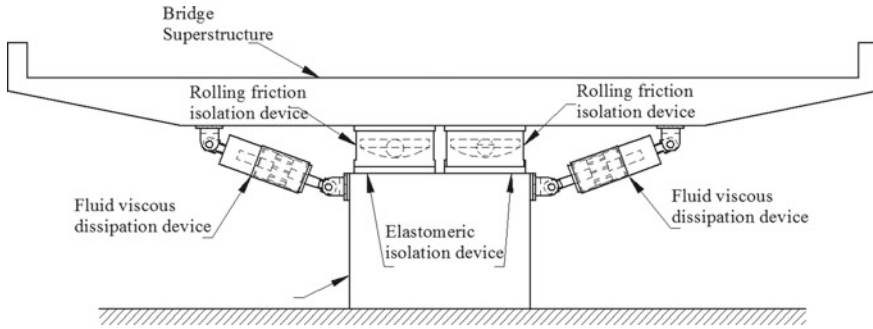


Fig. 1 Schematically representation of composed isolation system on a bridge structure

The schematic representation of the composed isolation system assembly on a bridge structure type is shown in Fig. 1.

Due to the disconnection made by means of composed isolation system, the foundation can move together with the ground while the superstructure has a different vibration period that protects it from the ground acceleration amplitudes.

The insulator system allows movement up to the limit of the sliding bearing and the elastic limit of the elastomeric system.

The displacements above this value are limited by the hydraulic dissipative system [4].

3 Modeling Aspects for the Pendulum Rolling Isolation System

The pendulum insulation system has concave geometry on the main sliding surface, thus allowing relative displacement between the two structural elements where it is mounted due to the activated degrees of freedom.

The translation movement in the plane is combined with a vertical lift, providing a significant energy consumption required for lifting the superstructure, as well as rotations that can occur simultaneously.

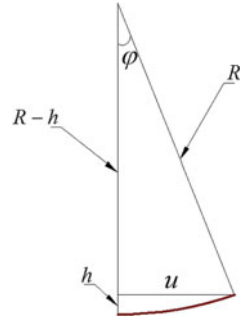
The mathematical modeling of the insulating pendulum supports is made taking into account the radius of curvature of the sliding surface and the displacements that may occur during the bearing operation.

The motion components are highlighted in Fig. 2 [5].

An imposed displacement (u) corresponds an angle (ϕ), as well as a vertical elevation (h), from where the relations corresponding to the triangle formed by the main rolling surface radius (R) and displacement (u) can be written [5]:

$$\sin \phi = \frac{u}{R}; \quad \cos \phi = \frac{R - h}{R} \tag{1}$$

Fig. 2 Simplified schematic representation of motion components on supports



$$R^2 = u^2 + (R - h)^2 \tag{2}$$

$$h^2 - 2Rh + u^2 = 0 \tag{3}$$

The accepted relation from the geometric conditions for vertical elevation (h) is the following [5]:

$$h = R - \sqrt{R^2 - u^2} \tag{4}$$

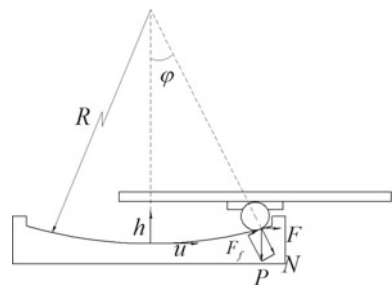
The simplified schematic presentation as well as the physical modeling of the spherical sliding system functioning based on the dry friction force (Coulomb) is shown in Fig. 3.

Physical modeling describing the operation of the spherical rolling pendulum support is performed and the relations describing the forces equilibrium involved in the operation of the friction insulating system are as follows [5]:

$$\begin{aligned} P - N \cos \varphi + F_f \sin \varphi &= 0 \\ F - N \sin \varphi - F_f \cos \varphi &= 0 \end{aligned} \tag{5}$$

By multiplying the two equations with $(-\sin \varphi)$ and $(\cos \varphi)$, respectively, are obtained the following equations:

Fig. 3 Physical modeling of the spherical rolling isolation support operation



$$\begin{aligned}
 -P \sin \varphi + N \sin \varphi \cos \varphi - F_f \sin^2 \varphi &= 0 \\
 F \cos \varphi - N \sin \varphi \cos \varphi - F_f \cos^2 \varphi &= 0
 \end{aligned}
 \tag{6}$$

The equations presented are relation forms between the forces involved in the physical modeling of the insulating support system, and the meaning of the used terms is the following:

P —static load on the support;

N —the normal load on the support;

F_f —the friction force;

φ —the angle resulting after the movement on the concave surface.

The nonlinear form of the equation describing the equilibrium of the forces involved in the operation of the sliding friction bearing supports on the concave surface is as follows [5]:

$$-P \sin \varphi + F \cos \varphi - F_f (\sin^2 \varphi + \cos^2 \varphi) = 0
 \tag{7}$$

Because earthquakes are unpredictable events, both in magnitude and propagation directions, insulation systems must be designed to achieve isolation from vibrations that come from many directions.

The rolling surface geometry ensures freedom of movement in any direction in the plane for translation as well as for rotations.

Pendulum isolation systems behave very well under a wide variety of seismic loads and are very effective in reducing accelerations transmitted to superstructures without inducing large displacements.

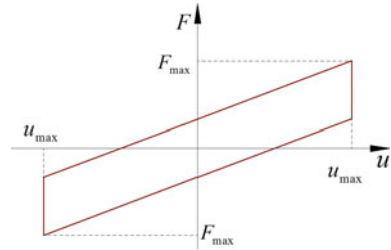
The use of these solutions for seismic isolation of building structures leads to an increase of the structure's flexibility in the horizontal plane, in order to increase the vibration period, so that the acceleration transmitted to the structure is considerably reduced.

Comparing the variations of the displacements and the forces acting on the structure, it is certain that with the change of the vibration period, an increase in the displacements at the base corresponds to a decrease of the forces acting on the structure.

The hysterical behavior of the dry friction bearings on the spherical surface is presented in Fig. 4. On the force–displacement diagram can be observed that up to a force limit value, there is no displacement and when this limit is exceeded, the movement begins on the support. The motion resistance increases progressively due to the geometry of the rolling surface that also allows the structure to return to its original position after the seismic action has passed.

The concave surface pendulum insulation system can withstand a relatively rigid superstructure, is effective for a large range of input frequencies from potential earthquakes, and can transmit a force described by the equation [5]:

Fig. 4 Force–displacement diagram for the pendulum insulation system



$$F = \frac{P}{R \cos \varphi} \cdot u + \frac{F_f}{\cos \varphi} \tag{8}$$

where

- R —the concave surface radius;
- u —displacement.

When there are small displacements on the supports, the equation of the lateral force becomes [5]:

$$F = \frac{P}{R} \cdot u + \mu \cdot P \cdot \text{sgn}(\dot{u}) \tag{9}$$

where

- μ —the coefficient of friction between the two surfaces;
- u —rolling velocity.

It should be noted that the normal load on the support consists of static load (P) correlated with the effect of the vertical acceleration of the foundation ground (\ddot{u}_v), as well as the additional seismic load provided by the twisting moment (p_s) [5]:

$$N = P \left(1 + \frac{\ddot{u}_v}{g} + \frac{p_s}{P} \right) \tag{10}$$

The sliding surface radius is the essential parameter in the operation of friction bearings and its choice influences the operating efficiency of the insulating system.

Also, the friction coefficient between the two surfaces in contact may influence the behavior of the insulating system and the insulated structure.

The isolation system is based on the dry friction force between the components surface in contact and develops a return force during the rolling motion on the bearing according to the surface geometry, and the vibration period can be described by the relation [5]:

$$T = 2\pi \sqrt{\frac{R}{g}} \tag{11}$$

The case of the free movement on the supports can be written in the relation for the effective vibration period (T_{ef}) based on the relation obtained for the effective stiffness as follows [5]:

$$T_{ef} = 2\pi \sqrt{\frac{P}{k_{ef} \cdot g}} \tag{12}$$

$$T_{ef} = 2\pi \sqrt{\frac{P}{P(\frac{1}{R} + \frac{\mu}{u}) \cdot g}} = 2\pi \sqrt{\frac{R \cdot u}{(u + \mu \cdot R) \cdot g}} \tag{13}$$

4 Numerical Analysis on Pendulum System Parameter Operation

Aiming to highlight the operating characteristics of the pendulum isolation system, two cases were considered having specific values of the key parameters represented by the static load on the supports, the rolling surface radius of curvature and the friction coefficient between the rolling piece and the concave surface. The data are presented in Table 1 for both cases.

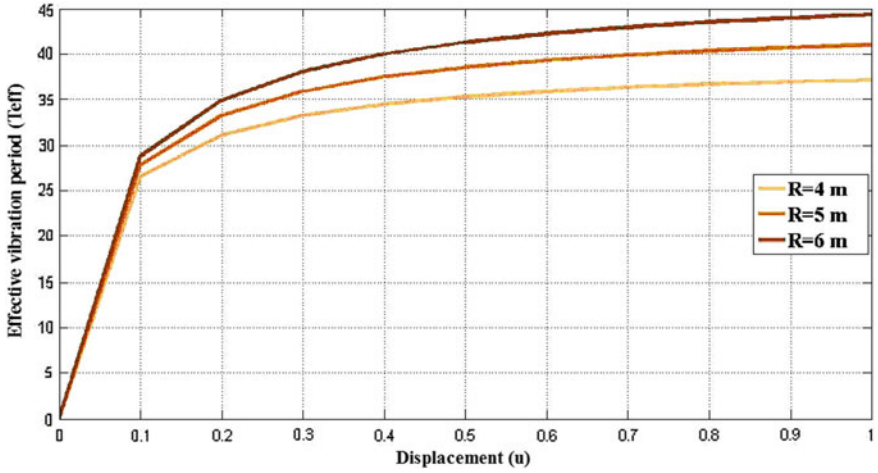
The graphical representation of the effective vibration period based on the displacement on the supports for the two cases is made based on the values considered for the calculation, and the case diagrams are shown in Fig. 5 [5].

By analyzing the diagrams shown in Fig. 5 regarding the effective vibration period depending on the displacement on the supports, it can be pointed out that for a higher value of the rolling surface radius a higher value is obtained for the vibration period of the insulating system.

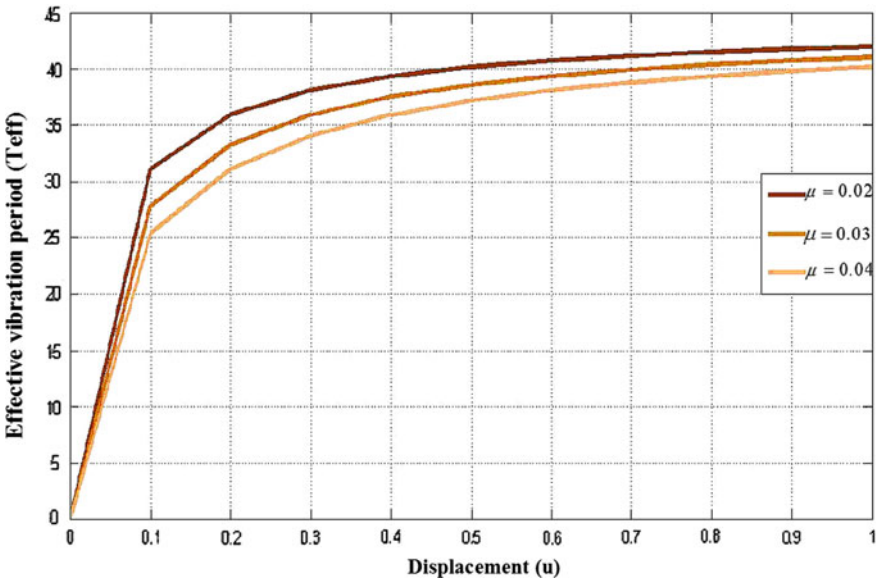
Also for the friction coefficient values used in the calculation, the effective vibration period is higher as the value for the friction coefficient between the contact surfaces being smaller.

Table 1 Values of parameters used in the analysis of the spherical sliding bearing support

Case number	Static load (P) (kN)	Radius of curvature (R) (m)	Friction coefficient (μ)
1.	200	4	0.02
		5	
		6	
2.	400	5	0.02
			0.03
			0.04



(a) Effective vibration period function of displacement by changing the radius of curvature of the main sliding surface - (case 1)



(b) Effective vibration period function of displacement by changing the friction coefficient at the main sliding surface – (case 2)

Fig. 5 Representation of the effective vibration period for the rolling pendulum isolation system

The effective damping for a specific displacement (u) on the support is described by the relation [5]:

$$A_{ef} = \frac{E_{dis}}{4\pi E_c} = \frac{2\mu R}{\pi(\mu R + u)} \quad (14)$$

Based on the corresponding values for the two analyzed cases, the graphical representations of the effective damping obtained by the movement on the supports are realized, as shown in Fig. 6 [5].

The maximum effective damping values are recorded for the higher radius of curvature values of the rolling concave surface, but also for the high frictional coefficient values between the two surfaces in contact.

5 Conclusion

A model of an insulating system that also has energy dissipative properties is presented in this paper which can be mounted on the bridge or viaduct construction structures.

It is a composed system having in composition rolling pendulum bearings utilizing the rolling motion of a spherical piece on a concave surface whose insulating action is combined with the energy dissipation action of a hydraulic system operating with viscous fluid.

By mounting at the insulated structure, the composite system disconnects the structural elements represented by the foundation and the superstructure, allowing the foundation to move along with the terrain required by the seismic shock wave, while the superstructure tends to maintain the inertial equilibrium.

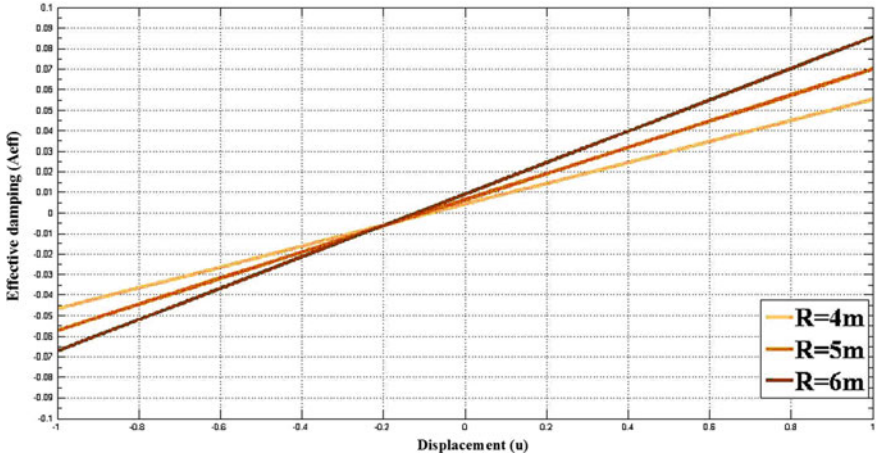
Due to an earthquake, displacements on the supports occur, which can be both translations in different directions, as well as rotations.

The concave shape of the sliding surface ensures the displacements and also the return to the initial position according to superstructure own weight.

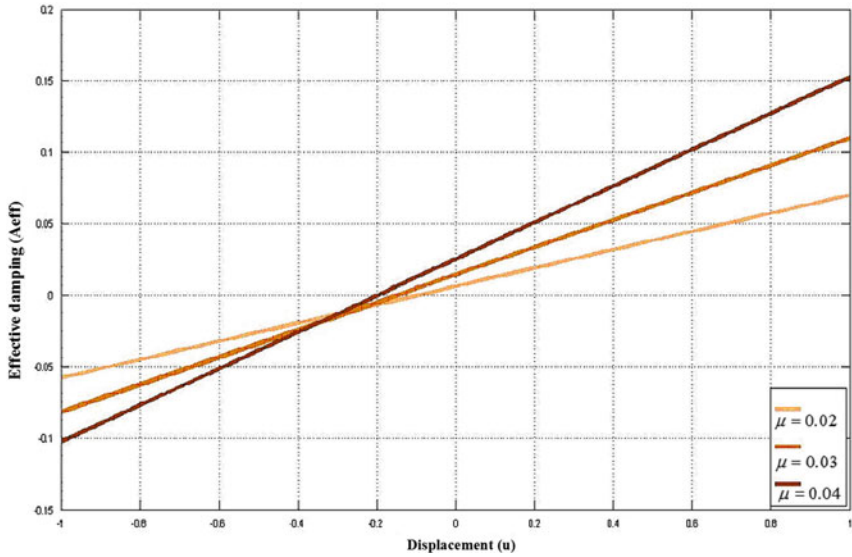
This composite system model can be used to isolate bridge structures, viaducts, as well as not very high buildings.

In the event of a severe earthquake, the structure can reach the upper boundary limit of the movement on the supports and there is the danger of support destruction.

To avoid this undesirable situation, the configuration of the isolator system has been modified by adding viscous fluid dissipative systems in order to limit dangerous displacements and providing anchoring points that add additional damping to the insulator assembly.



(a) Effective damping function of displacement by changing the radius of the main sliding surface - (case 1)



(b) Effective damping function of displacement with change of friction coefficient at main rolling surface - (case 2)

Fig. 6 Representation of effective damping function of displacement for the pendulum insulation system

References

1. G. Axinti, A.S. Axinti, *Acționări hidraulice și pneumatice*, vol. III (Editura Tehnica-Info, Chișinău, 2009)
2. S. Nastac, Working characteristics of the special isolation devices against vibratory actions, in *The Annals of Dunarea de Jos University of Galati, Fascicle XIV Mechanical Engineering* (Galati, 2007). ISSN 1224-5615
3. F.D. Scheaua, Special pattern of hydraulic dissipation system used for isolation of bridges against earthquakes, in *Analele Universității “Eftimie Murgu” Reșița, anul XXIV, No. 1, Reșița* (2017). ISSN 1453-7397
4. F.D. Scheaua, Description of a composed seismic isolation system for bridge structures, in *Analele Universității “Eftimie Murgu” anul XXII, No. 2, Reșița* (2015) ISSN 1453-7397
5. F.D. Scheaua, *Analiza comportării sistemelor de disipare cu frecare uscată la acțiuni dinamice*, PhD Thesis Dunarea de Jos University of Galati, Galati, 2013

Research of Acoustic Metamaterials at the University of Szeged, Faculty of Engineering



Péter Szuchy

Abstract Protection against dangerous and harmful vibration is an urgent problem all around the world. Considerable efforts are in progress for researching and developing acoustic metamaterials. One of these acoustic materials' working principles is the mass-in-mass subsystem that is an improved version of the 2-degree-of-Freedom system of dynamic reduction of vibration. The main goal of this paper is to introduce the actualities of practical research work on this field of the University of Szeged, Faculty of Engineering. First a short review of the theory is summarized, presenting effective mass, differences between linear and non-linear spring characteristics, results of rotating vector solution. The paper highlights the author's theory of the 5-degree-of-freedom subsystem of the "wall-paper"—like acoustic material. Then it shows the research instruments with the experimental system. It reveals the gap between the theory and the research results and features the present problems of the research, bringing into focus the practical side of it. It shortly introduces the used simulation software that reduces the number of the experiments. The other goal of this paper is to display the present state of the author's last year began PhD work and the planned further steps.

1 Introduction of the Theory

Significant part of acoustic vibrations has harmful impact, either it is a large energy vibration, like an earthquake, or a small one like a vibration in a car. However the most frequently occurring dangerous vibration is the noise that surrounds us almost all day. Its harmful effect in milder case can be only tiredness, stress, but in increased case it can bring high blood pressure, indigestion, or it can lead even to hearing loss. One method of the protection against noise is putting insulation between the source and the receiver, but the mass of it multiplied exponentially by increasing the noise-insulating ability. For example to improve the efficiency with 30 dB, the mass

P. Szuchy (✉)

Faculty of Engineering, University of Szeged, Mars Sqr. 7, 6724 Szeged, Hungary
e-mail: szpeter@mk.u-szeged.hu

© Springer Nature Switzerland AG 2021

N. Herisanu and V. Marinca (eds.), *Acoustics and Vibration of Mechanical Structures—AVMS 2019*, Springer Proceedings in Physics 251,
https://doi.org/10.1007/978-3-030-54136-1_49

of the absorber has to be multiplied to thirty-two times [1]:

$$\text{Transmission Loss} = 10 \log_{10} \left[1 + \left(\frac{\pi \rho h f}{c \rho_\alpha} \right)^2 \right] \tag{1}$$

where ρ is the density of absorber, h is the layer thickness of the absorber, f is the frequency, ρ_α is the density of air, c is the sound propagation speed in air [1]. It is for that reason the research of alternative sound-proof materials, including such materials which revealing features are terminated by their inner structure rather than their material quality (metamaterials) has been highly increased during the last decade. The basic unit of metamaterials with mass-in-mass subsystem represents a specific Two-Degree-Of Freedom (2DOF) oscillating system (see Fig. 1) [2, 3], which is the ground model for the theory of effective mass (see Fig. 2).

The essential result of the effective mass model is that: with proper parameters there exists an excitation frequency range where the excited m_1 mass stops or oscillates opposite to the excitation [4–6].

The effective mass can be expressed as function of the frequency of excitation on the basis of (2) (see Fig. 3) [1].

$$m_{eff} = m_1 + m_2 \frac{1}{1 - \frac{\omega_g^2}{\omega_2^2}} \tag{2}$$

where ω_g is the angular frequency of excitation, ω_2 is the natural angular frequency of the attached mass.

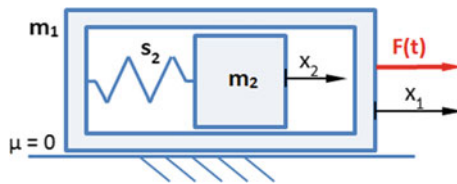


Fig. 1 Mass-in-mass subsystem model

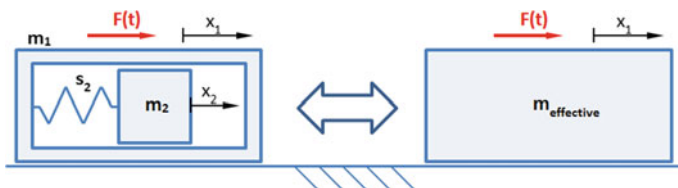


Fig. 2 Effective mass model

Fig. 3 Effective mass in function of excitation angular frequency

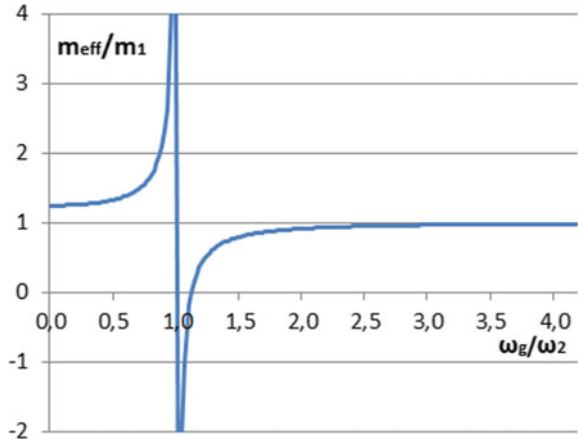
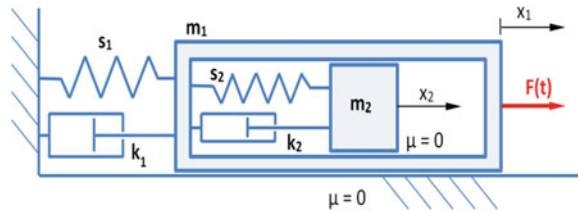


Fig. 4 Model of dynamic reduction of vibration



Negative effective mass occurs within a narrow frequency band above the natural angular frequency of the attached mass m_2 , which oscillates opposite to the m_1 mass.

The working principle of the mass-in-mass type metamaterials resembles in many aspects the dynamic reduction of vibration (see Fig. 4) [7], of which equations of motion with linear material characteristics were solved using rotating vectors [8].

The phase shift between the motion of m_1 and m_2 masses is written by the following equation where $D_2 = k_2/k_{2crit}$ is the Lehr-damping ratio [8]:

$$\varphi_2 = \operatorname{arctg} \frac{\frac{\omega_g}{\omega_2}}{\frac{1}{2D_2\left(\frac{\omega_g}{\omega_2}\right)^2} - \frac{1}{2D_2} + 2D_2} \tag{3}$$

and the amplitude ratio of the two masses is:

$$G_{21} = \frac{A_2}{A_1} = \sqrt{\frac{\left(2D_2\frac{\omega_g}{\omega_2}\right)^2 + 1}{\left(1 - \frac{\omega_g^2}{\omega_2^2}\right)^2 + \left(2D_2\frac{\omega_g}{\omega_2}\right)^2}} \tag{4}$$

If the spring and damping forces change linear with the displacement and velocity, than the equations of motion of the harmonic oscillation can be solved analytically, but in non-linear case there are only approximate solutions.

The equation of motion of progressive characteristic spring, linear viscous damping, one-degree-of freedom oscillation was written and solved by G. Duffing in 1918 [9]:

$$\ddot{x}(t) + ax(t) + \mu x^3(t) + \lambda \dot{x}(t) = F(t) \tag{5}$$

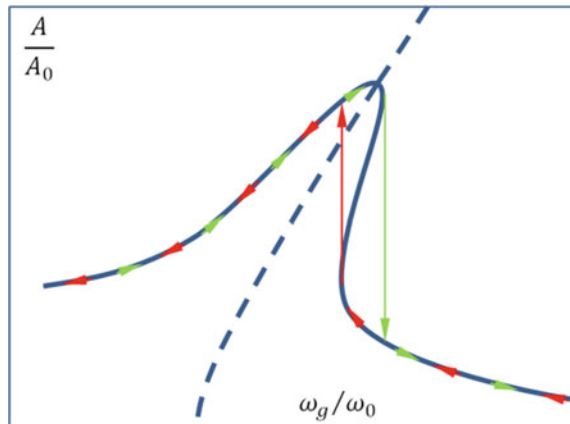
The non-linear characteristic was described by cubic function.

In rotating vector presentation the Duffing equation contains such a member that rotates not together with the other vectors' angular frequency, but three times faster. Therefore the phase shifts among the excitation force, displacement, velocity and acceleration vectors are not stationary, they vary during a period of motion.

Figure 5 shows the resonance of an oscillating system with non-linear, progressive characteristic spring. The green arrows present the change of amplitude during increase of excitation angular frequency, and the red arrows show the maximum displacement during decrease of the excitation angular frequency. It is visible that both directions of change of the excitation frequency lead to a discontinuous change of the amplitude, where the result depends on the initial parameters. The dashed line backbone (which is vertical in linear case) leans to right which means a wider resonance zone compared to the linear springs, that brings reduction of vibration in a wider range [10–12].

Figure 6 shows the rotating vectors of the Duffing equation. Compared to the linear equation, there is a new μx^3 member that contains a component that does not rotate with the $\Omega(\nu t)$ angular frequency as the other rotating vectors. This member can be unfolded to two vectors, both are directly proportional to the displacement, but one of them rotates with $\Omega(\nu t)$, the other rotates with $3\Omega(\nu t)$ angular frequency. That is enough to have no analytical solution with rotating vectors, only approximate.

Fig. 5 Resonance of progressive spring characteristic oscillating system



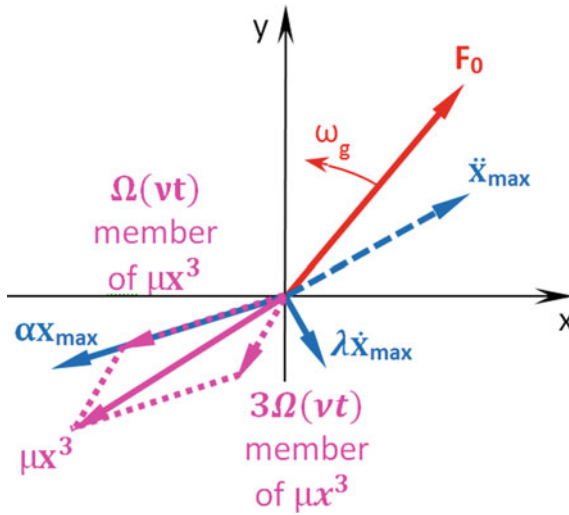


Fig. 6 Rotating force vector presentation of non-linear One-Degree-Of-Freedom oscillating system according to D’Alambert

2 Introduction of Measuring System

For the purposes of the research the University of Szeged, Technical Faculty established a new laboratory during the last year.

As a result of purchasing the following instruments are at service for measuring the reduction of vibration (see Fig. 7a, b.):

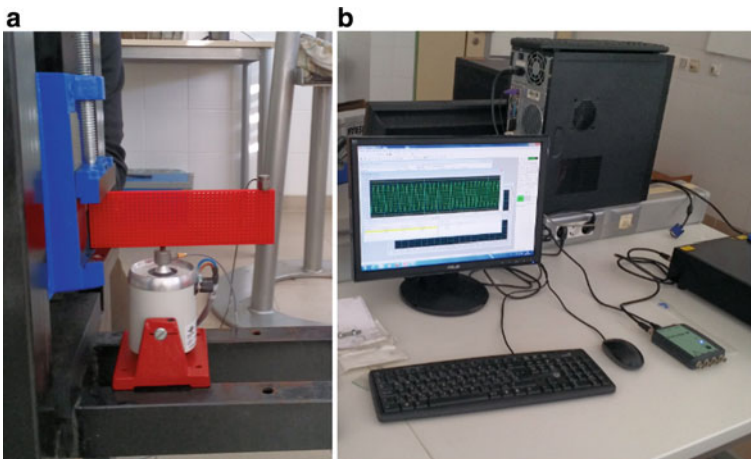


Fig. 7 **a** Basic arrangement, **b** PHOTON + dynamic signal analyzer

- Brüel&Kjaer PHOTON + Dynamic Signal Analyzer
- Brüel&Kjaer LDSvibrator with V201, M4 trunnion kit
- Brüel&Kjaer LDS LPA100 amplifier
- 8230 DeltaTron Force Transducer,
- Accelerometers
- Computer, rack.

As it was mentioned before the working principle of the metamaterial investigated resembles the dynamic reduction of vibration, but in a mass-in-mass arrangement. Accordingly, there is an external carrying case, the m_1 mass that is excited periodically. In this case there are some attached masses (m_2, m_3, m_4 etc.) arranged in a properly arranged geometrical formation. These attached masses take over the vibration energy of the case if the excitation frequency is closed to their natural angular frequency, reducing the vibration amplitude of the mass m_1 . During the experiment the attached masses are fixed to the case and the reduction of vibration is measured in the given frequency range changing the sweeping the excitation frequency.

Figure 7a presents one of the metamaterial cases (red color on Fig. 7a), gripped by a vice. Under it there is the LDS Vibrator that can shake with maximum 17.8 N force and 5 mm amplitude on a frequency between 10 and 13,000 Hz given by the signal generator. The 100–1000 Hz frequency range is the target range of the research because the vibrations in this range are the most harmful. The PHOTON + Signal Analyzer and Signal Generator gives signal for the vibrator through the LDS LPA amplifier. With a real time Fast Fourier Transformation (FFT) the PHOTON + analyzes the input signal as well (see Fig. 8) and produces a Frequency Response Function (FRF) as a ratio of output and input signals.

The vibrator controlling sinusoidal signal and the force transducer's signal are used as output signals. The input signal arrives from the accelerometer placed on the top of the metamaterial. From these signals the Frequency Response Function is calculated by the software of PHOTON + analyzer, and it is observed that the amplitude of the function decreases where the excitation frequencies just above the natural frequencies of the attached masses. With linear spring characteristics the

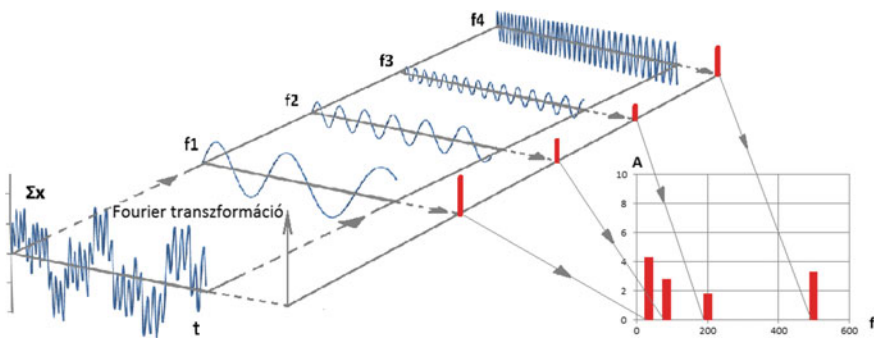


Fig. 8 Fast Fourier Transformation

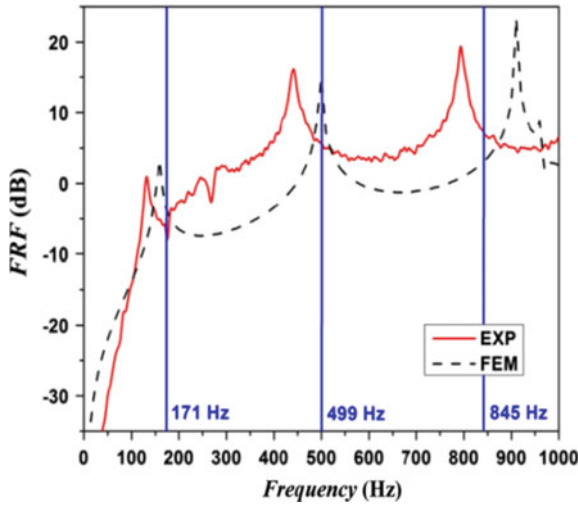


Fig. 9 Frequency Response Function of an experimental system [13]

frequency ranges where the amplitude decreases are narrow, with steep changes of the amplitude, while with non-linear springs the frequency ranges are wider, and the vibration is reduced in a broader frequency range (see Fig. 9).

3 Measuring the Reduction of Vibration of a 2-Degree-of-Freedom Subsystem

During the experiments a 2-Degree-Of-Freedom vibration system is investigated (see Figs. 10, 11) first. This mass-in-mass arranged system represents the subsystem of the searched metamaterials, so these measurements and calculations are the simplest. By these investigations the differences between the theoretical calculations and the measured results were studied. Since the presence (mass) of the used instruments (force transducer, accelerometers) influences the results of the measurements further work on corrections of the measure results is still needed.

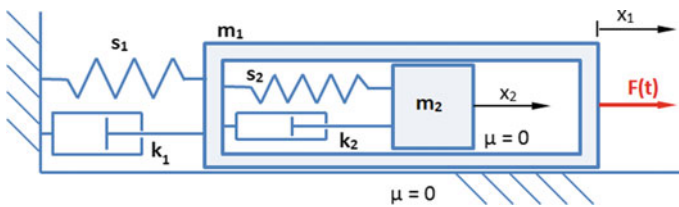
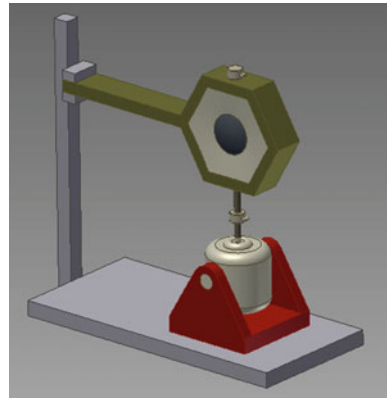


Fig. 10 Model of Two-Degree-Of-Freedom, mass-in-mass arranged vibrating system

Fig. 11 Measuring arrangement of 2DOF, mass-in-mass type vibrating system



For measuring and calculating the parameters of the 2-DOF model there are two different methods available: impulse excitation and sinusoidal excitation. With the impulse excitation are measured the decrease of the amplitude and the duration of n periods. Since the amplitude is not measured directly, the value of the A_1/A_n amplitude ratio is represented by the \ddot{x}_1/\ddot{x}_n quotient given by the accelerometer. The expression for the damping factor k , and the spring stiffness s are:

$$k = 2m \frac{\ln A_1/A_n}{nT} \tag{6}$$

$$s = m \left[\left(\frac{2\pi}{T} \right)^2 + \left(\frac{k}{2m} \right)^2 \right] \tag{7}$$

At sinusoidal excitation the phase shift φ between the excitation force and the displacement caused by the excitation, and the maximum displacement A_0 at the given ω_g and the static expansion A_{st} at $\omega_g = 1s^{-1}$ excitation have to be measured (the ratio of amplitudes is still represented by the acceleration rate). Without reduction and introducing a c factor:

$$c = \left(\frac{A_0}{A_{st}} \right)^2 (1 + \tan^2 \varphi) \tag{8}$$

$$s = m\omega_g \frac{c + \sqrt{c}}{c - 1} \tag{9}$$

$$k = \tan \varphi \frac{s - m\omega_g^2}{\omega_g} \tag{10}$$

This way the spring stiffness (s_2) and the damping factor (k_2) of the glue between the two masses, as well as the spring stiffness (s_1) and the damping factor (k_1) of the

gripping part of the periodically excited m_1 mass can be determined. Of course the s_1, k_1 parameters have to be measured without the m_2 mass, and the s_2, k_2 parameters can be found with fixed m_1 mass position, at excited m_2 mass.

As a plan of the future research the displacement should be measured too (with laser or inductive displacement transducer), than the measurement of the parameters will become much easier, and with laser measurement the problem of the mass of measuring elements will not appear at all.

4 “Wallpaper-like” Metamaterial

The design of the metamaterial being developed is similar to a wall-paper and its application is planned to be as same as a wall-paper: stuck on the wall. From the point of view of producibility no more then 4–5 attached masses can be considered. With well-set parameters the natural frequencies of the different attached masses are uniformly distributed within a relatively wide (600–800 Hz) frequency range thus representing a useful metamaterial for reduction of vibrations. Figure 12 represents the model of the metamaterial with the periodically excited mass m_1 and the masses m_2, m_3, m_4, m_5 attached to the first one in a mass-in-mass type arrangement.

This 5-Degree-Of-Freedom subsystem is the base of the author’s consideration of a useful acoustic vibration reducing wallpaper-like metamaterial. Figure 13 illustrates the construction. It consists of a carrier layer with a covering layer (m_1) and 4 in parallel attached different weight masses (m_{2-5}). The carrier layer (right side) and the covering layer (left side) are stuck together with adhesive (red color), and the attached masses are placed between the two layers in the cups of the covering layer.

The surrounding material of the masses provides the springs and dampings of the vibrating system that are considered to have linear characteristics. If the cups are empty around the m_{2-5} masses, the stiffness value can be a medium value ensured by the covering material, but the damping factor will be relatively low. If the stiffness and the damping factor are not large enough, the cups have to be filled with some flexible

Fig. 12 5-Degree-Of-Freedom vibrating system model in mass-in-mass arrangement

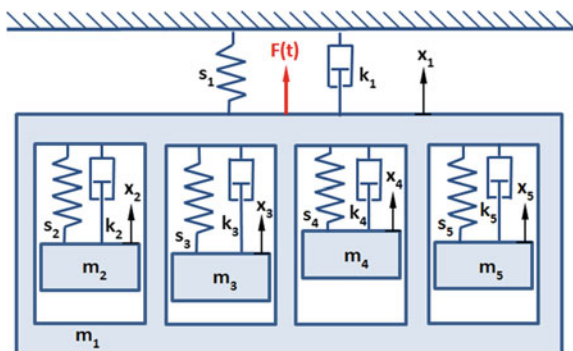


Fig. 13 “Wallpaper-like” construction

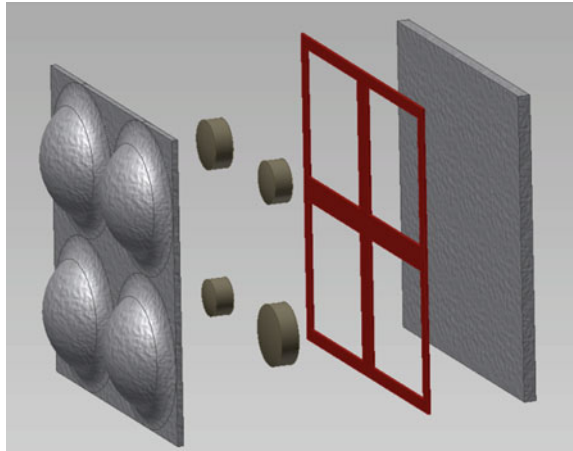


Table 1 Basic parameters

	Masses:	1.	2.	3.	4.	5.	
Given data	$F_o=$	100					N
	$S_n=$	2500	2500	2500	2500	2500	N/m
	$m_n=$	0.0625	0.0625	0.02778	0.01563	0.01	kg
	$k_n=$	5	1	1	1	1	Ns/m
Calculated data	$\omega_n=$	200	200	300	400	500	1/s
	$D_n=$	0.2	0.004	0.006	0.008	0.01	

material. The size of the basic unit is of the order of the magnitude of millimeter, and it is multiplied side by side on a flat carrier, so it looks like wallpaper.

The following example presents the usefulness of the model. The parameters are shown on Table 1.

Every spring stiffness s_n and damping factors k_n of the attached masses were set to the same values. The natural angular frequencies of the attached masses were set in difference of 100 1/s.

The amplitude ratios A_n/A_1 are presented by Fig. 14 in function of the angular frequency of excitation per natural angular frequency of mass m_1 (ω_g/ω_1). Figure 15 shows the phase shifts φ_n between the displacements d_n and d_1 in function of ω_g/ω_1 .

Figures 14 and 15 show the uniform distribution of the natural angular frequencies ω_n . The maximum amplitudes A_n and maximum phase shifts φ_n decrease as the damping ratios D_n increases.

The most important result is presented by the Fig. 16. The amplitude of $m_1(A_1)$ indicates the reduction of vibration. The continuous line represents the motion with the four attached masses and the dashed line without them. It is obvious that the reduction of vibration was quite successful in the frequency range around and over the natural angular frequency ω_1 of mass m_1 . But there occurred a problem: at about

Fig. 14 Amplitude ratio A_n/A_1 in function of angular frequency ratio ω_g/ω_1

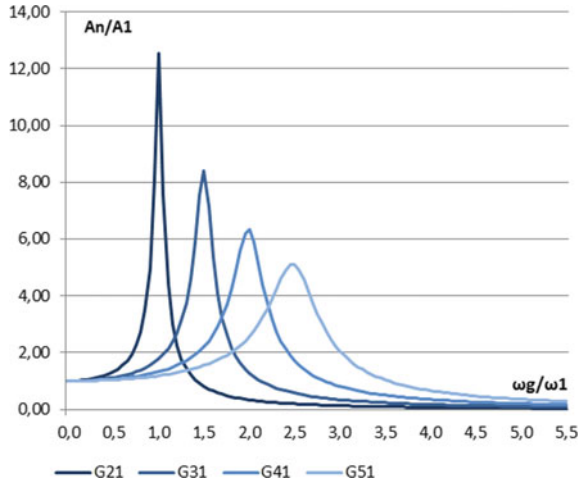
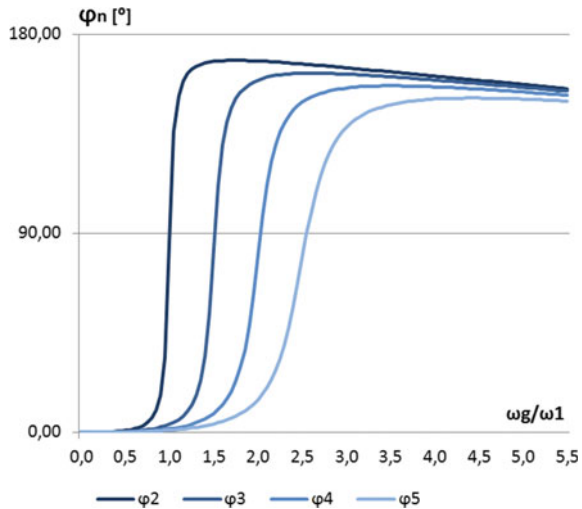


Fig. 15 Phase shifts between displacements d_n and d_1 in function of ω_g/ω_1



the half of ω_1 appears a new natural angular frequency, which is the resultant natural angular frequency ω_R of the five masses. The value of ω_R may be set with proper selection of the parameters of the model. If the excitation is not typically occurs in the lower range of ω_1 , these parameters can operate well. The phase shift between the excitation force and the displacement of mass m_1 is presented on Fig. 17.

There is an interesting question, what can be made with the energy of vibration that is captured by the wall-paper. The simplest answer is: let it diffuse in the form of heat into the surroundings. But there is a possibility to use it to useful purposes. For example if a piezo-electric quartz may be attached to the masses, which would generate electric current it could be a supplier of an electrical instrument or stored in accumulator.

Fig. 16 Amplitude per static extension of mass $m_1 (A_1/x_{st1})$ in function of ω_g/ω_1

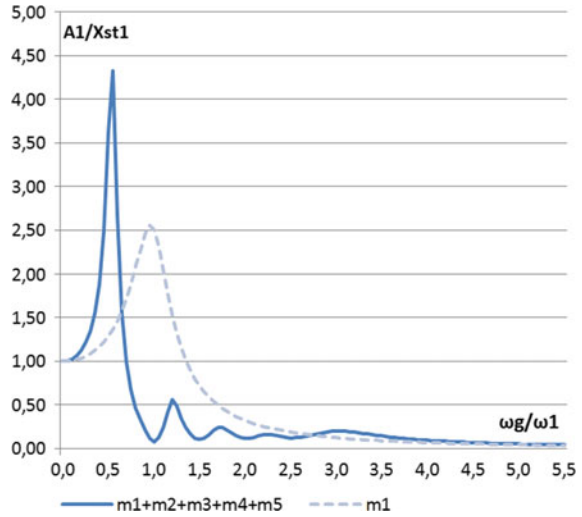
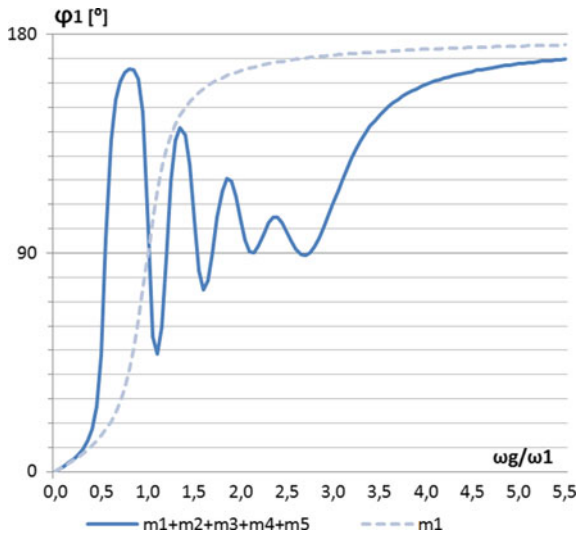


Fig. 17 Phase shift between the excitation force and the displacement of mass m_1 in function of ω_g/ω_1



5 Simulation Process

In order to reduce the number of the measurements different simulation softwares may be used. The Autodesk Inventor is available at the Faculty of Engineering and it has a moderate finite element analysis module (stress-analysis, displacement-analysis, modal-analysis), but it has neither Frequency Response Function (FRF), nor non-linear material features. The initial tests with ANSYS are encouraging, but

it needs very high qualified competence that takes too much time to improve. So the software support is still a question.

We lean on the MATLAB and the EXCELL software to verify the correctness of the analytical predictions and to study the motions with changing the different parameters.

6 Conclusion

It is obvious that have arrived to the most exciting part of the metamaterial research, because this is the point where the gathered theoretical knowledge turns to practical solution. The two and more degree-of-freedom vibrating models, the mass-in-mass arrangement, the differences between linear and non-linear material parameters have to be turned to reality and be verified by the measurements in order to move forward to the shaping, sizing, arranging and proper material finding of the carrier and the attached masses. And last but not least we will meet the problem of the miniaturizing and producibility as well. In conclusion, it can be stated we made a long way on metamaterials but the most is ahead of us.

References

1. L. Cveticanin, Gy Mester, Theory of acoustic metamaterials and metamaterial beams: an overview. *Acta Polytechnica Hungarica* **13**(7), 43–62 (2016)
2. P.F. Pai, Metamaterial-based broadband elastic wave undamped vibration absorber. *J. Intell. Mater. Syst. Struct.* **21**(5), 517–528 (2010)
3. H.H. Huang, C.T. Sun, G.I. Huang, On the negative effective mass density in acoustic metamaterials. *Int. J. Eng. Sci.* **47**, 610–617 (2009)
4. Bíró, I.: *Mechanikai lengések*, Szegedi Tudományegyetem Mérnöki Kar, Szeged, 2014. 122 p. ISBN 978-963-306-288-3
5. L. Cveticanin, M. Zukovic, Negative effective mass in acoustic metamaterial with nonlinear mass-in-mass subsystems. *Commun. Nonlinear Sci. Numer. Simul.* **51**, 89–104 (2017)
6. P.F. Pai, H. Peng, S. Jiang, Acoustic metamaterial beams based on multi-frequency vibration absorbers. *Int. J. Eng. Sci.* **79**, 195–205 (2014)
7. A. Hegedűs, *Fejezetek a kinetikából Rezgésttan* (Szent István Egyetemi Kiadó, Gödöllő, 2015). ISBN 978-963-269-468-9
8. P. Szuchy, I. Bíró, Damped 2-DOF subsystems of acoustic metamaterials, KOD 2018 IOP Conf. Ser. Mater. Sci. Eng. **393**, 012038 (2018). <https://doi.org/10.1088/1757-899x/393/1/012038>
9. A.F. Vakakis, A. Blanchard, Exact steady states of the periodically forced and damped duffing oscillator. *J. Sound Vib.* **413**, 57–65 (2018)
10. L. Cveticanin, *Strong nonlinear oscillators*. Springer International Publishing AG (2018). ISBN 978-3-319-58825-4
11. L. Cveticanin, M. Zukovic, Gy. Mester, I. Biro, J. Sarosi, Oscillators with symmetric and asymmetric quadratic nonlinearity. *Acta Mechanica* **227**(6), 1727–1742 (2016). IF (2015): 1,694

12. L. Cveticanin, G. Mester, I. Biro, Parameter influence on the harmonically excited duffing oscillator. *Acta Polytechnica Hungarica* **11**(5), 145–160 (2014). ISSN 1785-8860. IF: 0,649
13. R. Zhu, X.N. Liu, G.K. Hu, C.T. Sun, G.L. Huang, A chiral elastic metamaterial beam for broadband vibration suppression. *J. Sound Vib.* **333**, 2759–2773 (2014)

Crack Assessment Based on the Use of Severity-Adjusted Modal Curvatures of the Healthy Beam



Gilbert-Rainer Gillich , Cristian Tufisi , Magd Abdel Wahab ,
and Codruta Oana Hamat 

Abstract The current paper presents an algorithm for locating transverse cracks present in Euler–Bernoulli steel beams, by considering the relative frequency shifts (RFSs) measured for the weak-axis vibration modes and the mode shape curvatures. To apply the algorithm, we first determine, by means of the finite element method (FEM), the natural frequencies for the first four bending vibration modes for the healthy beam fixed-free and fixed-fixed end conditions. Afterward, we introduced transverse cracks with known depth and location and determined again the natural frequencies. As a next step, we use an original algorithm to plot the potential severity curves (PSCs) for the four modes and find the intersection, which indicates the crack severity and location. It was found that the method is reliable for determining the location of transverse cracks just by using the measured natural frequency and the squared normalized modal curvatures (SNMCs) for both imposed boundary conditions.

1 Introduction

As our society further develops, the need for more advanced methods for evaluating structural integrity of buildings, structures and mechanical aggregates is more of a priority. It is no surprise that structures failed over time due to faulty production technologies, natural aging phenomena and the lack of structural integrity analysis methods carried out over functioning time. Vibrational-based methods can evaluate a structure after its production and help determining its ability of maintaining functionality in real time, before structural failing happens [1]. Damage detection methods

G.-R. Gillich (✉) · C. Tufisi · C. O. Hamat
“Eftimie Murgu” University of Resita, P-ta TraianVuia 1-4, 320085 Resita, Romania
e-mail: gr.gillich@uem.ro

M. Abdel Wahab
Ghent University, 9052 Zwijnaarde, Belgium

© Springer Nature Switzerland AG 2021
N. Herisanu and V. Marinca (eds.), *Acoustics and Vibration of Mechanical Structures—AVMS 2019*, Springer Proceedings in Physics 251,
https://doi.org/10.1007/978-3-030-54136-1_50

based on natural frequency measurements have proven to be reliable and economically feasible for detecting, locating and evaluating damages [2–4]. The main argument is that the presence of cracks has a negative impact on the stiffness, decreasing the structure's capacity to store energy and changing its dynamic properties [5].

Cracks that are present in structures have a transversal form, but can become more complex as they branch and propagate through the material [6]. Studies have shown that every crack has its own signature, so it is possible to determine the location of a crack by knowing the frequency drop it produces for several bending vibration modes and the modal energy distribution, i.e., the modal curvature evolution along the beam.

The aim of the present paper is to study the precision of detecting and locating cracks by plotting curves resulted from the RFS obtained by measurements that are adjusted with the SNMC for several vibration modes. The resulted curves are, in fact, the PSC plotted for the severity of the real damage. It is shown in this paper that the intersection of such curves belonging to the first four out-of-plane vibration modes accurately indicates the crack position and severity for transverse cracks.

2 Materials and Methods

2.1 The Developed Method to Assess Cracks

The model predicting the frequency of the bending modes for a beam with a transverse crack, f_{i-D} , developed in previous studies [7], is defined by the frequency of the healthy beam f_{i-U} , a term $(\bar{\phi}_i''(x))^2$ that is the square of the normalized modal curvature (SNMC) and the damage severity $\gamma(0, a)$. The relation of the damaged beam's frequency takes the form:

$$f_{i-D}(x, a) = f_{i-U} [1 - \gamma(0, a) \cdot (\bar{\phi}_i''(x))^2] \quad (1)$$

The SNMC for a crack located at distance x from the left end of the beam indicates the energy stored by the healthy beam in an infinitesimal slice dx in which the crack is positioned. The SNMC is different for the different vibration modes and constraints.

The damage severity $\gamma(0, a)$ is the function representing the highest stiffness decrease due to a crack of depth a , which for the fixed-free as well as for the fixed-fixed beams occurs for the crack located at the fixed end. It can be derived using the beam deflection in healthy and damaged state and is similar, for a given beam cross section and damage, for all boundary conditions [8].

The frequency decrease is found from the following mathematical relation:

$$\Delta f_i = f_{i-U} - f_{i-D}(x, a) = f_{i-U} \cdot \gamma(0, a) \cdot (\bar{\phi}_i''(x))^2 \quad (2)$$

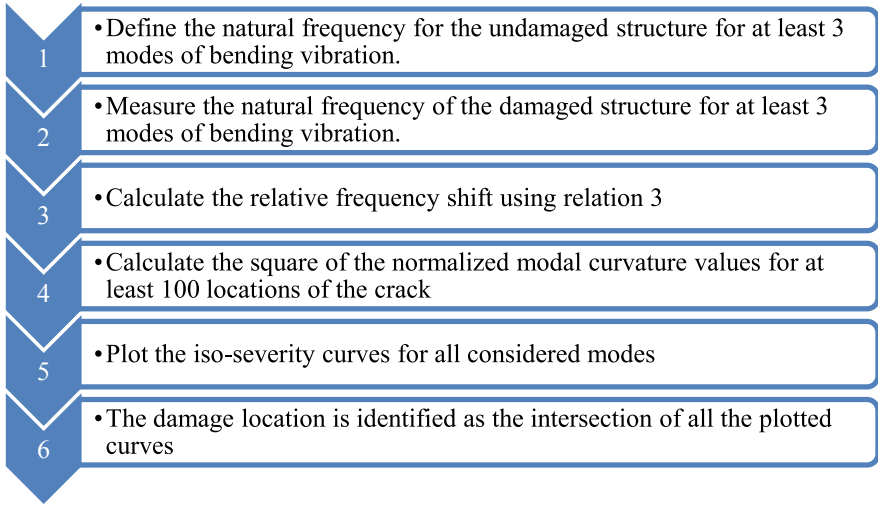


Fig. 1 Proposed damage indicating algorithm

The ratio between the frequency shift of a bending vibration mode i and the corresponding frequency of the healthy beam represents the RFS and is calculated as:

$$\Delta \bar{f}_i(x, a) = \frac{f_{i-U} - f_{i-D}(x, a)}{f_{i-U}} = \gamma(0, a) \cdot (\bar{\phi}_i''(x))^2 \tag{3}$$

It follows from relation (3) the severity for a crack placed at the location x and producing a known frequency drop as:

$$\frac{\Delta \bar{f}_i(x, a)}{(\bar{\phi}_i''(x))^2} = \gamma(0, a). \tag{4}$$

This finding is used in [9] to assess single cracks in beams. By employing relation 4, we can plot the PSC that considers the RFS and the SNMC. Obviously, the intersection of the PSC plotted for more vibration modes indicates the crack location, because here the combination of the SNMC and the damage severity fits the RFS for all considered modes. Finally, the severity can be found directly from the graphical representation or by involving relation (4). The algorithm is presented in Fig. 1.

2.2 The Simulation Scheme

For the proposed study, we have considered a beam both in healthy and in damaged states, with different end constraints. The geometry was modeled with the help of

Table 1 Beams' main dimensions and material properties

Length L (mm)	Width B (mm)	Thickness H (mm)	Mass density ρ (kg/mm ³)	Young's modulus E (N/m ²)	Poisson ratio ν (-)
1000	50	5	7850	2×10^{11}	0.3

the CAD software SolidWorks with its main dimensions and material properties presented in Table 1.

The modal analysis was performed by means of the ANSYS professional software, by defining the imposed end constraints and a fine hexahedral mesh with the maximum edge of 2 mm.

We have considered for this study transversal breathing cracks of 1.5 mm depth. The cracks are located at distance $x = 250$ mm from the left beam end in the first case, respectively, and $x = 550$ mm in the second case.

3 Results and Discussion

To assess the cracks, the proposed algorithm is applied for the damage scenarios described in the previous section. The results in terms of PSC are presented below (Fig. 2).

Figure 3 represents the ISC, from which the crack location is found at 248.5 mm that is very close to the real crack location, which is 250 mm. With the RFS calculated for the first mode and the SNMC calculated for the crack position, we determined with relation (4) the severity 0.00889. This severity corresponds to a crack depth 1.447 mm that is again very close to the real crack depth, which is 1.5 mm.

A similar study is made for the fixed-fixed beam, the beam and crack dimensions and geometry being maintained unaltered. The PSC is represented in Fig. 4. In the fixed-fixed case, the crack location is found both at 249 mm and symmetrically at 751 mm, the first value is very close to the real crack location, which is 250 mm, and the second value is resulted due to the modal curvature symmetry caused by the

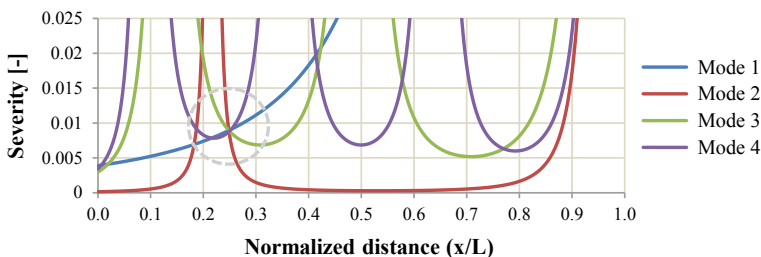


Fig. 2 Potential severity curves for the cantilever beam with a transverse crack having the depth $a = 1.5$ mm and located at $x = 250$ mm from the left end

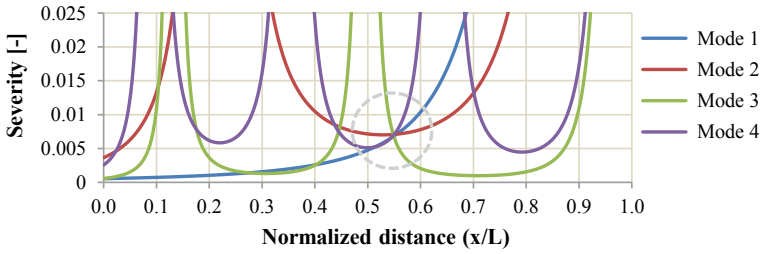


Fig. 3 Potential severity curves for the beam with fixed-free end conditions and a transverse crack having the depth $a = 1.5$ mm and located at $x = 550$ mm from the left end

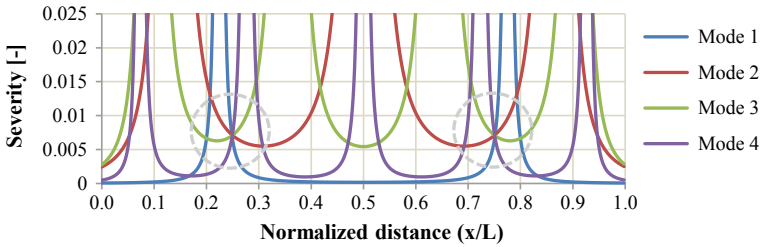


Fig. 4 Potential severity curves for the fixed-fixed beam with a transverse crack having the depth $a = 1.5$ mm and located at $x = 250$ mm from the left end

fixed-fixed constraint. The crack is also well recognized for the position 550 mm, since in Fig. 5 the positions 549 and 451 are found.

Regarding the severity, in both cases regardless of the end constraints and damage positions, it has the same value of 0.00889.

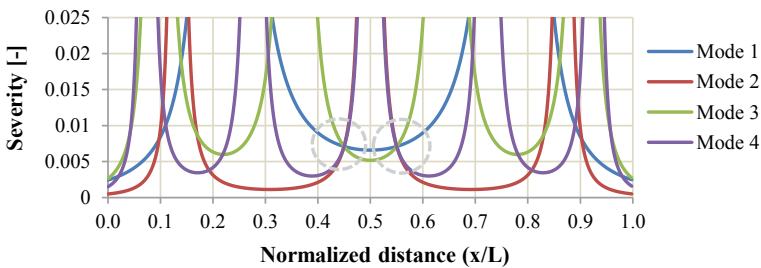


Fig. 5 Potential severity curves for the fixed-fixed beam with a transverse crack having the depth $a = 1.5$ mm and located at $x = 550$ mm from the left end

4 Conclusion

In the current study, we have plotted the PSC for a steel beam having one transversal crack of known dimensions and position, by employing an original relation that considers the RFS and the SNMC.

It was found that the intersection of the plotted PSC indicates precisely the damage location of all presented cases.

In the particular case where the beams end constraints are fixed-fixed, it was found that the PSC indicates two symmetric positioned damages, and this is due to the modal curvature symmetry caused by the constraint, showing that for this case it is enough to employ only half of the calculated severity values for locating the crack.

The study shows that the PSC algorithm is a very precise method for detecting, evaluating and locating damages in beam-like structures.

References

1. E. Mesquita, P. Antunes, F. Coelho, P. André, A. Arêde, H. Varum, Global overview on advances in structural health monitoring platforms. *J. Civ. Struct. Health Monit.* **6**(3), 461–475 (2016)
2. Z.B. Yang, M. Radzienski, P. Kudela, W. Ostachowicz, Damage detection in beam-like composite structures via Chebyshev pseudo spectral modal curvature. *Compos. Struct.* **168**, 1–12 (2017)
3. S. Khatir, K. Dekemele, M. Loccufer, T. Khatir, M.A. Wahab, Crack identification method in beam-like structures using changes in experimentally measured frequencies and Particle Swarm Optimization. *C. R. Mec.* **346**(2), 110–120 (2018)
4. R. Zenzen, I. Belaidi, S. Khatir, M.A. Wahab, A damage identification technique for beam-like and truss structures based on FRF and Bat Algorithm. *C. R. Mec.* **346**(12), 1253–1266 (2018)
5. M.H. He, T. Yang, Y. Du, Nondestructive identification of composite beams damage based on the curvature mode difference. *Compos. Struct.* **176**, 178–186 (2017)
6. J.T. Ravi, S. Nidhan, N. Muthu, S.K. Maiti, Analytical and experimental studies on detection of longitudinal, L and inverted T cracks in isotropic and bi-material beams based on changes in natural frequencies. *Mech. Syst. Signal Process.* **101**, 67–96 (2018)
7. G.R. Gillich, Z.I. Praisach, Modal identification and damage detection in beam-like structures using the power spectrum and time–frequency analysis. *Signal Processing.* **96**(A), 29–44 (2014)
8. Z.I. Praisach, G.R. Gillich, C. Protocsil, F. Muntean, Evaluation of crack depth in beams for known damage location based on vibration modes analysis. *Appl. Mech. Mater.* **430**, 90–94 (2013)
9. M. Dahak, N. Touat, M. Kharoubi, Damage detection in beam through change in measured frequency and undamaged curvature mode shape. *Inverse Prob. Sci. Eng.* **27**, 89–114 (2019)

Influence of Eccentricity of Drive Mechanisms and Sieve Vibrations on the Quality of Seed Separation



Constantin Popa, Adrian Costache, Alina Ovanisof,
and Roxana Alexandra Petre

Abstract In this paper, a theoretical and experimental study on the mechanical separation of seeds on the windrows is carried out. First, a study on the influence of vibrations on some quality indices of seed separation is carried out, and next to the kinematic of the drive mechanism (eccentric slider-crank) of the planar sieves, which is the active organ of the windrow, is analyzed. Next, the influence of the eccentricity of the crank mechanism was determined, on the seed quality indices of the first-quality and of the second-quality of the initial seed mass, for the wheat and barley seeds, respectively. It can be noticed that in the case of normal vibrations, as well as the reduced eccentricity of the sowing mechanism, the separation indices for the first and the second-quality seeds are higher than for the classical mechanisms. Correlation coefficients have very high values, which shows that the two curves, theoretical and measured, are very close.

1 Introduction

Seeds cleaning and sorting is an important phase in the conditioning of agricultural products.

In the paper [2], Cășandriou and Enescu studied the elasticity and vibrations of planar sieves, analyzing the separation block with kinematic excitation, the criteria for the selection of the elastic supports, determining the eigenfrequencies of the system, the degree of balance of forces due to elasticity, fatigue and buckling and the safety coefficients. The authors established the optimal construction solution.

In the article [6] Ion and Gherghe studied vibrocentrifuges for separation, as well as differential equations of seeds movement.

Dziki and Laskowsky study, in the paper [5], the physical properties and characteristics of wheat seeds prior to primary conditioning operations (cleaning and

C. Popa (✉) · A. Costache · A. Ovanisof · R. A. Petre
University Politehnica of Bucharest, Bucharest, Romania
e-mail: costel_popa_2004@yahoo.com

sorting) and prior to millings, such as density, hectolitre weight, as well as friction coefficients between seeds, between seeds and chaff, and between seeds and sieves.

In the paper [7], Ke Shun Liu studied the influence of vibrations and friction on the quality and efficiency of seed separation by sifting.

Also, Stendish made an extensive study of the movements, velocities and accelerations of the component parts of the drive mechanisms of the planar and cylindrical sieves in the article [10].

2 Materials and Methods

This paper aims to supply optimum ways of cleaning and sorting the wheat and barley seeds. An experimental stand has been used, made of two bodies out of which the higher one having adjustable slope ($1\dots 8^\circ$) and the lower one having a fixed slope (15°). The machine has also a centrifugal ventilator. Measurements were made for five values of the airflow velocity [8, 9].

A mixture of 30 kg of wheat seeds and 30 kg of barley seeds was used.

This experimental stand (Fig. 1) is intended for cleaning and sorting by size and aerodynamic properties of grains, pastures, technical crops obtained from combines or walking sticks. It is used for cleaning and sorting seeds of wheat, rye, barley, oats, rice, peas, beans, lentils, mustard, hemp, sunflower, millet and rape.

Experimental research was done for autumn wheat and autumn barley at three feed rates of the experiment stand, five airflow speeds set from the machine fan, and four values of the tilt angle β of the lower sieve of the upper block. The five speeds of the airflow are: $v_1 = 2.3 \text{ ms}^{-1}$, $v_2 = 3.8 \text{ ms}^{-1}$, $v_3 = 5 \text{ ms}^{-1}$, $v_4 = 6 \text{ ms}^{-1}$, $v_5 = 7 \text{ ms}^{-1}$. The four values of the angle β are: $\beta_1 = 2^\circ$, $\beta_2 = 4^\circ$, $\beta_3 = 6^\circ$, $\beta_4 = 8^\circ$. The angle of the upper block with sieves is $\alpha = 4^\circ$.

The above determinations were repeated using, at a time, four eccentric slider-crank mechanisms (eccentricities of 10, 20, 30 and 40 mm, respectively) instead of the classic slider-crank mechanism (eccentricity $e = 0$) previously used [7, 9].

Experiments are realized on the stand in Fig. 1 and with the equipment from Table 1. Sieves for the autumn wheat and barley seeds are selected, according to the seed sizes of these crops.

2.1 Determining the Amplitude of the Signal

A number of four determinations were made with signal transducers in three points of the windrow: P on the upper sieve of the upper block with a sieve (Figs. 2, 3, 4). All the determinations were performed for the windrow [2–4, 6, 7, 11].

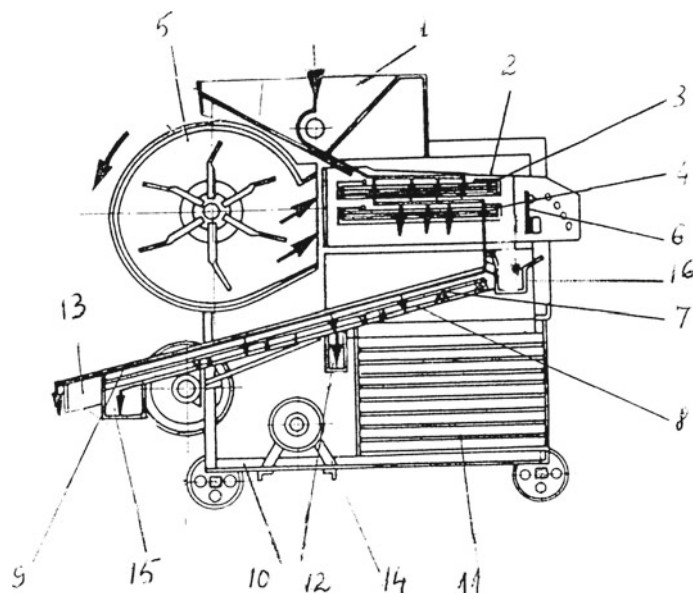


Fig. 1 Experimental stand: 1—food cart; 2—upper block with sieves; 3—the first sieve of the upper block; 4—the second sieve of the upper block; 5—fan; 6—shutter of chaff evacuation; 7—lower block with sieves; 8—the first sieve of the lower block; 9—the second sieve of the lower block; 10—frame; 11—the backup sieve box; 12—drain chamfer for small impurities and splinters; 13—first-quality seed drain chamfer (main culture); 14—electric engine; 15—second-quality seed drain chamfer; 16—drain chamfer for large impurities

Table 1 Appliance used in experiments

Current number	Device name	Measurement units	Number of pieces	Measuring accuracy	Measured values
1	Callipers	mm	1	± 0.1 mm	Dimensions
2	3 m reel with air bubble	mm	1	± 1 mm	Dimensions
3	Analytical balance	g	1	± 0.1 g	Masses
4	Suit type scale	kg	1	± 0.1 kg	Masses
5	Dynamometrical balance (scale)	kg	1	± 0.05 kg	Masses
6	Timer	s	1	± 0.1 s	Time
7	Anemometer with cups	ms^{-1}	1	± 0.05 m/s	Speeds
8	Laptop	Gb	1	HDD 500 Gb	Signals and signal spectra

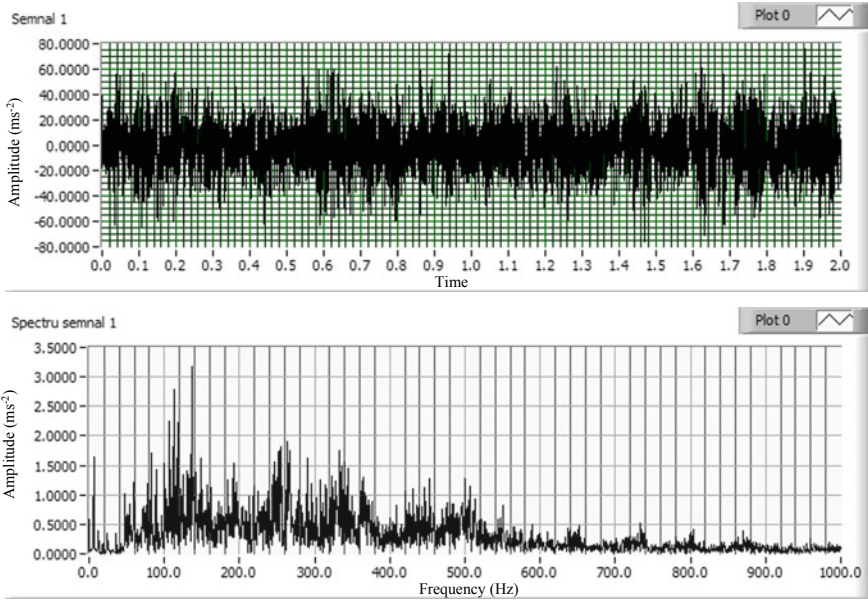


Fig. 2 Variation of acceleration amplitude with frequency and time in point *P*

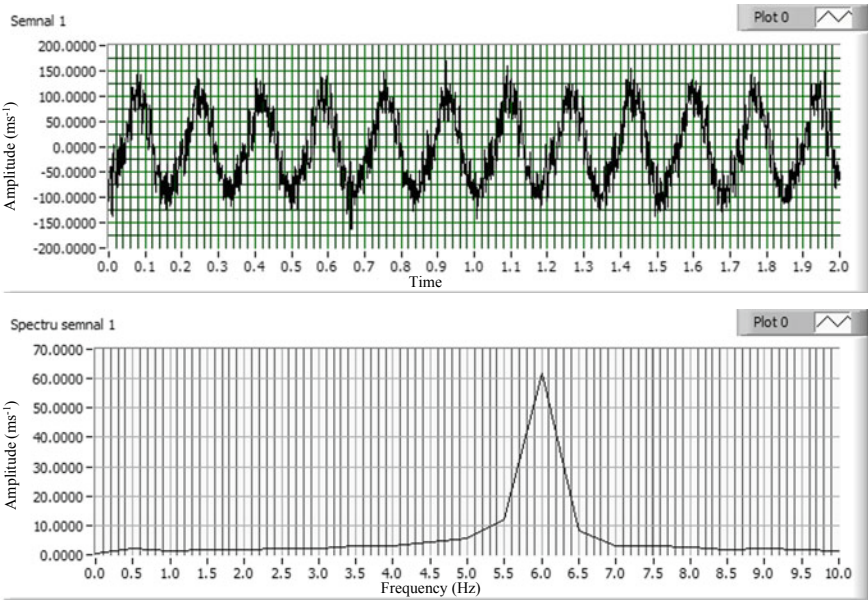


Fig. 3 Variation of velocity amplitude with frequency and time in point *P*

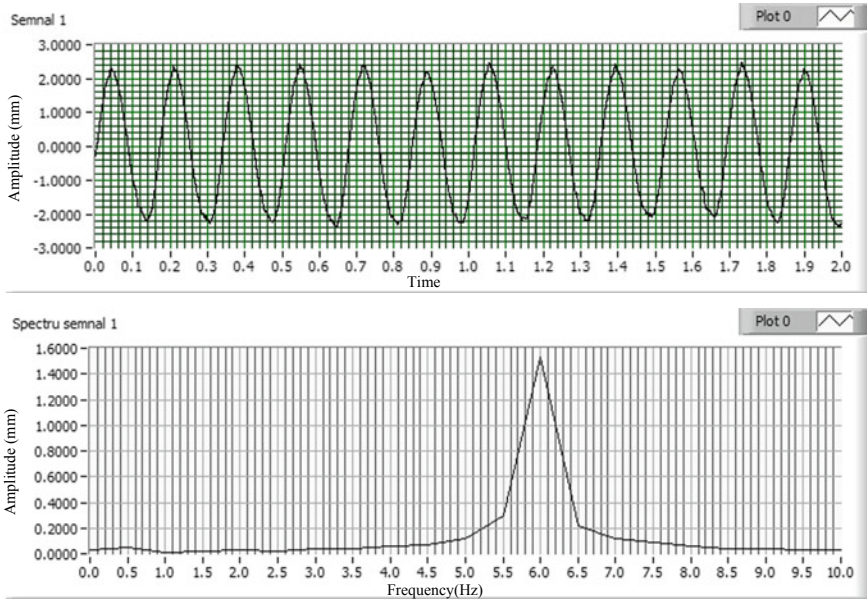


Fig. 4 Variation of displacement amplitude with frequency and time in point P

2.2 Determination of Seed Separation Degrees of First-Quality K_1 , Seeds of the Quality of the Second-Quality K_2 , from the Initial Seed Mass, Depending on the Eccentricity of the Drive Mechanism

The degree of separation of seeds of the first-quality k_1 is the percentage of the first-quality seeds, calculated from the initial seed mass [5, 8, 9].

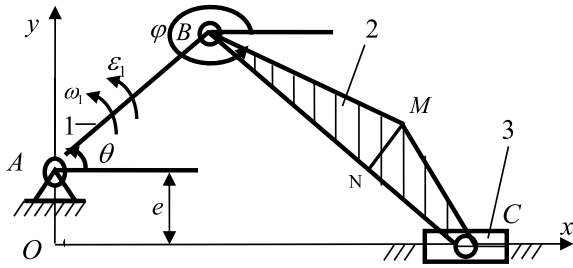
The degree of separation of seeds of the second-quality k_2 is the percentage of the second-quality seeds, calculated from the initial seed mass [5, 8, 9].

Determinations were made for each of the five airflow speeds mentioned above. The values of the tilt angles of the two upper block sieves, α and β , are: $\alpha = 4^\circ$ and $\beta = 4^\circ$. The angle of inclination of the chaff cover is $\gamma = 30^\circ$ and $\gamma = 60^\circ$.

3 Study of the New Sieve Drive Mechanism

For the eccentric slider-crank mechanism in Fig. 7 is known dimensions of the geometric elements and the law of motion of the element leader AB and are required trajectories, velocities and accelerations for the B, C and M of this type of mechanism. Therefore: $\theta = \theta(t)$, $\omega_1 = \dot{\theta}$, $\varepsilon_1 = \ddot{\theta}$, longer know OA, AB, BC, BN and NM. The question to determining parametric equations of the points: $B(x_B, y_B)$, $C(x_C, y_C)$

Fig. 5 Scheme of eccentric slider-crank mechanism for determining displacements, velocities and accelerations



and $M(x_M, y_M)$, angular trajectory φ , of point B , of the linear velocities for the points $B, C, M (v_B, v_C, v_M)$, the angular velocity to the plate 2, ω_2 , linear accelerations for the points $B, C, M (a_B, a_C, a_M)$ like and angular acceleration to the plate 2, ε_2 .

Are written the matrix equations for the position (trajectories, coordinates), velocity and acceleration from which deduced algebraic equations [1, 7, 10, 11].

3.1 Study of Displacements

To determine the displacements for the elements of the eccentric slider-crank mechanism (Fig. 5) using the following relations:

$$\begin{bmatrix} x_B \\ y_B \end{bmatrix} = \begin{bmatrix} 0 \\ OA \end{bmatrix} + \begin{bmatrix} \cos \theta & -\sin \theta \\ \sin \theta & \cos \theta \end{bmatrix} \cdot \begin{bmatrix} AB \\ 0 \end{bmatrix} \Rightarrow \begin{cases} x_B = AB \cdot \cos \theta \\ y_B = OA + AB \cdot \sin \theta \end{cases} \quad (1)$$

$$\begin{bmatrix} x_C \\ 0 \end{bmatrix} = \begin{bmatrix} x_B \\ y_B \end{bmatrix} + \begin{bmatrix} \cos \varphi & -\sin \varphi \\ \sin \varphi & \cos \varphi \end{bmatrix} \cdot \begin{bmatrix} BC \\ 0 \end{bmatrix} \Rightarrow \begin{cases} x_C = x_B + BC \cdot \cos \varphi \\ 0 = y_B + BC \cdot \sin \varphi \end{cases} \quad (2)$$

$$\begin{bmatrix} x_M \\ y_M \end{bmatrix} = \begin{bmatrix} x_B \\ y_B \end{bmatrix} + \begin{bmatrix} \cos \varphi & -\sin \varphi \\ \sin \varphi & \cos \varphi \end{bmatrix} \cdot \begin{bmatrix} BN \\ NM \end{bmatrix} \Rightarrow \begin{cases} x_M = x_B + \Delta x \\ 0 = y_B + \Delta y \end{cases} \quad (3)$$

Angle φ takes values in quadrants I and IV, so $\cos \alpha > 0$. The following notions are introduced:

$$\begin{cases} \Delta x = x_M - x_B = BN \cdot \cos \varphi - NM \cdot \sin \varphi \\ \Delta y = y_M - y_B = BN \cdot \sin \varphi - NM \cdot \cos \varphi \end{cases} \quad (4)$$

3.2 Study of Velocities

In order to determine the velocities of the points of the eccentric slider-crank mechanism (Fig. 5), the following formulas are used:

$$v_B = \omega_1 \cdot AB \quad (5)$$

$$v_{CB} = \omega_2 \cdot CB \quad (6)$$

The relations between the velocities are:

$$\begin{bmatrix} v_{Bx} \\ v_{By} \end{bmatrix} = \begin{bmatrix} \cos \theta & -\sin \theta \\ \sin \theta & \cos \theta \end{bmatrix} \cdot \begin{bmatrix} 0 \\ v_B \end{bmatrix} \Rightarrow \begin{cases} v_{Bx} = -v_B \cdot \sin \theta \\ v_{By} = v_B \cdot \cos \theta \end{cases} \quad (7)$$

$$\begin{bmatrix} v_{Cx} \\ v_{Cy} \end{bmatrix} = \begin{bmatrix} v_{Bx} \\ v_{By} \end{bmatrix} + \begin{bmatrix} \cos \varphi & -\sin \varphi \\ \sin \varphi & \cos \varphi \end{bmatrix} \cdot \begin{bmatrix} 0 \\ v_{CB} \end{bmatrix} \Rightarrow \begin{cases} v_C = v_{Bx} - v_{CB} \cdot \sin \varphi \\ 0 = v_{By} + v_{CB} \cdot \cos \varphi \end{cases} \quad (8)$$

$$\begin{bmatrix} v_{Mx} \\ v_{My} \end{bmatrix} = \begin{bmatrix} v_{Bx} \\ v_{By} \end{bmatrix} + \begin{bmatrix} \cos \varphi & -\sin \varphi \\ \sin \varphi & \cos \varphi \end{bmatrix} \cdot \begin{bmatrix} -\omega_2 \cdot NM \\ \omega_2 \cdot BN \end{bmatrix} \Rightarrow \begin{cases} v_{Mx} = v_{Bx} - \omega_2 \cdot \Delta y \\ 0 = v_{By} + \omega_2 \cdot \Delta x \end{cases} \quad (9)$$

3.3 Study of Accelerations

In order to determine the accelerations of the points of the slider-crank (Fig. 7), the following formulas were used:

$$\begin{cases} a_B^v = -\omega_1^2 \cdot AB \\ a_B^\tau = \varepsilon_1 \cdot AB \end{cases} \quad (10)$$

$$\begin{cases} a_{CB}^v = -\omega_1^2 \cdot BC \\ a_{CB}^\tau = \varepsilon_1 \cdot BC \end{cases} \quad (11)$$

The relations between the accelerations are:

$$\begin{bmatrix} a_{Bx} \\ a_{By} \end{bmatrix} = \begin{bmatrix} \cos \theta & -\sin \theta \\ \sin \theta & \cos \theta \end{bmatrix} \cdot \begin{bmatrix} a_{Bv} \\ a_{B\tau} \end{bmatrix} \Rightarrow \begin{cases} a_{Bx} = a_B^v \cos \theta - a_B^\tau \sin \theta \\ a_{By} = a_B^v \sin \theta + a_B^\tau \cos \theta \end{cases} \quad (12)$$

$$\begin{aligned} \begin{bmatrix} a_C \\ 0 \end{bmatrix} &= \begin{bmatrix} a_{Bx} \\ a_{By} \end{bmatrix} + \begin{bmatrix} \cos \varphi & -\sin \varphi \\ \sin \varphi & \cos \varphi \end{bmatrix} \cdot \begin{bmatrix} a_{CB}^v \\ a_{CB}^\tau \end{bmatrix} \\ &\Rightarrow \begin{cases} a_C = a_{Bx} + a_{CB}^v \cos \varphi - a_{CB}^\tau \sin \varphi \\ 0 = a_{By} + a_{CB}^v \sin \varphi + a_{CB}^\tau \cos \varphi \end{cases} \end{aligned} \quad (13)$$

$$\begin{bmatrix} a_{Mx} \\ a_{My} \end{bmatrix} = \begin{bmatrix} a_{Bx} \\ a_{By} \end{bmatrix} + \begin{bmatrix} \cos \varphi & -\sin \varphi \\ \sin \varphi & \cos \varphi \end{bmatrix} \cdot \begin{bmatrix} -\omega_2^2 \cdot BN - \varepsilon_2 \cdot NM \\ -\omega_2^2 \cdot NM + \varepsilon_2 \cdot BN \end{bmatrix}$$

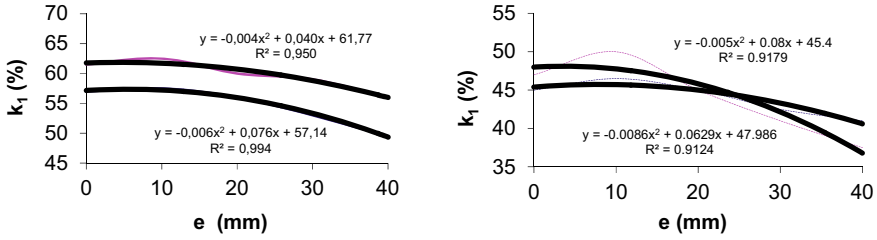


Fig. 6 Variation of the degree of seeds separation of the first-quality k_1 with respect to the eccentricity of the slider-crank mechanism, for the angles of inclination of the chaff cover $\gamma = 30^\circ$ and $\gamma = 60^\circ$, for wheat (left) and barley (right)

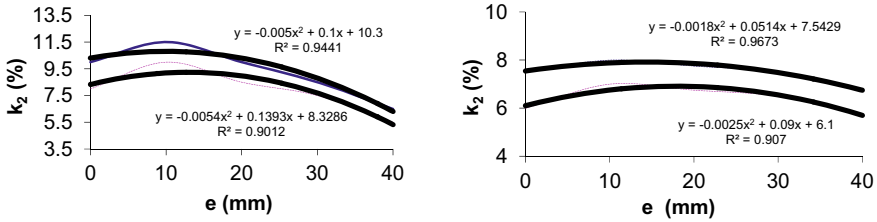


Fig. 7 Variation of the degree of seeds separation of the second-quality k_2 with respect to the eccentricity of the slider-crank mechanism, for the angles of inclination of the chaff cover $\gamma = 30^\circ$ and $\gamma = 60^\circ$, for wheat (left) and barley (right)

$$\Rightarrow \begin{cases} a_{Mx} = a_{Bx} - \omega_2^2 \Delta x - \varepsilon_2 \Delta y \\ a_{My} = a_{By} - \omega_2^2 \Delta y + \varepsilon_2 \Delta x \end{cases} \quad (14)$$

Replacing, at a time, the classic slider-crank mechanism with four eccentric slider-crank mechanisms ($e = 10, 20, 30$ and 40 mm, respectively) produced the results of Figs. 6 and 7 [9].

4 Results and Discussions

The variations $k_1 = f(e), k_2 = f(e)$ are illustrated in Figs. 6 and 7, respectively. The determinations were made using a classic slider-crank mechanism to drive the sieves and then repeated using four eccentric slider-crank mechanisms ($e = 0, 10, 20, 30$ and 40 mm, respectively). It is should be noticed that the seed separation of the first-quality, as well and of the second-quality, is optimal for the slider-crank mechanisms with eccentricity of approximately 10 mm.

The variation of the degree of separation of the seeds of the first-quality k_1 and of the second-quality k_2 with respect to the eccentricity of the slider-crank mechanism, for the angle of inclination of the chaff cover $\gamma = 30^\circ$ and $\gamma = 60^\circ$, is best

approximated by the second-order polynomial function $y = ax^2 + bx + c$, where coefficients a , b , c are real and non-zero.

The correlation coefficients have very high values, from which it follows that the two curves, real and theoretical, are very close.

The variations of the amplitude of the signal with the time and with the oscillation frequency, for seed accelerations, are presented in Fig. 2. The variations of the amplitude of the signal with the time and with the oscillation frequency, for seed velocities, are presented in Fig. 3. The variations of the amplitude of the signal with the time and with the oscillation frequency, for seed displacements, are presented in Fig. 4.

Therefore, the trajectories of the elements of the eccentric slider-crank mechanisms are trajectories of relative movements, trajectories of transport movements, and trajectories of absolute movements.

5 Conclusions

The variations of the amplitudes of the signal with respect to the time, given by the sensitive element of the vibration transducer, as well as the variations of the same amplitudes with respect to the frequency are random and are given by the graphical representations in Figs. 2, 3 and 4.

The seeds separation is better when the amplitude of sieve vibrations is situated in a certain range of values.

The variations in the qualitative working and exploitation indices in the separation of wheat and barley seeds depending on the eccentricities of the drive mechanisms are shown in Figs. 6 and 7; respectively.

Both seeds of the first-quality and the second-quality seeds are optimally separated for the values of the eccentricity of the sieves drive mechanism of approximately 10 mm.

References

1. O. Antonescu, P. Antonescu, *Mechanism and Machine Science: Course Book* (Politehnica Press Publishing House, Bucharest, 2016)
2. T. Căsandroi, N. Enescu, Some issues concerning the elastic elements of the separation and transport systems, vibrators used in agricultural machinery. *Constr. Mach.* **35**(7) (1983)
3. V. Chiroiu, T. Sireteanu, *Topics in Applied Mechanics*, vol. 1 (Romanian Academy Publishing House, Bucharest, 2003)
4. V. Chiroiu, T. Sireteanu, *Topics in Applied Mechanics*, vol. 2 (Romanian Academy Publishing House, Bucharest, 2004)
5. D. Dziki, J. Laskowsky, Wheat seeds physical properties and milling process. *Acta Agrophysica* **6**(1), 59–71 (2005)
6. E.E. Ion, G. Gherghe, Vibrations centrifugation of cereal mixtures. *META (Theoretical and Applied Mechanics Magazine)*, 3rd year, number 2, (5), pp. 55–58 (2002). (in Romanian)

7. K.S. Liu, Some factors affecting sieving performance and efficiency. *Powder Technol.* **193**(2009), 208–213 (2009)
8. N.N. Mohsenin, Physical properties of plant and animal materials, vol. 1, in *Structure, Physical Characteristics and Mechanical Properties* (Gordon and Breach Science Publishers, New York, 1970)
9. C. Popa, Researches on the influence of the constructive and functional parameters of the active organs of the equipment used for the cleaning and sorting of seeds on the qualitative working and exploitation indices. PhD. thesis (UASVM, Bucharest, 2004)
10. N. Stendish, The kinematics of batch sieving. *Powder Technol.* **41**, 57–67 (2005)
11. R. Voinea, I. Stroe, M.V. Predoi, *Technical Mechanics* (Politehnica Press Publishing House, Bucharest, 2010)

About the Forces and Moments that Influence the Behavior of a Friction Pendulum



Vasile Iancu and Lenuta Cindea

Abstract The paper presents the geometry of a seismic insulator, the friction pendulum, used in the seismic isolation of a 5 floors apartment building, which also has a technical basement, between the infrastructure and the foundation, where the seismic insulators will be mounted. Being built in the Banat area, the block has been designed with a Class III Reinforced Concrete Structure. It is known that in this area, the earthquakes happen close to the surface and have a magnitude between 3 and 5.7 on the Richter scale. These earthquakes are followed by replicas that extend over the period of several months. As a result of these earth movements, buildings are subjected to certain forces and moments that put them at risk of degradation or even demolition. Considering these inconveniences, we want to improve the dynamic behavior of buildings in the Banat area by decoupling the foundation from the infrastructure. Taking into account the forces and moments acting on it, knowing the value of the ground acceleration for the design, $a_g = 0.20$ g for IMR = 225 years and the value of the control period (corner) $T_C = 0.7$ for Resita, the solution chosen for the isolation of the building against earthquakes was the seismic friction pendulum with a single sliding surface.

1 Introduction

The protection against seismic activities has been a preoccupation since ancient times and is the main objective of seismic engineering. Seismic protection of buildings can be done either by designing the structure so that it has sufficient resistance, by introducing special structural devices into the structure of resistance [1].

The method of isolating the base of the structure involves the interposition between the infrastructure and the superstructure of seismic isolators to decouple the movement of the structure from the ground motion [2]. So during an important seismic event, there is no degradation of the structural and non-structural elements, but this

V. Iancu (✉) · L. Cindea
Eftimie Murgu University, Traian Vuia Square, Resita, Romania
e-mail: v.iancu@uem.ro

method involves a much higher initial cost. Some of the major advantages of the base insulation system are to ensure the continuous operations of the construction and to limit the maintenance works at the level of the seismic insulators [3].

The use of friction pendulum for the seismic isolation of constructions provides greater stability to earthquakes than conventional protective solutions [4]. They have very good performance characteristics compared to other types of seismic insulators, and they have a high fatigue strength and are characterized by slipping combined with the return force.

Due to their rectangular hysteresis loop, which most of these insulators present, it leads to the conclusion that they have a behavior similar to the Columbian-type friction.

2 The Working Model of the Friction Pendulum Isolator

In the paper is presented a block with 5 floors seismically isolated by means of friction pendulums, Fig. 1. The building is supposed to be located in Banat, known as a seismic area with earthquakes of magnitudes between 3 and 5 Richter degrees but not exceeding 5.6° Fig. 2.

In operation, the friction pendulum exhibits a low displacement, and their behavior is characterized by rigidity and strength. As shown in relation (1), the rigidity of the system is totally dependent on axial force G and radius of curvature R .

$$k = \frac{G}{R} \tag{1}$$

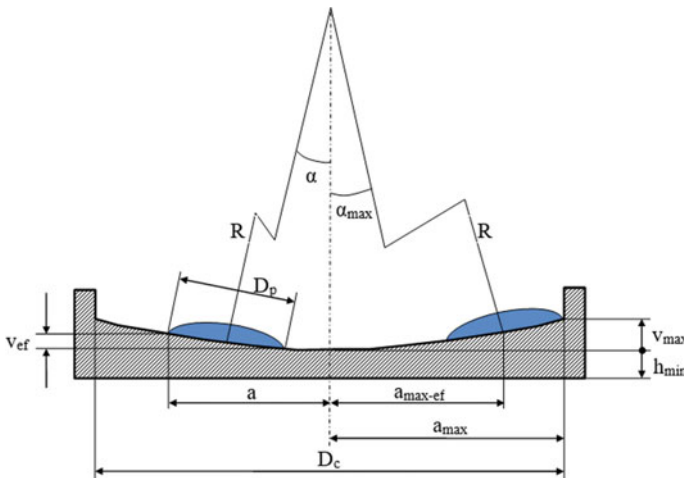


Fig. 1 Geometry and working mode of the friction pendulum

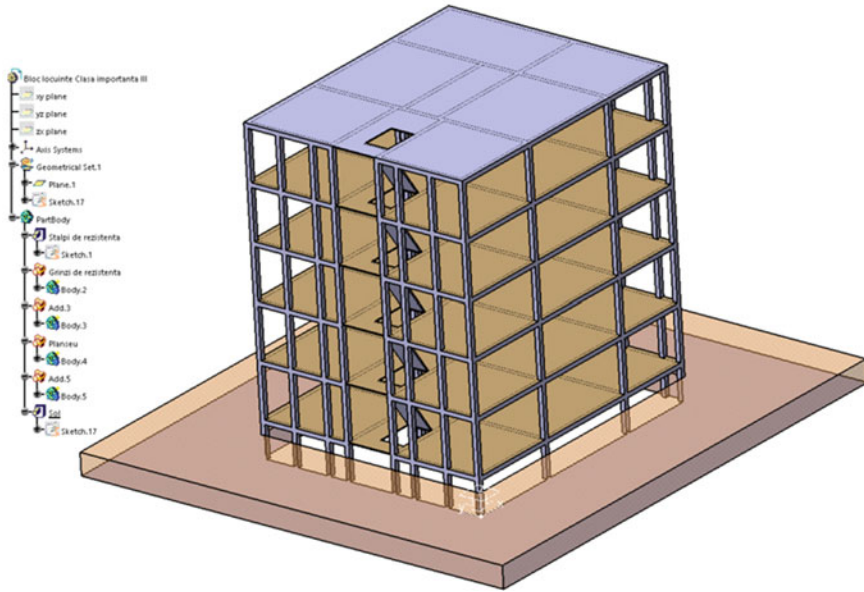


Fig. 2 5-story building isolated with friction pendulums

Designing seismic systems generally involves analyzing how the structure responds to a seismic action, but also defining the system acceleration to determine the period T in which the isolated structure oscillates [5].

The relationship of equivalent stiffness calculation is:

$$T = 2\pi \sqrt{\frac{G}{k_{ech}}} \tag{2}$$

where by the equivalent stiffness results as:

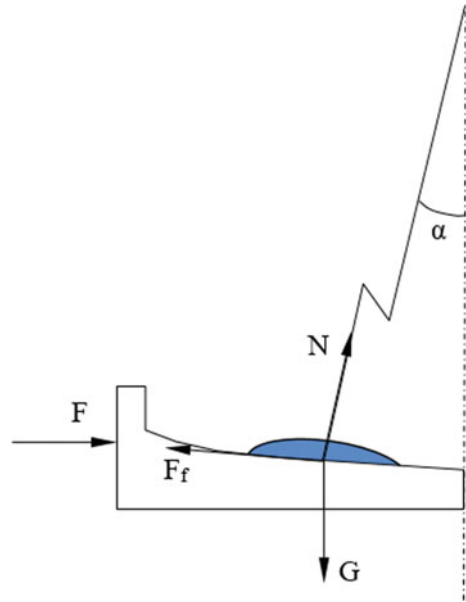
$$k_{ech} = \left(\frac{2\pi}{T}\right)^2 \cdot G \tag{3}$$

The aim of seismic isolators is to increase the flexibility of the base by reducing the acceleration transmitted to the structure by the seismic motion. Thus, if the variation of the forces and displacements acting on the construction compares, it is observed that changing the vibration period to the increase of the movement at the level of the structure base will decrease the forces acting on it [6].

The normal force N , which is composed of the static load G , the acceleration effect \ddot{u} , and the additional seismic load due to the torque M , acts on the sliding surfaces Fig. 3.

Normal force N is given by:

Fig. 3 Friction pendulum resistance to lateral loads



$$N = G \left(1 + \frac{\ddot{u}}{g} + \frac{M}{G} \right) \quad (4)$$

Because the frictional pendulum has no tensile strength and is almost rigid in compression, the response of the building is defined by a loss of energy Fig. 4.

The coefficient of friction has a more pronounced increase as a result of the phenomenon of adhesion between the pivot and the concave surface in the case of the complete absence of an oxide film. It is also affected by the deformation velocity and the relative sliding velocity between the pivot and the concave surface. In conclusion, as the deformation speed increases (i.e., the slip rate), the value of the friction coefficient decreases.

The relationship between force and lateral displacement in the case of a friction seismic system represented by a system of one degree of freedom, having the weight G , will have the form shown in Fig. 5 [7], the characteristics of this system being the force characteristic friction and post-elastic stiffness, k^* thereof.

During the earthquake, due to large deformations, certain elements of the structures may flow, so the hysteresis curve of unloading and recharging differs from the initial loading curve. This effect is due to the plastic behavior of the material, the system being inelastic.

The relationship between static force and displacement in such a system is no longer linear but dependent on the history and direction of loading:

$$F_s = F_s(a, v) \quad (5)$$

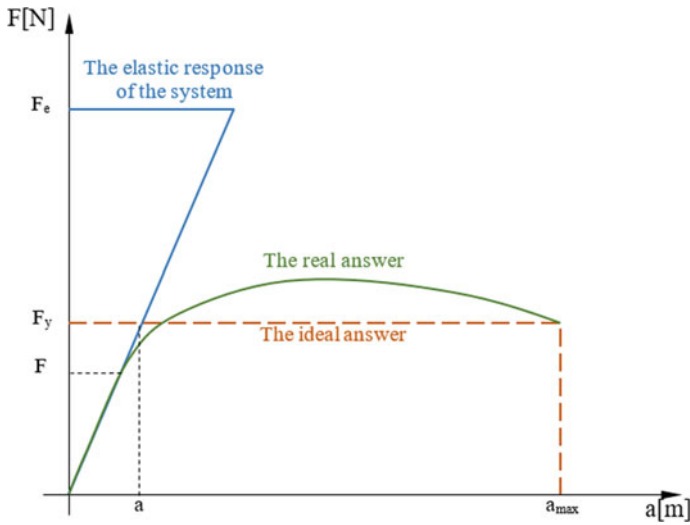
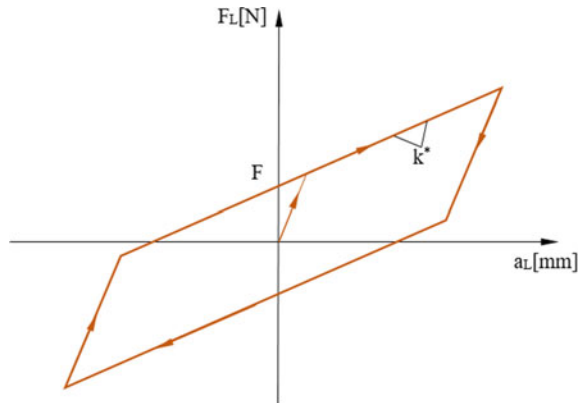


Fig. 4 Structural response of a seismically isolated building

Fig. 5 Ideal correspondence between the force and the displacement



where v represents the system speed.

In the case of friction isolators with large contact surfaces and lack of a lubricating fluid, the friction coefficient depends on the nature of the slip surfaces, the sliding speed, or the pressure exerted by the construction on the slip surface.

The response spectrum for damping greater than 5% shall be achieved by dividing the amortization acceleration with a damping coefficient or a depreciation loss factor B as follows:

$$S_a(T, \beta) = \frac{S_a(T, 5\%)}{B} \tag{6}$$

Table 1 Amortization reduction factor

β [%]	B		
	AASHTO	ASCE 1–10	Eurocod 8
≤ 2	0.8	0.8	0.8
5	1.0	1.0	1.0
10	1.2	1.2	1.2
20	1.5	1.5	1.6
30	1.7	0.7 or 1.8	1.9
40	1.9	1.9 or 2.1	2.1
50	2.0	2.0 or 2.4	2.3

in which: S_a is the spectral acceleration, T the period and β represents the damping factor.

In Table 1, we present the amortization reduction factor values extracted from AASHTO [8], ASCE 1–10 [9] and Eurocode 8 standards.

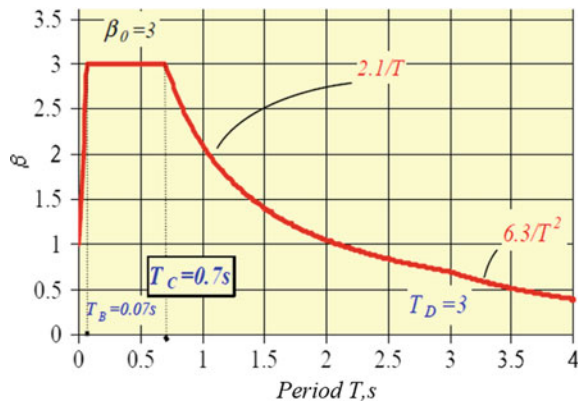
3 The Shape of the Friction Pendulum

Figure 6 shows the normalized elastic response spectrum for the horizontal components of the ground movement in areas where the seismic hazard is characterized by the absolute accelerations $a_g = 0.20$ g and $a_g = 0.16$ g under the seismic and terrain conditions of the Banat Romania region, with $\beta_0 = 3$ for the corner values $T_B = 0.07$ s, $T_C = 0.7$ s and $T_D = 3$ s.

Knowing the important class of the building, its total weight and the behavior factor, using the relation below, we can calculate the cutting forces acting on it:

$$F_t = \gamma_1 \cdot S_d(T_1) \cdot m \cdot \lambda \tag{7}$$

Fig. 6 Crusty sources in the Banat area



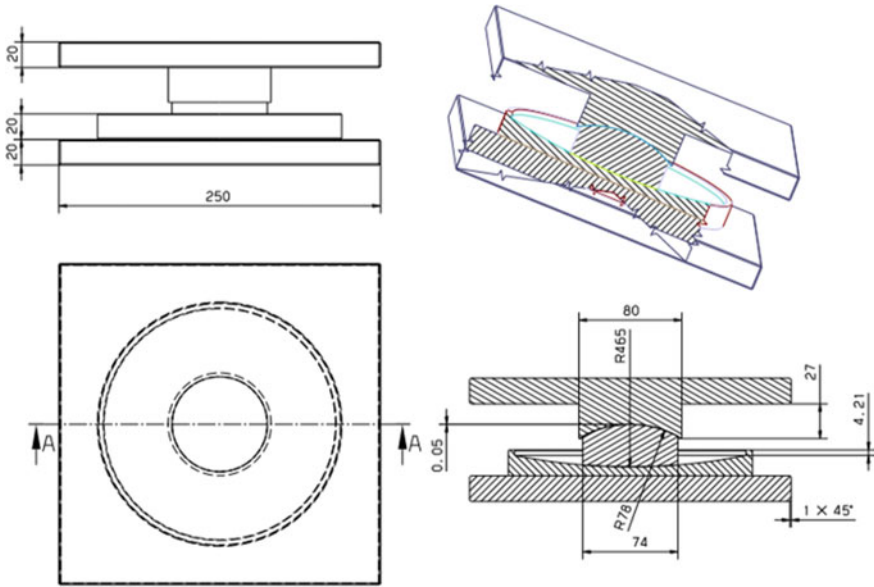


Fig. 7 Friction pendulum used for the earthquake isolation of the building

For the seismic isolation of the building presented in Fig. 2, we use a friction pendulum shown in Fig. 7.

Because the contact surface between the sliding and pivotal concave surface is subject to both frictional and crushing forces, the surface area is given by:

$$A_s = 2 \cdot \pi \cdot R \cdot h_s \tag{8}$$

And the crushing pressure is given by:

$$P_{ef} = \frac{G}{N_s \cdot A_s} \tag{9}$$

N_s the number of the pillars of the buildings.

4 Conclusions

Using the calculation of forces and moments which acts on the friction pendulum, used for the seismic isolation of the building, we reached to the geometry presented in the paper.

The simple friction pendulum presented is the optimal solution from a technological and financial point of view. Friction pendulum is more often used because

he has more strength and resolve much better the static and dynamic loads, than the rubber bearings.

References

1. M. Kumar, A.S. Whittaker, M.C. Constantinou, Characterizing friction in sliding isolation bearings. *Earthquake Eng. Struct. Dyn.* **44**(9), 1409–1425 (2015). <https://doi.org/10.1002/eqe.2524>
2. E. Pavlou, M.C. Constantinou, Response of nonstructural components in structures with damping systems. *J. Struct. Eng.* **132**(7), 1108–1117 (2006)
3. A.K. Chopra, *Dynamics of Structures Theory and Applications to Earthquake Engineering*, 2nd edn. (Prentice Hall, New Jersey, 2001)
4. J.M. Kelly, The role of damping in seismic isolation. *Earthquake Eng. Struct. Dyn.* 3–20 (1999)
5. G.-R. Gillich, A.A. Minda, N. Gillich, C.Ş. Jurcău, C.M. Iavornic, Robust friction pendulum with parameterized sliding surfaces, in *1st International Conference on Sustainable Development, Sustainable Chemical Industry, Pollution, Hazards and Environment*, pp. 13–15 (2012)
6. V.A. Zayas, S.S. Low, S.A. Mahin, A simple pendulum technique for achieving seismic isolation. *Earthquake Spectra* **6**, 317–333 (1990)
7. D. Nedelcu, V. Iancu, G.-R. Gillich, S.L. Bogdan, Study on the effect of the friction coefficient on the response of structures isolated with friction pendulums. *Vibroeng. Procedia* **19**, 6–11 (2018)
8. <https://www.nh.gov/dot/org/projectdevelopment/bridgedesign/documents/webbrmanual.pdf>. Last accessed 2019/05/12
9. <https://www.aisc.org/globalassets/aisc/publications/standards/seismic-provisions-for-structural-steel-buildings-ansi-aisc-341-16.pdf>. Last accessed 2019/05/13

The Influence of the Mesh Element Size on Critical Bending Speeds of a Rotor in the Finite Element Analysis



Ion Crăștiu, Dorin Simoiu, Calin Gozman-Pop, Paul Druța,
and Liviu Bereteu

Abstract All software used in mechanical engineering such as ANSYS, CATIA, SOLIDWORKS, and others contain modules for designing different components, as well as modules for dynamic behavior analysis. Determining the natural modes and the critical bending speeds of a rotor can be quite complicated by an analytical approach, but relatively simple if numerical analysis methods are used. Numerical analysis based on the finite element method (FEM) is the most commonly used in the modal analysis of a mechanical structure. Choosing a larger or smaller mesh size can increase the working time without affecting the accuracy required. In this paper, we are looking at the effect of the dimension of the finite element mesh size on the critical speeds of a rotor. The numerical results obtained by modal analysis are compared with the experimental results obtained by analyzing a vibroacoustic signal given by applying a mechanical impulse.

I. Crăștiu · D. Simoiu · C. Gozman-Pop · P. Druța · L. Bereteu (✉)
Mechanics and Materials Strength Department, Politehnica University of Timișoara, Bd. Mihai
Viteazul, Nr. 1, 300222 Timișoara, Romania
e-mail: liviu.bereteu@upt.ro

I. Crăștiu
e-mail: ion_crastiu@yahoo.com

D. Simoiu
e-mail: dorin.simoiu@upt.ro

C. Gozman-Pop
e-mail: calin.gozman@gmail.com

P. Druța
e-mail: paul.druta@yahoo.com

1 Introduction

At the bottom of the finite element analysis (FEA), the whole system is “fractured” in small parts that are incomparable with the dimensions of the analyzed system. From a mathematical point of view, the behavior of the whole system, i.e., the model response, is considered to be approximated by that of the discrete model obtained by connecting or assembling all elements. These pieces are called finite elements, and according to the FEA theory, the precision of the numerical calculations is all the greater as the dimensions of these elements are smaller, respectively, and the number of the finite elements is larger, but the time allocated to the numerical calculations is increasing.

In [1], static and modal analyses are performed on a rectangular steel plate to discuss the effects of the element size in the analysis of the finite elements. Bending deformation and von Mises stress for each model were calculated and compared, regarding the influence of the element size on the static analysis results. The finite element was used in the paper [2] for a study on the failure by compressing similar concrete geometry columns using different mesh sizes. Deflections and stress analysis of beam on different elements using ANSYS were the purpose of the paper [3]. The need for experimental verification of porous materials for the validation of the biomechanical behavior analysis by numerical calculations for different types, shapes, and dimensions of the finite elements is presented in paper [4]. Other studies show the influence of mesh density on the results of finite element analysis of the mechanical biocompatibility of dental implants [5], respectively, on the sensitivity of structural responses in fracture of coastal impact bones [6]. Some papers are oriented toward the dynamic behavior of mechanical structures, on modal analysis or impact analysis on a rectangular plate [1] as well as the influence of mesh size on the accuracy of the results [7]. The effect of the finite element size on the modal analysis of a heavy machine is analyzed in [8]. In [9], a study is made on finite element analysis of a cracked structure, and in [10], the natural frequency vibrations of a crankshaft of an internal combustion engine are simulated. In this paper, the influence of the mesh size on the natural frequencies, respectively, on the corresponding critical speeds of a rotor-shaft subjected to edge conditions, the simply supported ends, is analyzed.

2 Modal Analysis

Mechanical systems whose behavior is governed by differential equations with partial derivatives, perfect analytical solutions can be determined only if they are defined on a simple geometry. For complex geometries and nonlinear behaviors, approximate analytical methods and numerical methods have been developed. The last category is the FEM method, which consists of the approximation of the complex geometry of the mechanical system in a lot of other geometric entities with simple geometric shapes, called finite elements. The most used finite elements are triangular, tetrahedral, or

hexahedral shapes. For each element, special features are used that interpolate the unknown function. The FEM use procedure involves several steps. First of all, it is intended to generate a discrete representation of the studied object. The mesh generation stage is the most important step in this analysis, affecting the robustness and accuracy of the simulation results. Numerical simulation results are very sensitive to choose the type of material behavior, but also to select appropriate boundary conditions. For each element, a stiffness matrix and a mass matrix are established, and when internal friction is considered, also the damping matrix. At this stage, the choice of interpolation functions, number of elements, and number of nodes per element leads to an increase in the accuracy of the calculation, but also to the time consumption of the computer resources. The stiffness matrices, mass matrices, and damping matrices of the elements are then summed to form the global matrices $[K]$, $[M]$, and $[C]$. In the case of damping neglect, for a dynamic analysis, the integration scheme leads to solving the following system of linear differential equations.

$$[M]\{\ddot{u}\} + [K]\{u\} = \{0\}, \quad (1)$$

where $\{u\}$ are nodal displacements. The vibrations of the nodes can be expressed by harmonic functions such as:

$$\{u\}_i = \{U\}_i \cos(p_i t + \varphi_i), \quad (2)$$

where $\{U\}_i$ are the eigenvectors and p_i are corresponding circular frequencies. From these values, the natural frequencies, respectively, and the critical speeds are determined. The eigenvalues problem leads to solve the determinant:

$$|[K] - p^2[M]| = 0. \quad (3)$$

3 Numerical Results

The shapes of natural modes of vibration and natural frequencies of a rotor considered as a disk centered on a shaft were determined using the software provided by ANSYS 14.5. For the 3D modeling of the shaft and the rotor, the geometry of a solid element called SOLID 186, which is defined by 20 nodes, each having three degrees of freedom representing displacements in three perpendicular directions, was chosen.

This type of finite element exhibits square displacement behavior. To solve the eigenvalues problem, given by (3), the block Lanczos method is used because it is efficient to extract a large number of modes in most cases. The shape of the first bending vibration mode in the OXY plane is shown in Fig. 1, and the shape of the first bending vibration mode in the OXZ plane is shown in Fig. 2.

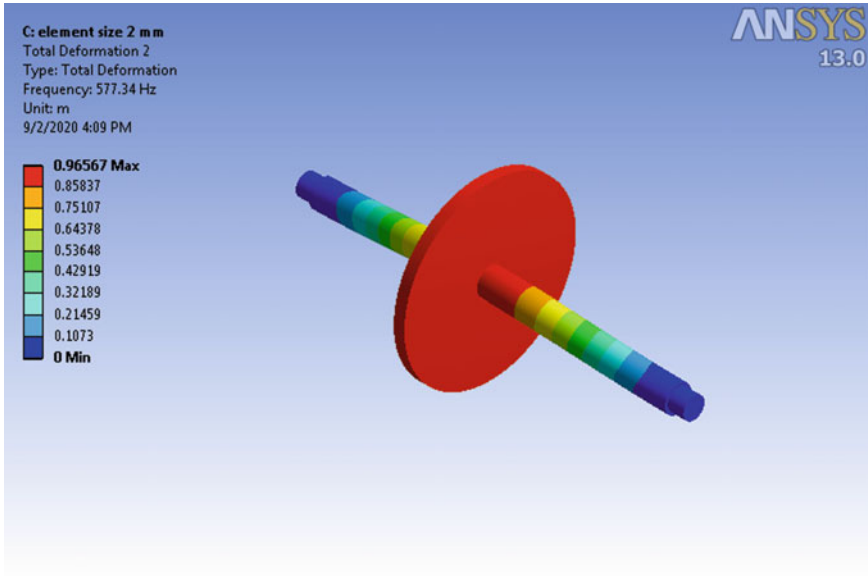


Fig. 1 First mode shape in OXY plane for a simple supported disk

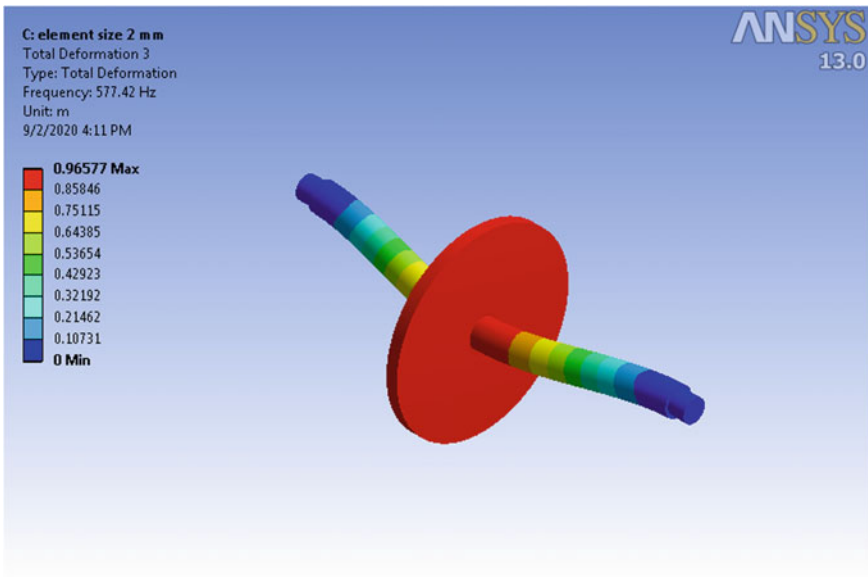


Fig. 2 First mode shape in OXZ plane for a simple supported disk

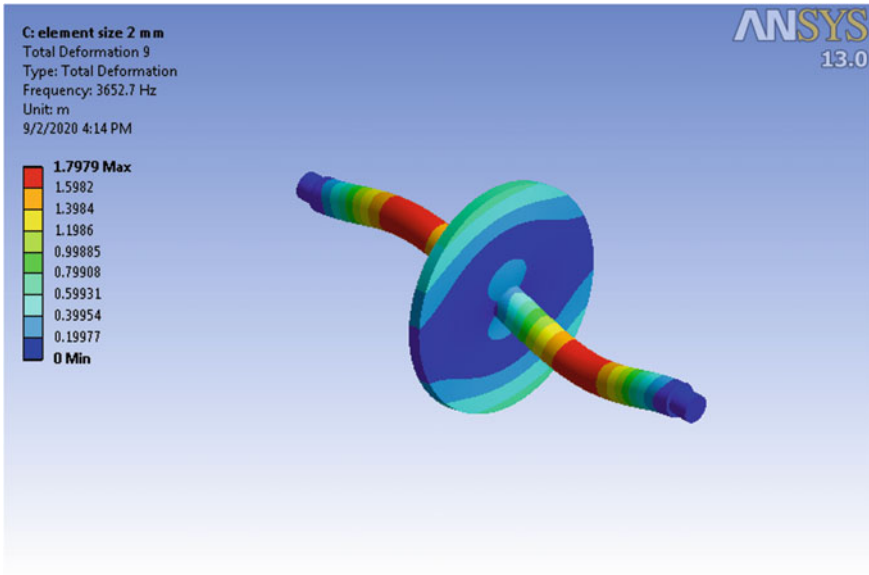


Fig. 3 Fourth mode shape in OXY plane for a simple supported disk

The shape of the fourth bending vibration mode of the rotor-shaft in the OXY plane is shown in Fig. 3, and the shape of the fourth bending vibration mode in the OXZ plane is shown in Fig. 4. For the numerical analysis, both the shaft and the rotor made of the same standard steel material with the elastic modulus $E = 200$ GPa, the density $\rho = 7850$ kg/m³ and the Poisson coefficient $\mu = 0.3$, were considered. Four cases corresponding to the 2, 3, 4, and 5 mm sizes of the finite element were analyzed.

Although the design of the rotor–shaft assembly taken up for meshing in ANSYS is perfectly symmetrical, however, in modal analysis, due to the size and the way the mesh is made, this assembly is treated as unsymmetrical and therefore will present vibration modes both in the OXY plane and in the OXZ plan.

Table 1 shows the number of elements, the number of nodes, the frequencies of the first four vibration modes corresponding to the 2, 3, 4, and 5 mm sizes, and mesh sizes that were used in the numerical simulation.

In many practical modal analysis applications, just a few of natural modes are of interest. One of the most common applications is to determine the critical speeds of the rotors. And in this case, it is enough to analyze just a few of natural modes. In this paper, only the first four natural modes are proposed. The effect of the mesh size on natural frequencies and therefore on critical speeds can be traced on the basis of the data presented in Table 1. At the same time, a suggestive view can be obtained graphically representing the variation of natural frequencies according to mesh size, so also as a function of the number of finite elements. This is shown in Figs. 5 and 6.

Table 1 Sizes of mesh elements and four natural frequencies of rotor–shaft

No. mode	Plane motion	Element size	Element size	Element size	Element size
		2 mm	3 mm	4 mm	5 mm
		Nodes 62119	Nodes 26179	Nodes 14103	Nodes 8074
		Elements 35116	Elements 14454	Elements 7548	Elements 4133
		Frequency [Hz]	Frequency [Hz]	Frequency [Hz]	Frequency [Hz]
1	OXY	577.34	579.83	581.85	583.4
1	OXZ	577.42	580.43	582.22	584.24
2	OXY	1128.7	1136.6	1140.1	1146.0
2	OXZ	1129.2	1137.6	1141.4	1147.5
3	OXY	2524.2	2530.3	2534.4	2540.7
3	OXZ	2524.2	2530.7	2535.6	2541.5
4	OXY	3652.7	3673.2	3688.3	3703.4
4	OXZ	3653.4	3676.2	3691.4	3708.6

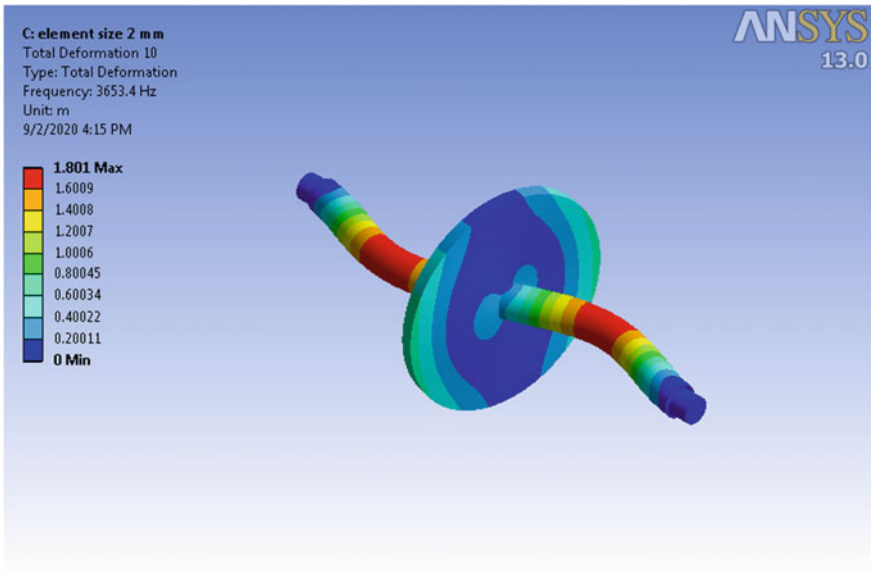


Fig. 4 Fourth mode shape in OXZ plane for a simple supported disk

By analyzing the frequencies of the first vibration mode for the largest number of nodes, i.e., for 2 mm elements, the deviation between the natural frequencies corresponding to the motion in the two planes, OXY and OXZ, is less than 0.014%. By doing the same, if the largest dimension of the element was chosen at 5 mm, the

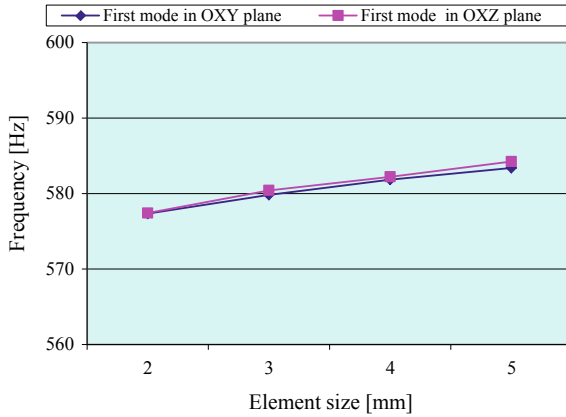


Fig. 5 Frequency variation of the first vibration mode in the two planes as a function of the size mesh

deviation between the two natural frequencies is 0.14%. Even if between the two situations, the deviations are in the second case 10 times higher than in the first case, in absolute values they are insignificant.

Now, if the natural frequencies corresponding to the fourth vibration mode are compared, for the largest number of nodes, i.e., with finite elements of 2 mm, it is found that between the frequencies of the movements in the two planes is a deviation of 0.019%. For the fourth natural mode way of vibration, it can be seen that between frequencies obtained for the greatest number of nodes and frequencies obtained for the smallest number of nodes is a percentage deviation of 1.5% (Fig. 6).

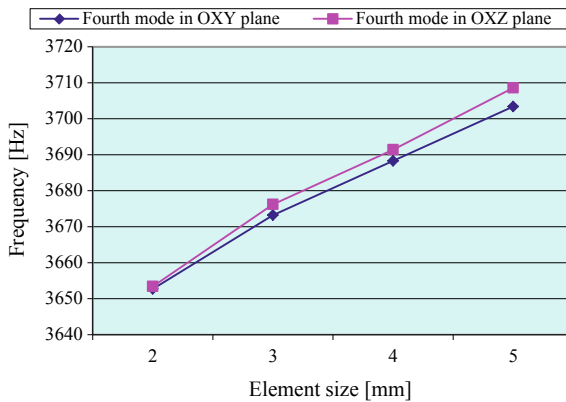


Fig. 6 Frequency variation of the fourth vibration mode in the two planes as a function of the size mesh

4 Experimental Results

The experimental model for recording a vibroacoustic signal is shown in Fig. 7.

The experimental stand, the impulser (consisting of a steel ball having a diameter of 15 mm, mounted in a flexible polymer rod with a length of 120 mm), the placement of the sensor, and the mechanical pulse application were made according to ASTM standard [11]. The sample consists of a shaft having a center disk **1**.

The considered mechanical system is placed on two supports of the mechanical structure constituting the experimental setup **2**. The signal is obtained by a mechanical pulse applied by means of a mini-hammer **3** having a steel ball at one end, and the handle is made of a plastic material. The signal is taken over by an acoustic sensor **4** which is actually a condenser microphone. This measurement system has the advantage of eliminating the contact between the probe and the sensor. The analog signal is picked up via a computer acquisition board **5**. This experimental stand was designed and used for other works [12–14], obtaining much better results than if a piezoelectric accelerometer had been used as a sensor.

The mass of the disk and of the axel has been measured by a precision digital balance which is accurate to one-hundredth of a gram. Average after six weighing, for the disk was $m = 800.333$ g, and $m_s = \rho AL = 700, 231$ g, for the shaft. The material was stainless steel with density $\rho_1 = 7850$ kg/m³.

To determine the critical speeds of the rotor–shaft a specialized, fast Fourier transform [15], software is required. Several signals have been acquired producing mechanical impulses so the displacement is possible in the OXY plane or in the OXZ plane.

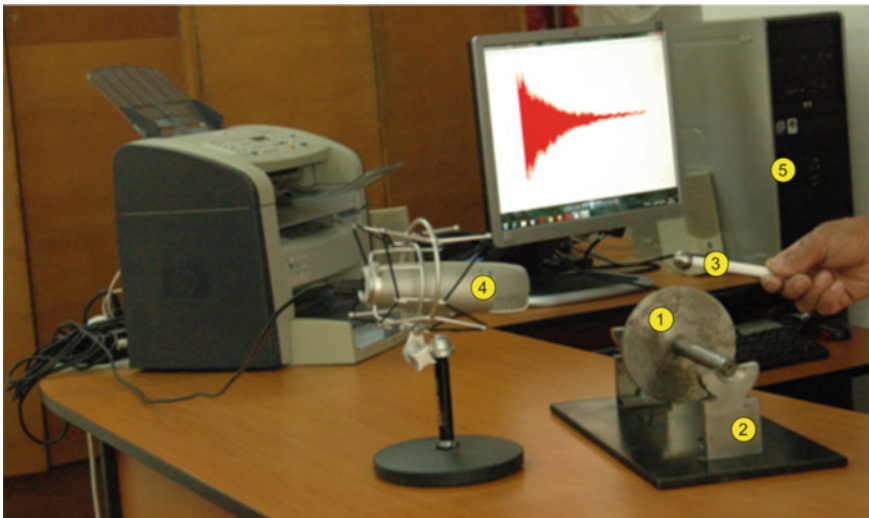
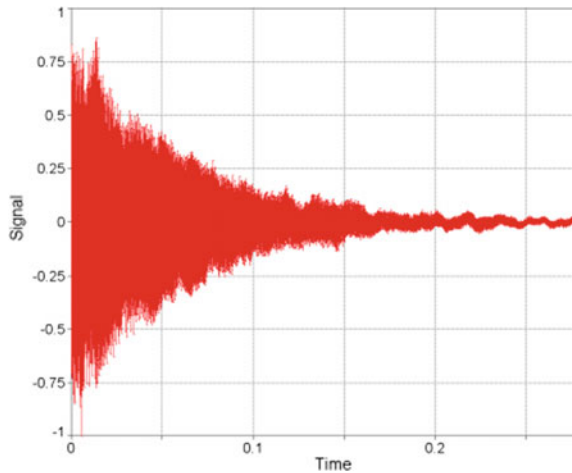


Fig. 7 Experimental stand

Table 2 Four natural frequencies of the rotor–shaft in two planes

No. mode	Four natural frequencies in OXY plane [Hz]	Critical speeds in OXY plane [rpm]	Four natural frequencies in OXZ plane [Hz]	Critical speeds in OXZ plane [rpm]
1	594.51	35,670.6	595.42	35,725.2
2	1152.3	69.138	1155.2	69.312
3	2551.7	153.102	2553.3	153.198
4	3723.4	223.404	3723.7	223.422

Fig. 8 Vibroacoustical signal in OXY plane



The read results were recorded, and the test was repeated 6 times, giving readings that are below 1% difference between each. The average of these values was used to determine natural frequencies. The results obtained from the all signals after their processing, as an average value, are given in Table 2.

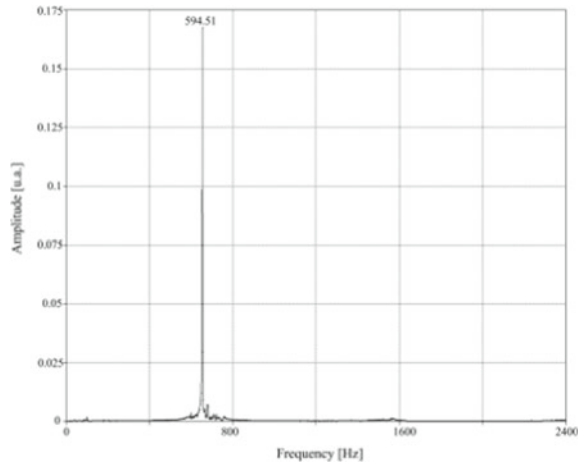
One of the countless recorded vibroacoustic signals is shown in Fig. 8. Each signal was filtered so as to remain a single component in the spectrum.

Fig. 9 showed the Fourier spectrum of a filtered signal for which the “passage” was possible around one of the natural frequencies known on the basis of numerical analysis. In this way, the frequencies of the “parasitic” sound introduced by the mini-hammer were also eliminated.

5 Conclusions

By analyzing how the rotor’s natural frequencies, i.e., the critical speeds, depending on the size of the mesh change, some conclusions can be done. First of all, the frequencies of the same vibration mode, so also the critical speeds, increase with the increase of the mesh size. Second, it can be seen that the effect of mesh size

Fig. 9 First mode frequency of the spectrum



is more pronounced in higher frequency modes. By comparing the experimentally natural frequencies, by FFT analysis obtained, of a vibroacoustic signal given by a mechanical impulse, it is found that they are higher than those obtained numerically. This is due to the fact that the rotor is placed on two supports in the experimental stand, which leads to an increase in the rigidity of the system. Another important conclusion to be drawn from this analysis is the fact that in the design and dynamic analysis of some rotors that have high-speed operating regimes, it is absolutely necessary to analyze with great accuracy, which implies a large number of elements, even if time increases. Safety in system operation is more important.

Very small differences are found between experimental results for the determination of the first natural frequency and the corresponding frequency determined by numeric method using modal analysis. The close results of the critical speed obtained from the numerical analysis of those obtained from the experimental determinations validate this method. From a practical point of view, it is interesting only the case for the shaft with simple support ends.

The results obtained by using FEM modal analysis in two planes are very close to those obtained by the measurements of the fundamental frequencies, that validates the proposed method. Also, small differences between values of critical speed obtained in numerical simulation and those obtained by experimental results come to reinforce the validity of this method.

References

1. Y. Liu, G. Glass, Effect of mesh density on finite element analysis, in *SAE International, Technical paper*, pp. 1–7 (2013)
2. M. Brocca, Z.P. Bazant, Size effect in concrete columns finite element analysis with microplane model. *J. Struct. Eng.* **127**(12), 1382–1390 (2001)

3. V. Debnath, B. Debnath, Deflection and stress analysis of beam on different elements using ansys APDL. *IJMET* **5**, 70–79 (2011)
4. G. Rotta, T. Sermak, On the necessity of experimental verification of numerical results in biomedical applications, in *Proceedings of Nineteenth National Conference Applications of Mathematics in Biology and Medicine*, Jastrzebia Gora, Poland, 16–20 September (2013), pp. 78–83
5. J. Zmudzki, W. Walke, W. Chadek, Influence of model discretization density in FEM numerical analysis on the determination stress level in bone surrounding dental implants. *Inform. Technol. Biomed.* **47**, 559–567 (2008)
6. Z. Li, M.W. Kinding, D. Subit, R.W. Kent, Influence of mesh density, cortical thickness and material properties on human rib fracture prediction. *Med. Eng. Phys.* **32**(9), 998–1008 (2010)
7. S. Roth, J. Oudry, M. El Rich, H. Shakourzadeh, Influence of mesh density on a finite element model under dynamic response loading. *J. Biol. Phys. Chem.* **9**(4), 203–209 (2009)
8. J. Wang, B. Song, J. Chen, T. Guo, D. Guo, Element size effect on the analysis of heavy-duty machine cross-rail, in *4th International Conference on Machinery, Materials and Computing Technology* (2016), pp. 964–970
9. J.R. Chaudhari, C.R. Patil, Study of Static and Modal Analysis of Un-Crack and Crack Cantilever Beam using FEA. *Int. J. Eng. Res. Technol.* **5**(4), 534–542 (2016)
10. P. Magryta, K. Pietrykowski, K. Skiba, FEM simulation research of natural frequency vibration of crankshaft from internal combustion engine, in *ITM Web of Conferences* vol. 15, Lublin, Poland (2017), pp 1–6
11. ASTM E 1876-01, Standard test method for dynamic young’s modulus, shear modulus, and poisson’s ratio by impulse excitation of vibration (2001)
12. O. Suciu, L. Bereteu, G. Draganescu, T. Ioanovici, Determination of the elastic modulus of hydroxiapatite doped with magnesium through nondestructive testing, in *Advanced Materials Research*, vol. 814 (Timisoara, Romania, 2013), pp. 115–122
13. O. Suciu, T. Ioanovici, L. Bereteu, Mechanical properties of hydroxyapatite doped with magnesium, used in bone implants, in *Acoustics and Vibration of Mechanical Structures*, vol. 430 (Timisoara, Romania, 2013), pp. 222–229
14. O. Suciu, L. Bereteu, G. Draganescu, Determination of mechanical properties of hydroxyapatite doped with magnesium, in *AIP Conference Proceedings, 12th TIM Physics Conference of the West-University-of-Timisoara, Romania*, vol. 1564 (2013), pp. 132–137
15. Autosignal Homepage. <http://www.sigmaplot.co.uk/downloads/trial/autosignal-trial.php>. Last accessed 2019/05/9